LEVEL II ③

Princeton University

JUN 1 6 1980

DTIC

Department of Mechanical and Aerospace Engineering

80 6 6 10 8

NITRAMINE MONOPROPELLANT DEFLAGRATION

AND

GENERAL NONSTEADY REACTING ROCKET CHAMBER FLOWS

TECHNICAL REPORT TO THE

OFFICE OF NAVAL RESEARCH

Submitted by

Moshe BenReuven and Leonard H. Caveny

DTIC
ELECTE
JUN 1 6 1980
C

January 1980

MAE Report No. 1455

Department of Mechanical and Aerospace Engineering
PRINCETON UNIVERSITY
Princeton, New Jersey 08544

Acknowledgments

ABSTRACT

A theoretical investigation is presented, concerning the deflagration of cyclic nitramines (RDX, HMX), which emerged recently as highly-energetic components in solid propellant formulations for rocket motors.

The first part of this study involves a steady state deflagration analysis of these monopropellants. This serves as a necessary preliminary step in the elucidation of the rather complex deflagration mechanism of these compounds within a propellant matrix.

Following the selection of a plausible chemical mechanism model from the published literature, an asymptotic theory is advanced for the gaseous deflagration wave, derived from the large difference between the chemical relaxation scales associated with the two overall reactions under consideration. These point to the plausibility of distinct near field and (much wider) far field regions in the gas phase, obtaining a singular, boundary layer type problem. This line of reasoning has led to the derivation of a unique burning rate formula, showing increasing pressure dependence as pressure becomes higher, in agreement with experimental observations. The analysis demonstrates the primary importance of the near field, through which heat feedback to the propellant surface is controlled, and the relative importance of the far field processes in determining the overall pressure dependence.

Further investigation of the near field processes is carried out through the formulation and subsequent numerical solution of a detailed nonlinear deflagration model, incorporating a reacting liquid phase. Calculations were performed with available thermophysical and kinetics data pertaining to RDX, throughout this study. Beside the details of the deflagration wave structure, solutions yield the linear pressure dependence of the flame speed eigenvalue, in agreement with the asymptotic theory predictions, and a quantitative measure for the role of subsurface exothermicity in determining the deflagration rate; within the pressure range below 4 MPa, this influence remains below 10%. The nonlinear model can serve as an analytical tool, by which various relevant chemical mechanisms and kinetics may be tested for adequacy.

The analysis in the second part is aimed at the behavior of nitramine-like propellants within an interior burning propellant grain. This was prompted by the notion of thick overall gaseous flame zone associated with nitramine compounds at pressures up to 5 MPa (at least), pointed out in the first part of this study.

First, the stationary behavior is analyzed, within a quasi one dimensional model of the viscous sublayer, where most of the gaseous reactions are carried out. This model is a simplified version of the lowest (zeroth) order formulation obtained in the aforementioned asymptotic analysis. Two necessary thermodynamic conditions are postulated, for coupling between the turbulent axial coreflow and the wall layer. A unique solution for the perturbed (or erosive) burning rate, as well as the extent of incomplete secondary reaction in the layer is obtained, through a perturbed expression for the deflagration rate eigenvalue. Actual calculations (with RDX data) reveal a progressive dependence of the perturbed burning rate upon the mean coreflow mass flux, G, and the existence of a critical G (threshold), below which coupling between the coreflow and the wall layer is suppressed. The retarding effects of

pressure increase and scale-up of interior port diameter are likewise shown. Amplification of far field signals is demonstrated, as relatively small deviations from fully-burnt state at the wall layer edge are associated with appreciable burning rate perturbations.

The above analysis indicates that residual exothermic reaction (with extent variable along the port) may be carried out in the core, due to incomplete wall layer reaction at the perturbed state. The final part of this analytical study addresses the problem of dynamic coupling between the axial acoustic field and the pressure-sensitive residual reaction in the core. A comparison of chemical relaxation (secondary reaction) and fluid-dynamic timescales indicates possible areas of Rayleigh-type coupling, in terms of the extent of residual reaction in the core, pressure and interior grain geometry. In a numerical solution of the time dependent, one dimensional core flowfield, along with a quasi-steady (instantaneously responding) wall layer, such dynamic coupling has indeed been demonstrated, in the form of spontaneous evolution of acoustic oscillations. [A spectral error analysis of the Rubin-Burstein finite difference algorithm employed tends to eliminate the time marching procedure as possible cause for these oscillations]. In case of vanishing core - wall layer interaction, such acoustic instability does not evolve. The intensity of turbulence heat feedback to the wall layer and the extent of secondary reaction fuel/oxidizer nonstoichiometry have a strong effect upon dynamic coupling in this form. The effects of mean pressure level and overall kinetics constant magnitude (for the residual reaction) were shown to be two-fold: on one hand, their increase tends to retard core - wall layer coupling; on the other, it enhances core exothermicity, and hence the possibility of Rayleigh-type coupling with the acoustic field.

This analysis points to the existence of an additional component to acoustic instability, namely, heat addition by residual reaction in the core; unlike nonsteady mass addition, however, this phenomenon must be studied within the realm of the particular chamber environment in consideration, as it combines propellant properties with the flow field configuration at any given point in space and time. It is directly associated with propellants having distended gaseous flame zones, which may lead to residual exothermicity in the main chamber flow.

TABLE OF CONTENTS

NOMENCLATURE

$A(x)$ = cross sectional area of propellant port, Chap. VIII, m^2

$\hat{A}$ = acoustic admittance for burning propellant, Chap. VII

A_1, A_2 = prefactor, Arrhenius kinetics constant for primary decomposition (1/s) and secondary reaction (m^3/mol-s) respectively

$A_{m,1}$ = prefactor, nitramine decomposition in the liquid phase, 1/s

a = adiabatic speed of sound, Chap. VIII, m/s

a_x = $d[\ln(A)]/dx$, chamber area cross sectional variation parameter

B = global (mass or heat) transfer number, Eq.(VI. 9). Also, Courant-Friedrichs-Lewy number, Chap. VIII

B^* = specific turbulence transfer number (between coreflow and wall layer), Eq.(VI. 40)

B_1, B_2 = quantities used in determination of relationship between spatial and timewise discretization, Chap. IV

B_p = pressure-reference parameter in asymptotic burning rate formula, Eq.(III. 19b), MPa

$B_{i,k}$ = Shvab-Zel'dovich coupling coefficients in the far field, Eqs. (VI. 28a,b)

b = nonstoichiometric fuel excess expressed in terms of mass fractions, Eq.(VIII. 11)

$C(y)$ = diagonal convective term tensor, Eq.(IV. 13); its nonsteady counterpart in Chap. IV is $\tilde{C}(t,y)$

CC_j = discretized cross correlation, Eq.(IX. 1)

C_f = dimensionless friction coefficient for blown wall layer, Eq.(VI. 8)

C_H = Stanton number for blown wall layer, Eq.(VI. 36)

C_p, C_c = specific heats for gas mixture (isobaric) and for condensed phase respectively, J/kg-K

C_v = isochoric specific heat for gas mixture, J/kg-K

$C_{i,P}$ = Shvab-Zel'dovich coupling coefficients in the near field, Eqs. (VI. 20a,b)

D = diffusion coefficient, gas mixture, m^2/s

D^*_{ss} = spurious diffusion term, due to generalized implicit finite differencing, Chap. IV

d = internal port diameter, cylindrical solid propellant cavity, m

d_F = nonstoichiometric fuel excess, expressed in terms of coupling coefficients, Eq.(IX. 4)

E_1, E_2 = Activation energy, primary decomposition and secondary reactions respectively, kcal/mol

E_B = normalized perturbed (erosive) burning rate parameter, Eq.(VI. 55)

E_{ml} = activation energy, liquid phase decomposition, kcal/mol

$e^{(h)}$ = residual in iterative procedure for nonlinear deflagration problem, Eq.(IV. 82)

F, f_i = forcing term vector and component respectively, in conservation equations

'F'   = fuel species (e.g., HCHO), far field or coreflow analyses

$G(y)$ = diagonal diffusivities tensor, Eq.(IV. 11); its nonsteady counterpart in Chap. IV is $\widetilde{G}(t,y)$

$G(x)$ = mean axial mass flux along chamber port, kg/m^2-s

g_c = normalized condensed phase exothermicity measure, Eq.(V. 7)

g_F, g_O = weighting constants in the definition of mean far field reactant concentrations, Eq.(VIII. 10)

g_R = heat release due to primary reaction in the far field, Eq.(III. 42)

h^*, h_T = specific thermal enthalpy, J/kg

I_{sp} = specific impulse of rocket motor, sec

K_f = number of spatial mesh divisions per unit near field length scale, Eq.(IV. 52)

K_T = thermal amplification factor, Eq.(VIII. 12b)

k = wave number in numerical coreflow analysis, Chap. VIII and App. G, 1/m

k_1, k_2 = kinetic constants, primary decomposition (1/s) and secondary reaction (m^3/mol-s) respectively

L = total chamber (coreflow control volume) length, m

Le   = Lewis number

M = Mach number

m, m_p = mass burning rate or mass flux perpendicular to propellant surface, kg/m^2-s

$\dot{m}_R$ = nitramine species mass flux at gas side of propellant surface, kg/m^2-s

N = total number of chemical species

NF = total number of interior spacewise meshpoints in finite difference analysis

n = burning rate pressure exponent

$\underset{\sim}{0}$ = null vector

'O' = oxidizer species (e.g., ONO) in far field and coreflow analyses

O( ) = Landau notation: the term referred to is, in absolute, at most a constant multiple of the quantity in parantheses

p = pressure, MPa (1 Mega Pascal = 10.013 atm)

P_{eq} = equivalent pressure, used in the definition of the perturbed wall layer eigenvalue, Eq.(VI. 52b), MPa

Pr = Prandtl number

Q = standard heat of reaction, J/mol (non SI units: kcal/mol)

Q^* = specific heat of reaction, Q/W, J/kg

$\dot{Q}_{inj}$ = mass injection heat loss to the coreflow, J/m^3-s

$\dot{Q}_R$ = heat release by chemical reaction in the coreflow, J/m^3-s

Q_s, Q_s^* = overall surface heat release (or depletion), J/kg

q_c = liquid side of the gas-liquid heat flux balance, Eq.(IV. 35b), J/m^2-s

q_{fb} = heat feedback from coreflow to the wall layer (turbulence transport), J/m^2-s

q_g = conductive heat feedback to propellant surface (gas side), J/m^2-s

R( ) = nitramine reactant in chemical mechanism: (g)vapor, and (liq)liquid phase

Re = Reynolds number

R_u = universal gas constant, 1.987 cal/mol-K; in equations of state, SI units

r = linear regression rate of burning propellant, m/s

Sc = Schmidt number

S_i = chemical species, in schematic reaction mechanism

s = specific entropy, J/kg-K

T = temperature, K

T_0 = ambient solid phase temperature, K

t = time, sec

t^* = chracteristic time scale, sec

t_D^* = diffusional time scale in the gas phase, Eq.(III. 5a), sec

t_P^* = diffusional time scale in the condensed phase, Eq.(VIII. 1), sec

t_{R1}^*, t_{R2}^* = reactive time scales for primary and secondary reactions respectively (gas phase), sec

$U(y)$ = dependent variable vector, Eq.(IV. 12); its nonsteady form in Chap. IV is $\tilde{U}(t,y)$

$U_0(x)$ = centerline velocity in the motor port, Chap. VI only, m/s

$U(x,t)$ = finite difference approximation of the dependent variable vector, Chap. VIII

$u(\ )$ = dependent variable vector. Also, gas velocity, m/s : perpendicular to propellant surface (Chaps. I-V) and parallel (axial), Chaps. VI-IX

u_{ms} = mean molecular velocity perpendicular to the surface, Eq.(IV. 78), m/s

u = frictional velocity, defined by the shear stress at the wall, m/s

V, V_n^j = finite difference approximation to nonsteady dependent variable vector, Chap. IV

$v(\ )$ = dimensionless dependent variable vector in finite difference algorithm, Chap. IV

v_s = gas velocity normal to surface at condensed-gas interface, m/s

$W_i, \bar{W}$ = molecular weight of species i and mean molecular weight of gas mixture, kg/mol

W_R = molecular weight of nitramine, kg/mol

w^* = tangential velocity scale for calculation of viscous sublayer thickness, Eq.(VI. 6)

$w_{k,i}$ = specific reaction rate k for species i, kg/m^3-s

$w_i(x,t)$ = generalized advective terms for coreflow formulation in conservation form, Chap. VIII

X_{CH} = chemical relaxation length scale, along chamber axis, Chap. VIII, m

x_n^j = spatial finite difference operator, generalized implicit algorithm, Eq.(IV. 47)

X_R = nitramine molar fraction

x = axial coordinate, coreflow

Y_i = mass fraction of species i

Y_F, Y_O = mass fraction of fuel and oxidizer species in secondary reaction

Y_R = nitramine mass fraction

y = flame zone coordinate, perpendicular to propellant surface

Y_1 = viscous sublayer thickness, Chap. VI

$Z_{F,i}$ = Coupling parameter for chemical species in the coreflow, Eq.(VIII.44)

z_n^j = right hand side of the generalized implicit discretization operator, Eq.(IV. 47)

GREEK ALPHABET

α_C = condensed phase thermal diffusivity, m^2/s

α_K = Knudsen accommodation coefficient, Eq.(IV. 77)

$\alpha_{k,i}$ = $W_i(\nu'' - \nu')_{k,i}/\bar{W}$, stoichiometric coefficient of species i in reaction number k

β = dimensionless viscous sublayer transfer number, Eq.(VI. 5)

β_1, β_2 = dimensionless activation energies, primary decomposition and secondary reaction respectively

γ = Cp/Cv, ratio of specific heats

Δ = difference, increment or decrement, for parameter following the symbol

$\Delta H_{f,i}^0$ = standard enthalpy of formation for species i, J/mol

Δh_D = heat flux defect at gas-liquid interface, due to liquid phase exothermicity, Eq.(V. 7), J/m^2-s

Δt = dimensional timestep in numerical integration

$\Delta \tilde{t}$ = $\Delta t/t_D^*$, dimensionless timestep in numerical solution, Chap. IV

Δx = dimensional space increment, coreflow numerical analysis, Chap. VIII

Δy = dimensional space increment, nonlinear deflagration numerical analysis, Eq.(IV. 52)

$\Delta \sigma$ = dimensionless specific entropy, Chap. VI

$\delta( )$ = variational operator: small increment of the parameter following the symbol

δ^* = length scale in flame field analysis

δ_D^* = diffusive length scale, gas phase: ratio of diffusivity to mass flux

δ_{Rk}^* = chemical relaxation length scales for primary decomposition (k = 1) and secondary reaction (k = 2)

δ_{RW} = chemical relaxation length scale in viscous sublayer (secondary reaction), Chap. VI

ε = small perturbation quantity, $0 < \varepsilon \ll 1$, Eq.(III. 30)

ε_t = dimensionless small quantity defining convergence to steady state of numerical integration, Eq.(IV. 65)

ε_R = normalized sublayer reactedness parameter (equivalently, normalized cutoff enthalpy), Eq.(VI. 35)

ε_T = turbulence diffusivity, Eq.(VI. 15a)

ζ = dimensionless near field coordinate

η = dimensionless viscous sublayer coordinate, section VI.B only

η_i = normalized mass fraction of species i

$\theta(\zeta, \varepsilon)$ = dimensionless near field enthalpy, Chap. III

θ = dimensionless temperature, Chap. V

θ' = generalized-implicit parameter, $0 < \theta' < 1$, numerical analysis, Chap.IV

θ_{fb} = normalized heat feedback to wall layer, Eq.(VI. 41)

Λ = flame speed eigenvalue, Eq.(III. 29)

λ = thermal conductivity, J/m-K-s

λ_{max} = maximal eigenvalue of advective coefficient matrix C, Chap. VIII only

μ = viscosity, kg/m-s

ν = kinematic viscosity = μ/ρ

$\nu_{i,k}$ = stoichiometric coefficient for reactant i in reaction k : ( )' denotes reactant and ( )'' denotes product

ξ = alternative dimensionless viscous sublayer coordinate, Eq.(VI. 15b)

π = $\pi_1 + \varepsilon\pi_2 + \ldots$ normalized pressure: asymptotic expansion, Chap.III

ρ = density, kg/m^3

σ_p = temperature sensitivity of the burning rate, Eq.(V. 17)

τ = h_T/Q_1^*, dimensionless thermal enthalpy

τ_w = frictional shear sterss at wall (with mass injection), Chap. VI

ϕ = p/B_p, normalized pressure, Eq.(III. 19) only

ϕ = u/u , normalized tangential velocity, viscous sublayer analysis, section VI.B only

ϕ_T, ϕ_i = overall dimensionless flux (convection and diffusion), for enthalpy and chemical species i, respectively

ψ = dimensionless form of liquid side of the heat flux balance at the gas-liquid interface, Eq.(V. 2)

Ω = frequency, cps

ω_k = overall reaction rate for primary decomposition (k = 1) and secondary reaction (k = 2), mol/m^3-s

ω_k^* = $\bar{W}$, overall reaction rate, kg/m^3-s

SUBSCRIPTS

a   = acoustic

CH   = chemical relaxation

C or COR   = core flowfield properties

c   = condensed phase property

D   = diffusional or molecular transport property

eq   = equivalent

f   = final flame position, where adiabatic flame temperature is attained

fb   = feedback (turbulence transport) from coreflow to wall layer

g   = gas phase property

i = integer denoting chemical species or vector component

k = integer denoting reaction number ($k = 1$ for primary decomposition and $k = 2$ for secondary reaction). Also, secondary reactants 'F' and 'O', Chap. VI

L = wall layer, Chap. VI

liq = liquid phase property

m = melting point in Chaps. I-V. Also, mean properties, Chaps. VI-IX

max = maximal

n = space mesh number in finite difference algorithm: $x_n = n\Delta x$

NR = nonreacting (condensed phase)

pert = perturbed (gaseous flame zone, burning rate), due to turbulence interference

RC = reacting (exothermic condensed phase)

ref = reference value

s = propellant surface: gas-solid or gas-liquid interface

ss = steady state

sub = sublimation

stg = stagnation

v = evaporation

0 = zeroth order term in asymptotic analysis of Chap. III. Also, initial conditions, Chap. IV-IX

SUPERSCRIPTS

(h),(k) = iteration level number, or harmonics serial number

j = timestep index, finite difference approximation, $t^j = j\Delta t$

0 = unperturbed, normal steady state property. Also, zeroth order property, Chap. III only

$\overline{(\ )}$ = (overbar), mean value, except in section VI.C.2, where it denotes far field properties

$(\ )^*$ = specific or characteristic property (dimensional, except for mass fractions, Y_i)

$\tilde{(\ )}$ = dimensionless or normalized quantity

CHAPTER I

INTRODUCTION

A. Cyclic Nitramine Deflagration at Steady State

Nitramine compounds like RDX and HMX were conceived originally as secondary explosives, due to their high energy content and relative stability. The chemical composition of RDX and HMX can be expressed by

$$N:O:H:C = a_1:a_2:a_3:a_4 = 2:2:2:1$$

containing almost stoichiometric proportions of oxygen and fuel material, as shown by the ratio,

$$(O)/[\ 0.5(H)\ +\ 2(C)\ ] = a_2/[0.5a_3 + 2a_4] = 2/3$$

(slightly fuel-rich), where final combustion products H_2O, CO_2 and N_2 were considered. Nitramines are known to deflagrate stably at pressures within the rocket operating regime, 1-10 MPa. These properties have led to a relatively new application for RDX and HMX, in solid propellant rocket motors. Relative to composite (inorganic oxidizer with plastic binder) or double base (nitrocellulose with nitroglycerin) propellants, RDX and HMX burn relatively slowly at low pressures and exhibit a rather high pressure sensitivity. Experimental evidence points to an increasing pressure exponent over a wide range of pressures, from 0.5 at low pressures, to 1.0 at high pressures. Further, high speed shadowgraphs taken during deflagration indicate extended heat release by exothermic reactions in the plume of strand-burning HMX samples (at 2.1 MPa), appreciably different from parrallel plume observations made with ammonium perchlorate (AP), where the extent of such heat release seems negligible in comparison.

Additionally, scanning electron micrographs of the deflagrating surface of RDX and HMX reveal the existence of a melt layer, at pressures within the rocket operating regime; the entrapped bubbles observed indicate the plausibility of subsurface decomposition under these conditions (liquid phase decomposition is also known to occur with AP).

These observations point to a possibly complex self-deflagration behavior, with a mechanism and structure which may differ from that of AP deflagration, at least with respect to the gas phase processes. The deflagration problem is further compounded when RDX and HMX are utilized in a granular bed, or in a propellant matrix requiring granular nitramine with various additives, (e.g., inert hydrocarbon binder), where the burning rate pressure exponent becomes discontinuous (upward shifts to values appreciably larger than 1.0) at pressures between 15-35 MPa.

An understanding of self deflagration of RDX and HMX is essential prior to any attempt to elucidate the inherently more complex propellant matrix combustion. This provides the motivation for the first part of the present study, being an analysis of nitramine monopropellant deflagration at steady state. The objectives for this part are as follows:

1. A rational theory of self deflagration, expressed in a mathematical model. The model would incorporate the gaseous flame zone and the condensed phase, with the associated physical and thermochemical processes.

2. An algorithm for solution of the deflagration model, in order to obtain qualitative insight as well as quantitative data regarding primarily the flame structure, the condensed phase processes and the overall pressure dependent behavior.

The corresponding subjects are covered in Chapters III through IV; they are preceded by the literature survey in Chapter II, which also serves as a source for the chemical mechanism employed and for the thermophysical and chemical kinetic properties.

The present analysis utilizes available experimental data regarding the chemical decomposition mechanism, its kinetics, and various thermophysical constants as essential input. This is opposed to certain analyses which employ observable deflagration behavior in order to calculate some of the afore-mentioned parameters, e.g., using the experimental burning rate pressure exponent to define the order of the apparent overall gas phase reaction. Indeed such practice can be justified only in certain limited cases, such as gaseous deflagration with simple reactant mixtures, but not over the entire class of solid propellant flames, involving quite complex chemical mechanisms. In other words, the physics of propellant deflagration do not guarantee the validity of a single overall chemical reaction under all pressures; in the same vein, based on comparable observed deflagration rates vs. pressure, one may not deduce that AP deflagration models should intrinsically apply to nitramine as well, with a mere change of input parameters.

To conclude, an enhanced complexity can be expected in the deflagration process of nitramines relative to that of AP, (in the gaseous flame zone particularly) which justifies a detailed investigation and a new approach, not limited to a single overall gaseous reaction term. Fortunately, the rapid advent of both applied mathematics (small perturbations) and numerical methods for differential equations in the last 15 years, make such analyses feasible.

B. Reacting, Nonsteady Rocket Chamber Flows

The first part of this study prompts extension of the investigation to the rocket chamber environment. This task is undertaken in the second part herein, including Chapters VI through IX. Considering propellants which exhibit relatively long, premixed gaseous flame zones within the rocket operation pressure regime, the following questions are addressed.

1. Stationary Interactions

Within a prismatic, longitudinal propellant grain cavity, what would be the physical interactions between the main axial gas stream (termed core flow) and the intensive gaseous flame region near the propellant surface. A comparison of blown, viscous sublayer thickness and the pertinent chemical reaction length scales shows that reactants may be swept into the core flow under favorable conditions (e.g., port diameter, axial position along cavity and pressure), with a certain extent of residual reaction in the core permitted. Therefore, since gases in the core are closer in the mean to the

fully reacted state than those at the outer edge of the viscous wall layer, a driving enthalpy potential arises, by which heat may be fed back to the reacting wall layer, through turbulence transport. This can cause effective perturbation of the gaseous flame region adjacent to the propellant surface (namely, a departure from the normal stationary deflagration mode, analysed in the first part of the study), leading to burning rate modification.

The physical interaction, resulting in a novel concept of enhanced burning in rocket motors employing propellants which have long, premixed gaseous reaction zones, is the subject of Chapter VI. The analysis is motivated by the well-known property of double base propellants to exhibit extended reaction well beyond the wall layer region in certain low pressure motor configurations, their susceptibility to erosive burning (typical to "low burning rate" propellants) and the mounting evidence that nitramines with plastic binders behave in a similar way. Modeling is done by use of the formulation developed for nitramines in the first part of the study, assuming certain analogy with double base propellants regarding the flame structure.

2. Dynamic Interactions

A direct outcome of exothermic, pressure-sensitive reactions in the core flow field is the possible modification of the dynamic core flow response. Most previous analyses of dynamic stability of solid propellant motors (acoustic or nonlinear) avoid this problem by addressing AP-propellant configurations, assuming short or collapsed gaseous flame zones. Thus, the core is considered an inert wave carrying medium; dynamic interaction is centered upon the propellant boundary, where nonsteady mass feeding, resulting from time-like relaxation of the condensed phase thermal wave, is coupled with pressure (and recently, velocity) fluctuations in the core flow field.

The question here is, what would be the effect of core reactions upon the dynamic stability of the motor configuration, considering small amplitudes. The particular coupling between chemical reactions in the core and (stationary) erosive burning within the present framework, leads to an added dimension to the propellant chamber dynamics: the history of the flow field must now be also considered. In other words, determination of the propellant admittance or burning rate response functions outside of the specific chamber environment cannot yield the sufficient input to the stability analysis.

This problem is investigated in Chapters VII through IX. A quasi one dimensional core flow model is formulated and solved numerically. The insights obtained may contribute toward the understanding of low amplitude, high frequency instabilities observed with double base propellants, bearing a striking resemblence to recent observations with nitramine propellants.

CHAPTER II

THE PROPERTIES OF CYCLIC NITRAMINES:
A LITERATURE SURVEY

A. Introduction

This chapter serves two major purposes in the present study. First, to introduce the properties of nitramines and provide details of the chemical mechanism involved in their decomposition. Second, to obtain a background for the overall deflagration characteristics of these substances. This is done through a review of published works. Particularly, in the first instance, the literature will serve as a source from which an idealized chemical mechanism is developed for subsequent nitramine deflagration analysis in the following chapters.

The plan or presentation herein is as follows. Molecular structure and thermophysical properties are given in Section B. Chemical decomposition mechanism and kinetics are reviewed in Section C. The chemical decomposition model is shown in Section D, and Section E contains the review on nitramine deflagration properties.

B. Structure and Thermophysical Properties

1. Molecular Structure

Cyclic nitramines are non-polymeric, molecular substances which may form crystals. In general, their chemical formula is

$$[-CH_2-N(NO_2)-]_i$$
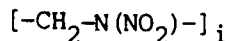
where i has integral values. In the present chapter, as well as in the remainder of this study, only properties of the cyclic nitramines 1, 3, 5 trinitrohexahydro-1, 3, 5 triazine (RDX, with i = 3) and 1, 3, 5, 7 tetranitro-1, 3, 5, 7 tetraazacyclooctane (HMX, where i = 4) shall be of interest. The structure and a representative conformations of these two substances are shown in Figs. II.1 and II.2, schematically.

Molecular conformations and associated bond energies of RDX were reported by Orloff, Muellen and Rauch[1] utilizing ultra-violet absorption spectra measurements in a molecular orbital study of the electronic structure. Of the four apparent conformations considered, three are of the chair type, observed experimentally in RDX crystals, with varying degrees of molecular symmetry (concerning the NO_2 groups) and one is a boat conformer. One of these chair conformers, shown in Fig. II.1 with the NO_2 groups in equatorial positions was considered most favorable in that its ground state energy lies lowest and it offers symmetry about 3 major axes. It has been concluded that different chair-type conformation most probably correspond to liquid and vapor states on one hand (with free molecule and high degree of internal symmetry) and to crystal on the other, as packing forces would interfere in the latter state. The authors[1] also report the various bond energies associated with the RDX molecular structure; these were mostly estimated by extrapolation (using electron overlap population data) and are summarized as follows:

CALCULATED RDX BOND ENERGIES:
N-C   80 kcal/mol
N-N   66 kcal/mol

Unfortunately, there are no analytical means by which to correlate these energies with actual activation energies in the process of decomposition.

The molecular structure of RDX was also investigated by Harris,[2] using X-ray diffraction.

2. The Crystalline Polymorphs of HMX

HMX in the solid state exhibits four distinct crystalline polymorphs, designated alpha, beta, gamma and delta. This is in contrast to RDX, having only a single observed crystalline form. The polymorphs of HMX were first described by McCrone[3] in 1942. In a more recent study utilizing hot stage microscopy, Teetsov and McCrone[4] reported the transition temperatures between the various conformations. The beta polymorph is the one stable at room temperature, up to 388.5 K where beta to alpha transition occurs; the beta to delta transition evolves at 439 K. The delta state is the most stable between 439 K and its melting point, at 554.5 K. Within the entire temperature range from ambient to melting, the gamma polymorph is unstable at ordinary pressures. The melting points of the other three pure crystalline polymorphs were also measured: 520 K, 530 K and 553 K for beta, alpha, and gamma HMX respectively. In comparision, the melting point of RDX is 478.5 K, measured by Hall.[5] The effect of thermal decomposition of HMX upon the above experimental results was assumed negligible, as good reproducibility was obtained over a wide range of heating times.

Maycock and Verneker,[6] in a study of HMX decomposition by thermogravimetric (TGA) and differential thermal analysis (DTA), suggested that transition from beta-HMX to delta-HMX is irreversible, as their delta-HMX samples, (obtained by heating from the beta polymorph) remained stable for more than 24 hours at room temperature after cooling. Further, the transition temperature from beta-HMX to delta-HMX was found to depend upon the heating rate: 458 K at 2 K/min and 473 K at 15 K/min.

The molecular structure of HMX in its four polymorphs was studied by Cady, Larson and Cromer,[7] who summarized the available X-ray diffraction data concerning the heavy atom positions. The structure of beta-HMX, the polymorph stable at room temperature, was reinvestigated by Choi and Boutin,[8] utilizing neutron diffraction techniques which enable the determination of the H-atom positions; three dimensional models of the beta-HMX molecule were built in this laboratory using their data.

Relative stability of HMX and RDX crystals was investigated by Belyayeva et al,[9] in a study utilizing rates and extents of decomposition below the melting points, as well as X-ray diffraction data. The range of temperatures considered for HMX was above 453 K , which is higher than the alpha-delta transition point[3,4,7] so that delta-HMX was probably involved. The article consistently refers to alpha-HMX as the stable polymorph above 453 K, which disagrees with the designation common to western literature (i.e., delta-HMX). These authors conclude[9] that HMX is more stable than RDX in the condensed phase, and attribute the difference in stability principally to differences in

the intermolecular distances between C---O atoms in the crystal lattice; they report a distance of 3.21 A for RDX and 3.01-3.12 A for HMX, resulting in a contribution of 7 kcal/mol to the intermolecular interaction energy for RDX and presumably a greater addition to HMX (the potential energy well becomes deeper as the C---O distance decreases). Overall, molecular potential interaction energies of 27 and 35 kcal/mol were calculated for RDX and HMX respectively, explaining the observed difference in stability of the crystals. The observations regarding the C---O atomic distance in HMX crystals tend to be corroborated by the values reported earlier by Cady et al[7] and by Choi and Boutin[8] for beta-HMX, reporting intermolecular distances less than 3.20 A between heavy atoms (3.02 A for C---O) and less than 2.60 A between H and heavy atoms.

Thermophysical properties of RDX and HMX are summarized in Table II.1, along with the literature sources.

3. Sublimation, Vaporization and Melting

Vapor pressure as function of temperature below the melting point and heats of sublimation were reported by Edwards[10] for RDX, by Rosen and Dickinson[11] for RDX and beta-HMX, and by Taylor and Crookes[12] for delta-HMX. The results in all cases were correlated by the logarithmic vapor pressure (p_v) equation,

$$\log_{10}(p_v) = A - B/T$$

where A = const relates (p_v, T) at some reference point, $B = Q_{sub}/2.3 R_u$, and Q_{sub} is the molar latent heat of sublimation. The results of all three works were summarized by Taylor and Crookes[12] and are given in Table II.2. Rosen and Dickinson[11] attribute the difference in their calculated molar heat of sublimation data, Q_{sub}(beta-HMX) $-Q_{sub}$(RDX) = 10.78 kcal/mol to the molecular weight difference, as indeed the resulting specific heats of sublimation for RDX and beta-HMX, 140.0 and 141.5 kcal/g respectively, are remarkably close. Considering the crystalline stability argument of Belyayeva et al,[9] based on intermolecular attraction dominated by the C---O proximity, it seems now more appropriate to assign this interaction an energy value closer to 10 kcal/mole, as possible explanation of the molar sublimation enthalpy difference between RDX and beta-HMX; note that[11] Q_{sub}(RDX)/3 = 10.37 kcal/mol, while Q_{sub}(beta-HMX)/4 = 10.47 kcal/mol, in support of the above line of reasoning. The small difference in interaction energies per C---O set might result from the small differences in the C---O distances for beta-HMX and RDX, observed earlier.

A somewhat large difference can be observed, cf. Table II.2, comparing the Q_{sub}(RDX) of Rosen and Dickinson[11] and of Edwards,[10] being 31.11 and 26.8 kcal/mol respectively. The former (and more recent) data seems to be more commonly accepted with the differences possibly emanating from the different experimental methods. A hypothetical small amount of gas phase decomposition, more pronounced in the experiments of Edwards[10] (due to the higher temperature range) must be ruled out as possible explanation; it can be shown to produce a trend opposite to the one observed, namely both higher A and Q_{sub}.

The relatively small difference in the HMX sublimation enthalpy data of Rosen and Dickinson[11] and of Taylor and Crookes,[12] being 3.89 to 2.59 kcal/mol is attributed in the latter work to the differences in the polymorphs

investigated, beta-HMX and delta-HMX respectively. This is verified by the results of Hall[5], in a DSC study of decomposition and phase transitions of various secondary explosives. The values reported[5] for solid-solid transition energies of HMX are approximately 1.9 kcal/mol for alpha to delta and 2.35 kcal/mol for beta to delta transitions.

The heat of fusion, Q_m, measured by Hall[5] for RDX is 8.5 kcal/mol. Similar measurements were not reported for HMX since it tends to decompose at temperatures below its melting point, at the heating rates utilized for thermal analysis (90 K/min is a high rate in common DSC devices) and the size of the melting endotherm is found to depend upon the heating rate, as will be discussed later. A first estimate of the molar heat of fusion for delta-HMX can be obtained from $(4/3)Q_{m,RDX} = 11.4$ kcal/mol, based on the foregoing crystalline intermolecular attraction arguments.

In conclusion, an important difference is observed between RDX and HMX: the latter melts with decomposition at moderate heating rates, to the extent that the decomposition exotherm obscures the melting endotherm, and its fusion enthalpy cannot be measured by conventional means; RDX under the same heating rates does not exhibit significant condensed phase reactions for $T @< T_m$.

C. The Chemical Mechanism and Kinetics of Thermal Decomposition of RDX and HMX

Melting of HMX is accompanied by decomposition at moderate heating rates, as mentioned in the foregoing section. When heated at a slow enough rate, both RDX and HMX are observed to decompose in the condensed phase at temperatures below their respective melting points. An appreciable acceleration of the rate of thermal decomposition is observed upon liquefaction, achieved even below the melting point due to interaction of RDX and HMX with initial decomposition products. Sublimation and evaporation of these compounds at temperatures below and above the melting point facilitates decomposition in the vapor phase, simultaneously with the condensed phase reaction; the vapor phase reaction is approximately 10 times faster than the condensed phase reaction at $T < T_m$.

The majority of the experimental studies of the decomposition process reviewed herein were performed at moderate heating rates and temperatures, and under relatively low pressures (up to 1 atm). These studies are divided into two categories, according to the temperature regime: $T > T_m$ in Section C.1 and $T < T_m$ in C.2. Investigations performed in temperature and pressure ranges corresponding to deflagration are treated separately in Section C.3, followed by a discussion of decomposition properties which concludes this section.

1. Studies of Thermal Decomposition Above the Melting Point

The decomposition kinetics of RDX and HMX were investigated by Robertson[13] at temperatures above the melting point using a manometric method (pressure rise in reaction vessel as function of time, with temperature as parameter). For RDX, decomposition of the pure substance as well as dilute solutions (2, 5, and 20%) in ester and TNT were tested, showing overall first order kinetics. Several of the gaseous product concentrations were measured, and the Arrhenius rate constants calculated; for pure RDX, $\log_{10}(k) = 18.5 - 47.5/2.3R_uT$, while for the RDX in TNT solution, $\log_{10}(k) = 15.55 - 41.5/2.3R_uT$. The rate in dilute solution was found lower than for pure RDX in the temperature range tested. The chemical mechanism suggested involves initially the transfer of

the O atom from a nitramino group to a neighboring carbon, forming an oxadiazole intermediate which breaks up subsequently to form CH_2O, N_2O and other products. The differences between pure and dilute solution decomposition was attributed to a short thermal chain reaction, effectively inhibited in the solution. A similar mechanism was assumed to prevail for HMX, but only the pure substance was tested. HMX was found to decompose vigorously upon liquefaction, somewhat below the melting point where an accelerative reaction was identified, much slower than the ensuing first order decomposition. The kinetic rate constant calculated for the latter is $\log_{10}(k) = 19.7 - 52.7/2.3R_uT$. All the kinetic data are summarized in Table II.3, along with the associated temperature range.

Rauch and Fanelli[14] investigated RDX decomposition at temperatures above the melting point, in the range 480 K – 500 K. Small samples were tested in initially evacuated glass vessels, using a manometric method. Concentration of gaseous decomposition products was measured, and the effects of reactor volume $(26 - 300 \ cm^3)$ and initial sample weight estimated. Concentration – time profiles of N_2O, CO_2 and NO_2 were reported; the NO_2 species was not reported in other studies, and despite its relatively low concentration, was found highly significant: NO_2 showed progressive dependence upon reactor volume, exhibited typical peaks not observed with N_2O and CO_2, and (on a per mole decomposed basis) was independent of the initial RDX sample weight. These strongly indicate a gas phase decomposition in which NO_2 is produced at the initial stage and then depleted. On the other hand, within the experimental error, the measured decomposition rates were found virtually independent of the reaction vessel volume. The authors concluded therefore that within the temperature range tested, decomposition proceeds simultaneously in the gas and the liquid phase, that the extent of gas phase reaction is relatively small due to the low RDX vapor pressure, and that the rate measured pertains to the liquid phase decomposition. The kinetic data was found to follow overall unimolecular first order and the kinetic constant calculated is shown to be in good agreement with that of Robertson[13] for pure RDX, cf. Table II.3. Different mechanisms were assumed to prevail in the liquid and in the gas phase. For the gas, the initial step proposed involves homolytic N–N bond rupture, producing NO_2 and other products; for the liquid, the authors cite the oxadiazole mechanism suggested by Robertson.[13]

Rogers and Smith[15] investigated the kinetics of RDX decomposition in the liquid state utilizing a method for determining the kinetic rate constant and overall reaction order from DSC data, where the order of reaction, s, is not necessarily unity. Prescribing s = 1, the Arrhenius parameters were in good agreement with those obtained by Robertson,[13] (who assumed first order kinetics). However, the calculated order (average) for RDX was 1.3, indicating a degree of complexity in the reaction, in which case the average (A,E) were both appreciably higher than the data of Robertson, cf. Table II.3. As the method is capable of calculating E at any point along the decomposition curve of a single DSC run, (for an assumed s), the authors concluded it was adequate for study of complex reactions exhibiting autocatalysis (E decrease) or inhibition (E increase), both of which seemed to occur in RDX decomposition. This particular method was not pursued in subsequent publications by Rogers[16,17] concerning RDX and HMX, where overall first order kinetics were considered.

HMX decomposition in the liquid phase, in the range of temperatures 554–558 K was investigated by Rogers,[16] utilizing DSC in isothermal mode. To

avoid the complexity of the induction and accelerative reaction periods, only the receding portions of the DSC decomposition-time curves were considered, corresponding to homogeneous liquid phase reaction at the maximal rate. Good correlation with first order kinetics was obtained, and the Arrhenius parameters are in excellent agreement with the data of Robertson.[13] The method is therefore particularly adequate for compounds melting with decomposition, exhibiting sigmoid (S-shaped) decomposition-time curves.

The kinetics of RDX decomposition in the temperature range 505-520K was further investigated by Rogers and Daub[17], using DSC in the isothermal mode described earlier.[16]

HMX was included in the study as well, but reported with lesser detail. This work is unique in its attempt to define the kinetics constants of vapor phase decomposition from composite DSC plots, despite the relatively small fraction of material decomposed in the gas. Simultaneous liquid and gas phase decomposition was detected, as the shape of the decomposition rate curves was found to depend upon sample cell volume and total cell-perforation area (the latter used for pressure equilibration). The vapor pressure, constant at a given temperature as long as a liquid exists, was determined at the instant the last liquid disappeared, by integration of the decomposition curves. From these data a clausius-Clapeyron plot was made for RDX, obtaining the heat of vaporization; a least-squares fit of the data, made in this study, yields Q_{vap} = 20.28 kcal/mol, smaller by 2.3 kcal/mol than the value obtained from the combined results of Rosen and Dickinson[11] and Hall,[5] cf. Table II.1. The resulting evaporation law parameters are given in Table II.2. The receding portion of the decomposition rate vs. time curves, used to determine the order and the rate of the reaction in the liquid and the gas, consist of two parts: a relatively long exotherm, corresponding to liquid phase reaction, followed (after a small transition interval) by a much shorter and somewhat steeper tail-off, corresponding to pure gas phase decomposition after the disappearance of the last liquid. Both reactions were shown to be very closely of first order overall for RDX; orders of 0.84 and 0.94 were found for the liquid and the gas respectively. For HMX the picture is more complex: 97% was found decomposed with an apparent order of 0.6, indicating a complex condensed phase reaction, while the remainder followed an order of 0.9, attributed to the gas. Arrhenius plots for the gas show distinctly more data scatter than the order plots from a single DSC run, particularly for HMX.

In the way of critique, it should be pointed out that the DSC apparatus is designed primarily for testing liquids or solids as heat conduction through the cell bottom facilitates reliable thermal measurement. Heat release from the gas phase reaction might not be measured with confidence due to convective losses through the cell top, thermal gradients in the gas (occupying more than 80% of the cell volume) and uncertainty in the initial equilibrium concentration of reactant, due to vaporization retarded by the presence of product gases. To these difficulties one may add the relatively small amounts reacting in the gas (less than 2.5% for RDX at the maximal temperature), which implies that the maximal deflection of the DSC exotherm was calibrated for the larger heat release from the liquid. To the extent of describing an initial intramolecular first order process, such as anticipated for the gas phase decomposition of RDX, the dilute solution phase decomposition data of Robertson[13] would seem relevant for comparison with the vapor phase data of Rogers and Daub [17] unfortunately, the Arrhenius parameters are far from agreement. The reported[17] gas phase kinetic data for RDX and HMX are given in

Table II.3. For the liquid phase decomposition of RDX, (A , E) were lower than those obtained by Robertson[13] for the pure liquid: differences of 100 1/s in A and 3 kcal/mol in E are observed. In a later note, Rogers[18] modified these values by subtracting the effect of the gaseous reaction from the overall decomposition curve and obtaining the rate for liquid decomposition alone; the corrected liquid RDX data is in very good agreement with the data of Robertson,[13] cf. Table II.3. Finally, regarding HMX, the liquid phase kinetic data of Robertson and the gas phase data of Rogers and Daub[17] are in excellent agreement.

2. Studies of Thermal Decomposition Below The Melting Point

Suryanarayana and co-workers at Picatinny Arsenal[19] published an isotope study of HMX decomposition. Using ^{15}N as tracer, 99% of which was shown to be located in the nitramino groups, the products of decomposition were measured at 230 C, 254 C and 285 C by mass spectrometry. These temperatures cover a range below and slightly above the melting point (281 C), where delta-HMX is the stable polymorph. Thus, the results pertain to condensed phase decomposition; HMX was found to decompose vigorously in the solid state before melting, as temperatures were raised above 200 C. The most important observation made was that nitrous oxide, formed in relatively large quantities (40% of total moles produced) was determined to consist mostly of the isotopic form $N^{15}NO$. The authors concluded, therefore, that the mechanism of thermal decomposition in the condensed phase involves rupture of the C-N bond, rather than that of the N-N bond (despite the much lower energy of the latter); this behavior was attributed to stabilization of the N-N bond by resonance of the NO_2-groups, following observations by Cady et al[7] that the N-N distance in the crystal was shorter than that of a single free standing N-N bond. A concerted intramolecular mechanism of decomposition was proposed as follows:

$$(II.1)$$
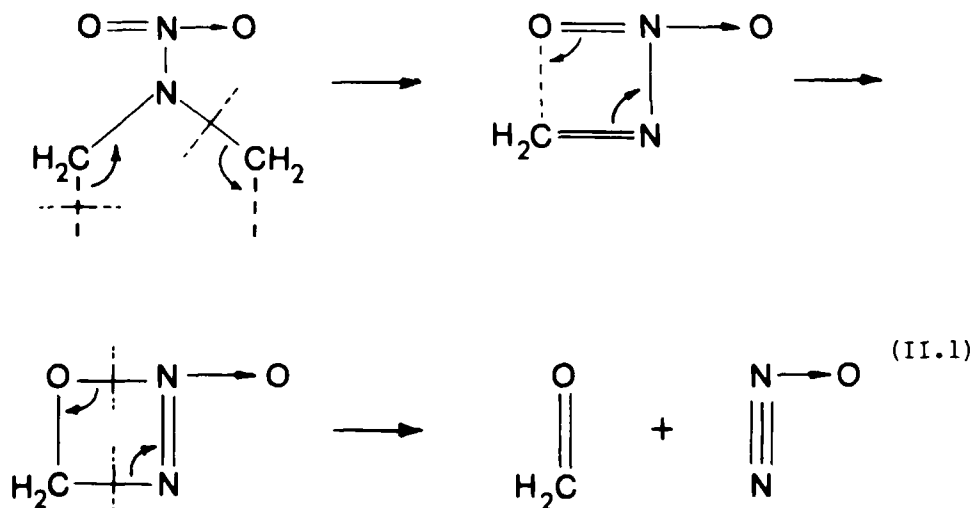
McCarty[20] has proposed three different intermediate-mechanisms of similar form, which to various degrees intend to improve the original scheme[19] in terms of observed molecular orbital symmetry, and better fitting of observed final decomposition products.

In contrast to the behavior of HMX described above, Cosgrove and Owen[21] reported that RDX tends to decompose mainly in the vapor phase at 195 C (below its melting point, at 205.5 C) with insignificant decomposition in the condensed phase under these conditions. The rate was found proportional to the reactor vessel volume (hence reaction in the gas phase), independent of initial sample weight (indicating an overall unimolecular process) and appreciably retarded when the reaction vessel was pre-pressurized by N_2, indicating influence of RDX vapor pressure, since N_2 would retard diffusion away from the surface. These conclusions were substantiated in two additional publications,[22,23] discussed later.

Investigations of the kinetics and mechanism of RDX decomposition at temperatures below the melting point were reported in a series of papers by Batten and Murdie[24,25] and Batten.[26,27] The kinetics were studied[24,25] utilizing a manometric method (pressure vs. time) with glass reactors of fixed volume, pre-pressurized to 100 Torr by nitrogen to suppress RDX sublimation.

Sigmoid-shaped decomposition-time curves were found and the periods of reaction identified:[24] induction, acceleration and maximal rate; different rates correspond to each period. The effect of sample configuration (confinement using holder tubes, or spreading on bottom of reactor) upon the kinetics was studied,[24,25] showing a rather strong influence: when the sample is more confined, the induction rate decreases and the acceleration rate increases; all geometries tend to the spread condition (frothing, gross partial liquefaction) and thus by the time maximal rate is achieved, all approach a uniform maximal rate.

These findings were attributed to interaction between the gaseous products of decomposition and the condensed unreacted RDX, not to the onset of liquefaction; inhibition, followed by a possible competing gaseous reaction which particularly depletes the inhibitor, and finally free escape of the inhibitor, were suggested at the three respective decomposition stages.

The activation energies in the temperature range 170-198 C for the various decomposition stages were calculated:[25] at the induction stage, 53 and 49 kcal/mol corresponding to spread and confined samples respectively, and 62 to 64 kcal/mol at the maximal rate, regardless of confinement conditions.

The higher activation energy results seem to be corroborated by the RDX decomposition data of Rogers and Morris,[8] (using DSC but in an undisclosed temperature range), 67 + 3 kcal/mol, and by Maycock and Verneker[3] (using TGA and DTA for a study of HMX decomposition) who found 63 + 2 kcal/mol. The lower activation energies, observed only for confined samples at the initial stages of decomposition, are closer to those reported for RDX above the melting point, e.g., Robertson.[13] However, the lack of complete definition of the kinetic constant in the present work[25] makes it difficult to make rate comparisons.

The effect of various gases upon decomposition below the melting point was tested, and a chemical mechanism proposed.[26] The gases used for pre-pressurization were typical products of decomposition, CH_2O and NO_2, were shown to effectively catalyze and inhibit the decomposition reaction, respectively. Other species, e.g. CO_2, CO, NO and H_2O were reported to have little or no effect. H_2O had an inhibiting effect. In addition, the nonvolatile residue (NVR) remaining after complete decomposition in condensed form was checked for possible influence on decomposition; it was shown to

strongly promote liquefaction and decomposition rate in nitrogen atmospheres. The decomposition mechanism proposed is intermolecular in its initial stages, based on the short $C---O$ distances observed[1] in RDX crystals. Attack by O of one molecule on CH_2 group of an adjacent one was therefore proposed, forming CH_2O, NO_2, N_2O and other gaseous products; assuming effective "caging" of the reaction products within the surrounding crystal lattice, these products may undergo further secondary reactions - in particular,

$$NO_2 + 5/7CH_2O \longrightarrow NO + 2/7CO_2 + 3/7CO + 5/7H_2O \qquad (II.2)$$
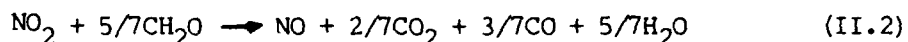
advanced by Pollard and Wyatt.[29,30,31] This reaction may explain the relative behavior of NO_2 and CH_2O in catalysis of RDX decomposition: NO_2 in excess depletes CH_2O (which was found catalyzing). The polarity of H_2O molecules was assumed to directly interfere with the $C---O$ intermolecular process, explaining the aforementioned retarding effect of water.

Catalysis of RDX decomposition is taken up in a separate report by Batten,[26] in the temperature range 170-197 C. Using only spread samples in CH_2O atmosphere, it was shown that the extent of decomposition catalysis by CH_2O increases with decreasing temperature, that the activation energy at all stages of decomposition remains close to 44 kcal/mol, comparable to the E previously obtained for confined samples[24,25] at the induction and acceleration stages (in nitrogen atmosphere). Actual rates observed, however, are 10 times faster for the "catalyzed, spread" configurations as compared to the "uncatalyzed, confined" ones. It was therefore concluded that the product CH_2O may promote autocatalysis in the bulk of the material undergoing decomposition; another possible role of CH_2O is to suppress attack by NO_2 on the nonvolatile residue mentioned earlier, and therefore indirectly promote liquefaction. The mechanism depicting the detailed involvement of CH_2O in the decomposition was written in terms of the unidentified nonvolatile residue.

An investigation of delta-HMX decomposition by Maycock and Vernecker,[6] mentioned earlier, was carried out under helium atmosphere in a temperature range about the melting point, 518-573 K. Experiments made with flowing (10 lit/hr) and stagnant (1 atm) helium were reported, obtaining S-shaped decomposition curves, similar to those reported by Rauch and Fanelli.[14] The calculated activation energies were 62 and 59 kcal/mol for flow and for stagnant atmospheres respectively, obtained from the maximal temperature measured in the adiabatic experiments. The associated frequency factors were not reported, probably due to the unresolved order of reaction. The decomposition exotherm for the stagnant gas was shown appreciably higher than that of the flowing helium, indicating interaction between gaseous products and the condensed phase decomposition process; further, liquefaction of the sample was sometimes observed visually prior to the melting endotherm signal, upon which decomposition was greatly accelerated. All of the above findings are in good agreement with the RDX-observations of Batten[24-27] corresponding to spread samples at a lower pressure and temperature range, and suggest a high degree of similarity between early stages of RDX and HMX decomposition.

Cosgrove and Owen[22,23] continued their investigation of RDX decomposition below the melting point,[21] using mass spectroscopy to identify the major products at various stages of the decomposition. Only results at 195 C were reported. The effects of reactor volume and initial sample weight were tested, for initially evacuated reaction vessels; the findings confirm those reported earlier,[21] namely that decomposition rate was independent of initial sample

weight and increased proportionally with the volume. Additionally, the effect
of various levels of pre-pressurization by nitrogen was estimated. Nitrogen
was found to suppress the (gaseous) decomposition rate; however, contrary to
the assumption of Batten and Murdie,[24,25] 100 Torr of nitrogen did not block
the RDX sublimation effectively (as shown by the products) and hence still
allows for gas phase decomposition.

Concentrations of N_2, N_2O, NO, CO, CO_2, CH_2O and other products (including
NO_2^- and NO_3^- were reported (Ref. 22) at various stages of the decomposition.
NO_2 was not detected, but the authors attribute the presence of NO_2^- and NO_3^- in
large quantities on NO_2 formed, reacting rapidly with nnofNO_3^- in large
quantities on NO_2 formed, reacting rapidly with CH_2O through the mechanism of
Eq. (II.2). In addition, the presence of hydroxymethyl formamide
(HCO-NH-HCHOH, denoted here HMF) is indicated by the observed amounts of HCOOH
and NH_3, combined with the equivalent amount of CH_2O; this compound (HMF) is
assumed to promote liquefaction of RDX below the melting point (by dissolution)
and hence more rapid decomposition, in the solution phase.

The authors[22] conclude that the gas phase decomposition of RDX under their
experimental conditions is of primary importance, and that two opposing
physical factors control decomposition: processes influencing the vaporization
of RDX, and those affecting solution-phase decomposition indirectly, through
influence upon HMF coming into contact with solid RDX.

In the second part of the same study, Cosgrove and Owen[23] continue the
investigation by assessment of the influence of various products upon the
decomposition of RDX at 195 C. N_2, N_2O, NO, CO_2, CO and H_2O were all found to
effectively retard the decomposition rate, when present at 214 Torr initially;
except for NO, the effect was shown equivalent to that of N_2 at the same
pressure.

HCHO was found to catalyze decomposition, in line with the results of
Batten;[26,27] when this substabnce was added, increased yields of NO, CO_2 and
CO were observed, cf. Eq. (II.2), while N_2 and N_2O yields were unaffected.
This points to indirect influence through the gas phase decomposition,
particularly as the effect was found greater at the later stages of
decomposition (attributed to retarding of RDX vaporization by CH_2O, initially).

Distinct reaction mechanisms were proposed[23] for gas and for condensed
phase decomposition of RDX. The initial stage in the gas involves fission of
the N-N bond to eliminate NO_2:

$$RDX(g) \rightarrow R\cdot + NO_2 \qquad\qquad (II.3a)$$

where the R$\cdot$ radical denotes RDX less one nitramino group, which decomposes
further:

$$R\cdot \rightarrow N_2 + CH_2O + O_2N-N-CH_2NH-CHO \qquad\qquad (II.3b)$$

$$O_2N-N-CH_2NH-CHO \rightarrow N_2O + \cdot CHOH-NH-CHO \qquad\qquad (II.3c)$$
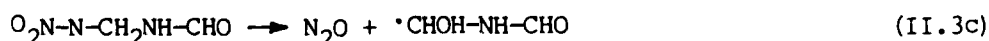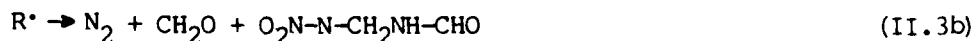
The hydroxymethyl formamide radical appearing in the last reaction may react
with a proton to form HMF or may dimerize; HMF can continue to react:

$$2CH_2OH-NH-HCO \rightarrow CH_2(NH-HCO) + H_2O + CH_2O$$

$$CH_2OH-NH-HCO + 3CH_2O \rightarrow (CH_3)_3N + 2CO_2 + H_2O \qquad (II.4)$$
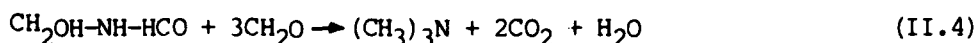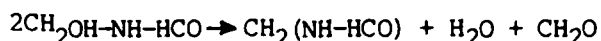
In addition, NO_2 and CH_2O can react to form NO, CO, CO_2 and H_2O, according to Eq. (II.2).

For liquid phase decomposition, the authors adopt the reaction proposed by Robertson,[13] which they advance one step further to ring opening:

$$RDX(liq) \rightarrow CH_2O + \text{[ring fragment structure]} \qquad (II.5)$$
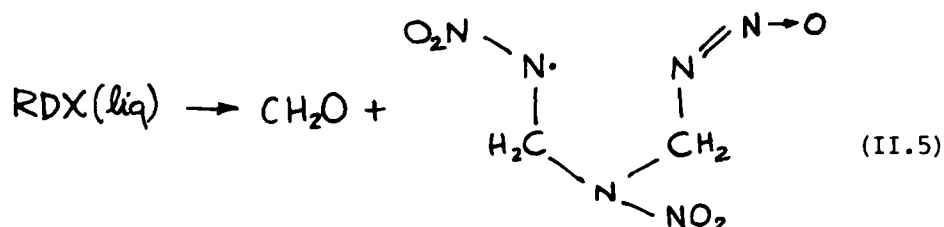
with elimination of HCHO shown reversible.[23] The ring fragment would subsequently break to produce two N_2O molecules. Note that the last step apparently involves two C-N bond fissions, but is not elementary (as originally proposed by Robertson, an oxadiazole intermediate would be involved).

Stals et al[32,33] investigated the decomposition process of polycrystalline RDX during the photochemical process induced by external radiation (medium intensity light source). The range of temperatures was 25 -60 C, and the system initially under vacuum. Pyrolysis products were indentified by mass spectrometer and their partial pressures reported;[33] these were N_2, NO, N_2O, CO_2, CO and HCN, as well as appreciably smaller amounts of CH_2O, NH_3, H_2O, NO_2 and other species. NO_2 in larger quantities was measured previously (Ref. 34) at lower temperatures, and its present near absence was attributed to possible secondary reactions or to photolytic degradation to ·NO + O. The authors recognize the presence of "dark" reactions in the vapor phase above the crystal (as opposed to the photolysis reactions inside the crystal), from which the major contributions to CO and CO_2 arose. They suggest that N_2O is formed in the condensed phase at the expense of N_2, in a secondary process, in line with the energetically favored intermolecular process,[26] and the C-N bond breaking postulated by Suryanarayana.[19]

Combined flow reactor-mass spectrometer, as well as DSC studies were reported by Goshgarian[35] in an investigation of HMX and RDX decomposition at temperatures up to the melting point.

In the range 523-557 K, three regions of HMX decomposition were identified from non-isothermal flow reactor data. In the interval 523-543 K, E = 38 + 2 kcal/mol, corresponding to sublimation (in agreement with the delta-HMX data of Taylor and Crookes[13]) or a combination of sublimation and vapor phase decomposition. In the interval 544-553 K, E = 42 + 2 kcal/mol, interpreted as solid phase reaction prior to melting (may correspond to the accelerative reaction observed by Rogers[15,16,18] and others[14,24,25]). Finally, upon melting, between 554-557 K, a very large activation energy is apparent, E = 120 + 10 kcal/mol, interpreted as two simultaneous homolytic C-N bond ruptures in the liquid, and elimination of HCH-NNO$_2$ (mass/charge = 74, not detected in the

mass spectrometer). Values comparable with this final activation energy were not reported elsewhere, and are not supported by the associated isothermal DSC measurements of the same study (67 kcal/mol) near the HMX melting point.

Gaseous product concentration profiles from the flow reactor-mass spectrometer for RDX and HMX show clearly increasing concentrations of N_2O, NO_2, CH_2O, NO, CO, H_2O, as temperature increases below the melting point. Heavier fragments, typically at mass/charge of 75, 128 and 148 were also observed. For HMX, NO_2, CH_2O and CO_2 sharply increase as T_m = 554 K is passed, and again as deflagration begins at T > 557 K; in the mean time, heavier fragments tend to peak out and gradually disappear as T increases up to T_m, observed only as trace amounts at $T > T_m$. In contrast, for RDX the passage through the melting point is smooth and breaks in the concentration profiles were not indicated. NO_2 seems to have the highest concentration, with CH_2O, NO and N_2 following closely. Further, heavy fragments continue to occur even at $T > T_m$; concentrations of mass/charge 75 (possibly hydroxymethyl formamide) and 132 are still increasing at T = 503 K.

Therefore, differences between the liquid phase decomposition of RDX and HMX are evident. Relative to RDX, HMX decomposes more vigorously, its melting and decomposition occur simultaneously (at low enough heating rates), as reaction rate increases abruptly at $T \stackrel{\sim}{<} T_m$. Although the HMX process seems more complex and the associated kinetics differ, the author concluded that basically the same primary decomposition mechanism applies to both RDX and HMX.

The appearance of NO_2 and its increasing concentration beyond T_m for both HMX and RDX confirms the findings of Rauch and Fanelli[14] and indicates an increasing involvement of gas phase decomposition as T increases, since NO_2 is simultaneously depleted by secondary reactions. It seems unlikely that secondary reactions could produce NO_2 faster than it would deplete by the NO_2 + CH_2O reaction.

3. Thermal Decomposition at Elevated Pressures and Temperatures

Several of the RDX and HMX decomposition studies were extended to higher pressures and temperatures, more closely resembling deflagration conditions than the low (p; T) commonly used in the analyses reviewed in the foregoing sections. The important question is of course whether the decomposition mechanism and kinetics available from low (p; T) data would be valid under typical deflagration conditions. Unfortunately, decomposition under elevated (p; T) is rather rapid and remains beyond the measurement capacity of available devices like the DSC. Therefore, chemical kinetic data is outside the scope of these studies, concerned mostly with final decomposition products, overall heat release and variations in thermophysical behavior such as phase transitions.

Bernecker and Smith[36] analyzed the combustion products of several secondary explosives by mass spectrometry, in the pressure range between 0.1 and 12 MPa. Helium was used to pre-pressurize the reaction vessel. For RDX and HMX, the main products observed were N_2 and the constituents of the water-gas reaction. Although H_2O was not measured, its calculated values (to produce the given O/C ratio present in the initial HMX or RDX) resulted in excellent overall balance of atomic species. The concentrations, in mole-percent of final products are almost identical for RDX and HMX, regarding the major species:

$$N_2 : CO : CO_2 : H_2 : H_2O = 33.5 : 22 : 11 : 11 : 22$$
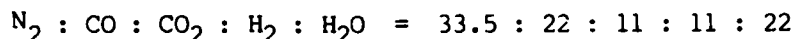
with only slight variations as pressure is increased above 2.5 MPa. NO and N_2O were also detected (as well as HCN), at relatively low concentrations; the concentration of N_2O increases appreciably at lower pressures, particularly for HMX. Small concentrations of CH_2O were also reported for HMX (not RDX) at the 0.1 MPa level, where ignition difficulties and nonsteady combustion were encountered.

Rocchio and Juhasz[37] studied the thermal decomposition and measured the gaseous product concentrations of beta-HMX and HMX propellant (75% HMX/25% polyurethane binder) over an extended range of temperatures, 450 - 1070 K, under 1 atm of helium. The major product concentrations for pure HMX decomposition at 1070 K are shown below, compared with the 1 atm data of Bernecker and Smith.[36]

N_2	CO	CO_2	MOLE-% OF FINAL PRODUCTS						
			H_2	H_2O	NO	N_2O	HCH	CH_2O	
13.5	12.	7.	-	21.	28.	10.5	8.	?	Rocchio[37]
16.3	10	4.9	.86	15.3	26.7	14.2	10.3	0.7	Bernecker[36]

Good overall agreement is demonstrated. No apparent change in product concentrations was observed between 450 - 620 K; however, between 620 and 870 K there appears an appreciable decrease in the ratios of $CH_2O/(CO + CO_2)$ and N_2O/NO. These findings indicate that at higher temperatures and pressures, secondary reactions involving primary decomposition products are enhanced appreciably (being typically second order overall), resulting in product concentrations closer to those observed after complete combustion.

Lenchitz and Velicky[38] attempted to correlate the burning rate of HMX and HMX propellent (HMX with nitrocellulose and inert binder) at various granulations, with the heat of reaction, measured in a high pressure calorimeter. The pressure regime covered by their experiments was 500 - 10^4 psi (3.4 - 68 MPa). Both strand burner and closed bomb were used for burning rate measurements. The heat of reaction, Q, of pure HMX (sample density was not reported) was found independent of granulation size, and appears to have four regions: (a) over the range 3.4 - 10 MPa, Q increases by 100 cal/g;   (b) over 10 - 20.5 MPa Q remains uniform, at a level of 1.5 kcal/g;   (c) following a marked rise at 20.5 MPa, Q increases again by 100 cal/g over 20.5 - 34 MPa, and   (d) over 34 - 68 MPa, Q remains fairly constant, at the level of 1.6 kcal/g. Similar variations in Q were also observed for the HMX propellants within the above range of pressures, but at lower overall levels of Q, and with certain deviation among the different HMX granulations used.

Experiments with pressurized DSC apparatus on various granular HMX samples were reported by Goshgarian,[35] for pressures between 0.1 - 13 MPa and temperatures below the melting point, 420 - 570 K. The DSC data for re-crystallized (purified) HMX shows both phase transition and decomposition kinetics quite invariant to pressure in the range tested. The "duration of melt" in arbitrary units, measured from the onset of melt endotherm to deflagration signal, was found variable with particle size. For coarse (>190 μm) granulation, the melt was not observed prior to deflagration at   5

MPa, whereas fine (9 μm) granulation showed prevailing melt even above 13 MPa. In all cases the duration of melt tends to decrease with increasing pressure. Increasing the sample heating rate resulted in increasing the duration of melt at a given pressure; for the 190 μm sample, it shifted the point of solid-to-deflagration (melt disappearance) to higher pressure.

It can be concluded that there is no evidence for changing of either the chemical mechanism or the kinetics of decomposition under the elevated (p; T) conditions tested. It may be then assumed that the findings of the foregoing sections remain valid and applicable, in general, within the (p; T) domain typical to deflagration. The observed accelerated variations in product composition and heat release indicate possibly the enhancement of certain reactions of secondary nature, involving lighter species like N_2O, CH_2O and H_2 as reactants.

It would be interesting to observe variations in temperature, products and intermediate species concentrations (such as CH_2, HCN, OH) within an actual RDX and HMX flame, as distance from the deflagrating surface and pressure are varied. These, then, should be compared to low (p; T) data. Such measurements were no reported; laser diagnostics of chemically reacting flows would be a possible method of obtaining these data.

4. Discussion: Primary Decomposition and Secondary Reactions

The current status of knowledge regarding the initiation of decomposition was summarized recently by Shaw and Walker.[39] Eight possible initial unimolecular steps in the thermal decomposition of HMX were postulated, in a study based on the literature. Using available thermochemical data for HMX and RDX (as well as an appreciable amount of data for similar compounds) the Arrhenius rate constants for three of the reactions of interest were estimated. The proposed initial steps are as follows.

a) Formation of an oxadiazole ring by transfer of an O atom from NO_2 to a neighboring CH_2, proposed by Robertson[13] and adopted by Rauch and Fanelli.[14]

b) Heterolytic C–N bond cleavage (subsequently forming CH_2O and N_2O) proposed by McCarty.[20]

c) Elimination of $(CH_2)NNO_2$ proposed by Stals.[34]

d) Concerted de-polymerization to $4(CH_2)NNO_2$, proposed by Suryanarayana et al.[19]

e) Homolytic N–NO_2 bond fission, proposed by Rauch[14] and by Cosgrove and Owen[22,23] for the gas phase process. The kinetic rate constant calculated is $\log_{10}(k) = 16.4 - 46.2/2.3R_uT$.

f) Homolytic C–N bond cleavage. The kinetic rate constant calculated is for ring opening (based on an estimate of the HMX ring strain, 7.5 – 11 kcal/mol) $\log_{10}(k) = 18 - 60/2.3R_uT$.

g) Five-center elimination of HONO. Although this reaction is not observed in nitramine decomposition, it is suggested nevertheless due to analogy with nitroalkanes. The estimated rate constant is

$$\log_{10}(k) = 10.8 - 38/2.3R_uT.$$

h) Four-center elimination of HNO_2. Similar to the reaction in (g), with the same estimated rate constant.

The chemical processes occuring during decomposition of RDX and HMX may be ideally divided into two major categories, not necessarily separate in time or site of occurance.

a) Primary decomposition may be defined as the reaction mechanism by which RDX and HMX molecules break down to simple products, e.g., CH_2O, NO_2, N_2O, HCN, NO — as well as (to some extent) to final combustion products, N_2, CO, CO_2, H_2, H_2O. These primary reactions would be fairly typical to RDX and HMX, and the overall reaction process can be described by first order kinetics.

b) Secondary reactions in this framework can be defined as reactions among products of primary decomposition, following typically second order (overall) kinetics. These may include $NO_2 + CH_2O$, $N_2O + CH_2O$, $2N_2O \quad 2NO + N_2$ and the water-gas reaction, all yielding final combustion products. Reactions involving larger fragments of RDX and HMX are excluded, cf. Eq. (II.4), being incorporated in the primary reaction mechanism. In contrast with the overall primary process, these reactions are not unique to cyclic nitramine decomposition.

The primary decomposition processes are expected to have relatively short characteristic (overall) kinetic times, defined $t_{c1} = 1/k_1(T)$, at temperatures above the melting point for both gas phase and liquid phase processes. This is indicated by the typically large pre-exponential factors associated with the rate constants, and demonstrated in the concentration–temperature profiles of Goshgarian[35] for HMX decomposition, by the rapid depletion of large HMX fragments at temperatures just below $T_m = 554$ K (RDX is expected to follow the same trend at temperatures somewhat above its $T_m = 478$ K).

The secondary reactions are expected to be less rapid in comparison, with characteristic times defined $t_{c2} = 1/[k_2(T)p/R_uT]$, typically longer than those of primary decomposition within the range of temperatures expected in the gas during deflagration. These reactions are more pressure sensitive, owing to their second order nature; this is demonstrated by the production–depletion of NO_2 in the concentration vs. time curves of Rauch and Fanelli,[14] and in the observation of N_2O, CH_2O and HCN at low (0.1 MPa) but not at higher (> 2.5 MPa) pressures, in the RDX and HMX experiments of Bernecker and Smith.[36]

Kinetic rate constants from various sources for primary decomposition of HMX and RDX in the gas and the condensed phase are compared in Fig. II.3. The liquid phase data for RDX and HMX are close (only Robertson's[13] kinetics drawn), indicating a similarity in the primary decomposition kinetics for these two substances in the liquid. If the validity of these kinetics constants is accepted, the reason for the observed faster HMX decomposition near its melting point (relative to RDX near its melting point) seems to emanate simply from the appreciable difference between the associated melting temperatures: $k(HMX,554K)/k(RDX,478$ K$) \doteq 10$. Likewise, the dilute RDX/TNT solution data of Robertson[13], assumed to adequately represent RDX(g) decomposition, is in good agreement with the calculated kinetics of homolytic N-N bond fission by Shaw and Walker[39] for HMX(g), indicating a similarity between the gas phase

decomposition kinetics. The line corresponding to RDX(g) decomposition, due to Rogers and Daub[17], has a somewhat smaller slope, and intersects the RDX/TNT solution line at $T \doteq 800K$. Even with this deviation, the agreement between all three gas phase decomposition lines drawn is remarkable, within the range 600-1000 K where most vapor phase decomposition can be assumed to occur.

Characteristic reaction times for primary decomposition and several plausible secondary reactions, according to the foregoing definitions, are plotted against 1/T in Fig. II.4. Comparison shows that the two overall secondary reactions involving N_2O are appreciably slower than the other kinetics plotted, at least up to temperatures of 2000 K. The accelerative effect of pressure on the secondary reactions is demonstrated. The $NO_2 + CH_2O$ reaction is shown faster than the primary decomposition kinetics up to roughly 600 K at 0.1 MPa, and up to 700 K at 10 MPa. This may explain the absence of NO_2 from many low-temperature decomposition product measurements. It should be mentioned, however, that the actual rate of the $NO_2 + CH_2O$ reaction in the gas phase of deflagrating RDX and HMX is expected to be appreciably slower than primary decomposition, when the mean temperature is taken (say) as 1000 K. Of course, many other secondary reactions may prevail in the gas phase, the kinetics time scales of which could differ appreciably from those shown in Fig. II.4; however, the N_2O and NO_2 reactions shown are highly relevant to nitramine deflagration[20], and the reactions involving CH_2O dominate in terms of their exothermicity. Therefore, in conclusion, secondary reactions are expected to have a strong influence upon the temperature and chemical composition of the gases at the outer region of the flame. These parameters are important to rocket motor performance, as the specific impulse, I_{sp}, depends on the temperature and mean molecular weight of the final combustion products. Primary decomposition, in comparison, is expected to control the deflagration rate to a large extent, through vapor and liquid heat release. This is due to the quickness of primary decomposition reactions (both in the liquid and the gas) along with their observed high exothermicity. The influence of secondary reactions upon the heat feedback to the propellant surface and the rate of deflagration is expected to be negligible if they occur at a distance from the burning surface (depending on the primary decomposition for reactant supply), but should be considerable if they occur close enough to the surface, namely, if they are fast enough. Thus, pressure may have an important effect in determining the relative influence of secondary reactions on the deflagration rate, as indicated in Fig. II.4. These reactions shall be discussed now in some detail.

Pollard and Wyatt[29,30,31] investigated the reaction between nitrogen dioxide and formaldehyde at low pressures (5 Torr) and proposed a mechanism, for which the overall step is,[29]

$$7NO_2 + 5CH_2O \rightarrow 7NO + 3CO + 2CO_2 + 5H_2O \qquad (II.6)$$
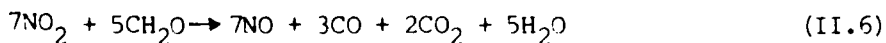
The overall reaction was observed to follow first order with respect to each of the reactants. A change in the kinetics was apparent at 430 K, leading to higher Arrhenius parameters (A, E), relative to the reaction at lower temperatures; the final product composition, however, remained unchanged. For T > 430 K, they reported the rate constant,

$$\log_{10}(k) = 6. - 19/2.3R_uT \qquad (II.7)$$

where k is in $m^3/mol.s$. The authors investigated the explosive reaction[30] as

well, at T > 450 K for low initial pressures, and showed that the product composition ratio of NO/N_2 increases appreciably with temperature, while CO_2 remained fairly constant.[2]

In a further study of the deflagration properties,[31] various CH_2O/NO_2 compositions were tested in spherical reactors at initial pressures of 4 – 8 Torr. The flame speed was measured and found independent of initial pressure, in line with their overall second order mechanism. Further, the maximal flame speed occured at a composition of CH_2O/NO_2 slightly CH_2O -rich relative to the stoichiometric ratio dictated by the overall reaction, Eq. (II.6), as expected. The flame speed was shown to be effectively retarded by the addition of argon (up to 0.3 mole fraction) to the initial mixture.

A more recent investigation of NO_2 reaction with aldehydes was carried out in a shock tube by Fifer[40] at elevatd pressures (7 – 12 atm) and temperatures (700 – 2600 K). The NO_2 + CH_2O experiments were performed with dilute reactant mixtures in argon, to avoid the explosive reaction discussed by Pollard and Wyatt.[30] The initial reactant percent ratios reported for NO_2/CH_2O were 5%/2% and 1.5%/3%; kinetic constants and reactant concentration were determined in separate experiments. The stoichiometry was shown to vary gradually with (p, T); increasing (p, T) resulted in concentrations of CO decreasing and CO_2 increasing for the NO_2 -rich mixture, with the reverse trend observed in the NO_2 -lean mixture. In contrast to Pollard and Wyatt,[29] N_2 appears as product. Eight pertinent elementary reactions were presented (none involves nitrogen) but no attempt was made to combine them into a single model of the overall reaction. The calculated reaction rate term involves the concentration of argon, being:

$$-d(NO_2)/dt = 10^{7.1}\exp(-26.7/R_uT)(Ar)^{0.40}(CH_2O)^{0.56}(NO_2)^{0.90} \qquad (II.8)$$

A large number of additional secondary reactions can be proposed, of which the following would be typical.

$$N_2O + M \longrightarrow N_2 + O + M \qquad\qquad (II.9a)$$

$$\underline{N_2O + O \longrightarrow 2NO} \qquad\qquad (II.9b)$$

$$2N_2O \longrightarrow 2NO + N_2, \quad Q = -3.94 \text{ kcal/mol.} \qquad (II.9c)$$
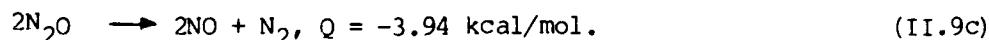
shown to be slightly endothermic overall. As given by Levy[41] in a recent update of available kinetics data of elementary reactions in flames, the second step in the mechanism is appreciably faster than the first (decomposition) step, with

$$\log_{10}(k) = 6.36 - 24.1/2.3R_uT \qquad\qquad (II.9d)$$

so that the first step would be rate determining, with a rate constant of

$$\log_{10}(k_2) = 8.7 - 58./2.3R_uT \qquad\qquad (II.9e)$$

Where k_2 are given in $m^3/mol.s$. Another plausible reaction involves CH_2O and N_2O, for which one of the many routes is:

$$CH_2O + M \longrightarrow CO + H_2 + M$$

$$N_2O + H_2 \longrightarrow H_2O + N_2 \qquad\qquad (II.10a)$$

$$\overline{CH_2O + N_2O \longrightarrow CO + N_2 + H_2O,\ Q = +76.1\ kcal/mol.}$$
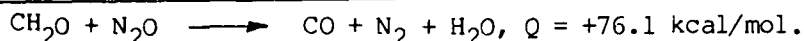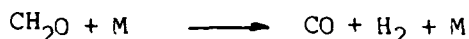
overall highly exothermic. For this reaction, the rate constant is extimated,[42]

$$\log_{10}(k_2) = 7.1 - 44/2.3R_uT \qquad\qquad (II.10b)$$

A rather extensive review of N_2O and CH_2O reactions was made by McCarty[20] within an overall nitramine-combustion literature survey. Twenty three elementary reaction steps involving N_2O and CH_2O were listed, partly with the associated kinetic constants. The overall reaction in Eq. (II.10a) can be obtained from the steps listed, but no attempt was made for a similar explicit model, as the reaction may proceed by different routes depending on location in the flame field, i.e., the availability of O or H atoms, other radicals, the local temperature, etc. Within the CH_2O/N_2O mechanism, a high activation energy corresponds to N_2O decomposition, as shown by Eqs. (II.9a,e), but reactions with $N_2O + H$ atoms, according to Fenimore and Jones,[43] have E = 12 kcal/mol; however, the probability for large enough concentrations of H atoms in the flame is severely impeded by the high dissociation energy of HCHO $\rightarrow$ H + CHO, being -76 kcal/mol. McCarty[20] considered the N_2O/CH_2O reaction as the major one occuring in the nitramine flame (primary decomposition of nitramine in the vapor phase was omitted), and concluded that since a chain mechanism is involved, radical traps would tend to decrease the burning rate. This picture of the deflagration process would hold for high enough pressures, where the major heat feedback contribution from the gas phase is due to secondary reactions. Other reactions, involving NO and NO_2 as oxidants were also reviewed, but in lesser detail.

A large number of elementary reactions involving NO_2 were listed in a study by Ford[44] and some of the associate rate constants were given. These may be useful for a detailed study of the secondary reaction mechanism, along with the tabulated data of Levy.[41]

A fundamental role of secondary reactions in propagating deflagration was assumed in the investigation by Fogel'zang et al,[45] where the combustion characteristics of nitramino, nitrosoamine, C-nitro and nitrate compounds were compared. The authors suggest that the reason nitramines (releasing N_2O in decomposition) burn much faster than C-nitro and nitrate compounds (releasing NO_2 in decomposition) at about the same final flame temperature is, that N_2O mixtures burn faster than similar NO_2 mixtures. This notion is based on a work by Parker and Wolfhard[46,47] which unfortunately excludes reactions involving aldehydes. The dark zone in the combustion of C-nitro compounds (typically nitrocellulose and double base propellants) was attributed to formation of NO by NO_2 reduction, leading to subsequent reduction of NO and N_2 formation which is endothermic; hence, these compounds are incapable for using all their chemical energy for flame propagation. N-nitro compounds, on the other hand, were assumed to react by a different route, producing N_2O which reacts rapidly and is highly exothermic. It should then be expected that all nitroso compounds burn slower than nitro compounds (e.g. nitramines) since NO is

likely to be formed. While this may hold in general, it has one prominent exception in nitrosoguanidine, $(NH_2)_2CNNO$, which was observed to burn faster than all nitramines; the reaction postulated for the explanation of this outstanding behavior still requires experimental proof, particularly for the existence of $(NH_2)_2CO$.

The authors[45] assume overall second order kinetics (burning rate pressure exponent n ≈ 1 for nitramines) and completely exclude the effect of primary decomposition. Further, their correlation of calculated final flame temperatures and burning rates of the afore-mentioned compounds (all at 40 MPa) implies strong coupling between the secondary reactions in the gaseous flame and the deflagrating surface. Although this might prevail at higher pressures, it certainly cannot apply to the entire pressure range, 0.3 - 40 MPa, considered in their study.

The decomposition characteristics of RDX and HMX may now be summarized as follows.

a) Decomposition can proceed in both the gas and the condensed phase. At temperatures below the melting point, condensed phase decomposition is slow, its rate being approximately 1/10 of the rate of gas phase decomposition.[21] Upon liquefaction, the condensed phase reaction rate accelerates appreciably.

b) At slow enough heating rates, both RDX and HMX melt with decomposition. (HMX decomposes more vigorously) exhibiting sigmoid shaped decomposition- time curves, with an induction period, an accelerative reaction, and finally a maximal rate. Autocatalysis was indicated in most of these experiments.[13,14,24-27]

c) In the range of temperatures below the melting point, the condensed phase decomposition depends strongly upon gaseous decomposition product concentrations. CH_2O and NO_2 catalize and inhibit the condensed phase decomposition respectively.[22,23,27] Hydroxymethyl formamide, produced in the gas phase, promotes liquefaction below the melting point, upon which condensed phase decomposition is accelerated appreciably.

In this respect, sample geometry (confinement) can have a pronounced influence on the reaction rate, due to effective "caging" of gaseous products.

d) Different chemical mechanisms pertain to gas phase and to condensed phase decomposition. In the gas, the most likely initial step is the homolytic $N-NO_2$ bond fission, producing NO_2.[14,22,23,39] The initial step in the condensed phase probably involves C-N bond breaking, (despite the unfavorably high C-N bond energy) and favors N_2O production, ultimately.[14,23] The differences could emanate from the strengthening of the N-N bond and intermolecular interactions in the crystal and liquid, as opposed to the relative freedom of the NO_2 rotor in gas phase conformations. Indeed, distinct Arrhenius rate constants for the gas and for the condensed phase were reported, (as shown by the grouping of the condensed phase and of the gas phase kinetics in Fig. II.3) mostly agreeing with overall first order kinetics, and showing a rather high frequency factor. The question

of intermolecular[26,27] versus intramolecular[13,19] initial decomposition processes in the condensed phase remains open at this time.

e) The observations of distinct decreases in the $CH_2O/(CO_2 + CO)$ and N_2O/NO ratios between 620 and 870 K by Rocchio and Juhasz,[37] the vanishing of N_2O, CH_2O and HCN above 0.2 MPa by Bernecker and Smith,[36] and the apparent 0.1 kcal/g increase in heat of reaction between 20.5 and 34 MPa by Lenchitz and Velicky[38] indicate an enhanced extent of secondary reactions, not a change in the decomposition mechanism.

D. Chemical Mechanism and Rate Constants for the Deflagration Model

Based on the foregoing observations, a model for the chemical process is now sought, for incorporation in the deflagration study.

Evidently, although many of the decomposition and self-deflagration properties of HMX and RDX are quite similar, a somewhat higher degree of complexity in the decomposition of HMX has been indicated, particularly in the region of solid-liquid transition. This has effectively impeded the measurement of the fusion enthalpy, as well as the definition of a detailed condensed phase decomposition mechanism of HMX.

In contrast, a rather complete set of thermophysical and chemical kinetic data can be readily assembled for RDX; the choice falls then naturally on this compound, for quantitative representation in the deflagration model. Hence, relatively speaking, for reasons of data availability and reliability, the decomposition model herein corresponds to RDX alone.

It must be stressed, however, that the monopropellant deflagration model developed in subsequent chapters applies equally well to RDX and HMX, the possible differences in the decomposition mechanism notwithstanding.

1. The Vapor Phase

The mechanism considered is based on the one proposed by Cosgrove and Owen[23] for RDX in the gas phase, with slight modifications. For completeness of the present discussion, the reactions are rewritten. The initial steps in the decomposition process are:

$$RDX(g) \longrightarrow R^{\cdot} + NO_2 \qquad \text{(II.11a)}$$

$$R^{\cdot} \longrightarrow N_2 + CH_2O + O_2N-N-CH_2NH-CHO \qquad \text{(II.11b)}$$

$$O_2N-N-CH_2NH-CHO \longrightarrow N_2O + {}^{\cdot}CHOH-NH-CHO \qquad \text{(II.11c)}$$
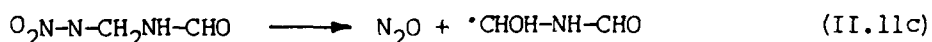
Reactions involving further decomposition of the last radical in Eq. (II.11c), leading ultimately to formation of HCOOH, NH_3, and hydroxymethyl formamide (all of which not observed in deflagration) are conveniently replaced by the following overall step, suggested by Valance et al:[48]

$$^{\cdot}CHOH-NH-CHO \longrightarrow 2CH_2O + 0.5N_2 \qquad \text{(II.11d)}$$
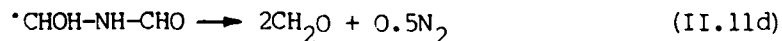
The four reaction steps shown in Eqs. (II.11 a,b,c,d) can be added, to obtain a net overall (unimolecular) primary decomposition reaction:

$$RDX(g) \longrightarrow NO_2 + N_2O + 3CH_2O + 3/2N_2, \quad Q_1 = 108 \text{ kcal/mol.} \quad (II.12a)$$
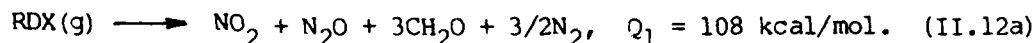
Simultaneously with the above step, the secondary reaction, involving NO_2 and CH_2O is, following Pollard and Wyatt:[29]

$$NO_2 + 5/7CH_2O \longrightarrow NO + 3/7CO + 2/7CO_2 + 5/7H_2O, \quad (II.12b)$$
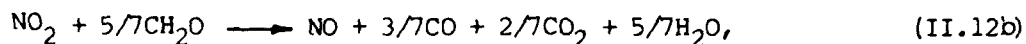
$$Q_2 = 46 \text{ kcal/mol.}$$

The last two overall reactions, Eqs. (II.12a,b), are intended for the modeling of the initial stages of the chemical process during RDX deflagration in the vapor phase.

Comparison with experimental RDX decomposition product concentrations of Cosgrove and Owen,[22] given in Table II.4, shows fairly good agreement, lending some credibility to the model proposed herein.

The kinetic constant for the primary decomposition reaction, Eq. (II.12a), is the one reported by Robertson,[13] for dilute solution phase decomposition of RDX in TNT,

$$\log_{10}(k_1) = 15.55 - 41.5/2.3R_uT \quad (II.13)$$

which seems best suited (at the present state of knowledge of the kinetics) for representation of the vapor phase process.

For the secondary reaction, Eq. (II.12b), the Arrhenius parameters were calculated by Pollard and Wyatt:[29]

$$\log_{10}(k_2) = 6 - 19/2.3R_uT \quad (II.14)$$

where $k(m^3/mol-s)$, obtained for $T > 430$ K. The kinetics follow first order with respect to each of the reactants.

2. The Liquid Phase

Experimental evidence points to distinct gas and condensed phase decomposition mechanisms for RDX and HMX, regarding the initial steps. In contrast to the gas (where N-N bond breaking is most likely the initial step) C-N bond fission or five center HONO elimination might be the initial steps in the liquid, as discussed by Shaw and Walker.[39] Still, apart from the concerted de-polymerization mechanism of Suryanarayana,[19] a detailed liquid phase decomposition mechanism is yet to be reported in the open literature; for this reason, the stoichiometry of the primary decomposition reaction presented in Eq. (II.12a) shall be adopted for the liquid phase as well, although the liquid phase mechanism might favor N_2O formation at the expense NO_2:

$$RDX(liq) \longrightarrow NO_2 + N_2O + 3CH_2O + 3/2N_2, \quad (II.15)$$
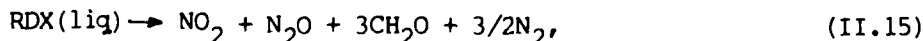
$$Q_1(liq) = 75.4 \text{ kcal/mol.}$$

The kinetic rate constant is taken from the pure liquid RDX data of Robertson,[13]

$$\log_{10}(k_1) = 18.5 - 47.5/2.3R_uT \qquad\qquad (II.16)$$

in agreement with most of the experimental works on the liquid phase decomposition kinetics. Secondary reactions are excluded from the liquid phase model, since they involve gaseous products of the primary decomposition, and their rates are expected to be negligible if the products are assumed to be dissolved in the remaining liquid.

E. Deflagration of Nitramines

1. Experimental Observations of Nitramine Deflagration

The following properties characterize the self-deflagration of RDX and HMX.

a) At low to intermediate pressures (up to 13 MPa) a layer of molten nitramine forms on the deflagrating surface where liquid phase decomposition occurs.[49-52] The melt layer thickness decreases with increasing pressure; for HMX, micrographs of quenched crystals after deflagration at 3.3 MPa show a melt thickness of 15-20 μm.[49,50]

b) The burning rates of RDX and HMX are quite similar over a wide range of pressures.[49,50] These rates are relatively low at low pressures, with a pressure exponent, n, which varies gradually from values of 0.5 (p < 0.1 MPa) to 1.0 (p > 10 MPa).

c) In granular matrices, distinct upward break in the pressure exponent and large increase in the burning rate occur as pressure is increased beyond a critical value. This was demonstrated experimentally with granular packed beds of RDX and HMX by Taylor[52] and by Bobolev et al,[53] where burning rates and pressure exponents (n > 1) much in excess of those observed in normal deflagration were shown to occur after transition. The critical transition pressure was found to correlate with the mean particle size of HMX and RDX: exponent breaks occur consistently at lower pressure for the larger particle size arrays; thus in the regime of accelerative burning (termed convective burning in Soviet literature) higher burning rate may correspond to larger particle size at a given p, in contrast with the behavior of AP propellants which exhibit the reverse trend in their normal deflagration regime.

d) Under normal deflagration conditions, crystals of pure RDX and HMX tend to crack.[49,54] The number of cracks observed increases with the pressure, attributed to steepening of the thermal profile within the crystal at the deflagrating surface.[54]

The deflagration of RDX and HMX propellants incorporating inert plastic (hydrocarbon) binders is discussed in the following.

e) In contrast to AP propellants, both burning rate and the final flame temperature, T_f, are depressed in the propellant configuration relative to pure nitramine. This may be explained by secondary

reactions involving binder fragments, e.g., $CH_2 + H_2O \rightarrow CO + 2H_2$ which is 30 kcal/mol endothermic. Such reactions may account for both cooling of the final product temperature and reduced heat feedback from the gas to the propellant surface. Meanwhile, the average molecular weight of products (relative to pure nitramine combustion) decreases. Since the I_{sp} is proportional to $(T_f/\overline{W})^{0.5}$, this property might not be as strongly affected, but the reduced burning rate is undesirable.

f) Upward breaks in the burning rate and the pressure exponent were observed for propellant configurations at pressures between 10 - 30 MPa (above the rocket operating regime), as reported by Zimmer-Galler,[55] Cohen,[56,57] Boggs et al[49] and McCarty.[58] This phenomenon strongly resembles the aforementioned transition to convective burning observed with granular beds of pure nitramines, but with some important differences, notably the much lower burning rates in the case of the propellant configurations. The pertinent properties may be summarized as follows.

$p < p_{crit}$	$p > p_{crit}$
n(comp) < n(HMX)	n(comp) > n(HMX)
r(comp) < r(HMX)	r(comp) > r(HMX)
r(20 μm, comp) > r(100 μm, comp)	r(20 μm, comp) < r(100 μm, comp)

Numbers in parentheses indicate granular mesh size. Similar trends were observed with RDX.[55] In some of the burning rate experiments incorporating coarse enough HMX granulations (> 200 μm) a second, downward shift in the pressure exponent was observed, as pressure was increased appreciably beyond p_{crit}: n and r both approach then the values for pure HMX.

2. Analyses of Nitramine Deflagration

Most analytical treatments of nitramine deflagration to date deal with propellant configurations, namely nitramine combined with inert binder or energetic additives, with the aim of explaining the observed discontinuities in the burning rate pressure exponent at high pressures. These lie outside of the main interest of the present investigation, and shall be mentioned only briefly. The review by McCarty[20] may serve as an excellent source of references, regarding U.S. (and Soviet) works on this subject, up to 1976.

Analyses of nitramine monopropellant deflagration are scarce, since they seem to provide no direct answer to the question of burning rate-pressure slope discontinuities, unique to pure granular nitramines or propellants containing granular nitramine configurations.

In both propellant and monopropellant analyses, a rather general trend is evident in the assumption that models which were developed for and apply to ammonium perchlorate (AP) should necessarily apply to nitramines as well, with an appropriate choice of thermophysical and kinetic parameters. This view is expressed explicitly in the works by Beckstead et al,[59,60] Cohen and co-workers[56,57] and by Boggs et al.[50,61] This assumption might hold at high enough pressures, where a single overall second order reaction step may adequately approximate the gas phase processes, strongly coupled to the

deflagrating propellant surface. Unfortunately, the AP-similarity is expected to break down in presence of multiple reactions having diverse characteristic time scales in the gas phase of deflagrating nitramines, as indicated in the discussion of primary decomposition and secondary reactions, Section C.4.

Beckstead and McCarty[59] used the Beckstead-Derr-Price model[60] to calculate the deflagration properties of nitramine monopropellants. A large section of their article was devoted to a survey of AP deflagration analyses, assuming full applicability of these models to deflagrating nitramines. In this context, the authors conclude that most deflagration models could predict the burning rate versus pressure (of AP) reasonably well, hence a test for the true validity of the model would be to predict the burning rate sensitivity to initial propellant temperature. Indeed a correlation of the temperature sensitivity data of Boggs et al[61,50] was carried out, in a trial and error optimization procedure. A value of the "surface" heat release was calculated, being 208 cal/g; this value seems to incorporate condensed phase exothermic reaction, latent heat of evaporation and heat release by primary decomposition in the gas. The authors conclude that greater initial temperature sensitivity is observed at lower pressures, since subsurface reactions control the deflagration process.

Of course, if primary decomposition in the gas phase and the condensed phase are lumped in the above manner, one may expect (1) rather high "surface temperatures", (2) a surface heat release which remains reasonably constant, and (3) relatively low activation energy of the surface pyrolysis law, all of which seem to be observed in this work.[59] In addition, at low p, assuming large flame "standoff" distance (by which the position of fully reacted flame is approximated) the burning rate temperature sensitivity expression of the BDP model reduces to

$$\sigma_p \equiv \left(\frac{\partial \ln r}{\partial T_0}\right)_p \doteq E_s/R_u T_s^2$$

where E_s is the surface pyrolysis activiation energy and T_s the surface temperature. Evidently, when an expression like $r = A_s \exp(-E_s/R_u T_s)$ is used, σ_p will increase sharply for decreasing r, due to its strong dependence on T_s.

It may be therefore concluded that the authors[59] successfully verified all of their initial assumptions, including those inherent in the BDP model. Unfortunately, their conclusion regarding deflagration control by condensed phase decomposition at lower pressures is unwarranted, although their results follow the experimental data, for the following reasons: (1) low pressure deflagration of nitramines was not adequately modeled, since primary decomposition on both sides of the condensed-gas interface was apparently lumped, and (2) information regarding the heat feedback from the gas phase could not be properly obtained by their model for quantitative comparison of gas/condensed phase heat generation effects on the deflagration rate.

Analyses of self deflagrating HMX were presented in two articles by Boggs et al.[50,61] The sensitivity of burning rate to variations in initial sample temperature, T_0, was the subject of the first investigation,[61] using their experimental burning rate data at T_0 = 300, 373 and 423 K within the pressure range 0.8 - 10 MPa as input to the analysis. An Arrhenius type pyrolysis law, and a modified verson of an overall heat balance (from the Beckstead-Derr-Price

model[60]) were utilized to provide two expressions defining the surface temperature, T_s. These were combined to form a single constraint in an optimization procedure, intended to obtain "optimal" values of the following six parameters: the surface pyrolysis law parameters (A,E), the heat of reaction, Cp, the kinetic constant and the order of reaction in the gas phase. Trial and error calculations were made, and a best fit of the experimental data was selected. The authors concluded that an extremely exothermic surface reaction prevails (involving roughly 85 kcal/mol), an activation energy $E \doteq 53$ kcal/mol, and a mixed order of 1.8; the surface temperature is $T_s \doteq 1470$ K.

Aside from the obvious question of validity of the calculation procedure (it seems that normally six independent constraints are necessary to uniquely define six unknowns, so that their system is highly under-determined), the results seem interesting mainly because the high surface temperature and heat release indicate that the data might correspond to the end of the primary reaction zone in the gas, not to the propellant surface.

In the second investigation,[50] the model described above was utilized to correlate further burning rate data, with similar results. The results were compared with those of Beckstead et al[50] who correlated the HMX burning rate data of Taylor,[51] using only two out of six parameters in the optimization procedure, the rest being frozen inputs. Not suprisingly reasonable agreement was demonstrated.

In conclusion, a detailed analysis of nitramine deflagration is definitely warranted, as a necessary first step toward the understanding of nitramine propellant combustion. Existing models which correspond to AP deflagration, intrinsically exclude important details characteristic of nitramines; selection of appropriate thermophysical and kinetic parameters cannot lead to proper nitramine representation by these models. in particular, when several gas phase reactions with diversely different kinetic time scales are involved, one cannot hope to obtain proper representation of the deflagration wave by using a single overall reaction (even if the reaction order is adjusted to twice the value of the burning rate pressure exponent) in the model. This argument points to the necessity of a specific nitramine deflagration model, a task taken up in the following chapters.

CHAPTER III

PHYSICAL INTERACTIONS IN THE GASEOUS
FLAME ZONE OF NITRAMINES

A. Introduction

Attention is focused in this chapter upon the gaseous reaction region of
deflagrating nitramines. The physical significance of this part of the
deflagration wave is implied by the relatively high observed burning rate
pressure exponent characteristic to these substances, discussed in the
foregoing chapter. This indicates a high degree of sensitivity to pressure,
and hence to gas phase processes.

Prior to the formulation of a comprehensive analytical solution of
deflagrating nitramines, it is necessary to obtain some physical insight into
the processes to be investigated. This may be started by a preliminary
calculation of the time scales and length scales associated with the two
proposed chemical reaction steps in the gas phase. The magnitudes of these
scales and how they relate to characteristic transport scales in the gaseous
region are crucial to posing the problem correctly in both a physical and
mathematical sense. For purposes of illustration, the specific properties of
RDX will be used in this section.

A strong motivation for this examination is provided by the kinetic
constants and the characteristic kinetic times of the associated reactions
shown in Figs. II.3 and II.4; indeed the large differences between both
activation energies and pre-exponential factors suggest a corresponding
diversity in the characteristic length and time scales associated with these
reactions. Therefore, the secondary reaction is expected to be much slower and
have a characteristic length much larger than the primary decomposition
reaction in the gas phase. The calculations that follow show this observation
to be correct. The question to which a qualitative answer is expected from
this preliminary analysis is: what are the physical and analytical implications
of a large difference between the various reactive and transport length scales.
More precisely,

1. How do the various reactive and transport scales in the gaseous flame
   region compare.

2. Would a separation of the gaseous flame region into a near field,
   where the nitramine decomposition reaction is dominant, and a far
   field, where the secondary reaction is dominant, be plausible.

3. If, indeed, such sub-regions in the flame field are indicated, what
   error is ivolved in neglecting the secondary reaction in the near
   field, where nitramine decomposition dominates the heat release.

In the following sections, temperatures in the gaseous flame region are
estimated. Then, appropriate mean reaction rates, $\bar{\omega}_1$ and $\bar{\omega}_2$, are
calculated. The corresponding reactive length scales, δ_{R1}^* and δ_{R2}^*, and
the transport scale, δ_D^* that evolve are compared and a discussion of the
physical and analytical implications is given.

B. Length Scales and Time Scales in the Gas Phase

    1. Definitions

Let the average reaction rates $\bar{\omega}_j$ (kg/m^3-s) be defined:

$$\bar{\omega}_1 \equiv \bar{\rho}\,\bar{k}_1\,\bar{W}\,\bar{Y}_R/W_R \tag{III.1a}$$

$$\bar{\omega}_2 \equiv \bar{\rho}^2\bar{k}_2\,\bar{W}\,\frac{\bar{Y}_F}{W_F}\,\frac{\bar{Y}_O}{W_O} \tag{III.1b}$$

with
$$\bar{k}_j = \bar{k}_j(\bar{T}_j) \equiv A_j\,exp\left[-\frac{E_j}{R_u\bar{T}_j}\right],\ j=1,2 \tag{III.1c}$$

A characteristic reactive length scale may be defined:

$$\delta_{Rj}^* \equiv m/\bar{\omega}_j \tag{III.2}$$

where m is the mixture mass flux, kg/m^2-s and the subscripts j = 1,2 herein refer to nitramine decomposition and the secondary reaction respectively. A characteristic diffusive or transport scale is:

$$\delta_D^* \equiv \rho D/m \doteq (\lambda/C_p)/m \tag{III.3}$$

The last equality in Eq. (III.3) evolves from the approximation Le = 1, assumed to hold in the present analysis. ρD is the mean mixture diffusivity, kg/m-s.

The average mixture density, $\bar{\rho}$ (kg/m^3) is defined by the equation of state for ideal gas:

$$\bar{\rho} = \bar{W}P/R_u\bar{T} \tag{III.4}$$

$\bar{W}$ is the average molecular weight of the mixture, kg/mol.

The characteristic time scales corresponding to transport processes and reaction may be now defined as follows:

$$t_D^* \equiv \bar{\rho}\,\delta_D^*/m \tag{III.5a}$$

is the diffusional time scale. The characteristic reactive time scales are given by

$$t_{Rj}^* \equiv \bar{\rho}/\bar{\omega}_j\ ,\ j=1,2 \tag{III.5b}$$

In the present steady state analysis, it is more convenient to deal with length rather than time scales; thus, most reference to scales in the forthcoming sections shall correspond to δ_D^* and δ_{Rj}^*.

Evidently, density and, in particular, reaction rates tend to vary appreciably from point to point within the gaseous combustion zone. Therefore, reasonable estimates of these properties will strongly depend upon suitable averages chosen for T, W_m, and the rest of the parameters.

2. Temperatures in the Gaseous Flame Region

The chemical equilibrium algorithm of Gordon and McBride[52] was employed to obtain the properties of the product gases at the outer end of the deflagration wave for RDX. The final isobaric flame temperature was found to vary between 3100 - 3200 K, within the pressure range 0.5 - 10 MPa. The concentrations at that point correspond to final combustion products at equilibrium, and remain fairly constant within the pressure range tested:

$$RDX(s) \longrightarrow 2.25CO + 0.72CO_2 + 1.98H_2O + 2.8N_2 + 0.81H_2$$
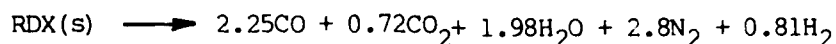
with a mean molecular weight of 24 g/mol.

Additional resolution of the flame field picture is warranted, with the consideration of the two overall reaction mechanism of Section II.D in the deflagration model, in view of the appreciable differences between the associated characteristic kinetic times. Indeed Fig. II.4 shows that t_{c2}/t_{c1} < 1/100 over the range of pressures 0.1 - 10 MPa for T > 700 K. This kinetic time scale relationship indicates that primary decomposition, cf. Eq. (II.12a), would be dominant on the average, within the gaseous region adjacent to the propellant surface.

Prior to continuing the present temperature calculations, the following classifications as to regions in the gas phase flame field are introduced. For present purposes, these definitions are utilized in order to properly choose the average properties associated with the mean reaction rates.

Let the region in the gas between the condensed surface and the point where nitramine decomposition reaction goes to completion (e.g., $Y_R < 10^{-7}$) be defined as the near field; the subsequent region, away from the condensed surface where only the secondary reaction exists, would be defined as the far field. The foregoing classification is based primarily upon physical relation to the condensed surface, not to be confused for the time being with their mathematical, small perturbation counterparts. They are, however, compatible with the mathematical definitions: "outer field" is where a zeroth order (i.e., 100%) change would cause large variations in the whole field, as in our case would doubling the ambient pressure (considered here a far field property, although uniform).

A fuller justification to the particular division of the flame field herein may be found when the average reaction rates and length scales are compared, and further when actual results of the nonlinear model are reviewed.

In an approximate manner, the secondary reaction shall be neglected for the time being in the near field, considering nitramine decomposition only. The parameters at the end of the near-field may then be readily evaluated.

Schematically, the nitramine decomposition reaction, Eq. (II.12a), is:

$$R \longrightarrow \sum_{i=1}^{N} V_{i,1}'' S_i + Q_1 \qquad \text{(III.6)}$$

the mass fractions and mean molecular weight at the end of the near-field are found,[63,64]

$$Y_i^* = V_{i,1}'' W_i / W_R, \quad i = 1, 2, \cdots N$$

$$1/\overline{W}^* = \sum_{i=1}^{N} Y_i^* / W_i \qquad \text{(III.7)}$$

Thus, for RDX, $Y_R^* = 0$, $Y_{N_2}^* = 0.19$, $Y_{N_2O}^* = 0.20$, $Y_{NO_2}^* = 0.21$, $Y_{CH_2O}^* = 0.40$, and $\overline{W}^* = 34.2$ g/mol. These values may be altered in the actual flame by interaction with the far field processes (e.g., diffusion outward of CH_2O and NO_2 due to depletion) and by the effect of the secondary reaction in the near field.

The temperature at the end of the near field, when nitramine decomposition alone is considered, may be calculated from[63]

$$\sum_{i=1}^{N} V_{i,1}'' \int_{T_0}^{T} C_{p_i}(T') dT' = Q_1 \qquad \text{(III.8)}$$

$$Q_1 \equiv -\sum_{i=1}^{N} V_{i,1}'' \Delta H_{f,i}^\circ + \Delta H_{f,R}^\circ \qquad \text{(III.9)}$$

where Q_1 represents the standard heat of reaction for nitramine decomposition, expressed in Eq. (III.6), kcal/mol; the stoichiometry of that reaction assumed valid over the range of pressures considered. C_{p_i} is the isobaric heat capacity for species i; the temperature dependence of C_{p_i} is taken here to the first power of T, viz.,

$$C_{p_i}(T) = \overline{A}_i + \overline{B}_i T, \quad i = 1, 2 \ldots N \qquad \text{(III.10)}$$

For RDX, the heat of sublimation[11] is 31.1 kcal/mol. Thus, when RDX(S), i.e., RDX in the solid state, is considered in Eq. (III.8), then

$$Q_1 = 108 - 31.1 = 76.9 \text{ kcal/mol.}$$

solution of the quadratic equation that results from Eqs. (III.8) and III.10) gives the temperature at the end of the near field, $T^* = 1330$ K.

Once primary decomposition of nitramine is complete at the end of the near field, it is expected that secondary reactions (similar to the $NO_2 + CH_2O$ reaction presently considered) would take over in the far field. For RDX, these should reduce the mean molecular weight from 34 to 24 g/mol, increase the

temperature from 1300 K to roughly 3000 K and produce CO, CO_2, H_2O, N_2, and H_2 as final combustion products.

3. Length and Time Scales

Now that a concept of a range of magnitudes associated with the various parameters in the gaseous flame region has been established, suitable average properties may be chosen. The concern here is to properly represent the point in the flame where both reactions co-exist. Such average properties are:

$$T_1 = \bar{T}_2 = 1000 \text{ K}$$

$$\bar{Y}_R = 0.1, \quad \bar{Y}_F = \bar{Y}_O = 0.2$$

$$\bar{W} = 40 \text{ g/mol}$$

The thermochemical data of Eqs. (II.13,14) is utilized in the range of pressures p = 10 to 40 atm. Calculations of mean densities and the corresponding reaction rates $\bar{\omega}_1$ and $\bar{\omega}_2$ are given in Table III.1 for 3 representative pressures within the given range. It is clear from these calculations that for the average properties employed, the reaction rates consistently differ by 2 orders of magnitude. The implications regarding the associated length and time scales should be obvious. These scales, defined in Section III.B, were calculated using values of mass flux, m, close to the experimentally observed ones for RDX deflagration at the pressures considered.[53]

The scale calculation results are summarized in Table III.1; the following observations can be made:

a) $\quad \delta_D^* \sim O(10 \text{ to } 1) \mu m$

   $\delta_{R1}^* \sim O(10); \quad \delta_{R2}^* \sim O(1000 \text{ to } 100) \mu m$

   $t_{R1}^* \sim O(10); \quad t_{R2}^* \sim O(1000) \mu s$

b) The pressure dependence of the diffusive length scale enters through $\delta_D^* \sim 1/m$. This is due to ρD being approximately pressure independent. Hence, $\delta_D^* \sim p^{-n}$ where n is the burning rate pressure exponent.

c) The reactive length scales δ_{R1}^*, δ_{R2}^* differ by 2 orders of magnitude. This results from the difference between the mean reaction rates. The pressure dependence of $\delta_{R1}^* \sim p^n/p = p^{n-1}$, while $\delta_{R2}^* \sim p^n/p^2 = p^{n-2}$. This is demonstrated in Table III.1 as a greater pressure sensitivity on part of δ_{R2}^*, compared with δ_{R1}^*.

d) In the pressure regime considered, it is important to realize that $\delta_D^* \sim \delta_{R1}^* \ll \delta_{R2}^*$. The flame region is thus convective-diffusive-reactive, with nitramine decomposition being the dominant reaction.

e) The reactive time scales exhibit the same magnitude difference as the length scales: t_{R1}^* and t_{R2}^* are 2 orders of magnitude apart. t_{R1}^*

however, is shown to be pressure independent for obvious reasons, while $t^*_{R2} \sim 1/p$.

C. Asymptotic Dependence of the Deflagration Rate on Pressure

1. Derivation of the Burning Rate Equation

The purpose of this section is to investigate in an approximate manner the relationship between the normal burning rate of nitramine and pressure in terms of the pertinent gaseous flame field processes.

A laminar, premixed one-dimensional flame region is considered, with a single mean overall reaction rate to represent all the chemical processes in the gas phase, such that

$$\omega_{eq} \sim \omega_1 + \omega_2 \tag{III.11}$$

An equivalent heat release Q_{eq}, associated with ω_{eq} is defined

$$Q_{eq}\,\omega_{eq} \sim Q_1 \omega_1 + Q_2 \omega_2 \tag{III.12}$$

Assume now that the entire flow, entering the gaseous flame field at $y = 0^+$ as a mixture of reactants, is leaving fully reacted at the end of the flame. Then,

$$\int_0^\infty \omega_{eq}\, dy \sim m \tag{III.13}$$

When suitable average values are employed, an associated overall length scale, δ_f, may be introduced:

$$\overline{\omega}_{eq}\, \delta_f = m \tag{III.14}$$

where

$$\overline{\omega}_{eq} \sim \overline{\omega_1 + \omega_2} \sim \overline{\omega}_1 + \overline{\omega}_2 .$$

The averages $\overline{\omega}_1$ and $\overline{\omega}_2$, cf. Eqs. (III.1a) and (III.1b), can be obtained by using temperature-explicit expressions for the kinetics constants, as well as for the mass fractions of 'R', 'F', and 'O'. The latter may be obtained by suitable approximate profiles. Employing a method similar to the centroid rule of Spalding:[65,66]

$$\int_{\tau_s}^1 \omega_j(\tau)(\tau - \overline{\tau}_j)\, d\tau = 0, \quad j = 1,2$$

where τ is a dimensionless temperature, normalized in the range where the particular ω_j is applicable, and $\overline{\tau}_j = \text{const}$ denotes the temperature-centroid, to be found from the above expression. The resulting $\overline{\tau}_j$ or $\overline{T}_j$ lead to unequivocal definitions of $\omega_1(\overline{T}_1)$ and $\omega_2(\overline{T}_2)$.

Neglecting kinetic energy, an overall enthalpy balance results from the first integral of the energy equation. Approximately, using the overall scale of Eq. (III.14):

$$m \overline{C_p} \Delta T_f + \overline{\lambda} \Delta T_f / \delta_f \sim Q_{eq} \int_0^\infty \omega_{eq} \, dy \qquad \text{(III.15)}$$

T_f being the net gain in temperature throughout the gaseous flame zone. After some modification, the result of substitution of Eqs. (III.13) and (III.14) into the energy balance, Eq. (III.15), is:

$$1 + \left[\overline{\omega}_1 + \overline{\omega}_2 \right] \frac{\overline{\lambda}}{\overline{C_p}} / m^2 \sim Q_{eq} / \overline{C_p} \Delta T_f \qquad \text{(III.16)}$$

In regular deflagration situations, convective, diffusive, and reactive processes are expected to be of equal importance. For such cases,

$$Q_{eq} / \overline{C_p} \Delta T_f \sim O(1)$$

It follows then from Eq. (III.16) directly, that

$$\left[\overline{\omega}_1 + \overline{\omega}_2 \right] \frac{\overline{\lambda}}{\overline{C_p}} / m^2 \sim O(1)$$

and hence,

$$m \sim \left[\frac{\overline{\lambda}}{\overline{C_p}} \left(\overline{\omega}_1 + \overline{\omega}_2 \right) \right]^{1/2}$$

This result is indentical with the well known expression obtained for laminar premixed deflagration, when $\overline{\omega}_{eq}$ is substituted for $\overline{\omega}_1 + \overline{\omega}_2$ (cf. Penner,[64] and Williams[65]).

Thus,

$$m \sim \left(\frac{\overline{\lambda}}{\overline{C_p}} \right)^{\frac{1}{2}} \overline{\omega}_2^{1/2} \left[1 + \overline{\omega}_1 / \overline{\omega}_2 \right]^{1/2} \qquad \text{(III.17)}$$

Using now the pressure dependencies of each of the elements in the last equation, namely, $\overline{\omega}_1 \sim p$ and $\overline{\omega}_2 \sim p^2$ one obtains:

$$m \sim p(1 + B_p/p)^{1/2} \qquad \text{(III.18)}$$

where B_p = const is formally pressure independent and has the dimension of pressure.

In order to define the parameters involved more explicitly, the following approximation is considered,

$$\overline{\omega}_{eq} \doteq B_1 \overline{\omega}_1 + B_2 \overline{\omega}_2$$

where B_1 and B_2 are dimensionless proportionality constants; this is in line with the proposed asymptotic behavior given by Eq. (III.11). Without loss of generality, let $B_1 = B$ and $B_2 = 1$. Hence, from Eq. (III.18),

$$m = a \phi (1 + 1/\phi)^{1/2} \qquad \text{(III.19a)}$$

where a is a proportionality constant,

$$\phi \equiv p/B_p$$

and

$$B_p \equiv \bar{B}\left(\frac{\bar{\omega}_1}{p}\right)\Big/\left(\frac{\bar{\omega}_2}{p^2}\right)$$

Alternatively, the last equation can be written in dimensional form:

$$m = b[p(p + B_p)]^{1/2} \qquad\qquad (III.19b)$$

where b is a proportionality constant.

Equations (III.19a) and (III.19b) constitute two-parameter formulae, with $(a;B_p)$ describing the burning rate of nitramine monopropellants over a wide range of pressures. Physical gas phase reasoning, incorporating two distinct chemical reactions, has led to the explicit pressure dependence shown.

To demonstrate the validity of the foregoing results, two groups of experimental data were correlated by use of Eq. (III.19b). The low pressure (0.5 to 6.6 MPa) mass burning rate measurements of Bobolev et al[53] made on porous columns of RDX, are correlated in Fig. III.1, with b = 2.57 $(kg/m^2-s)/MPa$, and B_p = 3.8 MPa. On the same plot, the measurements of Zimmer-Galler[55] for pressed RDX pellets burning in nitrogen atmosphere are depicted without correlation; the original results were in inches/sec, and the density of the pellets (not reported) was assumed that of pure RDX to facilitate plotting. In Fig. III.2, the linear regression rate data of Boggs et al[49] at pressures from 1 to 140 MPa, are correlated. The asymptotic burning rate correlation in this case yields B_p = 36.7 MPa; the reason for the O(10) difference between the B_p parameters is embedded in the data, with the high pressure measurements[49] somewhat on the low side, probably due to the small amount of polymer binder added. Overall, Eq. (III.19b) presents a good correlation in both cases separately, with the upward shift in the apparent burning rate pressure exponent clearly evident, as pressure increases. It should be said that the agreement in no way serves as proof for the theory. However, it demonstrates consistency between the predictions made and experimental observations.

2. Pressure-Dependence of the Length Scales

The burning rate pressure exponent, n , can be implicitly defined,

$$\phi^{n-1/2} \equiv m/a\phi^{1/2} = (1+\phi)^{1/2}$$

by use of Eq.(III.19a). Obviously, n is pressure dependent . Its values at the extreme limits of high (p >> B_p) and low (p << B_p) pressures can be readily derived,

$$\lim_{\phi \to 0} (n - \tfrac{1}{2}) = \lim_{\phi \to 0} \left[\tfrac{1}{2} \log (1 + \phi) / \log \phi \right] = 0 \implies n = \tfrac{1}{2}$$

$$\lim_{\phi \to \infty} (n - \tfrac{1}{2}) = \lim_{\phi \to \infty} \left[\tfrac{1}{2} \log (1 + \phi) / \log \phi \right] = \tfrac{1}{2} \implies n = 1$$

Therefore, at intermediate pressures, $0.5 < n < 1$ should be expected. Indeed, values of n between 0.7 and 0.8 have been reported [49,53,20] for $1 < p < 100$ MPa, and the burning rate data indicate increase of n as pressure is increased.[49,50,53]

The pressure dependence of the length scales is given explicitly, using Eq.(III.18):

$$\delta_D^* = \rho D / m \sim 1/m \sim p^{-1} (1 + B_p / p)^{-1/2} \tag{III.20a}$$

$$\delta_{R1}^* = m / \bar{\omega}_1 \sim (1 + B_p / p)^{1/2} \tag{III.20b}$$

$$\delta_{R2}^* = m / \bar{\omega}_2 \sim (1 + B_p / p)^{1/2} / p \tag{III.20c}$$

At the low pressure limit, when $p \ll B_p$, $n = 0.5$ and hence $\delta_D^* \sim \delta_{R1}^* \sim p^{-1/2}$, while $\delta_{R2}^* \sim p^{-3/2}$. Thus,

$$\delta_D^* \sim \delta_{R1}^* \ll \delta_{R2}^* \tag{III.21}$$

At the high pressure limit, when $p \gg B_p$, $n = 1$ and hence $\delta_D^* \sim \delta_{R2}^* \sim 1/p$, but the pressure dependence of δ_{R1}^* tends to vanish formally.

The δ_{R1}^* behavior here indicates that a first order overall reaction (such as that of primary decomposition), if it coexisted with a second order one, would tend to have a finite, constant length scale as the high pressure limit is approached:

$$\delta_D^* \sim \delta_{R2}^* \ll \delta_{R1}^* \sim const$$

The picture presented by the above relationship is misleading to a large extent, since thermal effects have been excluded. Consider the process in the flame zone as the high pressure limit is approached form below, in a

quasi-steady manner. The secondary reaction rate, possessing the most sensitivity to pressure, would be the fastest to increase; with it, δ^*_{R2} will decrease. This means that the secondary reaction would tend to occur to an increasing extent within the region previously dominated by primary decomposition. Hence, an enhancement of heat release in that zone (particularly pronounced near the outer edge where reactant concentrations and temperature are high enough for the secondary reaction) and increase of the mean temperature should result. This, in turn, would enhance appreciably the primary reaction, since its thermal sensitivity (represented by the typically large activation energy) is the greatest. What would thus be observed is an accelerated decrease of the primary reaction zone thickness, and with it the δ^*_{R1} scale, as follows from the linearized expression for small increments $\Delta p/p$ and $\Delta T_1/\bar{T}_1$:

$$\Delta \delta^*_{R1}/(\delta^*_{R1}) \sim (n-1)\Delta p/p + (1 - E_1/R_u \bar{T}_1)\Delta \bar{T}_1/\bar{T}_1 \qquad (III.22)$$

The first term of the right hand side is small absolutely and negative, for $n < 1$, but the second term contains an amplification factor, $(E_1/R_u \bar{T}_1) \sim O(10)$, representing a large decrement, as $\Delta T_1/\bar{T}_1 \sim \Delta p/p > 0$. So, one may find that δ^*_{R1} decreases $\sim 10\Delta p/p$, an order of magnitude faster than δ^*_{R2}, for which

$$\Delta \delta^*_{R2}/(\delta^*_{R2}) \sim (n-2)\Delta p/p \sim O(\Delta p/p) \qquad (III.23)$$

Note that the above process does not induce changes in T_2 associated with the secondary reaction -- T_2 being higher than the primary flame temperature. δ^*_D contains a weak (relatively speaking) temperature dependence that may be neglected here.

As higher pressures are reached in this manner, the primary reaction zone is pushed further against the condensed phase surface, its length scale diminishing in an accelerated manner. Hence, a more reasonable model for the deflagration process at the high pressure limit emerges:

$$\delta^*_D \sim \delta^*_{R2} \gg \delta^*_{R1} \qquad (III.24)$$

with the primary nitramine decomposition reaction tending to "collapse" or localize at the condensed/gas interface.

The three associated flame field length scales are plotted against pressure in Fig. III.3, over the range $0.1 < p < 100$ MPa. Equations (III.20 a,b,c) were utilized, with reference values:

$$\overline{\omega}^*_1(1 \text{ MPa}) = 7 \times 10^5 \text{ Kg/m}^3\text{-s}$$

$$\overline{\omega}^*_2(1 \text{ MPa}) = 5 \times 10^3 \text{ Kg/m}^3\text{-s}$$

$$\overline{\rho D}(1000K) = 6 \times 10^{-5} \text{ Kg/m-s}$$

Equation (III.19b) was used with the values of b and B_p from the Bobolev[53] burning rate correlation, Fig. III.1. For comparison, flame length data corresponding to double base (DB)[67,68] and to ammonium perchlorate (AP)[69-71] propellants are provided in Fig. III.3 as well. The observations are

summarized as follows.

a. The secondary reactive scale δ^*_{R2} is shown to be within an order of magnitude of the measured dark zone thickness of a DB propellant made by Kubota,[67] over a range $0.1 < p < 1.0$ MPa, and by Maltsev[68] at 1.5 MPa.

b. Regarding the foregoing discussion of the thermal effect within the near field, two lines represent the primary reactive scale, δ^*_{R1}. The upper line corresponds to $\bar{\omega}_1 \sim p$ (with $\bar{T}_1 = $ const) while the lower line contains a (maximal) equivalent pressure correction due to thermal effects, with $\bar{\omega}_1 \sim p^{1.5}$.

c. In the range $1 < p < 10$ MPa corresponding to rocket operation, δ^*_D, δ^*_{R1} and the pure-AP data of Guirao and Williams[69] are all within the same order of magnitude, with actual lengths varying between 20. and 0.8 μm.

d. The calculated lengths for AP composite propellant flames made by Steinz[70] are roughly one order of magnitude higher (for the oxidizer-fuel or secondary flame) and one order of magnitude lower (for the close-in $NH_3 + HClO_4$ flame) than the data discussed in (c). The close-in flame data[70] are corroborated by the single point estimate of Friedman et al.[71]

To conclude, the length scale comparison of Fig. III.3 indicates certain structural similarities between nitramine and DB flames. The diffusive and primary reaction scales, δ^*_D and δ^*_{R1} are close to the calculated close-in AP flame lengths, showing that the primary influence on the burning rate of nitramines would be exerted by the near field processes.

3. Critique

In the way of critique of the present treatment, the following arguments are pertinent.

a. Condensed phase processes were precluded from the present calculation, concerned with the gaseous flame zone. It was shown in Section II.C that nitramine decomposition occurs in the condensed phase and the extent of this reaction tends to increase with increasing pressure. Appreciable subsurface heat release may decrease the dependence of the deflagration rate upon heat feedback from the gas phase, and, hence, upon pressure. This may change the foregoing results, particularly those concerning asymptotic behavior at the high pressure limit.

b. The chemical mechanism leading to the present 2-reaction configuration has been derived largely from pyrolysis data. Consequently, it might not hold for high rate processes which occur under large pressures. Besides the expected modification of reaction paths, a substantial influence of pressure upon kinetic constants might be involved, as noted by Kamlet.[72]

Keeping in mind these limitations, it is still possible to draw a few conclusions here. Based on gas phase considerations alone, the burning rate

exponent being 0.7 to 0.8 in the low range of intermediate pressures may be explained; this is obtained from the combined influence of both first order overall nitramine decomposition and secondary (second order overall) reactions upon the heat feedback to the propellant surface.

At both high and low pressure limits, the gaseous flame zone would be characterized by convective-diffusive-reactive processes. The particular pressure dependence of the associated length scales brings about $\delta_D^* \sim \delta_{R1}^* \ll \delta_{R2}^*$ at the low pressure range. At the high pressure range, combined pressure and thermal effects bring about $\delta_D^* \sim \delta_{R2}^* \gg \delta_{R1}^*$.

The existence of 2 distinct length scales at the low pressure range leads to the concept of a boundary layer type problem, investigated in the next section. In contrast, the distinct length scales associated with the behavior at the high pressure range indicate a uniform (although probably quite thin) gaseous flame zone, with a single, second order overall chemical reaction term; the primary decomposition reaction may then be considered to be effectively "collapsed" at the condensed surface.

D. Gaseous Flame Field Theory at the Low Range of Intermediate Pressures

The present section is intended to demonstrate certain analytical features inherent in the problem of nitramine deflagration in the low range of intermediate pressures. The main objective is to demonstrate the validity of division of the gaseous flame zone into near field and far field in a rigorous manner.

The proportions found among the pertinent length scales in the problem lead directly to a boundary layer type formulation. This analysis is pursued to the point where statement of the gas phase problem in the form known as Matched Asymptotic Expansions[73,74] is made. The hierarchy of equations that results is used as the means by which the various physical and chemical interactions in the flame zone could best be illuminated. For this reason, actual solution to the problem is not attempted within this framework; however, the physical insight obtained will strongly influence the manner by which solution to the full nonlinear problem is sought, a task undertaken in the next chapter.

1. Overall Flame Field Configuration

The gaseous flame field is considered to be a laminar, pre-mixed one-dimensional flow at steady state. The assumptions leading to the equations of motion, as well as the equations, are stated in detail in Section IV.B. For simplicity, $\rho D = \lambda/Cp = \text{const}$ and $\overline{W} = \text{const}$ were assumed; these are in no way essential, and are employed only for the purpose of a clearer demonstration of the present ideas.

Properties that appear in both dimensional and dimensionless forms are marked herein with an asterisk when dimensional. The symbols follow those of Section C as closely as possible.

The overall mass and momentum conservation statements are, respectively:

$$m \equiv \rho u = const$$

$$p = const$$

The transport equations for the entire flame region in terms of the mixture enthalpy and species mass fractions are, for $0^+ < y^* < +\infty$:

$$m\frac{dh^*}{dy^*} - \left(\frac{\lambda}{c_p}\right)\frac{d^2 h^*}{dy^{*2}} = \omega_1^* Q_1^* + \omega_2^* Q_2^* \qquad \text{(III.25a)}$$

$$m\frac{dY_i}{dy^*} - (\rho D)\frac{d^2 Y_i}{dy^{*2}} = w_{1,i}^* + w_{2,i}^* , \qquad \text{(III.25b)}$$

$$i = 1, 2, \cdots N$$

h^* is the thermal enthalpy of the mixture, defined

$$h^* \equiv \int_{T^0}^{T} c_p(T')dT'$$

and $w_{k,i}^*$ are the specific rates (depletion or production) for the ith species in the kth reaction,

$$w_{k,i} = W_i \left(\nu''_{i,k} - \nu'_{i,k}\right)\omega_k^* / \overline{W} \qquad \text{(III.26)}$$

The following dimensionless parameters are introduced:

$$\tau \equiv h^*/Q_1^* , \quad \omega_1 \equiv \omega_1^*/\overline{\omega}_1 , \quad \omega_2 \equiv \omega_2^*/\overline{\omega}_2$$

$$y \equiv y^*/\delta^*$$

with δ^* being some overall length scale, defined more precisely later. The energy equation becomes, for $0^+ < y < +\infty$:

$$\frac{d\tau}{dy} - \frac{\lambda/c_p}{m}\frac{1}{\delta^*}\frac{d^2\tau}{dy^2} = \frac{\delta^*}{m/\overline{\omega}_1}\omega_1 + \frac{\delta^*}{m/\overline{\omega}_2}\frac{Q_2^*}{Q_1^*}\omega_2 \qquad \text{(III.27)}$$

A similar transform may be applied to the species equations (III.25b).

Consider now the lower range of intermediate pressures, where it has been found that

$$\delta_D^* \sim \delta_{R1}^* \ll \delta_{R2}^*$$

as defined previously. Since at the end of the gaseous flame zone all chemical processes go to completion by definition, a suitable global length scale would be $\delta^* \equiv \delta^*_{R2}$, including all possible reactions. Using this scale in the energy equation (III.27):

$$\frac{d\tau}{dy} - \varepsilon \frac{d^2\tau}{dy^2} = \frac{\Lambda}{\varepsilon}\,\omega_1 + \frac{Q_2}{Q_1}\,\omega_2 \qquad \text{(III.28)}$$

where

$$\Lambda \equiv \delta^*_D / \delta^*_{R1} = \frac{\rho D \overline{\omega}^*_1}{m^2} \sim O(1) \qquad \text{(III.29)}$$

and

$$\varepsilon \equiv \delta^*_D / \delta^*_{R2} = \frac{\rho D \overline{\omega}^*_2}{m^2} \ll 1 \qquad \text{(III.30)}$$

Clearly, the quantity $0 < \varepsilon \ll 1$ defined here is the ratio of 2 length scales of the flow field. Its appearance in the reduced differential operator, Eq. (III.28), as multiplier of the highest derivative gives the present flame zone formulation the properties of a singular perturbation problem of the boundary layer type.[73,74]

The boundary conditions (BCs herein) written in terms of the dimensionless variables are discussed next.

Denoting the condensed-gas phase interface by $y = 0$, the associated conservation relations for mass, energy and species are, after some modification,

$$m_g = m_p = m$$

$$\left[m h^* - \frac{\lambda}{c_p} \frac{dh^*}{dy^*} \right]_{0^+} - \left[m h^*_c - \frac{\lambda_c}{c_c} \frac{dh^*_c}{dy^*} \right]_{0^-} = -m Q^*_s$$

$$\left[m Y_i - \rho D \frac{dY_i}{dy^*} \right]_{0^+} - \left[m Y_i \right]_{0^-} = 0, \quad i = 1, 2; \cdots N \qquad \text{(III.31)}$$

following Scala and Sutton[75] and Williams.[76] The physical arguments leading to the energy and species interface balances are depicted schematically in Figs. III.4 and III.5 respectively.

In the foregoing equations, h^*_c and h^* denote thermal enthalpies on the condensed and gas sides of the interface, respectively, and Q^*_s is the net chemical enthalpy change across the interface ($Q^*_s > 0$ for net depletion, as for endothermic vaporization or sublimation). Molecular diffusion was assumed negligible within the condenses phase. In the case of exothermic subsurface reaction, Q^*_s may incorporate (in an approximate manner) the net heat produced by this reaction, and hence would depend upon the surface temperature, T_s.

Note that a no-slip condition applies to the interface temperature, namely, $T(0^+) = T(0^-) \equiv T_s$, but thermal enthalpies may differ across the

interface, as $h^*(0^+) \neq h_c^*(0^-)$, for obvious reasons.

The conservation conditions in dimensionless form are written,

$$\tau(0^+) - \varepsilon \frac{d\tau}{dy}(0^+) = \tau_c(0^-) - \frac{d\tau_c}{dy_c}(0^-) - \tilde{Q}_s \qquad \text{(III.32a)}$$

$$Y_i(0^+) - \varepsilon \frac{dY_i}{dy}(0^+) = Y_i(0^-), \quad i = 1, 2 \cdots N \qquad \text{(III.32b)}$$

where the following dimensionless condensed phase properties have been introduced: $\tau_c \equiv h_c^*/Q_i^*$, $\tilde{Q}_s \equiv Q_s^*/Q_i^*$ and the dimensionless condensed phase coordinate,

$$y_c \equiv y^*/(\lambda_c/mC_c) \qquad \text{(III.33)}$$

The species conservation condition, Eq. (III.32b) implies that in the case of nonvanishing diffusion on the gas side ($y = 0^+$) of the interface, a discontinuity in the mass fractions would occur across the phase boundary, viz., $Y_j(0^-) \neq Y_j(0^+)$. Such discontinuity is anticipated whenever the diffusional terms on both sides of the flow interface are unequal, in absence of rapid surface reactions, as discussed by Bird, Stuart and Lightfoot.[77]

Evidently, the left-hand sides of both enthalpy and species conservation conditions, Eqs. (III.32a,b), reduce exactly to the same form, involving total (convective and diffusive) flux terms.

The boundary conditions at $y^* \rightarrow \infty$ may be written in dimensionless form directly:

$$\tau(\infty) = \tau_f \qquad \text{(III.34a)}$$

$$Y_i(\infty) = Y_{i,f} , \quad i = 1, 2, \cdots N \qquad \text{(III.34b)}$$

where subscript f denotes the fully reacted final flame conditions.

The foregoing results strongly indicate the plausibility of casting the theory of the gaseous deflagration wave in terms of a near field and a far field. The near field, where primary decomposition of nitramine dominates, and the process is characteristically convective-diffusive-reactive, is a narrow, high gradient region adjacent to the propellant surface. The far field, on the other hand, occupies a relatively wide region, dominated by subsequent secondary reactions (second order, overall), e.g., $CH_2O + NO_2$, where gradients are low by comparison to the near field and the process is predominantly convective-reactive. This flame field configuration is illustrated in Fig. III.6, showing temperature and species profiles and reaction rates.

The derivation and discussion of the near field and far field asymptotic

theory is the subject of the remainder of this chapter.

2. The Near Field Flame Region

The near field can be depicted as a narrow region in the gas, in the neighborhood of $y = 0^+$ with length $O(\varepsilon)$, where nitramine decomposition dominates the chemical processes. Here, high rates of change (namely, high gradients) are expected; [73,74] particularly, the diffusive terms, d^2/dy^2 assume relatively high importance. This region, previously identified by comparison of chemical length scales alone, may now be fully realized analytically.

Let the magnified length coordinate applicable to this region, be defined:

$$\zeta \equiv y/\varepsilon \tag{III.35}$$

The corresponding dimensionless dependent variables for enthalpy and species are, respectively:

$$\theta(\zeta, \varepsilon) \sim \sum_{n=0}^{\infty} \mu_n(\varepsilon)\, \theta_n(\zeta)$$

$$\eta_i(\zeta, \varepsilon) \sim \sum_{n=0}^{\infty} \mu_n(\varepsilon)\, \eta_{i,n}(\zeta), \quad i = 1,2 \cdots N \tag{III.36}$$

represented by the above inner expansions as $\varepsilon \to 0$ with ζ fixed.

The functions $\mu_n(\varepsilon)$ are expected to be simply powers of ε, with leading term $\mu_0(\varepsilon) = \varepsilon^0 = 1$. Likewise, the leading terms of the dependent variable expansions are expected to be $\theta_0 \sim O(1)$ and $\eta_{i,0} \sim O(1)$, $i = 1,2 \ldots N$ for the dimensionless system. The reduced reaction rates $\tilde{\omega}_1(\theta, n_i \ldots)$ and $\tilde{\omega}_2(\theta, n_i \ldots)$ should be expanded in θ and η_i, about their zeroth order values. It can be shown that $\tilde{\omega}_1$ and $\tilde{\omega}_2$ would also have leading terms $\sim O(1)$.

The energy equation, after transformation to near field variables, reads:

$$\frac{d\theta}{d\zeta} - \frac{d^2\theta}{d\zeta^2} = \Lambda \tilde{\omega}_1 + \varepsilon \frac{Q_2}{Q_1} \tilde{\omega}_2 \tag{III.37}$$

The species conservation equations are similar. The near field BCs are constituted of the transformed $y = 0^+$ BCs of the general system. The outer (or $y \to \infty$) BCs cannot be satisfied by the near field equations, for obvious reasons.

$$\theta(0^+, \varepsilon) - \frac{d\theta}{d\zeta}(0^+, \varepsilon) = \phi_T(0^-, \varepsilon) \equiv \theta_c(0^-, \varepsilon) - \frac{d\theta_c}{dy_c}(0^-, \varepsilon) - \tilde{Q}_s(\varepsilon)$$

$$\eta_i(0^+, \varepsilon) - \frac{d\eta_i}{d\zeta}(0^+, \varepsilon) = \phi_i(0^-, \varepsilon) \equiv \eta_{c,i}(0^-, \varepsilon), \quad i = 1,2, \cdots N$$

$$\tag{III.38}$$

where suitable expansions, similar to Eq. (III.36) were taken for condensed phase and surface parameters.

The parameter Λ has the role of an eigenvalue in the present system, and must also be perturbed. Its expansion, which should be uniformly valid throughout the entire flame field:

$$\Lambda(\varepsilon) \sim \sum_{n=0}^{\infty} \gamma_n(\varepsilon) \Lambda^{(n)} = \Lambda^0 + \cdots \qquad \text{(III.39)}$$

again, with $\gamma_0(\varepsilon) = \varepsilon^0 = 1$, taken so that the leading term is $\sim O(1)$ for obvious reasons.

To lowest order in ε (zeroth order), the system reads:

$$\frac{d\theta_0}{d\xi} - \frac{d^2\theta_0}{d\xi^2} = \Lambda^0 \tilde{\omega}_{1,0}(\theta_0, \eta_{R,0}) \qquad \text{(III.40a)}$$

$$\frac{d\eta_{i,0}}{d\xi} - \frac{d^2\eta_{i,0}}{d\xi^2} = \Lambda^0 \tilde{\omega}_{1,0}(\theta_0, \eta_{R,0}), \quad i = 1, 2, \cdots N \qquad \text{(III.40b)}$$

where $\eta_i = Y_i \bar{W}/W_i(\nu''_{1,i} - \nu'_{1,i})$. The BCs for this system are (given at $y = 0$ only):

$$\theta_0(0^+) - \frac{d\theta_0}{d\xi}(0^+) = \phi_T^0$$

$$\eta_{i,0}(0^+) - \frac{d\eta_{i,0}}{d\xi}(0^+) = \phi_i^0, \quad i = 1, 2, \cdots N \qquad \text{(III.40c)}$$

3. The Far Field Flame Region

In the far field, the most difficulty seems to arise from the $\Lambda\omega_1/\varepsilon$ term, corresponding to nitramine decomposition. Let:

$$\omega_1 = Y_R K_1 \exp(-\beta_1/\tau)/\tau$$

$$K_1 \equiv (C_p\bar{T}/Q_1^*) \exp(+E_1/R_u\bar{T})/Y_R^* \qquad \text{(III.41)}$$

K_1 is a constant, chosen so that $\omega_1 = \omega_1^*/\bar{\omega}_1$ is satisfied, with $\bar{\omega}_1$ given by Eqs. (III.1a,c). It is expected that nitramine decomposition, due to its relatively rapid rate be close to completion at the outer end of the near field, where $y \sim O(\varepsilon)$ and $T \approx 1000$ K. This means that already at that point, relatively low concentrations of nitramine (small Y_R) should prevail. If indeed we take $Y_R \sim O(\varepsilon)$ in the far field, then $\Lambda\tilde{\omega}_1/\varepsilon \sim O(1)$ since $\tilde{\omega}_1 \sim Y_R$. Hence, when we let $\varepsilon \rightarrow 0$ the above term will not grow unbounded. Then, the problem concerning the $\Lambda\omega_1/\varepsilon$ term is settled for

all but the Y_R conservation equation itself, where the $1/\varepsilon$ term persists. This equation may be written:

$$\varepsilon \frac{d^2 Y_R}{dy^2} - \frac{dY_R}{dy} - \frac{\Lambda}{\varepsilon} \frac{W_R}{\overline{W}} \omega_1 = 0$$

where $y \equiv y^*/\delta_{R2}^*$, and with the boundedness condition being $Y_R(\infty) = 0$. Put in more explicit form, the Y_R equation is:

$$\varepsilon \frac{d^2 Y_R}{dy^2} - \frac{dY_R}{dy} - \frac{\tilde{q}_R}{\varepsilon} Y_R = 0 \tag{III.42}$$

where

$$\tilde{q}_R \equiv \Lambda (W_R/\overline{W}) k_1 \exp(-\beta_1/\tau)/\tau$$

For the RDX (in TNT solution[13]) properties of Table II.3, in the range of temperatures between 1000 and 3000 K (corresponding to the region $\varepsilon < y < \infty$) $\tilde{q}_R$ will increase from $O(10)$ to $O(10^5)$, through roughly 4 orders of magnitude. $\tilde{q}_R = \tilde{q}_R[\tau(y)]$ is a bounded, Lipschitz-continuous function of y in the domain of interest. An admissible solution of Eq. (III.42) is the trivial one, $Y_R(y) = 0$ which also satisfies the given condition of boundedness. This, however, poses a difficulty when matching with the near-field solution is attempted.

A non-trivial solution may be sought, utilizing the following transform of Y_R:

$$Y_R(y) = \exp[-\alpha(y)/\varepsilon] f(y) \tag{III.43}$$

where $\alpha(y)$ is a continuous function, possessing at least 2 derivatives; we leave it as yet unspecified. $f(y)$ represents the relatively slowly varying properties of Y_R. Substitution into Eq. (III.42) results, after some rearrangement:

$$\varepsilon f'' - (1 + 2\alpha') + [-\alpha'' + (\alpha')^2/\varepsilon - \tilde{q}_R/\varepsilon] f = 0 \tag{III.44}$$

where a prime denotes d/dy herein.

When the requirement for least degeneracy is invoked (remembering, however, that the far field should be predominantly convective-reactive), $\alpha(y)$ can now be defined by letting

$$(\alpha')^2 + \alpha' - \tilde{q}_R = 0 \tag{III.45}$$

which effectively eliminates the fast (or steep) variation associated with the $1/\varepsilon$ term, and restores the balance between the f' and the f terms. The solution to the quadratic equation (III.45) is:

$$G(y) \equiv \alpha' = [-1 + (1 + 4\tilde{q}_R)^{1/2}]/2 \tag{III.46}$$

where the negative root has been discarded, so that $G(y) > 0$ in the domain of interest, and the exponential term in the Y_R expression of Eq. (III.43) would decay in an accelerated manner as y increases. $\alpha(y)$ is given by the indefinite integral,

$$\alpha(y) = \int^{(y)} G(y)\,dy \qquad \text{(III.47)}$$

The equation for f(y) now can be written:

$$(1 + 2G)f' + G'f = \varepsilon f'' \qquad \text{(III.48)}$$

Expanding f(y) in the following asymptotic series,

$$f(y,\varepsilon) \sim \sum_{n=0}^{\infty} \varepsilon^n f_n(y) \qquad \text{(III.49)}$$

as $\varepsilon \to 0$ with y held fixed. Simple powers of ε are suggested here by both the $\varepsilon f''$ term and the near field solution structure; $f_n(y) \sim O(1)$ in the above expansion for all n.

Substitution of this expansion into Eq. (III.48) results in a hierarchy of equations for $f_n(y)$, $n = 1, 2, \ldots$. The lowest (zeroth) order equation is:

$$f_o'/f_o = -G'/(1 + 2G)$$

which integrates simply to yield

$$f_o(y) \propto \left[1 + 4q_R(y)\right]^{-1/4} \qquad \text{(III.50)}$$

where Eq. (III.46) for the definition of G was used, after integration. $f_0(y)$ will in general decrease with increasing y, but it has a much slower rate of decay than that described by the $\exp[-\alpha(y)/\varepsilon]$ term. Note that the integration constant was omitted; it is properly reserved for the full Y_R expression:

$$Y_R^{(0)}(y,\varepsilon) = c^{(0)} \exp\left[-\alpha(y)/\varepsilon\right]/\left[1 + 4q_R\right]^{1/4} \qquad \text{(III.51)}$$

which describes the lowest order of $Y_R(y)$ in the far field. The constant coefficient $c^{(0)}$ is to be determined by the conditions of matching with the near field solution.

Suppose now that at the outer end of the near field the nitramine concentration is such that $Y_R^{(1)}(\zeta \simeq 1) \sim O(\varepsilon)$. This implies

$$Y_R^{(0)} \sim O(\varepsilon), \quad c^{(0)} = \varepsilon c_1 + O(\varepsilon^2)$$

with $c_1 \sim O(1)$ provided that $\exp[-\alpha(\varepsilon)/\varepsilon] \sim O(1)$. Hence,

$\Lambda\omega_1(\tau, Y_R^{(0)})/\varepsilon \sim O(1)$ in the far field, causing this term to appear in the far field formulation to lowest order. The influence of ω_1 upon the far

field solution (for variables other than Y_R itself) should not be of great importance in this case, since $Y_R^{(0)}(y)$ would cause the ω_1 term to decay quite rapidly. On the other hand, coupling between the far field and the near field prevails to lowest order. Particularly, this means that Λ is influenced by the far field processes to lowest order. Of course, this is contrary to observed physical processes, since the strongest influence upon the burning rate eigenvalue (through the strong coupling between burning rate, m_p, and heat feedback to the condensed phase) would come primarily from processes in the immediate vicinity of the condensed/gas interface, i.e., the near field.

Thus, it is concluded here that:

$$ Y_R^{(0)} \sim O(\varepsilon^2) $$

(or less)

which will be shown to effectively de-couple the lowest order near field and far field problems. Therefore, it is assumed now:

$$ C^{(0)} = \varepsilon^2 C_2 + O(\varepsilon^3), \quad C_2 \sim O(1) \qquad \text{(III.52)} $$

To complete this discussion of the far field, we turn now to the rest of the dependent variables. Retaining the global coordinate and dependent variable notation for the far field, the latter are represented by the outer expansions:

$$ \tau(y, \varepsilon) \sim \sum_{n=0}^{\infty} \psi_n(\varepsilon) \tau_n(y) $$

$$ Y_i^{(0)}(y, \varepsilon) \sim \sum_{n=0}^{\infty} \psi_n(\varepsilon) Y_{i,n}(y) $$

$$ \text{(III.53)} $$

asymptotically, as $\varepsilon \to 0$ and y fixed. For $Y_R^{(0)}$, according to the foregoing line of reasoning, the leading term in the Y_R expansion is $\sim O(\varepsilon^2)$. The functions $\psi_n(\varepsilon)$ in the above formulation may be thought of as integral powers of ε, similar to the near field expansions.

The energy and species conservation equations are identical to those of the global system, Eq. (III.28) and shall not be repeated. Substitution of Eq. (III.53) into these conservation equations, utilizing suitable outer expansions for $\omega_1(\tau, Y_R)$ and $\omega_2(\tau, Y_F, Y_O)$ results in a hierarchy of ordinary differential equations. To lowest order in ε, the system reads:

$$\frac{d\tau_0}{dy} = \frac{Q_2}{Q_1} \omega_2^{(0)}(\tau_0, Y_F^0, Y_0^0)$$

(III.54)

$$\frac{dY_i^0}{dy} = \alpha_{2,i} \omega_2^{(0)}(\tau_0, Y_F^0, Y_0^0), \quad i \neq R$$

where

$$\alpha_{2,i} \equiv W_i(\nu_{2,i}'' - \nu_{2,i}')/\overline{W}$$

Note that

$$\Lambda^0 \omega_1^{(2)}(\tau_0, Y_R^{(2)})/\varepsilon \sim O(\varepsilon)$$

will appear for the first time in the first-order formulation of the far field. Consequently, all species that are associated with the ω_1 reaction only, will have homogeneous zeroth order equations. The BCs at $y = \infty$ are

$$\tau_0(\infty) = \tau_f, \quad Y_i^0(\infty) = Y_{i,f}, \quad i = 1, 2, \cdots N$$

(III.55)

with subsequent orders of the dependent variables having homogeneous conditions, (namely, conditions at $y = \infty$ remain unperturbed).

It is evident now that the far field is constituted of a hierarchy of first-order systems of equations for which the number of BCs given is adequate. To lowest (zeroth) order in ε, the preceding formulation of Eqs. (III.54) and (III.55) is independent of the near field; analytical solutions for this system can be obtained with relative ease. The method of solution is briefly outlined in the following. Noting the similarity between enthalpy and all species involved in the ω_2 reaction, suitable Shvab-Zeldovich coupling parameters can be formed:

$$C_i \equiv \frac{Q_1}{Q_2} \tau_0 - Y_i^0/\alpha_{2,i} = const$$

(III.56)

all of which satisfy $dc_i/dy = 0$ and are found from the given conditions at infinity. This allows, particularly, the expression of Y_F^0 and Y_O^0 as functions of τ_0. The problem then amounts to integrating the full equation (III.54), viz.,

$$\int^{(y)} dy = \frac{Q_1}{Q_2} \int^{(\tau_0)} \frac{d\tau_0}{\omega_2^{(0)}(\tau_0)}$$

(III.57)

Integration here may be carried out by use of asymptotic methods, utilizing the relatively large reduced activation energy of ω_2 as perturbation quantity. The method would be similar to that of Appendix B, for the simplified condensed

phase model.

4. The Flame Speed Eigenvalue

The expansions given in Eq. (III.39) is treated now with the objective of obtaining a more explicit relationship and further insight into the nature of the solutions. Consider the asymptotic burning rate formula of Eq. (III.19),

$$m = m_0 \left(1 + \varepsilon \overline{\overline{\pi}}\right)^{1/2} \tag{III.58}$$

Slightly re-written, with $m_0 \sim p^{1/2}$ and $\varepsilon\overline{\overline{\pi}} \sim p$. A plausible asymptotic expansion of the mass burning rate is therefore suggested,

$$m \sim m_0 \left[1 + \varepsilon\pi_1 + \varepsilon^2\pi_2 + \cdots\right]^{1/2} \tag{III.59}$$

as $\varepsilon \to 0$, at any point in the field. This expression may be now utilized in the development of the Λ -expansion, as follows.

The flame speed eigenvalue, in explicit form, is

$$\Lambda = \rho D \overline{\omega}_1^0 / m^2 \sim f(p)/m^2$$

with $f(p) \sim p$, since $\overline{\omega}_1^0 \sim p$. The expansion in general is, cf. Eq. (III.39),

$$\Lambda \sim \Lambda^0 \left[1 + \varepsilon\widetilde{\Lambda}^{(1)} + \varepsilon^2\widetilde{\Lambda}^{(2)} + \cdots\right]$$

where

$$\Lambda^0 = f(p)/m^2 \sim p^0 \sim const$$

and

$$\widetilde{\Lambda}^{(i)} \equiv \Lambda^{(i)}/\Lambda^0 , \quad i = 1, 2, \cdots$$

Substituting Eq. (III.59) in the expression, it becomes

$$\Lambda \sim \Lambda^0 / \left[1 + \varepsilon\pi_1 + \varepsilon^2\pi_2 + \cdots\right] \tag{III.60}$$

as $\varepsilon \to 0$, at any point in the field; using a Taylor series expansion in Eq. (III.60), the Λ-expansion may be written in short form,

$$\Lambda \sim \Lambda^0 \left(1 - \varepsilon\overline{\overline{\pi}}\right) \tag{III.61}$$

where

$$\varepsilon\overline{\overline{\pi}} = \varepsilon\widetilde{\Lambda}^{(1)} + \varepsilon^2\widetilde{\Lambda}^{(2)} + \cdots$$

implied by the required equivalence between Eqs. (III.60), (III.61) and (III.19). The important implications of the present development are summarized as follows.

a. Λ^0 = const is pressure independent for all pressures under which the theory is valid. Hence, zeroth order near field solutions are always self similar.

b.   By considering the zeroth order term Λ^0 alone, one may account for $m \sim p^{1/2}$ only, namely, zeroth order considerations may yield only the mass burning rate pressure dependence at the strict lower pressure limit.

c.   First order (and higher) considerations must be incorporated in order to bring about the true pressure dependence of both the eigenvalue and the burning rate, at the particular pressure range of interest. The actual magnitude of $\varepsilon\bar{\pi}$ relative to unity will determine the correct $m \sim p^n$ (or n, the pressure exponent) dependence, at the particular p investigated.

d.   The overall higher order effect in Λ , entering through the $\varepsilon\bar{\pi}$ term in Eq. (III.61) is a decrement, and its pressure dependence is always given by

$$\varepsilon\bar{\pi} \sim p \qquad\qquad (III.62)$$

at all pressures for which the theory is valid.

5.   Discussion

The matching of near field and far field expansions in an overlap domain of common validity is excluded here. Detailed discussions of this subject are given in the works of Van Dyke[73] and Cole.[74] In the most elementary case, matching between zeroth plus first-order far-field and zeroth near-field solutions would be attempted, since the matching procedure provides exact relations between finite, partial sums.[73]

Although to lowest (zeroth) order in the near-field system, Eq. (III.40) is considerably simpler than the fully nonlinear overall flame field problem, analytical solutions are still hard to obtain without further simplification. Note also that a full statement of the near field problem should involve the condensed phase process equations in a perturbed form, as required by the enthalpy and species BCs, Eq. (III.40c). These have been omitted here, since complete solution was not intended by the present method. Detailed treatment of the nonlinear condensed phase problem is given in Chapter IV, Section C.

There are a few works in which the method of matched asymptotic expansions was utilized in study deflagration problems, mostly with a single overall chemical reaction step. A brief review of these seems in order now.

The relatively large activation energy (or an equivalent property) associated with chemical reactions in most deflagration problems of interest[78] is utilized in all of the works described herein as a (large) perturbation quantity. This facilitates the definition of a relatively thin, high-gradient reactive zone within the overall deflagration wave, since under these

conditions the reaction would effectively occur under temperatures quite close to that of the fully reacted flame. The high activation energy concept forms the basis for the approximate analytical treatment of solid propellant deflagration advanced by Zel'dovich[79,80] essential for the assumption that the entire gas phase reaction is localized at the final flame temperature.

Jaine and Kumar[31] used a temperature-power expression of the form $\tau^n n^s$ where s = const and n denotes "activation energy", to represent the reaction rate term; this is similar to the temperature-explicit approximation proposed by Spalding.[65,66] Their calculated flame speed eigenvalues (equivalent to the defined in the present study) are admittedly difficult to compare with other data where Arrhenius-type reaction rates were used.

Bush and Fendell[82] used the method successfully to compute the flame speed eigenvalue up to second order in ε, for a single, first-order overall chemical reaction. A modified Arrhenius rate expression was used to overcome the cold boundary difficulty. The entire deflagration wave was divided into 2 sub-regions as follows: (a) a thin "downstream" reactive zone, where temperatures are close to that of the fully reacted flame, the process being characteristically reactive-diffusive-convective; and (b) a relatively thick "upstream" nonreacting region where temperatures are low, so the process is convective-diffusive. Normalized temperature was used as an independent variable, and the process of matching "inner" (a) and "outer" (b) solutions required an intermediate expansion. Using the 2 leading terms in the eigenvalue expansion, the above authors found very good agreement with the numerically computed values by Friedman and Burke:[83] errors within 1% were observed for normalized activation temperature of O(10).

Williams[84] has applied the methodology and lowest order result (namely Λ^0 = 1/2, with Le = 1) of Bush and Fendell[82] to the case of solid propellant deflagration. The equivalence of the pure gaseous pre-mixed deflagration and normal solid deflagration problems was shown for the case of large activation energy in the gas. The analysis does not go beyond zeroth order, and obviously applies to propellant configurations (and pressures) where the pre-mixed gas phase assumption applies.

Joulin and Clavin[85] considered a two-step reaction in the form

$$R \longrightarrow X \longrightarrow PRODUCTS + Q_{R2}$$
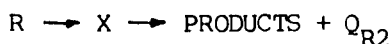
where X denotes an intermediate radical. Both steps were assumed to involve comparable high activation energies, but only the final step was allowed any exothermicity (Q_{R1} = 0 for the first step). Similar to the analysis of Bush and Fendell,[82] a narrow, high temperature reaction zone was postulated, the independent variable used being the reduced temperature. Zeroth order solution was obtained for the flame speed eigenvalue, and the effect of the intermediate X upon laminar flame speed shown within this framework, for the case that X possessed a distinct binary diffusion coefficient with the products (shown through the use of distinct Lewis numbers). Details of the solution procedure were completely omitted, and the source of the 0.5 factor in the Λ^0 expression (as well as its analytical expression) remain unclear.

The high activation energy of the primary decomposition reaction in the

present problem could be utilized (in a manner similar to the asymptotic analysis in the aforementioned studies[82,85] to obtain an approximate analytical solution for the zeroth order near field problem. However, this would involve an expansion-within-expansion, and was precluded herein.

6. Conclusions

(a) The burning rate eigenvalue expansion has a pressure independent term $\Lambda^0 \sim O(1)$ which appears only in the near field formulation, considering the zeroth order problem. Consequently, Λ^0 is fully determined by the zeroth order near field configuration, regardless of pressure. Λ^0 may be found, for instance, by applying the successive lower and upper bound iterative method of Johnson and Nachbar.[65]

The next higher order solution in Λ introduces influences due to the secondary reaction in the near field [by the ω_2 term, cf. Eq. (III.37)], due to far field processes (through matching) and due to the actual pressure in the field. This leads to the conclusion that the interaction between the secondary reaction and the gas burning rate, m_p, is not of primary nature quantitatively, but extremely important in a qualitative sense, e.g., elucidating the pressure dependence.

(b) For the particular range of pressures considered here, the actual values of ε for the case of RDX deflagration may be found using Table III.1. These are $\varepsilon \doteq 1/40$ to $1/20$. It is expected that the expansions proceed in integral powers of ε (as mentioned previously, using the *principle of least degeneracy of the equations*).

Hence, the error involved in any near field or far field variable, computed to zeroth order only, is expected to be $O(\varepsilon)$; using the values of ε for RDX, this amounts to 2.5 to 5% roughly, in the range p = 1.0 to 4.0 MPa. Nonlinear effects, such as temperature- and concentration-dependent properties might account for additional deviations from the exact solution.

(c) The pressure dependence of within the region of applicability of the theory, is given by

$$\varepsilon = \rho D \overline{\omega_2}/m^2 \sim p^2/m^2 \sim p^{2-2n} \qquad (III.63a)$$

with $0 < \varepsilon \ll 1$. Note that n, the apparent burning rate pressure exponent, is variable for large enough variations in pressure, as given by Eq. (III.19). The pressure dependence of Λ is given by

$$\Lambda = \rho D \overline{\omega_1}/m^2 \sim \frac{\Lambda^0}{1+\varepsilon \overline{\pi}} \sim \frac{1}{1+p} \qquad (III.63b)$$

At the low pressure limit, n = 0.5 and $\varepsilon \sim p$; since $p \rightarrow 0$ at that limit, Λ is pressure-independent. At this limit only, both near field and far field solutions to zeroth order are pressure-independent, namely self similar. Otherwise, the solutions depend explicitly on p through ε and Λ, and in this respect are dissimilar.

Although high pressures were intrinsically excluded from the preceding analysis, some interesting observations can be made regarding the behavior of

the system at the high pressure limit. For extremely high pressures, $n \doteq 1$ so that $\mathcal{E}$ tends to be pressure independent and $\Lambda \sim 1/p$. Up to that limit, as the pressure increases, $\mathcal{E} \sim p^{2-2n}$ increases as well; therefore, a switching or reversal of roles seems to occur between $\mathcal{E}$ and Λ (as between ω_1 and ω_2): now $\mathcal{E}$ may be considered as "eigenvalue" while $\Lambda \sim 1/p \ll 1$ as a small- perturbation quantity, provided that the thermal effects do not interfere significantly with the decreasing of Λ (being much more sensitive to temperature than $\mathcal{E}$ due to the high activation energy E_1, as mentioned earlier).

In the intermediate pressure range, where $0.5 < n < 1.0$, Λ is decreasing while $\mathcal{E}$ is increasing with p. Thus, with increasing pressure in the intermediate range one may observe a shift of main influence from the primary nitramine decomposition at the lower pressure range, to the secondary reaction at higher pressures. In the meantime, the distinction between near field and far field, based according to the foregoing arguments on $\mathcal{E}$ being small, tends to diminish and a uniform (but absolutely thin) flame region can be foreseen. This may be manifested by gradual decrease of the near field gradients, associated with an increase of the far field gradients, both in dimensionless form.

(d) The difficulty in obtaining analytical solutions by the present method was mentioned earlier. It is stressed here that the preceding theory was primarily intended to put the physical ideas which have evolved in the previous sections in a rigorous analytical form. The implied zeroth order results provide valuable guidance to the continuation of this study by solving the nonlinear deflagration model numerically. Therefore, at the pressure range considered, emphasis should be placed on the domain close to the condensed phase surface, where primary decomposition of nitramine dominates the chemical processes.

CHAPTER IV

STEADY DEFLAGRATION ANALYSIS OF A NITRAMINE MONOPROPELLANT IN
THE RANGE OF PRESSURES FROM 1.0 to 4.0 MPa

A. Introduction

Following the analysis of Chapter III and the conclusions therein, a
solution to the full deflagration problem is the subject of the present
chapter.

In this chapter the gas phase and condensed phase elements are treated
separately; they are combined in the complete solution through the solid-liquid
interface conservation conditions.

In order to represent physical reality as closely as possible, variable
thermophysical properties are necessary in the gas phase. With the two
proposed chemical reactions, this amounts to a nonlinear problem in which the
various coefficients are solution dependent. Hence, numerical techniques were
employed to facilitate solution. The formulation of the gas phase processes is
treated in Section B. Section D contains the details of the numerical
solution. Calculation of the thermophysical properties pertinent to the gas
phase is given in Appendix A, along with the corresponding data.

The condensed phase involves a liquid layer in which nitramine
decomposition is considered. Although thermophysical parameters in the
condensed phase were taken as constant because of insufficient data, the
situation here is also nonlinear. The condensed phase analysis is presented in
Section C; a special case (thin liquid layer), for which analytical solution
was possible, is treated separately in Appendix B.

In Section E the present analysis is concluded with the description of the
actual process of obtaining solutions to the deflagration problem, by combining
the various elements in an iterative manner.

B. Formulation of the Gas Phase Problem

The analysis of Chapter III has shown that distinct far field and near
field regions can be identified in the overall flame field, within the range of
pressures of interest. It was also shown that the near field processes have
primary influence upon the burning rate, while the far field processes exert a
weaker influence, although non-negligible.

Within the framework of a solution to the full deflagration problem,
attention is focused upon the gas phase behavior in the region adjacent to the
condensed-gas interface. In this particular region the intention is to
represent the process as accurately as possible. This amounts to having a
nonlinear problem, in general, with the two simultaneous chemical reactions
chosen to represent the chemical processes.

The treatment of the gas phase here is aimed at obtaining a mathematically
well-posed problem which is tractable. Not surprisingly, a two-point boundary
value problem evolves; for purposes of the present section, the boundary
conditions are considered to be known finite constants; the objective is to
obtain solutions for this gas phase formulation. These solution manifolds are

not to be confused with solution of the entire deflagration problem, since some
of them might correspond to eigenvalues which are not physically realistic.

1. Assumptions

The reactive gas phase region is considered essentially as a
one-dimensional, pre-mixed laminar flame. The pre-mixedness follows from the
assumed homogeneity of the nitramine monopropellant, in both chemical and
structural sense.

In setting up the formulation, assumptions common to theoretical gaseous
deflagration studies were employed. These follow very closely the assumptions
listed by Williams[65] and are presented here for completeness.
   (a) All binary molecular diffusion coefficients are assumed equal.
   (b) The Lewis number for individual species and for the mixture is taken
       equal to unity: Le = 1.
   (c) Pressure gradient- and thermal gradient-induced diffusion (the Soret
       and Dufor effects[65]) are negligible.
   (d) Viscous effects are negligible, as well as radiative transport.
   (e) The momentum statement for the gaseous flame field, typical to gaseous
       deflagrations, is

$$p(y) = const. \qquad (IV.1)$$

   (f) The gas mixture is assumed to have the properties of an ideal gas, for
       which the equation of state is:

$$p = \rho R_u T \sum_{i=1}^{N} Y_i / W_i \qquad (IV.2)$$

2. Nonlinear Gas Phase Deflagration Model

An inertial coordinate system is employed; the origin is affixed to the
condensed-gas interface, stationary in the observer frame of reference. The
interface is denoted $y = 0$, with y being the space coordinate. The gas phase
extends in the domain defined $0^+ < y < +\infty$, and flow is in the positive y
direction as illustrated in Fig. III.6.

According to the chemical mechanisms discussed in Chapter II, the
following reactions are considered here (given schematically):

a) Primary decomposition of nitramine in the gas phase:

$$R(g) \longrightarrow \sum_{i=2}^{N} \nu''_{1,i} S_i(g) + Q_1 \qquad (IV.3)$$
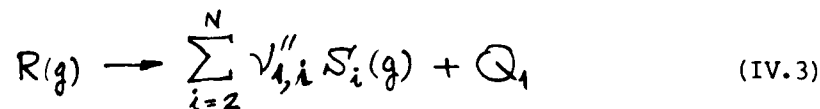
The S_i for which $\nu''_{1,i} \neq 0$ are products of this primary
decomposition; these involve typically the species NO_2, CH_2O, N_2O,
N_2, and others; mostly, they are not the final combustion products
observed at the end of the flame. Some of these species are involved
in subsequent secondary reactions.

b) Of all possible secondary reactions, a single representative one was chosen, second-order overall; written schematically:

$$F(g) + O(g) \longrightarrow \sum_{i=1}^{N} \nu''_{2,i} S_i(g) + Q_2 \quad \text{(IV.4)}$$
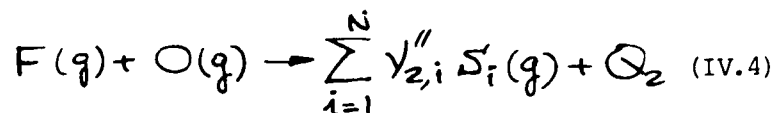
typically involving CH_2O and NO_2 as 'F' and 'O' respectively. This particular reaction, due to its relatively low activation energy, large pre-factor, and appreciable heat release Q_2, is most likely to influence the near field process. Note that although the reaction of Eq. (IV.4) involves 'F' and 'O' which are products of primary decomposition, both reactions are considered to be simultaneous; this is allowed by the sufficiently high temperature within the near field. The products of the secondary reaction are those species for which $\nu''_{2,i} \neq 0$; typically, these are CO_2, CO, H_2O, NO and others.

As indicated by the asymptotic analysis of Chapter III (in the range of pressures considered), secondary reactions would dominate the far field processes, but their effect upon heat feedback to the condensed surface is of secondary importance. In this respect, a more detailed secondary reaction mechanism would yield a better resolution of the far field part of the deflagration wave -- at the cost of appreciably increased computational effort. On the other hand, no great improvement upon the resulting flame speed eigenvalue can be expected.

To obtain a good resolution of the gas phase processes which influence heat feedback to the condensed phase the most, the region of interest in the gas shall be confined to the neighborhood of the condensed-gas interface; thus, a finite region is considered, such that $0^+ < y < y_f$, where

$$y_f = b \delta_D^* \quad \text{(IV.5)}$$

The dimensionless constant $b \geqslant 2$ typically; $\delta_D^* = \rho D/m$ is the diffusive length scale defined by Eq. (III.3).

The governing equations of motion for thermal enthalpy and species mass fractions are written in dimensional form:

$$\frac{d}{dy}\left(mh - \frac{\lambda}{c_p} \frac{dh}{dy} \right) = \omega_1 Q_1 + \omega_2 Q_2 \quad \text{(IV.6a)}$$

$$\frac{d}{dy}\left(mY_i - \rho D \frac{dY_i}{dy} \right) = \alpha_{1,i} \omega_1 + \alpha_{2,i} \omega_2, \quad \text{(IV.6b)}$$

$$i = 1, 2, \cdots N$$

for $0^+ < y < y_f$. The various parameters in Eqs. (IV.6a,b) are defined:

$$h \equiv \int_{T^0}^{T} c_p(T') dT' \quad \text{(IV.7a)}$$

$$\alpha_{k,i} \equiv W_i \left(\nu''_{k,l} - \nu'_{k,i} \right), \quad k=1,2 \ ; \quad i=1,2,\cdots N \qquad \text{(IV.7b)}$$

The overall reaction rate terms, ω_1 and ω_2 are defined by Eqs. (III.1a,b,c), but here local properties, i.e., $T(y)$ and $Y_i(y)$, $i = 1,2...N$ are to be used with the Arrhenius terms. The overall mass continuity statement is:

$$m \equiv \rho u = m_p \qquad \text{(IV.8)}$$

Due to assumptions (a) and (b), $\lambda / Cp = \rho D$ for all species. The derivation of Eqs. (IV.6a,b) involved the use of Fick's law for normal diffusion; likewise, the properties of ideal gas, uniform pressure, and overall continuity, Eqs. (IV.2), (IV.1), and (IV.8) have been utilized in the above derivation as well.

The parameters Cp and λ were taken dependent upon local temperature and species concentrations, so that:

$$C_p = \sum_{i=1}^{N} Y_i C_{p_i}(T) \qquad \text{(IV.9)}$$

$$\lambda / C_p = \rho D = f \left[T, Y_1, Y_2, \cdots Y_N \right] \qquad \text{(IV.10)}$$

A detailed discussion of the data and the modeling involved in actual calculations of Cp, λ and ρD are presented in Appendix A.

Equations (IV.6a,b) can be shown to constitute a system of N+1 coupled, nonlinear second order ordinary differential equations. Written in vector form,

$$G \, d^2U/dy^2 - C \, dU/dy + F = \underset{\sim}{0}, \qquad 0 < y < y_f \qquad \text{(IV.11)}$$

where

$$U^T(y) = (h \qquad Y_1 \qquad Y_2 \ldots Y_N) \qquad \text{(IV.12)}$$

defines the dependent variable vector. F is the vector of production terms; G is the diagonal diffusivities tensor and C the diagonal convective term tensor, containing elements of the form

$$m - d(\rho D)/dy \qquad \text{(IV.13)}$$

F, G, and C depend upon U(y), but not on y explicitly; hence the system of Eq. (IV.11) is termed autonomous.

The boundary conditions for the system of Eq. (IV.11) can be stated:

$$U(0^+) = U_s \qquad \text{(IV.14)}$$

$$dU/dy(y_f) = \underset{\sim}{0} \qquad \text{(IV.15)}$$

Equations (VI.11) through (IV.15) define the 2-point boundary value problem in the gas phase.

Comparison between Eq. (IV.14) and the rigorous condensed-gas interface constraints, Eqs. (III.31) and (III.32), reveals that no attempt is made at this point to satisfy the rigorous boundary conditions. Of course, the solution has to satisfy them eventually; more attention will be given this subject in Section D, dealing with the actual solution process. Thus, for the time being, in order to obtain a well-posed problem in the gas, the values of the dependent variable vector are simply imposed at $y = 0^+$, as given by U_s.

For a given set of ambient data, (P, T_0), the values of J_s and m are not known a priori; together, they form what may be termed here as a multi-dimensional flame speed eigenvalue (to borrow a phrase from deflagration analysis). This has to be ultimately defined in the complete solution of the deflagration problem.

Recalling the discussion of Chapter III, one may expect to find gradients dU/dy at y_f negligibly small compared with those near the $y = 0^+$ boundary. Hence, although the boundary condition of Eq. (IV.15) does not apply in a strict sense to any finite y_f in the gas, it is still expected to reasonably represent physical reality, within the realm of the present investigation of the near field.

Despite the similarity of the differential operators of Eq. (IV.11) for all species and enthalpy, the presence of multiple chemical reactions brings about F-vector components which prevent the simplification, usually obtained by forming suitable Shvab-Zeldovich coupling terms.[76,86] In other words, one may not reduce the problem to a single equation [of the form of Eq. (IV.11)] for one of the U-components, with the rest of the unknowns governed by homogeneous equations of the same form. Lees[87] has overcome this difficulty for the case of chain reactions in deflagration by formulating conservation laws for elements, rather than molecular species. The obvious advantage to Lees'[87] method is the homogeneity of the differential operators. Unfortunately, since certain molecular species profiles are of critical interest in the present study, Lees' method cannot be used.

Combining all chemical events into a single overall reaction step in the gas phase would greatly simplify the system formally, and allow the formation of Shvab-Zeldovich coupling parameters. This was done in a study of ammonium perchlorate monopropellant deflagration by Guirao and Williams.[69,88] The diversity of chemical length scales associated with the reactions considered here, at the low range of intermediate pressures, does not allow this simplifying procedure. Since numerical and not analytical solutions are sought for the present formulation, additional simplifying assumptions are not warranted. The clear advantage here is that relative effects of each reaction at any point of interest in the region $0 < y < y_f$ are directly revealed, as well as the effect of changes in the chemical mechanism or in the thermochemical parameters.

3. The System in Dimensionless Form

The system of conservation equations, Eqs. (IV.6a,b), may be re-cast in dimensionless form:

$$\frac{d\tau}{d\xi} - \frac{d^2\tau}{d\xi^2} = \Lambda F_\tau$$

$$\frac{dY_i}{d\xi} - \frac{d^2Y_i}{d\xi^2} = \Lambda F_i , \quad i = 1, 2, \cdots N \qquad \text{(IV.16)}$$

where the dimensionless specific (thermal) enthalpy is,

$$\tau(\xi) \equiv (W_1/Q_1) \int_{T^0}^{T} C_p(T')dT' \qquad \text{(IV.17a)}$$

and the dimensionless near field coordinate is defined,

$$\xi \equiv \int_0^y \frac{dy'}{(\rho D/m)} \qquad \text{(IV.17b)}$$

The production terms are

$$F_\tau \equiv \tilde{\omega}_1 + (Q_2/Q_1)(\mathcal{E}/\Lambda)\tilde{\omega}_2$$

$$F_i \equiv \alpha_{1,i}\tilde{\omega}_1 + (\mathcal{E}/\Lambda)\alpha_{2,i}\tilde{\omega}_2 , \quad i = 1, 2, \cdots N \qquad \text{(IV.17c)}$$

$\tilde{\omega}_1$ and $\tilde{\omega}_2$ are dimensionless reaction rates. Note that $\mathcal{E}$ and Λ are variable here, but defined similarly to their constant counterparts in Chap. III.

The boundary conditions at $\xi = 0^+$ for the above system are given by Eqs. (III.32a,b):

$$\tau(0^+) - d\tau/d\xi(0^+) = \phi_\tau(0^-)$$

$$\qquad \text{(IV.18a)}$$

$$Y_i(0^+) - dY_i/d\xi(0^+) = \phi_i(0^-), \quad i = 1, 2 \cdots N$$

A finite dimensionless near field length, b, may be chosen, cf. Eq. (IV.5); the imposed outer boundary conditions are

$$d\tau/d\xi(b) = dY_i/d\xi(b) \doteq 0 , \quad i = 1, 2, \cdots N \qquad \text{(IV.18b)}$$

The foregoing derivation is given here only for completeness of the mathematical model. For reasons of physical clarity, it has been decided in the development stages of the numerical algorithm to work with the original system, given by Eqs. (IV.6) through (IV.15), in dimensional form -- that is, in physical space.

C. Condensed Phase Analysis

1. The Liquid Layer

Experimental observations[35,37,49,51,52,56,57] confirm the existence of a liquid layer during deflagration of nitramines (HMX and RDX) at low to moderate pressures. According to Cohen and others,[56,57,35] the liquid layer tends to disappear at pressures higher than 70 atm. Regarding the relatively low melting point of nitramines (478 K for RDX) on one hand, and the strong exothermicity of the gaseous reactions adjacent to the propellant surface on the other, the existence of such a layer indeed seems plausible. This liquid layer separates effectively the solid and the gas phases in the range of pressures considered.

For temperatures above the melting point, nitramine decomposition in the liquid state has been studied by several investigators.[13-18] However, the rates of heating used in these thermochemical experiments (typically up to 90 degrees K per minute) are several orders of magnitude below those expected under normal deflagration situations; nevertheless, it is assumed that nitramine decomposition can occur in the liquid, under deflagration conditions. The studies mentioned here and the proposed chemical mechanism were discussed in Chapter II.

Scanning electron micrographs of deflagrating nitramine samples taken after extinction by Boggs, et al[49] and also by Cohen,[57] reveal entrapped gas bubbles under the extinguished surface. Unfortunately, extinguishment was achieved in all cases by rapid depressurization (following steady burning at 2 MPa in Boggs'[49] experiments); for this reason, one may not be certain about the actual presence of gas bubbles during the deflagration process itself.

Recently, experiments were conducted at Princeton University in which deflagrating HMX was rapidly extinguished at constant pressure by means of rapid deradiation.[89] The extinguished surfaces of these specimens are strikingly different from those extinguished by rapid depressurization -- the surfaces are smooth and froth is not detected on the surface or in the subsurface layer. A few isolated bubbles were observed, but their frequency of occurrence is much lower than observed by Boggs[49] and Cohen.[57]

Lengelle[90] has modeled the reacting liquid layer (endothermic) of a polymer undergoing pyrolytic degradation. This model was utilized by Guirao and Williams[69] in their analysis of deflagrating ammonium perchlorate (AP) monopropellant. A thin liquid layer was postulated, where 70% of the AP decomposition (exothermic) was assumed to occur. A uniform liquid phase temperature was assumed. In their case,[69] the exothermic gas phase reaction could not by itself support more than about 10% of the mass generation; in other words, the driving force sustaining steady deflagration was placed mostly in the exothermic liquid phase decomposition reaction. Therefore, with respect to the existance, reactivity and exothermicity of the liquid subsurface layer, an analogy can be drawn between deflagrating nitramine and AP monopropellant.

The subject of the remainder of this section is the theoretical analysis of the reacting liquid layer, incorporating the exothermic decomposition of nitramine in the liquid state.

2. Assumptions

The following assumptions are made, regarding the condensed phase analysis.

(a) The only reaction considered in the liquid phase is the overall unimolecular decomposition of nitramine, the products of which are gaseous. The actual reaction stoichiometry and the associated thermochemical parameters are given in Eq. (II.15) and in Appendix C. The specific case of RDX has been discussed in detail in Section II.D; for completeness, the reaction is written in general:

$$R(liq) \longrightarrow \sum_{i=2}^{N} \nu''_{1,i} S_i(g) + Q_{liq} \qquad (IV.19)$$
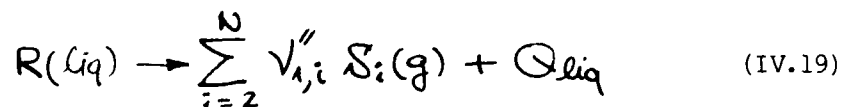
(b) Gaseous products of decomposition in the liquid are assumed to remain dissolved in the non-reacted liquid. These products are convected by the liquid toward the liquid-gas interface at $y = 0$. In the range of pressures considered in this study and with the relatively small extent of reaction expected, gas bubbles are not anticipated in the liquid.

(c) The liquid is assumed to be isotropic and to have uniform properties (density, thermal conductivity, heat capacity) throughout the entire width of the zone.

(d) Regarding the above thermophysical properties, actual calculations were performed using data which correspond to the solid state because of the lack of liquid phase information.

(e) Molecular (but not thermal) diffusivities in the liquid are assumed negligible compared with convection.

(f) Within the present framework, solid phase reactions or solid-solid phase transitions are not considered. In this respect, the present model is strictly applicable to RDX, for which such transitions are not observed, and to a somewhat lesser extent to HMX which exhibits such transitions; the heat involved in such transitions and the accompanying variation of thermophysical properties can be considered negligible here.

It is evident now that the present liquid phase model allows for nitramine decomposition and its associated heat release to occur anywhere in the liquid, under local (variable) concentration and temperature. No restriction is made a-priori on the physical thickness of the layer. Additional discussion of the liquid layer is included at the end of this section.

3. Comprehensive Condensed Phase Model

Consistent with the preceding gas phase analysis, the liquid phase is defined in the negative region $-y_m < y < 0$ where y_m denotes the liquid layer thickness; recall that the origin of the inertial coordinate system is affixed to the liquid-gas interface; relative to this origin, at steady state, the solid-liquid boundary is stationary: this boundary is uniquely defined as the

point where the substance is at its melting temperature, T_m, and the heat of fusion, Q_m, is depleted. Between the y_m and $y = 0$ boundaries, as solid liquefies at a constant rate, the liquid flows at a constant flux $m_p = m$ in the positive y direction.

The solid phase (taken as semi-infinite) is assumed to be adiabatic at infinity. As it translates at a constant rate r toward the $y = -y_m$ boundary, it is heated by conduction and its temperature increases from the ambient T_0 to T_m at $y = -y_m$.

The dimensional conservation equations for energy and nitramine (the only species followed explicitly) are, after some modification:

$$\frac{d^2 T}{dy^2} - \frac{r}{\alpha_c} \frac{dT}{dy} = -A_{m,l} \exp\left[-\frac{E_{m,l}}{R_u T}\right] Y Q_{liq} \frac{\rho_c}{\lambda_c} \tag{IV.20}$$

$$r \frac{dY}{dy} = -A_{m,l} \exp\left[-\frac{E_{m,l}}{R_u T}\right] Y \tag{IV.21}$$

$$-y_m < y < 0$$

The subscript 'R' was omitted from Y, which denotes nitramine here; the Arrhenius-type reaction rate term is shown explicitly. $r \equiv m/\rho_c$ is the linear regression rate, and $\alpha_c \equiv \lambda_c/\rho_c C_c$ the thermal diffusivity.

Transforming Eqs. (IV.20) and (IV.21) to dimensionless variables,

$$\zeta \equiv (y + y_m)/(\alpha_c/r) \tag{IV.22a}$$

$$\tau \equiv (T - T_m)/T^* \tag{IV.22b}$$

where $T^* \equiv Q_{liq}/C_c$, the system becomes:

$$\frac{d^2 \tau}{d\zeta^2} - \frac{d\tau}{d\zeta} = -F(\tau) Y \tag{IV.23a}$$

$$\frac{dY}{d\zeta} = -F(\tau) Y \tag{IV.23b}$$

with $F(\tau)$ being the temperature-dependent part of the reaction rate term. The dimensionless liquid layer thickness here is $a \equiv y_m/(\alpha_c/r)$; since the liquid layer thickness is not known beforehand, an auxiliary relation is provided by the energy balance at the liquid-solid interface:

$$\frac{d\tau}{d\zeta}(0^+) = [Q_m + C_c(T_m - T_0)]/C_c T^* \tag{IV.24}$$

The derivation of this equation is given in Appendix B. The boundary conditions of the system of Eqs. (IV.23) are:

$$\tau(0) = 0, \quad \tau(a) = (T_S - T_m)/T^* \equiv \tau_s, \quad Y(0) = 1. \quad \text{(IV.25)}$$

The total thermal flux in the negative ζ direction defines a new dependent variable:

$$\phi(\zeta) \equiv d\tau/d\zeta - \tau \qquad \text{(IV.26)}$$

The dimensionless system of Eqs. (IV.23) thus reduces to

$$\frac{d}{d\zeta}\begin{bmatrix} \phi \\ Y \end{bmatrix} = - F(\tau)Y \begin{bmatrix} 1 \\ 1 \end{bmatrix} \qquad \text{(IV.27)}$$

with the boundary conditions given by Eqs. (IV.24) and (IV.25).

The structure of Eq. (IV.27) obviously suggests the formation of a Shvab-Zeldovich-type coupling parameter, $\phi - Y$, for which $d(\phi - Y)/d\zeta = 0$ and hence,

$$\phi - Y = C_0 = \text{const} \qquad \text{(IV.28)}$$

with C_0 determined by the auxiliary condition and the boundary conditions, Eqs. (IV.24) and (IV.25) respectively, at $\zeta = 0$. Therefore:

$$C_0 = [Q_m + C_c(T_m - T_0)]/C_cT^* - 1. \qquad \text{(IV.29)}$$

These considerations eliminate one of the dependent variables (e.g., Y).

Finally, by a change of the independent variable, the problem is transformed to the phase plane; this is obtained by utilizing τ as the independent variable:

$$\frac{d}{d\zeta} = \frac{d\tau}{d\zeta}\frac{d}{d\tau} = (\phi + \tau)\frac{d}{d\tau}$$

This is allowed since $d\tau/d\zeta$ never vanishes in the region $0 < \zeta < a$, and $\tau(\zeta)$ is a continuous, monotonously varying function of ζ. The transformed system reads:

$$\frac{d}{d\tau}\begin{bmatrix} \phi \\ \zeta \end{bmatrix} = \frac{1}{\phi + \tau}\begin{bmatrix} (\phi - C_0)F(\tau) \\ 1 \end{bmatrix} \qquad \text{(IV.30)}$$

The boundary conditions are $\zeta(0) = 0$ and $\phi(0) = \phi_0$, where ϕ_0 is given by Eq. (IV.24), since $\tau(\zeta = 0) = 0$. The production term, given explicitly:

$$F(\tau) \equiv \frac{\alpha_c}{r} A_{m,1} \exp\left[- \frac{E_{m,1}}{\tau T^* + T_m}\right] \qquad \text{(IV.31)}$$

Thus, the original 2-point boundary value problem has been reduced to the equivalent non-autonomous initial value problem in $\phi(\tau)$ and $\zeta(\tau)$. Nitramine concentration at any point in the field is given by Eq. (IV.28). The remainder of the species' mass fractions are given by further coupling parameters, all of which reduce to the form:

$$Y_i = (1-Y)W_i (\nu''_{m,i} - \nu'_{m,i})/W_R, \quad i = 2, 3, \cdots N \qquad \text{(IV.32)}$$

Upper and lower bound estimates for $\phi(\tau)$ are obtained by selecting for the exponent in Eq. (IV.31) constant lower and upper values, respectively. Let

$$K_L \equiv F(\tau = 0), \qquad K_U \equiv F(\tau = \tau_s)$$

Denoting these in general by K, Eq. (IV.30) simplifies to:

$$\frac{d\phi}{d\tau} = -K(\phi - C_0)/(\phi + \tau) \qquad \text{(IV.33)}$$

for which the solution is given in implicit form:

$$K(\phi - C_o)^{1/K} [\tau + (\phi + KC_o)/(K + 1)] \equiv C_1 = \text{const.} \qquad \text{(IV.34)}$$

The integration constant C_1 is evaluated at the point [$\tau = 0$; $\phi(0)$]. As mentioned in the section dealing with the gas phase model, T_s and m are not known beforehand and should be specified during the process of solution. For a given value of m, specifying an unreasonably high T_s value for instance could lead to $d\tau/d\zeta = 0$ and a singularity would evolve. For this reason, it is important to obtain suitable estimates on $\phi(\tau_s)$ prior to attempting a solution; such estimates may be obtained by Eq. (IV.34) with $K \equiv K_U$.

To obtain a qualitative measure of the solution behavior, a more elementary model was set up. By assuming all heat release to be localized at the liquid-gas interface, yet allowing the chemical reaction to proceed within the layer [thereby excluding the production term from Eq. (IV.20) but not from Eq. (IV.21)], an analytical solution of the problem is made possible, using asymptotic methods. This concise model clearly approximates cases where only a small extent of nitramine decomposition occurs in the liquid phase. The concise model and its solution are the subject of Appendix B. A brief comparison of the two models (termed (1) "comprehensive" and (2) "concise" herein) follows in the remainder of the present section.

The liquid side of the $y = 0$ interface energy balance, cf. Eqs. (III.32a,b), can be written in dimensional form:

$$\phi^*_T (0^-) = mC_c(T_s - T^0) - q_c \qquad \text{(VI.35a)}$$

where T^0 is the reference temperature, and the solution-dependent part is defined:

$$q_c \equiv \lambda_c \frac{dT}{dy}_* (0^-) + m Q_s \tag{IV.35b}$$

In the absence of surface reactions, the term Q_s denotes in the comprehensive model the amount of heat required for gasification of the remaining nitramine at the surface:

$$Q_{s_1} \equiv Y_{R1}(0^-) Q_v \tag{IV.36a}$$

For the concise model, the Q_s term contains in addition the net heat release by the subsurface reaction, hence

$$Q_{s_2} \equiv Y_{R2}(0^-) Q_v - \left[1 - Y_{R2}(0^-)\right] Q_{liq} \tag{IV.36b}$$

since all of the condensed phase reaciton heat release is assumed to be localized at the $y = 0$ surface in the concise model. Turning now to the thermal gradients, at any point in the field $T_m < T < T_s$, the thermal gradient due to this model is larger than that due to the comprehensive one. This is due to the internal heat generation in the comprehensive model, which requires less conductive heat flux to maintain any particular temperature. Thus:

$$\left[\lambda_c dT/dy (0^-)\right]_1 < \left[\lambda_c dT/dy (0^-)\right]_2 \tag{IV.37}$$

for the same ambient conditions and (T_s, m). This in turn causes effectively that

$$y_{m1} > y_{m2} \tag{IV.38}$$

which can be deduced from physical scaling considerations involving Eq. (IV.37): $\Delta T \sim (T_s - T_m)$ and $\Delta y \sim y_m$. Now, from the inequality (IV.38), it is expected that:

$$Y_{R1}(0^-) < Y_{R2}(0^-) \tag{IV.39}$$

since the longer the residence time in the layer (which corresponds to the larger y_{m1}), the higher depletion of nitramine and, hence, lower $Y_{R1}(0^-)$. The heat of reaction, Q_{liq}, is typically 4 times larger than the heat of vaporization, Q_v. Thus, Eqs. (IV.36a,b) indicate that for small differences between $Y_{R1}(0^-)$ and $Y_{R2}(0^-)$, one obtains $Q_{s1} > Q_{s2}$.

Returning now to Eq. (IV.35), it is somewhat unanticipated that the Q_s and $\lambda_c dT/dy(0^-)$ effects combine in such a manner that q_c values obtained by both models are in excellent agreement; this is demonstrated graphically in the independent liquid layer results discussed in Chapter V.

Solutions to the independent comprehensive liquid layer model were obtained by integration of the system of Eqs. (IV.30a,b), utilizing a Runge-Kutta 4 procedure.

D. Numerical Solution

    The major subject of the present section is the solution of the gas phase problem. First, the numerical algorithm of the gas phase equations is derived and discussed for constant boundary conditions of the form given by Eqs. (IV.14) and (IV.15). Then, a method of varying dynamically the boundary data at $y = 0^+$ (in a manner which satisfies the interface conservation conditions) is presented. This naturally involves the incorporation of the condensed phase into the general solution procedure.

1. Pseudo Time Marching and the General Implicit Algorithm

    A convenient method for obtaining solutions to the steady state gas phase model is to formulate and solve the corresponding pseudo-nonsteady problem. The solution then is generated by time marching until equilibrium is achieved (in the sense that time variation has vanished).

    In the present configuration, the overall continuity and momentum statements remain strictly those of steady state, namely, m, p = const ; thus, the present pseudo-nonsteady formulation should not be confused with the rigorous time-dependent problem.

    The resulting system of nonsteady equations is obtained from Eq. (IV.11) and is of the parabolic type. Denoting now the nonsteady counterpart of the dependent variable vector U [defined in Eq. (IV.12)] by $\tilde{U}(t,y)$, the system is:

$$\frac{\partial \tilde{U}}{\partial t} = \tilde{G} \frac{\partial^2 \tilde{U}}{\partial y^2} - \tilde{C} \frac{\partial \tilde{U}}{\partial y} + \tilde{F}(\tilde{U}) \qquad \text{(IV.40)}$$

$$0 < y < y_f, \ t > 0$$

where $\tilde{G} = G/\rho$, $\tilde{F} = F/\rho$ and $\tilde{C} = C/\rho$; G, F, and C were defined for Eq. (IV.11). The boundary and initial data are:

$$\tilde{U}(t,0) = \tilde{U}_s, \quad \partial U/\partial y(t, y_f) = \underset{\sim}{0} \qquad \text{(IV.41a)}$$

$$\tilde{U}(0,y) = \tilde{U}_0(y) \qquad \text{(IV.41b)}$$

    A general-implicit finite difference algorithm is employed to solve the parabolic system given by Eqs. (IV.40) and (IV.41); denoting the numerical solution vector by $V(t,y)$, space and time are discretized: $y_n = n \Delta y$ and $t^j = j \Delta t$. The differential operations of Eq. (IV.40) are replaced by finite difference quotients as follows:

$$\left(\frac{\partial V}{\partial t}\right)_n^j \doteq (V_n^{j+1} - V_n^j)/\Delta t \qquad \text{(IV.42)}$$

which is forward-differencing (Euler form) in time, and

$$\left(\frac{\partial V}{\partial y}\right)_n^j \doteq \left(V_{n+1}^j - V_{n-1}^j \right)/2\Delta y \qquad \text{(IV.43a)}$$

$$\left(\frac{\partial^2 V}{\partial y^2}\right)_n^j \doteq \left(V_{n+1}^j - 2V_n^j + V_{n-1}^j \right)/\Delta y^2 \qquad \text{(IV.43b)}$$

which correspond to central differencing in space. Denoting the finite differenced right hand side of Eq. (IV.40) by R, after use of Eqs. (IV.42) and (IV.43) has been made, the general implicit algorithm reads:

$$V_n^{j+1} - V_n^j = \Delta t\, \theta' R_n^{j+1} + \Delta t(1-\theta') R_n^j \qquad \text{(IV.44)}$$

$$n = 1,2\ldots NF,$$

where $0 < \theta' < 1$ is the dimensionless general implicit parameter. All is considered to be known at time level j. The goal here is to obtain a linear algebraic system of equations involving the unknowns V^{j+1} at all space points. Due to the dependence of G, F, and C upon V [in the R_n^{j+1} expression of Eq. (IV.44)], these parameters must be quasi-linearized in order for Eq. (IV.44) to be linear in V_n^{j+1}. The quasi-linearization is done as follows:

(a) Using known data of time levels j and $j-1$, the value of V at time level $j+1$ is predicted:

$$V_n^{j+1,P} = 2V_n^j - V_n^{j-1} \qquad \text{(IV.45)}$$

At time level $j = 1$, one may simply use $V_n^{j+1,P} = V_n^j$.

(b) Using $V_n^{j+1,P}$, the terms in the coefficient tensors $\tilde{G}$ and $\tilde{C}$ can be calculated. These are denoted $\tilde{G}_n^{j+1,P}$ and $\tilde{C}_n^{j+1,P}$ at all points y_n.

The F vector is expanded to first order in a Taylor series about $V_n^{j+1,P}$:

$$\tilde{F}_n^{j+1} = \tilde{F}_n^{j+1,P} + \left(\partial\tilde{F}/\partial V\right)_n^{j+1,P}\left(V_n^{j+1} - V_n^{j+1,P}\right) \qquad \text{(IV.46)}$$

where $(\partial F/\partial V)_n^{j+1,P}$ denotes the proper Jacobian matrix, whose elements can be calculated explicitly from the known functional dependence of its terms upon V. The particular expansion of Eq. (IV.46) has better properties than an expansion about V_n^j for instance, since the reaction rate terms of $\tilde{F}$ depend on V in a stiff manner. R_n^{j+1} of Eq. (IV.44) can now be written more explicitly, in its present quasi-linearized form:

$$R_n^{j+1} = \tilde{G}_n^{j+1,P} \left[V_{n+1}^{j+1} - 2V_n^{j+1} + V_{n-1}^{j+1} \right]/\Delta y^2$$

$$- \tilde{C}_n^{j+1,P} \left[V_{n+1}^{j+1} - V_{n-1}^{j+1} \right]/2\Delta y$$

$$+ \tilde{F}_n^{j+1,P} + \left(\frac{\partial F}{\partial V}\right)_n^{j+1,P} \left[V_n^{j+1} - V_n^{j+1,P} \right]$$

$$\equiv \tilde{X}^{j+1,P} \cdot V_n^{j+1} \qquad\qquad (IV.47)$$

defining the quasi-linearized, spatial finite difference operator $\tilde{X}_n^{j+1,P}$. Utilizing this operator in Eq. (IV.44), after some rearrangement, results in

$$\left[I - \theta'\Delta t\, X_n^{j+1,P} \right] V_n^{j+1} = \left[V_n^j + (1-\theta')\Delta t\, R_n^j \right] \equiv Z_n^j \quad (IV.48)$$

where I is the identity matrix and Z_n^j is defined by the right hand side of Eq. (IV.48); Z_n^j at each step is given by the exact predictor:

$$Z_n^j = Z_n^{j-1} + (V_n^j - Z_n^{j-1})/\theta', \qquad \theta' > 0 \qquad\qquad (IV.49)$$

This follows from the identity $\qquad X_n^j V_n^j \equiv R_n^j,\qquad$ for converged solution at any time level j.

When all interior nodal points spacewise are considered, $n = 1,2,\ldots NF$, Eq. (IV.48) yields a set of NF algebraic equations in the unknown vectors V^{j+1}. This results in a block tridiagonal matrix equation (since each V_n^{j+1} is a vector of dimension N+1), solved by conventional decomposition and Gaussian elimination.[91,92] The specific algorithm used for this purpose is described in ? in Ref. 92.

The boundary conditions for the differential system, given by Eq. .41a), provide the required end-values for V:

$$V_{n=0} = U_s \qquad\qquad (IV.50a)$$

$$V_{NF+1} = V_{NF} \qquad\qquad (IV.50b)$$

where 0 and NF+1 denote the inner and outer boundary points, respectively.

The initial conditions, made necessary by the present pseudo-nonsteady configuration, are imposed in the form of second order polynomials to insure smoothness of the initial data:

$$V^{j=0} = \tilde{U}_0(y) = a + by + cy^2 \qquad\qquad (IV.51)$$

with the constant coefficient vectors a, b, and c determined by the conditions: $\tilde{U}_0(0) = U_s$, $d\tilde{U}_0/dy(y_f) = 0$, and $\tilde{U}_0(y_f) = V_f$. It was found that a convenient set of components for the vector V_f is provided by the conditions at the end of the near field (estimated, of course). Other sets of V_f-parameter configurations have been tried, yielding practically the same solutions. The following, however, must be observed:

(a) All mass fractions in the initial conditions must add up to unity.

(b) The chosen $T(y_f)$ must be sufficiently high to insure vigorous reaction initially, or else the system tends to "extinguish" within the first few time steps.

The finite difference algorithm described above is implemented in a predictor-corrector mode:

(a) The first (predicted) V^{j+1} solution is obtained by use of $X^{j+1,P}$ and V^j. This solution is used to re-calculate $X^{j+1,P}$.

(b) Using the re-calculated $X^{j+1,P}$ and V^j, the process is repeated to generate a new (corrected) V^{j+1} solution.

Although the predictor-corrector process can be repeated several times within each time step, it was found that a single passage through the (a) - (b) loop was sufficient, with additional passages producing negligible changes in V^{j+1}.

The subject of proper choice of Δy and Δt for this integration procedure is addressed next.

2. Space and Time Increments

The space increment is chosen:

$$\Delta y = \left[(\rho D)_s / m \right] / K_f \qquad (IV.52)$$

consistent with the specified y_f of Eq. (IV.5). The present difference algorithm utilizes a uniform mesh size, and the integer $K_f \sim O(10)$.

The pseudo-nonsteady system of Eq. (IV.40) is of the parabolic type. Consequently, the necessary and sufficient numerical stability criterion is[93] given by:

$$\bar{D} \Delta t / \Delta y^2 = B_1 \qquad (IV.53)$$

where $B_1 > 0$ is a finite constant and $\bar{D} = D_s$ is an average diffusion coefficient, chosen to represent the diagonal matrix $\bar{G} = G/\rho$. For values of $\theta > 1/2$, there is no formal restriction on the magnitude of B_1, since the algorithm of Eq. (IV.48) is termed unconditionally stable.[93] This should prevail throughout most of the region $0 < y < y_f$; however, as the domain of interest in the gas extends somewhat beyond the outer end of the near field, i.e., near y_f, the conditions are

$$d(\rho D)/dy \ll m$$

$$d^2 u/dy^2 \ll du/dy$$

Hence, as would be physically expected, the convective term dominates and to lowest order, the pseudo- nonsteady model for the neighborhood of $y \doteq y_f$ is:

$$\frac{\partial V}{\partial t} \doteq - \frac{m}{\rho} \frac{\partial V}{\partial y} + \tilde{F} \qquad (IV.54)$$

This configuration, in contrast to that given by Eq. (IV.40), is predominantly hyperbolic. For Eq. (IV.54), the Courant-Friedrichs-Lewy stability criterion is:

$$\frac{m}{\rho_f} \Delta t / \Delta y = B_2 \le 1 \qquad (IV.55)$$

where $\rho_f = \rho (y_f)$ which yields a maximal m/ρ .

It is evident now that the domain of interest in the gas, from the viewpoint of the pseudo-nonsteady algorithm, encompasses both parabolic-type (most of the space interval) and hyperbolic-type (near y_f) regions. To maintain numerical stability throughout the entire domain in space, both stability criteria, given by Eqs. (IV.53) and (IV.55), must be satisfied by the uniform choice of Δt. Of the two constraints mentioned, only the second one truly limits the choice of Δt, imposing an upper bound. Denoting by Δt_1 and Δt_2 the time increments associated with the conditions of Eqs. (IV.53) and (IV.55) respectively, their ratio is:

$$\Delta t_1 / \Delta t_2 = B_1 (\rho_s / \rho_f) / K_f \qquad (IV.56)$$

with $B_2 = 1$. Since most of the region $0 < y < y_f$ is parabolic, the choice falls naturally on the condition of Eq. (IV.53). In order not to violate the aforementioned hyperbolic constraint, it is required that $\Delta t_1 = \Delta t_2$ in Eq. (IV.56). Thus, the above equation constrains B_1:

$$B_1 \le K_f (\rho_f / \rho_s) \qquad (IV.57)$$

where $\rho_f / \rho_s \sim O(1/4)$ typically. Hence, $B_1 \stackrel{\sim}{<} 2.5$ is recommended.

3. Truncation Error Effects

The truncation error associated with the particular difference scheme described in the foregoing sections is the subject of the present treatment.

Expansion of V_n^{j+1} and R_n^{j+1} with respect to t about the point $(y_n; t^j)$ in Taylor series and substitution into Eq. (IV.44) yields:

$$\left(\frac{\partial V}{\partial t}\right)_n^j + \frac{1}{2!} \left(\frac{\partial^2 V}{\partial t^2}\right)_n^j \Delta t + O(\Delta t^2) =$$

$$\theta' \left[R_n^j + \left(\frac{\partial R}{\partial t}\right)_n^j \Delta t + O(\Delta t^2) \right] + (1-\theta') R_n^j \qquad (IV.58)$$

where it has been assumed that $V(y,t)$ and R are analytic in some small neighborhood of $(y_n; t^j)$. Hence, from Eq. (IV.58):

$$\left(\frac{\partial V}{\partial t}\right)_n^j = R_n^j + O(\Delta t) \qquad (IV.59)$$

Turning now to the difference quotients contained in R_n^j [cf. Eqs. (IV.43a,b) and (IV.47)] V_{n+1}^j and V_{n-1}^j are developed in

Taylor series with respect to y about the point $(y_n; t^j)$, obtaining:

$$R_n^j = \tilde{G}\left(\frac{\partial^2 V}{\partial y^2}\right)_n^j - \tilde{C}\left(\frac{\partial V}{\partial y}\right)_n^j + \tilde{F}$$

$$+ \Delta y^2\left[\frac{2\tilde{G}}{4!}\left(\frac{\partial^4 V}{\partial y^4}\right)_n^j - \frac{\tilde{C}}{3!}\left(\frac{\partial^3 V}{\partial y^3}\right)_n^j\right] + O(\Delta y^4)$$

$$\text{(IV.60)}$$

where the indices n, j have been omitted from G, C, and F. Equation (IV.60) can be written now explicitly

$$\frac{\partial V}{\partial t} = \tilde{G}\frac{\partial^2 V}{\partial y^2} - \tilde{C}\frac{\partial V}{\partial y} + \tilde{F} + O(\Delta t, \Delta y^2) \quad \text{(IV.61)}$$

The indices n, j have been omitted completely from the last equation; it is to apply to the entire region $0 < y < y_f$, $t > 0$.

To demonstrate consistency, the functional dependence $\Delta y = g(\Delta t)$ must be defined.[94] Utilizing Eq. (IV.53) for this purpose, it is evident that $\Delta y^2 \sim O(\Delta t)$. Now, letting $\Delta t \rightarrow 0$, the $O(\Delta t, \Delta y^2)$ terms uniformly vanish in Eq. (IV.61), assuming that the partial derivatives contained therein remain finite in the limiting process. Thus, consistency of the difference scheme with the original exact, pseudo-nonsteady configuration has been shown.

It should be emphasized that consistency and stability of the present pseudo-dynamic numerical algorithm are of interest only with regard to their influence upon the final steady state solution, namely for ensuring convergence. Yet, it is impossible to realize a final steady state with a numerically unstable difference algorithm, (implying no-convergence). For this reason, the numerical analysis herein is pursued as if the given differential system were genuinely time-dependent.

The truncation error is $O(\Delta t)$, or equivalently $O(\Delta y^2)$. Usually, finite, nonvanishing values of Δt and Δy are incorporated in actual numerical computations, and the physical implications of the associated truncation error terms are of interest. More specifically, we refer here to spurious diffusion (analog to artificial viscosity[95]), corresponding to the $\partial^2 V/\partial y^2$ member within the truncation error term.

Attending to the problem of the $O(\Delta t)$ term in Eq. (IV.58),

$$"O(\Delta t)" \sim \Delta t\left[\theta'\left(\frac{\partial R}{\partial t}\right) - \frac{1}{2}\left(\frac{\partial^2 V}{\partial t^2}\right)\right] \quad \text{(IV.62)}$$

According to Eqs. (IV.60) and (IV.61),

$$\Delta t \frac{\widetilde{\partial R}}{\partial t} = \Delta t \frac{\widetilde{\partial}}{\partial t} \left[\widetilde{G} \frac{\partial^2 V}{\partial y^2} - \widetilde{C} \frac{\partial V}{\partial y} + \widetilde{F} \right]$$

$$= \Delta t \frac{\widetilde{\partial}}{\partial t} \left(\frac{\partial V}{\partial t} \right)$$

where terms $O(\Delta t \cdot \Delta y^2)$ and higher have been neglected. Thus, the $O(\Delta t)$ expression is reduced to:

$$"O(\Delta t)" \sim \Delta t \left(\theta' - 1/2 \right) \left(\frac{\partial^2 V}{\partial t^2} \right) \qquad \text{(IV.63)}$$

When $\theta' = 1/2$, which corresponds to the Crank-Nicholson scheme,[96] the $O(\Delta t)$ term vanishes identically. For $\theta' > 1/2$ employed presently, the $O(\Delta t)$ term prevails throughout the nonsteady integration process, until steady state is reached; at the limit of steady state all time derivatives strictly vanish, and the $O(\Delta t)$ term uniformly vanishes.

Convergence to steady state may be defined in principle by the requirement that the dimensionless time-like variation of any gas field property not exceed an arbitrarily small quantity, ε_t, viz.,

$$\max_{n} \left| \Delta v / \Delta \widetilde{t} \right| \leq \varepsilon_t \qquad \text{(IV.64)}$$

at any time level, j. In the last equation, v denotes any dimensionless gas field variable, with the indices n,j omitted. $\Delta \widetilde{t} \equiv \Delta t / t_D^*$, and t_D^* is the associated near field time scale, defined by Eq. (III.5a). Using Eqs. (IV.52) and (IV.53), evidently $\Delta \widetilde{t} = B_1 / K_f^2$, since $\Delta y = \delta_D^* / K_f$.

An upper bound on the actual value of ε_t for practical purposes can be imposed through the requirement that the residual time variation at the convergent level be at most of the same order of magnitude as the truncation error, namely $O(\Delta t)$; finally, a somewhat more conservative value is given by

$$\varepsilon_t \sim O(\Delta \widetilde{t} \cdot \Delta y / \delta_D^*) \sim O(1 / K_f^3) \qquad \text{(IV.65)}$$

This amounts to $\varepsilon_t \sim O(1/1000)$ in practice.

Turning now to the $O(\Delta y^2)$ term in Eq. (IV.60), viz.,

$$"O(\Delta y^2)" = \Delta y^2 \left[\frac{2\widetilde{G}}{4!} \left(\frac{\partial^4 V}{\partial y^4} \right) - \frac{\widetilde{C}}{3!} \left(\frac{\partial^3 V}{\partial y^3} \right) \right] \qquad \text{(IV.66)}$$

the method of Roache[97] shall be employed to demonstrate stationary spurious diffusion. The main concern here is the solution at steady state; the $O(\Delta y^2)$ term does not vanish then. The differential operator to consider is:

$$\overline{D} \frac{\partial^2 V}{\partial y^2} - \overline{w} \frac{\partial V}{\partial y} + f V = 0 \qquad \text{(IV.67)}$$

using for purposes of demonstration a quasi-linearized version of Eq. (IV.40) at steady state, in any small neighborhood in the field. In the last equation, f is the Jacobian $(\partial F/\partial V)$, $D \doteq \tilde{G}$ and $\bar{w} \doteq \tilde{C}$, assuming local constant values for $\bar{D}$, f, and $\bar{w}$. The homogeneous linear operator of Eq. (IV.67) provides:

$$\bar{D} \frac{\partial^4 V}{\partial y^4} = \bar{w} \frac{\partial^3 V}{\partial y^3} - f \frac{\partial^2 V}{\partial y^2}$$

$$\frac{\partial^3 V}{\partial y^3} = \left(\frac{\bar{w}}{\bar{D}}\right) \frac{\partial^2 V}{\partial y^2} - \left(\frac{f}{\bar{D}}\right) \frac{\partial V}{\partial y}$$

$$\bar{w} \frac{\partial V}{\partial y} = \bar{D} \frac{\partial^2 V}{\partial y^2} + f V$$

The first two expressions can be utilized to eliminate the fourth and third order derivatives in Eq. (IV.66), and the last one to eliminate the $\partial/\partial y$ term which results from the substitution,

$$"O(\Delta y^2)" = \frac{\Delta y^2}{12} \left[-\left(\frac{\bar{w}}{\bar{D}}\right) \frac{\partial^2 V}{\partial y^2} + \left(\frac{f}{\bar{D}}\right)^2 V \right] \qquad (IV.68)$$

which consists entirely of dissipative-like terms. The stationary spurious diffusion term in Eq. (IV.68), defined:

$$D_{ss}^* \equiv -\Delta y^2 \bar{D} \left(\bar{w}/\bar{D}\right)^2 / 12 < 0 \qquad (IV.69)$$

is shown to be negative, regardless of the sign of $\bar{w}$.

Thus, the steady-state solutions to the gas phase problem, obtained by use of the present pseudo-nonsteady algorithm, correspond to a reduced diffusion coefficient (by a second order decrement in y). An approximate upper bound on D_{ss}^* can be obtained by considering the consistent set of parameters $\bar{D} = D_s$ and $\bar{w} \doteq m/\rho_s$ in Eq. (IV.69); using the definintion of Δy in Eq. (IV.52):

$$\left| D_{ss}^* / D_s \right|_{max} \sim O\left(1/12 \, K_f^2\right) \sim O\left(10^{-3}\right)$$

which represents a modest modification of approximately 0.1% in the value of D. A similar statement should hold, regarding the second term of Eq. (IV.68); since this term is positive-definite, it should tend to cancel with the $\partial^2/\partial y^2$ term wherever the latter is positive.

It should be emphasized here that the foregoing analysis, leading from Eq. (IV.66) to Eq. (IV.69), is approximate and intended only for purposes of physical interpretation of the truncation error term at the strict limit of steady state.

4. Properties of the Numerical Solution for the Gas Field

Actual stability of the present numerical algorithm was checked by perturbing several of the key parameters (e.g., m, activation energies, and pre-exponential factors). It was found that small variations introduced in these parameters and the boundary conditions cause correspondingly small changes in the solutions. Whereby, existence of neighboring solutions and smooth dependence upon the boundary data were demonstrated, indicating stable solutions.

Utilizing $\theta' = 0.8$ with Δy and Δt given by Eqs. (IV.52) and (IV.53) respectively, and with $B_1 = 1$ and $K_f = 12$, numerical instability was not encountered for any permissible set of boundary and initial data.

Although it would seem at this point that numerical solutions for the independent gas phase problem could be generated for any fictitious set of boundary data, this is strictly not the case. The existence of genuine solutions is definitely confined to certain intervals of valid boundary data and m, at any ambient pressure. Of all the observations regarding this property, the most interesting may be those resembling physical blowoff and flashback in actual gaseous deflagrations. These were obtained for fixed pressure and boundary data $\tilde{U}(t,0) = U_s$. Specifying too low mass flux, m, for the given conditions resulted in numerical flashback with gradients becoming steeper near $y = 0^+$ each timestep until numerical instability occurred. On the other hand, specifying too high m for the given conditions resulted in numerical blowoff, where gradients became finally vanishingly small and $\tilde{U}(t,y) \rightarrow U_s$. These phenomena occurred consistently throughout the pressure regime investigated and were reproducible. No attempts to pursue upper and lower limits of mass flux vs. pressure were made, since the solutions did not satisfy the rigorous condensed-gas interface conservation conditions and, to this end, remain no more than a numerical curiosity.

5. Relaxation Procedure for the Boundary Conditions at the Liquid-Gas Interface

Physically relevant solutions of the overall deflagration model must satisfy the rigorous conservation conditions at the liquid- gas interface, $y = 0$. This involves combination of the condensed phase and gas phase solutions.

As discussed in Section C, manifolds of condensed phase solutions can be generated numerically for specified (m, T_0, T_s) data. The results, concerning the $y = 0$ boundary only, written in dimensionless form:

$$\phi_T(0^-) = \phi_T^*(0^-)/mQ_1^*$$

$$\phi_i(0^-) = Y_i(0^-), \quad i = 1, 2, \cdots N$$

(IV.70)

defined by the right-hand sides of Eqs. (III.32), (IV.35), and (IV.36a).

Similarly, the gas phase may be integrated independently, for specified

sets of (p, m, U_s) data. Genuine gas phase solution manifolds thus obtained do not necessarily satisfy the physical interface conditions at $y = 0$.

According to Eqs. (IV.18), the dimensionless interface conservation conditions can be written in vector form:

$$\phi^- = v(0^+) - dv/d\xi(0^+) \qquad (IV.71)$$

where $v^T(0^+) \equiv [\tau(0^+) \quad Y(0^+) \quad \dots \quad Y_N(0^+)]$, with τ and ξ defined by the integrals of Eqs. (IV.17a,b), and $v(0^+) = v_s$ is the dimensionless counterpart of U_s. Consider now a fixed data set (T_0, m, p), along with a current value of the vector $v_s^{(k)}$, where k denotes the current pseudo-time level of $y = 0$ boundary conditions. The condensed phase solution yields $[\phi^-]^{(k+1)}$; the gas phase, integrated forward in pseudo-time, obtains all interior field point solutions, $v^{(k+1)}$. These values of $[\phi]^{(k+1)}$ and $v^{(k+1)}$ may be used in Eq. (IV.71) to obtain new values of the boundary vector, $v_s^{(k+1)}$.

The procedure involves the 3-point, second order accurate difference approximation for the surface gradients,

$$\frac{dv}{d\xi}(0^+) = \frac{v_1 d^2 - v_2 - v_s(d^2-1)}{\xi_2(d-1)} \qquad (IV.72a)$$

obtained by Taylor series expansion of v about $\xi = 0^+$, $d \equiv \xi_2/\xi_1$; ξ_n is the local dimensionless coordinate corresponding to the nth spatial mesh point. It is obtained by a second order Runge Kutta integration, from Eq. (IV.17b):

$$\xi_{n+1} = \xi_n + \left[\frac{m}{(\rho D)_n} + \frac{m}{(\rho D)_{n+1}} \right] \Delta y/2 \qquad (IV.72b)$$

for uniform increment Δy, nonuniform $\Delta\xi$ arises, due to the spatial variation of ρD, most pronounced near the $y = 0^+$ surface.

The actual iteration process is semi-implicit. Substitution of Eq. (IV.72a) into Eq. (IV.71) yields:

$$v(0^+)^{(k+1)} = \left[\phi^- + \frac{v_1 d^2 - v_2}{\xi_2(d-1)} \right]^{(k+1)} \Big/ \left[1 + \frac{d+1}{\xi_2} \right]^{(k+1)} \qquad (IV.73)$$

The boundary condition relaxation procedure is summarized by following steps.

(a) For $v_s^{(k)}$ and the ambient data, generate the gas field solution (involving interior gas-phase points), $v^{(k+1)}$. Note that these results need not be at full steady state for intermediate relaxation steps.

(b) Integrate the condensed phase to obtain $[\phi^-]^{(k+1)}$.

(c) Calculate ξ_1 and ξ_2 by Eq. (IV.72b).

(d) Using Eq. (IV.73), calculate $v(0^+)^{(k+1)}$, and obtain $v_s^{(k+1)}$.

Steps (b) through (c) may be repeated in a predictor-corrector manner. Any number of time-like forward integration steps (j) of the gas phase may be used between distinct surface relaxation steps (k); the most efficient, however, was found to relax the boundary conditions each gas phase integration step, namely, k = j.

   (e) Checking convergence of the surface relaxation procedure is done in a manner compatible with the steady state convergence requirement of the interior gas-field points:

$$\max_i \left| \Delta v_i(0^+) \right| \equiv \max_i \left| V_i(0^+)^{(k+1)} - V_i(0^+)^{(k)} \right| \leqslant \varepsilon_t \widetilde{\Delta t} \quad \text{(IV.74)}$$

where i denotes individual components of the vector $v(0^+)$. Thus, steady state is achieved when

$$\max_i \left| \Delta V_i \right| \leqslant \varepsilon_t \widetilde{\Delta t} \quad \text{(IV.75)}$$

for the entire gas phase region (including the boundary values at y = 0.

By employing the y = 0 surface relaxation procedure with the combined gas and condensed phase integration, manifolds of solutions corresponding to the specified (p, m, T_0) data can be generated. These solutions, when convergence to steady state is achieved, satisfy the rigorous species and energy conservation conditions at the liquid-gas interface.

E. Solution or the Deflagration Problem

The final step in the solution of the deflagration problem, namely defining the mass burning rate m   , is the subject of this section. At the conclusion of the foregoing section, a method was defined by which solution manifolds of the combined gas and comdensed phase problems could be generated, for given ambient data (p, T_0) and specified m. In order to uniquely define $m(p, T_0)$, an additional independent constraint is required. The constraint is provided by the nitramine evaporation law, which can be stated implicitly as

$$X_R(0^+) = f(T_s, p) \quad \text{(IV.76)}$$

where $X_R(0^+)$ is the nitramine molar fraction at the gas side of the liquid-gas interface. Utilizing this as an auxiliary constraint, the mass burning rate may be calculated iteratively.

1. The Nitramine Evaporation Law

Any process of evaporation involves molecules of the substance (R) leaving the liquid in an outward flux, $m_R(OUT)$, and an influx of molecules, $m_R(IN)$, effectively returning to the liquid from the vapor phase. When $m_R(OUT) = m_R(IN)$, the process is termed at equilibrium, and no net evaporation occurs, although the substance (R) exists in both liquid and vapor phases. When $m_R(OUT) > m_R(IN)$, net vaporization takes place; in this instance, the net flux of vaporizing material can be expressed[98] as

$$m_R = \alpha_k \rho_s u_{ms} \left[Y_R^{(eq)} - Y_R^+ \right] \quad \text{(IV.77)}$$

where $0 < \alpha_K < 1$ is the Knudsen accommodation coefficient, ρ_s is the gas density at the surface, $Y_R^{(eq)}$ is the equilibrium mass fraction and Y_R^+ is the actual mass fraction of (R) at the gas side of the interface. The mean molecular velocity perpendicular to the surface is[99]

$$u_{ms} = \left[R_u T_s / 2\pi W_R \right]^{1/2} \tag{IV.78}$$

Note that (regardless whether equilibrium prevails or not) the outward flux is always given by the equilibrium expression,

$$Y_R^{(eq)} = X_R(0^+) W_R / \overline{W}_s \tag{IV.79a}$$

where

$$1/\overline{W}_s \equiv \sum_{i=1}^{N} Y_i(0^+)/W_i \tag{IV.79b}$$

The equilibrium mole fraction is given by Dalton's law,

$$X_R(0^+) = P_R(0^+)/P \tag{IV.79c}$$

and the equilibrium partial pressure of (R) can be expressed by a Clausius-Clapeyron law,

$$\ln P_R(0^+) = \ln P_v - E_v \left[\frac{1}{T_s} - \frac{1}{T_v} \right] \tag{IV.80}$$

where (P_v, T_v) are reference vapor pressure and temperature, and E_v the latent heat of vaporization; parameters for the last equation were extrapolated from the data of Rosen and Dickinson[11] for RDX, and the values tabulated in Appendix C.

It should be mentioned that the net vaporizing flux, m_R, is the difference between two large numbers [owing to the magnitude of u_{ms}, being much larger than the mean convective velocity $u_s(0^+)$]. This implies that $Y_R^{(eq)}$ is comparable to Y_R^+, the actual mass fraction. Indeed, the assumption of equilibrium at the surface (even though net vaporization prevails) may yield a good approximation of Y_R^+, but should be relaxed when the actual outward mass flux, m_R, is sought.

Thus, with available surface data U_s, Eqs. (IV.77) through (IV.80) fully define $m_R(U_s)$. The expression for the full mass flux is,

$$m^* = m_R + m^* \left[1 - Y_R(0^-) \right]$$

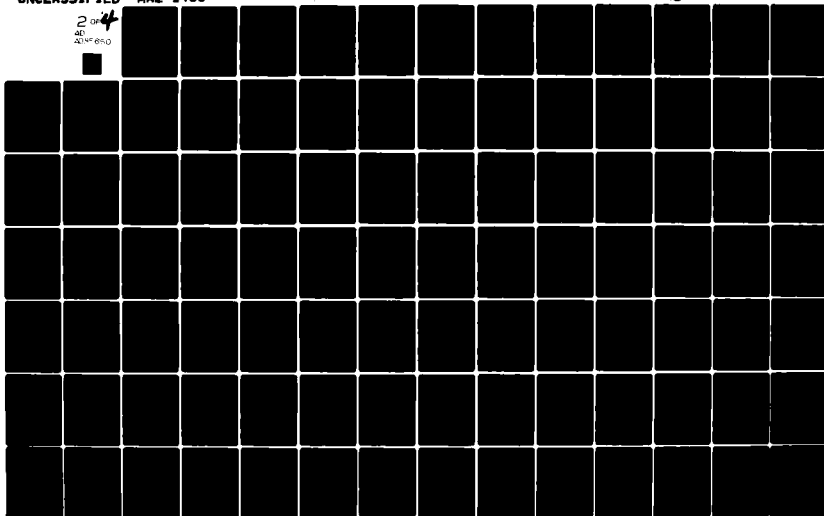accounting for subsurface gas generation; whereby,

$$m^* = m_R / Y_R(0^-) \tag{IV.81}$$

serves as the auxiliary relation sought.

2. The Iterative Procedure

The development of the relaxation procedure for boundary values at y = 0, described in Section D, followed from an intermediate relaxation configuration incorporating only the species boundary values, $Y_j(0^+)$, j = 1,2,...N. This method was essentially safer regarding convergence of the time-like integration to steady state, since as (T_s,m) are fixed, the condensed phase solution is fully determined and need not be repeated; hence, the $Y_j(0^+)$, j = 1,2,...N relaxation proceeds with invariant input from the condensed phase solution, namely, $Y_j(0^-)$ = const, j = 1,2,...N. In order to solve for (T_s,m) corresponding to the given ambient data at steady state, a multi-dimensional (2x2) Newton-Raphson procedure was employed, utilizing the energy conservation condition at y = 0 and the evaporation law as linearly independent constraints. The saving in computational effort over the relatively rapid convergence of the gas phase solution (including species $Y_j(0^+)$, j = 1,2,...N) was more than offset by the rather complex overall iteration procedure, requiring gas phase solutions at each (T_s,m)-iteration step, besides formation of the residual Jacobian, $\partial(e_1,e_2)/\partial(T_s,m)$. The procedure is not guaranteed to converge, even when solution is physically plausible. For instance, the residual function must be convex (the condition for which is that the Hessian matrix, possessing the diagonal terms $\partial^2 e_1/\partial T_s^2$, $\partial^2 e_2/\partial m^2$ must be positive semi-definite[100,101] as a necessary condition for convergence. The algorithm for this approach produced converged results in certain cases, but tended to overpredict the mass burning rate, m, consistently, for datum case properties. The multi-dimensional iteration algorithm has been abandoned in favor of the straightforward, single constraint method described in the remainder of this section, which incorporates relaxation of the entire boundary value vector, including T_s, within each iteration cycle.

The iterative procedure is based on satisfying the following constraint

$$\hat{e}^{(h)} = (m^* - m)/m = 0 \qquad (IV.82)$$

by converged steady state solutions, corresponding to fixed ambient data (T_0,p) and through suitable choice of m. m* in Eq. (IV.82) denotes the mass flux obtained by the converged steady state solution for a particular imposed $m^{(h)}$ through the procedure outlined in the previous section. superscript h denotes the current iteration index, and $e^{(h)}$, when nonzero, is the current residual or error.

Holding the ambient data fixed, $m^{(h)}$ can be varied within a Newton-Raphson or regula falsi iterative procedure, in order to minimize $\hat{e}^{(h)}$. Of course, each new iterative step (h+1), requires generation of new steady state solution for the $(p, T_0, m^{(h+1)})$ data.

The overall iterative procedure is considered converged, when

$$\hat{e}^{(h)} < \Delta\tilde{t}\cdot\Delta y/\delta_0^* \sim O(1/\kappa_f^3) \qquad (IV.83)$$

which is the allowable error in satisfying the y = 0 interface conservation conditions, at the final steady state level, cf Eqs. (IV.64), (IV.65) [not to be confused with the convergence criterion, Eq. (IV.75)].

Convergent steady state deflagration solutions for given ambient data (p, T_0) are therefore defined as those which satisfy all the imposed physical

constraints, including the evaporation law.

To conclude, the method described in this chapter can be used to generate solution manifolds for particular sets of (T_0, p) data within the pressure range of interest here. These constitute genuine solutions to the physical deflagration problem under the given ambient conditions, which was the objective for this part of the study.

A functional and structural description of the computer program NTRCOM (for combined condensed and gas phase solutions) is provided in Appendix C.

CHAPTER V

RESULTS OF THE STEADY STATE ANALYSIS, CONCLUSIONS AND RECOMMENDATIONS

A. Introduction

The solutions obtained by the nonlinear algorithms of Chap. IV are the subject of the present discussion. The framework for this chapter is as follows. The independent condensed phase solutions are discussed in Section B, where comparison is made between the comprehensive model of Section IV.C and the approximate (concise) one, given in Appendix B. Steady state solutions of the coupled condensed and gas phase models are described in Section C, including a summary of the pressure dependent behavior as well as the influence of various parameters. Conclusions and summary of observations are given in Section D, and recommendations for future study of nitramine deflagration are offered in Section E.

The converged steady state solutions discussed herein were obtained by NTRCOM, the numerical solution algorithm described in Appendix C, with prescribed mass burning rates, m, chosen close to the experimentally observed values at given ambient data. It must be stressed that solving for the mass burning rate $m(p, T_0)$ by the method of Section IV.E is entirely valid; however, with the extrapolated RDX evaporation data (E_v, P_v, T_v), cf. Appendix C, the $Y_R^{(eq)}$ tends to be consistently underpredicted, resulting in negative m_R. Rather than limit the validity and accuracy of the final results by the quality of the evaporation law parameters, it seems far better to employ values of m from available measurements, and make note of the error which evolves from the evaporation law constraint, Eq. (IV.82), at the converged state. The calculation of these errors requires knowledge of the Knudsen coefficient, α_K, appearing in Eq. (IV.77); in view of the uncertainty involved in the evaporation data, its value and the subsequent error term calculations would be highly speculative. Instead, the significant difference

$$d = Y_R^{(eq)} - Y_R(0^+)$$

is briefly noted. Its values are between -0.15 at 1 MPa to -0.06 at 4 MPa. For instance, at 4 MPa, specifying a mass burning rate 19% higher than the previously mentioned experimental value, results in $d = +0.12$. This is to emphasize that despite the aforementioned arguments, the actual data generated by the evaporation law, as well as the predicted values of the mass burning rate are in no way out of range. In comparison, the absolute magnitude of the residual errors involved in the dimensionless conservation conditions at y = 0, Eq. (IV.71), do not exceed 0.005 (or 0.5% considering unity as reference) at converged steady state.

The data used in all the numerical experiments considered herein are for RDX; the datum case properties are summarized in tabular form in Appendix C, and the associated thermophysical data given in Appendix A.

B. The Independent Condensed Phase

As shown in Section IV.C, the condensed phase can be formulated in terms of an (equivalent) initial value problem and solved independently. Thus, specifying (T_0, m) as well as a maximal surface temperature, T_s, can yield condensed phase solution manifolds outside of the framework of the entire

deflagration problem. These results are used to illustrate the reacting condensed phase behavior.

In each case, the results of the comprehensive model (Section IV.C) are compared with those of the concise model of Appendix B. All the independent solution data is summarized in Figs. V.1 through V.9. The condensed phase properties used are given in Table V.1. To avoid small differences in the numerical results due to varying integration step-size, the independent variable in the comprehensive system [given by Eqs. (IV.30a,b) and the associated initial conditions] was normalized:

$$\tilde{\tau}_c \equiv (T - T_m)/(T_s - T_m) \qquad \text{(V.1)}$$

such that $0 \leqslant \tilde{\tau}_c \leqslant 1$ in the domain of interest, and T_s is the current maximal surface temperature considered, which may vary with m. In the actual solution process of the coupled gas and condensed phase model, T_s is specified, and has to be matched by both gas and liquid solutions at $y = 0$. For the independent solution considered presently, the prescribed maximal T_s in each case was taken somewhat lower than that which brings about $d\tilde{\tau}_c/d\zeta_c = 0$.

For purposes of illustration, the independent variable axis was

$$\tilde{\tau}_c^* \equiv \tilde{\tau}_c (T_s - T_m)/(T_{s,ref} - T_m) = (T - T_m)/(T_{s,ref} - T_m)$$

in all the results plotted in Figs. V.1-5, where $T_{s,ref} = $ const. for all mass fluxes utilized, so that an absolute scale of reference is restored in the plots.

The three values of mass flux utilized in Figs. V.1 through V.9 were 7.2, 10.9 and 18 kg/m²s, close to those observed experimentally at 1, 2 and 4 MPa, and equal to the values prescribed in the combined gas-condensed phase solution.

Figures V.1 and V.6 show the mass fraction of nitramine in the liquid vs. temperature. As temperature is increased (toward the hot boundary at $y = 0$), the nitramine mass fraction decreases and the rate of depletion increases, both in an accelerated manner. This is due to the strong temperature sensitivity of the reaction rate term. As mass flux is increased, the residence time in the liquid layer decreases, and hence a tendency for less depletion of nitramine at higher m; however, the rate of supply of nitramine to the high-temperature reaction zone (by convection, mY_R) also increases, resulting in partial counter-balancing of the first effect. The concise model yields a slight over prediction of Y_R, the resons for which have been discussed in section IV.C.

Figure V.2 depicts the dimensionless thermal gradient; peaking of this function within the layer is due to the effect of reaction: as the hot boundary is approached and heat release by the reaction increases, less conducted heat flux is required to maintain a given temperature. In the region where the reaction is weak, the gradient is linear in $\tilde{\tau}_c^*$, since $d\tilde{\tau}_c/d\zeta_c - \tilde{\tau}_c \doteq$ const, as given by the concise-solution lines (where heat release within the liquid layer is precluded). For the various m-values shown, differences in the initial conditions, $d\tilde{\tau}_c/d\zeta_c(0^+)$, are entirely due to the scale transform, cf Eq. (V.1); larger T_s (corresponding to larger m) results in reduced $d\tilde{\tau}_c/d\zeta_c(0^+)$, cf Eq. (IV.24).

The total thermal flux in the negative ζ_c direction, $\phi \equiv d\tilde{\tau}_c/d\zeta_c - \tilde{\tau}_c$, is shown in Fig. V.3. Appreciable deflection downward from constant values (given by the ϕ = const. solution of the concise model) occur, as reaction heat release becomes more prominent, toward the hot boundary; the reasons for this have been discussed above.

A dimensionless form of the heat feedback term, q_c, defined by Eqs. (IV.35b) and (IV.36), viz.,

$$\psi \equiv q_c / m C_c (T_s - T_m) = \frac{d\tilde{\tau}_c}{d\zeta_c} + Q_s/C_c(T_s - T_m) \quad (V.2)$$

is drawn in Fig. V.4. The reasons for the good agreement between concise and comprehensive solutions here were discussed in detail in Section IV.C. The peaking of ψ within the range of temperatures considered, follows from similar behavior by the dimensionless thermal gradient. This property is of great importance to the matching of energy flux across the liquid-gas interface, as will be discussed later; matching corresponds to the receding portion of these curves.

The dimensionless distance from the solid-liquid interface within the liquid, $\zeta_c = (y + y_m)/(\alpha_c/r)$, is depicted in Fig. V.5. All the concise model solutions are self-similar since $\zeta_c = \log(\tilde{\tau}_c)$, and hence the lines for all m-values coincide. Departures from this single curve are observed for the comprehensive model: the smaller the mass flux, the lower the maximal temperature at a particular value of ζ_c (note that the layer thickness is not indicated by the ends of these lines). In other words, the larger the m, the smaller the maximal ζ_c.

Dimensional data is depicted in Figs. V.6 through V.9. The dimensional conductive heat flux, $-\lambda_c dT/dy$ is plotted against liquid phase temperature in Fig. V.7, showing that a higher mass flux m requires a higher conductive heat flux, at any given T. Figure V.8 showns the dimensional function q_c as function of T; here, too, the larger mass flux requires a large q_c at any temperature. Finally, the dimensional distance in the liquid layer is plotted against temperature in Fig. V.9, indicating that the liquid layer thickness tends to decrease as the mass flux increases.

C. The Combined Gas Phase and Condensed Phase Solution

The results discussed in this section correspond to converged steady state soltuions obtained by numerical experiments with the NTRCOM program. These tests cover the ressure range between 1 and 4 MPa, with imposed mass burning rates close to the experimental data available for RDX.

The part of the steady state solutions concerning the gas phase is summarized in Figs. V.10 through V.25, covering the near field properties as functions of distance from the condensed surface. Further distinct features of the deflagration solutions are given in Figs. V.26 through V.36.

1. Observation Regarding the Gas Phase

In all of the diagrams discussed in this section, four groups of data represent each parameter, at $p = 1, 2, 3,$ and 4 MPa.

Figures V.10 through V.12 depict temperature and species profiles vs. dimensional distance from the propellant surface. In Fig. V.10, as pressure is increased, the temperature at a given distance y is increasing, and the final temperature attained is higher. In Fig. V.11 the nitramine mass fraction is shown to decrease rather steeply with distance, reaching values $< 10^{-5}$ at the outer end of the region.

The reactants of the secondary reaction, NO_2 and CH_2O have rapidly rising concentrations near the surface, where nitramine depletion is faster than the rate of secondary reaction; these concentrations decrease slowly, once the primary reaction is close to completion. The mass fraction of N_2 and N_2O, not participating in any further reaction, increase as nitramine is depleted, and then remain constant. In Fig. V.12 products of the secondary reaction are shown, all of which have mass fractions 0.01, at least one order of magnitude below those of the primary reaction. The rise of the NO, CO_2, CO and H_2O species concentrations is slow relative to the species of Fig. V.11, as the characteristic rate of secondary reaction in the near field is relatively small.

A plot of reaction rates, $\log(\omega_1)$ and $\log(\omega_2)$ vs. distance from the propellant surface is given in Fig. V.13. The primary decomposition reaction is shown to be 2 orders of magnitude higher than ω_2 at the peak, falling to 2 to 3 orders of magnitude below ω_2 at the outer end of the near field. It is interesting to note that $\omega_2 > \omega_1$ at the surface, where $y \doteq 0^+$; this trend was indicated by the kinetics, cf. Fig. II.4. The secondary reaction rate rises monotonously throughout the near field, and is expected to peak only far from the surface, within the far field. Observing Figs. V.10 through V.13, as pressure is increased, the reaction rates ω_1 and ω_2 increase, the peak value of ω_1 is increasing, and the resulting mass fraction of nitramine near the surface is decreasing. Dimensional gradients, d /dy*, are increasing over the entire near field.

The reaction rate plot is repeated in Fig. V.14, using the dimensionless coordinate, given by the integral of Eq. (IV.17b). In this instance, peaking of the ω_1-curves and the region of fast gradient change for ω_2 are shown to occur at a unique position $\zeta \doteq 0.5$, regardless of pressure. This particular near field property, indicating a degree of self similarity, will be apparent with the rest of the dimensionless plots utilizing ζ for the abscissa.

Figure V.15 shows the dimensional conductive heat flux, $\lambda dT/dy$, as function of y. Near the surface, where the exothermic reactions are still weak, the conductive flux is high and rising. It reaches a peak in the near field, somewhat before $\omega_{1,max}$ is reached and then falls off rapidly; finally, dT/dy tapers slowly to approach zero in an asymptotic manner. Clearly, as pressure is increased, the dimensional gradient is increasing appreciably in the surface region. The fast-receding portion of dT/dy becomes steeper, and the peak becomes sharper, at higher pressures. This plot is repeated in Fig. V.16, depicting $\lambda dT/dy$ (dimensional) vs. ζ. Similar to the behavior observed in Fig. V.14, the conductive heat flux curves do not intersect as pressure is varied, and all the peaks occur at a unique $\zeta \doteq 0.35$ position,

regardless of pressure. Note that $\lambda\,dT/dy(0^+)$ increases with pressure.

A series of fully dimensionless plots is given in Figs. V.17 through V.21. Figure V.17 shows the dimensionless enthalpy, defined by Eq. (IV.17a), as function of ζ . A relatively rapid increase of τ to $\zeta \doteq$ 0.70 is followed by a shallow rise toward the outer end of the near field.

Mass fractions of the primary reaction species are depicted in Fig. V.18, as functions of ζ . Relative to Fig. V.11, these form now tighter clusters of curves, as the near field length coordinate is unified. In comparison, the secondary reaction products plotted in Fig. V.19 do not follow this tendency, as expected. As pressure is increased, the extent of secondary reaction within the near field increases, and the concentration curves for HCHO and NO_2 in Fig. V.18 move further apart when approaching higher values of ζ .

In a manner similar to that observed for the species concentrations in Fig. V.18, the dimensionless enthalpy gradient, $d\,\tau/d\zeta$, in Fig. V.20 shows tendency of all distinct pressure-data to cluster more tightly, when plotted against ζ . The trend toward self-similarity (i.e. all data falling on the same line, regardless of pressure) near the surface becomes weaker as the reaction rates (ω_1 , ω_2) increase toward $\zeta \sim 0.35$, where the dimensionless enthalpy gradients peak. Increasing pressure brings about smaller $d\,\tau/d\zeta$ in the near field, but at $\zeta \doteq 0.7$ crossing over occurs, and the largest gradient corresponds to the largest pressure, as expected from the theory of Chapter III. Clearly, a difference of 2 orders of magnitude exists between the values of $d\tau/d\zeta$ at $\zeta = 0^+$ and at $\zeta \gtrsim 1$, which shows the near field - far field arguments to be still valid within the pressure range considered.

Another parameter of interest in the near field is the total (convective and conductive) thermal flux, $\tau - d\tau/d\zeta$. Plotted against ζ in Fig. V.21, this function is negative for $0 < \zeta < 0.5$, and has a minimum at $\zeta \doteq 0.3$. As the gradient $d\tau/d\zeta$ decreases most rapidly near the point of maximal primary reaction rate, a steep linear ascent in that region follows, terminating in a monotonous shallow rise, where $d\tau/d\zeta$ is vanishingly small. The point $\zeta \doteq 0.5$, where $\tau - d\tau/d\zeta = 0$, coincides with the neighborhood of maximal ω_1, cf. Fig. V.14, for all pressures considered. This point is therefore physically significant in terms of the net dimensionless heat transfer, serving as a continental divide in the deflagration wave: upstream of it, net heat is fed back toward the propellant surface ($\zeta < 0.5$), conduction being dominant over convection; downstream ($\zeta > 0.5$) transport processes are weaker and convection dominates, as net heat is carried outward with the gas flow.

Figure V.22 depicts the distance from the condensed surface, y, in microns, plotted against the dimensionless near field coordinate ζ . For a given near field position, the larger distance corresponds to the smaller pressure (or mass burning rate, $m_p = m$), as given by the integral relationship of Eq. (IV.17b). The portions of the y-lines for $\zeta > 0.8$ appear linear, since the ρD variation there is small compared with that near the surface.

Three thermophysical parameters of interest are plotted in Figs. V.23 through V.25, as functions of the dimensionless coordinate ζ . In Fig. V.23, the isobaric specific heat, C_p, of the gas mixture is shown. The gas mixture diffusivity, λ/C_p is given in Fig. V.24. Both rise with the temperature in the near field. The mean molecular weight of the gas mixture,

W, is plotted in Fig. V.25, and shown to be a receding function of ζ: as nitramine is depleted and lighter species formed, W decreases. Data from all pressures of interest tend to merge near the outer end of the near field, since the secondary reaction (compared with nitramine decomposition) does not involve a significant change in mean molecular weight. As pressure increases, for a given near field position, Cp and λ/Cp increase, mainly due to the effect of rising temperature; W decreases, as the nitramine mass fraction decreases.

2. Summary of Pressure Dependent Characteristics in the Range Between 1 and 4 MPa

The results discussed in this section correspond to converged solutions of the nonlinear deflagration model, and involve observations of the overall pressure dependent behavior, obtained for the datum case data set.

In all the numerical experiments considered herein, the mass burning rate, m_p, was prescribed according to experimental values.[53] Within the pressure region considered, m_p has a pressure exponent $n \doteq 0.75$; the variation of $m_p(p)$ is depicted in Fig. V.26.

Nitramine concentrations at the liquid-gas interface are given in Figs. V.27a,b, as function of pressure. On the liquid side, the nitramine mass fraction decreases linearly with increasing pressure. For the pressure range considered, $0.98 > Y_R(0^-) > 0.91$, showning in Fig. V.27a that at 4 MPa nitramine decomposition in the liquid amounts to less than 10%. The nitramine mass fraction on the gas side also decreases with increasing pressure as shown in Fig. V.27b., but in a decelerating manner. The associated variation in mass fraction is $0.40 > Y_R(0^+) > 0.35$ about one half of total the variation on the liquid side. The surface temperature, T_s increases with pressure, as shown in Fig. V.28, in a decelerating manner. Within the pressure range considered, $625 < T_s < 690$ K; the variation of surface temperature with pressure is a marked departure from the assumption made by Spalding[66] that when a liquid phase is present on the deflagrating propellant surface, $T_s(p) \doteq$ const and equal to the boiling point temperature. Although actual boiling point data of RDX are not available at this time, one would tend to accept the observations of Zeldovich[79] that boiling of the liquid phase in similar secondary explosives marks the onset of detonation.

Although the deflagration process considered does not seem to be controlled by surface pyrolysis (such process was not included in the physical model), an attempt is made in Fig. V.29 to plot the prescribed $m_p(p)$ data against the converged solution data, $1/T_s(p)$. The result is a very good correlation [coefficient of determination, $(r^*)^2 = 0.9895$]; in the range of T_s and m_p considered, an apparent activation energy of 13 kcal/mol is found, with a prefactor of 2.68×10^5 kg/m^2-s.

The dimensionless gradients of thermal enthalpy and nitramine mass fraction at $y = 0^+$ are plotted in Fig. V.30 against pressure. These properties are of comparable magnitudes, as expected. Both decrease linearly over most of the pressure region, with the nitramine variation being steeper. The relatively small variation in the thermal gradient, between 0.52 and 0.54, indicates that as pressure increases, a slightly smaller amount of conductive feedback from the gas is needed--per unit mass of gas generated at the surface. Of course, absolutely, $\lambda dT/dy(0^+)$ increases with pressure, as shown in Fig. V.31. The logarithmic plot given, yields a linear correlation in the log-log

plane, showing that $\lambda dT/dy(0^+) \sim p^{0.715}$, as expected with the present gas phase-driven deflagration, where $\lambda dT/dy(0^+) \sim m$.

Figure V.32 shows $d\tau/d\zeta$ at $\zeta = 1.30$, toward the outer end of the near field. In contrast with the receding dimensionless gradients at $\zeta = 0^+$, this function is progressive in p. The observations regarding the gradients at $\zeta = 0^+$ and $\zeta = 1.3$ tend to verify the conclusion of Chap. III, that the near field - far field resolution becomes less distinct as pressure is increased, as near field gradients decrease, and far field gradients increase.

Full-logarithmic plots of $\omega_1^*(\zeta = 0.5)$ and $\omega_2^*(\zeta = 0.5)$ vs pressure are given in Figs. V.33 and V.34 respectively. Recall that $\zeta = 0.5$ is the near field coordinate where ω_1^* is maximal for all the pressures considered. Excellent linear correlations were obtained for both $\log(\omega_1^*)$ and $\log(\omega_2^*)$ vs. $\log(p)$. The pressure exponent of $\omega_2^*(0.5) \sim p^{2.08}$ is expected, but for the primary reaction, $\omega_1^*(0.5) \sim p^{1.34}$ is somewhat surprising, since this reaction is strictly first order overall. This behavior can be physically explained, when the thermal effect associated with heat release in the near field by the secondary reaction are taken into account. The overall variation of $\omega_1^* = f(\zeta = 0.5; p, T)$ with pressure is,

$$\frac{\delta \omega_i^*}{\delta p} = \left(\frac{\partial \omega_i^*}{\partial p}\right)_T + \left(\frac{\partial \omega_i^*}{\partial T}\right)_p \delta T^*/\delta p \qquad (V.3)$$

Assuming now that the variation δT^* is caused entirely by heat release due to the secondary reaction in the near field, viz.,

$$\delta \tau^* \sim \delta\left(\omega_2^*/m^2\right) = \frac{\partial}{\partial p}\left(\frac{\omega_2^*}{m^2}\right)\delta p \qquad (V.4)$$

Since $\omega_2^*/m^2 \sim p^{0.5}$ with the presently prescribed $n = 0.75$, and as $\delta\tau^* \sim c_p \delta T^*$, Eq. (V.4) yields $\delta T^*/\delta p \sim p^{-0.5}$, after the derivative is taken; note that although $\delta T^*/\delta p$ involves the small quantity $\varepsilon \ll 1$, the term $(\partial \omega_1^*/\partial T)_p$, multiplying it in Eq. (V.3) is large, due to the large activation energy associated with ω_1^*. Thus,

$$\frac{\delta \omega_i^*}{\delta p} \sim \left(\frac{\partial \omega_i^*}{\partial p}\right)_T + \left[\left(\frac{\partial \omega_i^*}{\partial T}\right)_p / p\right] p^{0.5} \qquad (V.5)$$

where $(\partial \omega_1^*/\partial p)_T$ and the term in square brackets are pressure independent. After integration, Eq. (V.5) leads to the explicit relationship,

$$\omega_1^* \sim c_0 p + c_1 p^{3/2}$$

which shows that the equivalent pressure dependence of the maximal ω_1^* is $\sim p^h$, with $1 < h < 3/2$, in the range of pressures considered - as observed in Fig. V.33.

Utilizing $\omega_2^*(\zeta = 0.5)$, the quantity $\varepsilon = \overline{\rho D \omega_2^*}/m^2$ is plotted against p on log-log scale in Fig. V.35. Actually, to obtain a more precise measure of the small quantity ε, the maximal $\omega_2 = f(\overline{T}_2)$ should have been used, as this is a far field property. However, $\overline{T}_2$ lies outside of the range of the present near field analysis, and ε shown in Fig. V.35 is provided only for comparison with the flame speed eigenvalue Λ, discussed next. The

linear (logarithmic) correlation shows that $\varepsilon \sim p^{0.626}$ and that $0.004 < \varepsilon < 0.015$ in the pressure range considered. Calculations at downstream positions, e.g., with ω_2^* ($\zeta = 1.30$), show somewhat higher values of ε, and that its pressure exponent tends closer to 0.5, the expected value.

Finally, the flame speed eigenvalue, Λ, calculated at $\zeta = 0.5$ is depicted as function of pressure in Fig. V.36. Evidently, an excellent linear correlation of Λ vs. p is obtained, with

$$\Lambda = 0.606 - 0.027 \, p$$

Thus, the flame speed eigenvalue in the pressure range tested is indeed given by a uniform $\Lambda^0 \sim O(1)$, independent of pressure, and a decrement $\propto p \ll 1$. This behavior confirms the predictions by the asymptotic gas phase theory of Section III.F, concerning the pressure dependence of Λ, and strongly indicates that the theory is valid within the pressure range tested.

3. The Role of the Reacting Condensed Phase

Observation of the steady state data points, over-plotted on the independent condensed phase diagrams, Figs. V.1 through V.9, shows the following trends:

a) The amount of nitramine depleted in the liquid phase, $1-Y_R(0^-)$, increases in an accelerated manner as pressure is increased; this is demonstrated in Figs. V.1 and V.6.

b) The liquid layer thickness decreases with increasing pressure, as shown in Fig. V.9, with slight deceleration.

c) The conductive heat flux at the liquid side of the y = 0 interface, shown in Fig. V.7, increases with pressure; however, at the T_s-coordinates of converged data, the difference between the comprehensive (exothermic reaction in liquid) and concise (heat release deferred to the surface y = 0) models is found to increase even faster.

These observations indicate that within the pressure range of interest, the dependence of the deflagration process upon the exothermic liquid phase decomposition reaction becomes stronger with increasing pressure. In the mean time, the liquid layer becomes thinner.

The first question of interest is, how does the increased subsurface exothermicity affect the pressure sensitivity of the burning rate. For qualitative demonstration, consider the simplified heat balance at the y = 0 surface, leading to

$$m = q_g / \left[C_c (T_s - T_0) + Q_s \right] \qquad \text{(V.6)}$$

where $q_g = \lambda_g T'(0^+)$ and all subsurface heat release (or depletion) is represented approximately by Q_s. Suppose now that two identical propellant systems are compared, both at exactly the same data (T_0, p, T_s, m), the only difference being that one has a somewhat higher subsurface exothermicity, viz., $\delta Q_s < 0$. It follows immediately that $\delta q_g < 0$, to maintain the required

invariance $\delta m = 0$. Now, within a narrow enough pressure range, $q_g \stackrel{\sim}{=} a p^b$, as shown in Fig. V.31, with a being a proportionality constant. Obviously, for $\delta a = \delta p = 0$, the requirement $\delta q_g < 0$ implies $\delta b < 0$. This shows that the pressure sensitivity of the deflagration rate m, cf. Eq. (V.6), must be reduced when subsurface exothermicity is enhanced.

To obtain a quantitative measure of the effect that the exothermic liquid phase reaction has upon the deflagration rate, m, the following dimensionless criterion is suggested:

$$g_c \equiv \frac{\Delta h_D}{\left[\lambda_g T'(0^+)\right]_{RC}} \qquad (V.7)$$

where

$$\Delta h_D \equiv \left[\lambda_g T'(0^+)\right]_{NR} - \left[\lambda_g T'(0^+)\right]_{RC}$$

subscripts RC and NR denote reacting and (hypothetical) non-reacting liquid phase configurations respectively, at the same converged steady state data, $(T_s; m, p)$.

The term Δh_D represents the conductive heat feedback defect (on the gas side of the $y = 0$ interface) due to exothermic liquid phase reaction; in this case, $\Delta h_D > 0$ always. An attempt shall be made now, to derive an expression for g_c which is directly useful for calculations. The derivation is followed by a discussion of the implied phenomena.

Neglecting the relatively small convective terms in the interface energy balance at $y = 0$ (typically two orders of magnitude smaller than the conductive terms), the balance yields

$$\left[\lambda_g T'(0^+)\right]_{NR} = \left[\lambda_c T'(0^-)\right]_{NR} + m Q_v$$

$$\left[\lambda_g T'(0^+)\right]_{RC} = \left[\lambda_c T'(0^-)\right]_{RC} + m Y Q_v \qquad (V.8)$$

where $Y = Y_R(0^-)$. Hence,

$$\Delta h_D = \left[\lambda_c T'(0^-)\right]_{NR} - \left[\lambda_c T'(0^-)\right]_{RC} + m Q_v (1-Y) \quad (V.9)$$

Comparing the comprehensive and concise reacting liquid layer solutions (recall that the thermal profile in the latter is that of a nonreacting liquid, since heat release was deferred to the $y = 0$ surface), one may approximate for present purposes:

$$\left[\lambda_c T'(0^-)\right]_{NR} - \left[\lambda_c T'(0^-)\right]_{RC} \stackrel{\sim}{=} m Q_{liq} (1-Y) \quad (V.10)$$

expressing the associated conductive heat flux defect on the condensed side of

the y = 0 interface. Substitution of Eq. (V.10) into Eq. (V.9) yields

$$\Delta h_D = m Q_{liq}(1 - \tilde{Q}_v)(1 - Y) \tag{V.11}$$

where Q_{liq} is the heat of reaction in the liquid, and $\tilde{Q}_v \equiv Q_v/Q_{liq}$.

Utilizing Eqs. (V.8) and (V.10), the denominator of Eq. (V.7) can be expressed as

$$\left[\lambda_g T'(0^+)\right]_{RC} = \left[\lambda_c T'(0^-)\right]_{NR} - m Q_{liq}(1 - Y) + m Y Q_v \tag{V.12}$$

Substitution of Eqs. (V.11) and (V.12) into Eq. (V.7), using dimensionless condensed phase variables, leads to

$$q_c = \frac{(1 - \tilde{Q}_v)(1 - Y)}{\left[\theta_s - \theta_0 + \tilde{Q}_m - (1 - Y) + Y\tilde{Q}_v\right]} \tag{V.13}$$

where $\theta_s \equiv T_s/T_c^*$, $\theta_0 \equiv T_0/T_c^*$, $\tilde{Q}_m \equiv Q_m/Q_{liq}$, and $T_c^* \equiv Q_{liq}/C_c$.

Derivation of the expression relating $[\lambda_c T'(0^-)]_{NR}$ and $\theta_s - \theta_0 + \tilde{Q}_m$ can be followed from Appendix B, using $y_c \equiv y/(\lambda_c/mC_c)$ as dimensionless distance. q_c was calculated according to Eq. (V.13), utilizing converged steady state data; it was found to vary between 0.02 at 1 MPa and 0.08 at 4 MPa, in an accelerated manner. Equation (V.13) shows that q_c increases with the extent of liquid layer reactedness, namely as 1-Y increases. Therefore, an increasing influence upon the deflagration rate by the exothermic liquid phase decomposition is indicated, within the pressure range considered. If this trend continues unrestricted into the higher pressure regime, a decreasing pressure dependence of m(p) might evolve, contrary to experimental observations involving nitramine deflagration (and analogous to plateau burning of certain catalized double base propellants). The question at this point is whether q_c will continuously increase, or, rather, undergo a maximum as pressure is raised.

To investigate the behavior of q_c outside of the pressure domain tested in this study, the following functional relationship is suggested,

$$Y(\theta) = 1 - \exp(-B/\theta)/\theta \tag{V.14}$$

where $\theta \equiv \theta_s - \theta_m$, and $\theta_m \equiv T_m/T_c^*$ is the dimensionless fusion temperature. The last equation involves converged steady state data (Y, θ_s), and B is an empyrical constant. A value of B = 1.044 was found to correlate the converged $Y_R(0^-)$ data set against θ to within 8%, using Eq. (V.14). According to this equation, $Y(\theta)$ is bounded in the $\theta > 0$ domain. At the extreme limits of $\theta = 0$ and $\theta \rightarrow \infty$, Y = 1. $Y(\theta)$ has a minimum at $\theta = 1/B$, where $Y = 1 - 1/Be \approx 0.65$.

A straightforward calculation shows that the point where $dq_c/d\theta = 0$ is a maximum, defined by

$$-Y'(\theta + c) - (1 - Y) = 0 \qquad\qquad (V.15)$$

followed directly from Eq. (V.13), where $Y' \equiv dY/d\theta$, and $c \equiv \theta_m - \theta_0 + \tilde{Q}_m + \tilde{Q}_v$. Utilizing $Y(\theta)$ from Eq. (V.14), the last equation yields the algebraic relationship

$$(B/\theta - 1)(\theta + c)/\theta^2 - 1/\theta = 0$$

and hence (for $\theta > 0$):

$$\theta^* = [(B - c) + (B^2 + 6 B c + c^2)^{1/2}]/4 \qquad\qquad (V.16)$$

The RDX condensed phase data of Table V.1 gives $c = 0.638$; with $B = 1.044$ one obtains $\theta^* = \theta_s^* - \theta_m^* = 0.688$, corresponding to $T_s \triangleq 1000$ K. At this maximal point, $Y(\theta^*) = 0.681$ by Eq. (V.14), and $g_c(\theta^*) = 0.246$; therefore, a maximal influence of the exothermic condensed phase reaction estimated is 24.6% by the physical criterion advanced in Eq. (V.7); the associated extent of reaction, $1 - Y$, is 32%.

Clearly, (c,B) depend upon practically all of the liquid phase properties, particularly Q_m, Q_v, Q_{liq}, T_m and the associated kinetics $(A,E)_{liq}$. However, both (c,B) are normalized; from the definition of c, it evidently varies slowly with respect to all of the parameters involved. Similar behavior is expected of B. Since the values of both c and B are close to unity, small variations in these parameters are expected to lead to small variations in θ^*, $g_c(\theta^*)$ and $Y(\theta^*)$.

The finding of extremal behavior of $g_c(\theta)$ is in agreement with the assumed functional relationship of $Y(\theta)$ in Eq. (V.14), where a minimum in $Y(\theta)$ has been anticipated. This particular property of $Y(\theta)$ is not (as it may seem) the direct cause for obtaining $g_{c,max}$; note that the point θ^* where g_c is maximal does not coincide with the point where $Y = Y_{min}$, i.e., $\theta^* = 0.69 < 1/B = 1/1.044$. Similar $g_c(\theta)$ behavior may also be found when a monotonously decreasing function, e.g., $Y(\theta) = 1 - \exp(-B'/\theta)$ is employed, with $B' \triangleq 0.72$ correlating (with somewhat less accuracy) the available (Y,θ) data. The value of θ^* obtained in this manner is 1.13, and the corresponding value of $g_{c,max} = 0.34$.

Therefore, despite the high margin of uncertainty involving the actual values of maximal g_c and θ^*, owing to the ad hoc nature of Eq. (V.14), the general indication of peaking behavior of g_c remains notwithstanding. As pointed out earlier, enhanced subsurface exothermicity tends to decrease the burning rate pressure sensitivity (i.e., to decrease its pressure exponent, n). This counteracts the tendency to increase n with increasing pressure, as discussed in Chap. III. Thus, the net increase of n, observed in practice as p is increased, can be expected to be somewhat slower than that predicted by gas phase reasoning alone.

4. Parametric Influences

The combined condensed phase and gas phase model involves a very large number of parameters. Most of these correspond to thrmophysical properties of individual gaseos species, cf Appendix A, which were not varied in the present study. The parametric influences discussed herein were obtained from condensed phase and gas phase solutions made separately,i.e., in decoupled form.

a. Primary Decomposition Kinetics

The baseline dataset for gas phase decomposition of RDX utilized the dilute TNT solution results of Robertson[13]. The effect of variation of vapor phase kinetics was studied by substitution of the data of Rogers and Daub[17] in a separate gas phase algorithm. Condensed phase and relaxation of the BCs at $y = 0$ were excluded,while liquid-gas interface properties, U_s, and m ,equal to the datum case properties were imposed at each pressure. The results show relatively small increases in the heat feedback to the surface, and somewhat lower maximal primary decomposition rate, at all pressures tested. Figure II .3 shows that the actual kinetics constants of Robertson[13] and of Rogers[17] are quite close, and that k[Robertson] < k[Rogers] for T < 800 K. Hence, in the neighborhood of the surface, a larger amount of heat release corresponds to Rogers' data, which explains the increment in $dT/dy(0^+)$. Such positive increments would lead to lower (T_s , m), since thermal balance at $y = 0$ is achieved at the receding portions of the q_c curves, as shown in Fig. V. 8. Another trend indicated with Rogers' data is a smaller overall variation of the maximal primary decomposition rate with pressure, explained by the lower activation energy (by 17%) relative to Robertson's data (through thermal coupling with the secondary reaction,discussed in Chapter III).

In the liquid phase, the effects of reduction of heat release, Q_{liq}, and the prefactor, A_{m1}, for RDX were investigated. Due to the high activation energy (47.5 kcal/mol), the two effects are roughly equivalent. To estimate the effect of change in the liquid phase decomposition mechanism, such that:

$$RDX(liq) \longrightarrow 3HCHO + 2N_2O + NO + 1/2N_2 , Q = 52.4 \text{ kcal/mol}$$
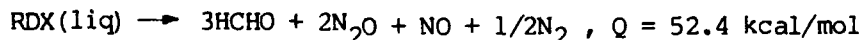
which is close to the mechanism proposed by Suryanarayana[19]. Therefore, a 30% reduction in the liquid phase heat release was tested, within the independent condensed phase solution framework. At 1 MPa and datum case (m , T_s , T_0), this was found to increase $Y_R(0^+)$ and q_c by 6% and 5% respectively. The retarding effect observed probably emanates from the relatively small extent of liquid phase decomposition even with the higher datum case heat of reaction .

b. Secondary reaction kinetics

Reduction of the secondary reaction prefactor , A_2 , by 99% (to 10^4 m^3/mol-s) using baseline data (p , m , U_s), resulted in reduction of the heat feedback to the surface by 7%, 11% and 16% at 1, 2 and 4 MPa, respectively. The maximal reaction rates were smaller, and their pressure exponent (in a log-log correlation with p) was reduced by 10%, closer to unity. The flame speed eigenvalue was reduced (closer to 0.5 in the mean) and its pressure decrement [cf Eqs. (III.61) and (III.62)] reduced to -0.014, by 50%. This demonstrates that the secondary reaction has a strong influence upon the pressure dependence of the system, although its overall quantitative effect is small at the pressure range considered.

c. Condensed Phase Properties

The formulation of Chapter IV shows that variation of the thermal conductivity, λ_c , is equivalent to variation of the thrmal diffusivity, α_c . Increasing λ_c by 30% resulted in higher nitramine depletion in the liquid, and, consequently, lower thermal gradients. At 1 MPa, the independent condensed phase solution for baseline data (m , T_s , T_0) showed reduction in both $Y_R(0^-)$ and q_c by 0.6% and 1.5% respectively. At 4 MPa, the respective figures are 4% and 5.5%. The relative deviations are more pronounced where the extent of subsurface decomposition is higher.

The specific heat, C_c , appears in the condensed phase formulation both within the thermal diffusivity group (in which its effect is inverse to that of thermal conductivity), and in the solid-liquid thermal balance, cf Eq. (IV. 24). Reduction of C_c leads to smaller requirement for solid heatup, through the term $mC_c(T_m - T_0)$. This, in turn, causes both thermal gradients and q_c to be lower, roughly in proportion to the amount of C_c reduction. Hence, compared to λ_c , the effect of C_c is expected to be much stronger .

A 30% reduction in C_c resulted in reduced $Y_R(0^-)$ and q_c by 0.6% and 21.5% respectively at 1 MPa, (4.6% and 26% at 4MPa) for baseline (m , T_s , T_0) data. Thus, a much stronger influence upon q_c is evident.

The effect of ambient solid temperature, T_0 , was studied in a similar manner. At 330 and 270 K, (i.e., ± 10%) the variations in $Y_R(0^-)$ and q_c were ∓0.3% and ∓5.4% at 1 MPa, (∓1% and ∓7% at 4 MPa) respectively. This demonstrates that elevated solid temperature leads to enhanced subsurface reaction, as well as to less solid heatup requirement, both of which cause q_c reduction. The latter, in particular, due to the heat balance constraint at the liquid-gas interface (y = 0), would lead to higher mass burning rate, to restore agreement with the gas-side heat feedback at the given pressure. With this argument, the temperature sensitivity implied by the foregoing results can be estimated indirectly, as follows. Matching of the heat fluxes at y = 0 requires that $q_c \triangleq \lambda dT/dy(0^+)$. The gas-side heat feedback , in turn, is proportional to m. Thus, the temperature sensitivity is,

$$\sigma_p \equiv \left[\frac{\partial(\ell n\, m)}{\partial T_0}\right]_p \sim -\left[\frac{\partial \ell n\, q_c)}{\partial T_0}\right]_p \simeq \left[\frac{\ell n\left(1+\frac{\Delta q_c}{q_c}\right)-\ell n\left(1-\frac{\Delta q_c}{q_c}\right)}{\Delta T_0}\right]_p \quad (V.17)$$

noting that $\Delta m \sim -\Delta q_c$. The aforementioned values of Δq_c yield σ_p = 0.0018 and 0.0022 1/K at 1 and 4 MPa respectively, in reasonable agreement with the HMX results of Boggs,[61] namely, 0.0015 1/K, for the given pressure interval.

D. Summary and Conclusions

An asymptotic theory and a subsequent nonlinear model were developed in this study, for the analysis of steady deflagration of nitramine monopropellants at the lower part of the rocket operating pressure regime. Physical reasoning has led to the two-zone, near field – far field concept of the nitramine gaseous deflagration wave, and to the derivation of the asymptotic burning rate equation. The asymptotic theory has put these concepts

within a rigorous mathematical framework, obtained an expression for the flame speed eigenvalue, and indicated the relative influence of the various flame regions upon the deflagration rate.

The nonlinear gas phase model, aimed mainly at the region close to the propellant surface, was solved by a numerical finite difference algorithm, coupling the chemically reacting liquid layer with the near field in the gas. The results of this analysis tend to verify the conclusions of the asymptotic theory within the pressure range tested. In addition, the detailed structure of the near field in terms of temperature and chemical species distributions, as well as thermophysical properties has been defined.

The capability of dealing with multiple simultaneous reactions in the flow field (without resort to lumping into a single overall reaction step), with thermophysical properties dependent upon local temperature as well as on species concentrations, and the coupling of the condensed and gas phase processes through the rigorous interface conservation conditions, has been demonstrated. It provides a reliable (yet not too complex) framework, through which the uncertainty in the results is largely confined to the thermophysical and thermochemical data available.

The main insights obtained by the analytical work herein, pertaining to the deflagration process are summarized as follows.

1. The near field and far field distinction in the gas phase holds true within the pressure range considered, as verified by the numerical analysis.

2. Over a wide range of pressures, the burning rate exhibits a variable pressure dependence, increasing from $n = 0.5$ at low pressures, to $n = 1.0$ at high pressures. Consequently, simple burning rate formulae incorporating a single pressure exponent, n, are expected to be limited to relatively narrow pressure intervals. This result of the asymptotic theory is in agreement with measured burning rate data at both low and high pressures.

3. The calculated surface temperature was found to vary with pressure, and correlate with the imposed burning rate to yield an Arrhenius-type relationship.

4. The nonlinear analysis has shown the flame speed eigenvalue to decrease linearly with pressure, as $\Lambda = 0.6 - 0.03p$, predicted by the asymptotic theory.

5. The primary deocmposition reaction rate is thermally enhanced by the presence of the considerably weaker secondary reaction. This points to a mechanism of indirect coupling between the far field processes (secondary reactions) and the burning rate, through which the far field effect is amplified. In this respect the near field region with its dominant primary deocmposition has fundamental importance in governing heat feedback to the propellant surface. Thus, it is anticipated that as pressure increases, a relatively small change in final flame temperature would correspond to an appreciable change in burning rate.

6. Compared to the primary decomposition reaction, the secondary reaction incorporated in the gas phase model has typically a smaller effect on the deflagration rate, involving from 7% to 16% of the net conductive heat feedback to the condensed surface within $1 < p < 4$ MPa; yet it accounts for the entire pressure-variation of the flame speed eigenvalue. This indicates a rather profound effect upon the overall pressure behavior of the system, although quantitatively small within the range tested.

7. The calculated effect of exothermic liquid phase decomposition upon the deflagration rate is from 2% at 1 MPa to 8% at 4 MPa, while the corresponding extent of decomposition within the liquid is between 2% and 9%. Although increasing in an accelerated manner for $1 < p < 4$ MPa, this effect is expected to reach a maximum of 25% at higher pressures (provided the liquid phase model is still valid), and then to decrease as pressure is increased further.

The foregoing conclusions, along with the results of the analysis contribute in a major way toward an improved understanding of the deflagration process of pure nitramines. Relative to previously published analyses of nitramine deflagration, the conclusions regarding the overall behavior, as well as the details of the deflagration wave structure are entirely new.

The theory and analytical model developed in this study are aimed at obtaining a rational framework within which the normal deflagration of nitramines can be studied under a variety of plausible chemical reactions and kinetic parameters, thermophysical input properties and ambient data – as long as the physical assumptions remain valid. In this respect, success is not measured by the ability of the model to predict burning rate close enough to that observed by experiments, under a particularly fortuitous set of input parameters; rather, it is measured by the model's adaptability to various propellants of the same family, chemical mechanisms and sets of input data, and by its ability to consistently provide both detailed structure and overall behavior of the deflagration mechanism.

E. Recommendations

1. Extention of the Analysis over the Far Field

To obtain a more complete picture of the gaseous deflagration wave of nitramine monopropellant, a more thorough investigation of the far field processes is required. This necessarily involves the following additions to the present algorithm.

a) Extension of the space coordinate over the entire gaseous reaction region. This may be achieved in either of two ways. (1) Direct modification to the numerical algorithm, utilizing variable space-mesh size, with small increments in the near field and progressively larger divisions in the far field. (2) Transformation of the equations of motion to the phase plane, (using thermal enthalpy as independent variable), or transform of the semi-infinite space domain in y to a finite domain, such as

$$\xi = 1 - exp(-sy) \qquad \text{(V.18)}$$

with s > 0, which requires re-derivation of the equations of motion, but the numerical algorithm in this case may utilize uniform mesh size for the independent variable ξ .

b) Modification of the chemical mechanism, to include a better representation of the far field processes. This requires the incorporation of more secondary reactions, such as $N_2O + CH_2O$, CH_2O decomposition, further reactions involving NO, NO_2 and other plausible reactions.

2. Extension of the Analysis over the Entire Rocket Operating Pressure Regime

This involves analysis at ambient pressures up to O(10 MPa), and definitely requires a more complete representation of the far field processes, as discussed above. It might further require modifications to the primary decomposition mechanism of nitramines, as the mechanism and data used presently are based on low pressure measurements, at slow heating rates.

3. Improved Chemical Reaction Mechanism

Representation of the chemical processes in the flame field in terms of elementary reaction steps, as mentioned earlier, is highly desirable. Unfortunately, the kinetic data in existence at present is insufficient for carrying out actual calculations with confidence, especially within the framework of a nonlinear model, where various influences may not be simply superimposed. An intermediate step in this direction would be to incorporate several (more than two) overall reaction steps, such that the final flame temperature and product compositions agree with experimental observations. Coupled with an adequate far field representation, the more detailed chemical mechanism could contribute toward further understanding of the deflagration process.

4. Stationary Critical Behavior

The liquid phase observed at low to intermediate pressure deflagration, tends to decrease in thickness and then possibly disappear altogether, as higher pressures are approached. This is expected to lead to considerable changes in the combustion mechanism, which would now be entirely driven by heat feedback from the gas phase, with a positive surface heat release, provided by the rapid gaseous decomposition of nitramine in a thin layer near the solid-gas interface (cf. discussion in Chapt. III).

Investigation of the behavior in the neighborhood of this critical phenomenon should involve an extensive re-modeling of the liquid phase process, to allow for the possible presence of observed bubbles containing gaseous products of decomposing nitramine in the liquid. This amounts to a two phase analysis, with strong emphasis on heat exchange between the interpenetrating gas and liquid media.

The appearance of such gas bubbles in the liquid layer of deflagrating secondary explosives, is sometimes associated with transition to denotation.[79] In this instance, the investigation may be expected to provide valuable insight into the process of transition to detonation and steady deflagration limits of pure nitramines.

5. Other Nitramine Compounds and Nitramines with Non-Energetic Binders

The present investigation was intentionally limited to the properties of RDX, the simplest cyclic nitramine compound, for the purpose of clearly demonstrating the outstanding features of the entire nitramine group. Utilizing the algorithm developed herein, the deflagration characteristics of other nitramine coupounds (such as HMX) may be readily evaluated. This involves possibly changes in the chemical mechanism, and use of appropriate thermochemical data. However, as long as the general near field-far field distinction remains valid (as it is certianly the case with HMX), only minor modifications to the input can be forseen.

A considerably more difficult problem is presented by the incorporation of non-energetic binder materials in the propellant composition. The difficulties are mainly in that the propellant loses its homogenity, which implies dependence upon granulation size distributions, necessitates consideration of different melting temperatures and involves irregular surface structure; in addition, strictly speaking, the premixed gaseous flame field assumption used herein is devalidated. Thus, at first glance, the deflagration process in this instance appears much more complex than that formulated for the monopropellant.

Still, some valuable preliminary insight may be obtained by retaining the present model, with the binder and associated species and reactions added. The following modeling stage would inherently involve more complex gas phase fluid dynamic mechanism (e.g., use of the Granular Diffusion Flame concept[102] for gasified binder pockets in a reacting premixed atmosphere), as well as an irregular condensed phase surface.

The consideration of energetic additives (such as AP) seems only one step further in the same direction, but the diverse phenomena introduced truly exclude any realistic discussion of the analysis for this case, within the present framework.

CHAPTER VI

STEADY OPERATION OF PROPELLANTS WITH EXTENDED
GASEOUS REACTION ZONES IN THE ROCKET CHAMBER

A. Introduction

In the first part of this work, it has been indicated that pure nitramine propellants exhibit relatively thick flame zones in the normal, rocket-operating pressure regime. The flame zones are extended by relatively slow secondary chemical reactions, in a premixed manner; double base (DB) propellants are known to show the same tendency,[67,68] although, when modified by energetic additives (ammonium perchlorate at the 20 to 30% level), their flame thicknesses tend to diminish. The variation of flame height with pressure for several practical solid propellants under normal, steady state (or strand) burning conditions is depicted in Fig. III.3; experimental and theoretical results are shown. It is evident that, in general, nitramine and DB propellants have gaseous flame zones much thicker than ammonium perchlorate (AP) composite propellants at the same pressure. This difference may extend over two or three orders of magnitude, with the flame thickness of pure AP being $O(10 \ \mu m)$ typically, while that of nitramine and DB may reach $O(1000 \ \mu m)$, under the same ambient conditions.

For rocket motor applications, the length of the gaseous reaction region is of great practical importance in determining the combustion behavior under both steady-state and dynamic operating conditions. Propellants with relatively long gaseous reaction regions have an increased tendency to erosive burning (as will be shown in the present chapter) and, in extreme cases, would even fail to achieve the expected specific impulse, I_{sp}, due to continued reactions beyond the exit nozzle. Therefore, propellants which differ appreciably in the length of their flame zones, under the same ambient conditions, are expected to differ significantly for similar motor configurations in both stationary and dynamic behavior.

Interior burning motor configurations shall be considered in the present discussion, that is, motors with a prismatic, longitudinal cavity in the propellant. Thus, at any particular axial station, the propellant regresses in a direction perpendicular to that of the main axial flow. The generally three-dimensional flow field may be approximated by the following division into two distinct regions:

(a) the core, extending over most of the cavity cross-sectional area, where the mean flow is axial and inviscid,

(b) a wall layer, adjacent to the propellant surface, where the only flow direction considered is perpendicular to the propellant surface.

This simplified physical configuration is shown schematically in Figs. VI.1a and VI.1b. A similar idealization was considered by Zeldovich,[103] in his analysis of propellant combustion in a gas flow.

Within the wall layer, characterized by dominant viscous transport and relatively small axial velocity component (as opposed to predominant axial motion and turbulence transport in the core), the question is what is the proportion between its thickness, y_1, and a chemical relaxation scale, δ_{RW},

associated with the extended gaseous reactions in the flame zone. Evidently, if $y_1 / \delta_{RW} \gg 1$, the gaseous reactions would go to completion well within the wall layer, the core flow would consist of fully reacted combustion products, and the core-wall layer interface (an imaginary surface) is expected to represent an adiabatic boundary. In this instance, roughly speaking, there is no interaction between the fluid dynamic processes in the core and the gaseous flame, and the propellant burning is unperturbed.

On the other hand, when $y_1 / \delta_{RW} \gtrsim 1$, the secondary reaction would not be fully completed within the wall layer, reactants may be swept out into the core, and the core flow can include now chemical reactions. In the presence of sufficiently high turbulence intensity in the core, heat may be fed back to the outer region of the wall layer (by the turbulent mechanism, with the local core – wall layer enthalpy difference serving as driving potential). The mode of propellant burning may now differ substantially from that in a quiescent environment, due to the disturbance of the outer flame region; thus, interaction between the propellant combustion and the fluid dynamic processes in the core would prevail.

Indirect experimental evidence to the existence of relatively slow chemical reactions in the core flow of solid propellant motors has been reported by Battista,[104] involving double base propellants. The observations consist mostly of low L-star effects (dynamic instability induced by low ratio of propellant cavity volume to nozzle throat area, leading to insufficient time for complete gaseous reactions) and the tendency of exhaust gases to burn beyond the nozzle.

The thickness of the wall layer region, y_1, is not expected to be uniform along the axis, as shown in Fig. VI.1a and discussed in the following section. y_1 is expected to be relatively large near the head end, and become thinner at downstream positions; neglecting for the moment the weak pressure gradient along the port, the chemical scale, δ_{RW}, would be relatively uniform in comparison. Therefore, a region where $y_1 > \delta_{RW}$ (no interaction) may prevail near the head end, while $y_1 < \delta_{RW}$ (interaction) could evolve at downstream core positions within the same motor.

In a stationary sense, interaction between the core flow field and the reacting layer can lead to perturbed burning, as differs from the normal, steady state deflagration mode. When nonsteady operation is considered, namely, fast varying phenomena in the combustion chamber, non-interacting and interacting cases may differ substantially, due to the presence of exothermic reaction in the core and heat exchange between the core and the wall layer in the latter case.

The dynamic effects of the chemically reacting core flow, coupled to the wall layer are the subject of the treatment in the following chapters. The present chapter serves to introduce the concept of the reacting wall layer and its coupling with the core at steady state. In this respect, the present analysis may be regarded as an intermediate step between the foregoing part of this work, which dealt with the steady, normal burning of nitramine monopropellants, and the second part, dealing with nonsteady burning of such propellants in a rocket chamber environment. Section B is a comparison between the blown, viscous sublayer thickness and the relevant secondary reaction scale. The reacting wall layer model and interaction criteria are given in

Section C and D. The solution procedure is described in Section E, and the results of the analysis discussed in Section F.

B. Comparison of Blown, Viscous Sublayer Thickness with the Chemical Relaxation Scale.

An approximate treatment of a viscous, blown wall layer region is offered in this section, with the objective of obtaining an estimate of its thickness based on fluid dynamic criteria. This wall layer thickness is then compared with a chemical length scale, representative of the chemical process in the propellant gaseous deflagration wave; the comparison would be indicative of the extent of reaction in the wall layer. The present analysis is intended only to verify the plausibility of the physical concepts used in the models of reacting wall layer and core flow of subsequent sections. Fluid dynamic criteria of interaction between the wall layer and the core flow (such as velocity matching) are not pursued beyond this point.

1. Viscous Sublayer Analysis

A viscous, chemically inert wall layer is considered, with mass injection at the inner boundary. A turbulent outer region exists, separated from the viscous layer by an intermediate (or buffer) zone, where turbulent and viscous transport are comparable. The physical picture is depicted in Fig. VI.1a.

Following the treatment by Tennekes,[105] the momentum equation for the viscous layer is

$$\rho v \frac{\partial u}{\partial y} = \frac{\partial}{\partial y}\left(\mu \frac{\partial u}{\partial y}\right), \quad \frac{\partial p}{\partial x} \simeq \rho u \frac{\partial u}{\partial x} \simeq 0 \quad \text{(VI.1)}$$

Assuming further that $\partial \rho u / \partial x \simeq 0$, it follows from continuity that

$$m = \rho v(\eta) = const \quad \text{(VI.2a)}$$

Using dimensionless variables $\phi \equiv u/u_\tau$ and

$$\eta \equiv \int_0^y \frac{dy}{(\mu/m)} \quad \text{(VI.2b)}$$

where the frictional velocity is defined $u_\tau \equiv (\tau_w/\rho_0)^{0.5}$, the momentum equation reduces to the following self-similar form,

$$\frac{d\phi}{d\eta} = \frac{d^2\phi}{d\eta^2}, \quad m \neq 0 \quad \text{(VI.3)}$$

The solution to this equation which satisfies the no-slip condition $\phi(0) = 0$ is

$$\phi(\eta) = \frac{1}{\beta}\left[e^\eta - 1\right] \quad \text{(VI.4)}$$

where β is an integration constant. For cases of blowing, m > 0 and the above solution tends to infinity as $\eta \to \infty$, and hence is not valid for matching with the outer zone solution. However, for small values of η it is expected to suffice, recalling that the present analysis is intended merely for an estimate of the viscous sublayer thickness. Therefore, β may not be evaluated by matching; instead, it can be determined by the shear stress at the wall (incorporating the effect of mass injection):

$$\tau_w = \mu \, \partial u / \partial y (0) = m \, u_\tau / \beta$$

and hence,

$$\beta = m \, u_\tau / \tau_w = m (\rho_o \, \tau_w)^{1/2} \qquad \text{(VI.5)}$$

The position of the outer end of the viscous sublayer, y_1, is assumed to be at the point where the velocity is equal to a common velocity scale w* for both viscous sublayer and intermediate zone: $u(y_1) = w^*$. Utilizing the linear expression obtained by Tennekes[105] for cases of blowing or suction,

$$\frac{w^*}{u_\tau} \doteq 2.3 \left[1 + 9 \frac{v_s}{u_\tau} \right] = 2.3 \left[1 + 9 \frac{\rho_o}{\rho_s} \beta \right] \qquad \text{(VI.6)}$$

where the last equality follows from the definition of u_τ , and $\rho_s = \rho(0)$. Thus, letting $\phi(\eta_1) = w^*/u_\tau$, Eqs. (VI.4) and (VI.6) yield an expression for the dimensionless viscous sublayer thickness:

$$\eta_1 = \ln \left[20.7 \frac{\rho_o}{\rho_s} \beta^2 + 2.3 \beta + 1 \right] \qquad \text{(VI.7)}$$

A more explicit expression for β can be obtained by use of C_f, the blown wall friction coefficient, defined by

$$\tau_w = \frac{1}{2} \rho_o U_o^2 C_f$$

where U_0 is the centerline axial velcity in the core. Defining $G \equiv \rho_0 U_0$, Eq. (VI.5) yields

$$\beta = \frac{m/G}{\sqrt{\frac{1}{2} C_f}} \qquad \text{(VI.8)}$$

Plots of $\phi(\eta)$ versus η are given in Fig. VI.2, with $\rho_0/\rho_s = 1$, and β as parameter. Evidently, η_1 depends only on β (neglecting for the moment the effect of $\rho_0/\rho_s < 1$), which can be termed the viscous sublayer transfer number. This parameter differs somewhat from the global transfer number defined by Lees,[87]

$$B = \frac{m/G}{\frac{1}{2} C_f} \qquad \text{(VI.9)}$$

for cases of blowing. The difference emanates from the use of the free stream velocity U_0 as reference velocity in the boundary layer by Lees,[87] as opposed

to the more appropriate frictional velocity u_τ used for the viscous sublayer in the present analysis; note that

$$u_\tau / U_0 = \sqrt{C_f} = \beta/B$$

according to the foregoing definitions.

To complete the calculation of η_1 as function of G/m, the values of C_f must be defined. Using the global transfer number B, the ratio of blown to impervious (m = 0) friction coefficients is approximated by

$$C_f/C_f^0 \doteq 1.2 \, B^{-0.77} \tag{VI.10}$$

This correlation is due to Marxman,[106] intended for the range $5 < B < 100$ and expected to apply to higher values of B as well. The impervious-wall friction coefficient is approximated by the Blasius formula[107]

$$\frac{1}{2} C_f^0 = 0.03 \, Re_x^{-0.2} \, Pr^{-2/3} \tag{VI.11}$$

using the core flow Reynolds number as function of axial position x,

$$Re_x \equiv Gx/\mu = \frac{G}{m} \left(\frac{md}{\mu} \right) \frac{x}{d} \tag{VI.12}$$

where d is the port diameter and μ the core viscosity. Re_x is used rather than $Re_d = Gd/\mu$ to compensate for the expected developing nature of the core velocity profiles, neglected so far due to the assumptions of $\partial u/\partial x \doteq \partial p/\partial x = 0$. For the turbulent core flow, $Pr \doteq 1$ shall be assumed henceforth.

Given the values of (G/m, x/d, md/μ, ρ_0/ρ_s), the calculation may proceed as follows.

(1) Using Eqs. (VI.11) and (VI.12) to eliminate C_f^0 from Eq. (VI.10), this equation yields $C_f/2 = f(B)$.

(2) Combining the last result with Eq. (VI.9), B can be calculated.

(3) $C_f/2$ can now be obtained, using B in Eq. (VI.9).

(4) Using $C_f/2$ in Eq. (VI.8), β can be defined.

(5) Substituting β in Eq. (VI.7), η_1 can be obtained.

(6) To obtain y_1, the spatial distribution of $\mu(y)$ must be defined. Approximately,

$$\mu/\mu_s = \left(T/T_s \right)^{1/2} \tag{VI.13a}$$

Assuming now, for instance, a linear temperature profile within the layer,

$$T/T_s = 1 + a\tilde{y} \qquad \text{(VI.13b)}$$

where $a \equiv (T_1 - T_s)/T_s$, $T_1 = T(y_1)$ at the layer edge, and $\tilde{y} \equiv y/y_1$. Under these conditions, the integral of Eq. (VI.2b) can be shown to yield

$$y_1 = \eta_1 \frac{\mu_s}{m} \frac{a/2}{\left[(1+a)^{0.5} - 1\right]} \qquad \text{(VI.13c)}$$

Note that for the last calculation m is required explicitly, and that $\rho_0/\rho_s = T_s/T_1$ [when $p(y) \doteq$ const and the mean molecular weight $W(y) \doteq$ const].

For purposes of the present analysis, a uniform mass injection rate is assumed, viz., $m(x) = m = $ const. Assuming in addition a flat velocity profile in the core, as shown in Fig. VI.1b, G(x) then represents the mean mass flux in the core for a cylindrical grain port with these idealizations,

$$G/m = 1 + 4x/d$$

where the core mass flux at the head end is $G(0) = m \neq 0$.

2. Discussion of Results

The calculations were carried out with $\rho_0/\rho_s \doteq 1$ and $\mu(y) = \bar{\mu} \sim \sqrt{(T_1 + T_s)/2}$ in Eqs. (VI.7) and (VI.2b) respectively. Consider a typical case of combustion, with $T_s = 650$ and $T_1 = 2600$ K; $T_1/T_s = 4$, and $\rho_0/\rho_s = 1/4$. This particular set of data implies an overestimate of η_1 by 8% at $\beta = 1000$, and by 18% at $\beta = 10$. For y_1, employing the uniform mean viscosity results (with $a = T_1/T_s - 1 = 3$) in an overestimate by 5%. These deviations by no means offset the physical significance of the results.

The results are plotted as functions of G/m in Figs. VI.3 through VI.6. The viscous sublayer transfer number, β, is depicted in Fig. VI.3 with the blowing Reynolds number, md/μ, as parameter. A hyperbolic decrease with G/m is demonstrated, as

$$\beta \sim (m/G)^{1.8} (md/\mu)^{0.43}$$

The blown friction coefficient ratio, C_f/C_f^0, is plotted in Fig. VI.4 with md/μ as parameter. This function increases parabolically with G/m,

$$C_f/C_f^0 \sim (G/m)^2 (md/\mu)^{-0.66}$$

As expected, C_f/C_f^0 approaches unity as the blowing ratio m/G decreases, in an accelerated manner. The dimensionless sublayer thickness, η_1, is drawn in Fig. VI.5, for $\rho_0/\rho_s = 1$. The variation follows that of β on a logarithmic-scale.

The viscous sublayer thickness, $y_1 = (\mu/m)\eta_1$, is plotted against G/m in Fig. VI.6, at various values of (m;d). The y_1 profiles resemble those of η_1: the sublayer thickness becomes smaller as the blowing ratio, m/G, decreases, for fixed (m;d), and increases for larger port diameters, d, at fixed (G/m;m). Unlike η_1, however, y_1 depends inversely on the blowing rate, m, at a given

(G/m , d). The secondary reaction scale associated with the sublayer process,

$$\delta_{RW} = m/\overline{\omega}_2^* \sim m/p^2$$

is overplotted for comparison with y_1. Since a uniform pressure has been assumed within the port, it follows that $\delta_{RW}(G/m) = \text{const}$. The three values of δ_{RW} shown correspond to the values of m(p) used in the calculation of y_1 (from RDX burning rate data). The kinetics of the $CH_2O + NO_2$ reaction (slightly modified, with $A_2 = 3 \times 10^6$ m^3/mol-s) were employed in the calculation of $\overline{\omega}_2^*$, and δ_{RW} is otherwise defined similarly to the secondary reactive scale shown in Fig. III.3 and discussed in Section III.B. The straight lines of $\delta_{RW}(m,p)$ are shown to intersect the associated $y_1(m)$ curves in Fig. VI.6. For a given (md/μ), $\delta_{RW}/y_1 \sim m^2/p^2$ which decreases with increasing pressure. Thus the points of crossover, where y_1 becomes smaller than δ_{RW}, occur at higher values of G/m as the pressure increases. To a lesser extent, this also occurs for a given (m;p) as the port diameter, d, is increased.

The axial velocity component within the viscous sublayer is expected to be small compared to the mean core velocity, U_0, due to the combined effects of wall proximity and blowing. In addition, the sublayer thickness is relatively insensitive to the actual value of the axial velocity chosen for its definition, $\phi^* \equiv w^*/u_\tau$, cf. Eq. (VI.6). This is due to the logarithmic dependence $\eta_1 \sim \log(\beta\phi^* + 1)$. Thus, for large enough β, $\Delta\eta_1 \sim \Delta\phi^*/\phi^*$; if instead of w^* one choses $0.1w^*$ for the definition of η_1, then $\Delta\phi^*/\phi^* = -0.9$, and $\Delta\eta_1/\eta_1 \doteq -0.9/10 = -9\%$, where $\eta_1 \doteq 10$ typically, near the head-end.

In conclusion, the analysis indicates that for $1 < p < 6$ MPa and the conditions tested, the blown viscous sublayer thickness is comparable to the chemical relaxation scale associated with secondary reactions in the flame zone of nitramines. Further, the sublayer thickness for small G/m (as near the head-end of the port) tends to be larger than the chemical scale δ_{RW}, while the reverse holds for large G/m (downstream port positions). The extent of the region near the head end, where $y_1/\delta_{RW} > 1$, tends to increase with pressure and port diameter.

3. Critique of the Viscous Sublayer Analysis

The preceding analysis was intended only for the purpose of estimating the ratio δ_{RW}/y_1 along the propellant port. In the way of critique, the following points can be made.

(a) The concept of a purely laminar viscous sublayer seems artificial, in that it neglects the generation of turbulence near the wall. The dissipative member, $\partial(\mu\,\partial u/\partial y)/\partial y = \partial\tau/\partial y$ in Eq. (VI.1) should have contained an additional term, such that

$$\tau = (\mu + \varepsilon_T)\,\partial u/\partial y$$

$$\varepsilon_T \equiv (k^* y^2)^2 \rho\,\partial u/\partial y \qquad \text{(VI.15a)}$$

ε_T in the last equation involves the Prandtl mixing length concept, ℓ_T^2,

approximated near the wall by the Hama correlation,[108] as $\ell_T \doteq K^* y^2$. Substitution of Eq. (VI.15a) in Eq. (VI.1) right hand side, and transforming to dimensionless coordinates, the differential equation for the viscous sublayer becomes, after one integration:

$$\xi^4 \left(\frac{d\phi}{d\xi}\right)^2 + \alpha_T \left[\frac{d\phi}{d\xi} - (\beta\phi + 1) \right] = 0 \qquad \text{(VI.15b)}$$

where $\xi \equiv y/(\nu/u_\tau)$, the kinematic viscosity is $\nu = \mu/\rho$ and $\alpha_T \equiv (1/K^*)/(\nu/u_\tau)$. α_T is the ratio of a turbulent length scale to the viscous, laminar length scale. Note that $\nu/u_\tau = \beta \cdot (\mu/m)$. When α_T is large and ξ small, the present configuration reduces to the former one, whose solution is given by Eq. (VI.5). Using the data of Hama,[108] for impervious-wall pipe flow, $\alpha_T \sim O(100)$ and, thus, $\alpha_T^2 \sim O(10^4)$. Dividing Eq. (VI.15) through by α_T^2, the first term becomes negligible (assuming all derivatives and ξ of order unity), and the solution, by Eq. (VI.4), would be a zeroth order approximation.

(b) The effects of combustion with the large associated temperature (and composition) variation across the reaction zone were discussed to some extent in the foregoing sections, where density and viscosity variations were considered. As mentioned earlier, these considerations do not offset the physical significance of the results. Additionally, as noted by Lees,[87] variations in the Stanton number (or the thermal enthalpy transfer coefficient) due to Mach number, pressure gradient, and stagnation-to-surface enthalpy ratio are surprisingly small. Analogously, C_f is not expected to vary appreciably due to the above effects.

Experimental observations of blown, turbulent boundary layers with and without combustion were made by Wooldridge and Muzzy,[109] simulating the behavior of hybrid rocket systems, where combustion is non-premixed. Similarity of the velocity profiles (between combustion and cold flows) in the turbulent region were found. The ratio

$$\frac{C_f(comb)}{C_f(cold)} \approx \frac{(\mu/y_1)_{comb}}{(\mu/y_1)_{cold}}$$

was calculated and found to lie between 1.6 and 0.80, for the range $2 < B < 55$. The values of μ_{cold} are, of course, lower than those corresponding to high-temperature combusting mixtures, which may explain the large observed upward deviation.

To conclude, it seems that the viscous sublayer analysis of the present section, despite its approximate nature, yields a reasonable estimate of the sublayer thickness, y_1. The estimates regarding the extent of interference between the core and the wall layer reaction, based on the ratio δ_{RW}/y_1, should therefore be valid.

The relatively small tangential velocity components and turbulence effects within the sublayer indicate the plausibility of a one-dimensional approximation of the reacting wall layer region. This would offer great analytical simplicity, yet allow for a reasonable representation of the physically important phenomena.

C. The Chemically Reacting Wall Layer at Steady State

1. Physical Considerations

The present approach is based on the following assumption: to a first approximation, both turbulence effects and velocity components tangent to the propellant surface are negligible within the wall layer region. This region is conceptually similar to the viscous sublayer discussed in Section B herein. A one-dimensional, reacting wall layer is postulated for the portion of the gaseous deflagration wave residing within the wall layer region. The physical processes in the wall layer remain, therefore, the same as those in the gaseous deflagration region at the normal burning mode.

For certain local core conditions, the entire gaseous deflagration zone of the propellant might be included within the viscous sublayer region, as indicated in Section B by $\delta_{BW}/y_1 < 1$. In this instance, the flame zone would remain unperturbed locally, and propellant burning should proceed in a manner identical to that of normal deflagration under the given ambient conditions, $[p(x), T_0]$. This configuration is commonly observed in practice with propellants having sufficiently thin gaseous flame zones, burning in a rocket chamber environment.

When the local core mass flux, $G(x)$, is sufficiently large, the turbulent intensity in the neighborhood of the wall layer edge may reach a high enough level such that interference with the outer zone of the gaseous reaction would occur. The interference is manifested by the effective removal of reactants from the final stages of the flame and the supply of heat (through the turbulent convective mechanism) to the outer edge of the wall layer. In this case, propellant burning would be perturbed, following the disturbance of the outer portion of the gaseous deflagration wave.

The basic difference between perturbed and unperturbed wall layer configurations lies in the manner and extent of coupling with the adjacent core flowfield. The unperturbed case depends on a single core state-variable, $p(x)$. The perturbed case, in addition, (as will be shown) is coupled rather strongly with fluid dynamic core variables such as the mean core mass flux, $G(x)$, and stagnation enthalpy, $h_{stg}(x)$. The core flowfield, in turn, will depend only upon the mass flux, m, and the enthalpy, h^*, of the fully-reacted, injected gas in the unperturbed case. For the perturbed case, the core flowfield will depend, in addition, on the reactant concentration of the gas injected, as well as on the heat balance, due to injected enthalpy, heat feedback to the wall layer edge, and heat generation by local chemical reaction in the core. The latter case clearly presents a much stronger coupling between the wall layer and core flow field.

Matching of local tangential velocity components at the outer edge of the viscous wall layer is a plausible criterion of interaction with the core flow, and requires a two dimensional analysis of the wall layer region. The present quasi one dimensional wall layer configuration precludes such matching; instead, a thermodynamic interaction condition is postulated, based on matching of the specific heat feedback supplied from the core and that required within the wall layer at its outer (cutoff) edge. The definition of perturbed states hinges upon this condition.

The particular properties of nitramine propellants will be utilized in the
present section, in order to make the results directly applicable to actual
propellants having thick, premixed gaseous reaction regions (with slight
modifications, the analysis can apply to double base propellants as well).
For this purpose, a simplified version of the two-zone, reacting gas phase
theory, developed in Chapter III, will be employed.

The term perturbed state is intended as a generalization of stationary
erosive burning associated usually with the enhancement of burning rate by
turbulent heat transfer from the main flow. The range of perturbed states
considered included both enhancement and retardation (termed negative erosion
and observed in the composite-propellant experiments of Dickinson and
Jackson[110]) as two sides of the same physical phenomenon, namely, interference
between the coreflow and the outer portion of the gaseous flame zone. Roughly
speaking, the specific enthalpy feedback to the wall layer edge, θ_{fb}, may not
match the specific enthalpy flux, θ_e^0, required for the normal unperturbed
configuration at the same cutoff enthalpy. When $\theta_{fb} > \theta_e^0$, physical equilibrium
within the layer would be achieved at a mass burning rate such that $m > m^0$. Of
course, when there is no interference, $m = m^0$ should be recovered. In cases of
cross-over (as δ_{RW}/y_1 becomes larger than unity at downstream sections of
the port), the so-called critical or threshold erosive velocity (in the core)
is realized as the point where the turbulent mechanism in the core begins to
effectively interfere with the reacting wall layer; this occurs as the wall
layer thickness decreases with increasing axial position, x, exposing the outer
reaction region. Similar explanations (regarding the threshold velocity) have
been suggested by Vandenkerchove[112] and discussed by Yamada, et al,[113] although
without any of the details of the flame zone structure considered presently.

In the remainder of this section and in the following one, the formulation
of the wall layer is given, and the physical ideas regarding the reacting wall
layer concept and the interaction criteria are put in a more rigorous form.

2. Analytical Model for the Unperturbed Reacting Wall Layer

The lowest order formulation regarding the gaseous deflagration of
nitramines is employed along with the pertinent assumptions. These have been
detailed in Section III.F. The two-zone, near field and far field concept is
therefore adopted for the purpose of describing the reacting wall layer
processes, assumed to be applicable within the range of pressures presently
considered.

Enthalpy and chemical species concentrations, as functions of distance in
the layer, y, are not required, as well as the details of the near field
interior. The analysis is pursued to the point where the fluxes of total
enthalpy and species can be solved for, as functions of local thermal enthalpy
in the far field.

a. The Near Field Formulation

The near field conservation equations, written for the total flux terms at
the zeroth order, are:

$$\frac{d\phi}{d\zeta} = \Lambda \tilde{\omega}_1, \qquad 0 < \zeta < \infty \qquad \text{(VI.16)}$$

The total flux terms (convection and diffusion) are defined:

$$\phi_T(\zeta) \equiv \tau - d\tau/d\zeta, \quad \tau \equiv h_T/Q_i^* \quad \text{(VI.17a)}$$

$$\phi_i(\zeta) \equiv \eta_i - d\eta_i/d\zeta, \quad \text{(VI.17b)}$$

$$\eta_i \equiv Y_i W_R / W_i (\nu'' - \nu')_{i,1}, \quad i = 1, 2 \cdots N$$

The dimensionless near field coordinate is $\zeta = y/(\lambda/m \cdot C_p)$; Le = 1, m = const and p = const have been assumed. Subscript 'R' denotes the nitramine species in particular, or, more generally, the homogeneous propellant molecular species undergoing primary decomposition in the near field. The flame speed eigenvalue is

$$\Lambda = \frac{\lambda/C_p}{m^2} \overline{\omega_i^*} \quad \text{(VI.18)}$$

similar to the definition in Eq. (III.29). The dimensionless, first order overall decomposition reaction rate, $\tilde{\omega}_1$, is given by the Arrhenius expression

$$\tilde{\omega}_1 = \frac{1}{\overline{\omega_i^*}} A_1 e^{-\beta_1/\tau} \rho Y_R \quad \text{(VI.19)}$$

where $\overline{\omega_i^*}$ in the last two equations is a suitable mean value of ω_1. Shvab–Zeldovich coupling terms can be formed for the total flux parameters,

$$C_{TR} = \phi_T - \phi_R = \text{const} \quad \text{(VI.20a)}$$

$$C_{i,R} = \phi_i - \phi_R = \text{const}, \quad i \neq R \quad \text{(VI.20b)}$$

These constant coupling terms can be evaluated by use of the available boundary conditions at the condensed-gas interface:

$$\phi_i(0^+) = \eta_i(0^-) \quad \text{(VI.21a)}$$

$$\phi_T(0^+) = \phi_c(0^-) \quad \text{(VI.21b)}$$

where the specific heat flux to the surface is

$$\phi_c(0^-) = f_1[\tau(0^+), m, T_0] \quad \text{(VI.21c)}$$

f_1, along with $\eta_i(0^-)$, i = 1,2,...N are given by the solution of the condensed phase discussed in Section III.C and Appendix B.

For the lowest order representation herein, the interface between the near field and far field must be defined to facilitate coupling. Let this be at the point where the total flux of initial decomposition reactant,'R', vanishes,

$$\phi_R(a^-) = 0 \qquad \text{(VI.22)}$$

and initial decomposition is virtually complete. Note that with the present notation, Eq. (VI.22) is satisfied only when both η_R and its gradient vanish simultaneously. The coordinate $a \equiv y_a/(\lambda/m\,C_p)$ denotes the position of this point in the field. The rest of the flux terms, $\phi(a^-)$, may be obtained through the use of the coupling parameters. For instance,

$$\phi_T(a^-) = C_{TR} = \phi_T(0^+) - \phi_R(0^+)$$
$$= \phi_T(0^+) - \eta_R(0^-) \qquad \text{(VI.23)}$$

Similar expressions hold for the chemical species.

To close the near field formulation, the mass burning rate correlation is introduced:

$$f_2\left[\tau(0^+), m\right] = 0 \qquad \text{(VI.24a)}$$

which, in practical application has the form

$$m = A_s \exp\left[-\beta s/\tau(0^+)\right] \qquad \text{(VI.24b)}$$

similar to an Arrhenius pyrolysis law; actually, this is a least–squares regression of the data obtained by the solution of the comprehensive nitramine model, described in Chapter V.

Prior to consideration of the far field, it should be pointed out that the gradient,

$$\frac{d\tau}{d\xi}(0^+) = \left[\frac{\lambda dT/dy(0^+)}{m}\right]\Big/ Q_1^* \qquad \text{(VI.25)}$$

is the heat feedback to the condensed phase per unit gas-mass generated, normalized by the specific heat of primary reaction, $Q_1^* = Q_1/W_R$. This term will have an important role in the remainder of the present analysis.

b. The Far Field Formulation

The dimensionless far field conservation equations, to zeroth order, are

$$\frac{d\bar{\tau}}{d\bar{y}} = (Q_2/Q_1^*)\,\tilde{\omega}_2 \qquad \text{(VI.26a)}$$

$$\frac{d\bar{\eta}_i}{d\bar{y}} = \tilde{\omega}_2\,, \quad \bar{\eta}_i \equiv Y_i/W_i(\nu''-\nu')_{i,2}\,, \quad i=1,2\cdots N \quad \text{(VI.26b)}$$

for $0^+ < y < \infty$. The far field dimensionless coordinate is $y \equiv y/(m/\bar{\omega}_{2,L})$. An overbar is used to denote the far field variables, except for $\bar{\omega}_{2,L}$ which

is a suitable mean value of the secondary reaction within the far field. The dimensionless secondary reaction rate is given by the following Arrhenius expression:

$$\tilde{\omega}_2 = \frac{1}{\tilde{\omega}_{2,L}} \, A_2 e^{-\beta_2/\bar{\tau}} \, \bar{\rho}^2 \, \frac{Y_F}{W_F} \, \frac{Y_O}{W_O} \qquad (VI.27)$$

Shvab-Zeldovich coupling parameters for the far field may be introduced:

$$B_{T,F} = (Q_1^*/Q_2)\bar{\tau} - \bar{\eta}_F = const \qquad (VI.28a)$$

$$B_{i,F} = \bar{\eta}_i - \bar{\eta}_F = const \qquad (VI.28b)$$

To zeroth order, the systems describing the near and far field processes, given by Eqs. (VI.16) through (VI.28), are essentially decoupled, as shown in Section III.F; rigorous coupling between the near field and far field processes would enter through consideration of higher order terms. Consequently, since the present analysis is limited to lowest order, an approximate coupling condition must be imposed. This involves matching of the total flux terms at the interface point, $y = y_a$. Of course, forced-coupling in this manner has nothing to do with rigorous matching of the inner and outer asymptotic expansions in a region of common validity, discussed in Chapter III. Thus,

$$\bar{\tau}(\bar{y}_a) = \phi_T(a^-) = C_{T,R} \qquad (VI.29a)$$

$$\bar{\eta}_i(\bar{y}_a) = \phi_i(a^-)/W_R = C_{i,R}/W_R \,, \, i \neq R \qquad (VI.29b)$$

are imposed, where the point 'a' has been defined by Eq. (VI.22). Note that total flux terms on both sides of the intermediate surface $y = y_a$ are equated; on the far field side, to lowest order, these involve only the convective terms (namely, diffusion terms do not appear).

The final thermal enthalpy, at $y = +\infty$, is given by the coupling term between $\bar{\tau}$ and the leanest far field reactant, say 'O':

$$\bar{\tau}_2 = B_{T,O} \qquad (VI.30)$$

where $B_{T,O}$ is defined similarly to $B_{T,F}$ in Eq. (VI.28a).

The foregoing formulation can now be solved, to the extent that no details of the near field, e.g., $\phi(\xi)$, are required, and only the far field is of interest.

As will become clear in Section 3 herein, the particular spatial dependence of the far field solution is not of interest presently. Instead, the explicit dependence of the far field properties upon $\bar{\tau}$, through $\hat{\omega}_2(\bar{\tau})$, shall be exploited. This dependence is demonstrated as follows. According to the caloric equation of state,

$$\bar{\rho} = \frac{\gamma}{\gamma-1} \, P/h_T = \frac{\gamma}{\gamma-1} \, \frac{P/Q^*}{\bar{\tau}} \qquad \text{(VI.31)}$$

Utilizing the far field coupling terms,

$$\bar{Y}_k/W_k = \frac{Q_1^*}{Q_2} (\nu''-\nu')_{k,2} \left[\bar{\tau} - \tilde{B}_{T,k}\right] \qquad \text{(VI.32)}$$

where $\tilde{B}_{T,k} \equiv B_{T,k} Q_2/Q^*_1$, and $k =$ 'O' or 'F'. Thus, the Arrhenius expression for $\tilde{\omega}_2$, in Eq. (VI.27) becomes

$$\tilde{\omega}_2(\bar{\tau}) = \tilde{A}_2 \, e^{-\beta_2/\bar{\tau}} \prod_{k=O,F} (1 - \tilde{B}_{T,k}/\bar{\tau}) \qquad \text{(VI.33a)}$$

and the dimensionless prefactor is

$$\tilde{A}_2 = \frac{A_2}{\bar{\omega}_{2,L}} \left(\frac{\gamma}{\gamma-1} P\right)^2 \prod_{k=O,F} (\nu''-\nu')_{k,2} /Q_2^2 \qquad \text{(VI.33b)}$$

Recall that $\bar{\omega}_{2,L} = \omega_2(p, \bar{\tau}_m)$ where $\bar{\tau}_m$ is a suitable mean value for $\bar{\tau}$ within the far field.

Therefore, $d\bar{\tau}/dy$ depends only on $\bar{\tau}$, as follows from Eqs. (VI.26) through (VI.33). $\bar{\tau}(\bar{y})$ is expected to be monotonously varying and Lipschitz-continuous in the domain $\bar{y}_a < \bar{y} < \infty$; thus, instead of considering the infinite domain in $\bar{y}$, one may consider the finite domain $\bar{\tau}_a < \bar{\tau} < \bar{\tau}_2$, where $\bar{\tau}_a \equiv \bar{\tau}(\bar{y}_a)$. This property will prove most useful when the core-far field interaction is considered in the following section. For this matter, the following two far field farameters are of interest in the subsequent analysis.

The specific heat feedback at any point within the far field is defined by

$$\theta \equiv \varepsilon \, d\bar{\tau}/d\bar{y} = \lambda \frac{d\bar{T}}{dy} / m Q_1^* =$$
$$\varepsilon \frac{Q_2}{Q_1^*} \tilde{\omega}_2(\bar{\tau}) \qquad \text{(VI.34)}$$

analogous to the near field quantity $d\tau/d\zeta \, (0^+)$, in Eq. (VI.25). $\varepsilon \equiv (\lambda/m \, C_p)/(m/ \, \bar{\omega}_{2,L}) \ll 1$, the ratio of the near field to far field length scales, defined in Eq. (III.30); note that $d\bar{\tau}/d\bar{y} \sim O(1)$.

The local reactedness parameter, defined:

$$\varepsilon_R \equiv \frac{\bar{\tau} - \bar{\tau}_a}{\bar{\tau}_2 - \bar{\tau}_a} \qquad \text{(VI.35)}$$

for $\bar{\tau}_a \leq \bar{\tau} \leq \bar{\tau}_2$. This property represents the extent of reaction within

the far field, as $Le = 1$ has been assumed. The above statement of $\mathcal{E}_R$ can be equivalently written in terms of any of the partinent reaction mass fraction parameters $\bar{\eta}_i$ or $\bar{Y}_i$.

3. Solution Procedure for the Unperturbed Case

Solutions to the far field of the wall layer may be obtained now for specified sets of ambient data, (p, T_0). These comprise a single manifold in terms of $\tau(0^+)$ or m. Near field details beyond d /d (0^+), $\phi(0^+)$, and $\phi(a^-)$ are not required, but the use of these variables requires implicitly the existence of solutions to the near field problem.

For a solution to be of any physical significance, $\tau(0^+)$ or m must correspond uniquely to the given ambient data. Therefore, the only admissible solution for any given set, (p, T_0), is that which pertains to a unique value of the flame speed eigenvalue, $\Lambda(p, m)$. This conclusion is drawn from the equivalence between the near field problem herein and the eigenvalue problem investigated by Johnson and Nachbar.[114,115] They have shown that to any $\tau(0^+)$ (within a certain interval), there must correspond a unique Λ.

This property of the wall layer solutions is of great importance to the subsequent attainment of unique solutions for the perturbed case.

One particular way to obtain unperturbed solutions to the wall layer formulation would be to specify $\bar{\tau}_2(p)$, being the adiabatic flame temperature at the given pressure. The following iterative procedure can be utilized.

a) Impose $\tau(0^+)$, by which $m[\tau(0^+)]$ may be calculated, through the burning rate correlation, Eq. (VI.24).

b) Generate the condensed phase solution for the data set $[\tau(0^+), m, T_0]$; obtaining $d\tau/d\xi(0^+)$, $\eta_i(0^-)$, $i = 1, 2, \ldots N$. The vector $\phi(a^-)$ may now be calculated, using the near field coupling terms, Eqs. (VI.21) through (VI.23).

c) Using $\phi(a^-)$ in Eqs. (VI.28) and (VI.29), the far field coupling parameters, $B_{T,F}$, $B_{T,O}$ can be calculated.

d) Let the genuine unperturbed solution properties be denoted by $(\ )^0$. If the calculated leanest species coupling term, $B_{T,O}$, and the imposed $\bar{\tau}_2(p)$ are equal, according to Eq. (VI.30), then the solution obtained is valid, and $\tau(0^+)^0 = \tau(0^+)$ and $m^0 = m$ correspond uniquely to the given ambient data. If, however, $\bar{\tau}_2(p)$ $\neq B_{T,O}$, then $\tau(0^+)$ is corrected, and the entire iteration loop repeated.

With the attainment of $\tau(0^+)^0$, m^0, etc., the far field properties are uniquely defined as functions of $\bar{\tau} \in [\bar{\tau}_a, \bar{\tau}_2]$. In particular, $d\bar{\tau}/dy(\bar{\tau}; p, T_0)$ is given explicitly, as all the parameters in Eqs. (VI.33) and (VI.26a) are now known.

D. Thermodynamic Interaction Criteria Between the Core and the Reacting Wall Layer

1. Turbulent Heat Feedback

The subject of heat, mass, and momentum transfer through a reacting, turbulent boundary layer has been discussed by numerous authors. Notably, Lees[87] has provided a most thorough treatment in which the physical interactions are made clear. Marxman and co-workers[106,116,117] and Wooldridge and Muzzy[109] investigated the interior ballistics problem of hybrid propellant rockets both experimentally and analytically. Although the reactants in these systems are primarily separate and combustion is essentially not premixed, the explicit treatment of turbulent transport through the layer renders some of the results of these works[87,106] highly applicable to the present analysis.

Assuming that Le = Pr = Sc = 1, and invoking the Reynolds analogy between heat, mass, and momentum transfer, Lees[87] has shown that the heat flux to the wall, q_w, through a turbulent boundary layer, is given by

$$q_w = G C_H \Delta h \qquad \text{(VI.36)}$$

where G is the mean core mass flux, C_H the turbulent Stanton number (or enthalpy transfer coefficient), and Δh the total enthalpy difference between the core and the wall, including chemical enthalpy and kinetic energy. Once the Reynolds analogy is accepted, C_H can be replaced by its momentum counterpart, $C_f/2$ being the turbulent wall friction coefficient (cf. Section B herein). When the heat flux, q_w, is used entirely to gasify the condensed wall material, resulting in a mass flux, m, perpendicular to the wall, it may be readily shown from Eq. (VI.36) that B = $\Delta h/(q_w/m)$, where the global transfer number is defined normally as B = m/GC$_H$. These relations form the basis for the solid fuel regression rate expression in the hybrid rocket, developed by Marxman.[106,116,117] The present analysis utilizes the expression of Eq. (VI.36) for heat feedback from the turbulent core to the reacting wall layer edge, with certain modifications.

The region where turbulent transport should be prominent is between the core and the outer edge of the laminar wall layer. Therefore, the above expression for heat feedback, denoted presently by q_{fb}, is more appropriate in this region. Δh is now reduced to the total enthalpy difference between the core and wall layer outer edge, which has the role of a driving potential. Consequently, a modified definition of B is also required.

With the present one-dimensional model of the wall layer, the axial velocity component is neglected within the layer; thus, the no-slip condition at the wall is effectively displaced to the wall layer outer edge, where, actually, some finite, relatively small u* > 0 prevails, assuming u*/U$_0$ << 1. Thus, approximately

$$C_H = C_H^0(C_H/C_H^0) = 0.03 Re_x^{-0.2} Pr^{-2/3} \frac{C_H}{C_H^0} \qquad \text{(VI.37)}$$

similar to Eq. (VI.11), with Pr ≠ 1 due to turbulence effects. The use of Re$_x$ = Gx/μ in the last equation, as well as in Eq. (VI.11) is intended for

approximate representation of the developing nature of the velocity profiles along the port. Experimental cold-flow results of Yamada[113] indicate that the maximal turbulence intensity increases along the port, and tends to move closer to the injected wall. The velocity profiles obtained are corroborated by the earlier measurements of Dunlap, Willoughby and Hermsen,[118] and are in good agreement with the cosine-shaped analytical velocity profiles derived by Culick[119] for the inviscid core flow. In anticipation of the relatively small transfer numbers, B*, for the present configuration, Marxman's[106] logarithmic correlation may be used:

$$C_H/C_H^0 \doteq \ln(1+B^*) / B^* \qquad (VI.38)$$

B* is defined equivalently to B in the foregoing discussion,

$$B^* \equiv \frac{\Delta h/Q_i^*}{d\tau/d\zeta(0^+)} \qquad (VI.39)$$

Finally, the total enthalpy difference, Δh, is represented by

$$\Delta h/Q_i^* = \tau_{stg}(x) - \bar{\tau}^*$$

where $\tau_{stg}(x)$ is the reduced thermal stagnation enthalpy in the core, and $\bar{\tau}^*$ is the reduced thermal enthalpy at the outer dege of the wall layer, defining the cutoff point. Therefore, written explicitly:

$$B^* = \frac{\tau_{stg} - \bar{\tau}^*}{d\tau/d\zeta(0^+)} \qquad (VI.40)$$

Returning now to Eq. (VI.36), an expression is derived for the specific (per unit mass generated at the propellant surface) turbulent heat feedback; after replacing q_w by q_{fb} and some manipulation:

$$\theta_{fb} \equiv \frac{q_{fb}}{mQ_i^*} = \frac{GC_H}{m} B^* \frac{d\tau}{d\zeta}(0^+) \qquad (VI.41)$$

By definition, $B \equiv m/GC_H$ for the global transfer number; the last equation yields, therefore, an interesting relationship between B* and B:

$$B^*/B = \frac{\theta_{fb}}{d\tau/d\zeta(0^+)} \qquad (VI.42)$$

which will be discussed later.

Finally, the dimensionless heat feedback expression can be written

explicitly, using Eqs. (VI.37), (VI.38) and Eq. (VI.41):

$$\theta_{fb} = 0.03 G Re_x^{-0.2} \ln(1+B^*) \frac{d\tau}{d\xi}(0^+)/m \qquad \text{(VI.43)}$$

with B* defined by Eq. (VI.40).

The first thermodynamic interaction constraint between the core and the wall layer can now be stated:

$$\theta_{fb}(\bar{\tau}^*) = \theta(\bar{\tau}^*) = \varepsilon \frac{d\bar{\tau}}{d\bar{y}}(\bar{\tau}^*) \qquad \text{(VI.44)}$$

which amounts to the requirement of continuity of heat transfer through the interface between the core and the wall layer, assuming no sources or sinks of heat exist at the interface.

Thus, by Eqs. (VI.42) and (VI.44), $B^*/B \sim \varepsilon \ll 1$, with $d\bar{\tau}/d\bar{y} \sim d\tau/d\xi(0^+) \sim O(1)$. The mass generation equivalent for the external heat feedback (or, equivalently, for the outer portion of the deflagration wave which has been cut off) may be defined as $\Delta m \equiv m\theta_{fb}$. Evidently, $\Delta m/m = \theta_{fb} \sim \varepsilon$; this demonstrates that the expected range of interference regarding induced mass generation is absolutely limited to $O(\varepsilon)$, relative to the total mass generation, m, at the perturbed state. The quantity Δm should not be confused with the excess (or defect) in mass generation due to the erosive effect.

2. Closure of the Interaction Criteria: The Auxiliary Constraint.

Suppose that at a specific axial position in the core, a particular set of conditions (G, τ_{stg}, p, T_0) prevails. Eliminating these known parameters from the formulation, it is therefore possible to write

$$\theta_{fb} = q_1(\tau(0^+), \bar{\tau}) \qquad \text{(VI.45)}$$

according to Eq. (VI.43); recall that m and $d\tau/d\xi$ (0^+) are uniquely defined for given sets of [$\tau(0^+)$, T_0], following Eqs. (VI.24) and (VI.21c). For the same conditions, the functional dependence of θ by Eqs. (VI.33) and (VI.34) is given by :

$$\theta = q_2(\tau(0^+), \bar{\tau}) \qquad \text{(VI.46)}$$

The heat balance requirement of Eq. (VI.44) implies that $\theta_{fb} = \theta$ for the same set [$\bar{\tau} = \bar{\tau}^*$, $\tau(0^+)$]. Clearly, only a single constraint for the definition of two parameters has been provided so far, since at the perturbed state, there exists no way to uniquely relate [m; p(x)] or [$\tau(0^+)$; p(x)] -- unlike the unperturbed, normal burning case. An additional constraint is sought, therefore, to render the perturbed state system fully determined.

The obvious equality of $\bar{\tau}_-^* = \bar{\tau}_+^*$ at the-core wall layer interface has

been inferred previously in an implicit way; a thermal shock, as for $\bar{c}_-^* \neq \bar{c}_+^*$ cannot be supported by any physical process at hand (for instance, the pressure across the interface is uniform). Likewise, the possibility of discontinuous heat transfer rate, by which $\theta(\bar{c}_-^*) \neq \theta_{fb}(\bar{c}_+^*)$, is ruled out, since it would lead to abrupt heating or cooling of a gas parcel upon passage through the interface. Continuation of this line of reasoning leads to the auxiliary constraint, for which the derivation is as follows.

By the second law of thermodynamics,

$$\Delta\sigma \geq \frac{\Delta\theta}{\bar{c}} = \frac{\theta-\theta_{fb}}{\bar{c}} \tag{VI.47}$$

where an imaginary infinitesimal process at the core wall layer interface is considered, by which the dimensionless temperature increases from $\bar{c}^*$ to $\bar{c}^* + \delta\bar{c}^*$. The corresponding change in the specific entropy being $\Delta\sigma \equiv \Delta s/C_p$. The first variation of Eq. (VI.47) with respect to $\bar{c}$, which has the role of action coordinate, yields:

$$\frac{\delta(\Delta\sigma)}{\delta\bar{c}} \geq \frac{1}{\bar{c}}\left[\frac{\partial\Delta\theta}{\partial\bar{c}}\right]_{p,Y_i\cdots} - \frac{\Delta\theta}{\bar{c}^2} \tag{VI.48}$$

Thus, a necessary condition for the vanishing of $\delta(\Delta\sigma)$ is given by:

(a) $\Delta\theta = 0$, which is satisfied by the requirement of Eq. (VI.44), and

(b) $(\partial\Delta\theta/\partial\bar{c})_{p,Y_i} = 0$ at the interface, which implies :

$$\frac{\partial\theta}{\partial\bar{c}}(\bar{c}_-^*) = \frac{\partial\theta_{fb}}{\partial\bar{c}}(\bar{c}_+^*) \tag{VI.49}$$

The last equality holds if, and only if, $\partial(\Delta\theta)/\partial\bar{c} = \Delta(\partial\theta/\partial\bar{c})$, which is not obviously satisfied, but, rather, indicated by the assumed continuity of θ, θ_{fb}, $\bar{c}$, p, etc., in the neighborhood of the interface.

When the equality in Eq. (VI.48) holds (reversible process), and with conditions (a) and (b) satisfied, Eq. (VI.48) is equivalent to the requirement that the rate of change of entropy across the interface is constant, viz.,

$$\delta(\Delta\sigma) = 0.$$

With the choice of Eq. (VI.49) as the additional constraint needed for closure of the system of equations, the problem now becomes fully determined. Fortunately, $\partial\theta/\partial\bar{c}$ and $\partial\theta_{fb}/\partial\bar{c}$ can be found explicitly through use of Eqs. (VI.33), (VI.34), (VI.40), and (VI.43):

$$\frac{\partial\theta_{fb}}{\partial\bar{c}} = -0.03G Re_x^{-0.2}/m(1+B^*) \tag{VI.50}$$

$$\frac{\partial \theta}{\partial \overline{\tau}} = \varepsilon (Q_2/Q_1^*) \frac{\partial \widetilde{\tilde{\omega}}_2}{\partial \overline{\tau}} =$$

$$\varepsilon \frac{Q_2}{Q_1^*} \widetilde{A}_2 \, \overline{e}^{\beta_2/\overline{\tau}} \left[\beta_2 \prod_{k=F,O} (1 - \widetilde{B}_{T,k}/\overline{\tau}) \right.$$

$$\left. + (1 - \frac{\widetilde{B}_{T,F}}{\overline{\tau}}) \widetilde{B}_{T,O} + (1 - \frac{\widetilde{B}_{T,O}}{\overline{\tau}}) \widetilde{B}_{T,F} \right] / \overline{\tau}^2 \qquad \text{(VI.51)}$$

The thermodynamic coupling criterion between the core and the wall layer can now be stated as follows.

At a given position along the core axis, for the particular prevailing conditions $(G, \overline{\tau}_{stg}, p, T_0)$, coupling between the core and the reacting wall layer can exist only if both interaction constraints are satisfied at the interface, namely, that $\theta = \theta_{fb}$ and $\partial \theta / \partial \overline{\tau} = \partial \theta_{fb} / \partial \overline{\tau}$, at $\overline{\tau} = \overline{\tau}*$.

As will be shown in the following section, this criterion by itself does not insure unique solutions to the perturbed state cases, although it provides closure of the system.

The variation of θ and θ_{fb} vs $\overline{\tau}$, in the case that both interaction constraints are satisfied, is plotted in Fig. VI.6. At the point where $\overline{\tau} = \overline{\tau}*$, the θ and θ_{fb} curves are tangent. The particular $\tau(0^+)$ which obtains this configuration generally differs from that of the unperturbed case, and consequently, $m \neq m^0$.

E. The Reacting Wall Layer at the Perturbed State

1. Uniqueness: The Equivalent, Unperturbed Deflagration Eigenvalue

In Section C.3. herein, the eigenvalue-nature of the reacting wall layer model was pointed out for the unperturbed case. The conclusion was that to each $\tau(0^+)$ within a certain range, there must correspond a unique $\Lambda(p,m)$, the flame speed eigenvalue. This insures that the mass generation rate, m, corresponds uniquely to the ambient data. It will be shown in this section that the same principle must apply for the perturbed model as well.

In the perturbed case, the far field boundedness condition, namely $\overline{\tau}(\infty) = \overline{\tau}_2(p)$, corresponding to normal deflagration, is replaced by the heat feedback conditions imposed at $\overline{\tau} = \overline{\tau}*$ within the far field. For a given $p = p(x)$, m may now vary with $G(x)$ and $\tau_{stg}(x)$, as imposed by the interaction constraints, independently of p.

Consider hypothetically a perturbed case for which the interaction constraints were satisfied, leading to far field heat feedback larger then that corresponding to an unperturbed case under the same pressure. This should cause burning rate enhancement, namely increased m relative to the unperturbed case. However, the far field length scale, $m/\bar{\omega}_{2,L}$ would then increase, and (roughly speaking) the associated gradients would decrease, particularly $\lambda d\overline{T}/dy \sim \omega_2/m$, contrary to physically expected behavior.

Additionally, increasing m implies increased $\tau(0^+)$ according to the correlation in Eq. (VI.24b); since $d\tau/d\varsigma(0^+)$ is relatively insensitive to variations in m, an increase of $\phi_T(0^+) = \tau(0^+) - d\tau/d\varsigma(0^+)$ would ensue. Now, as $\tau(0^+)$ and m increase, $Y_R(0^-) = \phi_R(0^+)$ decreases, as shown in the results of Chapter V. These lead to an increase of $\bar{\tau}_a$, through Eqs. (VI.23) and (VI.29a), and consequently to increasing $\bar{\tau}_2$ (since $\bar{\tau}_2 - \bar{\tau}_a = const$ for a fixed far field reaction stoichiometry). Therefore, as m increases, although $\lambda d\bar{T}/dy$ would decrease over most of the domain $\bar{\tau}_a < \bar{\tau} < \bar{\tau}_2$, a small portion near $\bar{\tau}_2$ (due to $\bar{\tau}_2$ increase) would obtain higher gradient than that in the associated unperturbed case. This indicates that the interaction point (where $\lambda dT/dy$ and q_{fb} are tangent in the $\theta - \bar{\tau}$ plane) may not be unique.

Consistency with physically observed behavior and uniqueness of the interaction point are restored by invoking the eigenvalue concept. The far field, to the present first approximation, lacks any means of communicating information upstream to the near field and the propellant surface. This is due to the absence of diffusion from the zeroth order far field formulation. Thus, the only way by which valid solutions at the perturbed state may be obtained is through the eigenvalue Λ. One way to properly implement the eigenvalue concept with the present perturbed state formulation is to consider $\Lambda(P_{eq}, m)$, where m is the mass flux in the perturbed case and P_{eq} is the equivalent pressure corresponding to this mass flux at the unperturbed, normal burning state. This, of course, follows from the uniqueness of Λ for a given $\tau(0^+)$, and the unique correspondence between m and $\tau(0^+)$. It should be pointed out that the near field problem, in both perturbed and unperturbed states, remains exactly identical. Therefore,

$$\Lambda_{pert.} = \Lambda^{(eq)}_{unpert.} \tag{VI.52a}$$

with

$$m_{pert.} = m^0(P_{eq}) \tag{VI.52b}$$

Hence,

$$\left[\rho D \bar{\omega}_i^* / m^2\right]_{pert.} = \left[\rho D \bar{\omega}_i^* / m^2\right]_{eq.}$$

where P_{eq} is defined by Eq. (VI.52b) as the equivalent near field pressure in the unperturbed case. Generally, $\bar{\omega}_1 = F_1(\bar{T}_1)p$; assuming for the present purposes that the same $F_1(\bar{T}_1)$ applies to both perturbed and equivalent-unperturbed cases, the last equation yields an expression for the modified mean far field diffusivity,

$$(\rho D)_{pert.} = (\rho D)_{eq.} P_{eq}/p \tag{VI.53}$$

after elimination of $F_1(\bar{T}_1)$ and use of Eq. (VI.52b). This modification restores proper behavior to the far field model as follows.

$$\lambda \frac{d\overline{T}}{dy}\Big|_{pert} = \left[\frac{\rho D}{m}\right]_{pert} Q_2 \omega_2 = \left[\frac{\rho D}{m}\right]_{eq.} \frac{P_{eq}}{P} Q_2 \omega_2 \qquad (VI.54)$$

Since $m_{eq} \sim p_{eq}^n$ and $n < 1$ within the relatively narrow pressure regime considered presently, $\lambda dT/dy$ clearly increases with m over the entire domain $\overline{\tau}_a < \overline{\tau} < \overline{\tau}_2$, and the interaction point is unique for a given set of conditions (τ_{stg}, G, p, T_0), as shown schematically in Fig. VI.7: once a perturbed state solution is found, pn increase of m would result in separation of the θ and θ_{fb} curves; conversely, a decrement in m would cause the curves to intersect at two points. In both cases the original solution is lost, as the interaction constraints cannot be satisfied. Therefore, solutions to the perturbed states (if they exsist) are unique.

Physically, the effect of turbulence interference upon the far field processes can be considered as twofold. First, enhancement of the overall diffusivity by an added turbulent term, directly increasing the local heat feedback within the outer part of the wall layer. Second, turbulence would tend to decrease the extent of laminar reaction and the dependence of its overall rate upon local state variables (e.g. pressure), introducing a turbulent premixed reaction term which would depend on local fluid dynamic variables. Combined laminar - turbulent reactions of this nature have been suggested by Spalding[120,121] in his eddy breakup models. Effects of *unmixedness*, *due to turbulent fluctuations*, on the overall reaction rate were modeled in an analysis by Spiegler, Wolfshtein and Timn it,[122] and mixedness correlations were studied by Varma, Fishburne and Beddini[123] in a model for reactions in chemical lasers. Within the present simplified analysis, these effects are represented approximately through the modified P_{eq}, being the equivalent near field pressure. The equivalent far field pressure can be represented by $(p\, P_{eq})^{1/2}$, as would appear in a modified ω_2 expression, cf Eq. (VI.43). With this interpretation, the far field length scale is

$$\left[m/\overline{\omega}_2\right]_{pert} \sim P_{eq}^n / (p\, P_{eq})$$

which is decreasing whenever m is enhanced at the perturbed state.

Obviously, the pressure physically prevailing within the wall layer is equal to the local core pressure, p(x). The use of P_{eq} presently is merely an analytical device by which the proper eigenvalue nature of the perturbed wall layer problem is restored, and a certain deficiency of the far field zeroth order model (namely, the inability to communicate information upstream) is overcome; it does not imply any pressure jump across the core wall layer interface.

In conclusion, the consideration of unique pairs of data (P_{eq},m) for the perturbed layer solution insures uniqueness of the solution at the perturbed state and restores proper physical behavior. The equivalent pressure, P_{eq}, is defined through the corresponding unperturbed burning rate eigenvalue. It has been shown that disregarding the eigenvalue concept in the present 2-point boundary value problem may lead to physical inconsistency.

2. Solution Procedure for the Perturbed, Reacting Wall Layer

Generally, the solution of the perturbed and unperturbed configurations is similar, in that matching of inner and outer conditions is required. However, due to the presence of an auxiliary constraint, the perturbed case solution involves an additional iteration loop.

For a given particular set of data, (G, τ_{stg}, p, T_0), the solution process is summarized as follows.

(a) The Outer Loop

Steps (a) through (c) of the unperturbed case solution process are repeated with slight modification; cf. Section C.3.

(1) $\tau(0^+)$ is imposed, and $m[\tau(0^+)]$ calculated; P_{eq} is found by the simple burning rate relationship, $m = a \, p_{eq}^n$, where n and a correspond to the range of pressures considered.

(2) The vector $\phi(a^-)$ is calculated by generation of the condensed phase solution and use of the near field coupling parameters.

(3) The far field coupling terms, $B_{T,F}$, $B_{T,0}$ are calculated utilizing $\phi(a^-)$.

(4) The first three steps fully define the far field configuration. Consequently, using Eqs. (VI.33), (VI.34), and (VI.51), θ and $\partial\theta/\partial\tau$ may be calculated. Note that $(p \, P_{eq})^{1/2}$ is to be used instead of p in Eq. (VI.33b). Likewise, since m and $d\tau/d\zeta(0^+)$ are known, θ_{fb} and $\partial\theta_{fb}/\partial\tau$ can be obtained by Eqs. (VI.43) and (VI.50).

(b) The Inner Loop

(1) The point τ , where the second interaction constraint is satisfied, i.e., $\partial\theta/\partial\tau = \partial\theta_{fb}/\partial\tau$, is sought without changing $\tau(0^+)$ or m. This is not necessarily the point where $\theta = \theta_{fb}$. Therefore, the difference $\theta - \theta_{fb}$ is calculated at this coordinate.

(2) The magnitude and sign of the error $\theta - \theta_{fb}$ is considered; if absolutely small, within an allowable error margin, then the procedure has converged, and all interaction criteria satisfied at the current values of $\tau(0^+)$, m, $\tau = \tau^*$, θ_{fb}, etc. If the error is still large, $\tau(0^+)$ is corrected and the procedure repeated form step (a.1) of the outer loop.

One way to execute the above solution procedure is by using two iteration loops, one within the other. The outer loop involves changes of $\tau(0^+)$ and satisfying the $\theta_{fb} = \theta^*$ constraint; the inner loop involves only search for the coordinate $\tau = \tau^*$, where $\partial\theta_{fb}/\partial\tau = \partial\theta/\partial\tau$, at a fixed $\tau(0^+)$. Actual calculations were made by this procedure, using two regula falsi (method of false position) loops.

Whenever the point τ^*, where both interaction criteria are satisfied, lies outside the range $\tau_a < \tau^* < \tau_2$, interaction is impossible, and

$\tau(0^+) = \tau(0^+)^0$ is then assumed, for the prevailing $p(x)$.

F. Discussion of Results

The reacting wall layer model, described in the foregoing sections, can now be utilized in order to obtain some quantitative insight into the processes involved in the wall layer and core interaction. To facilitate calculation at this stage, a simplified core flow field is imposed as follows. For an interior burning, straight cylindrical grain, $T_0(x)$, $d(x)$, $p(x)$, and $\tau_{stg}(x) = \bar{\tau}_2(p)$ are assumed constant.

Additionally, $G/m = 1 + 4x/d$ is assumed, with $m = m^0(p)$ in this calculation. The iteration scheme of Section E.2 is implemented, using a digital computer.

Note that the assumption $m = m^0(p)$ is made regarding the calculation of G/m and Re_x only, required in Eqs. (VI.43) and (VI.50), for calculating θ_{fb} and $\partial\theta_{fb}/\partial\tau$. Considering the effect of G in $Re_{ex}^{-0.2}$ to be quite weak, the resulting uncertainty in calculating $\varepsilon_R(G/m)$, $m(G/m)$, etc., introduced by the above simplification is expected to be small. However, ε_R and m as functions of x/d are only approximate. The results of these calculations are depicted in Figs. VI.9 through VI.14. Figure VI.8 shows the variation of $1 - \varepsilon_R$ with G/m for a single port diameter at pressures between 1 and 6 MPa. Figure VI.8 shows the variation of $1 - \varepsilon_R$ vs. G/m for various chamber diameters, d, at a single pressure. $1 - \varepsilon_R$ depends progressively on G/m, indicating the expected increase in degree of interference between the core and the wall layer as G(x) increases. For a given G/m, lower pressure and smaller port diameter cause $1 - \varepsilon_R$ to increase. The region of non-interaction near the head end where $\varepsilon_R = 1$ is extended downstream as p and d increase, clearly showing a threshold effect. These observations are consistent qualitatively with the comparison of fluid dynamic wall layer thickness and chemical reactive scale, shown in Fig. VI.6, at various pressures and port diameters.

The perturbed burning rate effect is defined by the dimensionless parameter

$$E_B \equiv m/m^0(p) - 1 \qquad (VI.55)$$

Figure VI.10 shows curves of E_B vs. G/m for a single chamber diameter, at various pressures; Fig. VI.11 depicts E_B vs. G/m at various port diameters with p = const. The behavior of E_B follows the same trends observed for $1 - \varepsilon_R$ in Figs. VI.8 and VI.9 respectively, with the non-interacting regions and threshold effects obviously coincident for E_B and $1 - \varepsilon_R$.

The major difference between E_B and $1 - \varepsilon_R$ lies in their actual numerical values. For a given set of conditions (τ_{stg}, p, T_0, d), E_B varies considerably more steeply than $1 - \varepsilon_R$ for the same range of G/m values. To compare their relative sensitivities, cross-plots of E_B vs $1 - \varepsilon_R$ were made. In Fig. VI.12, curves with d = const and p varied as parameter are given (combining data from Figs. VI.8 and VI.10), showing decreasing sensitivity (E_B slope) as pressure increases. In Fig. VI.13, data from Figs. VI.9 and VI.11 are combined, where p = const and d is varied as parameter; in this instance all the data fall on a single curve, showing that the proportion between E_B and $1 - \varepsilon_R$ is independent of port diameter. Figures VI.12 and VI.13

demonstrate that a relatively small degree of interference, expressed by $1 - \mathcal{E}_R \triangleq 0.01$ can correspond to appreciable modification of the burning rate, as $E_B \triangleq 0.10$. Thus, $E_B \sim 10 \times (1 - \mathcal{E}_R)$, showing a ten-fold amplification.

This behavior has its analogue in the steady state variation of deflagration rate of N-nitro compounds (e.g., HMX and RDX) and C-nitro compounds (e.g., double base propellants) with the adiabatic flame temperature at a constant pressure. Correlations of m with T_f (p = 400 atm) were made by Fogel'zang and co-workers,[45] and correlations between m and the heat of combustion for various double base formulations at 100 atm were reported by McCarty.[20] For instance, comparing two different high-energy double base compositions,[20] denoted 'A' and 'B' :

	r, in/s	Q, cal/g
A	1.0	1460
B	1.15	1500

Thus an increase of heat of combustion by 3% is associated with a rise of 15% in the burning rate, showing amplification by a factor of 5. It should be pointed out that the propellants considered in the aforementioned studies[20,45] exhibit extended secondary reaction zones during deflagration, similar to those discussed in Chapter III and shown in Fig. III.3.

The critical (or threshold) values of G/m, as function of pressure and of port diameter are plotted in Fig. VI.14, using data from Figs. VI.10 and VI.11. For a fixed port diameter, the variation of (G/m) at threshold is linear with p; at a fixed pressure, the dependence on diameter is shallower in comparison, and tends to decrease in slope as diameter increases.

Two basic assumptions in the present theory are similar to those employed by Zeldovich,[103] in his analysis of propellant burning under a gas flow. These are the assumption of quasi-one dimensional flame zone near the propellant surface, and the notion that when the entire gaseous reaction zone is included within the viscous sublayer, the burning rate can not be affected by fluid dynamic variables of the core flow. Enhancement of burning in the Zeldovich model occurs through modification of the transport properties in the flame (particularly thermal conductivity) by turbulence, employing the Prandtl mixing length concept. Trends similar to those observed in the present analysis were reported,[103] regarding E_B as function of G/m_0. However, the pressure sensitivity and the effect of port diameter were considered only through the dependence of $G/m_0 \sim p^{1/18} d^{1/12}$ in a particular propellant grain; consequently, the sensitivity of E_B to these parameters is much smaller than that found in the present study.

Beddini[124,125] employed an advanced two dimensional (second-order-closure) turbulence model for the entire channel flow, allowing a single, premixed, gaseous reaction near the propellant surface, in an analysis of erosive burning. Numerical solutions were generated for the reacting boundary layer configuration, for various imposed centerline velocities, U_0. Pressure sensitivity (through variation of m_0) and geometry scaling effects were investigated, showing trends similar to those observed in the present study, regarding both $E_B = f(G/m)$ and the sensitivity to (p;d). An earlier investigation of erosive burning, through a reacting (premixed) boundary layer

analysis was reported by Tsuji,[126] but turbulence effects were entirely precluded; further, the burning rate was assumed uniform along the propellant grain. Similarity solutions were obtained analytically, for a linearly varying outer velocity, $U_0 \sim x$. It was concluded that the axial gradient dU_0/dx was the only factor determining erosive burning under these conditions, contrary to experimental observations.

Erosive burning of double base propellants was investigated experimentally by Osborn and Burick.[127] The apparatus employed a solid propellant gas generator, firing into a test section with a planar propellant sample. In this respect the experiments resemble those of Marklund and Lake,[128] (who used ammonium perchlorate composite propellants exclusively) except for the acutal method of sample burning rate measurement. Three different propellant compositions were tested, at various values of (G, p, τ_{stg}). Unfortunately, the number of data points reported is too small (each point corresponding to different G and p) to allow construction of plots of $E_B = f(G/m; p)$ in the manner of Fig. VI.10. In a typical set of experiments, propellant with $T_f = 2600$ K was used in the gas generator, while a composition with $T_f > 3000$ K served as test sample. The results (six data points) showed insignificant effect due to the reduction in mainstream temperature, lying relatively close to those obtained when the same $(T_f > 3000$ k) propellant was used in the gas generator. The authors concluded that heat transfer from the main stream to the propellant surface is not the primary mechanism driving erosive burning; rather, mechanical erosion was proposed (without analysis). Finally, the authors[127] do not mention the possible effect of pressure, and it seems that the experiments were conducted as if this parameter had little or no effect upon erosive burning. However, plotting a set of their data in the form E_B vs G/m shows clearly the same trend observed in Fig. VI.10, namely, that a higher G/m is required to obtain the same E_B at a higher pressure.

In conclusion, the perturbed burning theory of this chapter demonstrates that enhanced burning due to interaction with the fluid dynamic processes in the core is not a property of the propellant alone. Unlike normal deflagration, it can not be readily studied outside of the specific rocket chamber environment. Perturbed burning at a particular position along the port depends on local core variables such as G and p, but also upon the local turbulence intensity and τ_{stg}, which are flow-history dependent. Consequently, experiments like those of Marklund and Lake[128] or Oborn and Burick,[127] involving isolated propellant sections in externally generated tangential flow, do not necessarily simulate enhanced burning conditions within any particular motor.

CHAPTER VII

BACKGROUND TO THE NONSTEADY ANALYSIS

This section provides a background for the present nonsteady investigation of solid propellants with extended gaseous flame zones in the rocket chamber environment, through a survey of the literature. The discussion is focused on several of the central questions of the present analysis, as reflected by the subdivision into the various categories herein. The questions of interest are summarized as follows:

o Acoustic excitation and damping mechanisms in the main chamber flow.
o Gaseous reactions in nonsteady solid propellant combustion.
o Erosive burning and its relation to acoustic stability.
o Nonsteady rocket motor operation involving double base and nitramine
    propellants.
o Nonlinear analyses of nonsteady solid propellant chamber processes.

A. Mechanisms for Enhancement or Damping of Acoustic Vibrations Within the Core Flow

The Rayleigh criterion[129] is of particular interest to the present reacting coreflow configuration, as it deals directly with thermal excitation of acoustic oscillations. Advanced for explaining "singing flames", it postulates that heat addition made at the proper point in space (such as a pressure antinode), in the proper time (heat added when the pressure is maximal, and extracted when the pressure is minimal) may lead to local enhancement of acoustic vibrations. The same mechanism could lead to suppression of oscillations, as heat is extracted when pressure is maximal and added when pressure is minimal. Thus, in order to generate acoustic oscillations, the net heat flux, q_v, into a local control volume, should have an oscillatory component in phase with the pressure perturbation. Stated somewhat less strictly, acoustic oscillations would be enhanced for time-wise phase angles $\text{Arg}(q_v, p') < \pi/2$, and damped for $\pi/2 < \text{Arg}(q_v, p') < \pi$, where p' denotes the complex pressure perturbation: the Rayleigh criterion may then be written in differential form, as

$$\left[\frac{\partial q_v}{\partial p}\right]^0_{\rho^0, h^0} > 0$$

where superscript 0 denotes the reference mean steady state. Satisfying this condition does not insure that oscillations will persist locally with ever-growing amplitude, since nonlinear damping may take over as the amplitude increases. Neither does it imply that the amplitude of oscillations would increase over the entire field following a local heat perturbation. Indeed, Glushkov and Kareev[130] have shown recently that the Rayleigh criterion consists of a necessary (not sufficient) condition for acoustic instability in the presence of dissipative processes (viscosity, diffusion); their work concerns a perturbed quiescent gas with zero mean flow.

Utilization of the Rayleigh criterion in works related to solid propellant combustion instability is quite rare. Smith and Sprenger,[131] in an early work concerning the tangential (spinning) acoustic modes in tubular solid propellant cavities, have stated it without formulation as a possible cause of "sonance"

burning, in the sense of self-excitation, i.e., the enhancement of observed acoustic vibrations by nonsteady heat release. The nonsteady heat source considered was the gaseous flame zone adjacent to the propellant surface; they have identified the pressure-dependent, exothermic gas phase reaction as likely to have an in-phase component with the imposed standing acoustic pressure modes. Unfortunately, due to a lack of complete formulation ragarding the site of the nonsteady heat release (in the chamber control volume or as a boundary condition), as well as lack of actual propellant data, it remains difficult to verify the adequacy of their heat- and pressure-oscillation coupling.

Cheng[132] considered the effect of heat addition in the main chamber flow upon acoustic stability, within the framework of solid propellant combustion with reactive additives (e.g., aluminum powder). The Rayleigh criterion was invoked for the purpose of an explanation of the coupling between nonsteady, distributed heat sources in the chamber flow and the acoustic field. Two distinct cases were analyzed: first, the effect of insensitive heat sources, through the distortion of the acoustic modes by imposing variation in the mean density and temperature in the flowfield; second, an end-burning case, with oscillatory, pressure-sensitive heat sources. Both models are based on modifications to previous analyses[133,134] by the same author, employing the Crocco time-lag assumption. The conclusions were as follows. In the first instance, the effect upon stability is indirect, entering through modification of the axial acoustic mode amplitude and frequency at the nozzle entrance section: if this particular mode is enhanced (assuming it is the most affected mode in terms of the non-dissipative nozzle damping), the acoustic energy content of the gas leaving the chamber is greater and, hence, damping would ensue. In the second case, the Rayleigh criterion is verified by the prediction of the effect of distributed sensitive heat sources upon acoustic stability: strongest effect was found near pressure antinodes, while vanishing effect was predicted in pressure nodal regions; the oscillatory heat sources and mass sources (the latter due to nonsteady gas generation at the fully reacted flame edge near the head end) tend to counteract in the neighborhood of the fundamental acoustic mode, and augment each other at even harmonic frequencies.

In this conjunction, it is interesting to point out that finite-time chemical relaxation processes, in the neighborhood of the equilibrium state in the main flow of the solid propellant chamber, are considered strictly dissipative. The acoustic analysis, presented in the textbook by Williams, Barrere and Huang[135] based on small departures from equilibrium, clearly demonstrates that the dissipative coefficient, α_n [for an exponential dissipative component, $\exp(-\alpha_n t)$ corresponding to the frequency Ω_n] is maximal at $\Omega_n / \Omega_{ch} = 1$, where α_n is the perturbation frequency, and $1/\Omega_{ch}$ the characteristic chemical relaxation time scale. However, the analysis is based on the assumption of zero entropy perturbation,[136,137] which leads to the homogeniety of the modified wave equation; although expected to be valid in the neighborhood of the equilibrium point, the assumption is rather inadequate for the description of a chemically reacting flow, with the reaction term appearing in the zeroth order formulation.

The Rayleigh mechanism is only one of several possible means by which excitation or attenuation of acoustic vibration is possible. Salant and Toong[138,139] discuss the effects of non-uniform mean flow properties ($d\bar{u}/dx$, $d\bar{\rho}/dx$, and $d\bar{s}/dx$, in a one dimensional, inviscid case), in addition to the influence of nonsteady distributed mass and heat sources, upon the acoustic

field. A strong coupling between the steady, nonuniform, mean flow and
traveling acoustic perturbations was demonstrated. In the absence of sources,
Salant and Toong[139] identify two types of coupling mechanisms. First,
dispersive processes, involving changes in acoustic wave impedance and group
velocity, which are energy conservative (with respect to the acoustic field).
The associated attenuation coefficient derived, α_1, depends explicitly on
$d\bar{u}/dx$, $d\bar{\rho}/dx$, and $d\bar{s}/dx$; attenuation occurs for positive values of these
gradients and amplification occurs if all are negative. Secondly, dissipative
processes, involving irreversible exchange of energy with the mean flow (this
effect vanishes for a perturbed, uniform, quiescent gas). The attenuation
coefficient in this instance, α_2, was shown to depend only on $d\bar{s}/dx$ and
$d\bar{u}/dx$; attenuation or amplification would occur for positive or negative values
of these gradients, respectively.

In a recent work by Cummings,[140] the effect of temperature gradient upon
the acoustics of a quiescent gas in a duct were investigated, using the WKBJ[141]
method, for a one-dimensional case. The predictions of the asymptotic theory
were verified by experiments (in air) and numerical solution. Amplification of
a pressure wave, traveling in the $x > 0$ direction was found for $dT/dx < 0$; the
frequency tested was 4.5 kHz and the temperature variation between
720 and 350 K over a 1 m span, accompanied by a pronounced increase in the mean
specific heat ratio of the gas, $d\gamma/dx > 0$. Further, conservation of acoustic
energy is indicated (the only component of acoustic intensity, being $I = \overline{p'u'}$,
remained uniform in space), which can be attributed to the absence of mean
flow. These findings are in line with the results of Salant and Toong.[139] It
should be noted that a slight induced flow could have resulted from the local
heating at $x = 0$; the indication of uniform acoustic intensity, however, shows
that this effect must have been negligible.

B. Gaseous Reactions in Nonsteady Solid Propellant Combustion

Finite rate gaseous reactions in nonsteady solid propellant combustion
analyses are traditionally excluded by invoking the quasi-steady assumption
regarding the gas phase region adjacent to the propellant surface. Motivated
by the analysis of Hart and McClure,[142] two notable exception to the above
statement exist in the works of Williams [143] and of Tien.[144]

Hart and McClure,[142] in a study aimed at obtaining analytical expression
for the burning rate response function, assumed that (a) the entire gas phase
reaction occurs within a thin flame sheet at a distance form the propellant
surface, and (b) the reactant flow region from the propellant to the flame,
termed induction zone, is entirely convective, namely, diffusion and reaction
in this region are assumed negligible. The resulting response function,
although containing implicitly the effect of finite reaction zone thickness, is
not adequate for describing the influence of finite rate reaction and diffusion
upon the response function. These deficiencies were pointed out by the
authors.

The investigation by Williams[143] goes one step further in terms of
formulation. The full diffusive-convective-reactive model of the gaseous flame
zone was employed. The nonsteady first order perturbation problem was
rigorously posed, but the analysis stops short of solution, which could have
been obtained numerically. The final results were limited to small values of
the imposed perturbation frequency [however, since the typical time scale in
the gas phase used may be shown to be $\sim O(0.1~\mu sec)$, actual frequencies of

the order of 10^4 cps could still fall within that category] and to very high values of the gas phase activation energy. Under the foregoing fundamental constraints, the acoustic admittance function,

$$\hat{A} \equiv \frac{u'(y\to\infty)/\bar{u}}{p'/\bar{p}}$$

was derived, and its real part, A_R, plotted against dimensionless frequency, Ω; the quantity $H_v \equiv -d(Q_v/R_u T_s)/dT_s$, related to the surface-gasification activation energy, was utilized as a parameter. A_R was shown to rise from zero to a maximum and then fall monotonously to negative values (without indication of recovery) as Ω increases. Higher values of H_v tend to cause higher peaks of A_R (occurring at larger Ω) and steeper declines. Unfortunately, the attenuating (negative) portions of A_R occur at regions of $\Omega \gg 1$ outside of the domain of validity specified by the simplifying assumptions. Interestingly, as pointed out by the author, the admittance function derived does not exhibit any explicit dependence upon the thermochemical data of the distributed flame zone reaction, unlike analyses which are closer to employing the collapsed flame surface approximation, e.g., the work of Denison and Baum,[145] where kinetic parameters appear explicitly in the results. This may be directly attributed to the elimination of the inhomogeneous reaction terms in the first order (perturbation) formulation, by the assumption of high activation energy.

Ten years later, apparently independent of the work by Williams, Tien[144] presented a study of the same problem. In this instance, the zeroth order (steady state) and first order (nonsteady perturbation) equations were solved numerically, after assuming for the dimensionless perturbation quantities the form $\Phi'(x,t) = \hat{\Phi}(x)\ \exp(i\Omega t)$, which reduces the perturbed system to ordinary differential equation form, in the unknowns, $\hat{\Phi}(x)$. No limitations were made a priori as to the acutal magnitude of Ω or the gas phase activation energy. Two comments regarding this analysis are in order : (1) The boundary condition at the flame outer edge was $Ds/Dt(y = +\infty,t) = 0$, namely, entropy is conserved for a fluid particle leaving the flame. Consequently, the resulting perturbed boundary condition is expected to be valid only for large enough frequencies, such that $1/\Omega^*$ is much smaller than typical thermal relaxation times. To an observer close enough to the flame edge from outside, the flow would appear to contain entropy waves, propagating at the fluid velocity; this phenomenon was studied by Krier and Summerfield.[146] (2) The fast gas phase time scale was used for the solution of the nonsteady heat conservation equation in the condensed phase. This gives rise to a coefficient $a^* \equiv \rho(cond)/\rho(gas,y = \infty) \gg 1$, multiplying the time derivative. At high enough frequency, this results in a singular problem for the perturbed condensed phase, implying a thin, high-frequency "boundary layer" within the solid near the surface. For the purpose of investigating this phenomenon, the regular length scale used in the analysis is inadequate. The real part of the acoustic admittance function, A_R, was calculated numerically and plotted against the dimensionless frequency $\Omega \equiv \Omega^* t(gas)$, with a^* and the characteristic time scale ratio, $b^* \equiv t(gas)/t(cond)$, as parameters. For ($a^* = 1000$, $b^* = 0.001$), the $Re(\hat{A})$ curve has a positive peak at low frequencies (resembling the well known quasi-steady gas phase results, cf. Denison and Baum[145]) and a negative minimum at high frequency, indicating attenuation in the latter case. With smaller a^* and larger b^* values, the positive peak is displaced to higher Ω-values, somewhat reduced, and the negative part vanishes.

The possibility of residual reaction (and heat release) in the main chamber flow of solid propellant motors is mentioned in several works dealing with nonsteady combustion, but without specification of the explicit mechanism; for instance, the heat release terms appearing in several of the acoustic chamber formulations by Culick.[147,148] In other investigations, of non-acoustic, L*-instability behavior, the comparable magnitudes of chamber gas residence time and flame zone reaction (for double base propellants) were cited as probable causes of nonsteady behavior at low frequencies.[149,150]

C. Erosive Burning and Nonsteady Solid Propellant Motor Operation

The significance of erosive burning to the problem of overall acoustic stability in the solid propellant motor has been investigated by several authors.

The analyses by Hart, Bird, and McClure[151-153] at Johns Hopkins University provided preliminary insights regarding the coupling between the acoustic chamber modes and a propellant combustion response, related to the gas velocity component tangent to the propellant surface, v. The erosive burning model used was highly idealized, in that the dynamic erosive burning component is assumed to depend upon the absolute magnitude of the tangential velocity perturbation (approximately pure axial) and its time derivatives. Specific details of the erosion mechanism, as well as the question of erosive threshold velocity, were not discussed.

In a linearized, three-dimensional acoustic study,[152] the erosive burning influence upon acoustic stability was estimated indirectly as follows. Since the solution of pure pressure-coupled acoustic modes is relatively straightforward, the dynamic erosion effects were formally absorbed in a modified, pressure-coupled burning rate admittance function. Considering only neutrally stable modes (those with pure real frequencies), the authors solved for the pressure-coupled acoustic modes. This way, the influence of the erosive component witin the admittance function upon the characteristic frequencies was assessed. Non-degenerate cases (radial, spinning and axial characteristic frequencies all differ), as well as degenerate modes (a pair of equal characteristic frequencies, leading to singularity) were investigated.

For zero threshold velocity, the perturbed burning rate component, $m'(eros) \sim |v| \sim |\sin \Omega t|$ can respond at twice the incident frequency, this nonlinear feature was termed rectification,[151] appearing already at infinitesimal acoustic amplitudes. This was shown to lead to amplification of otherwise stable modes, or to growth-limitation of otherwise unstable modes.[151] The complex wave forms which may result from finite acoustic perturbation velocities through erosive coupling were discussed in an additional study.[153] Several of the stability implications inherent in these analyses were reviewed by Price,[154,155] using the admittance function and associated phase angle approach; the effect of finite threshold velocity upon erosive response rectification (and subsequent acoustic stability) was qualitatively argued.[154]

In the way of critique, the following points can be made regarding the analyses by Hart, Bird and McClure.[151-153]

(a) Obviously, stability analyses based on stable modes do not yield any information about the time-evolution of small disturbances into finite ones. Only conclusions regarding the stability of certain

mode configurations, if they exist, are possible.

(b) Considering nonlinear effects, the presence of an erosive component to the overall burning rate (threshold velocity permitting) may significantly alter the burning rate pressure response to lowest order of approximation. Such a trend is hinted by the stationary analysis of Chapter VI; it does not mean that the pressure and tangential velocity perturbation effects are inseparable, but their mean coefficients (in quasi-linear form) are strongly coupled. In this instance, subtracting the pure calculated or otherwise separately measured pressure response from the apparent, overall burning rate response function to obtain the erosive burning component thereof is strictly meaningless.

(c) For the fundamental axial acoustic mode, containing most of the acoustic energy in the system, the region most susceptible to dynamic erosive burning is about the grain port half length, in the velocity antinode neighborhood; this is also the region of the pressure node. The converse holds for the grain ends. Thus, neglecting for the moment the velocity effect of the spinning modes, the consideration of an overall equivalent pressure coupling response function is quite speculative, in view of the dominance-area separation, (with v' and p' being out of phase by $\pi/2$) -- if the actual magnitudes of pressure and velocity excitations at a given point $(\underset{\sim}{x},t)$ are to have any significant effect on stability.

Lengelle[156] formulated a stationary erosive burning model utilizing blown turbulent boundary layer analysis and the Granular Diffusion Flame model of Summerfield (GDF).[102] A turbulence diffusivity parameter (based on the mixing length hypothesis of Prandtl) was derived, and used to modify the overall diffusivity, $[\rho D]_{tot}$. Assuming that the tubulent Schmidt and Lewis numbers are close to unity, it was shown that the GDF-theory length scale, X, (corresponding to the flame thickness) is invariant to the effect of turbulence. Thus, since $m \sim \lambda(T_f - T_s)/X$ and $\lambda \sim C_p[\rho D]_{tot}$, the resulting overall burning rate is $m \sim [\rho D]_{tot}$, and the erosive effect enters through the turbulent contribution to the overall diffusivity, effectively enhancing the heat feedback to the propellant surface. The analysis is clearly aimed at modeling the combustion of certain AP composite propellants; it was extended to the nonsteady acoustic domain, assuming a quasi-steady flame zone, and the burning rate response function was calculated for several hypothetical propellant configurations. It was found that the pressure response is strongly amplified when the erosive burning effect becomes more pronounced. For critical values of a parameter related to the energy stored in the propellant, the presence of an erosive effect could entirely reverse the response function values. These findings tend to support argument (b) above, for the particular case of AP composite propellants.

D. Nonsteady Observations with Double Base and Nitramine Solid Propellant Motors

Direct observations of nonsteady behavior associated with double base propellant rocket motors were reported by Trubridge and Badham [157] at the Summerfield Research Center (England). A systematic study of motors with diameters ranging between 6 and 19 inches was made. The various effects of operating pressure, propellant composition, ambient propellant temperature,

length and shape of propellant grain, and acoustic instability suppression devices (inert rods) were tested. The data are presented in p(t) vs t form, without frequency analysis. Two major types of nonsteady behavior are reported: (1) one, roughly close to ignition time, is an irregular, very high amplitude, low frequency (about several cps) phenomenon; (2) a more orderly, periodic, small amplitude pressure fluctuation in the estimated 10^3 cps range. In all cases, instability was spontaneous, without external stimulation. The various effects found are listed as follows.

(a) Ambient propellant temperature. In most cases, pre-conditioning to temperatures above 300 K resulted in destabilization, while lower ambient temperatures tended to stabilize.

(b) Propellant composition. The only indication given is the adiabatic flame temperature at constant pressure. Propellants with $1900 < T_f^0 < 2250$ K (total of 3 tested) tended to be stable. With the more energetic propellants, $2300 < T_f^0 < 2800$ K (total of 5 tested), instability was invariably encountered. Addition of aluminum powder did not always result in stabilization.

(c) Operating pressure. Unmodified propellants (or propellants operating below their plateau burning pressure regime) tended to stabilize when the operating pressure was raised. Conversely, a propellant operating above its plateau regime was stabilized by lowering the operating pressure.

(d) Scaling (motor diameter) tended to have little effect for motor diameters varied between 6 and 13 inches. Scaling effects were suggested in a comment by L. Green, in the discussion following the presentation.

(e) Several tubular grain samples, extinguished after undergoing high frequency instability, were found to have a region of enhanced absolute burning rate near the grain center (the region of velocity antinode for the fundamental axial mode, and possibly the region of highest spinning mode velocity amplitude).

In a somewhat earlier publication by Angelus,[158] a series of experiments utilizing a small, laboratory-scale, interior burning tubular grain was reported. The effects of propellant ambient temperature and operating pressure upon regular (acoustic) and irregular (high amplitude) instability were investigated. The frequency and amplitude analyses presented tend to support the effects described above in (a), (c), and (e), but with much more quantitative detail. In addition, a reduction in the motor specific impulse was observed whenever appreciable nonsteady behavior occured; the effect was attributed to possible incomplete combustion of the gases upon leaving the chamber. Unfortunately, the effect of operating pressure change is given through the ratio of burning surface to throat area, and it is not clear whether different interior grain diameters were used. This, as indicated by Section VI.F., could have a strong bearing upon the extent of erosive burning present in the various configurations.

Recent experiments by the group at Thiokol,[159] regarding irregular instability involving nitramine propellants, bear a striking qualitative resemblance to the instability behavior described above for double base

propellants.

E. Nonlinear Analyses of Nonsteady Solid Propellant Chamber Processes

This section deals mainly with nonlinear analyses, with some reference made to quasi-linearized works. All of the existing nonlinear studies published employ one-dimensional axial models of the chamber main flow for which finite difference numerical solutions are utilized. Since thin, fully reacted, (quasi-steady) flame zones and an aluminum particle phase are assumed, these works are aimed mainly at AP composite propellant modeling.

Kooker and Zinn[160] investigated finite amplitude axial modes in a tubular solid propellant rocket motor cavity. The consideration of rather strong disturbances and their effect upon stability is also inherent in the experiments performed by Brownlee and Marble[161] where pulsing of laboratory-size motors by small detonating charges was performed. The aluminum particle phase is considered adiabatic and, hence, may contribute only to damping of acoustic modes. A premixed model of the flame zone was used (with a uniform mean, pressure-sensitive reaction rate) to facilitate an explicit expression for a pressure sensitive heat feedback to the condensed surface. Numerical solutions to the axial core flowfield were obtained by the method of shock-following, developed by Moretti.[162] The condensed phase nonsteady heat equation was also solved numerically, utilizing the version of method of lines as developed by Vichnevetsky.[163]

The model obtains solutions to the nonlinear, nonsteady chamber processes for cases that involve *no velocity coupling* of the burning rate response. The chief conclusion was that small amplitude disturbances might evolve into high amplitude oscillations, through driving of such disturbances by the pressure-coupled, nonsteady propellant burning.

Levine and Culick,[164] in a first version of a similar study, used the method of characteristics for numerical solution of their partial differential equation system. A linear, pressure-coupled, burning rate response function was incorporated, facilitating calculation without solution of the nonsteady heat wave in the solid propellant. This obviously limited the applicability to very small amplitude disturbances. In a later work by these authors,[165] some of the deficiencies of the earlier model and algorithm were resolved by adding the nonsteady condensed phase solution and utilizing a more versatile numerical algorithm, that of Rubin and Burstein,[166] for the solution of the core flow equation. This model[165] was applied to the T-burner combustion problem, where cases of instability were obtainable. The application to a small laboratory motor model enabled reproduction of limit cycle behavior (persistent oscillation at constant amplitude, after perturbing the initial conditions) for non-aluminized propellant cases, in good agreement with experimental observations. However, instability in the rocket motor modeling could not be induced.

Culick,[147] in an earlier axial mode analysis of "nonlinear acoustics", formulated the wave equation in terms of the pressure perturbation, $p'(x,t)$. After selecting proper spatial distributions (of standing modes) for p', the resulting nonlinear time-dependent problem was solved by the method of Krylov and Bogoliubov.[167]

Compared with the numerical algorithms, the analytical approximations

have, in general, the advantages of being fast, costing less, and having freedom from numerically-induced stability limitations and errors. Further, the physical interaction incorporated are clearer. Unfortunately, to this end, they are limited to small perturbations, and effects distinctly nonlinear may not be properly represented. The numerical models, on the other hand, incorporate less restrictive assumptions and allow for more realistic representation (and more imaginative modeling) of the solid propellant burning process.

CHAPTER VIII

ANALYSIS OF NONSTEADY SOLID PROPELLANT ROCKET CHAMBER WITH CHEMICAL REACTION

A. Introduction

Chapter VI dealt with the steady-state interaction between an imposed core flowfield and the reacting wall layer for solid propellants possessing extended gaseous deflagration zones. For the case of interference between the core and the wall layer, Chapter VI shows the influence upon stationary burning rate of the propellant. One by-product of this interference is the injection of reactants into the core, where exothermic reactions may continue. The subject of the present chapter is the investigation of the influence of this particular propellant configuration upon the overall dynamic chamber behavior. More precisely, the objective is to advance an analytical model of the nonsteady chamber processes incorporating the wall layer concept and subsequent reaction in the core.

As shown in Chapter VII, analyses of nonsteady solid propellant chamber behavior were traditionally limited to propellants having short gaseous flame regions. This is thought to naturally encompass the most widely used class of propellants, namely, ammonium perchlorate composites; it excludes, however, double-base propellants and nitramine composite propellants. The collapsed flame zone assumption affords, in these cases, great analytical simplicity, in that the chamber flowfield can be considered as merely a wave-carrying medium, and the instability problem is therefore necessarily centered upon pressure-coupled, nonsteady mass generation. Even with this simplification, nonsteady chamber analysis remains formidable, and prediction of actual behavior by the various models is inconclusive in many instances.

Considering now propellants with extended gaseous reaction regions, a simple extension of the existing theories seems to be ruled out for two principal reasons. First, the existence of exothermic core reaction modifies the stability problem, as one must take into account the additional coupling between the nonsteady heat generation and the oscillatory pressure field; this may no longer be studied outside the particular chamber environment (like the solid propellant acoustic admittance, for instance). Secondly, mass generation by the propellant is expected to be strongly coupled with the core reaction (or, rather, with the core thermal balance) as shown by the interaction constraints of Section VI.D; the propellant dynamic burning response would then be expected to involve an additional component, besides that due to pressure coupling.

This necessitates casting of the analysis in terms of a reacting core flowfield, with appropriate conservation laws for energy and chemical species. Further, the assumption of adiabatic boundary between the core and the gaseous reaction zone (as for the case of collapsed flame) must be discarded in favor of the more complex, non-adiabatic interaction criteria mentioned above.

In order not to complicate immensely the present approach, the chamber flowfield is modeled in a quasi one-dimensional form; the nonsteady phenomena are studied within the framework of the fundamental axial acoustic mode and its first harmonics. The resulting analytical model is nonlinear, although sharp

variations of properties (as in shock waves or ultra-high harmonics), as well as high amplitudes, are excluded. The physical chamber configuration is depicted in Fig. VIII.1.

The plan of presentation for this Chapter is as follows. Section B contains a time-scale analysis based on the data obtained by the stationary model in Chapter VI. This is used to obtain a preliminary estimate of regimes of possible interaction between the oscillatory core flowfield and the exothermic reaction in terms of the work parameters, e.g., pressure, geometry, and frequency of oscillations. Sections C and D detail the elements of the analytical chamber model, namely, the condensed phase coupled with the reacting wall layer and the core flowfield, respectively. Section E describes the numerical algorithm for the coreflow model.

B. Characteristic Time Scales

The present section deals with the definition of appropriate time scales for the coreflow, the reacting wall layer and the propellant. This is followed by a discussion of possible interactions among these time scales.

1. Definitions

a. The solid phase

The characteristic thermal relaxation time for the burning solid propellant is

$$t_p^* = \alpha_c / r^2 \qquad\qquad \text{(VIII.1)}$$

where $\alpha_c = \lambda_c / \rho_c C_c$ is the condensed phase thermal diffusivity and $r = m/\rho_c$ is the linear regression rate of the propellant.

In presence of condensed phase reaction, an additional chemical relaxation scale is involved:

$$t_{p,CH}^* = \rho_c / \overline{\omega}_{1,COND}^* \qquad\qquad \text{(VIII.2)}$$

The present analysis employs the assumption of thin reaction zone in the condensed phase, viz.,

$$m / \overline{\omega}_{1,COND}^* \ll \alpha_c / r \qquad\qquad \text{(VIII.3)}$$

This assumption has led to the elementary reacting condensed phase model in Appendix B. It implies that $t_{p,CH}^* \ll t_p^*$.

b. The Reacting Wall Layer

The characteristic chemical relaxation time within the gaseous reacting wall layer involves the mean secondary reaction rate in the layer; as reference, consider

$$\overline{\omega}_{2,LR} = \omega_{2,L}(\overline{\tau}_m, p) \qquad\qquad \text{(VIII.4a)}$$

where $\overline{\tau}_m$ denotes the mean thermal enthalpy within the layer similar to that

defined in Section III.E. The dependence upon mean mass fractions of fuel and oxidizer, $\overline{Y}_F$ and $\overline{Y}_0$ has been absorbed into $\overline{\tau}_m$, through suitable Shvab-Zeldovich coupling. However, due to thermal enhancement in the layer, a more appropriate definition of the mean reaction rate is

$$\overline{\omega}_{2,L} = (P_{eq}/p)\,\overline{\omega}_{2,LR} \qquad\qquad \text{(VIII.4b)}$$

where P_{eq} is defined by Eq. (VI.52b). According to the discussion in Chapter VI,

$$P_{eq}/p = (E_B + 1)^{1/n} \doteq \left[K_L(1 - \varepsilon_R) + 1\right]^{1/n}$$

where the second equality is only approximate, implied by the results in Figs. VI.12, 13; in the last equation, n is the burning rate pressure exponent (for a small enough pressure interval), ε_R is the layer reactivity parameter, defined by Eq. (VI.35) and $K_L \sim O(10)$ is the amplification factor discussed in Section VI.F. Thus,

$$\overline{\omega}_{2,L} \doteq \overline{\omega}_{2,LR} \left[K_L(1 - \varepsilon_R) + 1\right]^{1/n} \qquad\qquad \text{(VIII.5)}$$

The associated chemical relaxation time is defined,

$$t_L^* = \overline{\rho}_L(\overline{\tau}_m, p)/\overline{\omega}_{2,L} \qquad\qquad \text{(VIII.6)}$$

The primary decomposition zone within the wall layer can be shown to have a characteristic time scale much smaller than that of the far field; choosing the diffusive scale for this purpose,

$$t_{L,1}^* = (\lambda/mc_p)/(m/\overline{\rho}_1)$$

following the analysis of Chapter III, $t_{L,1}^* \ll t_L^*$.

c. The Core Flow

Defined similarly to t_L^*, the characteristic chemical relaxation time in the coreflow is,

$$t_{CH}^* = \overline{\rho} / \overline{\omega}_{2,COR} \qquad\qquad \text{(VIII.7)}$$

where

$$\overline{\omega}_{2,COR} = f\left[\overline{\tau}_2, p, (Y_F^* Y_0^*)\right]$$

is the mean rate of secondary reaction in the core. Its definition is based on the maximal, fully burnt thermal enthalpy, and the reactant mass fractions at the cutoff edge of the wall layer. These mass fractions can be expressed in terms of ε_R; by definition,

$$Y_k^* = Y_{k,b} - (Y_{k,b} - Y_{k,a})(1 - \varepsilon_R) \qquad \text{(VIII.8)}$$

where k represents fuel or oxidizer (F and O, respectively) and subscripts b and a denote the fully burnt and nonreacted states in the wall layer, respectively.

The characteristic acoustic chamber time is given by the mean period of the fundamental axial acoustic mode,

$$t_a^{*0} = 2L/\bar{a} \qquad \text{(VIII.9a)}$$

where L is the chamber length and $\bar{a}$ the mean adiabatic speed of sound in the core. The ratio of frozen to equilibrium speed of sound is expected to be only slightly larger than unity; hence, it suffices for the present estimate to consider

$$\bar{a} \doteq \left[(\gamma - 1) \bar{\tau}_2 Q_1^* \right]^{1/2} \qquad \text{(VIII.9b)}$$

utilizing suitable mean values of $\bar{\tau}_2$ and $\gamma = Cp/Cv$. Higher harmonics of the fundamental mode are given by

$$t_a^{*(k)} = t_a^{*0}/k, \quad k = 2, 3, \cdots$$

2. Time Scale Interactions

To assess the possibility of dynamic coupling between the coreflow and the wall layer, the magnitude of the ratio t_L^*/t_{CH}^* is of interest. This ratio is largely determined by the relationship between the associated mean reaction rates. As shown by Eqs. (VIII.5) and (VIII.8), both $\bar{\omega}_{2,COR}$ and $\bar{\omega}_{2,L}$ depend on $(1-\varepsilon_R)$. However, for purposes of the present comparison, it can be shown that, for $0.95 < \varepsilon_R < 1$ and $n \doteq 0.75$, the variation of $\bar{\omega}_{2,L}(\varepsilon_R)$ is relatively small, and $\sim \bar{\omega}_{2,LR}$. The mean mass fractions in the wall layer can be written,

$$\bar{Y}_k = Y_{k,b} + g_k (Y_{k,a} - Y_{k,b}) \qquad \text{(VIII.10)}$$

where k denotes F or O, and the constants $g_k \doteq 0.5$ typically. In general, the case of nonstoichiometric proportions of F/O is of interest; e.g., suppose F is in excess, such that $Y_{F,b} = b$ and $Y_{O,b} = 0$. Using Eqs. (VIII.8) and (VIII.10),

$$Y_F^* Y_O^* = \bar{Y}_F \bar{Y}_O \; \frac{(1 - b/\bar{Y}_F)}{g_F g_O} \left[(1 - \varepsilon_R)^2 + \frac{g_F(1 - \varepsilon_R)}{\bar{Y}_F/b - 1} \right] \qquad \text{(VIII.11)}$$

Therefore,

$$t_L^* / t_{CH}^* \doteq (\bar{\rho}_L / \bar{\omega}_{2,LR}) / (\bar{\rho}_{COR} / \bar{\omega}_{2,COR}) =$$

$$K_T \left[(1 - \varepsilon_R)^2 + \frac{g_F (1 - \varepsilon_R)}{\bar{Y}_F / b - 1} \right] \qquad \text{(VIII.12a)}$$

where

$$K_T \equiv \frac{1 - b / \bar{Y}_F}{g_F g_0} \left(\frac{\bar{c}_m}{\bar{c}_2} \right) \exp \left[-\beta_2 \left(\frac{1}{\bar{c}_2} - \frac{1}{\bar{c}_m} \right) \right] \qquad \text{(VIII.12b)}$$

Within the range of parameters considered, $K_T \sim 0(10)$. For $0.95 < \varepsilon_R < 1$, in the near-stoichiometric case: $b \ll \bar{Y}_F$ and

$$t_L^* / t_{CH}^* \sim K_T (1 - \varepsilon_R)^2 \ll 1 \qquad \text{(VIII.13a)}$$

On the other hand, for a higher extent of non-soichiometry, suppose $Y_{F,a} / b \doteq 10$, then $g_F / (\bar{Y}_F / b - 1) \doteq 0.1$ and

$$t_L^* / t_{CH}^* \sim (1 - \varepsilon_R) \ll 1 \qquad \text{(VIII.13b)}$$

In both instances, therefore, the wall layer time scale is much shorter than that of the coreflow, over the range of ε_R expected. Note that very large departures from stoichiometric F/O proportions are precluded.

Invoking the Rayleigh criterion, it is obvious that in order to observe any interaction between the acoustic field and the chemical reaction in the coreflow, the two processes should necessarily have comparable time scales, viz.,

$$t_a^{*0} \sim t_{CH}^* \qquad \text{(VIII.14)}$$

Additional time scale relationships most likely to appear in practice are

$$t_P^* \sim t_a^{*0} \qquad \text{(VIII.15)}$$

excluding only extremely large or small motor length configurations; and, as indicated by Eq. (VIII.10), $t_L^* \ll t_{CH}^*$. Combining the last three relations, one obtains

$$t_L^* \ll t_a^{*0} \sim t_{CH}^* \sim t_P^* \qquad \text{(VIII.16)}$$

The extreme cases of very thick wall layers and ultra-high or very low frequencies are evidently ruled out. Therefore, at the moderate frequencies allowed by the time-scale configuration of Eq. (VIII.16), the acoustic field may interact with nonsteady heat release in the core, as well as with nonsteady mass addition by the propellant.

The associated frequency $\Omega_{CH} = 1/t^*_{CH}$ can now be calculated, using available thermochemical data for the $HCHO + NO_2$ reaction in $\bar{\omega}_{2,LR}$, and the explicit relations of Eqs. (VIII.12a,b). Ω_{CH} is plotted against $1 - \mathcal{E}_R$ in Fig. VIII.2 at various pressures, for a small value of $b > 0$. Since $\Omega_{CH} \sim p \cdot f(1 - \mathcal{E}_R; b)$, the frequency is shown to increase with p at any given $\mathcal{E}_R$. In Fig. VIII.3, the same plot is repeated at a single pressure for small departures from stoichiometric F/O, with $b > 0$ as parameter; Ω_{CH} is shown to increase with b at any fixed $\mathcal{E}_R$ and p.

To relate Ω_{CH} to the fundamental acoustic chamber mode, $t^{*0}_a = 1/\Omega_{CH}$ is imposed; this facilitates calculation of an associated characteristic chamber length,

$$X_{CH} = \bar{a}/2\Omega_{CH} \qquad \text{(VIII.17)}$$

through Eq. (VIII.9a). Imposing $\bar{a} = 920$ m/s, X_{CH} is plotted against $1 - \mathcal{E}_R$ in Fig. VIII.4, for a small value of $b > 0$, and with pressure as parameter. For a given pressure, X_{CH} decreases with increasing $(1 - \mathcal{E}_R)$ through several orders of magnitude; at a given $\mathcal{E}_R$, X_{CH} decreases with increasing p and (although not shown) expected to follow the same trend with respect to b.

The problem now is one of selecting parameter configurations most likely to exhibit coupling between the fundamental acoustic chamber mode and the core reaction. In other words, suitable pressure, chamber diameter, and length (p, d, L) need to be defined, such that optimal conditions for this coupling arise. This can be done now in an approximate manner, utilizing the results of Section VI.F.

Recall that Fig. VI.9 depicts the interaction parameter, $1 - \mathcal{E}_R$, against $1 + 4x/d$ at $p = \text{const}$, and with the port diameter, d, as parameter. Drawing $1 - \mathcal{E}_R = \text{const}$ lines results in intersections with the $d-$ curves, and pairs of data (x,d) can be obtained for each d. This plot was reconstructed as follows, in Fig. VIII.5. The geometry factor $4x/d$ is shown as function of axial distance x at various values of d. Overplotted are several curves of $1 - \mathcal{E}_R = \text{const}$, connecting points on the various d-lines, as obtained from Fig. VI.9. The interval of $1 - \mathcal{E}_R$ and of d drawn, defines a region of axial distances, x, over which those particular values of $1 - \mathcal{E}_R$ are attainable.

Now, with the selection of a particular set (p,L), and when equality of the characteristic frequencies, $\Omega_{CH} = \Omega^0_a$ is imposed, $1 - \mathcal{E}_R$ is determined (e.g., by taking $X_{CH} = L$ in Fig. VIII.4). To find the diameter that should produce this interaction, the map of $1 - \mathcal{E}_R$ vs. d in Fig. VIII.5 is entered, with the value $x = L$. The particular $1 - \mathcal{E}_R$ in question will determine the required diameter, d.

As an example, consider $p = 2$ MPa and $L = X_{CH} = 0.4$ m. From Fig. VIII.4, $1 - \mathcal{E}_R = 0.015$. Now, taking $x = L = 0.4$ m in Fig. VIII.5, the intersection with the $1 - \mathcal{E}_R = 0.015$ curve yields $d \triangleq 1.2$ cm. Actually, a better probability for interaction would arise when the particular $1 - \mathcal{E}_R$ is obtained upstream of the port exit plane, so that a somewhat smaller d is required.

It should be said that the foregoing arguments in no way ensure positive

interaction between the acoustic field and the reaction within the coreflow, neither do they indicate whether such interaction would be destabilizing. They merely comprise a necessary condition for such interaction: that the associated characteristic times t_a^{*0} and t_{CH}^* should be comparable.

Evidently, interaction would be most effective at the regions of pressure antinode: for the fundamental mode, these are in the neighborhood of $x = 0$ and of $x = L$. The analysis of Chap. VI has indicated that $1 - \mathcal{E}_R = 0$ near $x = 0$ (threshold) which leaves only the aft end. Here, however, there is less of a chance for overall excitation, due to the nozzle effect (through which acoustic energy is leaving the system by convection). Moreover, acoustic vibrations would tend to be damped when travelling upstream, against the velocity (and as expected, temperature) gradient, as pointed out by Salant and Toong.[138-139] Therefore, coupling between the fundamental acoustic mode and reaction in the core, if such coupling existed, may well be confined to the downstream region close to the port exit plane.

C. The Condensed Phase and the Quasi-Steady Reacting Wall Layer

1. The Condensed Phase

The condensed phase is assumed quasi-one-dimensional in a direction perpendicular to the propellant surface. Chemical reactions and the associated heat release are assumed to be concentrated within a collapsed, thin region at the condensed/gas interface. The propellant is considered homogeneous and isotropic, with uniform thermophysical properties. Thus, the only process followed within the condensed phase is the nonsteady energy transport.

a. Formulation

With the coordinate origin affixed to the receding propellant surface, the thermal diffusion equation is written in dimensionless form:

$$\frac{\partial \tilde{\mathcal{T}}}{\partial t_c} = \frac{\partial^2 \tilde{\mathcal{T}}}{\partial y_c^2} + V(t_c) \frac{\partial \tilde{\mathcal{T}}}{\partial y_c} \qquad \text{(VIII.18)}$$

for $0 < y_c < +\infty$, $t_c > 0$. The dimensionless temperature is defined $\tilde{\mathcal{T}} = T/T_0$, and the independent variables are $y_c = y/(\alpha_c/r_{ss})$, $t_c = t/(\alpha_c/r_{ss}^2)$; the dimensionless linear regression rate is $V = r(t)/r_{ss}$, where subscript ss denotes the steady state value. Overall mass continuity implies, assuming incompressibility:

$$V = V(t_c)$$

Strictly speaking, the coordinate system is non-inertial, so that the origin does not translate (relative to the stationary laboratory coordinate system) at constant speed. However, since only small departures from steady state are anticipated, the effect of small coordinate system acceleration is considered negligible. This difficulty was recognized by Williams[143] in his small perturbation study of nonsteady solid propellant combustion.

The following Dirichlet-type boundary conditions are imposed,

$$\tilde{\mathcal{T}}(0,t_c) = \tilde{\mathcal{T}}_0(t_c) \, ; \quad \tilde{\mathcal{T}}(\infty,t_c) = 1 \tag{VIII.19}$$

the second of which is a boundedness condition. The initial conditions are given at steady state, for which the solution is known:

$$\tilde{\mathcal{T}}(y_c,0) = \tilde{\mathcal{T}}_{ss}(y_c) = \left[\tilde{\mathcal{T}}_{0,ss} - 1 \right] e^{-y_c} + 1 \tag{VIII.20}$$

where $\tilde{\mathcal{T}}_{0,ss}$ is the dimensionless surface temperature at steady state.

b. Numerical Solution

To integrate the energy equation in time, an explicit numerical method is utilized. The semi-infinite region in y_c is approximated by the finite domain $0 < y_c < y_{cf}$, where y_{cf} is defined by

$$y_{cf} = - \ln \left[\frac{\tilde{\mathcal{T}}_f - 1}{\tilde{\mathcal{T}}_{0,ss} - 1} \right] \tag{VIII.21}$$

where $\tilde{\mathcal{T}}_f - 1 = 5 \times 10^{-4}$ typically. Variable mesh size in space is used, to facilitate an overall low number of nodal points (typically, 7), yet represent the high gradients near the $y_c = 0$ surface properly. For this purpose, the logarithmic stretching coordinate is used:

$$y_{c,n} = S_1 \left[e^{S_2 n} - 1 \right] \tag{VIII.22}$$

where S_1 and S_2 are adjustable constants, to achieve any desired configuration; n denotes the current nodal point index. The algorithm involves central differences in space, and is Euler-explicit timewise. Written in terms of the numerical approximation, U_n^j to $\tilde{\mathcal{T}}(y_c,t_c)$:

$$U_n^{j+1} = U_n^j + \Delta t_c \left[\frac{U_{n+1}^j - U_n^j}{\Delta y_{n+1}} - \frac{U_n^j - U_{n-1}^j}{\Delta y_n} \right] / \tfrac{1}{2} \left(\Delta y_n + \Delta y_{n+1} \right)$$

$$+ V^j \Delta t_c \left[U_{n+1}^j - U_{n-1}^j \right] / \left(\Delta y_n + \Delta y_{n+1} \right) \tag{VIII.23}$$

where $\Delta y_n = y_{c,n} - y_{c,n-1}$, $\quad n = 2,3,\ldots NF$.

Only interior points in the domain are included. With the algorithm being explicit in its time marching, the numerical stability criterion is:

$$\Delta t_c / \Delta y_{c,1}^2 < 0.5 \tag{VIII.24}$$

Δt_c is determined by the time increment used in the coreflow, Δt, in order to maintain coherence between the two time integration processes:

$$\Delta t_c = \Delta t / (\alpha_c / r_{ss}^2) \tag{VIII.25}$$

Δt, in turn, is determined by the Courant-Friedrichs-Lewy criterion (CFL) imposed by the core flowfield. Therefore, the method by which Δt_c and S_1, S_2 are obtained is as follows: as Δt is imposed, Δt_c is calculated by Eq. (VIII.25), and used in Eq. (VIII.24) to determine Δy_1 with a suitable choice of right hand side; e.g., $\Delta t_c / \Delta y_1^2 = 0.4$. Using Eq. (VIII.22), let $y_{c,1} = \Delta y_1$ so that one algebraic equation is provided, involving S_1 and S_2. The second equation is obtained by suitable choice of NF, the maximal number of interior nodal points, and $\tilde{\tau}_f - 1$ in Eq. (VIII.21). Since the time scale for coreflow variation, typically $1/\Omega_a$, is somewhat smaller than t_p^*, imposing Δt from the core does not result in numerical stability problems (for instance, unusually large or small Δy_1).

The accuracy of the given algorithm, Eq. (VIII.22), is described by the truncation error, which is $\sim 0(\Delta t_c, \Delta y_n^2)$. The space representation tends to become worse at stations deeper within the propellant, due to the progressive stretching of the $y_{c,n}$ coordinate; in the mean time, the higher space derivatives diminish in absolute value, compensating for the space increment growth. This would result in a fairly uniform truncation error effect, over the entire space domain considered.

c. The Auxiliary Energy Interface Condition

The condensed phase solution is required to satisfy the instantaneous energy conservation condition at the condensed/gas interface; in dimensional form:

$$\lambda \frac{\partial T}{\partial y}(0^+, t) = -\lambda_c \frac{\partial T}{\partial y}(0^-, t) + \rho_c r Q_s \tag{VIII.26}$$

where the condensed phase coordinate has been reversed. 0^+ and 0^- denote the gas side and condensed side of the interface, respectively, and Q_s is the net heat generation or depletion (by subsurface reaction and evaporation); $Q_s > 0$ for net heat depletion in the present notation. Further, overall mass continuity at the interface implies that

$$\rho_c r = m \tag{VIII.27}$$

where m is the mass flux.

Written in terms of condensed phase dimensionless properties, the right hand side of the energy condition is

$$\lambda \frac{\partial T}{\partial y}(0^+, t) = m C_c T_0 \left[-\frac{\partial \tilde{\tau}}{\partial y_c}(0, t_c) + \tilde{v} \tilde{Q}_s \right] \tag{VIII.28}$$

where $\tilde{Q}_s = Q_s / C_c T_0$. To evaluate $\partial \tilde{\tau} / \partial y_c (0^+, t_c)$ numerically,

$$\left(\frac{\partial U}{\partial y_c} \right)_0^j = \left[-a U_2^j + (a - 1/a) U_0^j - (1/a) U_1^j \right] / \Delta y_2 \tag{VIII.29}$$

which is a three point, second order accurate algorithm, and where
$a = 1/(1 + \Delta y_2/ \Delta y_1)$.

Note that the Dirichlet boundary condition of Eq. (VIII.19) incorporates the dimensionless surface temperature, common to both gas and condensed phase.

2. Condensed Phase and Reacting Wall Layer Coupling

a. The Quasi-steady Reacting Wall Layer

The time evolution of the coreflow equations at any particular point (x,t) is strongly influenced by the source terms which represent the heat and mass exchange across the core-wall layer boundary. These source terms are generated by the quasi-steady solution of the reacting wall layer formulation, similar to that described in Section VI.E; justification of the quasi-steady assumption, regarding the wall layer, is detailed in Appendix D.

Conceptually, the solution process may be described as follows. For a given set of coreflow data $[G(x,t), \tau_{stq}(x,t), p(x,t), etc.]$, the reacting wall layer solution is sought. Regardless of the nature of the coreflow process, being steady or nonsteady, it follows from the quasi-steady layer postulate that the prevailing core properties define uniquely the heat feedback per unit gas-mass generated within the layer, $\theta(\varepsilon_R)$, and, consequently, $\theta_{fb}(\varepsilon_R)$; these far field parameters are therefore fully determined by the external conditions in the core, at (x,t).

Further, as follows from $\theta(\varepsilon_R)$ being fully determined, the amount of heat feedback reaching the propellant surface [namely, $d\tau/d\zeta(0^+)$] must also retain its steady-state value (under the given instantaneous coreflow conditions). Otherwise, heat accumulation or depletion within the wall layer would result; since this heating or cooling is strictly time-dependent, the quasi-steady assumption would be violated.

In order to generate the above unique wall layer properties to match the given coreflow data set, a steady state solution is obtained by the method described in Section. VI.E. Of this solution, $\theta_{fb}(\varepsilon_R)$, ε_R, and $d\tau/d\zeta(0^+)$ are the only parameters of interest; the corresponding mass flux, m_{ss} and $\tau(0^+)$ are entirely fictitious. Since matching between the wall layer and the coreflow is achieved with the steady state wall layer solution, it remains to match between the wall layer and the condensed phase. For this purpose, $d\tau/d\zeta(0^+)$ serves as a key element, through the use of the condensed/gas energy constraint, Eqs. (VIII.26) and (VIII.28). The matching procedure is, therefore, based on satisfying the energy constraint at $y = 0$ in an iterative manner.

b. Solution Prodedure for the Coupled Condensed Phase and Wall Layer

Rewritten in terms of the dimensionless heat feedback to the propellant surface, $d\tau/d\zeta(0^+)$, the energy constraint is

$$\Phi_g = (C_c T_0/Q_1^*)[-\Phi_c + \tilde{v}\tilde{Q}_s] \qquad (VIII.30)$$

where $\Phi_g \equiv d\tau/d\zeta(0^+)$ and $\Phi_c = \partial\tilde{\tau}/\partial y_c(0^+, t_c)$.

The wall layer solution obtains Φ_g^{j+1}, corresponding to the time t^{j+1} which remains invariant for the process of iteration. The following steps describe the ineration process; it involves the condensed phase solution only.

(1) A value of $\tilde{\tau}_0^{j+1,k}$ is assumed for the dimensionless surface temperature. $k = 1$ is the current iteration index.

(2) The condensed phase heat equation is integrated forward in time, utilizing the finite difference algorithm of Eq. (VIII.23), with $\tilde{\tau}_0^{j+1,k}$ as boundary condition.

(3) After the solution has been obtained, the condensed side dimensionless heat flux at $y = 0$, $\Phi_c^{j+1,k}$ is calculated by the three-point difference formula of Eq. (VIII.29), with $U_0^{j+1,k} = \tilde{\tau}_0^{j+1,k}$.

(4) The mass burning rate correlation, Eq. (VI.24), and the elementary reacting condensed phase model of Appendix B are utilized to calculate

$$\tilde{V}^{j+1,k} = f(\tilde{\tau}_0^{j+1,k})/m_{ss} \qquad \text{(VIII.31)}$$

and

$$\tilde{Q}_s^{j+1,k} = g(\tilde{\tau}_0^{j+1,k}) \qquad \text{(VIII.32)}$$

respectively.

(5) Φ_g^{j+1}, $\Phi_c^{j+1,k}$, $\tilde{V}^{j+1,k}$, and $\tilde{Q}_s^{j+1,k}$ are now substituted into Eq. (VIII.30). Normally, a residual would arise, defined

$$R_s^{(k)} = \Phi_g^{j+1} - q(\Phi_c, \tilde{V}, \hat{Q}_s)^{j+1,k} \qquad \text{(VIII.33)}$$

When $R_s^{(k)}$ is sufficiently close to zero, the procedure is considered converged, and $\tilde{\tau}_0^{j+1} = \tilde{\tau}_0^{j+1,k}$, $m^{j+1} = m_{ss}V^{j+1,k}$. The condensed phase thermal profile is then stored for the purpose of the next time integration. If, on the other hand, $|R_s^{(k)}|$ is still large, the procedure is repeated from step (2) and on, after suitable correction is made to $\tilde{\tau}_0$ and the iteration index is raised to $k + 1$. Note that the condensed phase integration is repeated in this case, using the old thermal profile at t^j, not the previous iterate at $t^{j+1,k}$. A regula falsi procedure (or any other rapid-convergence method) may be used for this iteration procedure, with $'x' = \tilde{\tau}_0^{j+1,k}$ and $'y' = R_s^{(k)}$.

After convergence, the proper current values of the coreflow source terms at time t^{j+1} may be calculated using Θ_{fb}, ε_R, m, and $\tilde{\tau}_0$.

D. The Core Flowfield

1. Physical Description

A straight-prismatic propellant cavity is considered, closed at the head-end by propellant and a short, sonic nozzle at the aft-end. At the time of observation, the entire propellant is burning. Typical diameter and length dimensions are $O(1\ cm)$ and $O(10\ cm)$, respectively, corresponding to existing laboratory test configurations. The diameter may vary along the axis within 5% of its mean value.

The propellants of interest have properties which were discussed in previous chapters. Within the operating pressure regime considered, $1.0 < P < 6.0$ MPa, this type of propellant is expected to burn with a thick flame zone, $O(1\ mm)$, relative to ammonium perchlorate propellants which possess thin flame zones, $O(10\ \mu m)$.

A reacting wall layer with a finite thickness (yet small, compared with cavity diameter) is therefore considered, separating the coreflow region and the condensed propellant. Gas velocity and molecular transport within the layer are predominantly in the y-direction, perpendicular to the propellant surface. At any particular axial station, depending on the degree of interference between the wall layer and the core, chemical reaction within the layer may be incomplete and gaseous reactants, along with inert combustion products, are injected into the core.

Hence, a certain amount of premixed, exothermic residual reaction, considerably slower than that in the wall layer, may proceed within the core flowfield. At any axial station, this reaction is supported by reactant supply from upstream stations, as well as injection from the outer edge of the wall layer. The existence and extent of this reaction in the core is strongly coupled to erosive burning phenomena, as shown in Chapter VI.

The dynamic or time-dependent processes within the core flowfield are of interest. In particular, the interaction between the fundamental axial acoustic mode and the nonsteady heat generation in the core, by chemical reaction, is sought. The time scale for observation is, therefore, the period of the fundamental mode, $1/\Omega_a^0$, discussed in Section B herein. This time scale is short compared with the typical volume increase time (due to propellant regression), represented by d/r. For the duration of many oscillatory cycles, the chamber volume may, therefore, be considered as constant.

The analytical coreflow model is based on the foregoing physical description. The coreflow control volume boundaries in the chamber are drawn at the outer edge of the reacting wall layer, where the point of interaction (or layer cut-off) is denoted by the cut-off enthalpy, and the thermodynamic interaction constraints of Section VI.D are satisfied.

Additional simplifying assumptions, regarding the coreflow analytical model are discussed in the next section, followed by the core flowfield formulation.

2. Simplifying Assumptions

The basic assumptions for the coreflow model are as follows.

(a) The core flowfield is quasi-one-dimensional, with the axial (longitudinal) coordinate, x, being the only space variable considered. Variation of core properties in directions perpendicular to the axial, (y,z), are excluded, along with the associated velocity components, (v,w).

(b) Molecular transport, namely, diffusion, conductivity, and viscosity are negligible in the axial direction within the core control volume, along with turbulent effects. Therefore, the mean coreflow representation is formally laminar.

(c) Lateral mixing of gases entering the core at the wall layer boundary with the core gas is considered instantaneous. Thermal and chemical composition profiles, at any axial position, are therefore uniform over the cross-sectional area.

(d) Radiative heat transfer and body forces in the core are negligible.

(e) Thermophysical properties in the core are uniform. $\overline{W}$, Cp, γ = Cp/Cv are constants, their values taken at the typical high temperature of the core gases.

(f) The nozzle at the motor aft-end is considered to have a short convergent section and a sonic throat is maintained at all times. The throat may be periodically modulated to produce low amplitude wave excitation in the chamber.

Assumption (a) is clearly an idealization of a more complex, three-dimensional flowfield, most likely turbulent over most of its span $0 < x < L$. The quasi-one-dimensional coreflow assumption is severest near the head-end, where axial and radial velocity components are comparable; it becomes more plausible, however, several diameters downstream, as the axial mass flux, G, is rapidly amplified (for a cylindrical grain), and the ratio G/m approaches values $\sim O(100)$. Experimental cold flow evidence pointing to sinusoidal-shaped axial velocity profiles[113,118,119], tends to further weaken the confidence in this assumption regarding the lateral uniformity of the core parameter profiles. In this respect, the coreflow dependent variables should be considered only as mean values, over the cross-sectional channel area:

$$F(x,t) = \frac{1}{A(x)} \iint_{(A)} f(x,y',z',t)\,dy'dz' \qquad \text{(VIII.34)}$$

where F is the mean coreflow property. Of course, the last equation is used only conceptually; rigorous averaging would require application of the integral operator of Eq. (VIII.34) to the full, three-dimensional system of conservation equations.

Considering $Le \doteq Sc \doteq Pr \doteq 1$, it can be shown, with the available thermophysical data, that $\rho D/G \ll d < L$. Thus, molecular transport processes

have a range typically much shorter than any characteristic chamber dimension. In addition, sharp discontinuities or high gradients are excluded in the present study. These support the first part of assumption (b).

Near the core centerline, the Reynolds stress is roughly $-u'v' \sim u \, \partial u/\partial y$, showing a tendency to vanish as the velocity gradient, $\partial u/\partial y \to 0$ on the centerline. Turbulence intensity in the region of the core centerline is, therefore, close to zero. It increases, however, in the neighborhood of the channel walls; the intensity being $\sim (k_m y)^2$ using the Prandtl mixing length concept. These two opposing trends cause a peak of turbulence intensity within the core near the wall layer boundary. Using the data of Yamada et al,[113] peak intensity increases along the axis, as $\sim G/Re_d^{0.2}$, while its position, $y_T \sim \exp(m/G)$ tends closer to the wall as m/G decreases along the axis.

Hence, the low-turbulence region near the core centerline widens for increasing x in support of the laminar core representation. Turbulence effects, however, are incorporated in the coreflow model, as they most strongly affect the lateral heat and mass transfer across the wall layer boundary. Suitable turbulent correlations are utilized for this purpose, cf., Section VI.D.

Assumption (c) is an idealization, intended to facilitate the use of distributed source terms in the present quasi one-dimensional model in place of the lateral boundary conditions at the core/wall layer interface.

3. The Analytical Model

The governing equations are written in Eulerian conservation form, for the control volume of Fig. VIII. 1 .

Overall mass continuity:

$$\frac{\partial \rho}{\partial t} + \frac{\partial}{\partial x}(\rho u) = -\rho u \lambda_x + \tilde{M} \tag{VIII.35}$$

Momentum:

$$\frac{\partial}{\partial t}(\rho u) + \frac{\partial}{\partial x}(\rho u^2 + p) = -\rho u^2 \lambda_x + \tilde{M} u \alpha^* \tag{VIII.36}$$

Energy, in terms of the thermal enthalpy:

$$\frac{1}{r}\frac{\partial}{\partial t}(\rho h_T) + \frac{\partial}{\partial x}(\rho u h_T) - u\frac{\partial P}{\partial x} =$$

$$+ \dot{Q}_R + \dot{Q}_{fb} + \dot{Q}_{inj} \tag{VIII.37}$$

$$- \rho u h_T \lambda_x + \tilde{M} u^2 \left(\tfrac{1}{2} - \alpha^*\right)$$

Chemical species, $i = 1, 2, \ldots N$

$$\frac{\partial}{\partial t}(\rho Y_i) + \frac{\partial}{\partial x}(\rho u Y_i) = -\rho u Y_i a_x + \tilde{M} Y_i^* + w^{(i)} \qquad \text{(VIII.38)}$$

The various parameters are defined $a_x = d(\ln A)/dx$, $\gamma = C_p/C_v$, $\tilde{M} = mb_p/A$, and $\alpha^* = \tan \alpha$, where α is the angle between the channel side wall and the axial centerline for the case of variable channel area and b_p is the burning perimeter of the channel. The source terms in the energy equation are defined:

$$\dot{Q}_R = Q_2\, \omega_{2,C}, \quad \dot{Q}_{fb} = -q_{fb} b_p/A, \quad \text{and} \quad \dot{Q}_{inj} = \tilde{M}\, h_T^*$$

being the heat release by chemical reaction, the heat feedback to the wall layer edge, and the injection enthalpy (for gases entering the core at the control volume boundary), respectively. The heat feedback and injection terms, q_{fb}, h_T^*, and Y_i^* are obtained by satisfying the core/wall layer interaction constraints at each point (x,t). The thermal enthalpy, h_T^*, is defined by the integral of Eq. (IV.7a), and the caloric equation of state,

$$p = \rho h_T (\gamma - 1)/\gamma \qquad \text{(VIII.39)}$$

is utilized to eliminate the pressure, p, from the governing equations.

The chemical reaction considered in the core is overall second order, schematically represented by

$$\nu_F' S_F + \nu_O' S_O \longrightarrow \sum_{i=3}^{N} \nu_i'' S_i \qquad \text{(VIII.40)}$$
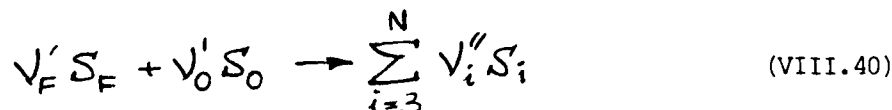
where the right hand side species are inert products of combustion, and ν_F', ν_O' are close to unity. The associated reaction rate in the core is represented by the Arrhenius expression,

$$\omega_{2,C} = \rho^2 A_2 \exp\left(-\beta_2/h_T\right)\left(\frac{Y_F}{W_F}\right)\left(\frac{Y_O}{W_O}\right) \qquad \text{(VIII.41)}$$

Similar to the secondary reaction within the wall layer, involving exactly the same species, thermochemical and stoichiometric data. The reaction rate for each of the species participating, in kg/m^3-s, is given by

$$w^{(i)} = W_i (\nu'' - \nu')_{2,i}\, \omega_{2,C} \qquad \text{(VIII.42)}$$

Shvab-Zeldovich-type coupling terms may be employed now, among the chemical species involved, to obtain some simplification in the partial differential equation (PDE) system. These are defined:

$$Z_{F,i} = Y_i\, \frac{W_F (\nu'' - \nu')_{2,F}}{W_i (\nu'' - \nu')_{2,i}} - Y_F, \quad i = 2, 3, \cdots \qquad \text{(VIII.43)}$$

where species F is used as a reference. Subtracting each of the species conservation equations for $i \neq F$ from the reference equation, $i = F$, Eq. (VIII.38) yields:

$$\rho \frac{\partial Z_{F,i}}{\partial t} + \rho u \frac{\partial Z_{F,i}}{\partial x} = \widetilde{M}(Z_{F,i}^* - Z_{F,i}), \quad i \neq 1 \tag{VIII.44}$$

The last equation is in convective form, obtained by using Eq. (VIII.35). $Z_{F,i}^*$ denote the coupling terms among species injected into the core from the wall layer, equivalent to the terms defined within the wall layer by Eq. (VI.28b), namely, $B_{i,F}$. Note that $B_{i,F}(x,t) = $ const for all i, due to the fixed primary decomposition stoichiometry employed, cf Eq. (VI.29b). This implies,

$$Z_{F,i}^*(x,t) = \text{const} \tag{VIII.45}$$

$Y_i^*(x,t)$, however, would be most likely variable. Now, the same chemical mechanism applies in both the wall layer and the core flow field. Further, neither boundary nor initial conditions involve imposed arbitrary chemical species compositions. For these reasons,

$$Z_{F,i}(x,t) = Z_{F,i}^* = \text{const} \tag{VIII.46}$$

Equations (VIII.44) are trivially satisfied by the relationship of Eq. (VIII.46), (along with the boundary and initial conditions, as will be shown), for all species $i \neq F$. This affords a great simplification in that it leaves only a single reference-species equation, in the form of Eq. (VIII.38), with $i = F$.

The partial differential system consists now of four first order equations in four dependent variables, defined as follows:

$$u_1 \equiv \rho, \quad u_2 \equiv \rho u, \quad u_3 \equiv \rho h_T, \quad u_4 \equiv \rho Y_F \tag{VIII.47}$$

where $u_i = u_i(x,t)$, $i = 1,2...4$. The original system may be rewritten now in terms of these variables:

$$\frac{\partial u_1}{\partial t} + \frac{\partial u_2}{\partial x} = F_1 \tag{VIII.48a}$$

$$\frac{\partial u_2}{\partial t} + \frac{\partial}{\partial x}\left[\frac{u_2^2}{u_1} + \frac{\gamma-1}{\gamma} u_3\right] = F_2 \tag{VIII.48b}$$

$$\frac{\partial u_3}{\partial t} + \frac{\partial}{\partial x}\left[\gamma\,\frac{u_2 u_3}{u_1}\right] - (\gamma-1)\frac{u_2}{u_1}\frac{\partial u_3}{\partial x} = F_3 \qquad \text{(VIII.48c)}$$

$$\frac{\partial u_4}{\partial t} + \frac{\partial}{\partial x}\left[\frac{u_2 u_4}{u_1}\right] = F_4 \qquad \text{(VIII.48d)}$$

where

$$F_1 \equiv u_2 \partial_x + \widetilde{M}$$

$$F_2 \equiv \frac{u_2}{u_1}\left[-u_2 \partial_x + \alpha^* \widetilde{M}\right]$$

$$F_3 \equiv \gamma\left[-\frac{u_2 u_3}{u_1}\partial_x + \left(\frac{u_2}{u_1}\right)^2 \widetilde{M}\left(\tfrac{1}{2}-\alpha^*\right)\right. \qquad \text{(VIII.49)}$$

$$\left. + \dot{Q}_R + \dot{Q}_{fb} + \dot{Q}_{inj}\right]$$

$$F_4 \equiv -\frac{u_2 u_4}{u_1}\partial_x + Y_F^* \widetilde{M} + w^{(F)}$$

The eigenvalues of this PDE system along with the compatibility (or characteristic) equations are derived in Appendix E. All four eigenvalues are real, and two are identical (the repeated eigenvalues correspond to the fluid particle path). Despite this degeneracy, following the generalized classification of Courant and Hilbert,[168] the system is hyperbolic.

The set of first order partial differential equations (VIII.48), is allowed four boundary conditions and four initial conditions.

The x = 0 boundary is drawn near the propellant head-end closure, taken planar in the present physical model. The available physical conditions are, therefore:

$$u_2(0,t) = m(0,t) \qquad \text{(VIII.50a)}$$

$$h_T(0,t) = h_T^*(0,t) \qquad \text{(VIII.50b)}$$

$$Y_F(0,t) = Y_F^*(0,t) \qquad \text{(VIII.50c)}$$

These involve flame cutoff parameters, derived from the conditions of the

lateral flame at the control volume periphery, (x = 0, y = d/2). It is assumed here that the influence of the head-end axial flow over the lateral surface is the same as the effect of radial flow over the head-end plane (from the periphery). Of course, this represents a rather crude approximation of the actual two- or three-dimensional flowfield. The above conditions may not be imposed directly, since the wall layer solution requires specified core data. They may, however, be satisfied in an iterative manner, in which the core data and the wall layer solution at x = 0 are brought to relax mutually. The actual procedure is given in Appendix F.

The fourth physical boundary condition is given at the nozzle end, x = L. This is the sonic throat condition for the (frozen) gas mixture leaving the port:

$$f\left[M^2(L,t), \, A_t(t)/A(L) \right] = 0 \qquad \text{(VIII.50d)}$$

In the actual, explicit form of the last equation, use of the one-dimensional, isentropic flow equations is made, justified by the short, adiabatic nozzle assumption.

The four initial conditions are written as

$$u_i(x,0) = u_i^0(x), \quad i = 1, 2, \cdots 4 \qquad \text{(VIII.51)}$$

added here only for the formal closure of the present discussion. They have an important role in the framework of the numerical solution, discussed in the following section.

E. The Numerical Solution

   1. The Rubin-Burstein Difference Scheme

The system of governing equations, Eq. (VIII.48), written in vector form:

$$\frac{\partial u_i}{\partial t} + \frac{\partial W_i}{\partial x} = f_i \qquad \text{(VIII.52)}$$

$W_i(u_1, \ldots u_4)$ and $f_i(u_1, \ldots u_4, x, t)$ are the generalized flux and source terms, respectively, defined by Eqs. (VIII.48) and (VIII.49). The system is hyperbolic, as shown in Appendix E.

The Rubin-Burnstein[166] finite difference scheme is utilized for the numerical solution of the system, Eq. (VIII.52), with some modification due to the presence of the source terms f_i, which have not been considered by the original authors. The algorithm is generally a two-step Lax-Wendroff[169,170] procedure, explicit in its time marching; it is applied directly to the system of equations in conservation form.

Denoting the numerical approximations of u_i, w_i, and f_i by U, W, and F, the two-step procedure is given as follows:

(a) <u>Predictor step</u> (midpoint, spacewise)

$$U_{n+1/2}^{j+1,P} = \frac{1}{2}\left(U_{n+1}^{j} + U_{n}^{j}\right) - \frac{\Delta t}{\Delta x}\left(W_{n+1}^{j} - W_{n}^{j}\right)$$
$$+ \frac{\Delta t}{2}\left(F_{n+1}^{j} + F_{n}^{j}\right) \qquad \text{(VIII.53)}$$

(b) <u>Corrector step</u>

$$U_{n}^{j+1} = U_{n}^{j} - \frac{\Delta t}{2}\left[\frac{W_{n+1}^{j} - W_{n-1}^{j}}{2\Delta x} + \frac{W_{n+1/2}^{j+1,P} - W_{n-1/2}^{j+1,P}}{\Delta x}\right]$$
$$+ \frac{\Delta t}{2}\left[\frac{F_{n+1/2}^{j+1,P} + F_{n-1/2}^{j+1,P}}{2} + F_{n}^{j}\right] \qquad \text{(VIII.54)}$$

The computational molecule associated with the discretization is shown in Fig. VIII.6. Evidently, from Eq. (VIII.48c), the thermal enthalpy equation does not reduce exactly to conservation form, and an additional term involving $(u_2/u_1)\,\partial u_3/\partial x$ appears. This term is treated separately; denoting $V \triangleq U_2^1/U_1^1,$ the predictor step right hand side has the additional term

$$\Delta t(\gamma-1)\,V_n^{j}\left[U_{3,n+1}^{j} - U_{3,n-1}^{j}\right]/\Delta x \qquad \text{(VIII.55a)}$$

The corrector step right hand side, for the energy equation, contains the additional term:

$$\frac{\Delta t}{2}(\gamma-1)\left\{V_n^{j}\,\frac{U_{3,n+1}^{j} - U_{3,n-1}^{j}}{2\Delta x}\right.$$
$$\left. + \frac{1}{2}\left(V_{n+1/2}^{j+1,P} + V_{n-1/2}^{j+1,P}\right)\frac{U_{3,n+1/2}^{j+1,P} - U_{3,n-1/2}^{j+1,P}}{\Delta x}\right\} \qquad \text{(VIII.55b)}$$

For purposes of analysis of the numerical algorithm, this deviation from conservation form need not be of concern. The energy equation, when written in terms of total stagnation energy of the mixture, can be easily shown to reduce to conservation form.

The present numerical algorithm utilizes central space-differences for representation of the $\partial/\partial x$ terms. Therefore, it requires all four dependent variables of the numerical scheme, u, to be fully specified at both x = 0 and x = L boundaries. In terms of the mathematical model employed, cf., Eqs. (VIII.48) through (VIII.51), as well as physically, there are formally only four such BCs available. Four additional constraints arise from the four compatibility relations, along the characteristic lines, at the boundaries. These so-called extraneous BCs are a property inherent in the hyperbolic system. An investigation and subsequent treatment of the numerical boundary conditions for fluid dynamic equations was carried out by Vichnevetsky,[171] whose method is followed here. Details of the derivation and the particular calculation procedures are given fully in Appendix F.

2. Consistency and Truncation Error

For purposes of the present analysis, the convective form of the system, Eq. (VIII.52), is used

$$\frac{\partial u_i}{\partial t} + C_{ik} \frac{\partial u_i}{\partial x} = f_i, \quad i = 1, 2, \cdots 4 \qquad \text{(VIII.56)}$$

where $C_{ik} = \partial w_i / \partial u_k$ is the Jacobian matrix of the flux terms, and summation convention is applied over repeated indices. The system is now considered in the small, i.e., over a small region in the x,t plane, where an appropriate quasi-linearized form of Eq. (VIII.56) applies. The mathematical justification of this approach to nonlinear hyperbolic systems (with all $f_i = 0$) was discussed by Lax.[172] Thus,

$$\frac{\partial u}{\partial t} + C \frac{\partial u}{\partial x} = f u \qquad \text{(VIII.57)}$$

where indices have been omitted. $u(x,t)$ is the dependent variable vector, and C, f are constant matrices. The RB difference scheme may now be applied to the linearized Eq. (VIII.57); substitution of the predictor into the corrector step results in the combined difference algorithm:

$$U_n^{j+1} = \left(1 + f\Delta t/2\right) U_n^j - C \frac{\Delta t}{\Delta x} \left(1 - f\Delta t\right) \left[U_{n+1}^j - U_{n-1}^j\right]/2$$

$$+ \frac{C^2}{2} \left(\frac{\Delta t}{\Delta x}\right)^2 \left[U_{n+1}^j - 2 U_n^j + U_{n-1}^j\right]$$

$$+ f\frac{\Delta t}{8} \left(1 + f\Delta t\right) \left[U_{n+1}^j + 2 U_n^j + U_{n-1}^j\right] \qquad \text{(VIII.58)}$$

With $f = 0$, the last equation is identical with the same result obtained by Rubin and Burstein[166] for the original Lax-Wendroff scheme.

The standard method of defining consistency and truncation error shall be used now. Assuming analyticity of $U(x,t)$ within the small domain considered, the following Taylor series expansions are made:

$$U_n^{j+1} = U_n^j + (\partial U/\partial t)_n^j \Delta t + \frac{1}{2!} (\partial^2 U/\partial t^2)_n^j \Delta t^2 + O(\Delta t^3)$$

$$U_{n+1}^j = U_n^j + (\partial U/\partial x)_n^j \Delta x + \frac{1}{2!} (\partial^2 U/\partial x^2)_n^j \Delta x^2 + O(\Delta x^3)$$

and so on. Substitution into Eq. (VIII.58), after some rearrangement:

$$U_t + \frac{1}{2} U_{tt} \Delta t + O(\Delta t^2) = -C U_x + O(\Delta x^2)$$
$$+ \frac{1}{2} f \cdot 2U + O(\Delta x^2)$$
$$+ \frac{1}{2} C^2 U_{xx} \Delta t + O(\Delta t \Delta x^2)$$
$$+ C f U_x \Delta t + O(\Delta t \Delta x^2)$$
$$+ \frac{f^2 \Delta t}{8} \cdot 4U + O(\Delta t \Delta x^2) \qquad \text{(VIII.59)}$$

The $(\ )_n^j$ indices have been omitted. To carry out the limiting process where the time increment is approaching zero, the functional relationship $\Delta x = g(\Delta t)$ should be defined. The Courant-Friedrich-Lewy (CFL) stability constraint may serve this purpose, being

$$C \Delta t / \Delta x = B \leq 1 \qquad \text{(VIII.60)}$$

Therefore, as $\Delta t \to 0$, Δx and Δt will approach zero uniformly. Collecting now terms of same orders in Δt, Eq. (VIII.59) yields:

$$U_t + C U_x - f U$$
$$+ \frac{\Delta t}{2} \left[U_{tt} - C^2 U_{xx} + C f U_x - f^2 U \right] + O(\Delta t^2, \Delta x^2) = 0 \qquad \text{(VIII.61)}$$

Now, as $\Delta t, \Delta x \to 0$ uniformly, consistency of the modified RB scheme is demonstrated, in the sense that the difference approximation, $U(x,t)$, satisfies the exact partial differential operator of Eq. (VIII.57), cf the first term in Eq. (VIII.61). When this holds, the $O(\Delta t)$ term in Eq. (VIII.61) vanishes identically, as

$$\frac{\partial U}{\partial t} + C \frac{\partial U}{\partial x} - f U = 0$$

Thus, the truncation error of the RB scheme is of second order, namely $O(\Delta t^2, \Delta x^2)$. The original Lax-Wendroff scheme has the same order of truncation error[169,179] as expected.

The actual choice of Δt in the numerical solution process is made through use of the maximal eigenvalue of C in the entire field,

$$\lambda_{max} = \max_n \left(a_n + u_n \right)$$

cf appendix E. This value is then utilized in the CFL constraint,

$$\lambda_{max} \Delta t / \Delta x = B < 1$$

which insures that Eq. (VIII.60) is satisfied over the entire domain.

3. Conclusions

From the standpoint of practical investigation of nonsteady oscillatory behavior, a major concern is the quantitative definition of amplification and attenuation (of particular frequency components), resulting from the discretization algorithm. In other words, the questions of amplitude and of phase velocity errors are of great importance. Unfortunately, since $f \neq 0$ in general, answers cannot be obtained from standard stability analyses, and the relation between exact and numerical solution components must be considered. For this purpose, a linearized error analysis was carried out in Appendix G. The results indicate that using the CFL number $B = 0.5$ leads to attenuation, involving small stepwise amplitude errors in the domain of wave numbers of interest, i.e.,

$$k = j/2L, \quad j = 1,2,\ldots10$$

where $j = 1$ denotes the fundamental mode. Higher frequency components ($j \gg 10$) are more readily attenuated, in comparison.

This particular conservative approach (favoring attenuation) has been undertaken since one of the primary objectives of the present analysis is to demonstrate amplification of acoustic vibrations through coupling with the exothermic reaction in the coreflow. In this respect, care must be taken to preclude possible numerically-induced amplification.

In practical calculations performed with CFL number $B = 0.5$, the solutions were found free of numerical instability under a wide variety of ambient and geometrical conditions. The existence of neighboring solutions was likewise demonstrated.

CHAPTER IX

NONLINEAR ACOUSTIC INSTABILITY INDUCED BY EXOTHERMIC REACTION

The discussion herein is divided into three major parts. First, a summary
of the results due to numerical analysis, for the model described in Chapter
VIII, given in Section A. Second, conclusions regarding nonsteady motions
coupled with the core reaction and the wall layer, in Section B. Finally,
recommendations for future study are offered in Section C.

A. Results

1. Physical Considerations

The results were obtained by the numerical algorithm described in Chapter
VIII. The full nonsteady one dimensional coreflow processes were considered,
along with the reacting wall layer model developed in Chapter VI, in quasi
steady form. Within the present framework, the solid propellant was considered
in the quasi steady mode as well, in the sense that it adjusts instantaneously
to any external perturbation. This assumption can not be justified physically
in general, and was made to enable a clear identification of the coupling
between the coreflow acoustics and the chemical process. This assumption
eliminates possible dynamic effects due to thermal relaxation in the solid
phase (investigated extensively in the literature, cf. Chapter VII) which
could obscure the phenomena presently of interest. It should be mentioned,
however, that under very high external perturbation frequencies, the solid
phase heat transfer problem becomes singular. The behavior in this regime can
be investigated analytically by postulating a thin, high-frequency boundary
layer within the solid, at the surface. Since the layer is thin, the
associated relaxation time is short, and a near-instantaneous response results.
This notion is corroborated to some extent by the (calculated) receding portion
of the propellant response function, which, after peaking at frequency O(1000)
cps for most propellants of interest, approaches zero asymptotically as the
frequency tends to very high values. This lends some credibility to the
present quasi steady assumption, provided the frequencies considered are high
enough.

When a reacting flow is undergoing acoustic oscillations, and Rayleigh
type coupling is considered, as explained in Chapter VII, the role of an
exothermic, overall second order reaction is quite clear. It would always
obtain a component of heat release in phase with the attendant pressure
oscillation, and hence promote instability. In this respect, there would be no
novelty in demonstration of acoustic enhancement in a flow where the reaction
is pressure sensitive and the reactant composition is prescribed. What makes
the present analysis worthwhile is therefore the combination of the various
elements within the propellant cavity; in particular, the interaction between
the coreflow and the wall layer, in simulation of actual rocket chamber
processes. The net dynamic effect of coupling between these elements is not
straightforward; the following factors must be considered.

(a) The presence of a mean (nonuniform) flow field, temperature, pressure
and velocity gradients in the core, imply that pure standing acoustic
modes can not be achieved exactly and some travelling wave content
should be expected.

(b) The region of core-wall layer interaction is usually confined to the downstream portion of the port, which means that waves produced in that region (due to possible dynamic coupling) should travel upstream, against velocity and temperature gradients; according to the arguments of Chapter VII, this should result in attenuation and nonuniformity of the standing modes.

(c) When the instantaneous pressure perturbation at a point is positive, the velocity perturbation (nearly out of phase) should be negative. The direct effect of both is to retard $1 - \mathcal{E}_R$, decreasing reactant injection. On the other hand, the core reaction is enhanced (both higher p and longer residence time) which tends to increase the stagnation enthalpy, and hence, increase $1 - \mathcal{E}_R$. Since pressure and stagnation enthalpy perturbations are not in phase generally, the two opposing trends clearly lead to dynamic interaction.

2. Datum Case

Enhancement of naturally evolving acoustic oscillations is clearly demonstrated in Figs. IX.1 through IX.3, for the datum case properties given in Table IX.1. These diagrams show pressure, velocity and stagnation temperature evolution against time, over many periods of oscillation. The following observations can be made.

(a) The fundamental mode is attenuated, within roughly two periods of oscillation, followed by persistent, high frequency, nearly sinusoidal waves.

(b) The frequency of the ensuing oscillations is close to (within 10%) the first harmonic frequency, which in this case is roughly 10^4 cps.

(c) The amplitude of the oscillations (pressure in particular, cf. Fig. IX.1c) is shown to increase slowly with time.

(d) The amplitude is highly nonuniform, being highest in the region of $x = L$ and appreciably smaller near $x = 0$, both regions of pressure antinode.

(e) In addition to the standing wave mode, some travelling wave content is evident. Particularly, oscillations are shown at $L/2$, the neighborhood of velocity node for the first harmonic.

(f) Whereas velocity and stagnation enthalpy seem to reach constant mean values, the pressure continues to rise in the average, although its mean gradient ($\partial \bar{p}/\partial t$) decreases with time. This is due to the initial data employed, which does not take into account erosive burning when an appropriate (fixed) supercritical nozzle is calculated. This need not be of concern, since the mean (in the bulk) pressure rise time is much longer than a typical period of oscillations.

In comparison, when interaction between the core and the wall layer is naturally retarded, as shown in Figs. IX.4a and IX.4b, the foregoing type of acoustic instability does not occur; both the fundamental mode and its first harmonic are attenuated, and the pressure-time profiles tend to be smooth.

A discretized cross correlation, defined

$$CC_j = \frac{1}{n} \sum_{i=1}^{n} \hat{q}_{Ri}\, \hat{P}_{i+j_P} \qquad (IX.1)$$

was carried out numerically, between the normalized fluctuations of reactive heat release in the core,

$$\hat{q}_{Ri} \equiv \dot{Q}_R(L-\Delta x, t^j)\big/\dot{Q}_R(L,t^j) - 1 \qquad (IX.2)$$

and the local pressure,

$$\hat{P}_{i+j_P} \equiv P(L-\Delta x, t^{i+j_P})\big/P(L,t^{i+j_P}) - 1 \qquad (IX.3)$$

where i, and $j_p = 0, \pm 1, \pm 2, \ldots$ denote the time and timewise phase index respectively. A comparison between three distinct cases is shown in Fig. IX.5. (A) is the strongly interacting, oscillatory datum case, where two prominent peaks are observed, at -0.36π and at $+0.24\pi$. This indicates a phase shift between Q_R and p, resulting from comparable characteristic times $t^*_a{}^{(I)}$ and t^*_{CH}. (B) is a case with vanishing interaction, corresponding to a smaller port diameter (d = 0.6 cm) and a reduced global turbulent heat feedback coefficient, at the baseline geometry factor (4L/d = 40). It obtains only a single peak, at $j_p = 0$, showing complete entrainment of the core reaction by pressure oscillations. (C) is another oscillatory case, but with weaker interaction than (A), obtained at a lower pressure (2 MPa). Actual mean values of Q_R for cases (B) and (C) were lower by 1 and 2 orders of magnitude respectively from those of case (A).

3. Parametric Influences

The effect of various parameters upon the time evolution of the coreflow system was studied by separate numerical experiments. All were made by perturbation of one or two parameters out of the baseline data set.

a. Fuel - oxidizer stoichiometry

This property is, of course, pre-determined by the propellant composition (however, turbulence effects might contribute to nonstoichiometry even in a premixed system). In the datum case, the fuel species 'F' is allowed to be in excess, such that the difference

$$d_F \equiv B_{T,F} - B_{T,O} = 0.02 \qquad (IX.4)$$

cf Eq. (VI.33a) and the discussion in Section B.2 of Chapter VIII. When $d_F = 0.002$ is employed, interaction between the core and the wall layer is appreciably retarded, [$1 - \varepsilon_R$ smaller by 30% in the mean] and the extent of core reaction decreases [$\dot{Q}_R$ is reduced by an order of magnitude, in the mean]. Consequently, heat release in the core can not effectively couple with the acoustic field, and vibrations do not evolve.

b. <u>Turbulent</u> <u>heat</u> <u>feedback</u>

This property was controlled by uniform reduction of the Blasius coefficient, C_{BL}, from its datum case value of 0.03 to 0.02, cf Eqs. (VI.11) and (VI.37). As expected, the behavior is similar to that described in (a) for d_F reduction. Time-traces were plotted in Figs. IX.4a,b for stagnation enthalpy, velocity and pressure at x = L. The results of a related case (smaller port diameter, d = 0.6 cm, at the baseline geometry factor of 4L/d = 40) were used for curve (B) in Fig. IX.5, discussed earlier. Note that due to the negligible extent of reaction in the core, the normalized stagnation enthalpy and velocity fluctuations are similar, which is the reason for the single trace in Fig. IX.4b.

c. <u>Pressure</u>

A reduction of the pressure from the baseline value of 5 MPa to 2 MPa was found to result in more core - wall layer interaction initially (higher erosive effect, as discussed in Section VI.F and in Chapter VIII); however, at later stages, the oscillations evolved had a much smaller amplitude than those at the datum case. The curve (C), plotted in Fig. IX.5 corresponds to these results: it shows a single peak at $-0.24\,\pi$. In this respect the behavior is similar to that of the datum case, in that a timewise phase is indicated between p and the core reaction; yet, oscillations tend to be attenuated in this case. The mean $\dot{Q}_R$ is roughly an order of magnitude lower than the datum case value, which might explain the relative weakness of coupling between the acoustic field and the core exothermicity.

d. <u>Reaction</u> <u>rate</u>

Variation of the kinetics constant prefactor for the reaction considered was carried out with values of A_2 in a range from 10^6 to 5×10^6 m^3/mol-s. The behavior found was not monotonous, as shown schematically in Fig. IX.6, where the mean amplitudes of pressure oscillation at x = L were compared. At the baseline value of 3×10^6 m^3/mol-s, the amplitude is maximal, while both above and below this value the amplitudes tend to decrease. When increased, this parameter has two opposing effects: it causes reduced core - wall layer interaction (the reactive region shrinks within the wall layer due to smaller secondary reaction length scale); on the other hand, it enhances $\dot{Q}_R$ globally. Therefore, the peaking behavior shown in Fig. IX.6 can be anticipated, since the first effect tends to retard, and the second to enhance dynamic coupling between the acoustic field and the core exothermicity. In this respect, the effect of A_2 is similar to that of pressure, although to a lesser extent.

e. <u>Geometry</u>

Within the present one dimensional coreflow configuration, chamber length variation controls the frequency of the natural standing acoustic modes; in addition, the geometry factor, 4L/d, indicates the extent of core - wall layer coupling (in a stationary sense). The effect of chamber length and port diameter is as follows.

(1) Decreasing port diameter to 0.6 cm at the baseline geometry factor of 40, was shown to initially enhance core - wall layer interaction, but attenuation ensued at later stages and the final amplitudes were

smaller than in the datum case, although oscillations persisted, at a frequency close to that of the first harmonic of the fundamental mode (note that a smaller chamber length was employed).

(2) At the same reduced diameter (0.6 cm), increasing the geometry factor to 4L/d = 60 (L = 9 cm), resulted in reduced coupling at the final stages and enhanced damping of vibrations.

These results indicate that the effect of geometry scaling is not straightforward. When, relative to the baseline, both smaller port diameter and larger L/d are employed, the net dynamic effect migh still lead to enhanced attenuation, as coupling conditions betwen the standing acoustic modes and core exothermicity may favor damping of vibrations. It should be stressed that coupling in this manner can lead to attenuation as well as to amplification of acoustic vibrations in the core.

B. Conclusions

A theoretical model for nonsteady, reacting flow within a solid propellant cavity has been developed and solved numerically, using a digital computer. The model explicitly applies to propellants resembling nitramines in that they possess extended gaseous reaction regions under rocket operating pressures. The conclusions drawn from the results of the analysis are summarized as follows.

1. The existence of oscillatory near-harmonic solutions with slowly varying amplitude, evolving naturally from smooth initial data has been demonstrated. The most likely mechanism responsible for these nonsteady solutions is the dynamic coupling between the reacting coreflow and the wall layer (the latter considered quasi steady), through the Rayleigh criterion.

2. The high frequencies of oscillation obtained by the present solutions resemble those observed in the firing of laboratory sized test motors containing nitramine composite propellants,[159] with comparable grain geometries. Their magnitude, O(10 KHz) tends to exclude possible interaction with the nonsteady heat wave relaxation in the solid phase, (being roughly one order of magnitude slower) and points to the novel interaction mechanism in (1) as plausible explanation.

3. Dynamic coupling between the wall layer and the reacting coreflow has been shown only for axial acoustic modes, owing to the one dimensional modeling. However, it could apply equally well to any of the transverse (spinning, radial) acoustic chamber modes.

4. From a practical standpoint, the present mode of instability may seem potentially less hazardous than the form provided by interaction between the acoustic field and solid phase dynamics, since the latter is available throughout the chamber, and hence may couple more effectively with the attendant pressure oscillations. Dynamic coupling with the reaction in the core, in comparison, is localized at the downstream portion of the port, whereby acoustic energy is lost through the nozzle, and attenuation occurs as waves travel upstream through the nonreacting upstream region. Nevertheless, this mode of coupling is important, since it may entrain or resonate with other components of the system, could effectively change the

overall frequency response of the chamber and lead to thrust fluctuations.

5. The crucial element in the dynamic chamber configuration analyzed herein is, of course, the exothermic residual reaction in the core. Its extent and pressure dependence determine mostly whether or not instability should evolve. Therefore, propellant additives (such as AP at the 10% level) which tend to decrease the flame zone thickness, or geometries (sufficiently large effective port diameters) which tend to supress the extent of residual core reaction are recommended, to avoid this particular mode of instability.

C. Recommendations

1. Incorporation of Solid Phase Dynamics

The most immediate extension of the analysis can be made by the addition of solid phase dynamics to the system. This would involve solution of the nonsteady heat wave in the solid, the model for which is described in Section VIII.C. A higher level of computational effort is required in this instance, since matching of thermal fluxes at the solid-gas boundary requires iterations at any point of interest along the axis. The advantage would be the ability to simulate more closely actual motor behavior from the instant of ignition within the present one dimensional coreflow model. This should enable comparison with experimental data. However, such data are not available in sufficient quantity at the time of this writing. Therefore, the analysis may suggest appropriate diagnostic measurements and scaling factors for experimental laboratory devices.

2. Turbulent Reaction Model

An important refinement of the present coreflow model would be obtained by allowing for fluid dynamic variables to affect the reaction rate in the core, in addition to the state-variable influence presently employed (through use of the laminar reaction rate in the mean). This may be achieved by including a turbulent reaction term in balance with the laminar one, e.g., in the manner suggested by Spalding.[120,121] Admittedly, the available turbulent reaction models[120-123] involve an appreciable uncertainty, owing to the present lack of knowledge about turbulence. However, incorporating these effects would allow for more realistic modeling of the residual coreflow combustion process, which is of primary importance in the determination of dynamic behavior in the present model.

This extension is impossible within a strictly one dimensional coreflow model, and requires accounting for lateral variations in the flow field. As a first step, two dimensional effects may be introduced approximately, by the local use of the lateral solution profiles derived analytically by Culick,[119] calculated for the main flow conditions at any point (x,t). The uncertainty in this approximation is no greater than that involved in the turbulent reaction model.

3. Frequency Response Analysis

The present coreflow model is provided with the capability to modulate or vary the (sonic) nozzle throat area in a prescribed manner. This may be used for a systematic investigation of forced oscillations (as well as response to a

step function perturbation). However, the resulting frequency response (or gain function) would lack any generality, being highly specific to the overall system's geometry, ambient data and the particular values of parameters, such as the extent of nonstoichiometric fuel excess (d_F), which are quite speculative.

This type of analysis has its merit whenever a particular motor configuration or laboratory experiment prove unstable, and remedies (e.g., rescaling) are sought. Its application must therefore await the attainment of a sufficiently wide experimental data base, and should incorporate the two aforementioned model extensions.

4. Two Dimensional Modeling of the Turbulent Coreflow

Despite the order of magnitude increase expected in computational effort, it is tempting to suggest this analysis for the future. It would allow replacement of the current turbulent heat feedback correlation and purely laminar flow field and reaction rate by more realistic models, allowing for turbulence effects, and relaxing the strong assumption of one-dimensionality near the head end (as well as over the entire core). When extended to include the wall layer region, this analysis may serve to check the adequacy of the core-wall layer interaction constraints of Chap. VI, necessitated by the present quasi one dimensional approach.

Unfortunately, in addition to the computational inconvenience, this approach has several strong drawbacks: current lack of confidence in turbulence modeling, lack of proper experimental measurements to justify the correlations utilized, and finally, loss of possible physical insight due to the complexity of the model itself. Although such models for multidimensional reacting flows are in existence (e.g., the second order closure models used by Varma[123] and by Beddini[124,125], their application to solid propellant chamber analysis has not been attempted.

5. Experimental Verification

The foregoing theory of rocket chamber processes, in both steady state and nonsteady parts, requires experimental verification. In addition to the diagnostic experiments suggested in Chap. V for the nitramine deflagration wave, similar experiments should be performed under transverse flow conditions. More specifically:

a. Steady state experiments with propellant burning under transverse flow conditions, to identify intermediate radicals such as OH, CH beyond the wall layer. This may eventually be done by laser-diagnostic methods currently under development (e.g., Coherent Anti Raman Spectra) and would verify or refute the postulate of extended reactions in the coreflow.

b. Systematic rocket motor experiments in which combined propellants and motor geometry effects would be studied. The propellants would be formulated to have a range of extended flame zone reactions.

REFERENCES

1. Orloff, M. K., Mullen, P. A. and Rauch, F. C., "Molecular Orbital Study of the Electronic Structure of Spectrum of Hexahydro 1, 3, 5 Trinitro-s-Triazine", Journal of Physical Chemistry, Vol. 74, No. 10, May 1970, pp. 2189-2192.

2. Harris, P. M., "An Investigation of the Crystalline Structure of Aromatic Trinitro- and Related Compounds", Ohio State Univ. Research Foundation, AFOSR-TR-59-165.

3. McCrone, W. C., "The Polymorphism of HMX", Progress Report, OSRD No. 694, June 30, 1942 and OSRD No. 1227, January 1943.

4. Teetsov, A. S. and McCrone, W. C., "The Microscopical Study of Polymorph Stability Diagrams", The Microscope, Vol. 15, No. 1, Nov.-Dec. 1965, pp.13-29.

5. Hall, P. G., "Thermal Decomposition and Phase Transitions in Solid Nitramines", Trans. Faraday Society, Vol. 67 (Part 2), 1971, pp. 556-562.

6. Maycock, J. N. and Verneker, V. R. P., "Thermal Decomposition of delta-HMX (Cyclotetramethylene Tetranitramine)", Explosivstoffe, No. 1, 1969, pp. 5-8.

7. Cady, H. H., Larson, A. C. and Cromer, D. T., "The Crystal Structure of alpha-HMX and a Refinement of the Structure of beta-HMX", Acta Cryst. 16 (1963) pp. 617-623.

8. Choi, C. S. and Boutin, H. P., "A Study of the Crystal Structure of beta-Cyclotetramethylene Tetranitramine by Neutron Deffraction", Acta Cryst., B.26 (1970), pp. 1235-1240.

9. Belyayeva, M. S., Klinenko, G. K., Dabaytseva, L. T. and Stolyarov, P. M., "Factors Determining the Thermal Stability of Cyclic Nitroamines in Crystalline State", Moscow, May 1978, (work in translation).

10. Edwards, G., "The Vapour Pressure of Cyclo-Trimethylene-Trinitramine (Cyclonite) and Pentaerythritol-Tetranitrate", Trans. Faraday Society 1953, 49, pp. 152-154.

11. Rosen, J. M. and Dickinson, C., "Vapor Pressures and Heats of Sublimation of Some High Melting Organic Explosives", Journal of Chemical and Engineering Data, Vol. 14, No. 1, January 1969, pp. 120-124.

12. Taylor, J. W. and Crookes, R. J., "Vapour Pressure and Enthalpy of Sublimation of 1, 3, 5, 7 Tetranitro-1, 3, 5, 7-tetra-aracyclo-octane (HMX)", Journal of the Chemical Society, Faraday Transactions I, Vol. 3, pp. 723-729, 1976.

13. Robertson, A. J. B., "The Thermal Decomposition of Explosives, Part II. Cyclotrimethylenetrinitramine and Cyclotetramethylenetetranitramine", _Trans. Faraday Society_, No. 45, pp. 85-93, 1949.

14. Rauch, F. C. and Fanelli, A. J., "The Thermal Decomposition Kinetics of Hexahydro, 1, 3, 5-trinitro-s-triazine Above the Melting Point: Evidence for Both a Gas and Liquid Phase Decomposition", _The Journal of Physical Chemistry_, Vol. 73, No. 5, May 1969, pp. 1604-1608.

15. Rogers, R. N. and Smith, L. C., "Application of Scanning Calorimetry to the Study of Chemical Kinetics", _Thermochimica Acta_, No. 1, 1970, pp. 1-9.

16. Rogers, R. N., "Differential Scanning Calorimetric Determination of Kinetic Constants of Systems that Melt with Decomposition", _Thermochimica Acta 3_, 1972, pp. 437-447.

17. Rogers, R. N. and Daub, G. W., "Scanning Calorimetric Determination of Vapor-Phase Kinetic Data", _Analytical Chemistry_, Vol. 45, pp. 596-600, March 1973.

18. Rogers, R. N., "Determination of Condensed Phase Kinetic Constants", Note, _Thermochimica Acta_, No. 9, pp. 444-446, 1974.

19. Suryanarayana, B., Graybush, R. J. and Autera, J. R. "Thermal Degradation of Secondary Nitramines: A Nitrogen-1 Tracer Study of HMX (1, 3, 5, 7 Tetranitro-1, 3, 5, 7- Tetraazacyclooctane)", _Chemistry and Industry_, pp. 2177-2178, December 30, 1967.

20. McCarty, K. P., "HMX Propellant Combustion Studies: Phase 1, Literature Search and Data Assessment", AFRPL-TR-76-59, December, 1976.

21. Cosgrove, J. D. and Owen, A. J., "The Thermal Decomposition of 1, 3, 5 Trinitrohexadydro-1, 3, 5 triazine (RDX)", _Chemical Communications_, 1968, p. 286.

22. Cosgrove, J. D. and Owen, A. J., "The Thermal Decomposition of 1, 3, 5 Trinitro Hexahydro 1, 3, 5 Triazine (RDX) Part I The Products and Psysical Parameters", _Combustion and Flame_, No. 22, 1974, pp. 13-18.

23. Cosgrove, J. D. and Owen, A. J., "The Thermal Decomposition of 1, 3, 5 Trinitro Hexahydro 1, 3, 5 Triazine (RDX) Part II: The Effects of the Products", _Combustion and Flame_, No. 22, 1974, pp. 19-22.

24. Batten, J. J. and Murdie, D. C., "The Thermal Decomposition of RDX at Temperatures Below the Melting Point. Part I: Comments on the Mechanism, _Aust. Journal of Chemistry 23_, 1970, pp. 737-747.

25. Batten, J. J. and Murdie, D. C., "The Thermal Decomposition of RDX at Temperatures Below the Melting Point. Part II: Activation Energy", Aust. Journal of Chemistry 23, 1970, pp. 749-755.

26. Batten, J. J., "The Thermal Decomposition of RDX at Temperatures Below the Melting Point. Part III: Toward Elucidation of the Mechanism", Aust. Journal of Chemistry 24, 1971, pp. 945-954.

27. Batten, J. J., "The Thermal Decomposition of RDX at Temperatures Below the Melting Point. Part IV: Catalysis of the Decomposition by Formaldehyde", Aust. Journal of Chemistry 24, 1971, pp. 2025-2029.

28. Rogers, R. N. and Morris, E. D., "On Estimating Activations Energies with a Differential Scanning Calorimeter", Analitical Chemistry, Vol. 38 (1966), pp. 412-414.

29. Pollard, F. H. and Wyatt, R. M. H., "Reactions Between Formaldehyde and Nitrogen Dioxide. Part I: The Kinetics of the Slow Reaction", Trans. Faraday Society, Vol. 45, 1949, pp. 760-767.

30. Pollard, F. H. and Woodward, P., "Reactions Between Formaldehyde and Nitrogen Dioxide. Part II: The Explosive Reaction", Trans. Faraday Society 45, 1949, pp. 767-770.

31. Pollard, F. H. and Wyatt, R. M. H., "Reactions Between Formaldehyde and Nitrogen Dioxide. Part III: The Determination of Flame Speeds", Trans. Faraday Society 46, 1950, pp. 281-289.

32. Stals, J., Buchanan, A. S. and Barraclough, C. G., "Chemistry of Alyphalic, Unconjugated Nitramines. Part 5: Primary Photochemical Processes in Polycrystalline RDX", Trans. Faraday Society 67, 1971, pp. 1749-1755.

33. Stals, J., Buchanan, A. S. and Barraclough, C. G., "Chemistry of Alyphalic, Unconjugated Nitramines. Part 6: Solid State Photolysis of RDX", Trans. Faraday Society 67, 1971, pp. 1756-1767.

34. Stals, J., "Chemistry of Alyphalic, Unconjugated Nitramines. Part 7: Interrelations Between the Thermal, Photochemical and Mass Spectral Fragmentation of RDX", Trans. Faraday Society 67, 1971, pp. 1768-1775.

35. Goshgarian, B. B., "The Decomposition of Cyclotrimethyl-enetrinitramine (RDX) and Cyclotetramethylenetetranitramine", AFRPL-TR-78-76, October 1978.

36. Brenecker, R. R. and Smith, L. C., "On the Products Formed in the Combustion of Explosives. Freeze Out of the Water-Gas Reaction", Journal of Physical Chemistry, 71, No. 8, 1967, pp. 2381-2390.

37. Rocchio, J. J. and Juhasz, A. A., "HMX Thermal Decomposition Chemistry and Its Relation to HMX-Composite Propellant Combustion", 11th JANNAF Combustion Meeting, CPIA Publication No. 261, December 1974, pp. 247-265.

38. Lenchitz, C. and Velicky, R. W., "The Role of Thermochemistry in HMX Propellant Burning", 12th JANNAF Combustion Meeting, CPIA Publication 273, Vol. II, Dec. 1975. pp. 301-321.

39. Shaw, R. and Walker, F. E., "Estimated Kinetics and Thermochemistry of Some Initial Unimolecular Reactions in the Thermal Decomposition of 1, 3, 5, 7 Tetranitro-1, 3, 5, 7 tetraazacyclooctane in the Gas Phase", The Journal of Physical Chemistry, Vol. 81, No. 25, pp. 2572-2576, 1977.

40. Fifer, R., "Shock Tube Study of the High Temperature Kinetics and Mechanism of Nitrogen Dioxide - Aldehyde Reactions" Modern Development in Shock Tube Research ,Proc. 10th International Shock tube Symposium, Kyoto, Japan, 1975, pp. 613-620.

41. Levy, J. B., "Examination of Chemical Kinetics Data Used in Induction Zone Calculations for the Combustion of Cordite", BRL CR-310, Aug. 1976.

42. Vallance, W. G., Private communication, 1974.

43. Fenimore, C. P. and Jones, G. W., "The Rate of Reaction $O + N_2O = 2NO$", 8th Symposium (International) on Combustion, The Combustion Institute, Pittsburgh, PA, 1962, pp. 127-133.

44. Ford, H., "Thermal Mechanisms Related to the Photolysis of Nitrogen Dioxide", 8th Symposium (International) on Combustion, The Combustion Institute, Pittsburgh, PA, 1962, pp. 119-127.

45. Fogelzang, A. E., Svetlov, B. S., Azhemian, V. Ya. Kolyasov, S. M. and Sergienko, O. I., "The Combustion of Nitramines and Nitosamines", Translated from Docladi Academi Nauk, SSSR, Vol. 216, No. 3, May 1974, pp. 603-606.

46. Parker, W. G. and Wolfhard, H. G., "Some Characteristics of Flames Supported by NO and NO2", 4th Symposium (International) on Combustion, The Combustion Institute, Pittsburgh, PA, 1953, pp. 420-428.

47. Wolfhard, H. G. and Parker, W. G., "Spectra and Combustion Mechanism of Flames Supported by Oxides of Nitrogen", 5th Symposium (International) on Combustion, The Combustion Institute, Pittsburgh, Pa., 1955, pp. 224-230.

48. Valance, W. G., Ben-Reuven, M., Vichnevetsky, R. and Summerfield, M., "Flame Model for Deflagration of RDX", Presented at 11th JANNAF Combustion Meeting, Dec. 1974.

49. Derr, R. L., Boggs, T. L., Zurn, D. E. and Dibble, E. J., "The Combustion Characteristics of HMX", 11th JANNAF Combustion Meeting, CPIA Publication 261, Vol 1, Dec. 1974, pp. 231-241.

50. Boggs, T. L., Price, C. F., Zurn, D. E., Derr, R. L. and Dibble, E. J., "The Self-Deflagration of Cyclotetrametylenetetranitramine (HMX)", Paper No. 77-859, AIAA/SAE 13th Propulsion Conference, Orlando, Florida, July 1977.

51. Taylor, J. W., "A Melting Stage in the Burning of Solid Secondary Explosives", Combustion and Flame, Vol. 6, June 1962, pp. 103-107.

52. Taylor, J. W., "The Burning of Secondary Explosive Powders by a Convective Mechanism", Transactions of the Faraday Society, Vol. 58, No. 471, 1962, pp. 561-568.

53. Bobolev, V. K., Margolin, A. M. and Chuiko, S. V., "Stability of Normal Burning of Porous Systems at Constant Pressure", Journal of Combustion, Explosion and Shock Waves, Vol. 2, No. 4, 1966, pp. 15-20.

54. Isom, B. K., "A Window Bomb Study of HMX Combustion", 11th JANNAF Combustion Meeting, CPIA Publication 261, Vol. 1, pp. 243-246.

55. Zimmer-Galler, R., "Correlation Between Deflagration Characteristics and Surface Properties of Nitramine-Based Propellants", AIAA Journal, Vol. 6, No. 11, Nov. 1968, pp. 2107-2110.

56. Cohen, N. S. and Price, C. F., "Combustion of Nitramine Propellants", Journal of Spacecraft and Rockets, No. 12, Oct. 1975, pp. 608-612.

57. Cohen, N. S. and Strand, L. D., "Nitramine Propellant Research", 13th JANNAF Combustion Meeting, CPIA Publication No. 281, Vol. 1, 1976, pp. 75-87.

58. McCarty, P., "Review of Nitramine Propellant Combustion Studies", 13th JANNAF Combustion Meeting, CPIA Publication No. 281, Vol. 1, 1976, pp. 377-393.

59. Beckstead, M. W. and McCarty, K. P., "Calculated Combustion Characteristics of Nitramine Monopropellants", 13th JANNAF Combustion Meeting, CPIA Publication No. 281, Dec. 1976, pp. 57-68.

60. Beckstead, M. W., Derr, R. L. and Price, C. F., "The Combustion of Solid Monopropellants and Composite Propellants ", 13th Symposium (International) on Combustion, The Combustion Institute, Pittsburgh, PA, 1971, pp. 1047-1056.

61. Boggs, T. L., Price, C. F., Zurn, D. E., Derr, R. L. and Dibble, E. J., "Temperature Sensitivity of Deflagration Rates of Cyclotetrametulenetetranitrmine (HMX)", 13th JANNAF Combustion Meeting, CPIA Publication No. 281, Dec. 1976, pp. 45-56.

62. Gordon, S. and McBride, B., "Computer Program for Calculation of Complex Chemical Equilibrium Compositions, Rocket Performance, Incident and Reflected Shocks and Chapman Jouget Detonations", NASA SP-273, Washington, D.C., 1971.

63. Penner, S. S., Chemistry Problems in Jet Propulsion, Pergamon Press, New York, 1957, Chapter 13, "Calculation of Adiabatic Flame Temperature and Equilibrium Compositions", pp. 136-157.

64. Penner, S. S. (63) op. cit., Chapter 24, "Laminar Flame Propagation in Premixed Gases", pp. 317-344.

65. Williams, F. A., Combustion Theory, Addison-Wesley, Reading, Mass., 1965, Chapter 5, "Laminar Flame Theory", pp. 95-136.

66. Spalding, D. B., "The Theory of Burning of Solid and Liquid Propellants", Combustion and Flame, Vol. 4, March 1960, pp. 59-76.

67. Kubota, N., "The Mechanism of Super-Rate Burning of Catalyzed Double Base Propellants", Ph. D. Thesis, Princeton University, Department of Aerospace, Princeton, NJ, 1973.

68. Maltsev, V. M. Law, R. J., Ryan, N. W., Bare, A. D., and Summerfield, M., "On the Mechanical Effect of the Catalytic Additives PbSa and CuSa in the Combustion of Double-Base Propellants", Unpublished Paper, Princeton, 1972.

69. Guirao, C. and Williams, F. A., "A Model for Ammonium Perchlorate Deflagration Between 20 and 100 atm", AIAA Journal, Vol. 9, No. 7, July 1971, pp. 1345-1356.

70. Steinz, J. A., "The Burning Mechanism of Ammonium Perchlorate-Based Composite Solid Propellants", Ph. D. Thesis, Princeton University, Department of Aerospace, Princeton, NJ, 1969.

71. Friedman, R., Hertzberg, M., McHale, E. T. and vonElbe, G., "Composite Solid Propellant Flame Microstructure Determination", Atlantic Research Corp. Report for NASA, NASA CR-66677, 1968.

72. Kamlet, M., "Changes in Chemical Reaction Mechanism with Increasing Pressure for HMX-Based Propellants", Research Brief, NSWC, White Oak, Silver Springs, MD, July 1976.

73. Van Dyke, M., Perturbation Methods in Fluid Mechanics, The Parabolic Press, Stanford, California, 1975 (Annotated edition), Chapter 5, "The Method of Matched Asymptotic Expansions", pp. 77-79

74. Cole, J. D. Perturbation Methods in Applied Mathematics, Blaisdell Waltham, Mass, 1968, pp. 1-78.

75. Scala, S. M. and Sutton, G. W., "Energy Transfer at a Chemically Reacting or Slip Interface", ARS Journal, Feb. 1959, pp. 141-143.

76. Williams, F. A., (65) op. cit., Chapter 1: "Summary of Basic Fluid Dynamics and Chemical Kinetics, pp. 1-17.

77. Bird, R. B., Stewart, W. E. and Lightfoot, E. N. Transport Phenomena, John Wiley, New York, 1960, Chapter 17: "Concentration Distributions in Solids and in Laminar Flow", pp. 519-553.

78. Williams, F. A., "Theory of Combustion in Laminar Flows", Ann. Rev. Fluid Mechanics, Vol. 3, edited by M. VanDyke and W. G. Vincenti, Annual Reviews, Palo Alto, California, 1971, pp. 171-188.

79. Zeldovich, Ya. B., "On the Theory of Combustion of Powders and Explosives", Journal of Theoretical and Experimental Physics, Vol. 12, No. 11-12, 1942, pp. 498-524 (translated from Russian).

80. Zeldovich, Ya. B., "Chain Reactions in Hot Flames--An Approximate Theory for Flame Velocity", International Chemical Engineering, Vol. 2, No. 2, April 1962, pp. 227-235.

81. Jain, V. K. and Kumar, R. N., "Theory of Laminar Flame Propagation with Non-Normal Diffusion", Combustion and Flame, Vol. 23, June 1969, pp. 285-294.

82. Bush, W. B. and Fendell, F. E., "Asymptotic Analysis of Laminar Flame Propagation for General Lewis Numbers", Combustion Science and Technology, 1970, Vol. 1, pp. 421-428.

83. Friedman, R. and Burke, E., "A Theoretical Model of a Gaseous Combustion Wave Governed by a First Order Reaction", Journal of Chem. Physics, Vol. 21, 1953, pp. 710-714.

84. Williams, F. A., "Quasi Steady Gas Phase Flame Theory in Unsteady Burning of a Homogeneous Solid Propellant", Tech. Note, AIAA Journal, Vol. 11, No. 9, Sept. 1973, pp. 1328-1330.

85. Joulin, G. and Clavin, P., "Asymptotic Analysis of a Premixed Laminar Flame Governed by a Two-Step Reaction", Combustion and Flame, 25, 1975, pp. 389-392.

86. Penner, S. S. and Mullins, B. P., Explosives, Detonations, Flammability and Ignition, AGARDograph, No. 31, Pergamon Press, New York, 1959, Chapter 1: "Fundamentals of Aerothermochemistry", pp. 5-15.

87. Lees, L., "Convective Heat Transfer with Mass Addition and Chemical Reaction", 3rd AGARD Colloquium on Combustion and Propulsion, Pergamon, New York, 1958, pp. 451-497.

88. Guirao, C. and Williams, F. A., "Sublimation of Ammonium Perchlorate", The Journal of Psysical Chemistry, Vol. 73, Vol. 12, Dec. 1969, pp. 4302-4311.

89. Caveny, L. H., Personal communication, April 1978.

90. Lengelle, G., "Thermal Degradation Kinetics and Surface Pyrolysis of Vinyl Polymers", AIAA Journal, Vol. 8, No. 11, Nov. 1970, pp. 1989-1996.

91. Isaacson, E. and Keller, H. B., Analysis of Numerical Methods, J. Wiley, N. Y., 1966, Chapter 2.3.2: "Tridiagonal or Jacobi Matrices", pp. 55-61.

92. Hawrusik, F. and Vichnevetsky, R., "Block Tri-Diagonal Subroutine TRIBLC", Report NAM 146, Sept. 1974, Rutgers University, Department of Computer Science, Livingston College, NJ.

93. Richtmyer, R. D. and Morton, K. W. Difference Methods for Initial Value Problems, Interscience Publishers, N. Y., 1967, Chapter 8.4: "Effect of Lower Order Terms on Stability", pp. 195-198.

94. Richtmyer, R. D. and Morton, K. W., Difference Methods for Initial Value Problems, Interscience Publishers, N. Y., 1967, Chapter 3.2: "Finite Difference Approximations", pp. 42-44.

95. VonNeumann, J., and Richtmyer, R. D., "A Method for Numerical Calculation of Hydrodynamic Shocks", Journal of Applied Physics 21, March 1950, pp. 232-237.

96. Crank, J. and Nicholson, P., "A Practical Method for Numerical Integration of Solutions of Partical Differential Equations of the Heat-Conductive Type", Proc. Cambridge Philos. Society, Vol. 43, 1947, p. 50.

97. Roache, P. J. "On Artificial Viscosity", Journal of Computational Physics, 10, 1972, pp. 169-184.

98. Plesset, M. S., and Prosperetti, A., "Bubble Dynamics and Cavitation", Annual Reviews of Fluid Mechanics, Vol. 9, 1977, pp. 145-185.

99. Williams, F. A., Journal of Computational Physics, 10, 1972, App. B-5: "The Rates of Heterogeneous Processes", pp. 382-388.

100. Bellman, R. E. and Kalaba, R. E., Quasilinerization and Nonlinear Boundary Value Problems, American Elsevier, New York, 1965, p. 413.

101. Jacobi, S. L. S., Kowalik, J. S. and Pizzo, J. T., Iterative Methods for Nonlinear Optimization Problems Prentice Hall, New York, 1972, pp. 10-12.

102. Summerfield, M., Sutherland, G. S., Webb, M. J., Taback, H. J., Hall, K. P., "Burning Mechanism of Ammonium Perchlorate Propellants", Solid Propellant Rocket Research, Progress in Astronautics and Rocketry, Vol. 1., Ed. M. Summerfield, Academic Press, NY, 1960, pp. 141-182.

103. Zeldovich, Ya, B., "Theory of Propellant Combustion in a Gas Flow", Journal of Combustion, Explosion and Shock Waves, 1972, pp. 399-408.

104. Battista, R. A., Caveny, L. H. and Summerfield, M., "Nonsteady Combustion of Solid Propellants", Aerospace and Mechanical Sciences Report No. 1049, Oct. 1972, Princeton University, Princeton Nj.

105. Tennekes, H., "Similarity Laws for Turbulent Boundary Layers with Suction or Injection", Journal of Fluid Mechanics, 21, part 4, 1965, pp. 689-703.

106. Marxman, G. A. and Wooldridge, C. E., "Research on the Combustion Mechanism of Hybrid Rockets", Advances in Tactical Rocket Propulsion, AGARD Conference Proc. No. 1, Technivision, England, 1968, pp. 425-477.

107. Bartz, D. R., "Survey of the Relationship Between Theory and Experiment for Convective Heat Transfer from Rocket Combustion Gases", Advances in Tactical Rocket Propulsion, AGARD Conference Proceedings No.1, Technivision, Maidenhead, England, Aug. 1968, pp. 291-381.

108. Hama, F. R., "On the Velocity Distribution in the Laminar Sublayer, and Transition Region in Turbulent Shear Flows", Journal of Aeronautical Sciences, Vol 20, No. 9, Sept. 1953, pp. 648-649.

109. Wooldrige, C. E. and Muzzy, R. J., "Measurements in a Turbulent Boundary Layer with Porous Wall Injection and Combustion", Proceedings, 10th Symposuim (international) on Combustion, the Combustion Institute, Pittsburgh, PA., 1965, pp. 1351-1362.

110. Schultz, R., Green, L. Jr. and Penner, S. S., "Studies on the Decomposition Mechanism, Erosive Burning, Sonance and Resonance for Solid Composite Propellants", 3rd AGARD Colloquium on Combustion and Propulsion, Pergamon Press, NY, 1958, pp. 367-427.

111. Dickinson, L. A. and Jackson, F., "Combustion in Solid Propellant Rocket Engines", 5th AGARD Colloquium on High Temperature Phenomena, Pargamon Press, the Macmillan Co., NY, 1963, pp. 531-550.

112. Vandenkervchove, J. A., "Erosive Burning of Colloidal Solid Propellant", Jet Propulsion, Vol. 28, 1958, pp. 599-603.

113. Yamada, K., Goto, M. and Ishikawa, N., "Simulative Study on the Erosive Burning of Solid Rocket Motors", AIAA Journal, Vol. 14, No. 9, Sept. 1976, pp. 1170-1177.

114. Johnson, W. E. and Nachbar, W., "Deflagration Limits in the Steady Linear Burning of a Monopropellant with Application to Ammonium Perchlorate", 8th Symposium (International) on Combustion, Baltimore, MD, Williams and Wilkius, 1962, pp. 678-689.

115. Johnson, W. E. and Nachbar, W., "Laminar Flame Theory and the Steady Burning of a Monopropellant", Archive for Rational Mechanics and Analysis, Vol. 12, No. 1. 1963, pp. 58-92.

116. Marxman, G. A. and Gilbert, M., "Turbulent Boundary Layer Combustion in the Hybrid Rocket", 9th Symposium (International) on Combustion, The Combustion Institute, Pittsburgh, PA, 1963, pp. 371-383.

117. Marxman, G. A., "Combustion in the Turbulent Boundary Layer on a Vaporizing Surface", 10th Symposium (International) on Combustion, The Combustion Institute, Pittsburgh, PA, 1965, pp. 1337-1349.

118. Dunlap, R., Willoughby, P. G. and Hermsen, R. W., "Flowfield in the Combustion Chamber of a Solid Propellant Rocket Motor", AIAA Journal, Vol. 12, No. 10, Sep. 1974, pp. 1440-1442.

119. Culick, F. E. C., "Rotational Axisymmetric Mean Flow and Damping of Acoustic Waves in a Solid Propellant Rocket", AIAA Journal, Vol. 4., No. 8, Aug. 1966, pp. 1462-1464.

120. Spalding, D. B., "Mixing and Turbulent Reaction in Steady Confined Turbulent Flames", 13th Symposium (International) on Combustion, The Combustion Institute, Pittsburgh, PA, 1971, pp. 645-657.

121. Spalding, D. B., "Development of the Eddy Break-Up Model of Turbulent Combustion", 16th Symposium (International) on Combustion, The Combustion Institute, Pittsburgh, PA, 1976, pp. 1657-1663.

122. Spiegler, E., Wolfshtein, M. and Timnat, Y., "A Model of Unmixedness for Turbulent Reacting Flows", Acta Astronautica Vol. 3, 1976, pp. 265-280.

123. Varma, A. K., Fishburne, E. S. and Beddini, R. A., "Modeling of Turbulent Mixing and Reactions in Chemical Lasers", AFOSR-TR-77-0584, Jan. 1977.

124. Beddini, R. A., and Fishburne, E. S., "Analysis of the Combustion-Turbulence Interaction Effects on Solid Propellant Erosive Burning", AIAA Paper No. 77-931, AIAA/SAE 13th Propulsion Conference, Orlando, FL, Jul. 1977.

125. Beddini, R. A., "Effect of Grain Port Flow on Solid Propellant Erosive Burning", AIAA Paper No. 78-977, AIAA/SAE 14th Joint Propulsion Conference, Las Vegas, NEV., Jul. 1978.

126. Tsuji, H., "An Aerothermochemical Analysis of Erosive Burning of Solid Propellant", 9th Symposium (International) on Combustion, the Combustion Institute, Pittsburgh, PA, 1963, pp. 384-393.

127. Osborn, J. R. and Burick, R. J., "Erosive Combustion of Solid Rocket Propellants", Jet Propulsion Center, Purdue University, Lafayette, IN, Jun. 1967, JPC Report NO-F-67-4.

128. Marklund, T., and Lake, A., "Experimental Investigation of Propellant Erosion", ARS Journal, Feb. 1960, pp. 173-178.

129. Lord Rayleigh, "The Theory of Sound", Dover Publications, NY, 1954, Vol. II, pp. 226-230.

130. Glushkov, I. S. and Kareev, Yu. A., "Acoustic Instability in a Nonadrabatic Gas", Trans. Teplofizika Vysokikh Temporatur, Vol. 8, No. 5, Sep.-Oct. 1970, pp. 957-962.

131. Smith, R. P. and Sprenger, D. F., "Combustion Instability in Solid Propellant Rockets", 4th Symposium (International) on Combustion, The Combustion Institute, Pittsburgh, PA, 1953, pp. 893-906.

132. Cheng, S. I., "Combustion Instability in Solid Rockets Using Propellants with Reactive Additives", Solid Propellant Rocket Research, Progress in Astronautics and Rocketry Vol. 1, Ed. M. Summerfield, Academic Press, NY, 1960, pp. 393-422.

133. Cheng, S. I., "High Frequency Combustion Instability in Solid Propellant Rockets", Jet Propulsion, part 1, Jan.-Feb. 1954, pp. 29-32, part 2, Mar.-Apr. 1954, pp. 102-109.

134. Crocco, L. and Cheng, S. I., "Theory of Combustion Instability in Liquid Propellant Rocket Motors", AGARDograph No. 8, Butterworth Scientific Publications, London, 1956.

135. Williams, F. E., Barrere, M. and Huang, N. C., "Fundamental Aspects of Solid Propellant Rockets", AGARDograph No. 116, Technivision, Slough, England, 1969, Chap. X: Theoretical Analyses of Combustion Instability, pp. 609-673.

136. Williams, F. E., (65) op. cit., Chap. IV. Reactions in Unsteady, Three Dimensional Flow, pp. 72-92.

137. Vincenti, W. G. and Kruger, C. H., Introduction to Physical Gas Dynamics, J. Wiley, NY, 1967, Chap. VIII. Flow with Vibrational or Chemical Nonequilibrium, pp. 245-315.

138. Salant, R. F., and Toong, T. Y., Oxidation and Combustion Reviews, C. F. H. Tipper, Ed., Elsevier, Amsterdam, 1967, Vol. 2, pp. 185-206.

139. Salant, R. F., and Toong, T. Y., "Amplification and Altenuation of Acoustic Waves in Nonhomogeneous Steady Flows", Journal of Acoustic Society of America, Vol. 49, No. 5 (part 2), 1971, pp. 16655-1666.

140. Cummings, A., "Ducts with Axial Temperature Gradients: An Approximate Solution for Sound Transmission and Generation", Journal of Sound and Vibration, 51(1), 1977, pp. 55-67.

141. Bender, C. M., and Orszag, S. A., Advanced Mathematical Methods for Scientists and Engineers, Chap. 10: WKB Theory, McGrawHill, NY, 1978, pp. 484-539.

142. Hart, R. W. and McClure F. T., "Combustion Instability: Acoustic Interaction with a Propellant Burning Surface", Journal of Chemical Physics, Vol. 30, Sep. 1959, pp. 1501-1514.

143. Williams, F. A., "Response of a Burning Solid to Small Amptitude Pressure Oscillations", Journal of Applied Physics, Vol. 33, No. 11, Nov. 1962, pp. 3153-3166.

144. Tien, J., "Oscillatory Burning of Solid Propellants Including Gas Phase Time Lag", Combustion Science and Technology, Vol. 5, 1972, pp. 47-54.

145. Denison, M. R. and Baum, E., "A Simplified Model of Unstable Burning in Solid Propellants", ARS Journal, Vol. 31, 1961, pp. 112-1122.

146. Krier, H. and Summerfield, M., Mathes, H. B. and Price, E. W., "Entropy Waves Produced in Oscillatory Combustion of Solid Propellants", AIAA Journal, Vol. 7, No. 11, Nov. 1969, pp. 2079-2086.

147. Culick, F. E. C., "Stability of 3-D Motions in a Combustion Chamber", Combustion Science and Technology, Vol. 10, 1975, pp. 109-124.

143. Culick, F. E. C., "Nonlinear Behavior of Acoustic Waves in Combustion Chambers", California Institute of Technology Report, Los Angeles, CA, Apr. 1975.

149. Tien, J., Sirignano, W. A. and Summerfield, M., "Theory of L* Combustion Instability", AIAA paper No. 68-179, 6th Aerospace Sciences Meeting, NY, Jan. 1968.

150. Caveny, L. H., Battista, R. A. and Summerfield, M., "Pressure Transients of Solid Rockets with Slow Gas Phase Reaction", AIAA paper No. 73-1301, AIAA/SAE 9th Propulsion Conference, Las Vegas, NEV, Nov. 1973.

151. McClure, F. T., Bird, J. F. and Hart, R. W., "Erosion Mechanism for Nonlinear Instability in the Axial Modes of Solid Propellant Rocket Motors", ARS Journal, Vol. 32, No. 3, Mar. 1962, pp. 374-378.

152. Hart, R. W., Bird, J. F. and McClure, F. T., "The Influence of Erosive Burning on Acoustic Instability in Solid Propellant Rocket Motors", Solid Propellant Rocket Research, Progress in Astronuatics and Rocketry, Vol. 1, Ed., M. Summerfield, Academic Press, NY, 1960, pp. 423-451.

153. Bird, J. F., Hart, R. W. and McClure, F. T., "Finite Acoustic Oscillations and Erosive Burning in Solid Fuel Rockets", AIAA Journal, Vol. 3, No. 12, Dec. 1965, pp. 2248-2256.

154. Dehority, G. L. and Price, E. W., "Axial Mode, Intermediate Frequency Combustion Instability in Solid Propellant Rockets", Naval Weapons Center TP-5654, China Lake, CA, Oct. 1974.

155. Price, E. W. and Dehority, G. L., "Velocity Coupled Axial Mode Combustion Instability in Solid Propellant Rocket Motors", Proceedings, 2nd ICPRG/AIAA Solid Propulsion Meeting, Anaheim, CA, 1967, pp. 213-227.

156. Lengelle, G., "A Model Describing the Velocity Response of Composite Propellants", AIAA Paper No. 73-1224, AIAA/SAE 9th Propulsion Conference, Las Vegas, NEV, Nov. 1973.

157. Trubridge, G. F. P. and Badham, H., "Experimental Studies of Unstable Combustion in Solid Propellant Rocket Engines", 5th AGARD Colloquium, High Temperature Phenomena, McMillan Co., NY, 1963, pp. 497-530.

158. Angelus, T., "Unstable Burning Phenomenon in Double Base Propellants", Solid Propellant Rocket Research, Progress in Astronautics and Rocketry series, Vol. 1, Ed. M. Summerfield, Academic Press, NY, 1960, pp. 495-526.

159. Glick, R. L., Personal Communication, Thiokol Corp. Huntsville, AL, Oct. 1977.

160. Kooker, D. E. and Zinn, B. T., "Numerical Investigation of Nonlinear Axial Instabilities in Solid Rocket Motors", BRL CR 141, Aberdeen, MD, Mar. 1974. also,

    Kooker, D. E., and Zinn, B. T., "Numerical Solution of Axial Instabilities in Solid Propellant Rocket Motors", Proceedings, 10th JANNAF Combustion Meeting, CPIA Publication No. 243, Vol. I, 1973, pp. 389-415.

161. Brownlee, W. G. and Marble, F. E., "An Experimental Investigation of Unstable Combustion in Solid Propellant Rocket Motors" Solid Propellant Rocket Research, Progress in Astronautics and Rocketry, Vol, 1, Ed. M. Summerfield, Academic Press, NY, 1960, pp. 455-494.

162. Moretti, G., ""A Critical Analysis of Numerical Techniques: The Piston Driven Inviscid Flow", Polytechnic Institute of Brooklyn, Dept. of Aerospace, Report PIBAL 69-25, July 1969. also,

    Moretti, G., "The Choice of a Time Dependent Technique in Gas Dynamics", Polytechnic Institute of Brooklyn, Dept. of Aerospace, Report PIBAL 69-26, July 1969. also,

    Moretti, G., "Complicated One Dimensional Flows", Polytechnic Institute of Brooklyn, Dept. of Aerospace, Report PIBAL 71-25, Sept. 1971.

163. Vichnevetsky, R. and Shieh, Y. S., "On the Numerical Method of Lines for One Dimensional Water Quality Equations", Rutgers University, Dept. of Computer Sciences, Technical Report, No. 20, Nov. 1972.

164. Levine, J. N. and Culick, F. E. C., "Numerical Analysis of Nonlinear Longitudinal Combustion Instability in Methalized Propellant Solid Rocket Motors", AFRPL TR-72-88, Jul. 1972.
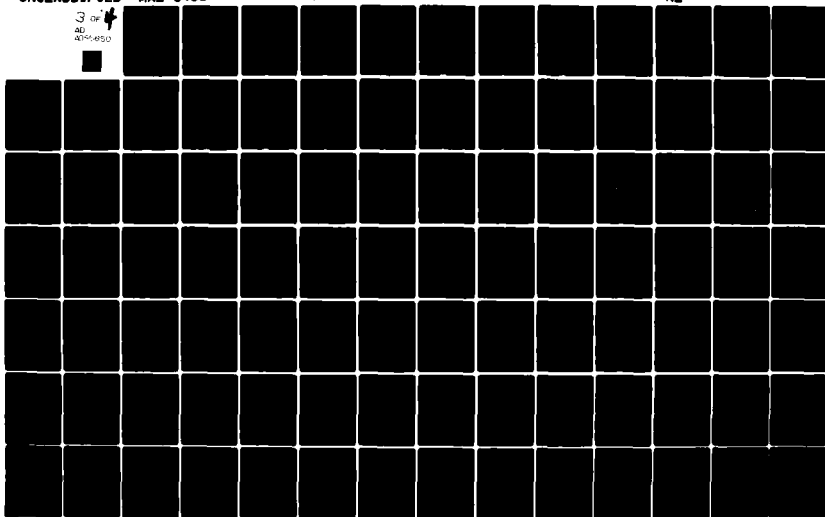
165. Levine, J. N. and Culick, F. E. C., "Nonlinear Analysis of Solid Rocket Combustion Instability", AFRPL TR-74-45, Oct. 1974.

166. Rubin, E. L., and Burstein, S. Z., "Difference Methods for the Inviscid and Viscous Equations of a Compressible Gas", Journal of Computational Physics 2, 1967, pp. 178-196.

167. Krylov, N., and Bogolivbov, N., "Introduction to Nonlinear Mechanics", Translated by S. Lefshetz, Princeton University Press, Princeton, NJ, 1947.

168. Courant, R. and Hilbert, D., Methods of Mathematical Physics, Vol.II: Partial Differential Equations, Interscience Publishers, NY, 1962, Chap. III.2: Classification in General and Characteristics, pp. 170-173.

169. Lax, P. D. and Wendroff, B., "Systems of Conservation Laws", Commun. Pure and Applied Mathematics 13, 1960, pp. 217-237.

170. Richtmyer, R. D. and Morton, K. W., (93) op. cit., Chap. 12.7, Conservation Form and the Lax-Wendroff Equations, pp. 300-306.

171. Vichnevetsky, R., "Treatment of Boundary Conditions in Difference Methods for One Dimensional Fluid Dynamic Equations", Electronic Assocaites Inc., Princeton, NJ, Tech. Report TR-70-21, Sept. 1970.

172. Lax, P. D., "Nonlinear Hyperbolic Equations", Commun. Pure and Applied Mathematics, Vol. VI, 1953, pp. 231-258.

TABLE II.1

THERMOPHYSICAL PROPERTIES OF RDX AND HMX

SOURCE	PROPERTY	UNITS	RDX	HMX
JANNAF,[102]	ΔH°_{f}, standard heat of formation @ 300 K	kcal/mol	-20.1	-17.9
Rosen[11]	Q_{sub}, heat of sublimation	kcal/mol	31.1	41.89
Hall[5]	Q_{m}, heat of fusion	kcal/mol	8.52	11.4 (a)
Hall[5]	T_{m}, melting temperature	K	478.5	554.
	Q_{str}, T_{str}: solid-solid transition enthalpy and temperature	kcal/mol·K		
Hall[5]	$\beta \rightarrow \delta$-HMX	kcal/mol·K		2.35 @471K
Hall[5]	$\alpha \rightarrow \delta$-HMX	kcal/mol·K		~1.9 @ 460K
Army,[100] AMCP-	W_{R}, molecular weight	g/mol	222	296
706-177	ρ_{c}, density	g/cc	1.82	1.90
	C_{c}, specific heat capacity (solid)	cal/g·K	0.32-0.45	0.43

(a) Estimate based on intermolecular bond energy similarity with RDX

TABLE II.2

VAPOR PRESSURE AND SUBLIMATION ENTHALPY
DATA FOR HMX AND RDX

$$\log_{10}(P_v) = A - B/T$$

where P_v(Torr) and B(K)

SOURCE	TEMPERATURE RANGE, °C	A	B(K)	Q_{sub} or Q_v, kcal/mol
(a) Rosen,[11] RDX(S)	55.7-97.7	14.18	6799	31.11
(b) Edwards,[10] RDX(S)	110.6-138.5	11.87	5850	26.8
(d) Rogers,[17] RDX(ℓ)	232 - 247	10.59	4433	20.28
Rosen,[11] β-HMX(S)	97.6-129.3	16.18	9154	41.89
(c) Taylor,[12] δ-HMX(S)	188 - 213	14.73	8296	38.0
(c) Taylor,[12] δ-HMX(S)	188 - 213	15.17	8596	39.3

Notes: (a) By the Langmuir method

(b) By the Knudsen method

(c) With two different orifices in the sample holder cover

(d) Evaporation from liquid, using DSC in isothermal mode.

TABLE II.3

PRIMARY DECOMPOSITION RATE CONSTANTS FOR RDX AND HMX

SAMPLE	SOURCE	ORDER	PREFACTOR $\log_{10}(A, 1/s)$	ACTIVATION ENERGY, E kcal/mol	TEMPERATURE RANGE °C
RDX (liq.)	Robertson[13]	1	18.5	47.5	213-299
	Rogers & Smith[15]	1	18.8	48.2	207-252
	Rogers & Smith[15]	1.3	20.4	52.0	" "
	Rogers & Daub[17]	1.	18.3	47.1	232-247
	Rauch & Fanelli[14]	1.	19.23	48.7	207-287
RDX (g)	Rogers & Daub[17]	1.	13.5	34.1	232-247
(a) RDX (sol.)	Robertson[13]	1.	15.55	41.5	195-281
HMX (liq.)	Robertson[13]	1.	19.7	52.7	271-276
"	Rogers[16]	1.	18.8	51.3	271-285
"	Goshgarian[35]	1.	--	120.0	280-285
HMX (g)	Rogers & Daub[17]	1.	20.2	52.9	273-287
(b) "	Shaw & Walker[39]	1.	16.4	46.2	---
(c) "	"	1.	18.0	60.0	---
(d) "	"	1.	10.8	38.0	---

Notes: (a) RDX in dilute TNT solution
(b) homolytic N-N bond fission, (c) homolytic C-N fission, (d) five-center elimination of HONO

TABLE II.4

COMPARISON OF FINAL PRODUCT CONCENTRATIONS
FOR RDX DECOMPOSITION

		PRODUCT MOLES/MOLE OF RDX DECOMPOSED						
SOURCE		N_2	NO	N_2O	CH_2O	CO	CO_2	H_2O
(a) Cosgrove & Owen[22]		1.26	0.85	1.08	1.41	0.70	0.36	0.51
(b) Present model		1.50	1.00	1.00	2.30	0.29	0.43	0.71

Notes: (a) Calculated from Table 1 therein, (for 210 min. reaction
time), slightly modified: the original 0.37 HCOOH +
0.34 NH_3 was replaced by the equivalent atomic mass
0.37 CH_2O + 0.34 NO + (0.34 x 3/2 = 0.51) H_2O, by adding
0.51 O; the resulting fraction of O recovered in products
is improved: from 0.895 to 0.992.

(b) Obtained from addition of the primary and secondary
reaction steps, Eqs. (II.12a) and (II.12b).

Table III.1

COMPARISON OF REACTIVE TIME AND LENGTH
SCALES FOR PRIMARY AND SECONDARY REACTIONS
IN THE FLAME ZONE OF NITRAMINES

P MPa	m kg/m^2-s	δ_D^* μm	Primary Decomposition (RDX)			Secondary Reaction (NO_2 + CH_2O)		
			$\bar{\omega}_1^*$ kg/m^3-s $\times 10^5$	δ_{R1}^* μm	t_{R1}^* ms	$\bar{\omega}_2^*$ kg/m^3-s $\times 10^3$	δ_{R2}^* mm	t_{R2}^* ms
1	5	12	2.3	22	21	1.1	5	4.5
2	9	7	4.6	20	21	4.3	2	2.2
4	16	4	9.2	17	21	17.5	0.9	1.07

AVERAGE PROPERTIES USED FOR THE MEAN REACTION RATES $\bar{\omega}_1^*$ AND $\bar{\omega}_2^*$

	UNITS	PRIMARY (1)	SECONDARY (2)
T_i	K	1000	1000
$\bar{W}m$	kg/mol	0.04	0.04
$\bar{k}_i(\bar{T}_i)$		3×10^6 1/s	42 m^3/mol-s
$\bar{Y}$		$\bar{Y}_R$ = 0.1	$\bar{Y}_F = \bar{Y}_0$ = 0.2

TABLE V.1

DATUM CASE, CONDENSED PHASE PROPERTIES
FOR RDX

		SOURCE
DENSITY	1.82 g/cm^3	(a)
THERMAL CONDUCTIVITY	0.0007 cal/cm-k-s	(a)
SPECIFIC HEAT	0.45 cal/g-k	(a)
MOLECULAR WEIGHT (RDX)	222 g/mol	
FUSION TEMPERATURE	478.5 K	Hall[5]
FUSION ENTHALPY	8.52 kcal/mol	Hall[5]
HEAT OF VAPORIZATION	22.6 kcal/mol	Rosen[11]

KINETIC DATA [primary decomposition, liquid phase,
cf. Eqs. (II.15), (II.16)] :

PREFACTOR	$A_{ml} = 10^{18.5}$ 1/s	Robertson[13]
ACTIVATION ENERGY	$E_{ml} = 47.5$ kcal/mol	Robertson[13]
HEAT OF REACTION	$Q_{liq} = 75.4$ kcal/mol	(b)

(a) Explosive Series, Properties of Explosives of Military
Interest, AMCP 106-177, Headquarters, U. S. Army Material
Command, Mar. 1967, p. 69.

(b) The kinetics of Eq. (II.15).

Table IX. 1

DATUM CASE PROPERTIES FOR REACTIVE CHAMBER DYNAMICS

port diameter	$d(cm)$	= 1.
geometry factor	$4L/d$	= 40
propellant cavity length	$L(m)$	= 0.1

fuel excess parameter, Eq. (IX.4)	d_F	= 0.02
Blasius coefficient	C_{BL}	= 0.03
nominal initial pressure	$\bar{p}(MPa)$	= 5.
port exit Mach number	$M(x=L)$	= 0.15
sonic-throat to port area ratio	$A^*/A(x=L)$	= 0.2527
adiabatic flame temperature (at 5 MPa)	$T_f(K)$	= 2400.
CFL number	B	= 0.5
integration timestep size	$t(sec)$	= 1.86×10^{-6}
No. of interior spatial mesh points	NF	= 25

Secondary reaction thermochemical data:

prefactor	$A_2(m^3/mol\text{-}s)$	= 3×10^6
activation energy	$E_2(kcal/mol)$	= 19.
heat of reaction	$Q_2(kcal/mol)$	= 46.7

Condensed phase properties: see Table V. 1

Surface pyrolysis correlation data: see Fig. V. 29

Burning rate law (for narrow pressure range): $m = a\, p^n$ kg/m^2-s,

with $a = 5.2$ and $n = 0.78$.
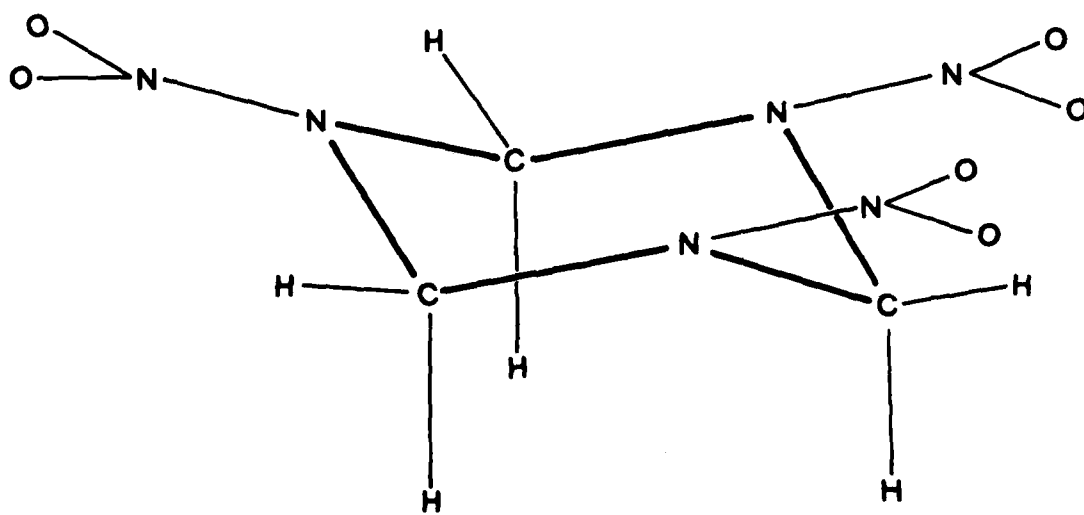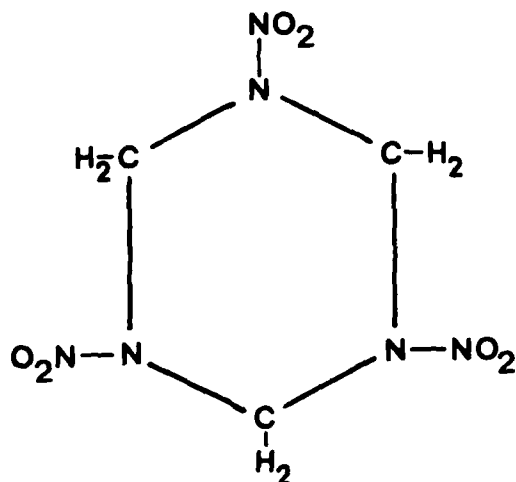
Fig. II.1
Molecular structure of RDX. Chair conformations are favored energetically in all states and observed in X-ray diffractions of RDX crystals; the conformer shown: after Orloff et al.
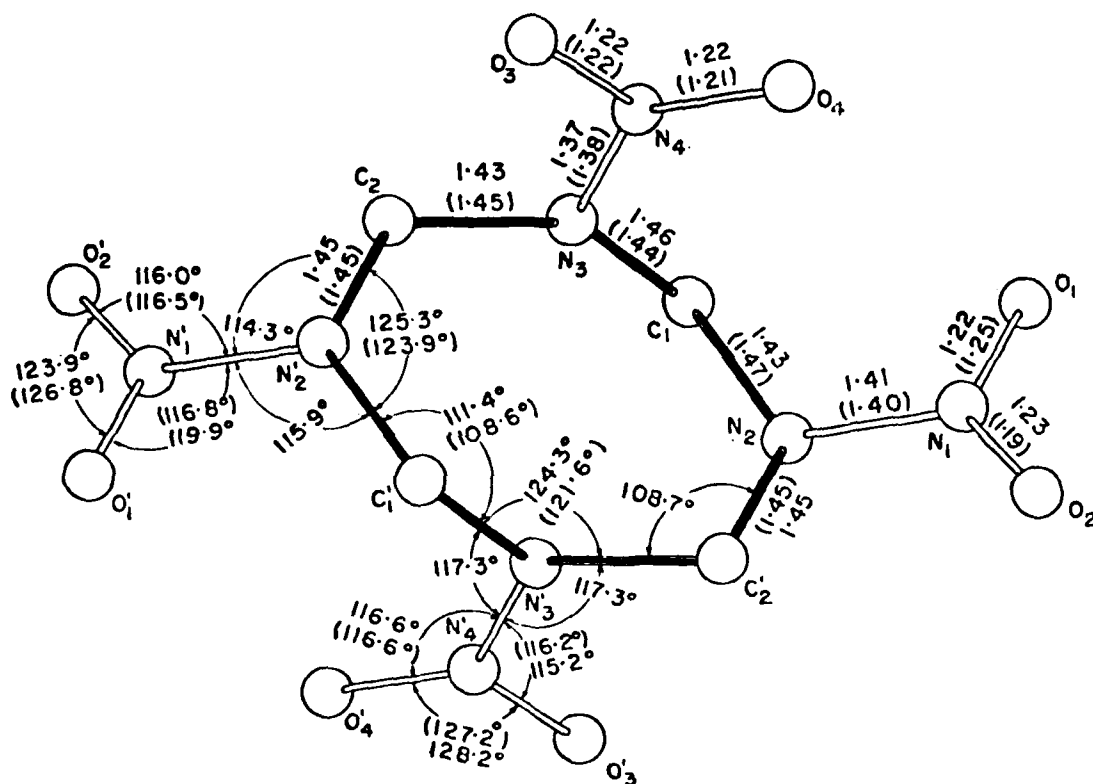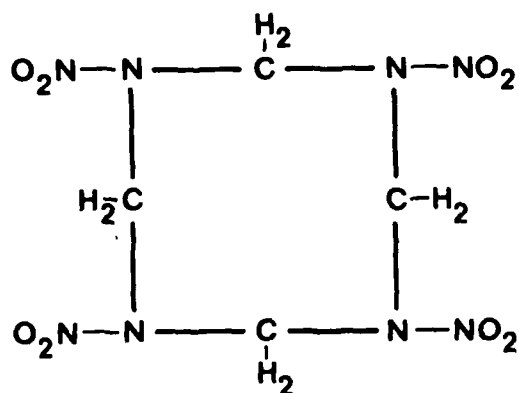
Fig. II.2
Molecular structure of HMX. The crystalline polymorph shown is beta-HMX, from Cady et al,
Ref. 7 ,is one of four known crystal configurations. It has bi-pyramid shape and is the one
HMX polymorph stable at room temperature.
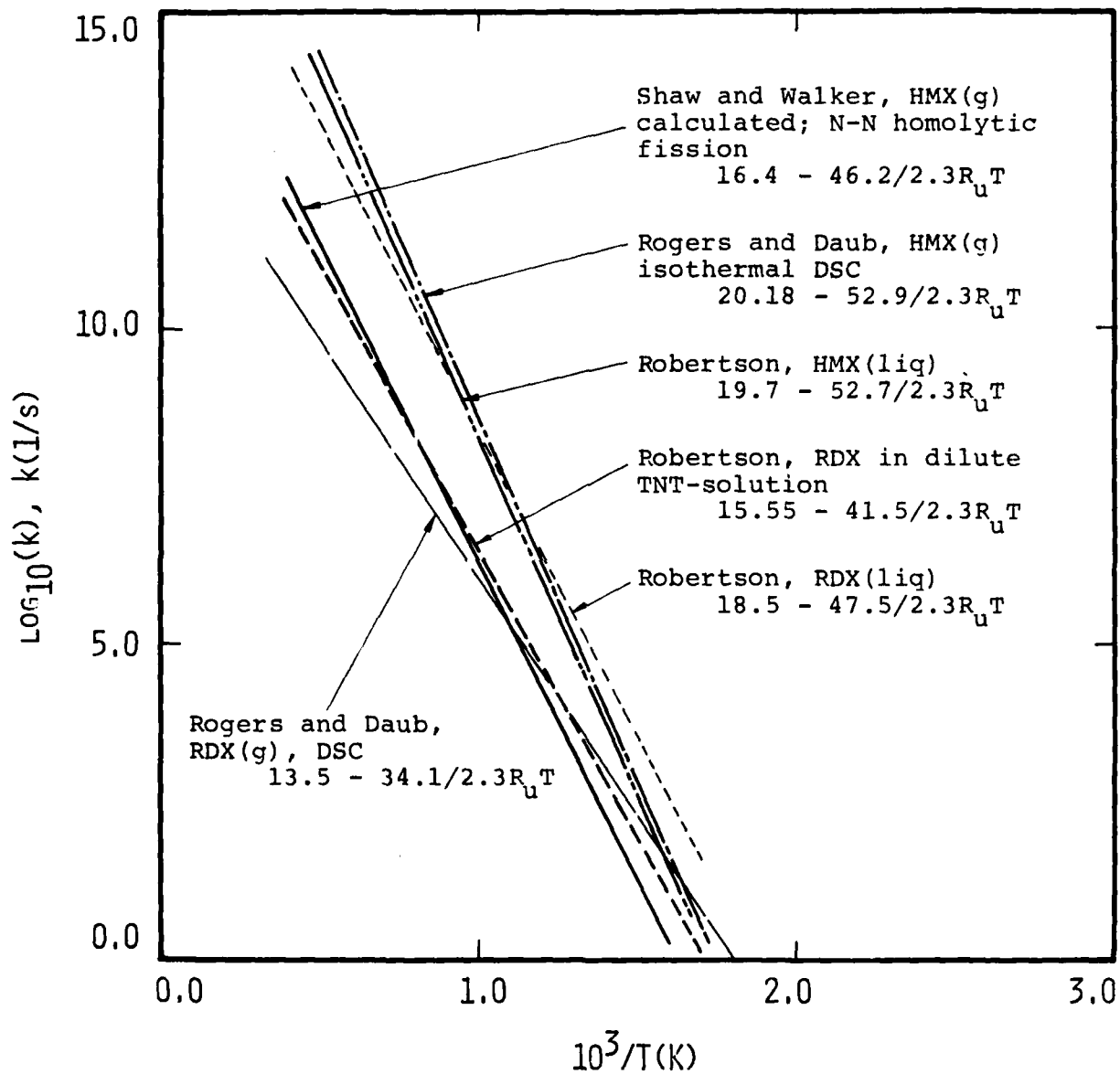
Fig. II.3

Comparison of kinetic data for primary decomposition of RDX and
HMX in the gas and in the liquid phase, for consideration in the
deflagration model.
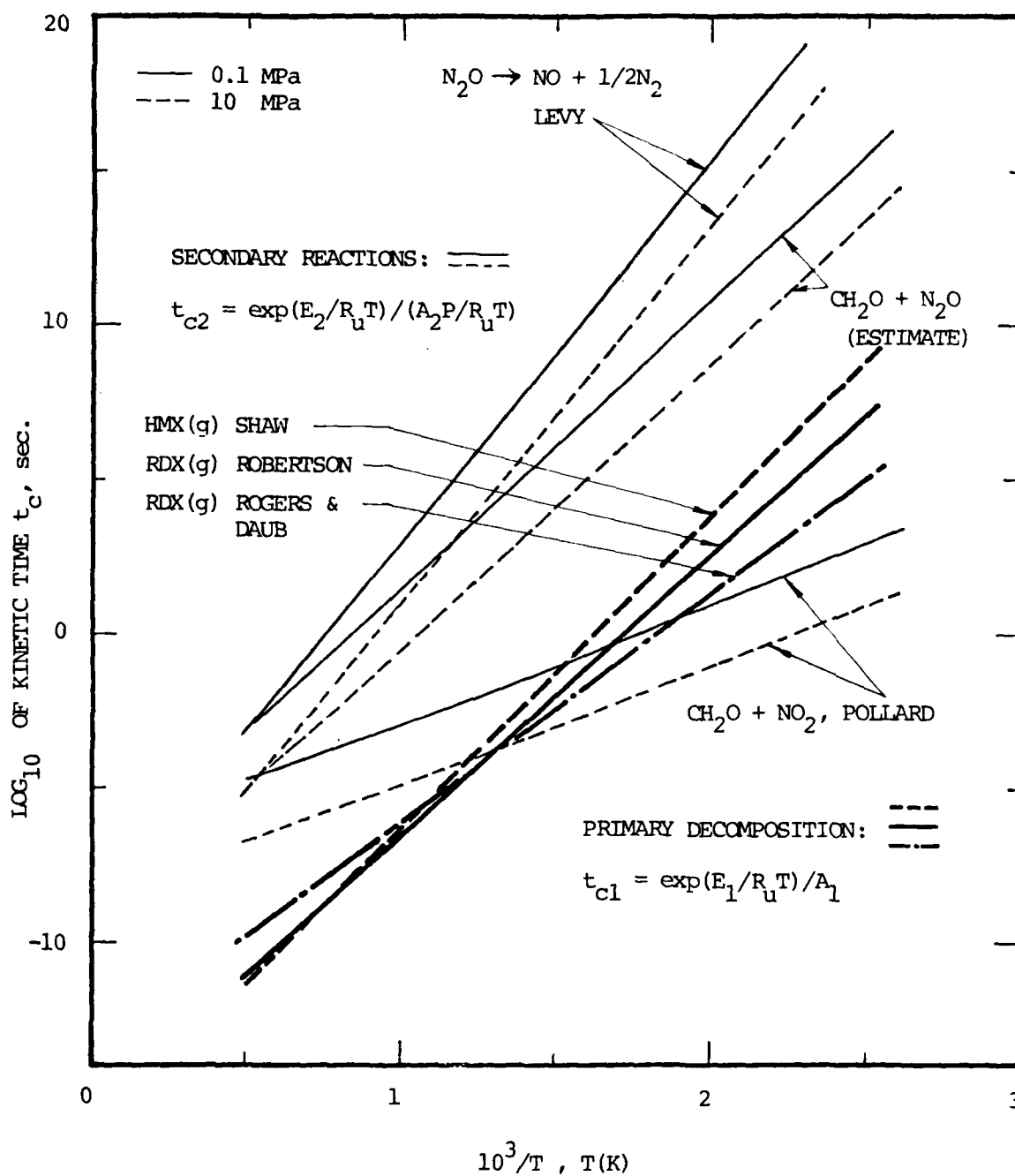
Fig. II.4

Comparison of characteristic kinetic times for primary decomposition and secondary reactions in the gas phase, plotted against inverse temperature. Primary decomposition is considerably faster for temperatures above 600 K.
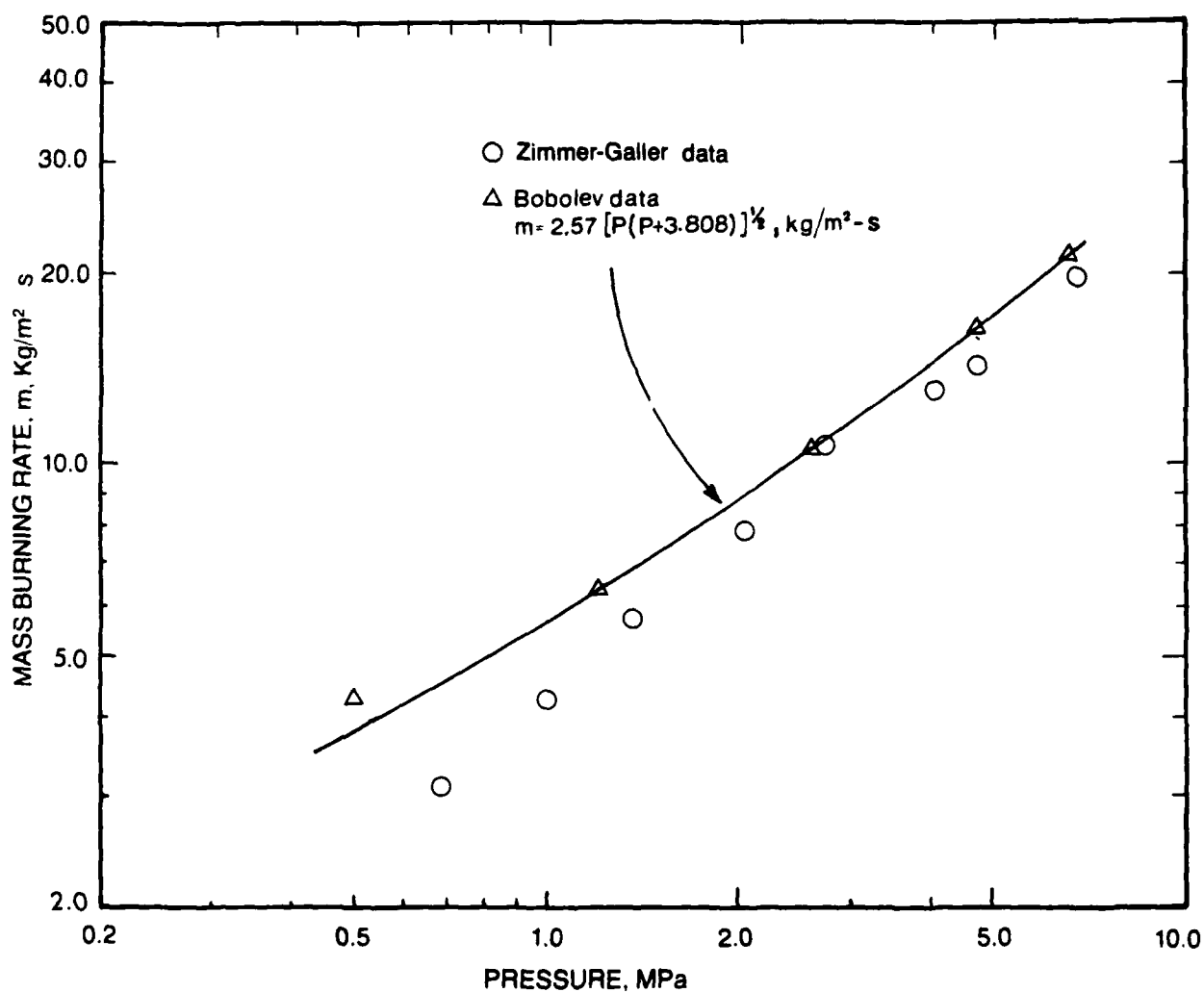
Fig. III.1
Experimental burning rate data of RDX against P, in the low-intermediate pressure range. The data of Bobolev et al, [53] taken over a wide range of granulations, is correlated by the asymptotic m(P) formula, Eq. (III.19.b). The data of Zimmer-Galler is shown without correlation; it was calculated from the r(P) reported, assuming a density of 1.82 g/cc. Fluctuations in the latter data may have been caused by density differences between the samples tested.
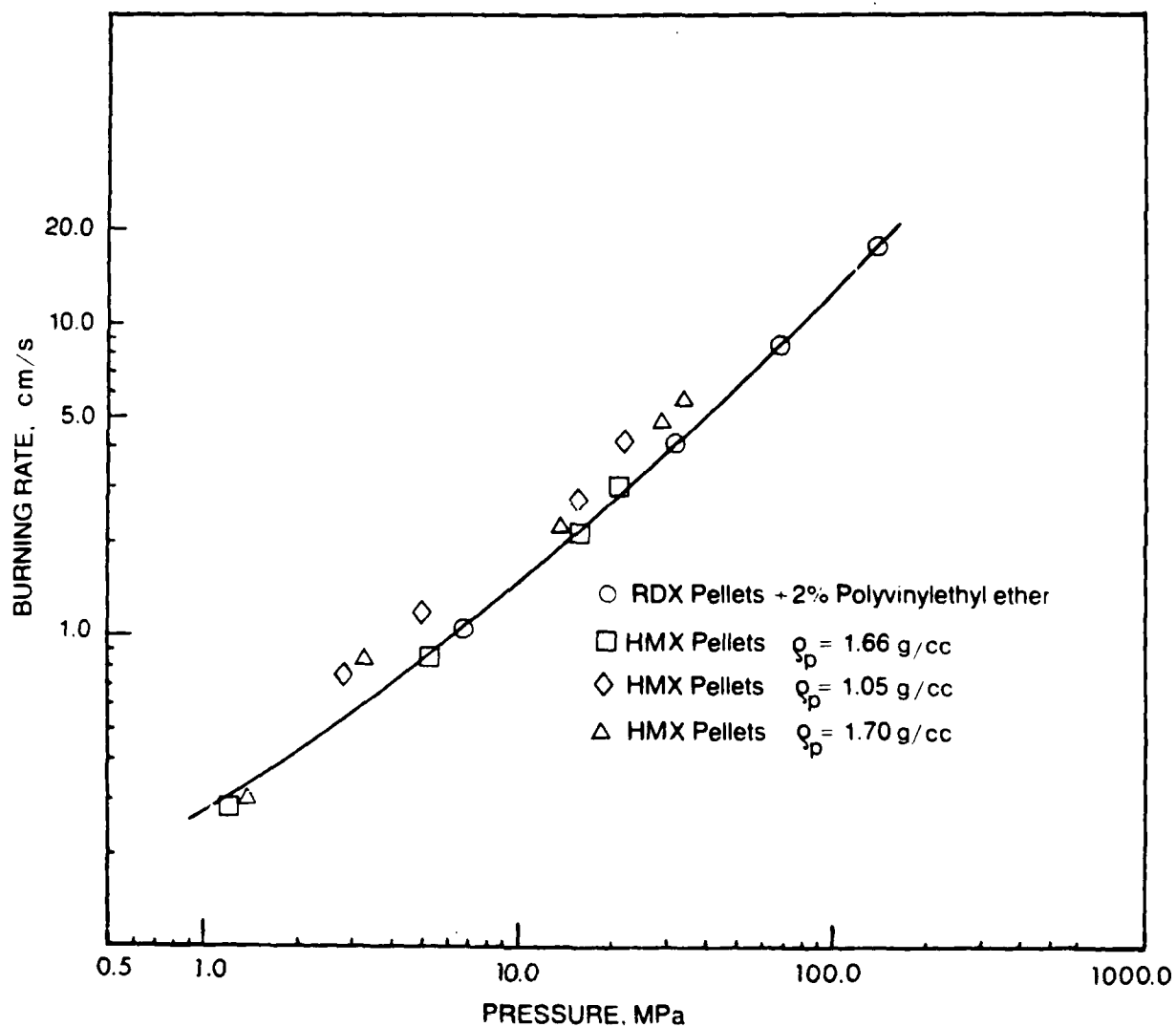
Fig. III.2
Measured linear burning rate data for HMX and RDX in the pressure range between 1. and 200. MPa. The RDX data was correlated by the asymptotic burning rate formula. Eq.(III.19.b). Note the closeness of the HMX and RDX points; no attempt was made to correlate the HMX results.
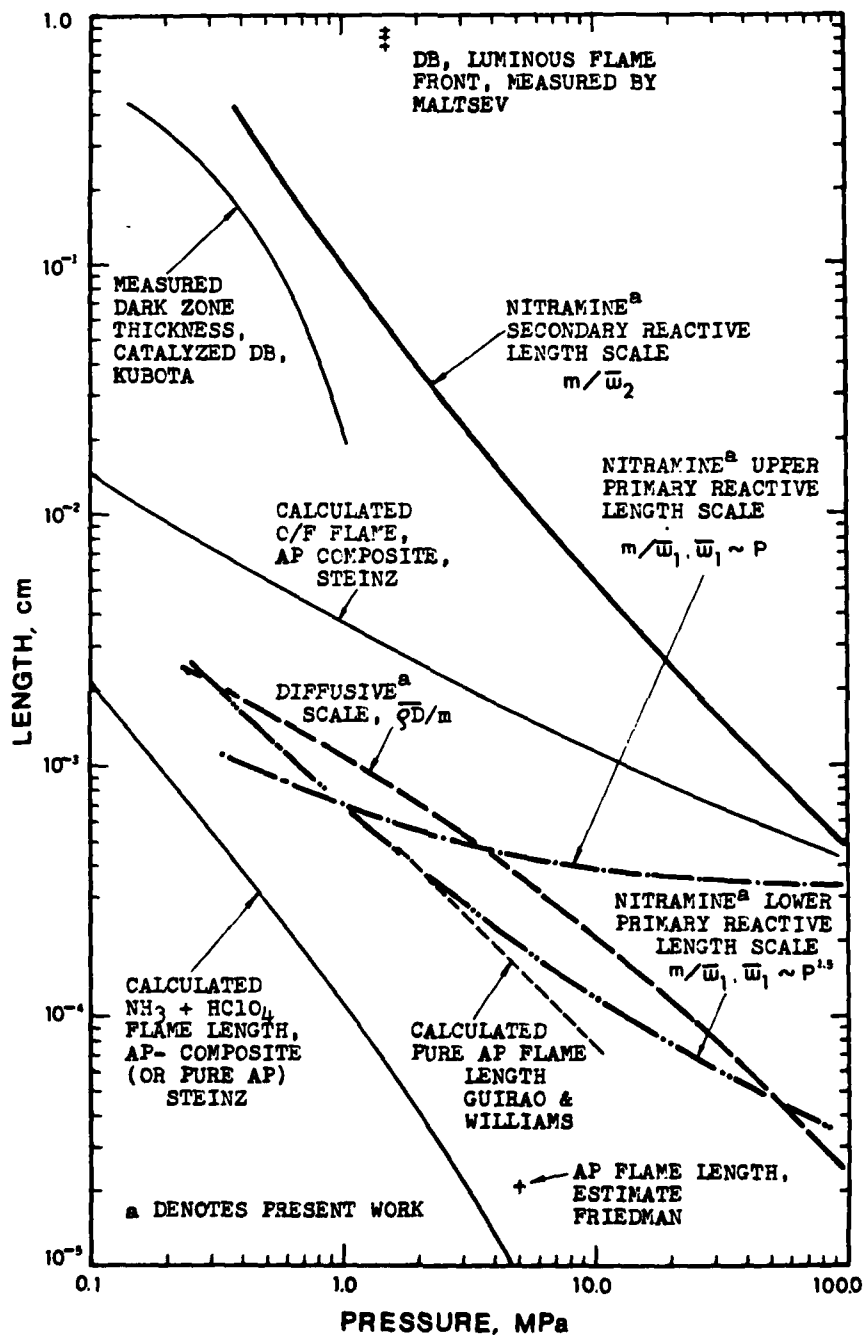
Fig. III.3
Theoretical and experimental length scales in the gaseous flame region vs pressure, in the range between 0.1 and 100 Mpa. Comparison is made between pure AP, AP propellant, DB propellants and the various scales arising in the nitramine monopropellant flame model. Sources are indicated. The upper δ_{R1} scale corresponds to $\bar{\omega}_1 \sim P$; the lower δ_{R1} scale is obtained by assuming a non-vanishing thermal effect in the near field due to the secondary reaction, such that $\bar{\omega}_1 \sim P^{1.5}$.
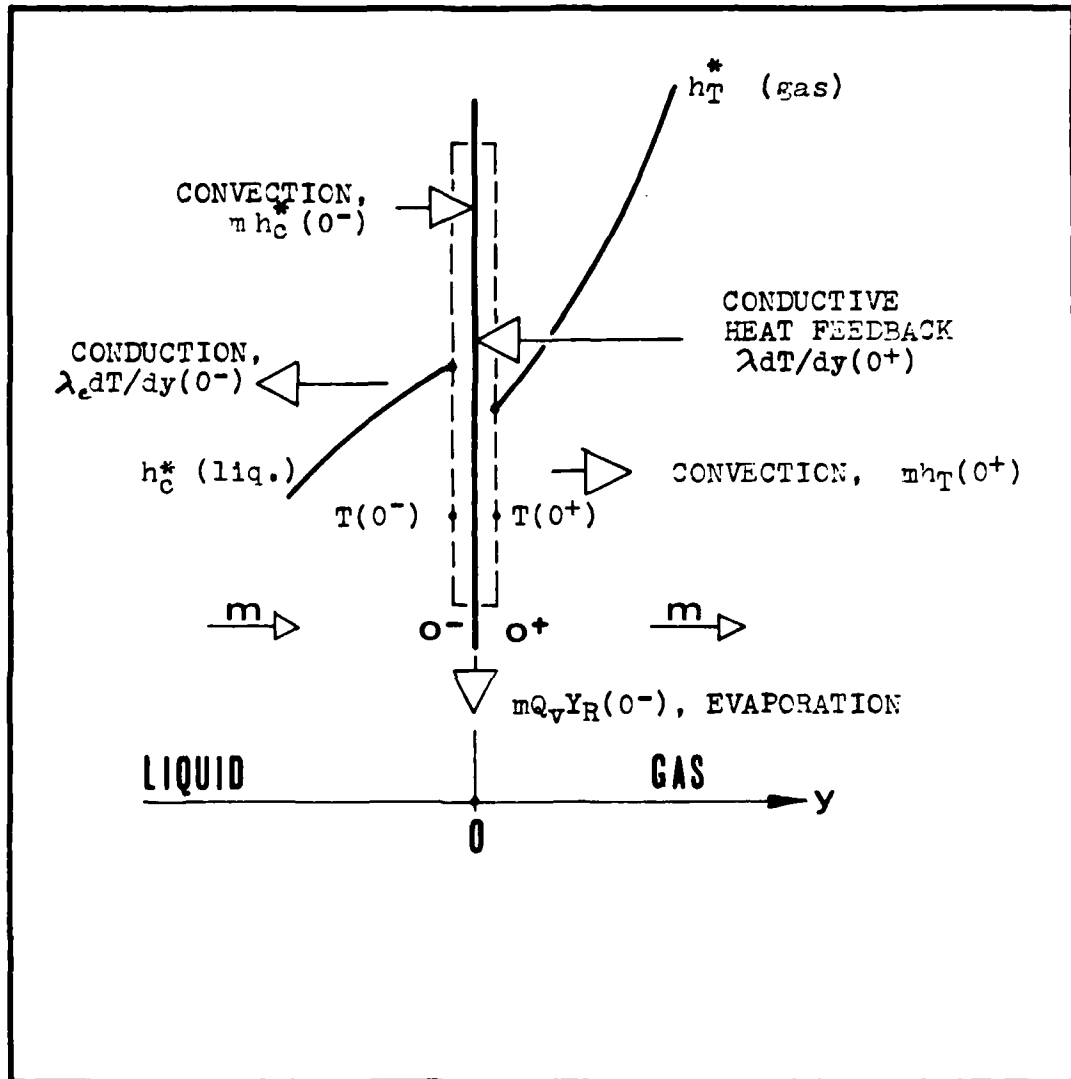
Fig. III.4

   Schematic diagram of the liquid-gas boundary control volume (in dashed line, prior to the limiting process letting the volume approach zero) showing the energy balance at y = 0.
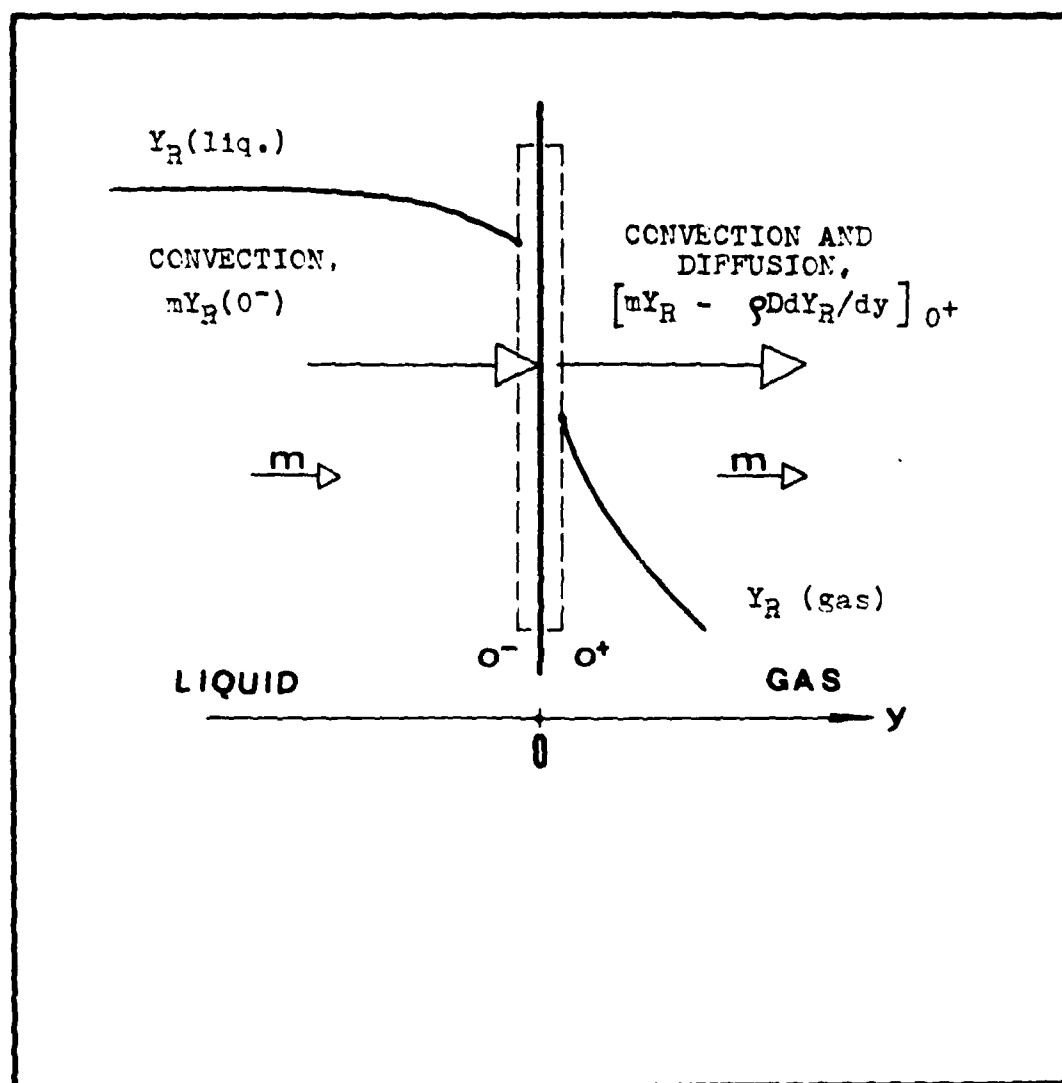
Fig. III.5
Schematic diagram of the liquid-gas boundary control volume (in dashed line, prior to the limiting process letting the volume approach zero) depicting the balance of chemical species' concentrations. Only the nitramine mass fraction is shown; the discontinuity in $Y_R(0^-) \neq Y_R(0^-)$ is due to the difference in transport (diffusion) between the two sides of the interface.
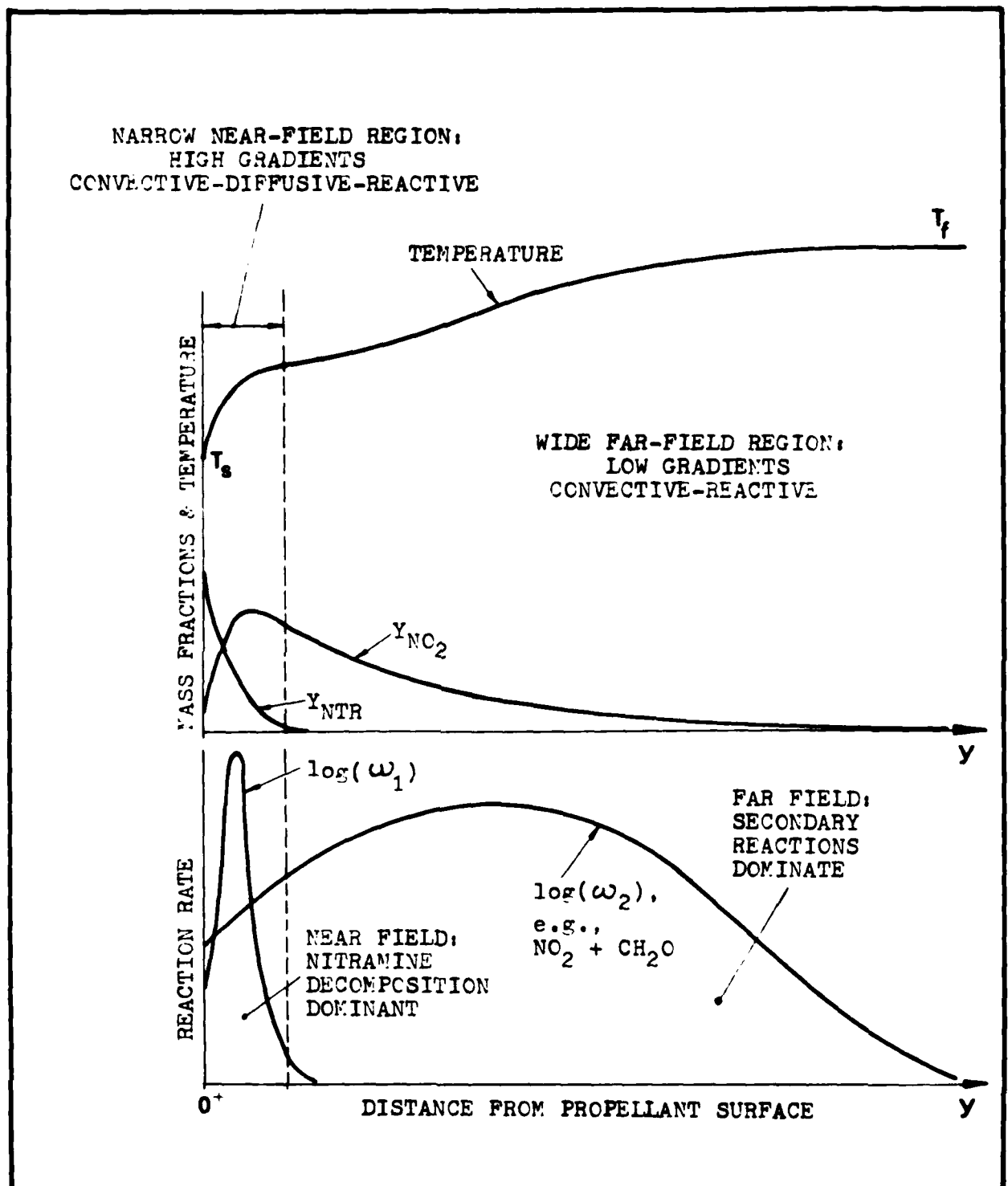
Fig. III.6

Schematic gas phase diagram, showing the near field and far field configuration for the nitramine deflagration wave. The near field region is magnified for clarity.

NITRAMINE
MASS FRACTION
Y_R

$Y_R = 1.$

T_s

$\underset{\Rightarrow}{m}$

$\underset{\Rightarrow}{m}$

$\underset{\Rightarrow}{m}$

HEAT FEEDBACK
FROM LIQUID

$\lambda_c dT/dy(-y_m^+)$

$\lambda dT/dy(0^+)$
HEAT FEEDBACK
FROM GAS

TEMPERATURE

mQ_m,
MELTING

$mY_R(0^-)Q_v$,
VAPORIZATION

$Q_{1,liq}$
HEAT RELEASE
BY NITRAMINE
DECOMPOSITION

T_m

SOLID   LIQUID   GAS

$-y_m$ 0   y
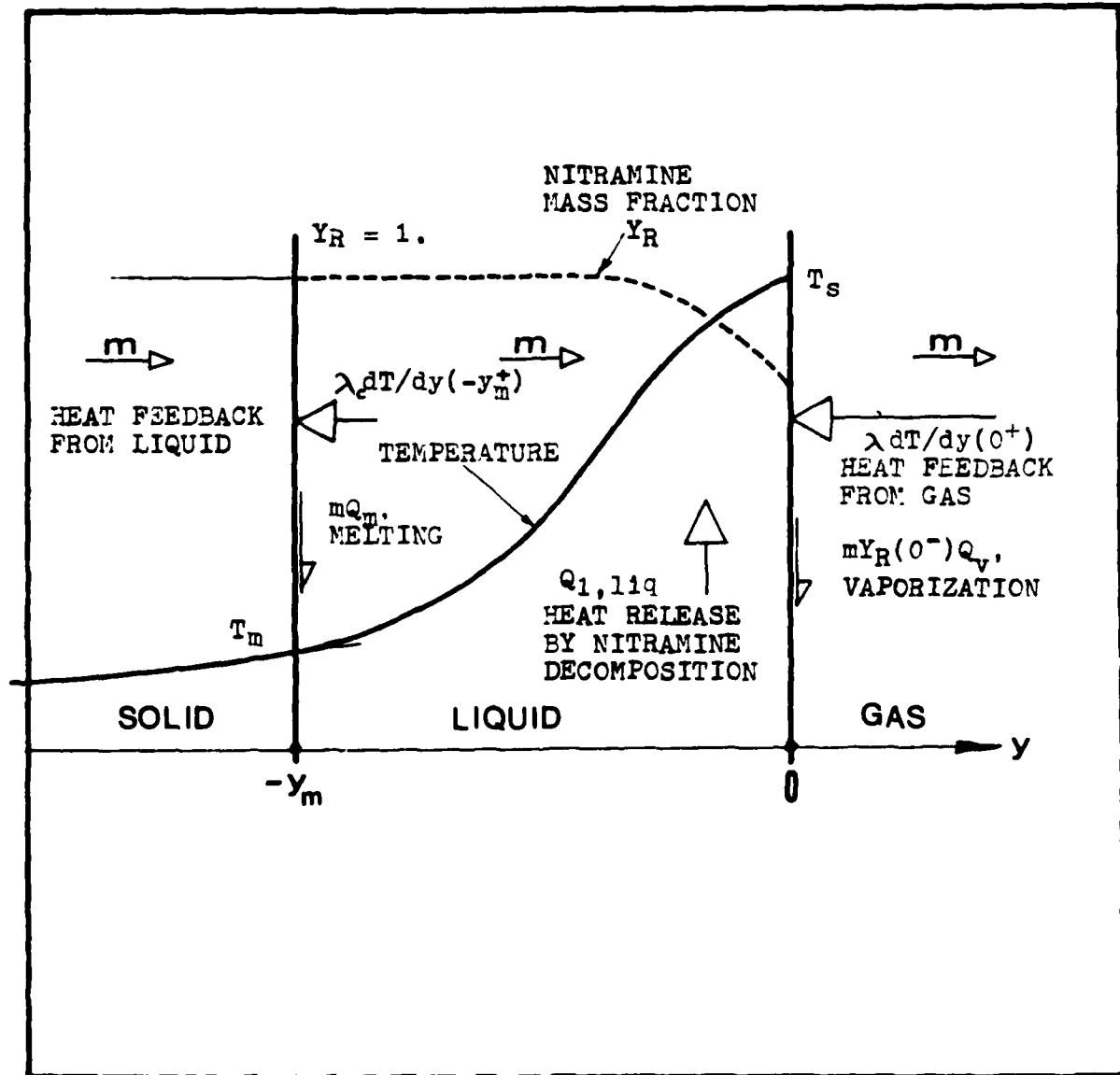
Fig. IV.1

Schematic diagram of the liquid phase processes for deflagrating nitramine monopropellant at moderate pressures. The rate and extent of decomposition depend upon both local temperature and residence time, with the latter inversely dependent on the flame speed. The reaction rate is a function of (T, Y_R) at each point; gaseous products are assumed dissolved in the liquid.
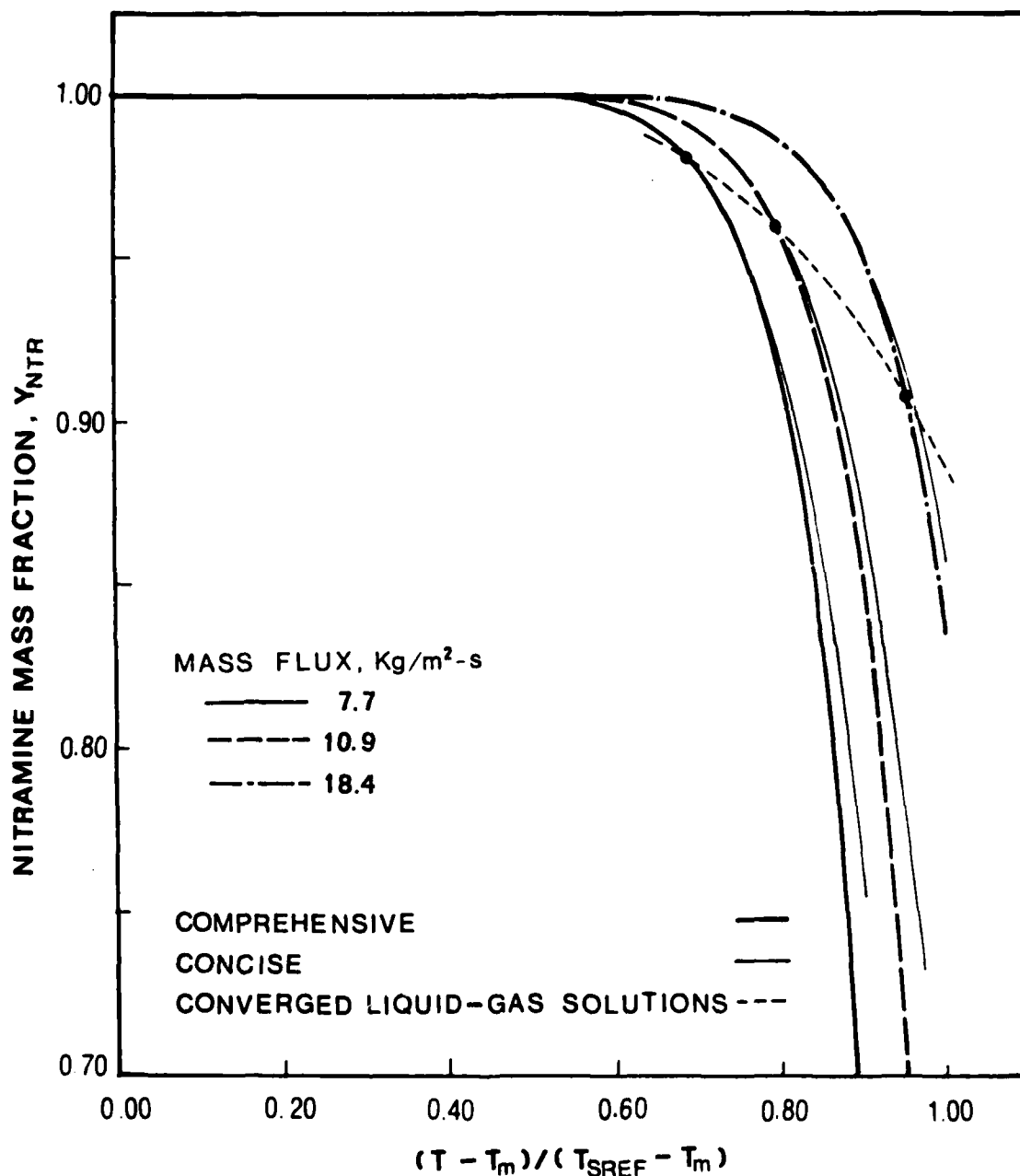
Fig. V.1

Nitramine mass fraction in the reacting liquid phase vs. normalized condensed phase temperature. At a given temperature, more depletion corresponds to lower mass flux, due to longer residence time; the converged surface points show an increased extent of reaction as m increases, since higher overall temperature counterbalances the shorter residence time. Note the closeness of the comprehensive and concise solution lines.
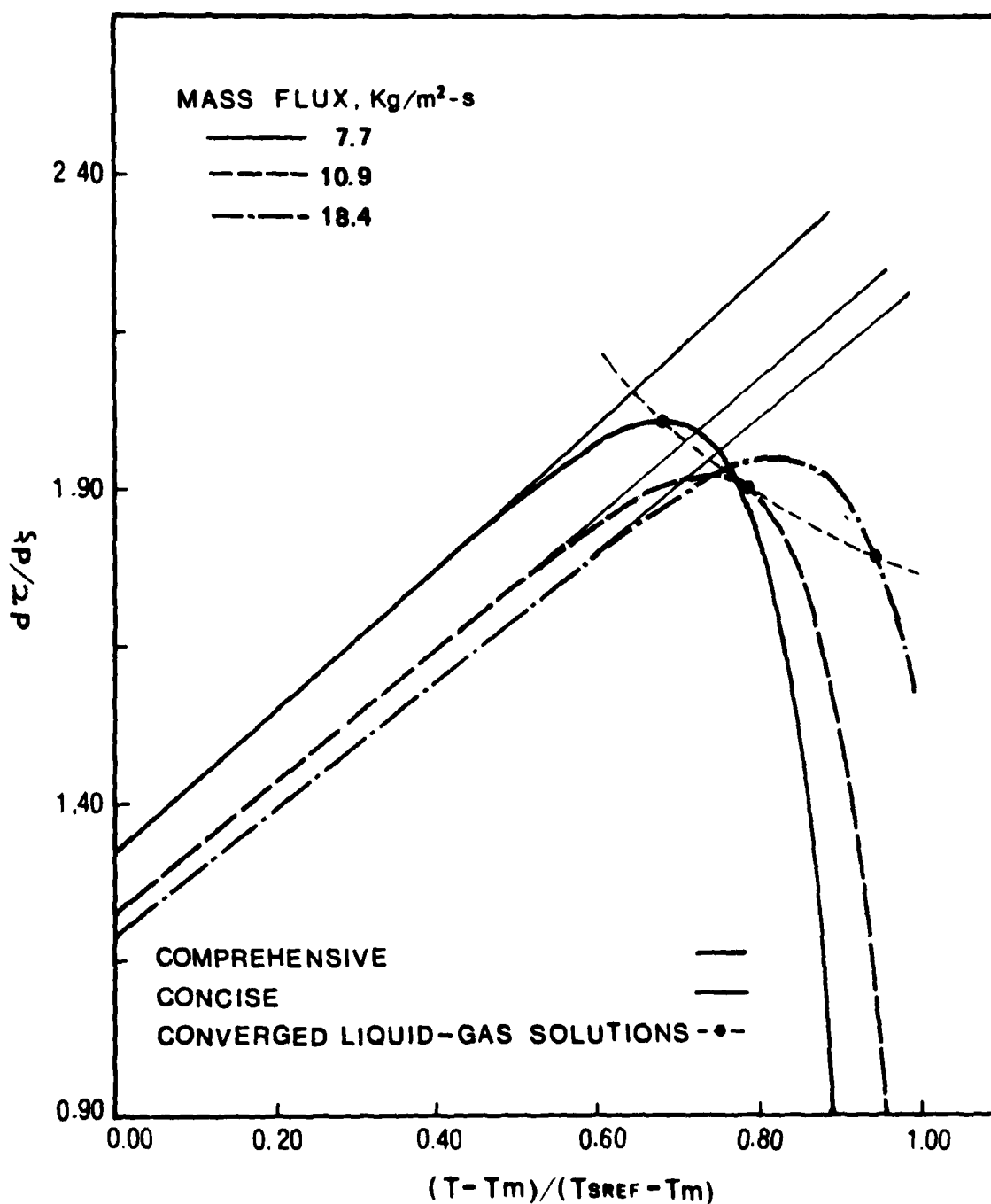
Fig. V.2

Dimensionless thermal gradient vs. normalized condensed phase temperature. Peaking of the comprehensive solution lines is due to heat release by primary decomposition within the layer, as less heat feedback is required to maintain a given temperature, whereas the concise solution (heat release localized at the surface) yields a linear relationship between temperature and its gradient.
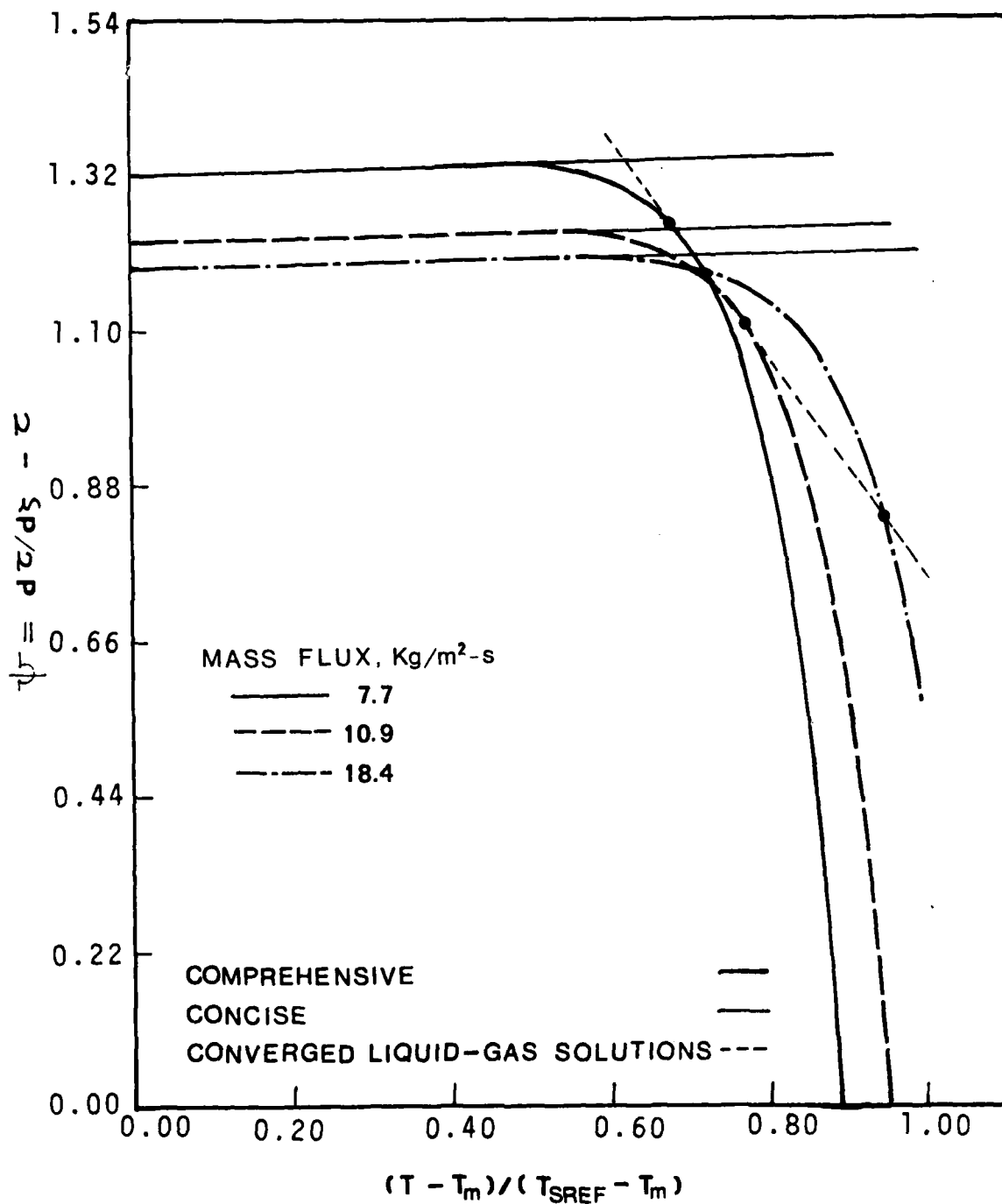
Fig. V.3
Total dimensionless thermal flux, ψ vs. normalized temperature in the liquid phase. As heat release by decomposition becomes larger, ψ decreases and hence the departure from the constant initial value, noting that reaction is negligible in the low temperature region.
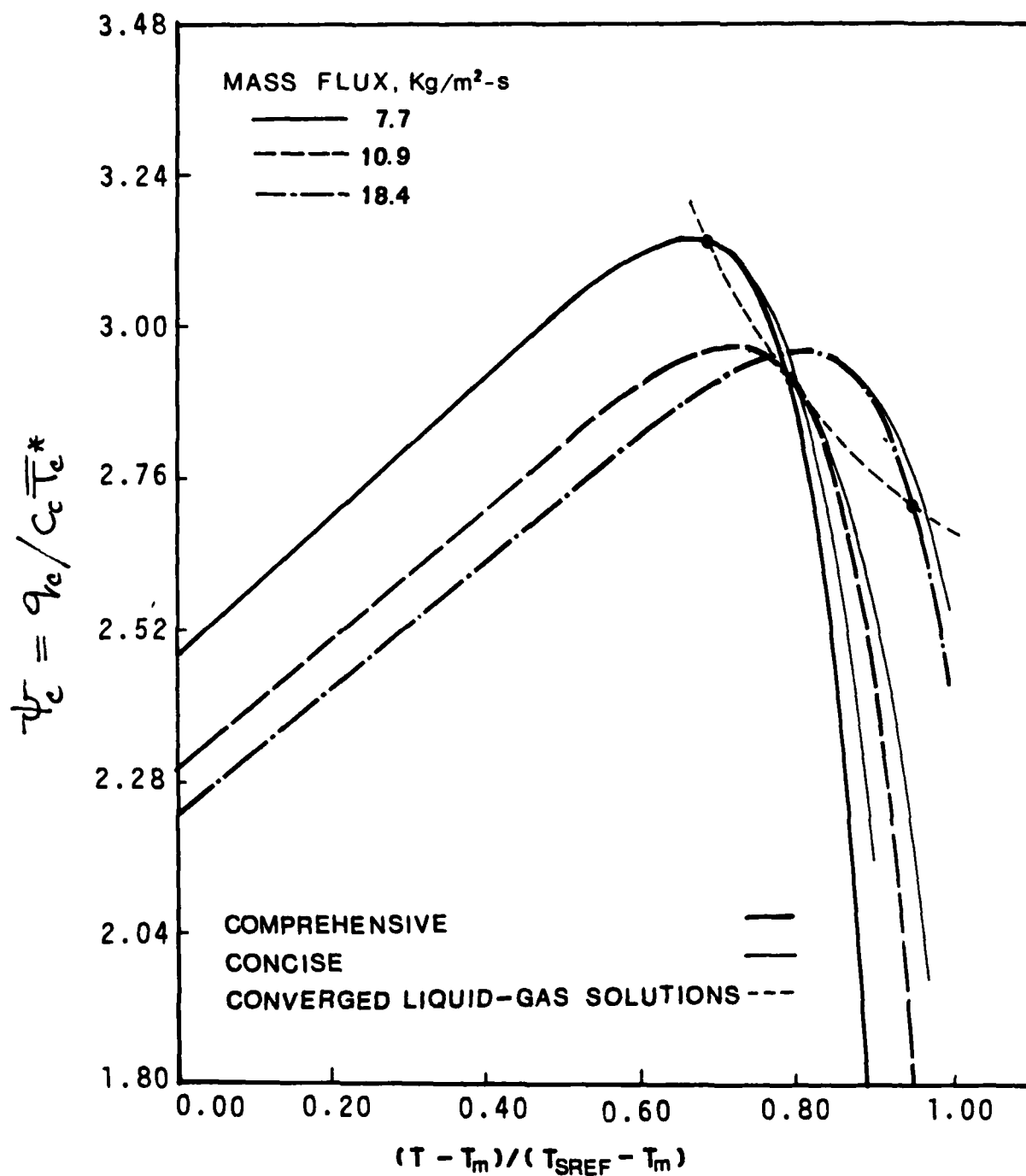
Fig. V.4

Dimensionless q_c, comprising the solution-dependent part of the liquid-gas interface energy balance vs. normalized temperature. Q_s is the net chemical enthalpy change across the surface (evaporation and reaction) and has different definitions for the comprehensive and the concise solutions, cf. Eqs. (36a,b). Note the close agreement, resembling that of Fig. V.1.
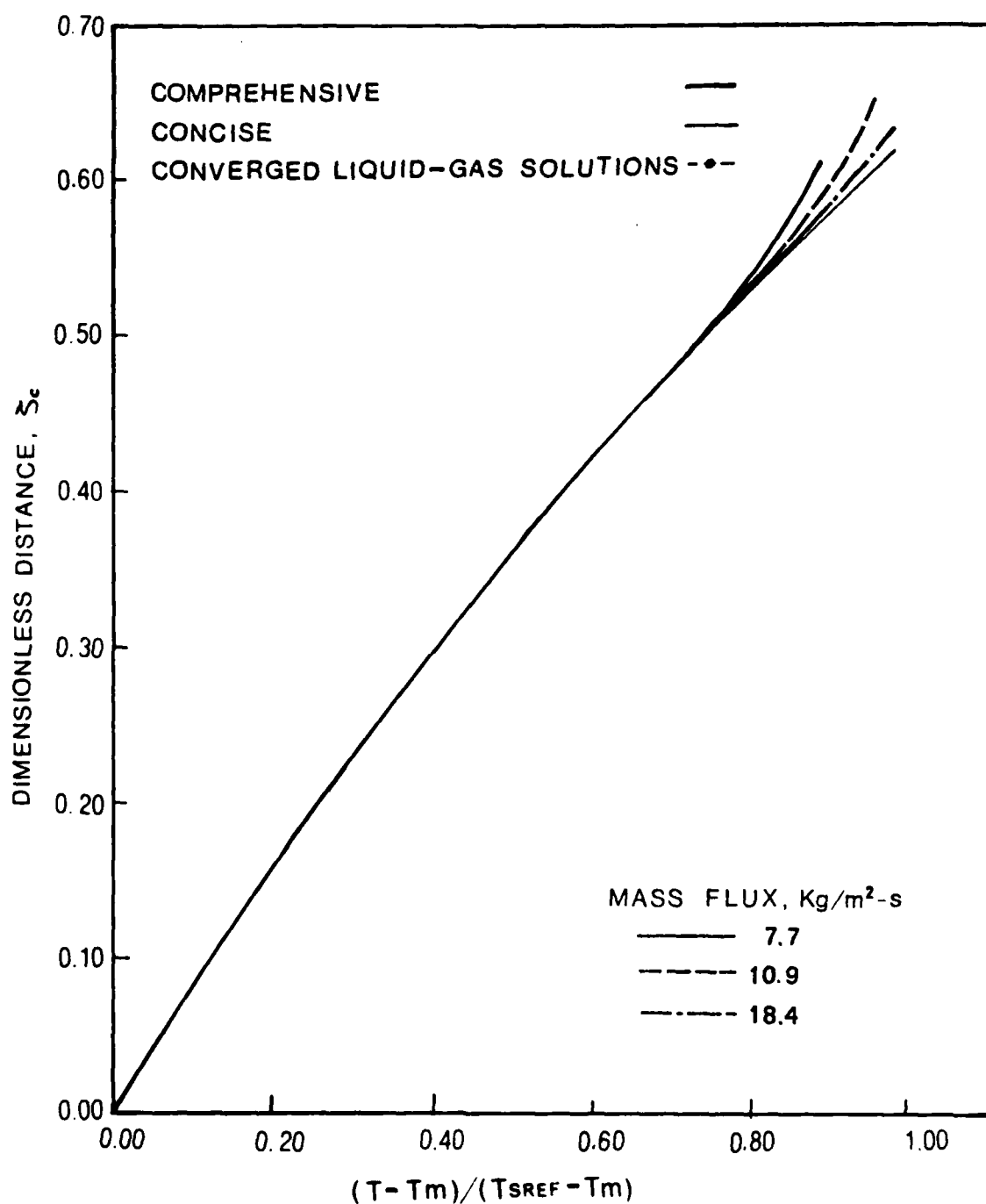
Fig. V.5

Dimensionless distance in the liquid layer from the solid-liquid interface, ξ_c vs. normalized liquid phase temperature. In the absence of heat sources (concise model) self-similarity is evident, as $\xi_c = \ln \tau_c$ regardless of the mass flux.
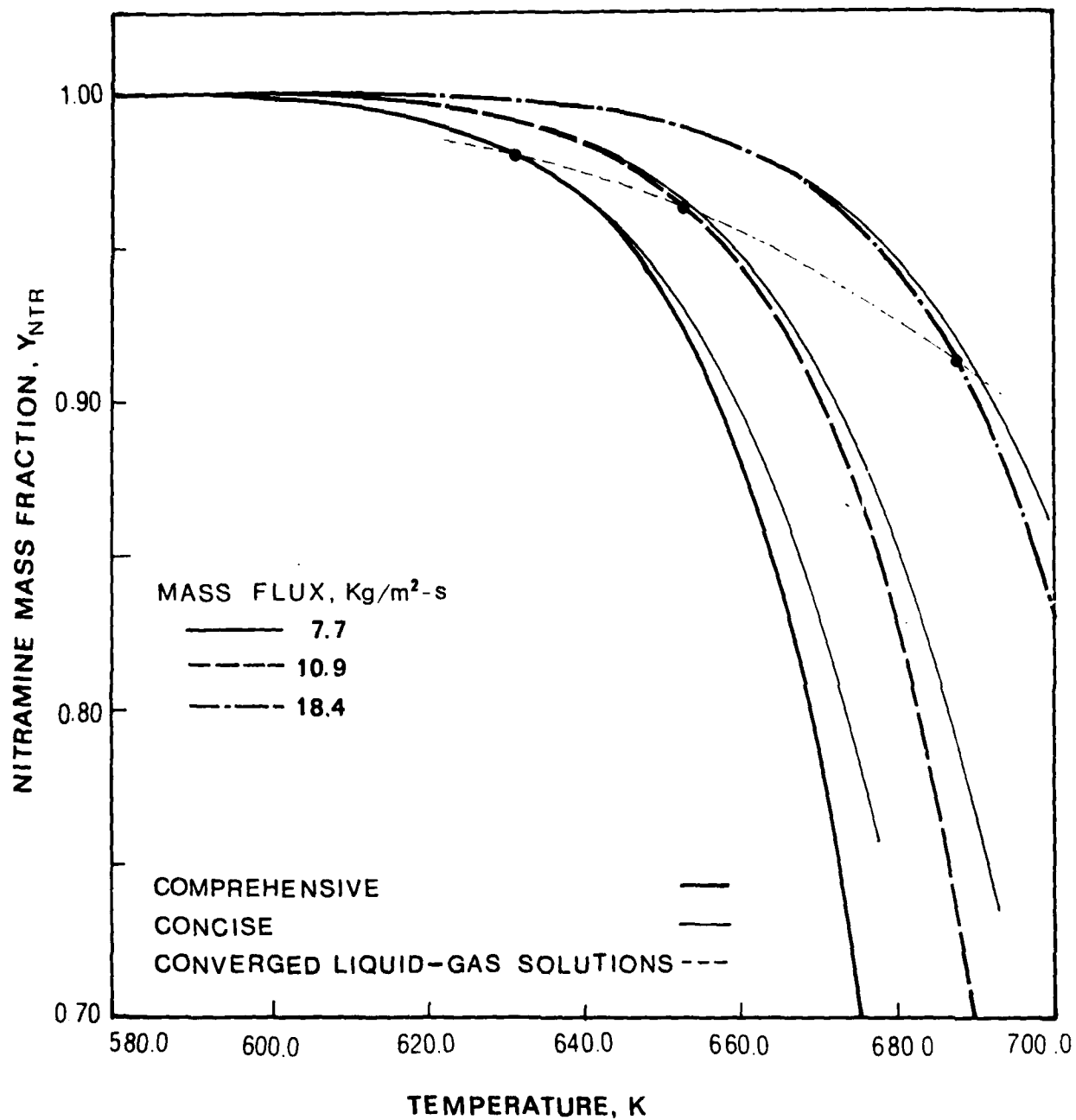
Fig. V.6
Nitramine mass fraction vs. temperature in the liquid layer.
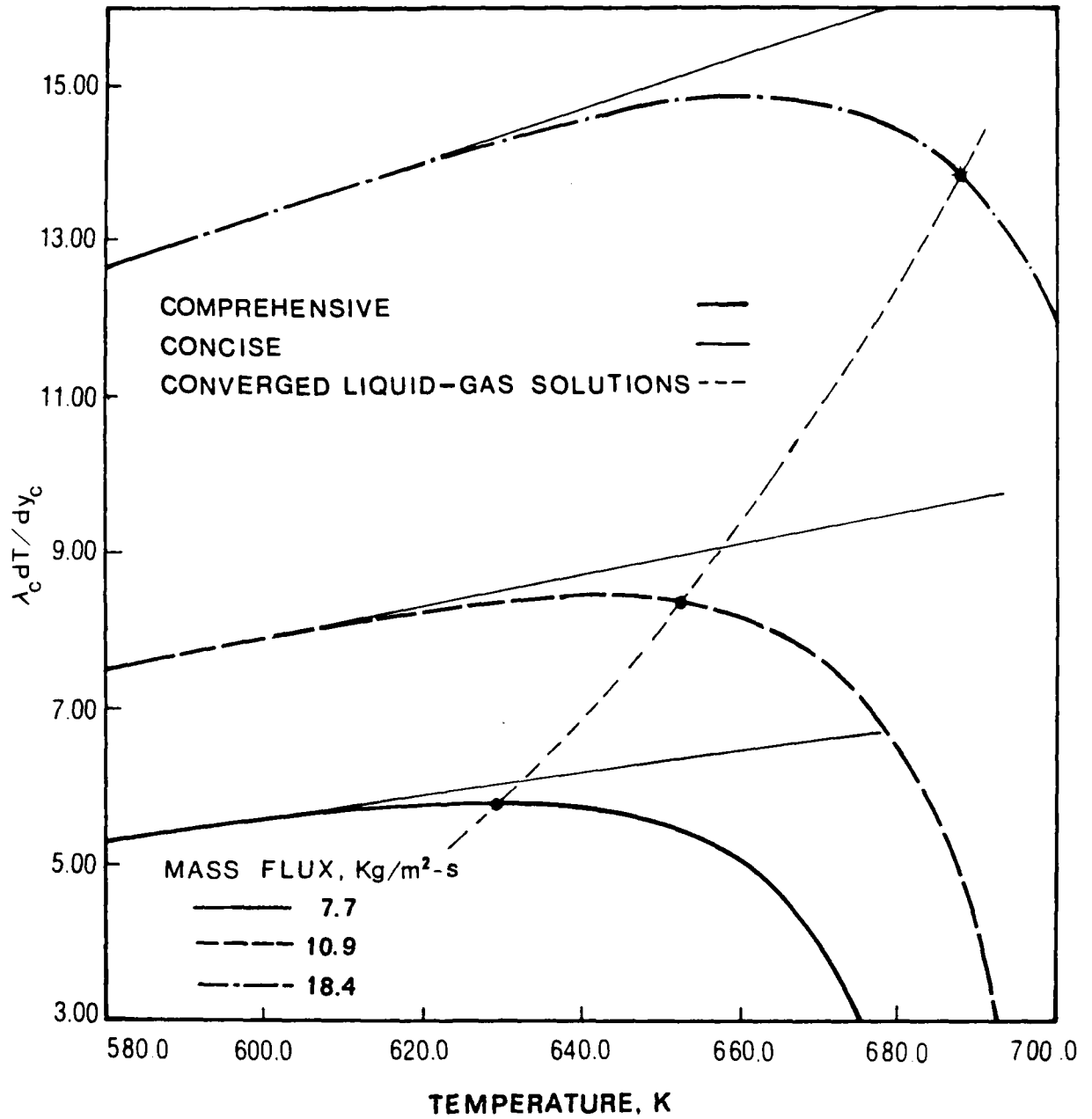
Fig. V.7
Conductive heat flux vs. temperature in the liquid layer, positive in the direction of the solid-liquid interface, showing growth with increasing mass flux, cf. Fig. V.2.
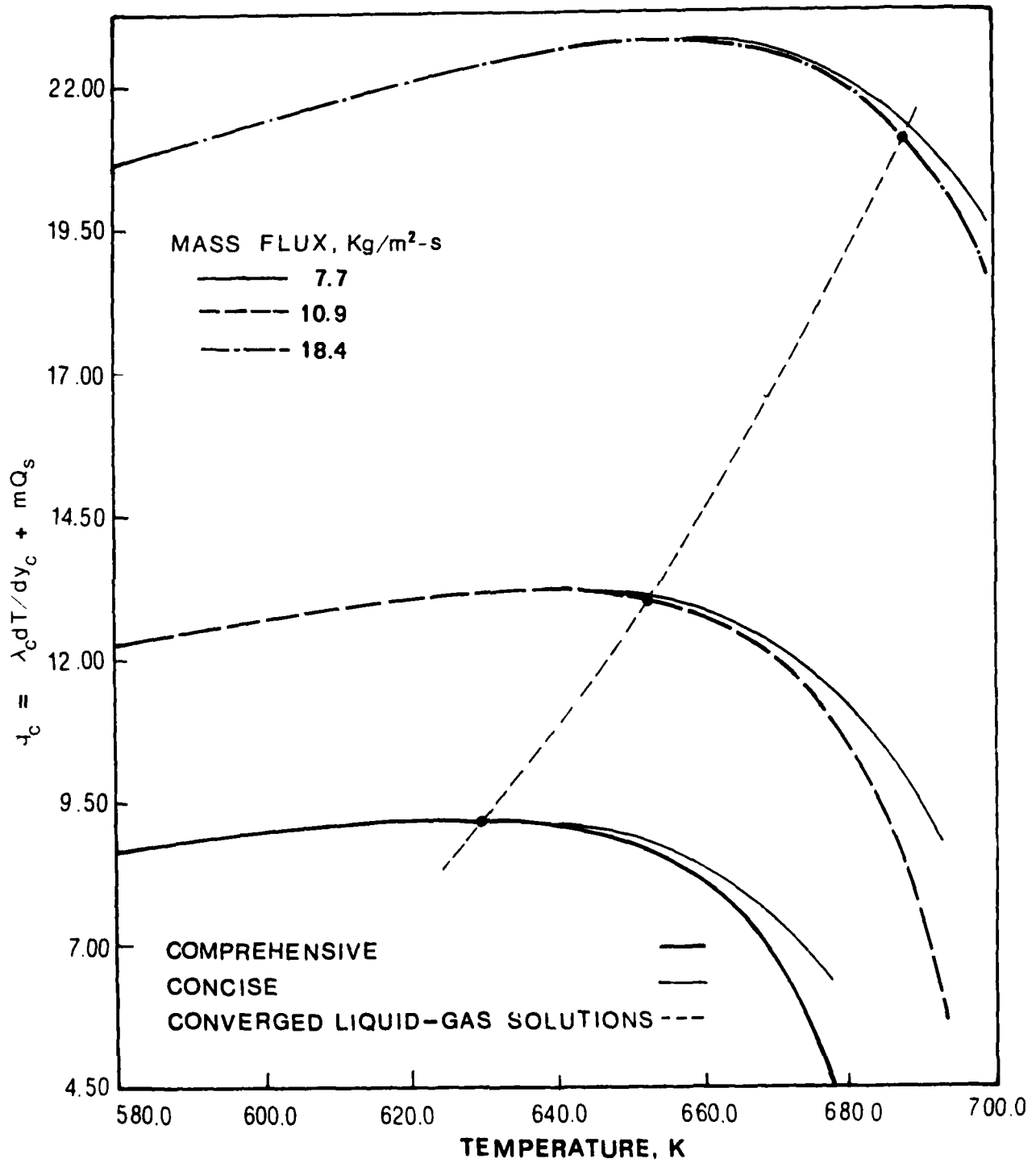
Fig. V.8

Dimensional q_c, the solution-dependent part of the energy balance at the liquid-gas interface vs. temperature in the liquid layer; cf. Fig. V.4.
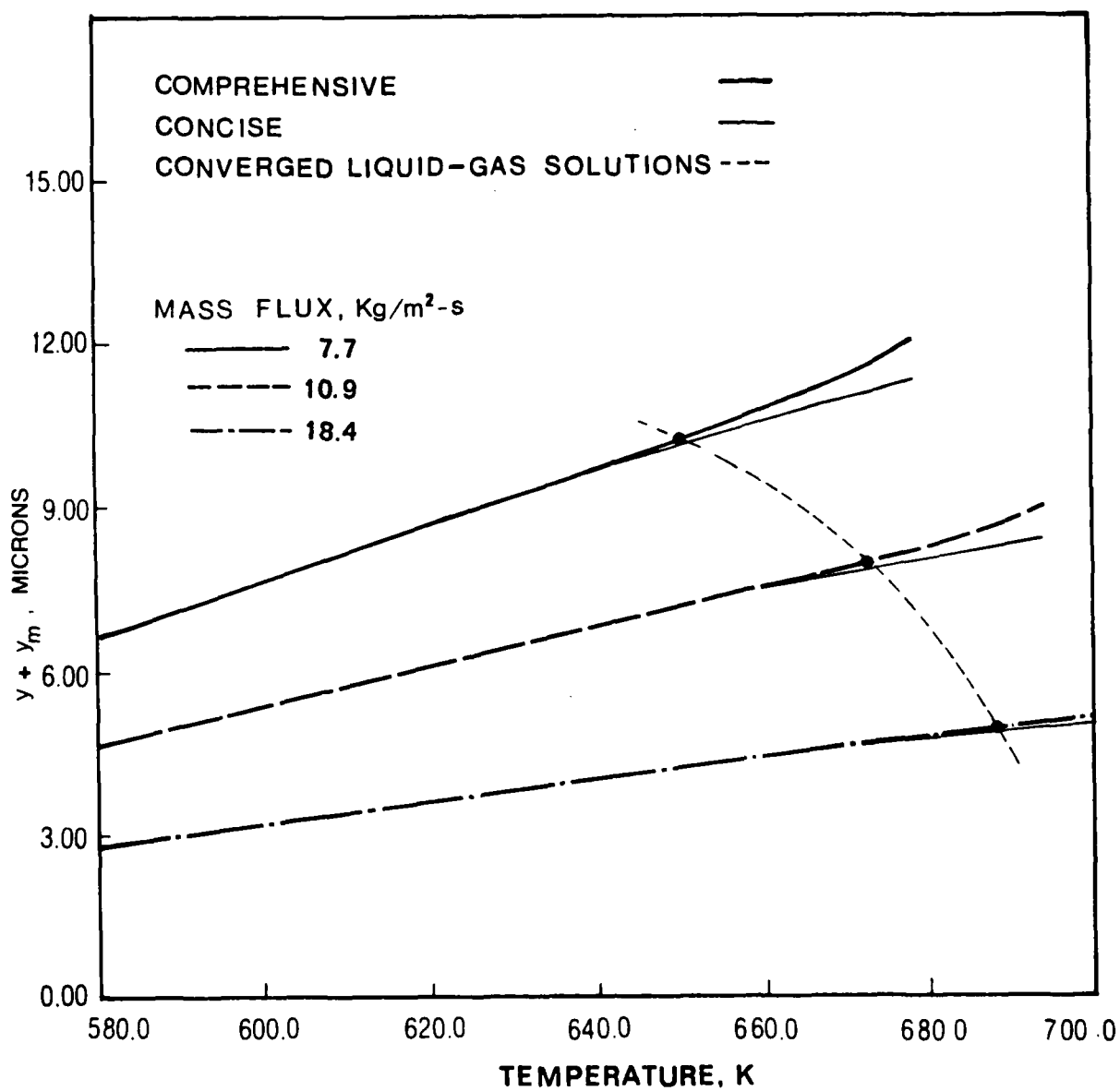
Fig. V.9
Distance in the liquid layer (from the solid-liquid interface) vs. temperature. The layer thickness, regarding the converged surface points, is shown to decrease with increasing mass flux in an accelerated manner.
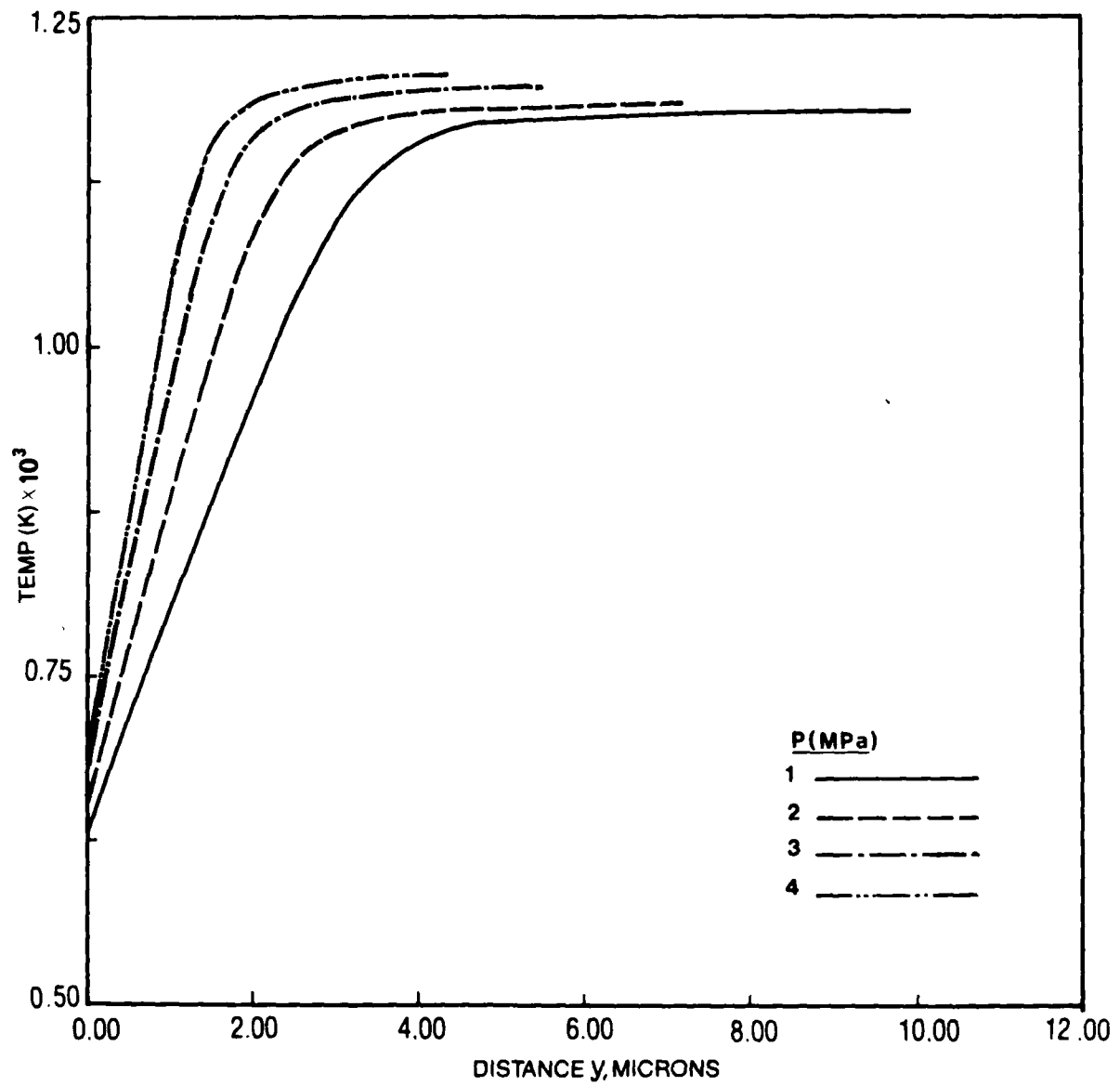
Fig. V. 10

Near field temperature distributions, as function of distance from the propellant surface.
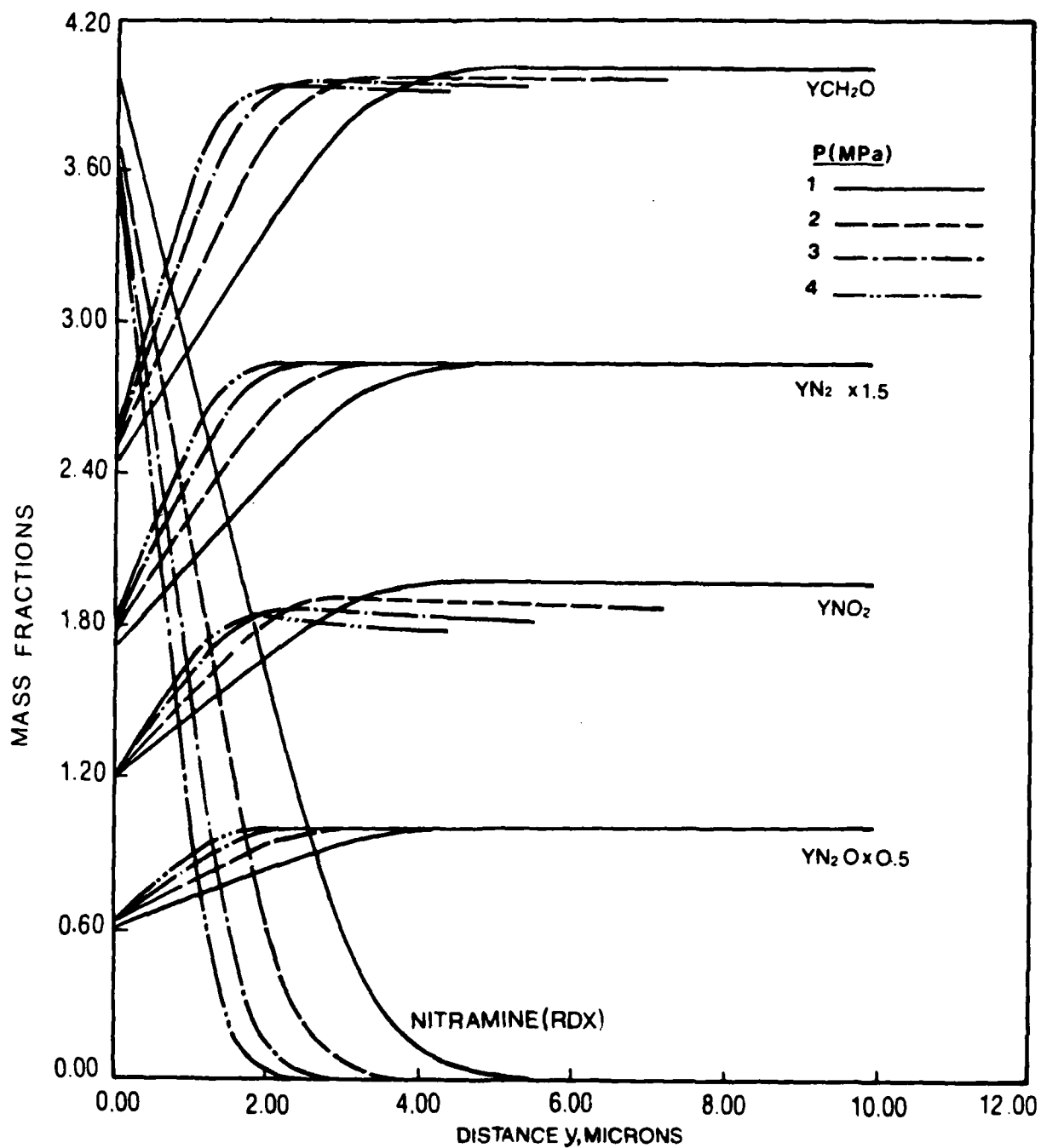
Fig. V. 11
Primary reaction mass fraction distributions, as functions of distance within the inner flame field.
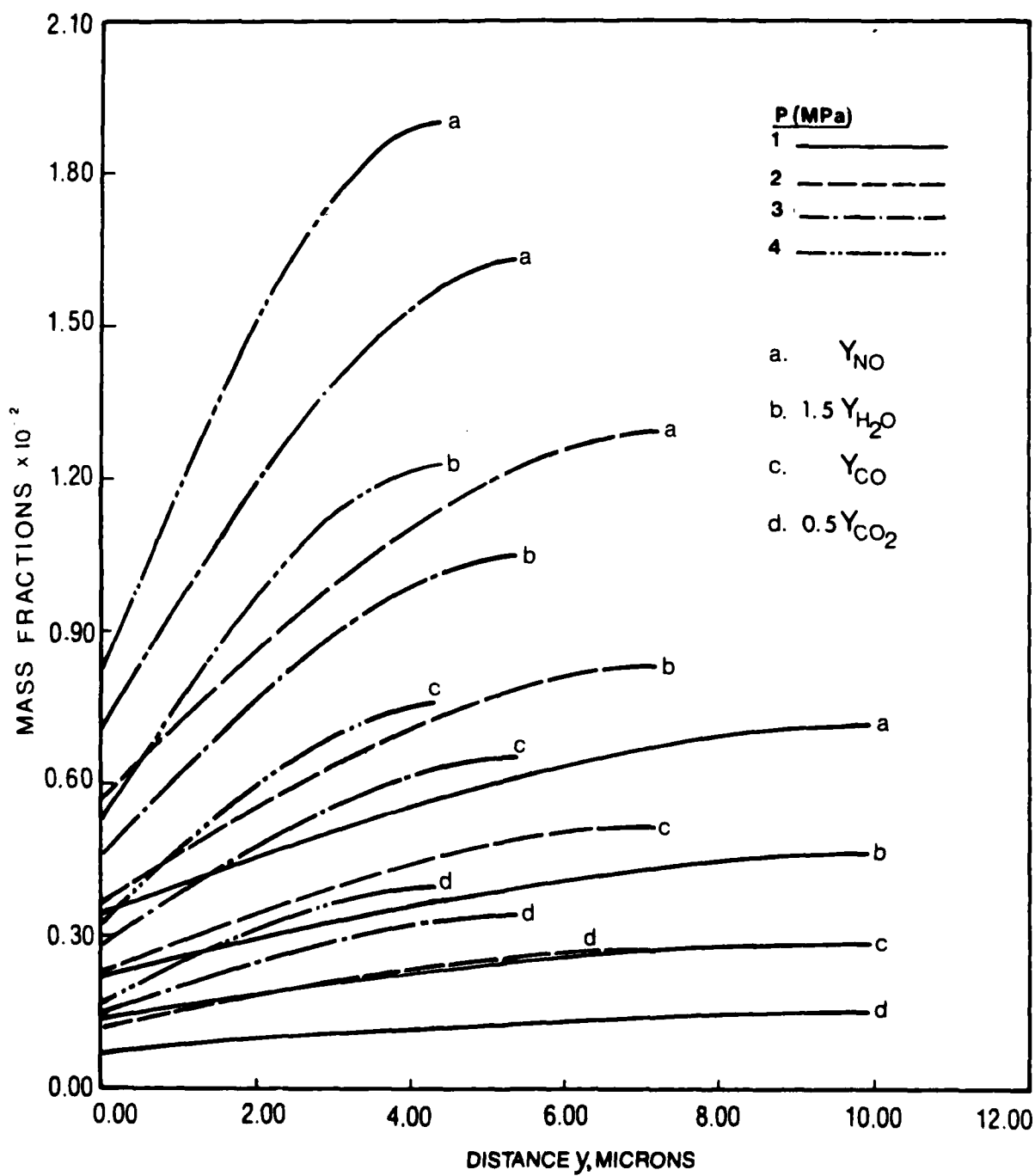
Fig. V. 12
Mass fraction distributions of secondary reaction products as functions of distance within the inner flame field.
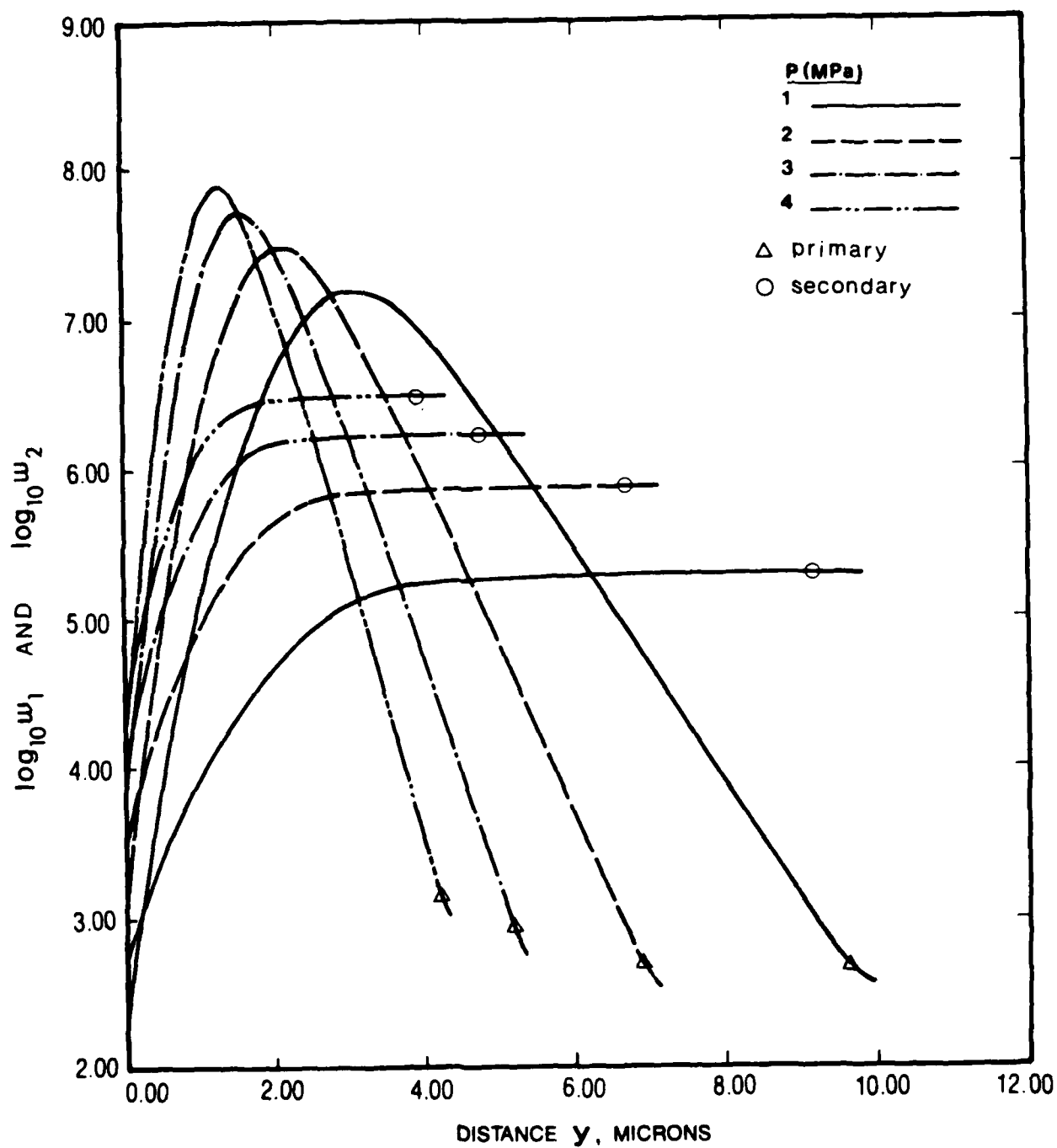
Fig. V. 13
Logarithms of the primary and secondary reaction rates within the inner flame field, as functions of distance from the propellant surface.
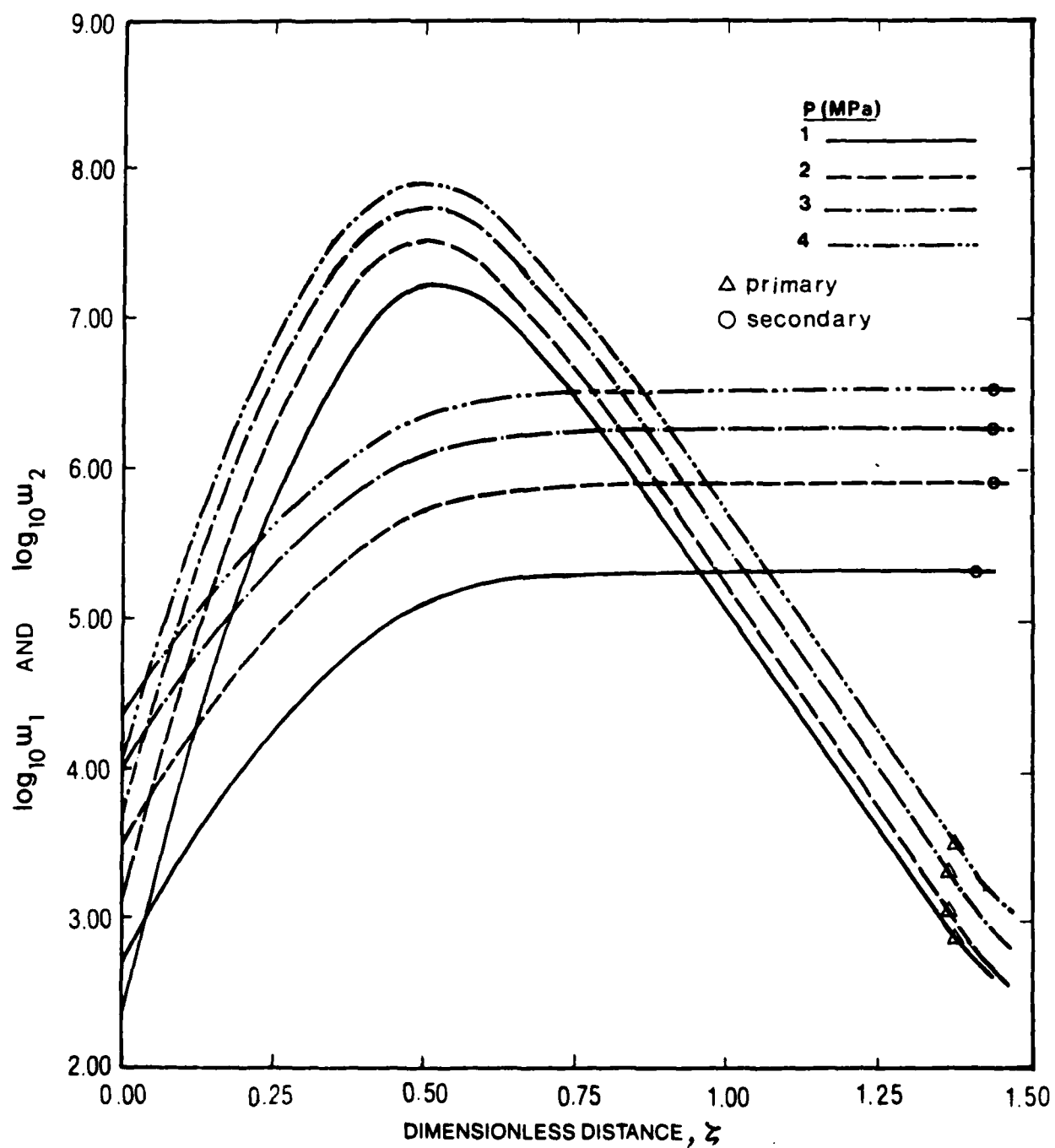
Fig. V. 14
Logarithms of the primary and secondary reaction rates in the inner flame field, plotted against dimensionless distance from the propellant surface.
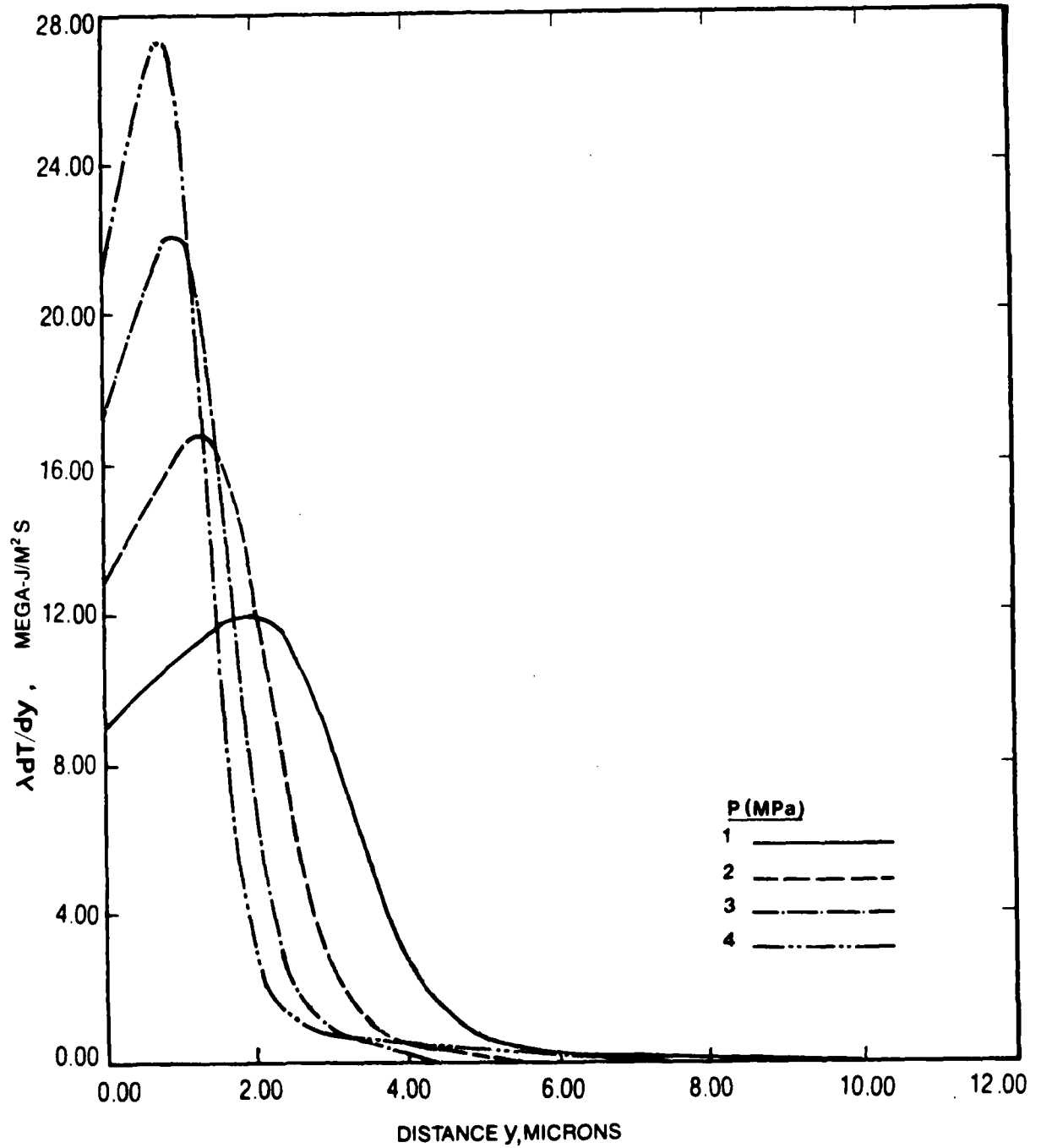
Fig. V. 15
Conductive thermal flux in the near field, as function of distance from the propellant surface.
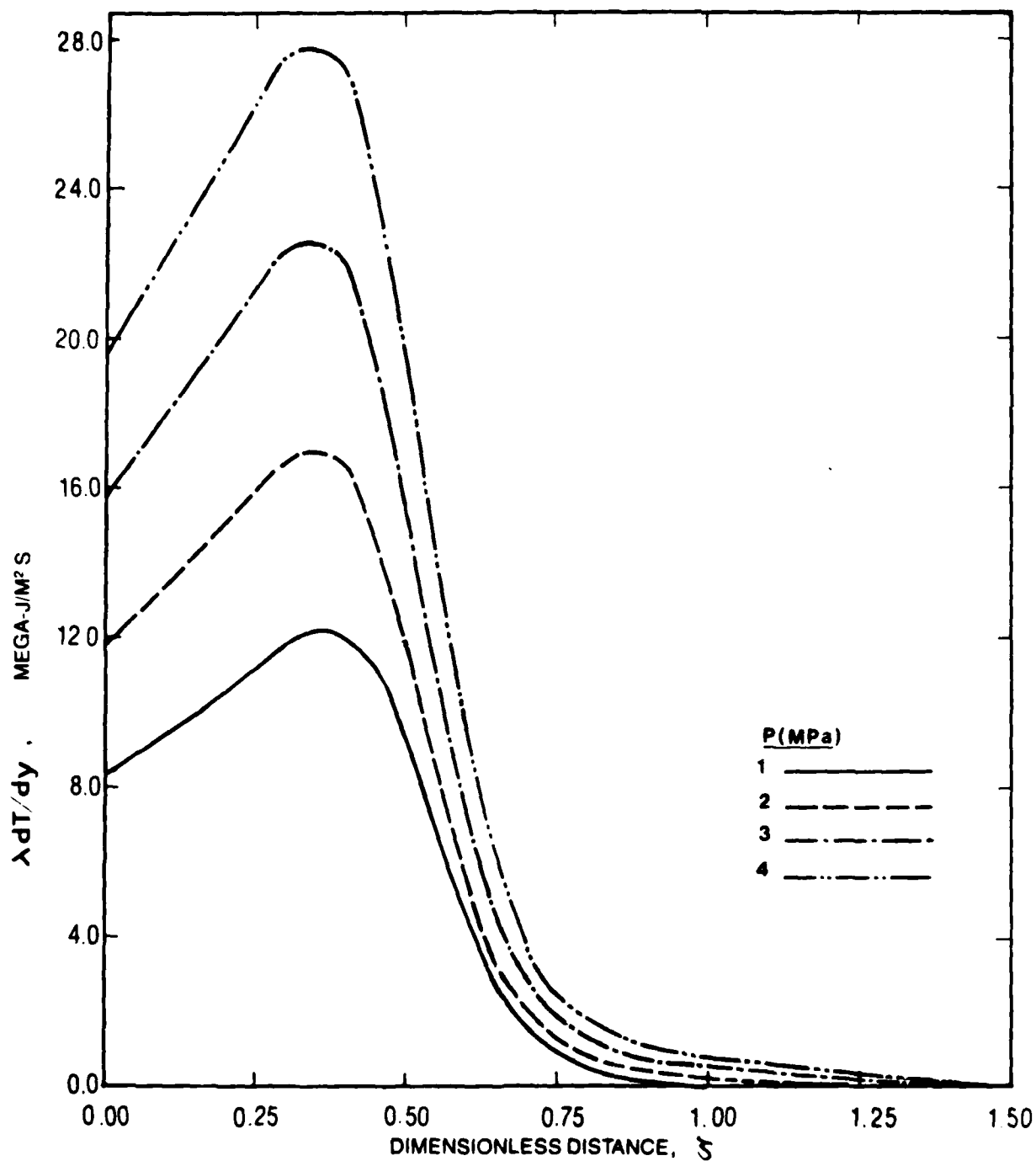
Fig. V. 16
Conductive thermal flux within the inner flame zone, in upstream direction, plotted against the dimensionless near field coordinate.
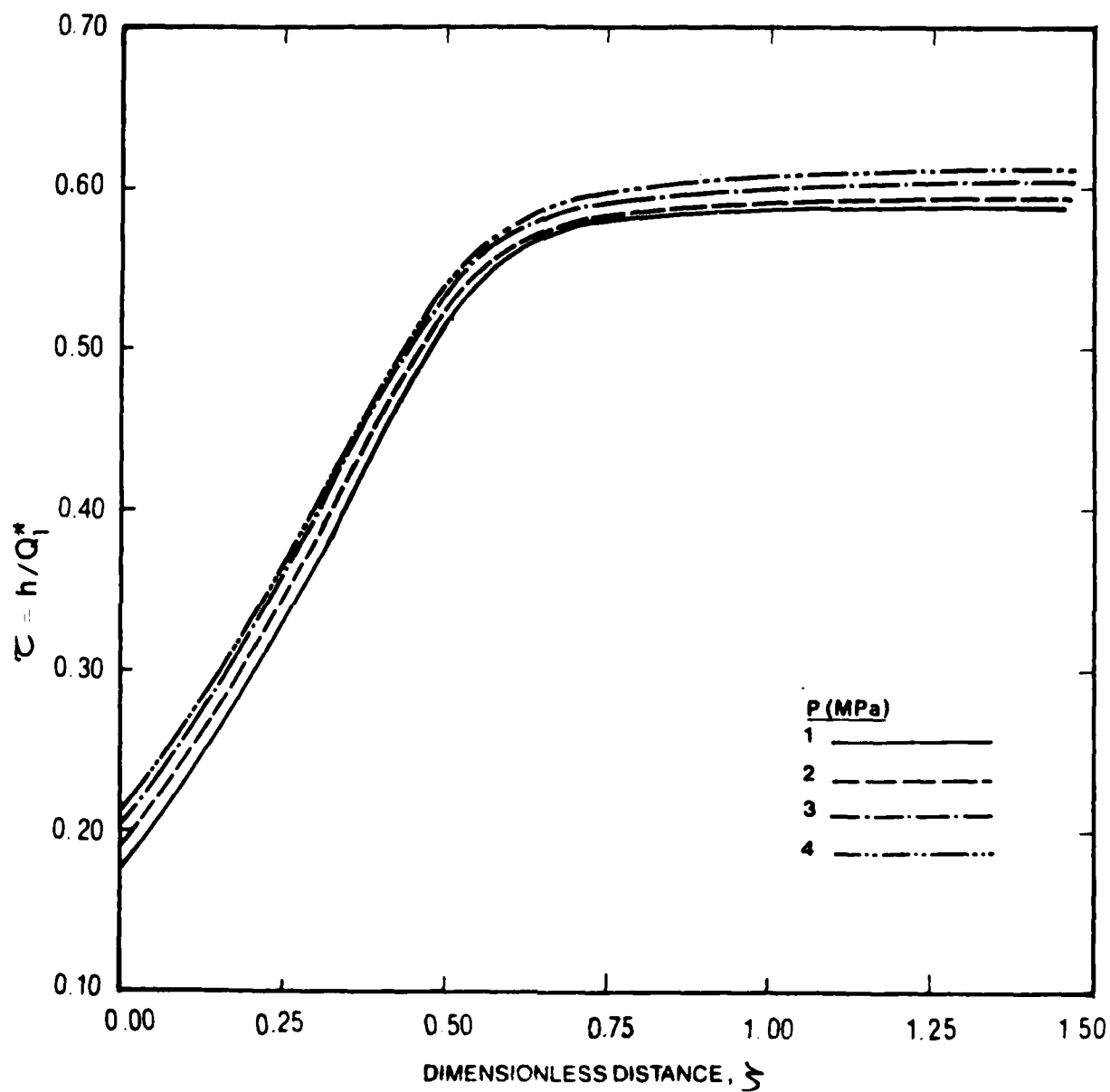
Fig. V. 17
Dimensionless thermal enthalpy distribution in the inner flame zone, as function of the dimensionless near field coordinate.
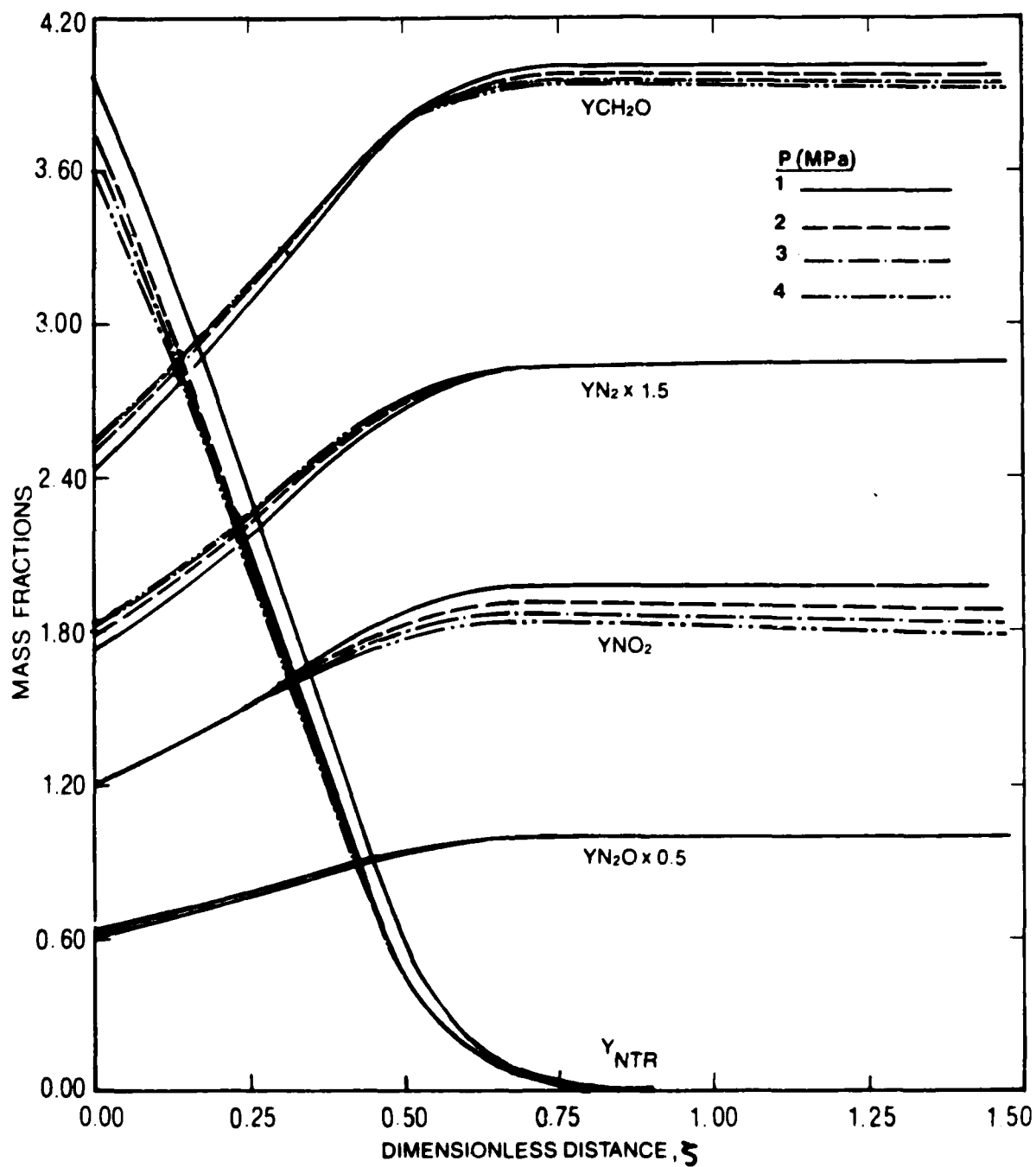
Fig. V. 18
Mass fraction distributions for the primary reaction, as functions of the dimensionless near field coordinate
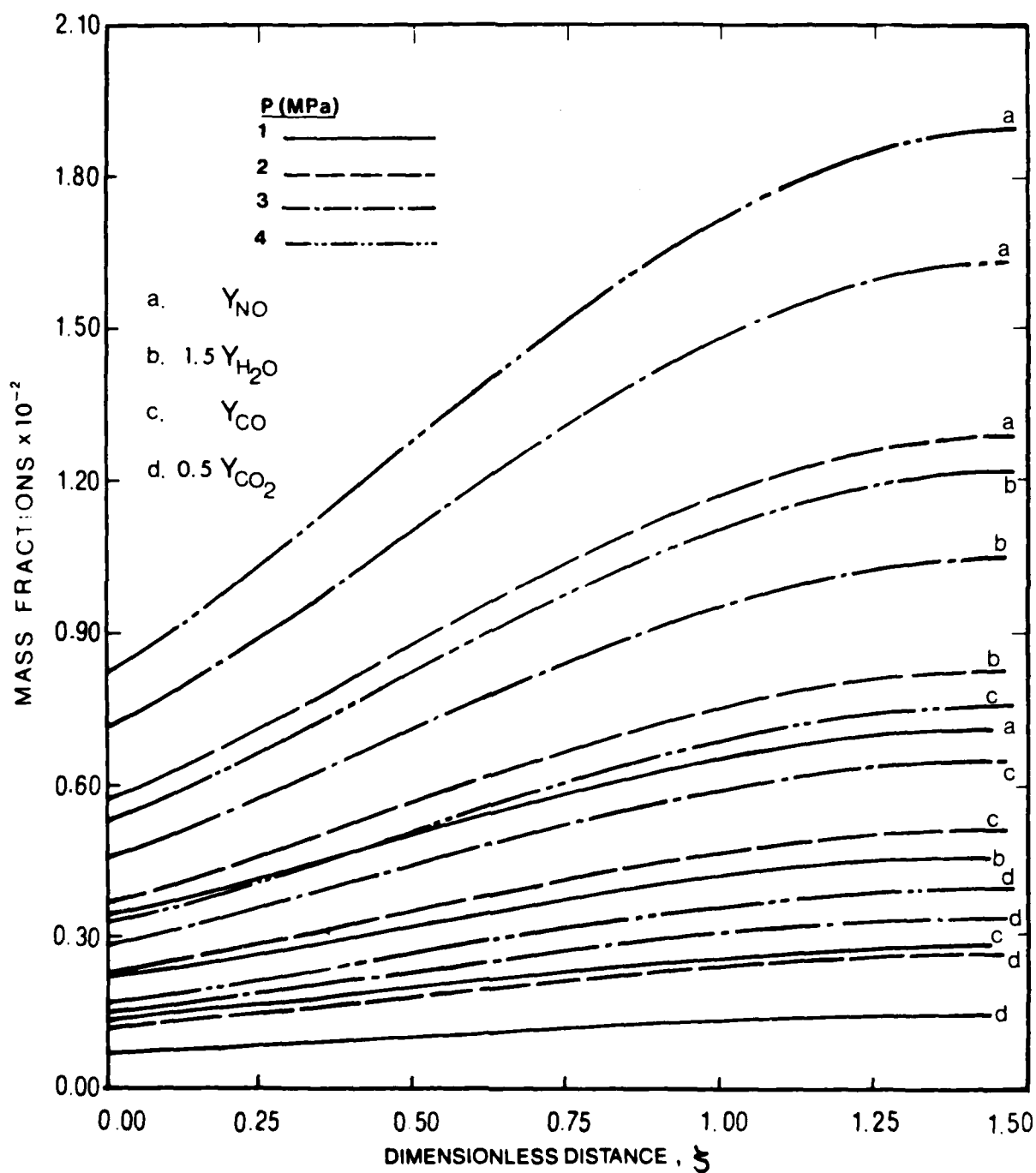
Fig. V. 19

Mass fraction distributions of the secondary reaction in the near field, as functions of the dimensionless near field coordinate.
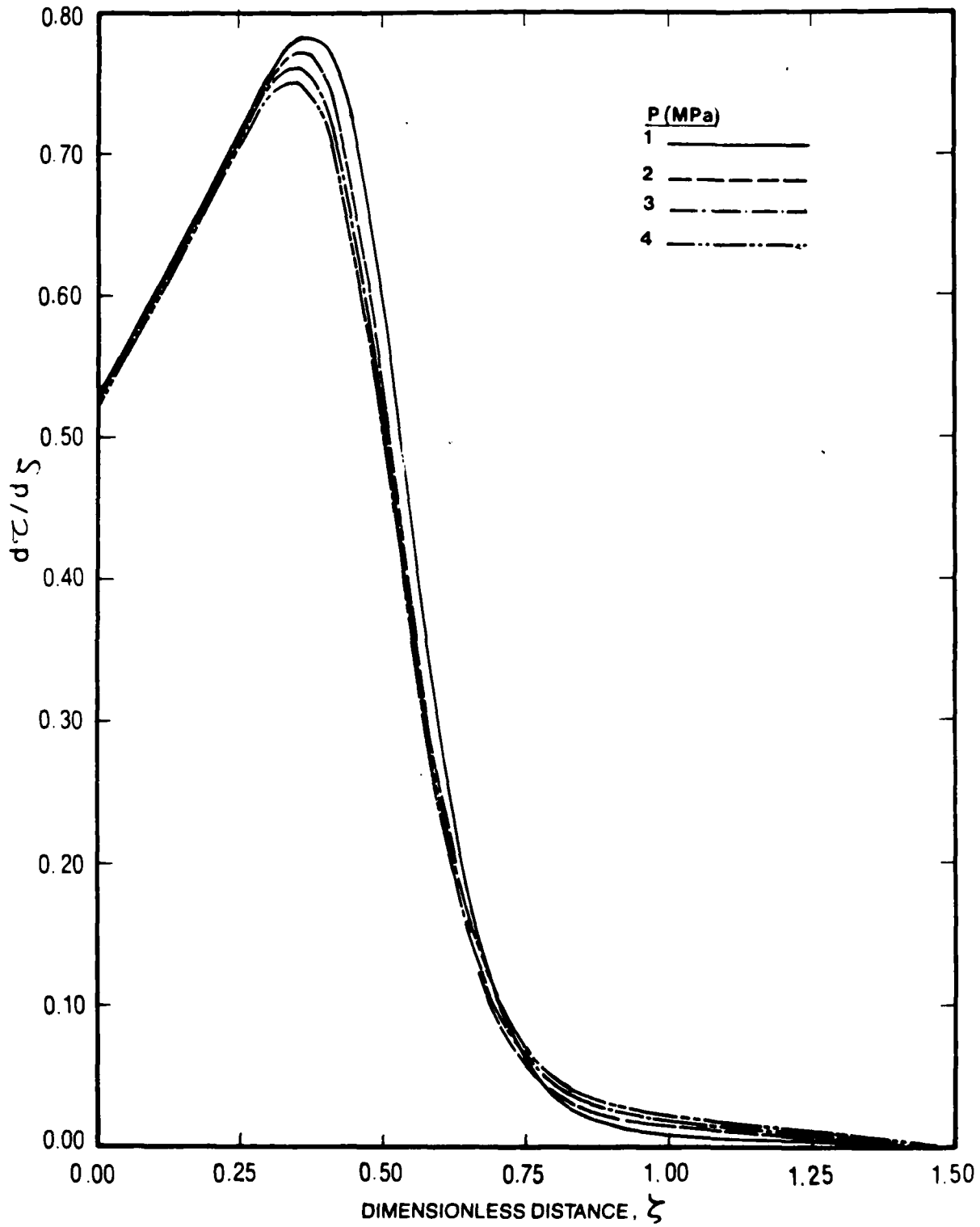
Fig. V. 20

Dimensionless thermal gradient, $d\tau/d\zeta$, in the inner flame zone, as function of the dimensionless near field coordinate. As pressure is increased, the inner gradients become smaller, while those at the outer end become larger.
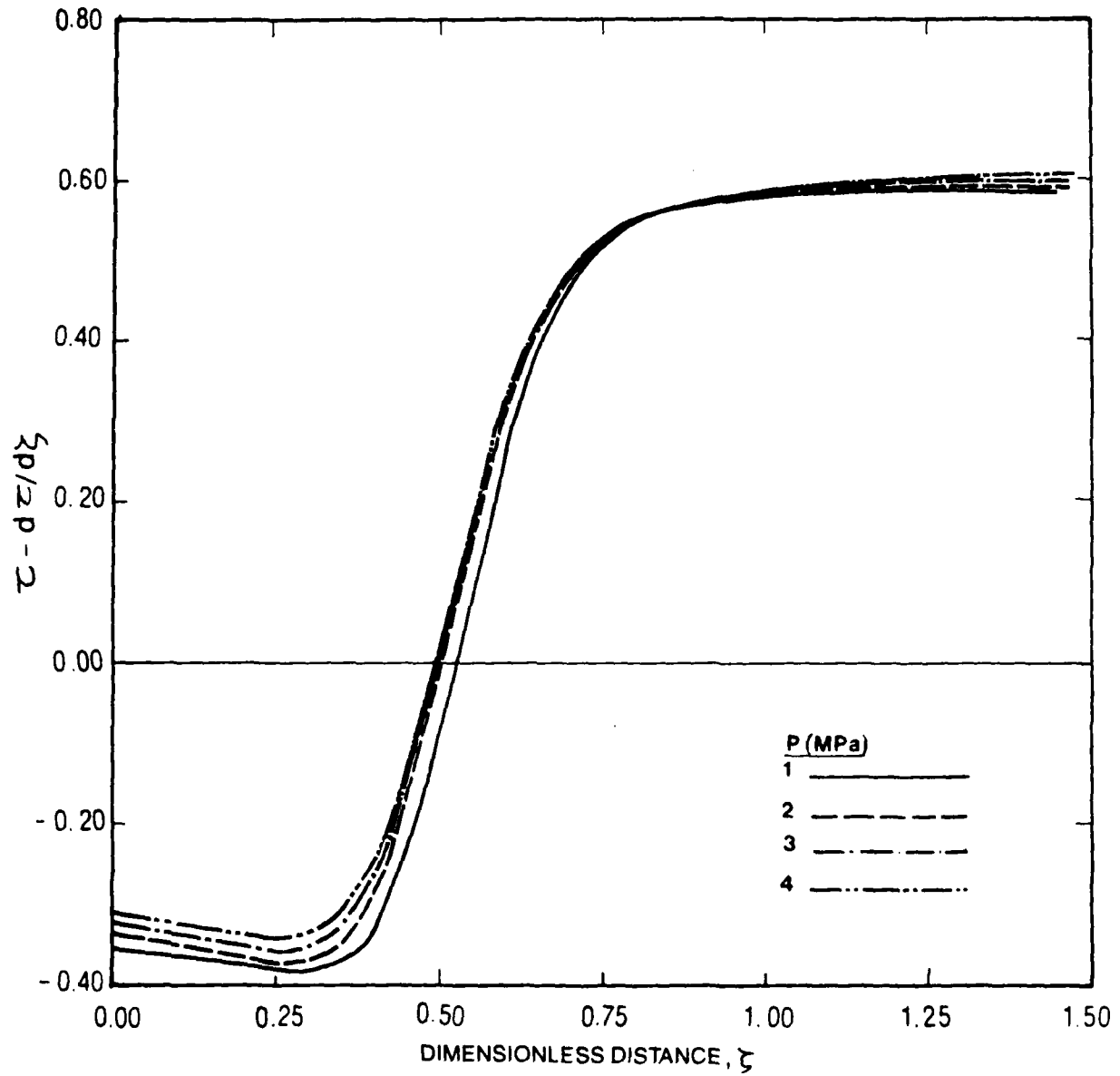
Fig. V. 21

Dimensionless total (convective and conductive) thermal enthalpy flux, τ-dτ/dζ, within the inner flame zone, as function of the dimensionless near field coordinate ζ.
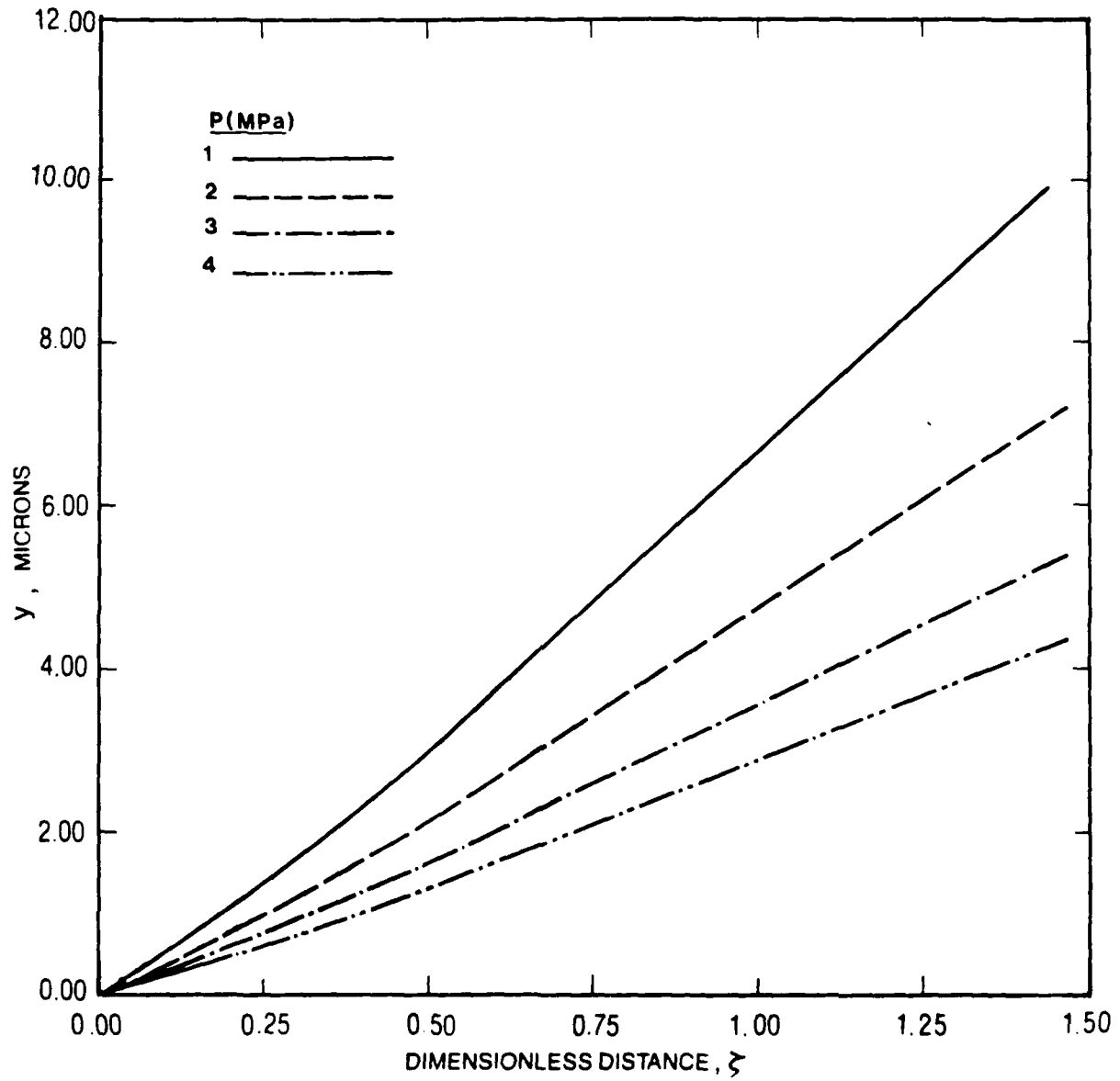
Fig. V. 22
Distance from the propellant surface y, as function of the dimensionless near field
coordinate, ζ . Increasing pressure brings about a decrease in the near field region
thickness.
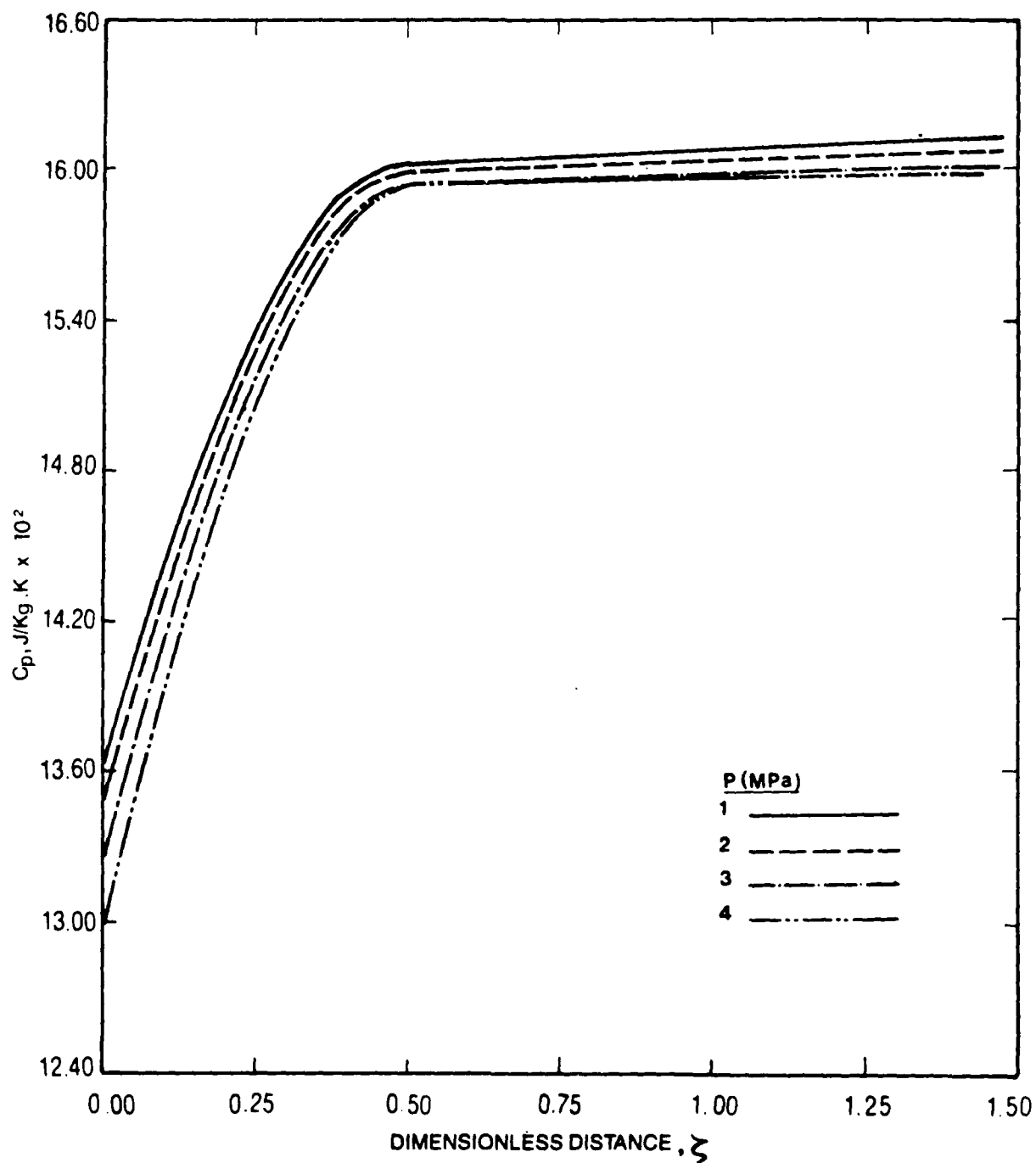
Fig. V. 23
Isobaric specific heat of the gas mixture, C_p, as function of the dimensionless near field coordinate, ζ
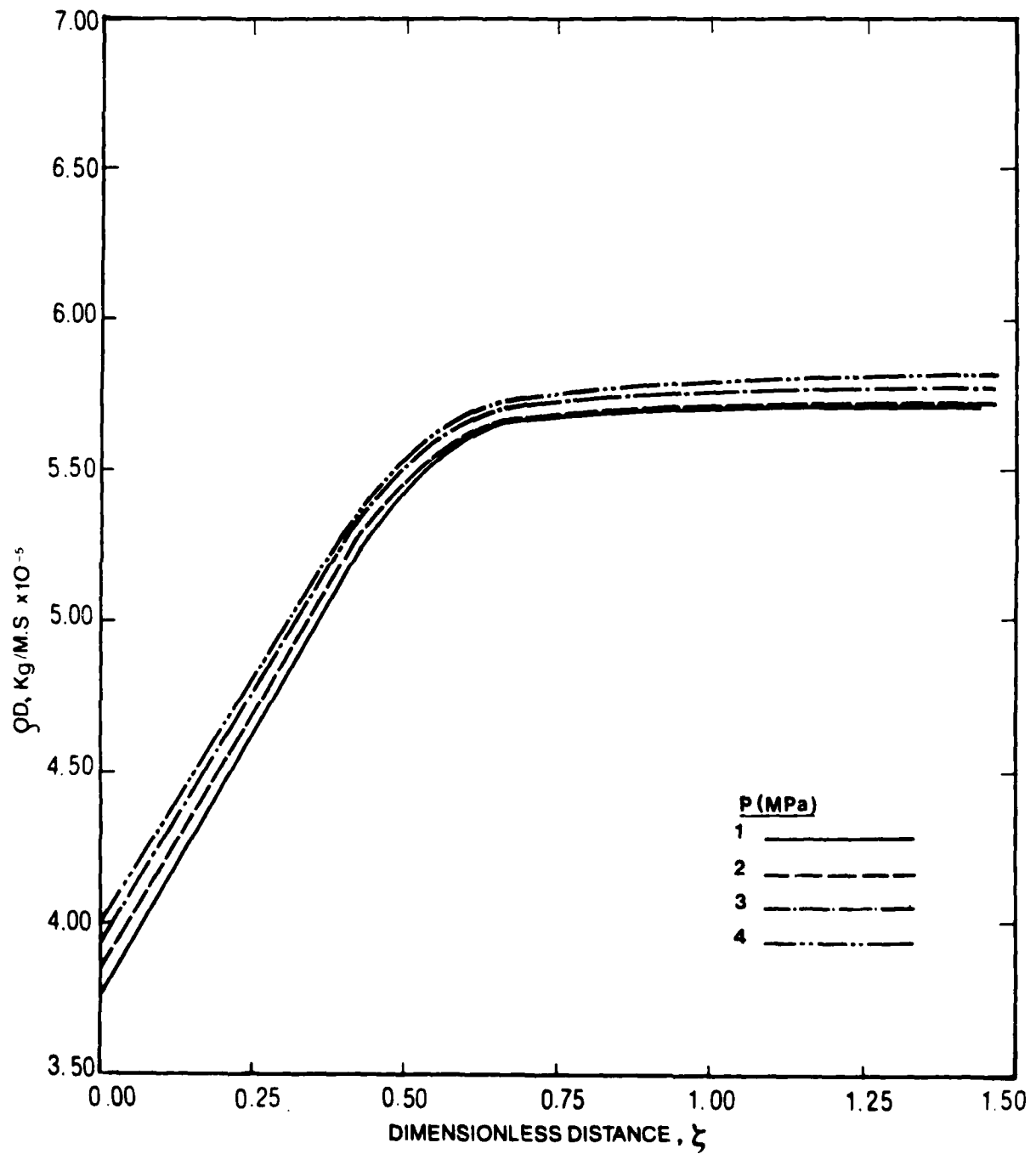
Fig. V. 24
Mean molecular diffusivity of the gas mixture, ρD, as function of the dimensionless near field coordinate.
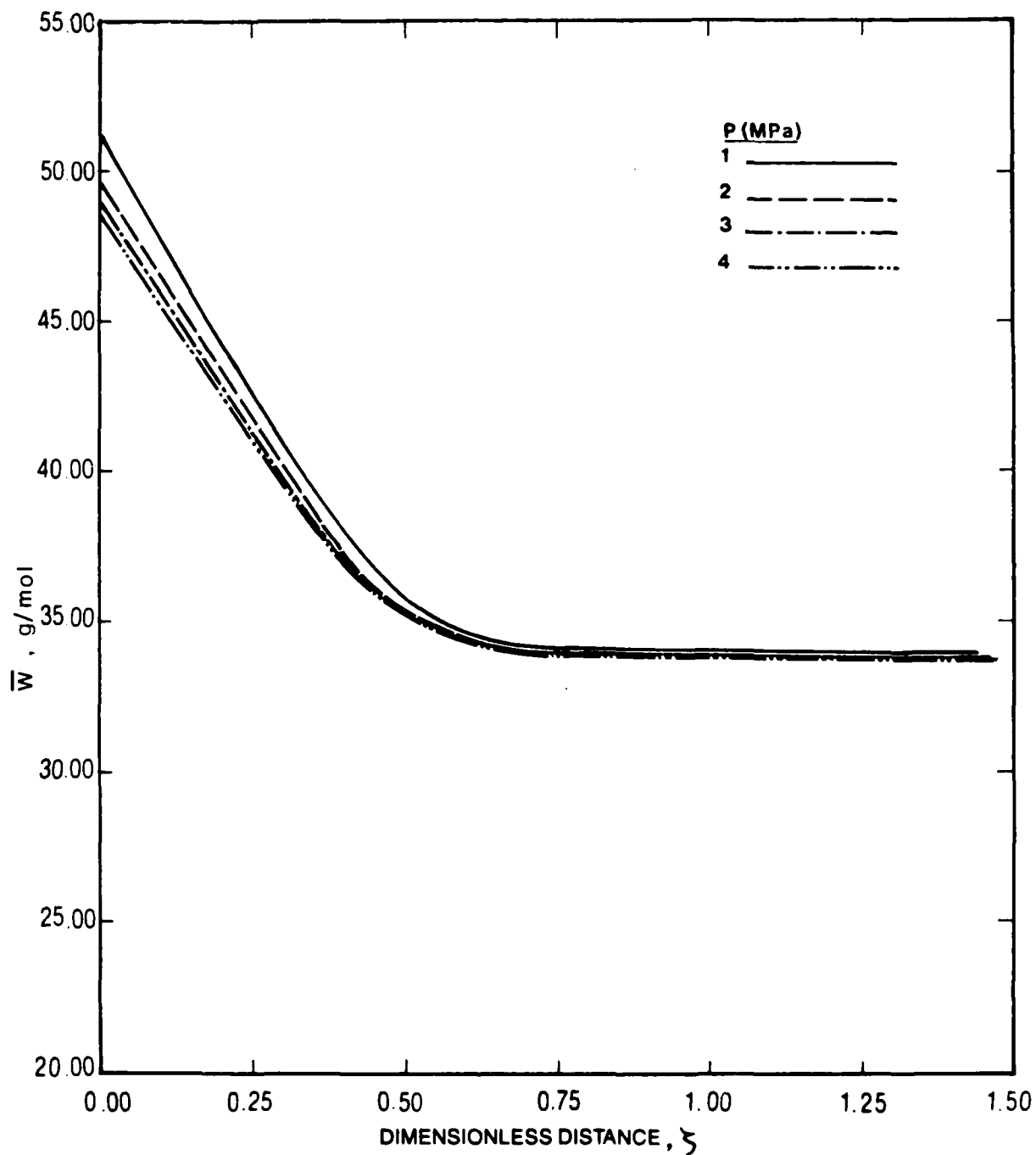
Fig. V. 25
Mean molecular weight of the gas mixture, as function of the dimensionless near field coordinate.
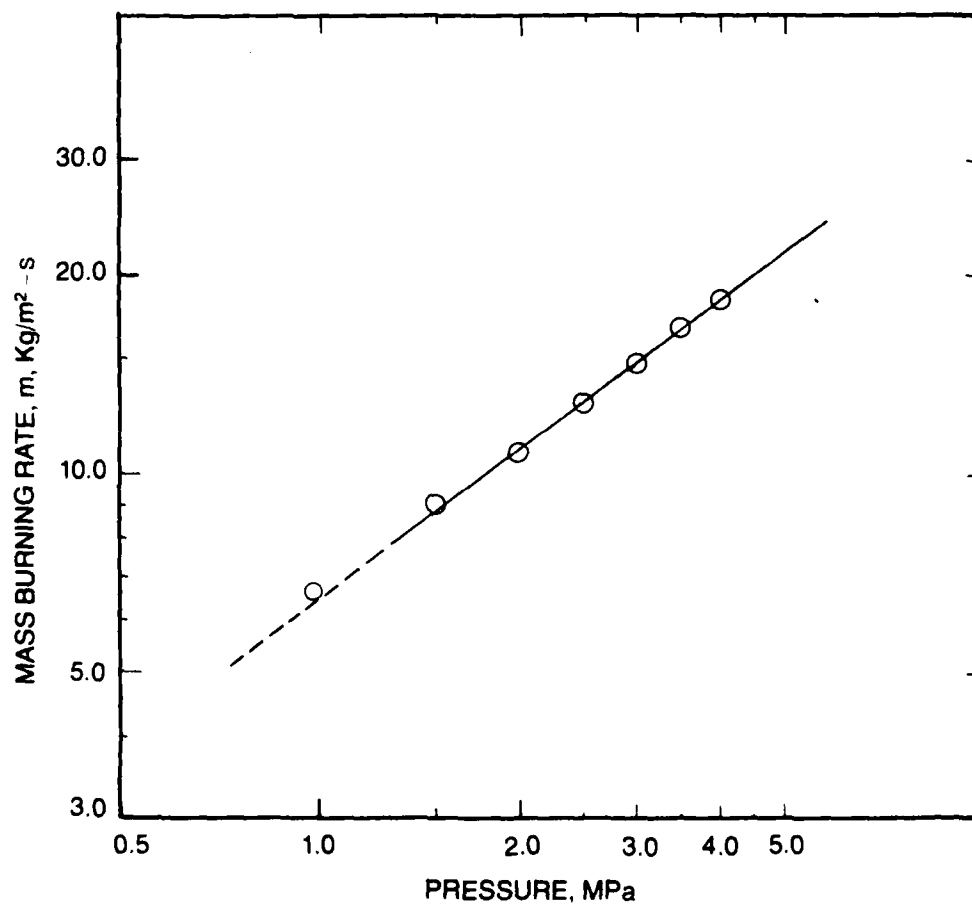
Fig. V.26
Logarithmic plot of the imposed mass flux vs. pressure, in the study of pressure dependent behavior. In the range of pressures considered, the exponent has a constant value, n = 0.75.

-220-
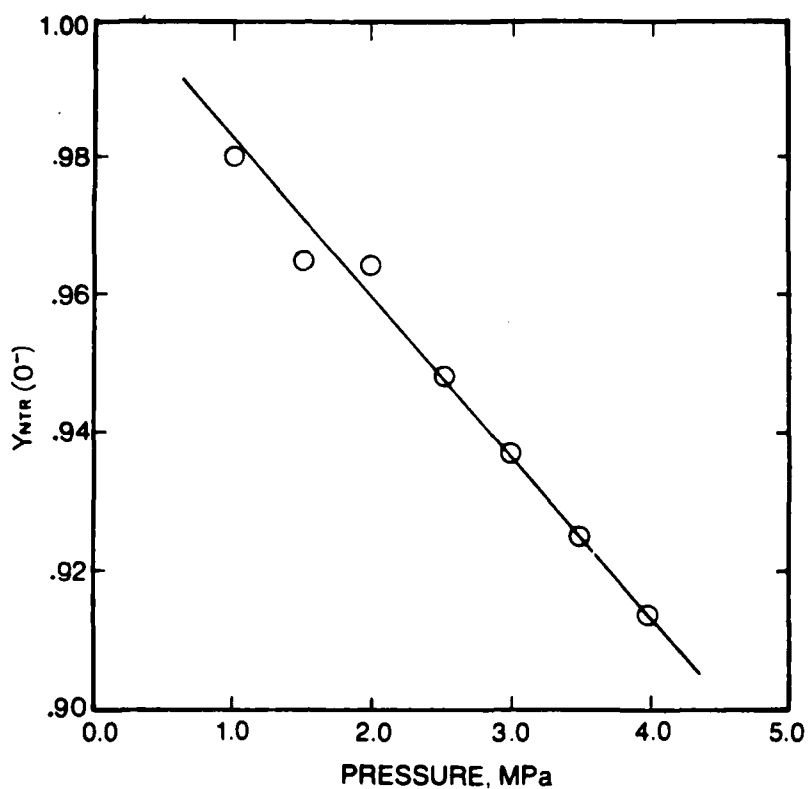
Fig. V.27a
Nitramine mass fraction on the liquid side of the liquid-gas interface vs. pressure, showing pronounced decrease with increasing pressure.
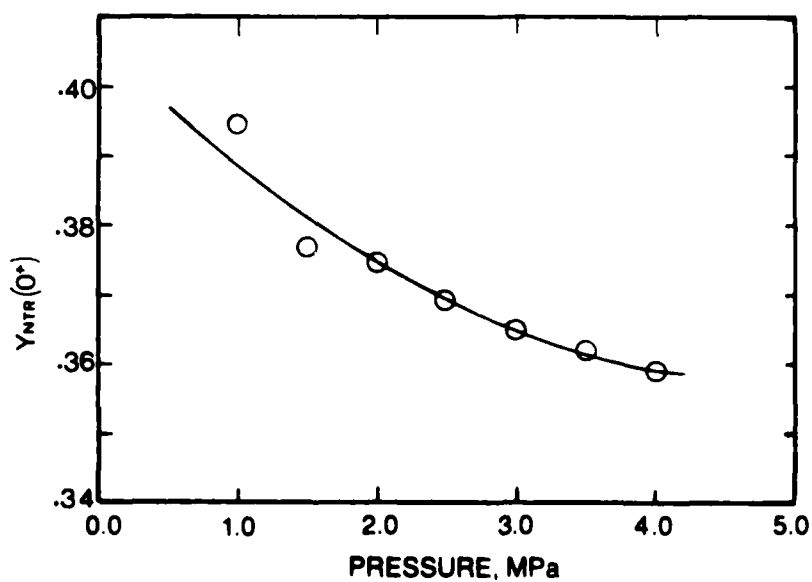
Fig. V.27b
Nitramine mass fraction on the gas side of the liquid-gas interface vs. pressure, showing relatively small decrease as pressure is increased.
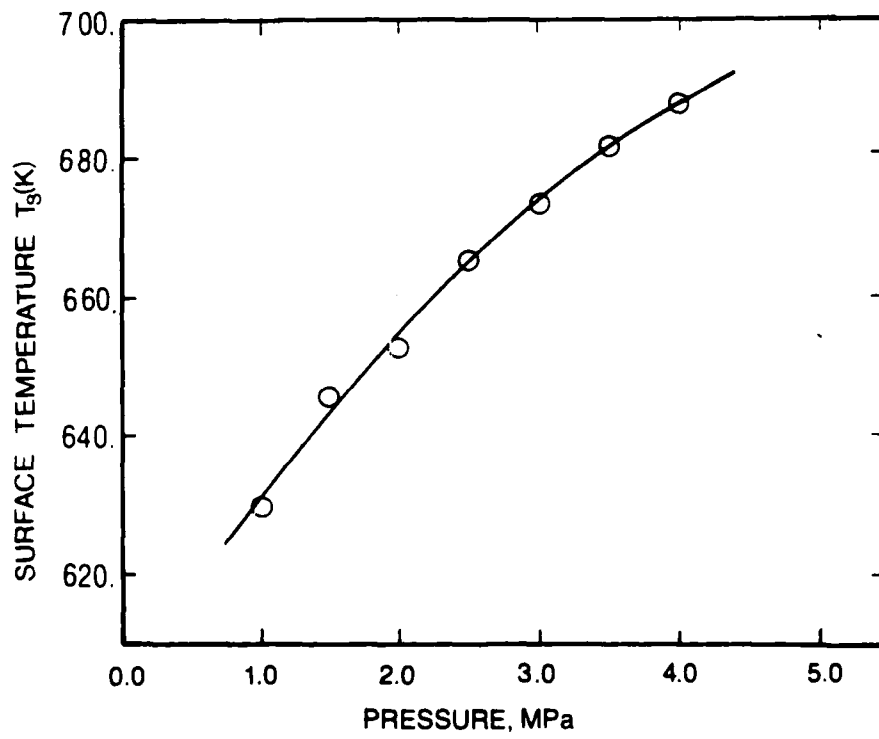
Fig. V.28
   Calculated surface temperature vs. pressure for converged solutions, showing T$_s$ to increase with pressure in a decelerating manner.
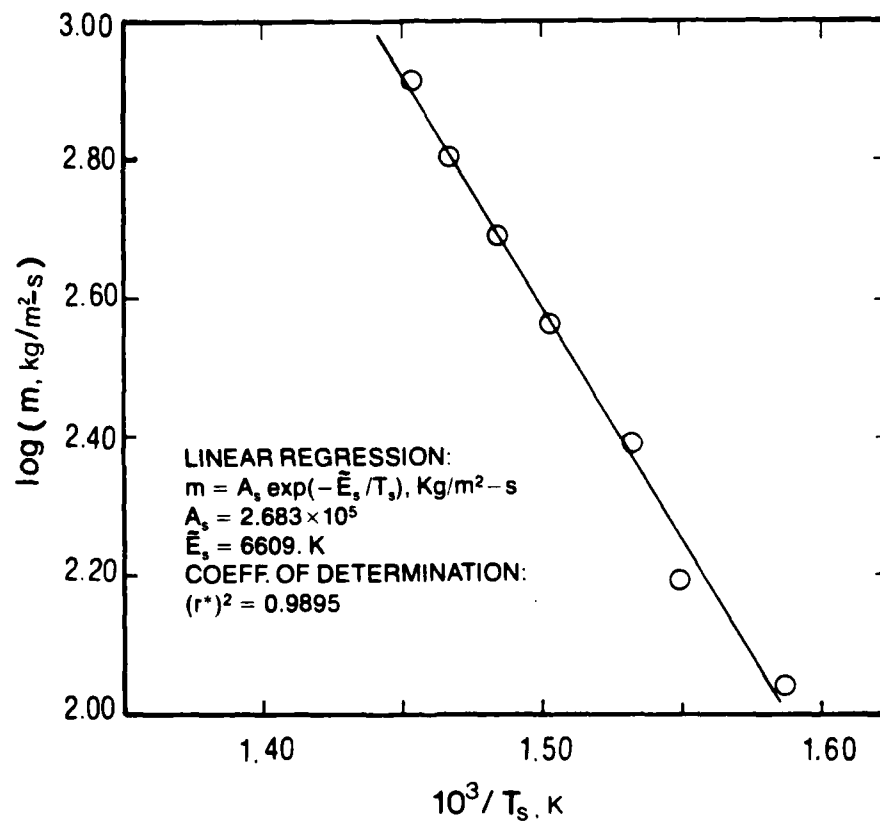
Fig. V.29
Correlation of the imposed mass flux logarithm with the inverse of the calculated surface temperature obtained from converged solutions. An Arrhenius type relationship is demonstrated, although no surface pyrolysis term was included in the model.
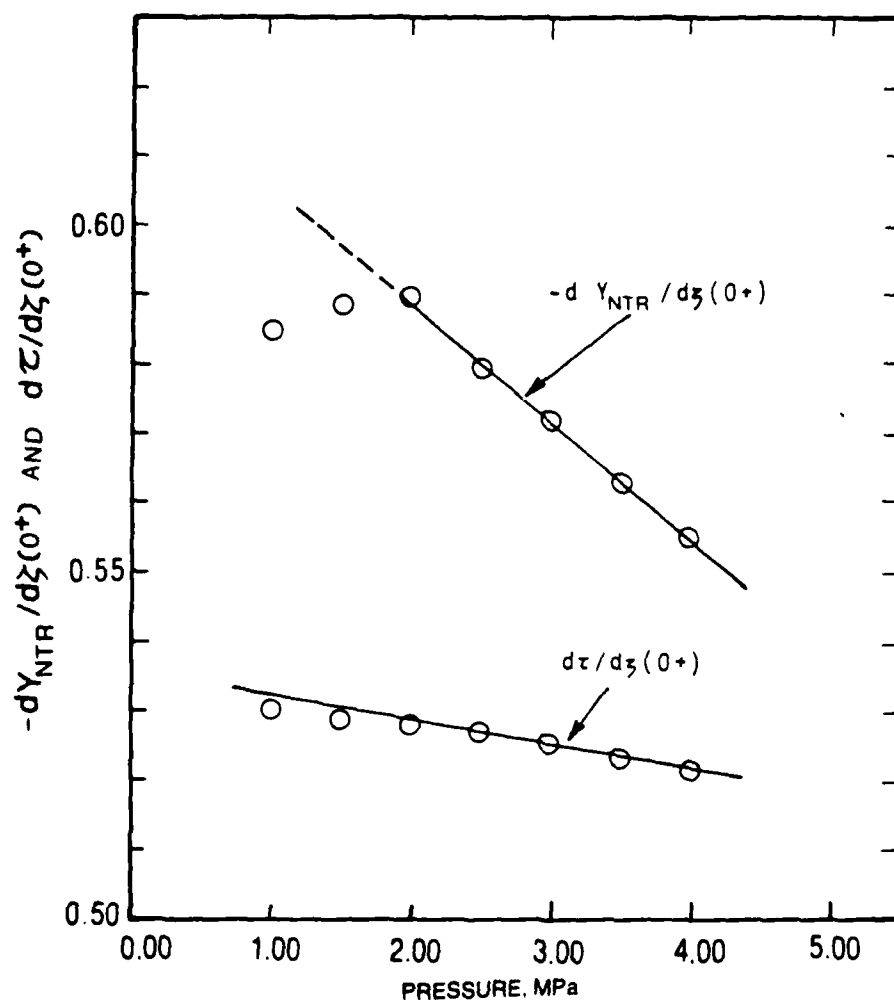
Fig. V.30

Dimensionless spatial enthalpy and nitramine mass fraction gradients on the gas side of the liquid-gas interface vs. pressure. Both parameters tend to decrease linearly with p, the thermal gradient being appreciably slower. The maximal deviation of the two low-pressure points from the upper line drawn is 3%.
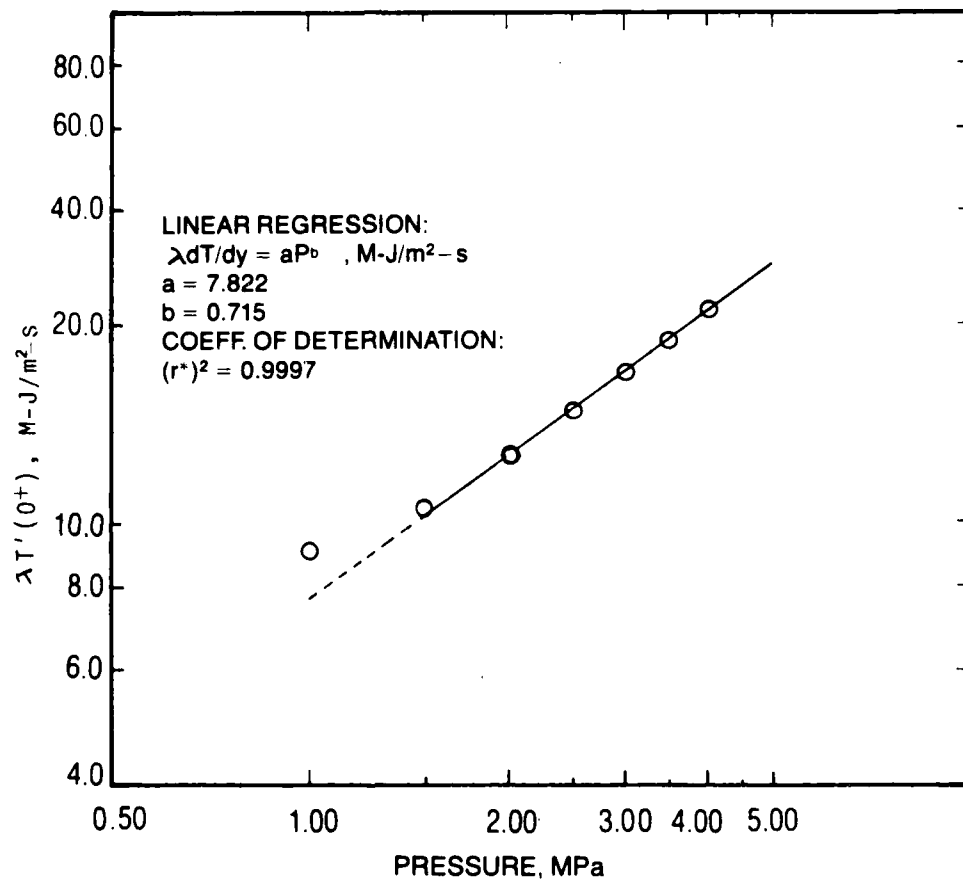
Fig. V.31

Logarithmic plot of the conducted heat feedback from the gas to the liquid surface vs. pressure. excellent linear correlation is demonstrated, with a pressure exponent of 0.715, close to that of the mass burning rate (n=0.75) cf. Fig. V.26.
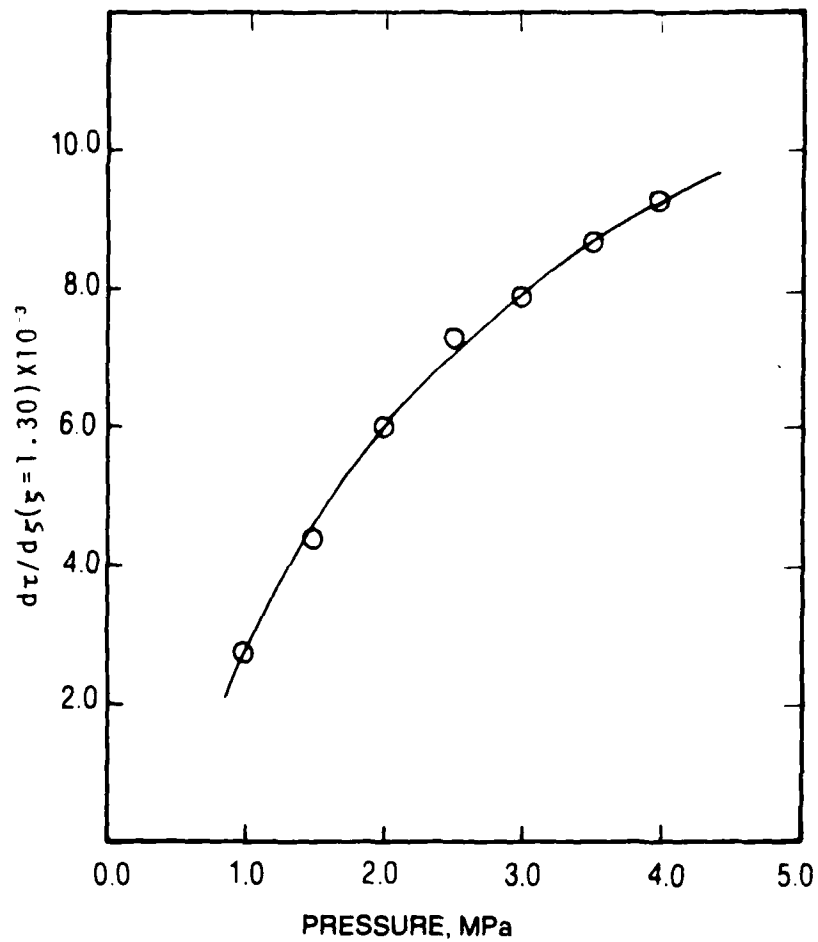
Fig. V.32

Dimensionless thermal enthalpy gradient at a fixed downstream position in the gas vs. pressure. In contrast to $d\tau/d\varsigma(0^{\cdot})$ which decreases slowly with P, cf. Fig. V.30, the dimensionless gradients toward the end of the near field tend to increase with P, as predicted by the asymptotic analysis of Chap. *III*.
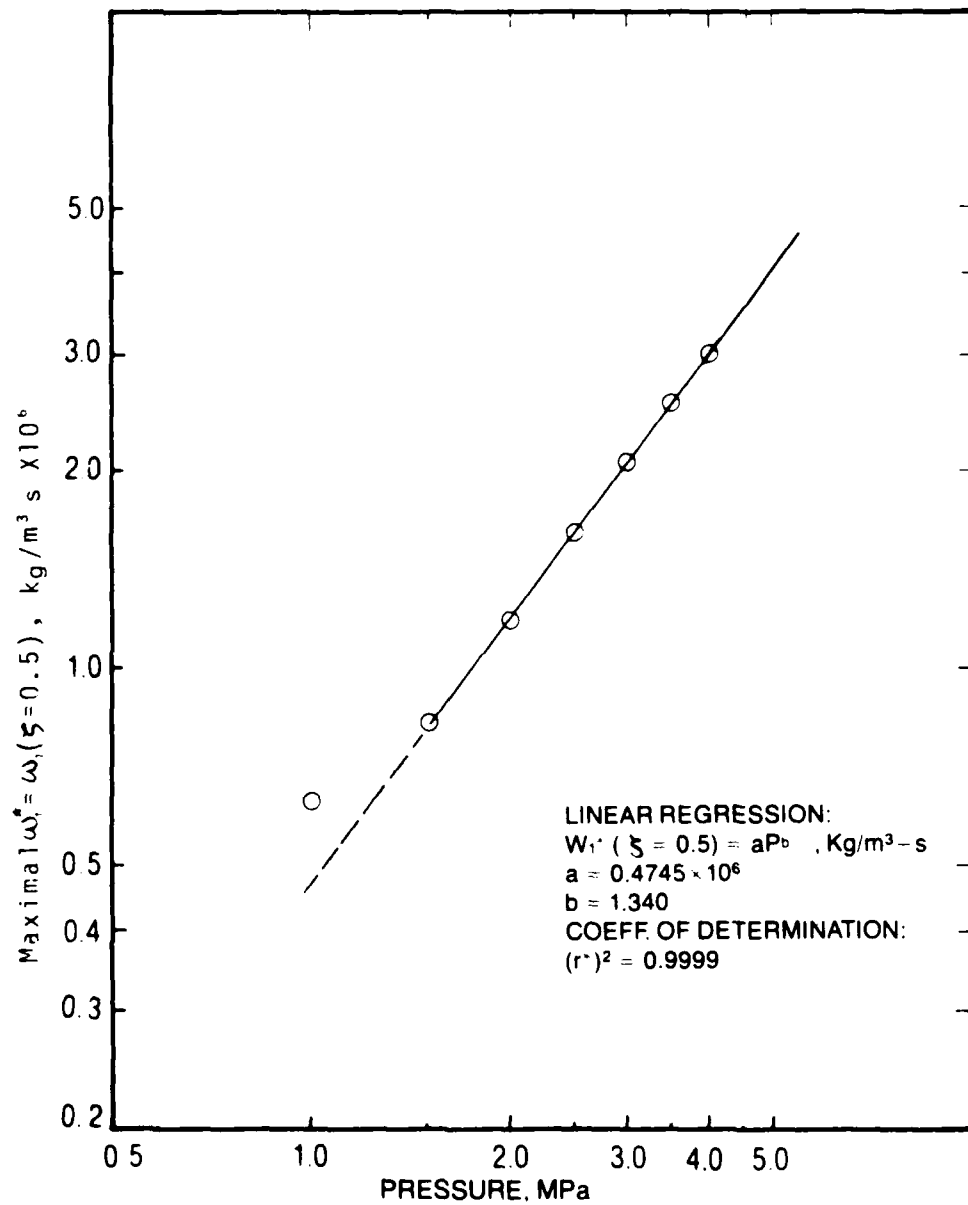
Fig. V.33

Logarithmic plot of the primary reaction rate at its maximum (ζ = 0.5, as shown in Fig. V.14) vs. pressure. A uniform pressure dependence is demonstrated by the linear correlation. The pressure exponent of 1.34 is larger than unity, explained by the induced thermal effect of the secondary reaction within the near field.
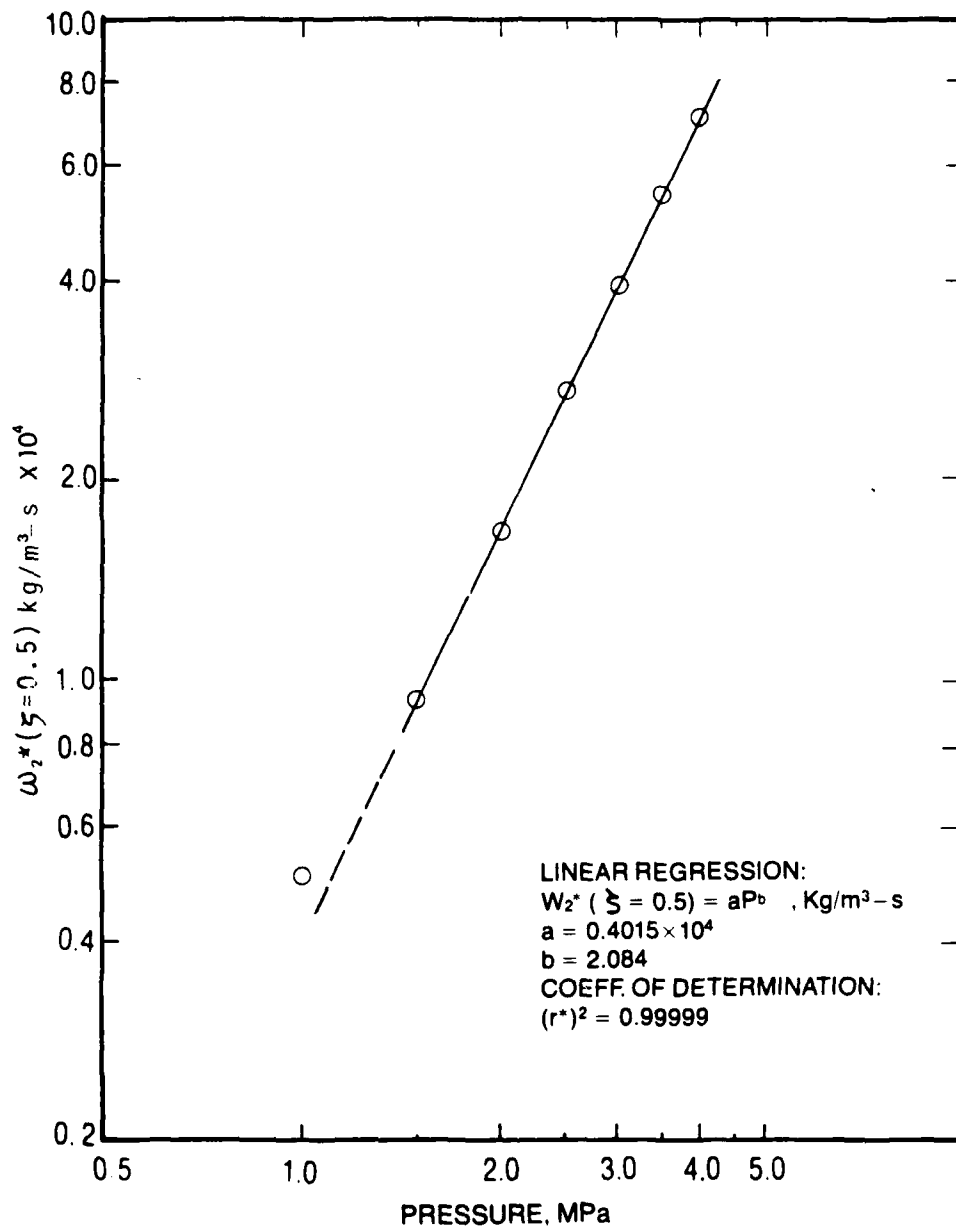
Fig. V.34
Logarithmic plot of the secondary reaction rate at $\zeta = 0.5$ vs. pressure. The linear correlation obtains a pressure exponent close to the overall second order imposed, not affected by the presence of the primary reaction.

LINEAR REGRESSION:
$\varepsilon = aP^b$
$a = 5.018 \times 10^{-3}$
$b = 0.6260$
COEFF. OF DETERMINATION:
$(r^*)^2 = 0.9940$
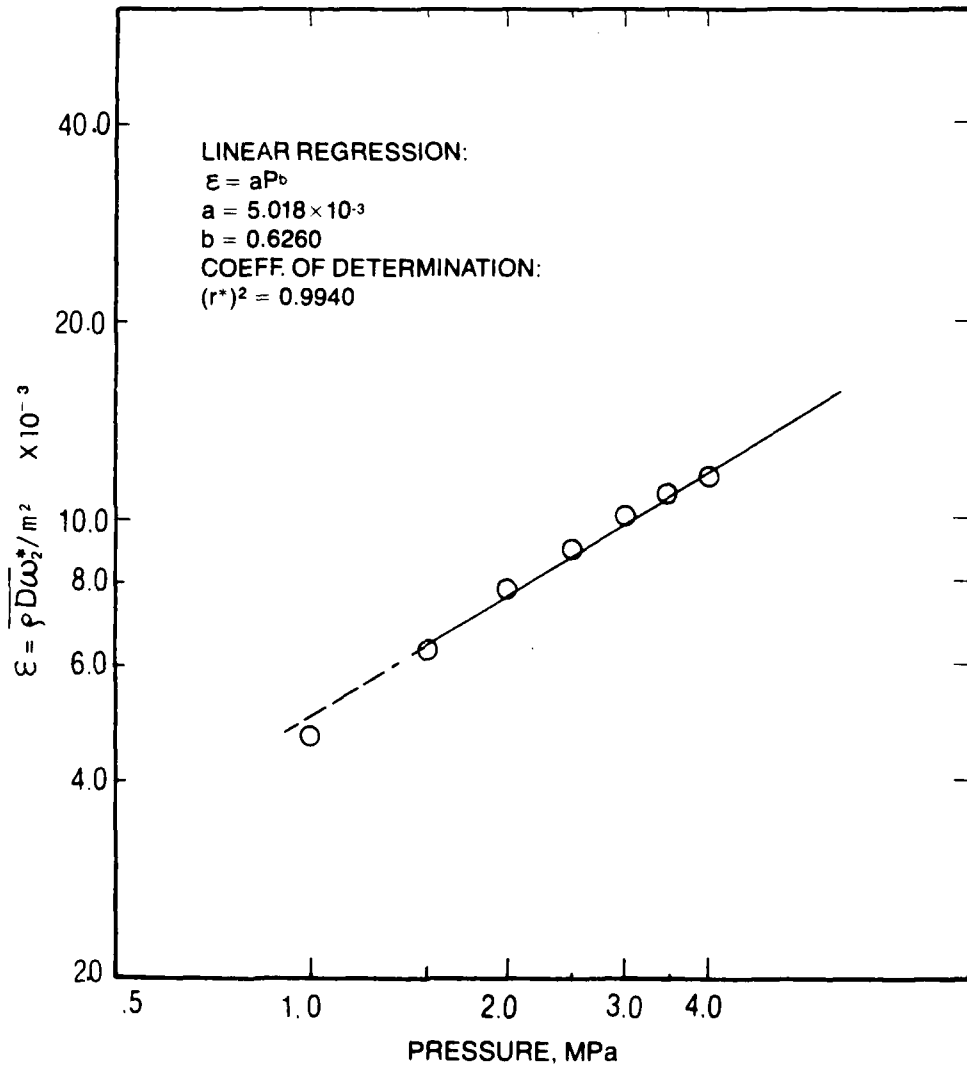
PRESSURE, MPa

Fig. V.35

Logarithmic plot of the small perturbation quantity $0 < \varepsilon \ll 1$ of the asymptotic deflagration analysis vs. pressure. Calculation was made with $W_2(\zeta = 0.5)$ and ε is shown to increase with pressure, verifying the predictions of Chap. *III* regarding the tendency to breakdown of the asymptotic assumptions at high pressures.
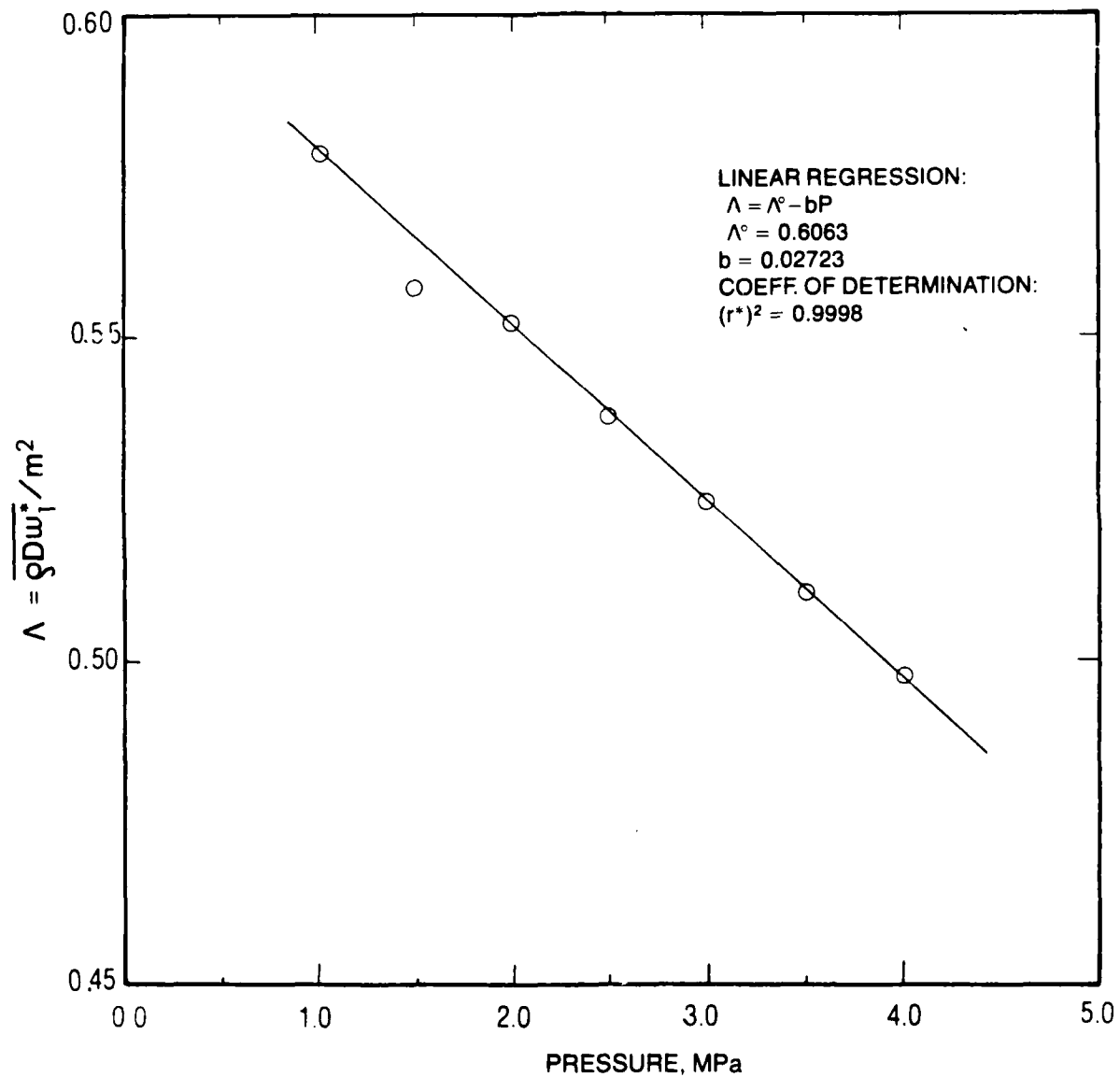
Fig. V.36
The flame speed eigenvalue calculated with W_1 ($\zeta = 0.5$) vs. pressure. This parameter is shown to decrease slowly with increasing P in a linear manner. The $\Lambda° = $ const is due to zeroth order near field effect, whereas the pressure decrement is a contribution of a first order effect by the secondary reaction.

TURBULENT CORE FLOW REGION
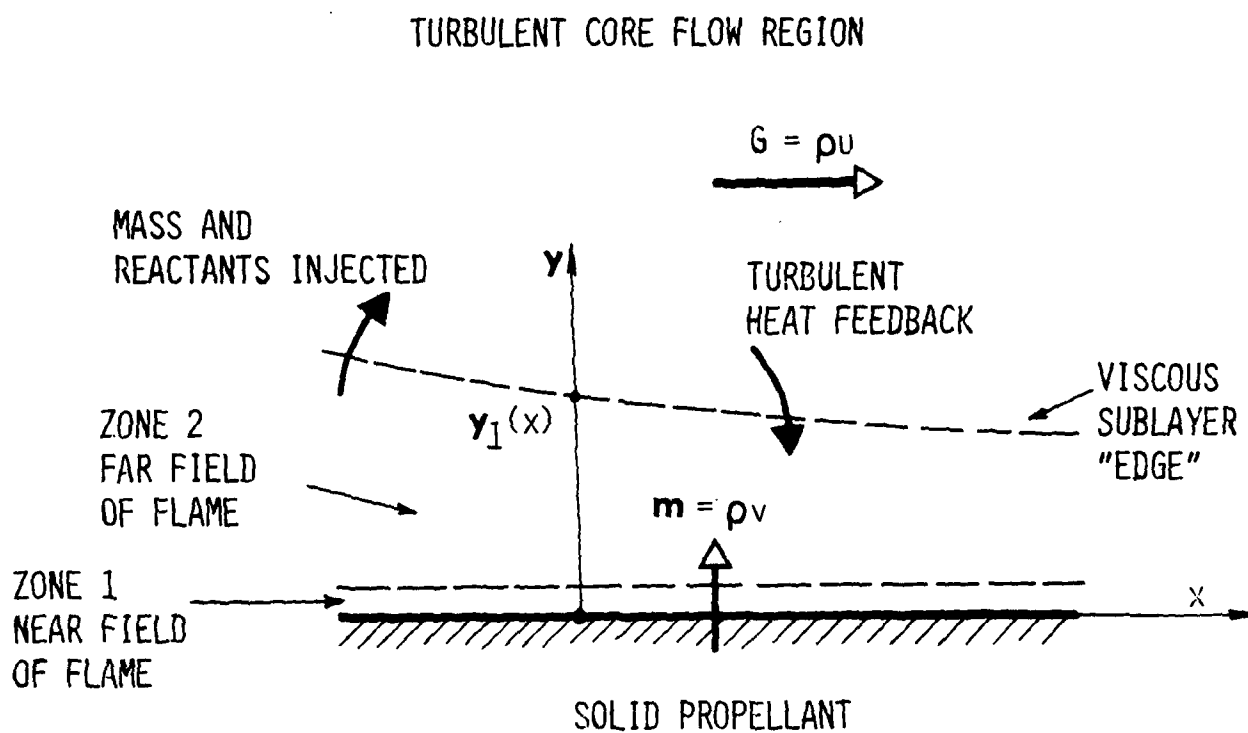
Fig. VI.1a Schematic diagram of the viscous sublayer configuration adjacent to the burning propellant surface. The viscous sublayer edge is defined approximately as the point where the interior velocity matches the intermediate (viscous-turbulent) velocity scale.
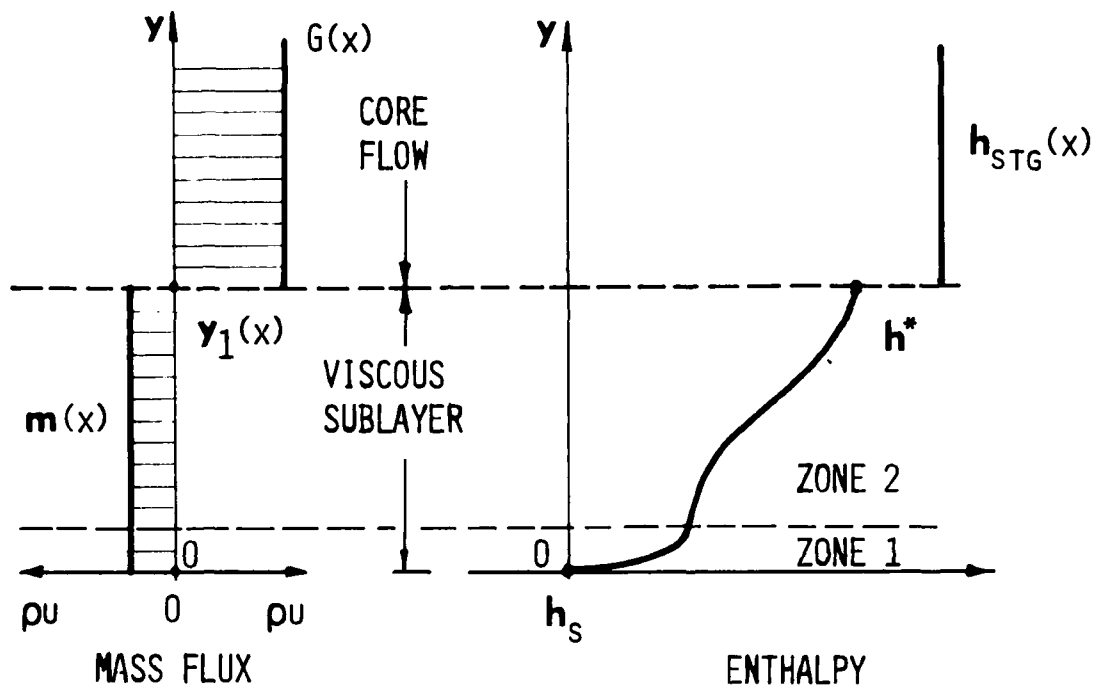
Fig. VI.1b Velocity and enthalpy distributions in the idealized sublayer and core configuration, showing the quasi-one dimensional sublayer (u = 0 within) and core flow (mass injection considered as distributed sources).
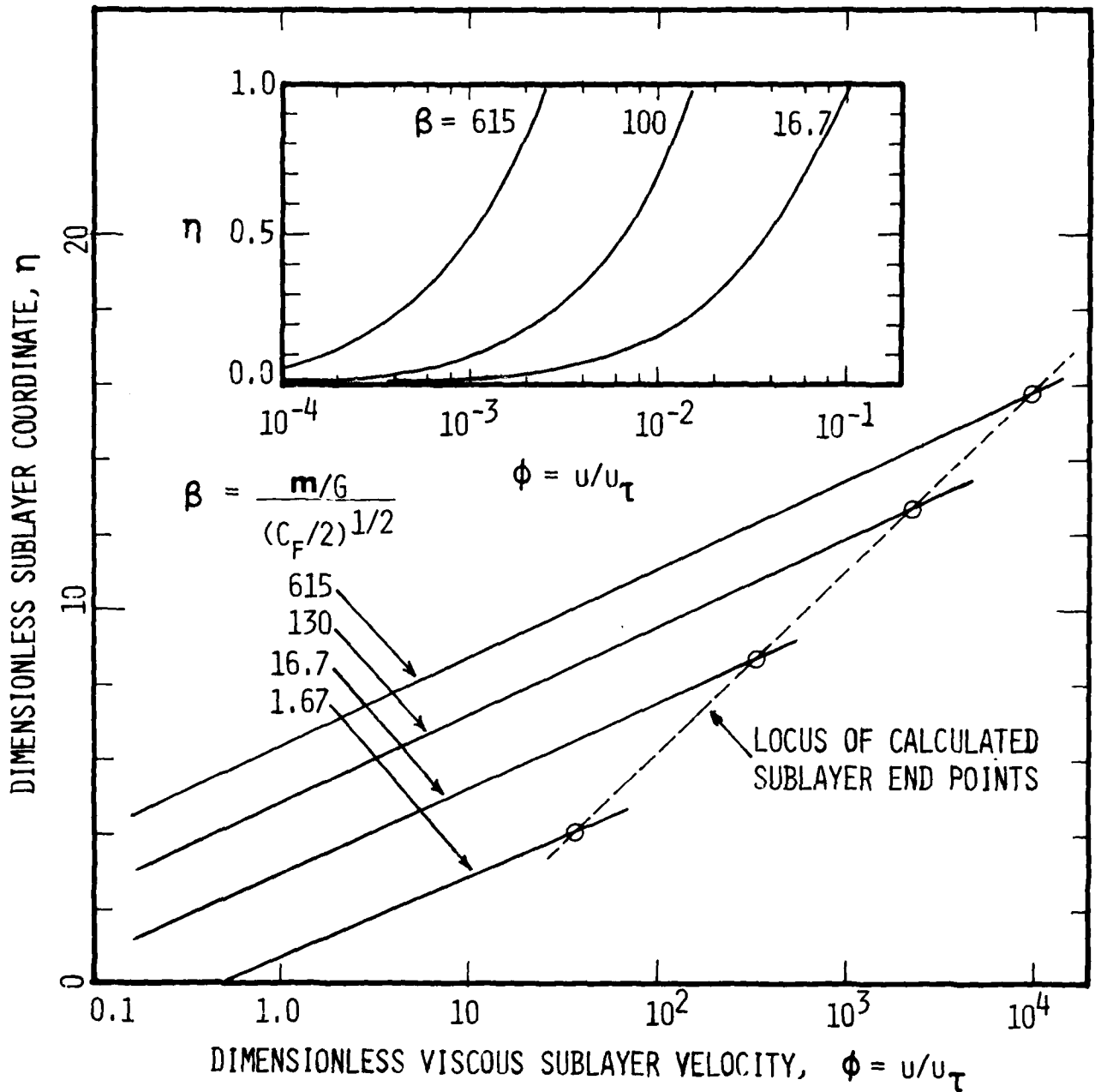
Fig. VI.2 Dimensionless tangential velocity profiles in the blown viscous sublayer at three values of the sublayer transfer number, β. The frictional velocity $u_\tau^2 \equiv \tau_w/\rho_0$ used as reference is for the blown layer. Calculated values of (η,ϕ) at the layer "edge" are shown to vary linearly on the scale used.
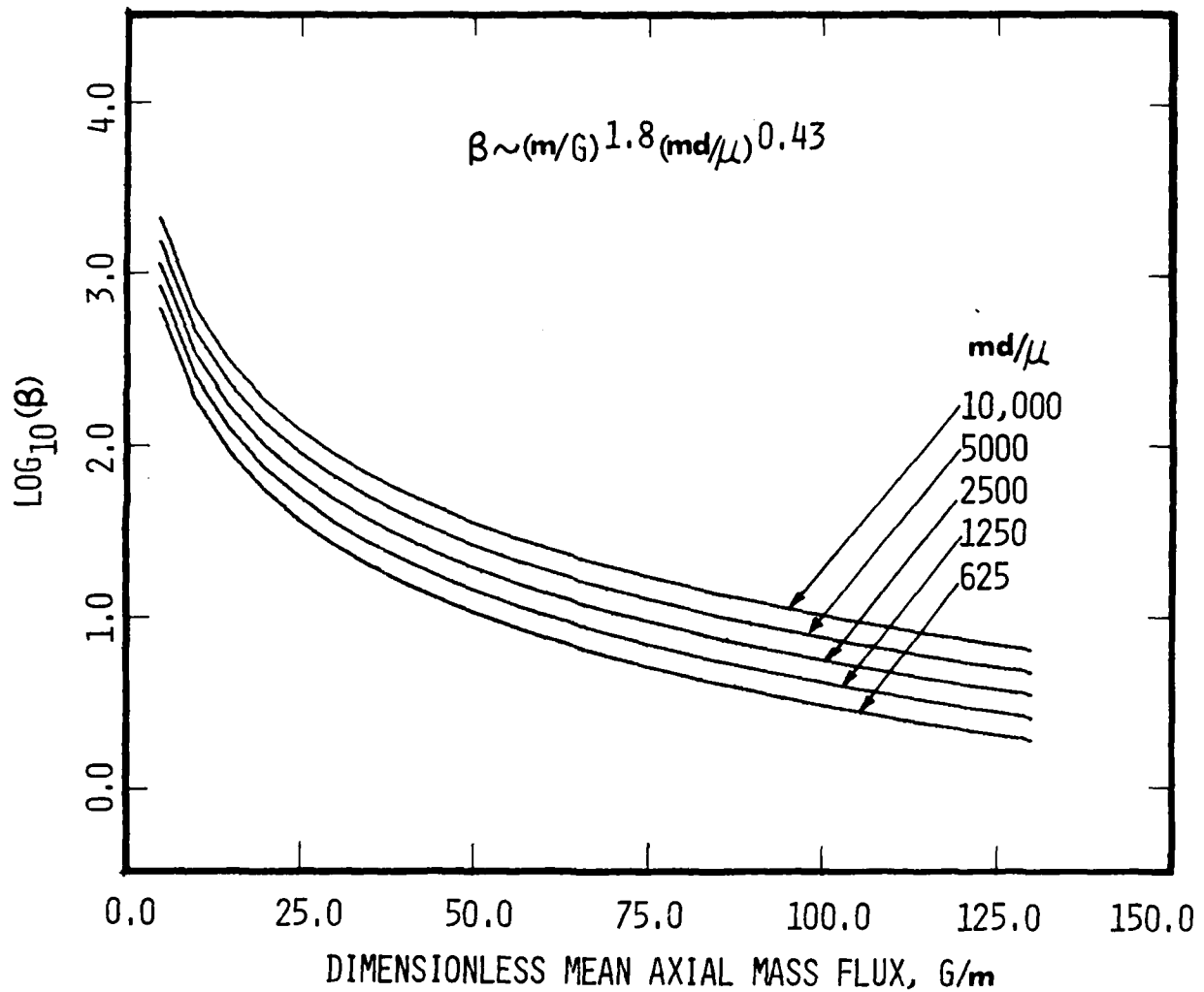
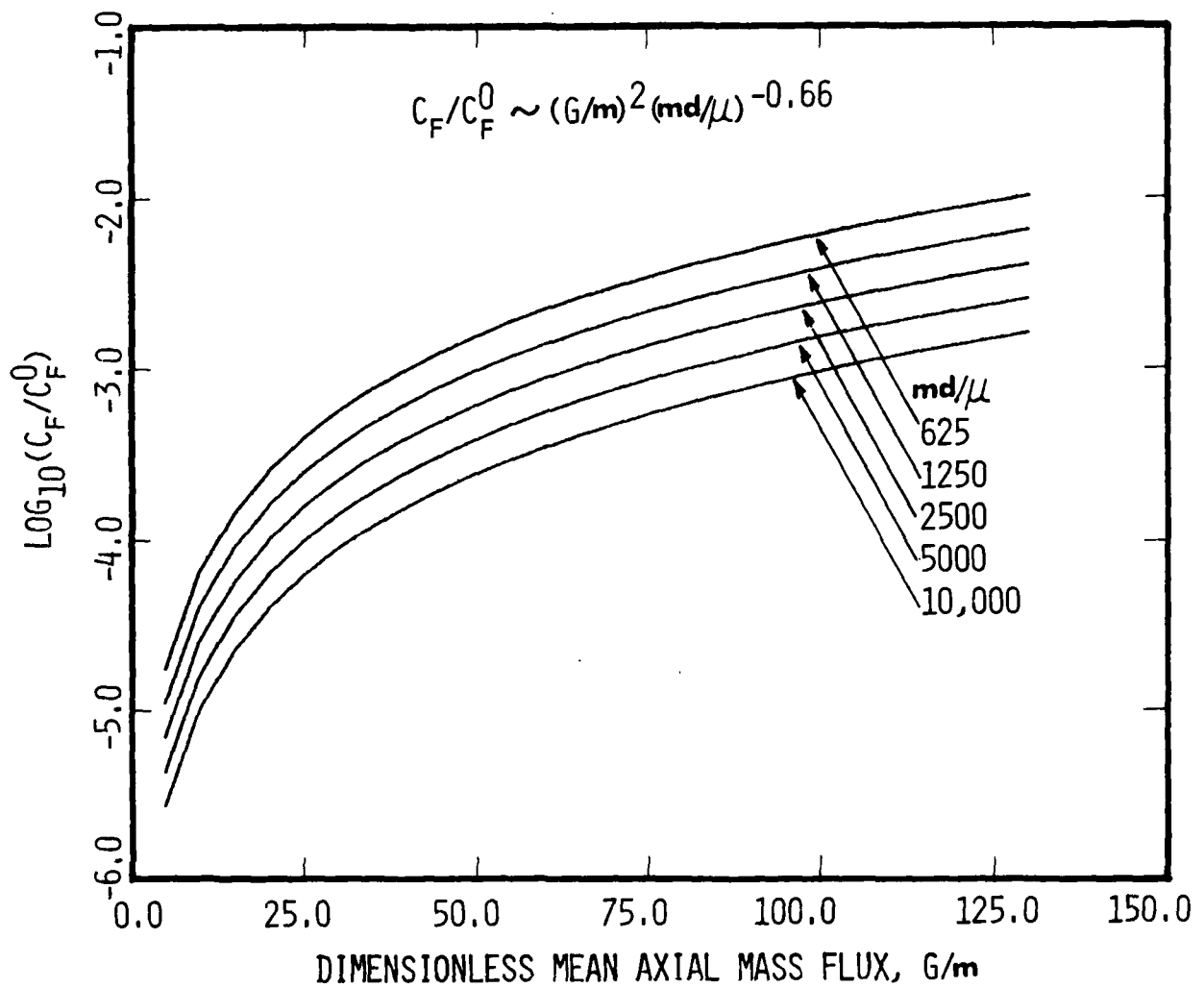Fig. VI.3 The viscous sublayer transfer parameter versus G/m, at various values of the blowing Reynolds number, md/μ. The hyperbolic behavior is due to $\beta \sim (m/G)^{1.8}$.

Fig. VI.4 The blown friction coefficient ratio versus G/m at various values of the blowing Reynolds number, md/μ. The parabolic behavior is due to $C_f/C_f^0 \sim (G/m)^2$.
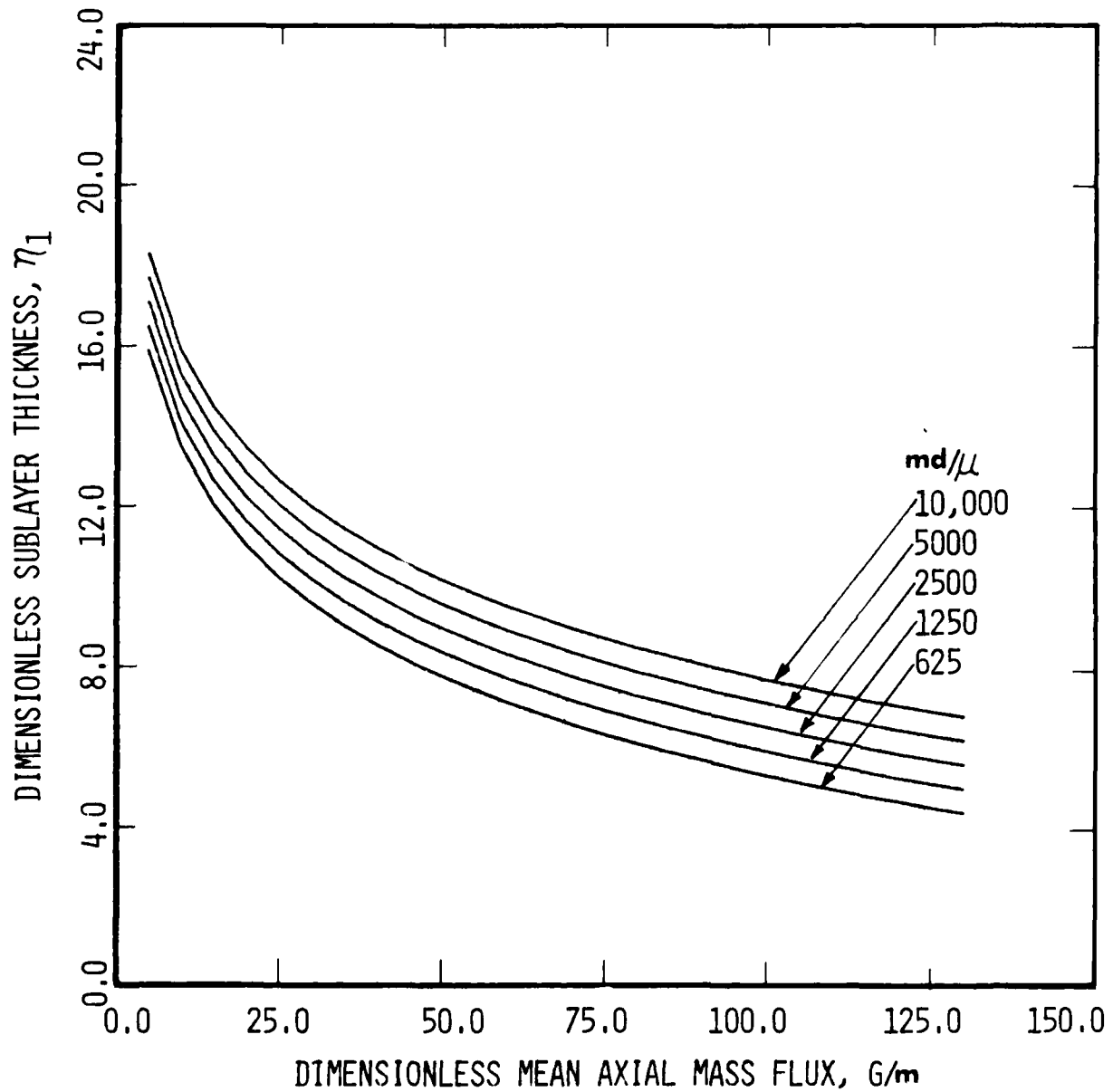
Fig. VI.5 The dimensionless blown sublayer thickness η_1 versus G/m, at various values of the blowing Reynolds number, $\dot{m}d/\mu$. The behavior of η_1 follows the logarithmic-scale variation of β.
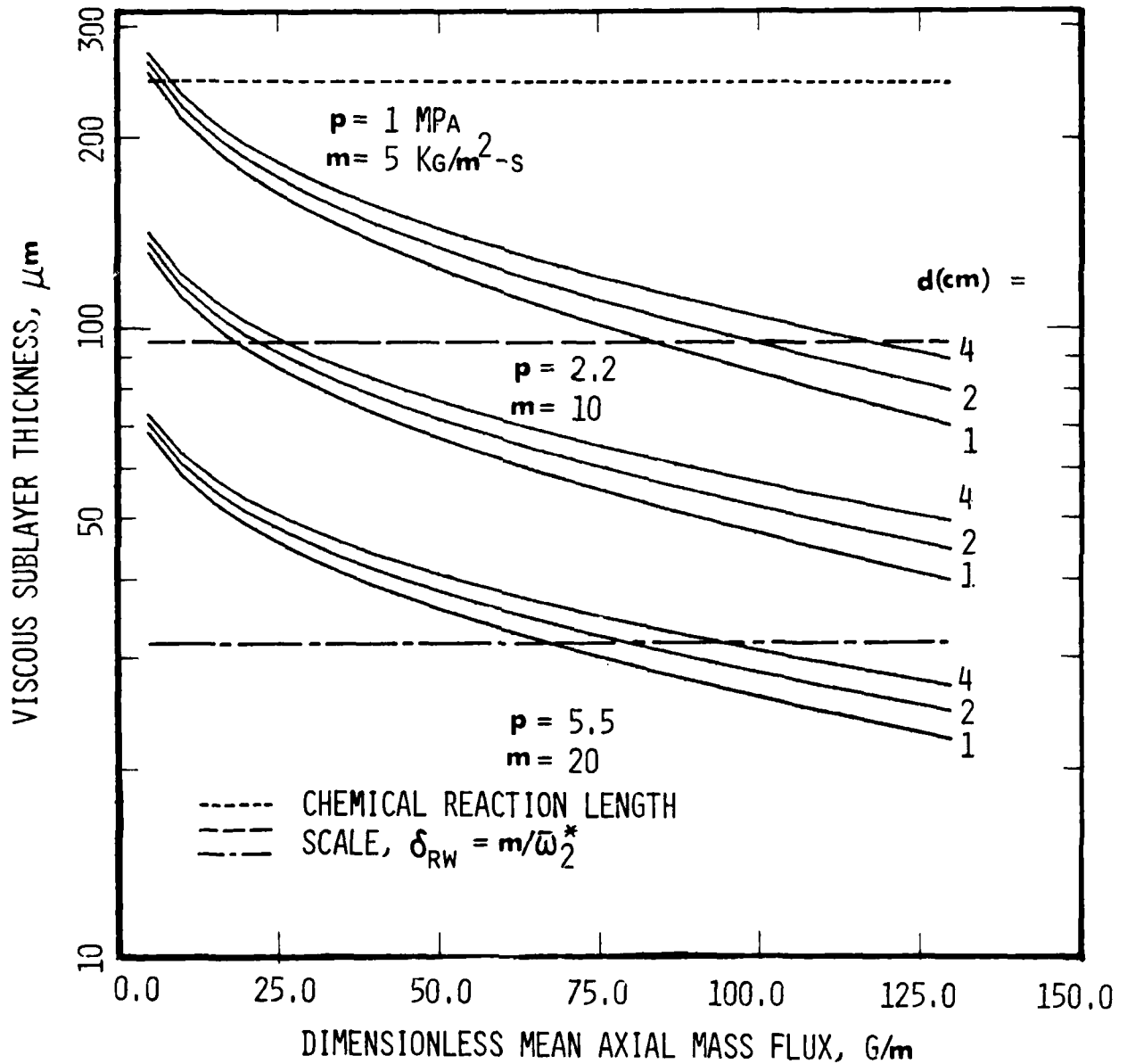
Fig. VI.6 The viscous sublayer thickness, $y_1 = (\mu/m)\eta_1$ versus G/m at various blowing rates and port diameters,(m , d). The chemical reaction length scales δ_{RW} are overplotted, at pressures corresponding to the values of m (p) used. The intersection points between y_1 and δ_{RW} shift to higher values of G/m as pressure increases, since δ_{RW}(p) decreases faster than $y_1\left[m(p)\right]$.
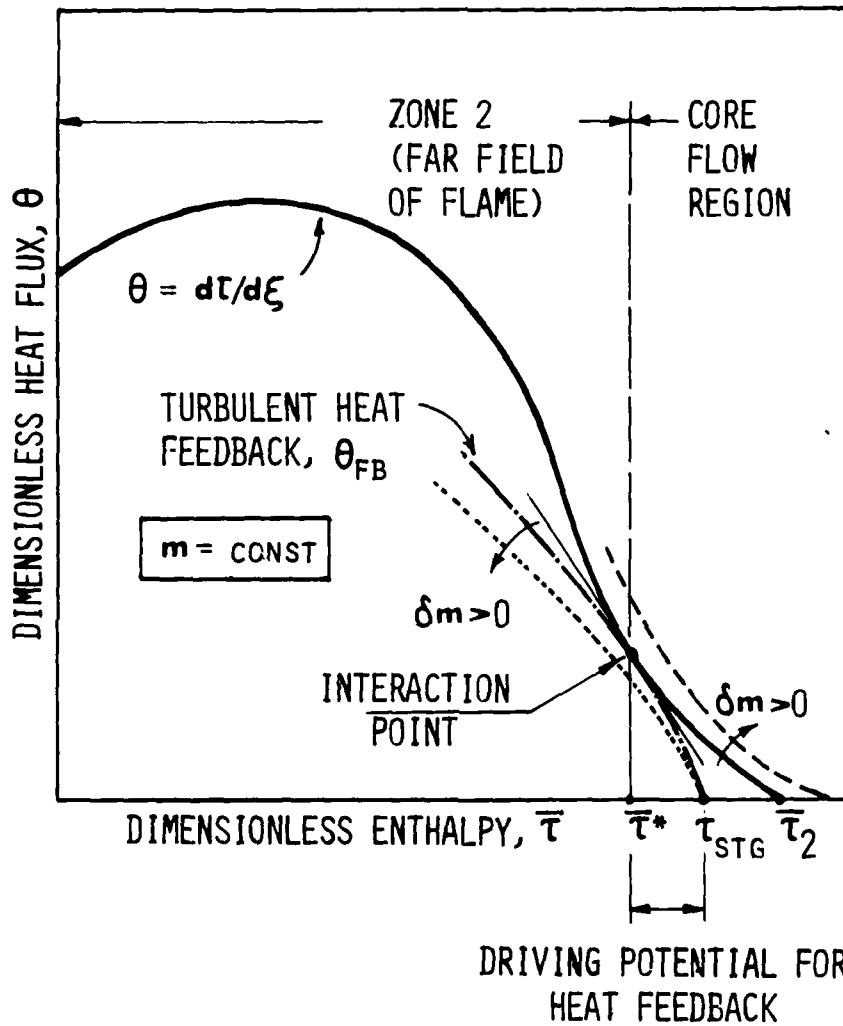
Fig. VI.7 Schematic diagram of the heat flux distribution in the sublayer and the turbulent heat feedback as functions of enthalpy, at a particular perturbed burning rate, m, for which the interaction conditions are satisfied.
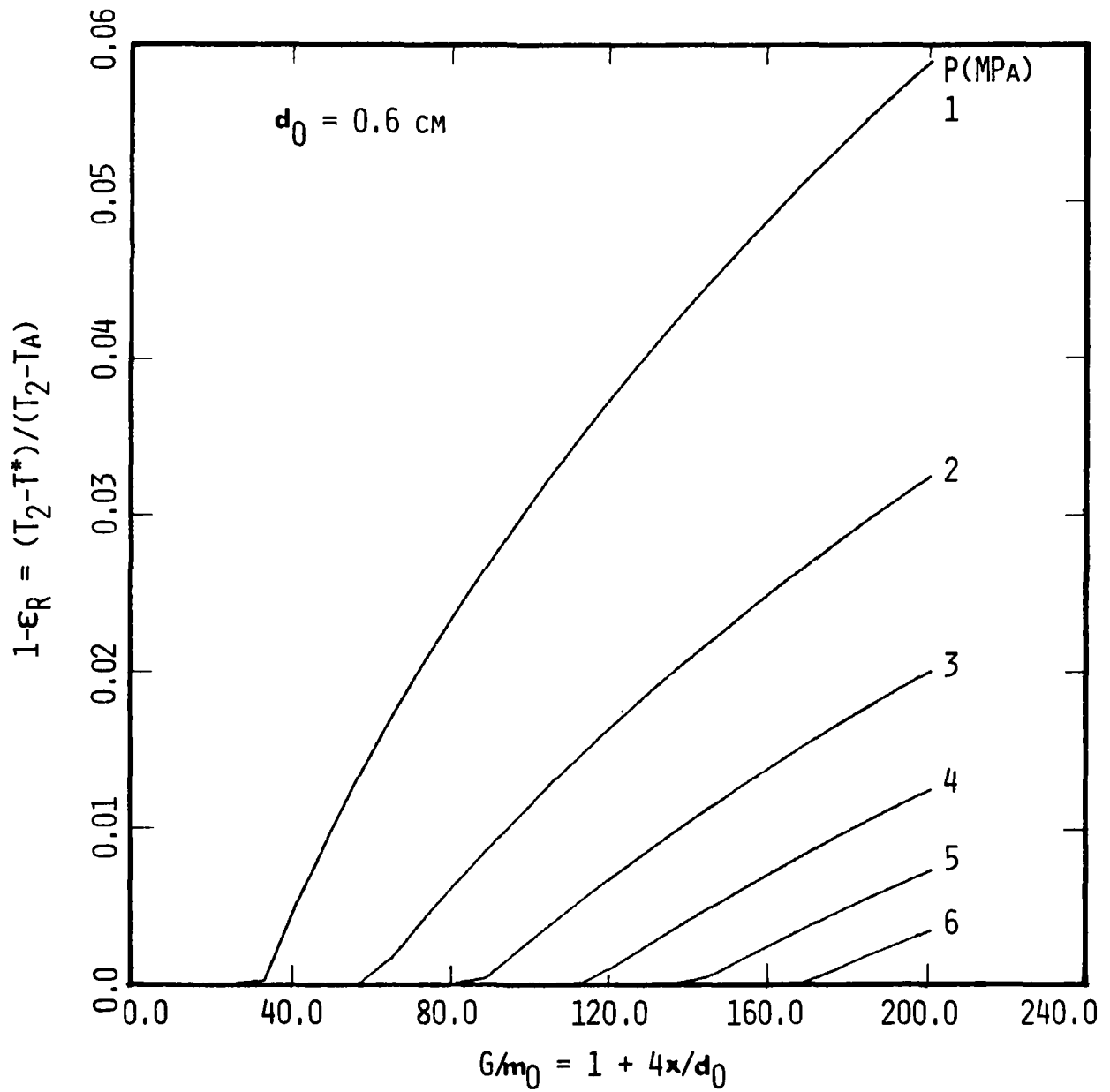
Fig. VI.8 Fraction of reactant injected, expressed in terms of the reduced cutoff enthalpy, versus dimensionless mean axial mass flux, at various pressures. Increasing the chamber pressure results in higher threshold values of G/m_0 and lower interaction.
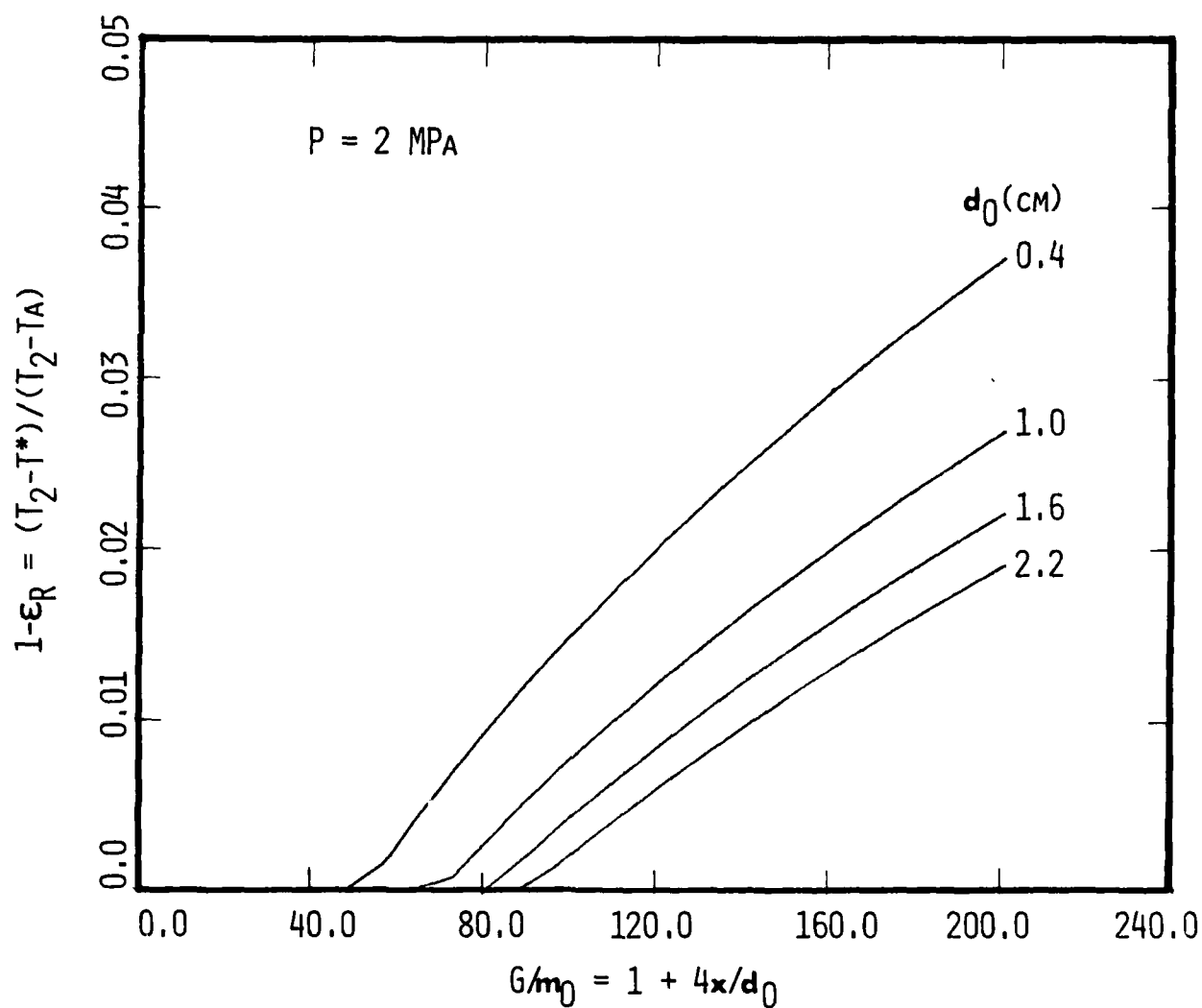
Fig. VI.9   Fraction of reactant injected versus mean dimension-less axial mass flux at various chamber diameters. Increasing the diameter has an effect similar to pressure increase in that interaction is decreased and the threshold G/m_0 increases.
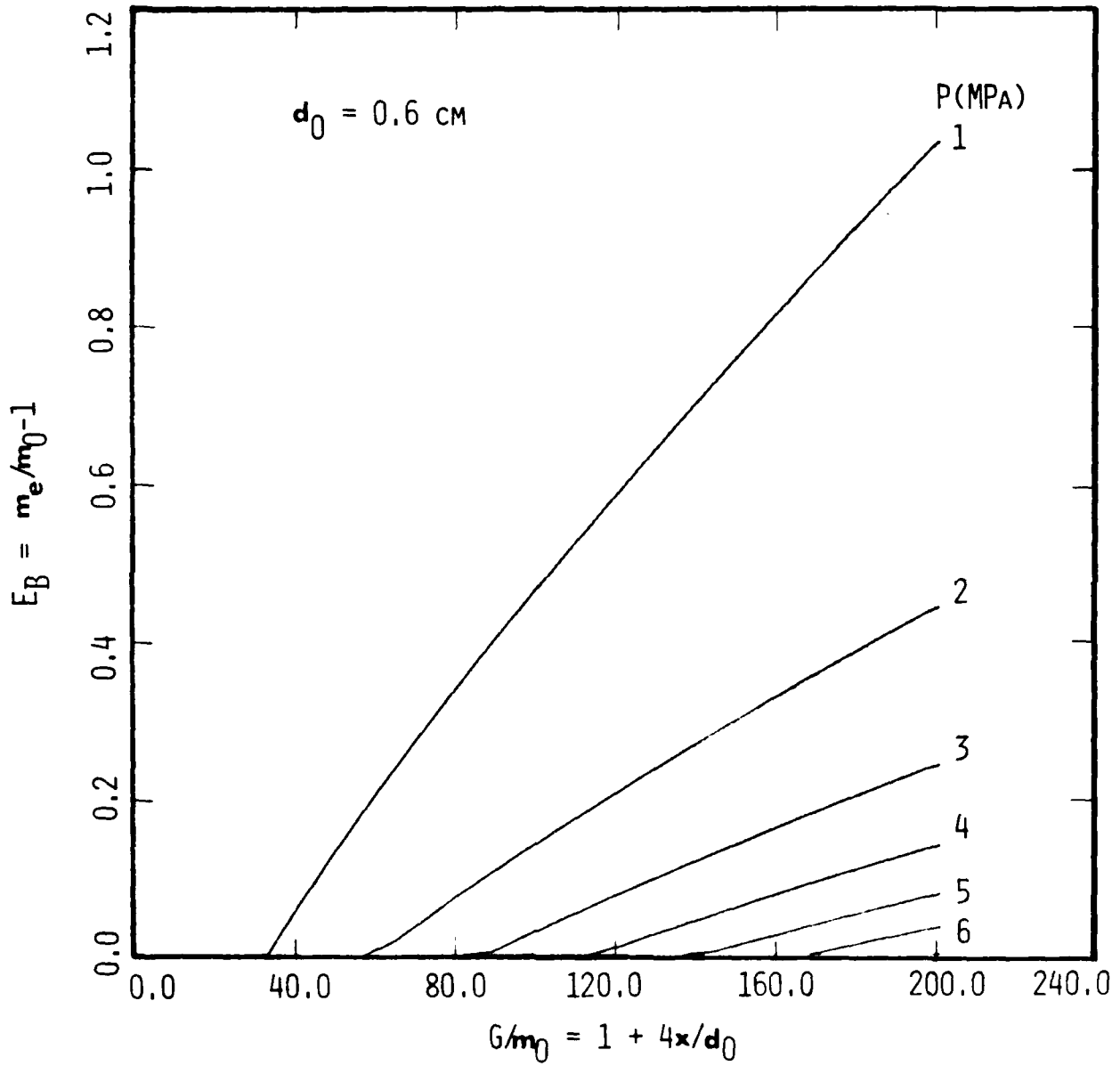
Fig. VI.10 Normalized erosive burning versus dimensionless mean axial mass flux, at various pressures. Increasing the pressure results in reduced erosive burning and higher threshold values for G/m_0.
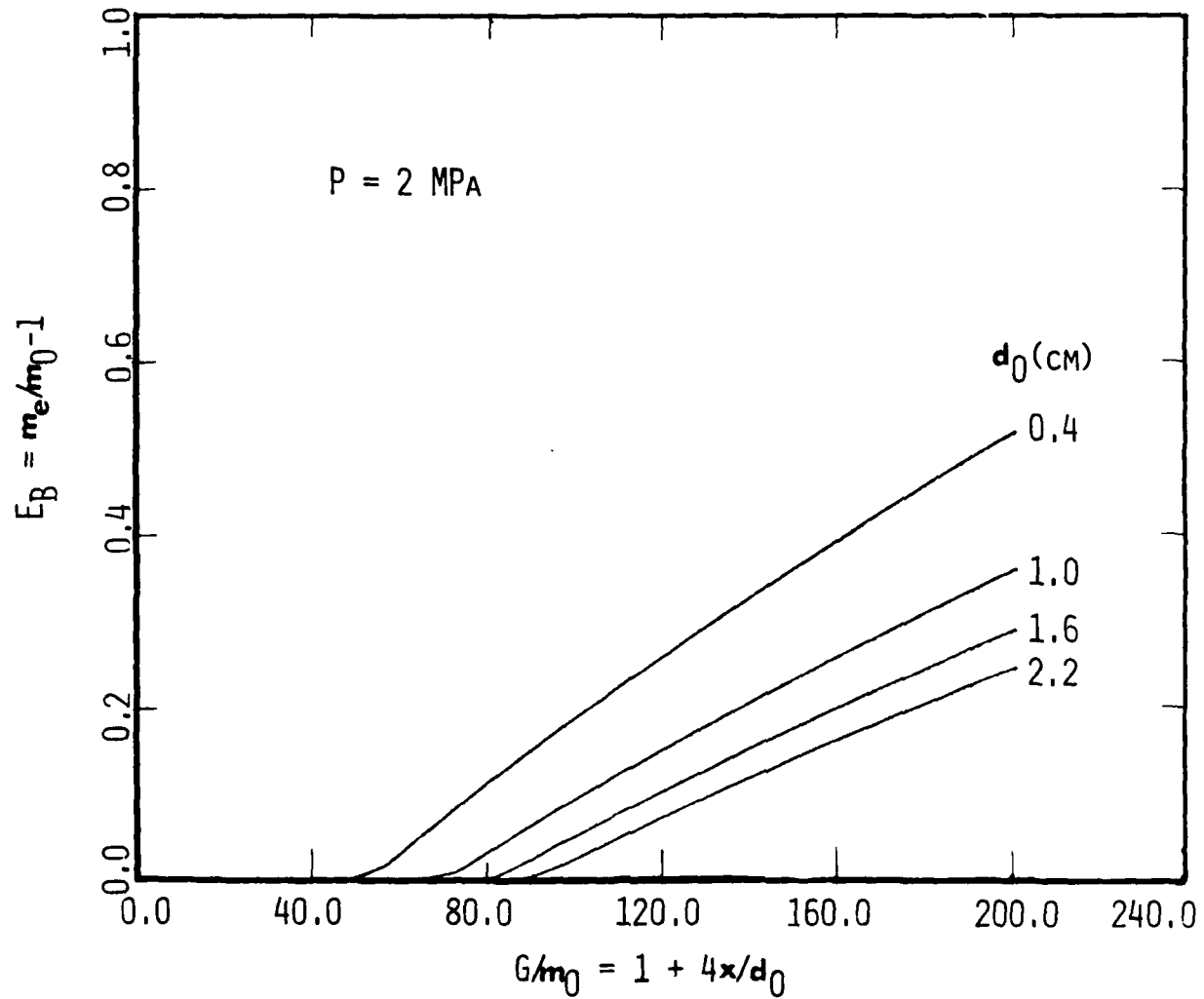
Fig. VI.11 Normalized erosive burning versus mean dimension-
less axial mass flux at various chamber diameters. A nontrivial
scaling effect is clearly shown: the erosive effect decreases
and the threshold values of G/m_0 increase as the diameter is
increased.
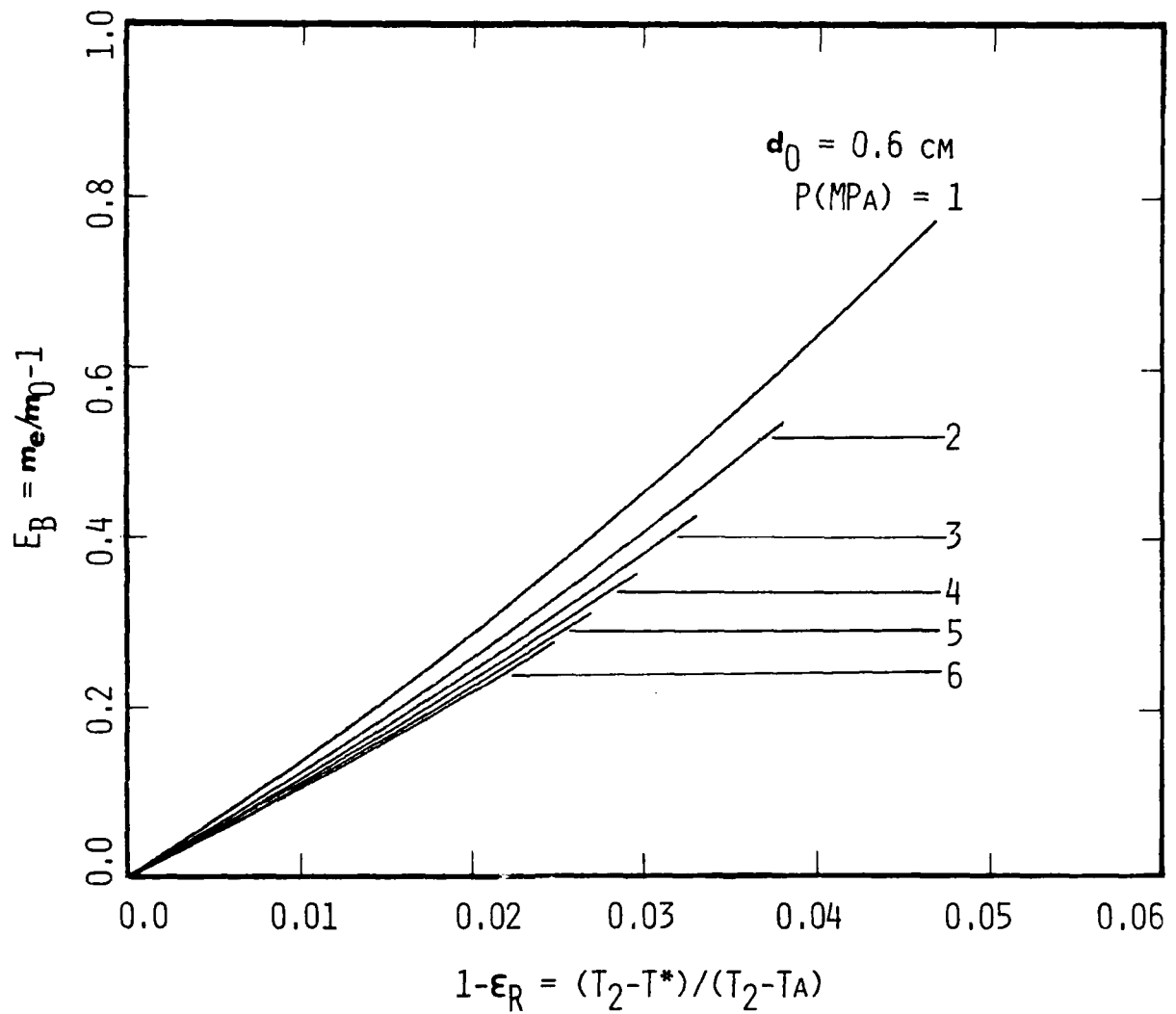
Fig. VI.12 Erosive burning versus reduced cutoff enthalpy at various pressures. Amplification of the burning rate (erosive effect) due to the far field perturbation is clearly shown; e.g., a value of $1 - \varepsilon_R \doteq 2\%$ corresponds to $E_B \doteq 20\%$.
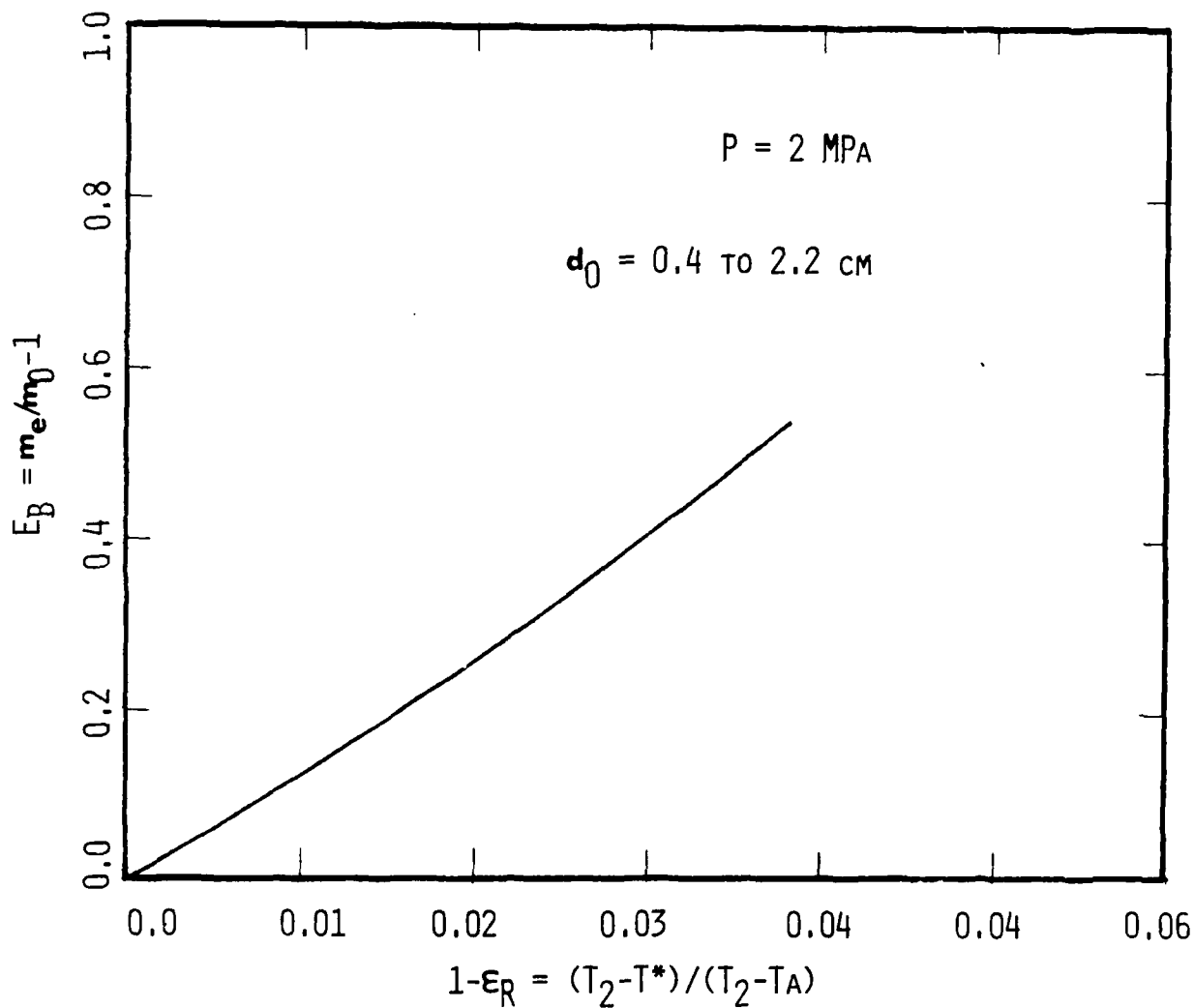
Fig. VI.13 Erosive burning versus reduced cutoff enthalpy at various port diameters (P = const). The erosion effect is self similar with respect to the port diameter, and all the lines coincide.
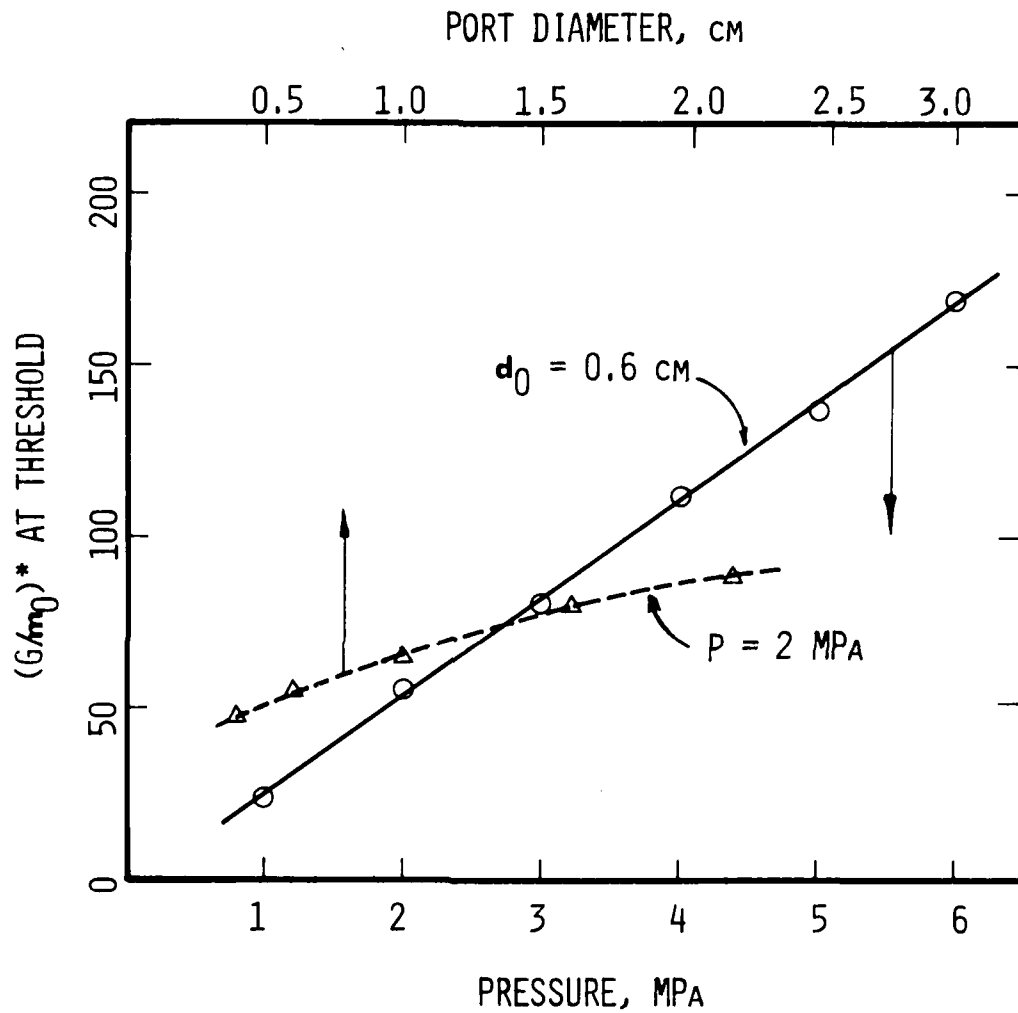
Fig. VI.14 Threshold effect (critical G/m_0) as function of pressure and port diameter. The behavior at fixed d_0 is close to linear, while a lower (and decreasing) sensitivity is demonstrated as d_0 varies at constant pressure.

COREFLOW CONTROL VOLUME

SONIC THROAT

$x=0$

$x=L$
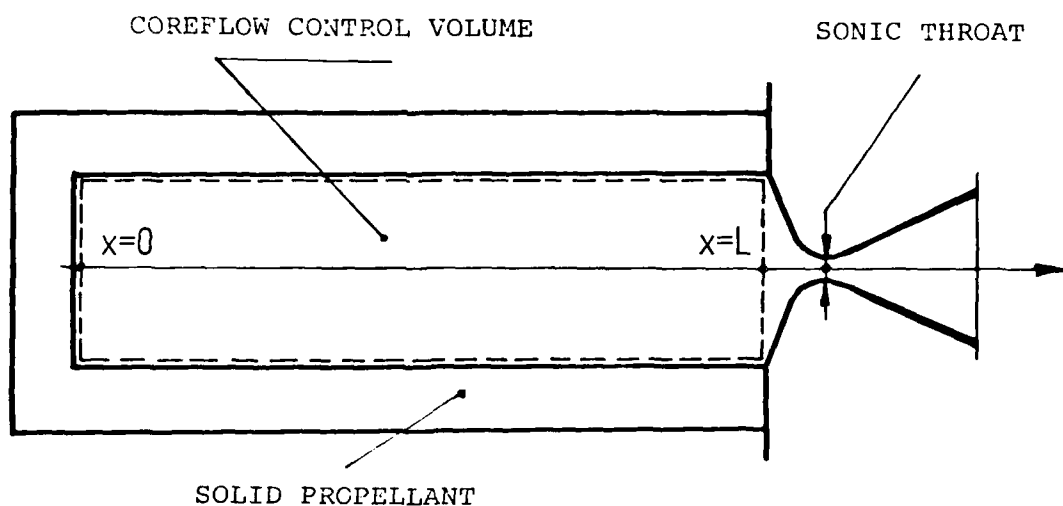
SOLID PROPELLANT

SOLID PROPELLANT CHAMBER CONFIGURATION

$\dot{Q}_{FB}$

Y

X

$m\ Y_i$

$\rho(x)$
$G(x)$

$h(x)$
$Y_i(x)$
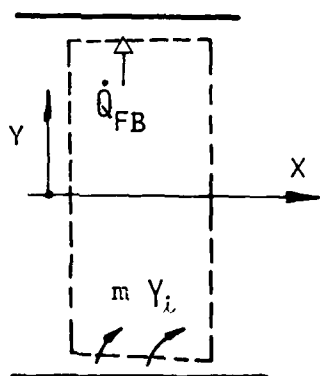
CONTROL VOLUME
SECTION
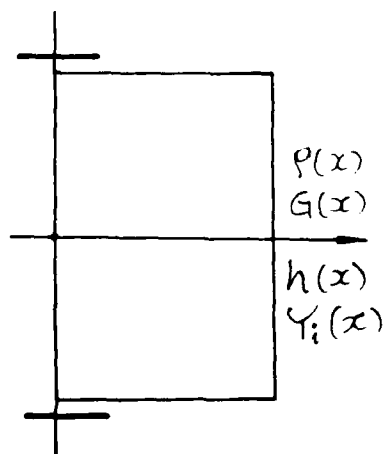
LATERAL CORE
PROFILES

Fig. VIII.1

Schematic of the solid propellant chamber and coreflow control
volume for the one-dimensional approximation employed. Details
show the injection of reactants and turbulent heat feedback at
lateral boundary (source terms in the model), and the uniformity
of profiles in y-direction.
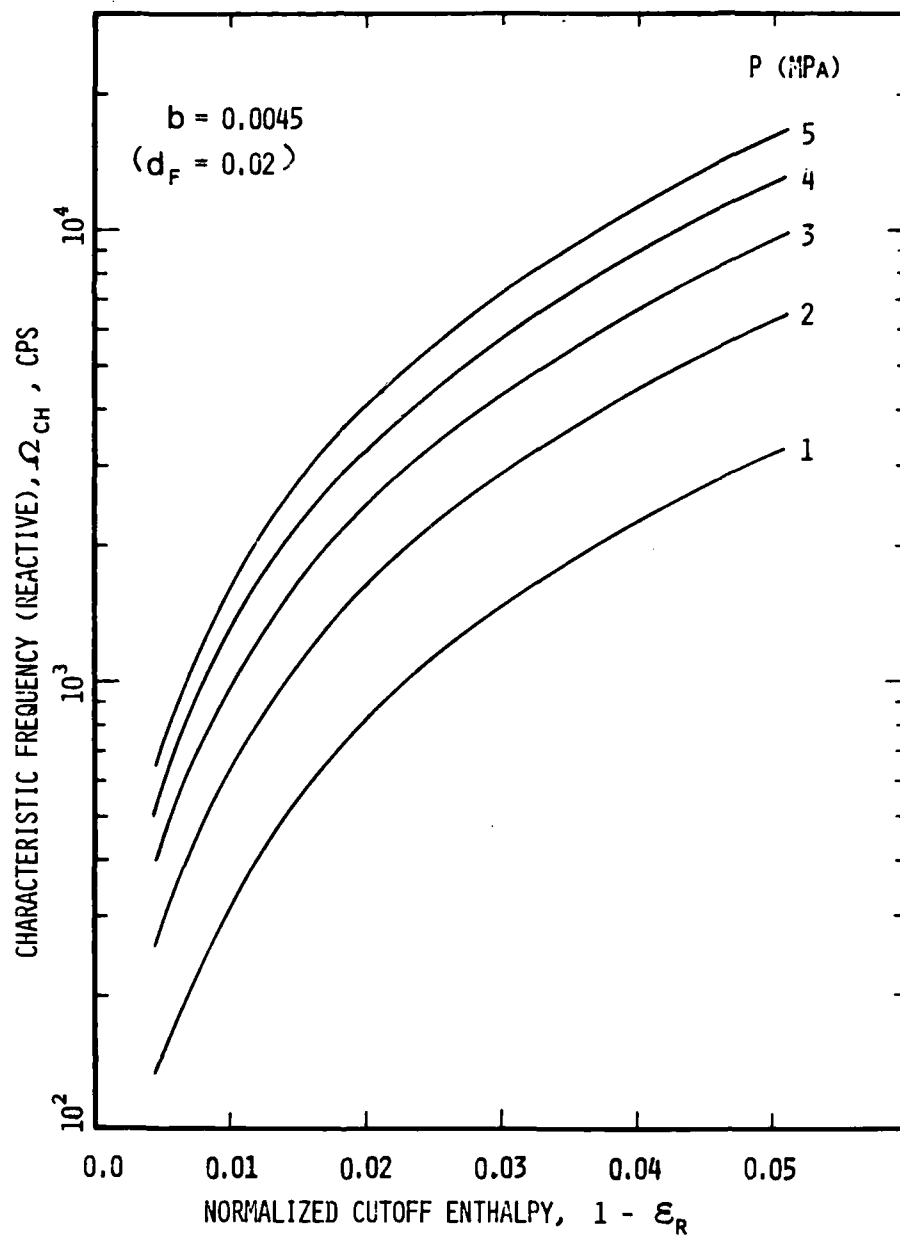
Fig. VIII.2

Characteristic core-reaction frequency vs. normalized cutoff enthalpy (core-wall layer coupling parameter), $1-\varepsilon_R$, with pressure as parameter, at a fixed fuel-excess, b.
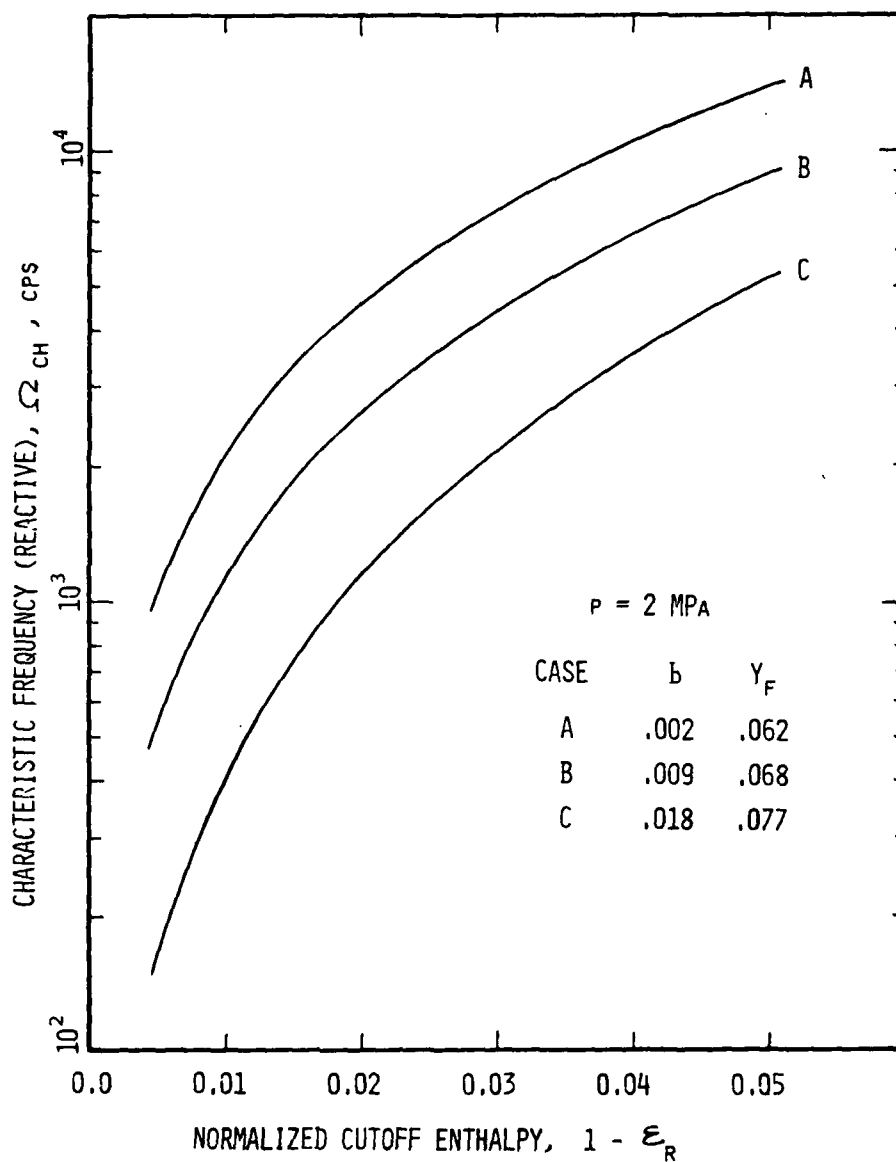
Fig. VIII.3

Characteristic core-reaction frequency vs. normalized cutoff
enthalpy, $1-\varepsilon_R$, with fuel-excess as parameter, at a fixed pressure.
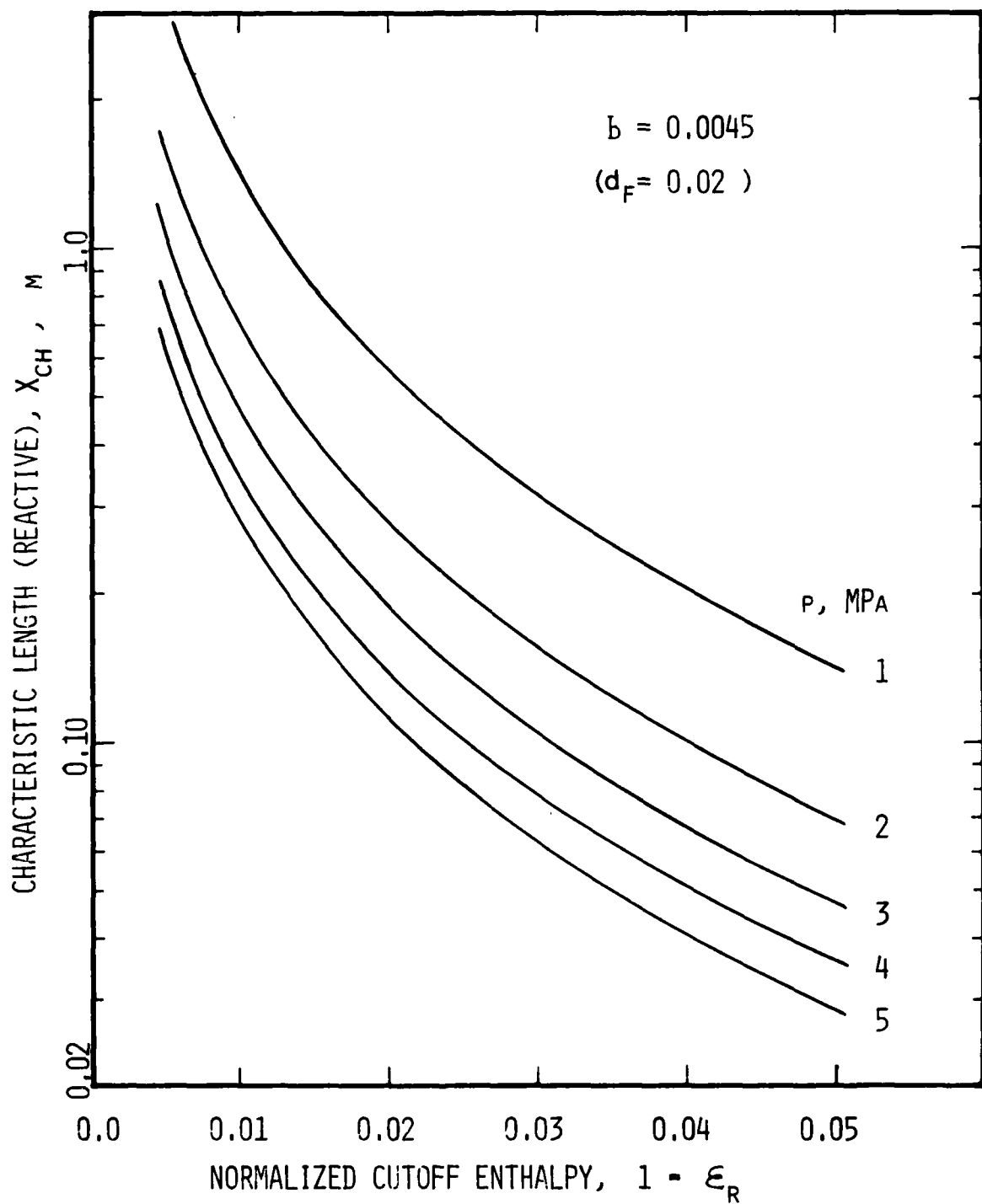
Fig. VIII.4

Characteristic axial length associated with residual coreflow
reaction vs. normalized cutoff enthalpy, $1-\epsilon_R$. Pressure is
varied as parameter, at a fixed fuel-excess, b.
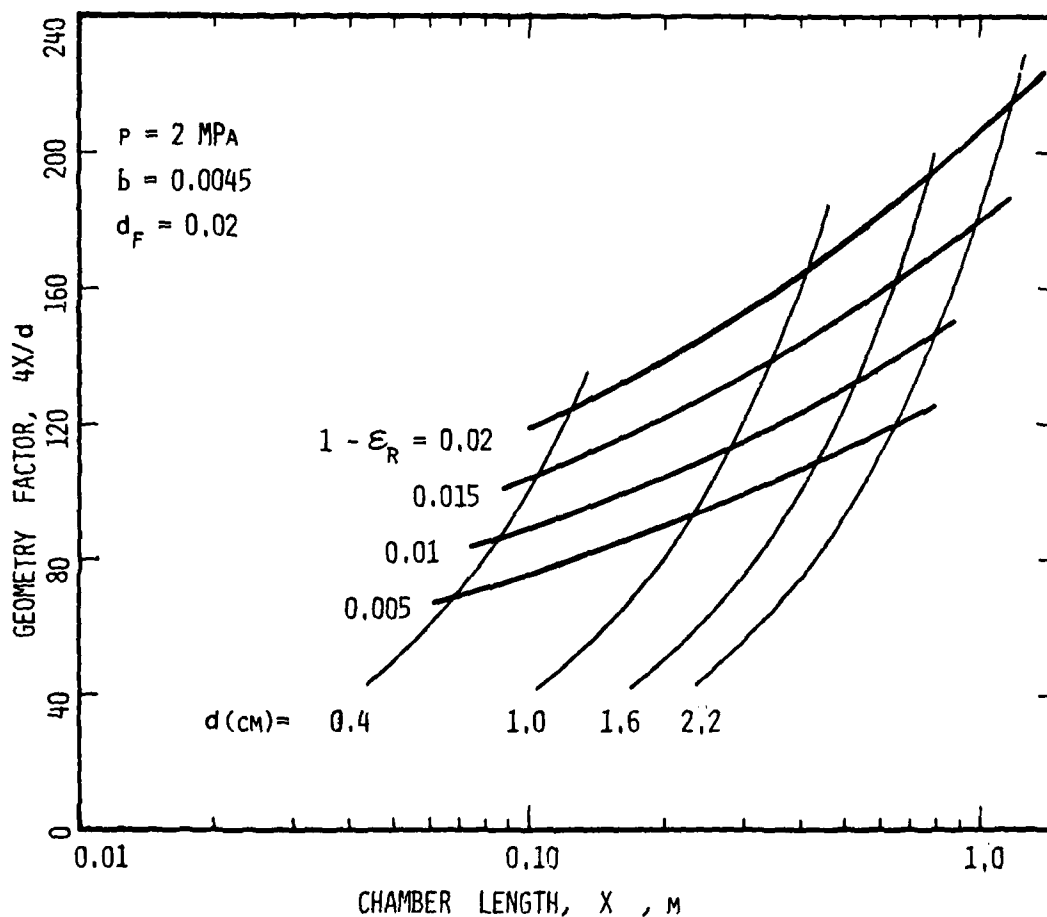
Fig. VIII.5

Normalized cutoff enthalpy and port diameter map (at fixed p), reconstructed from Fig. VI.9. Along with Fig. VIII.4, this map is used to suggest geometries (d,L) for cases likely to exhibit strong interaction between core exothermicity and the acoustic field.
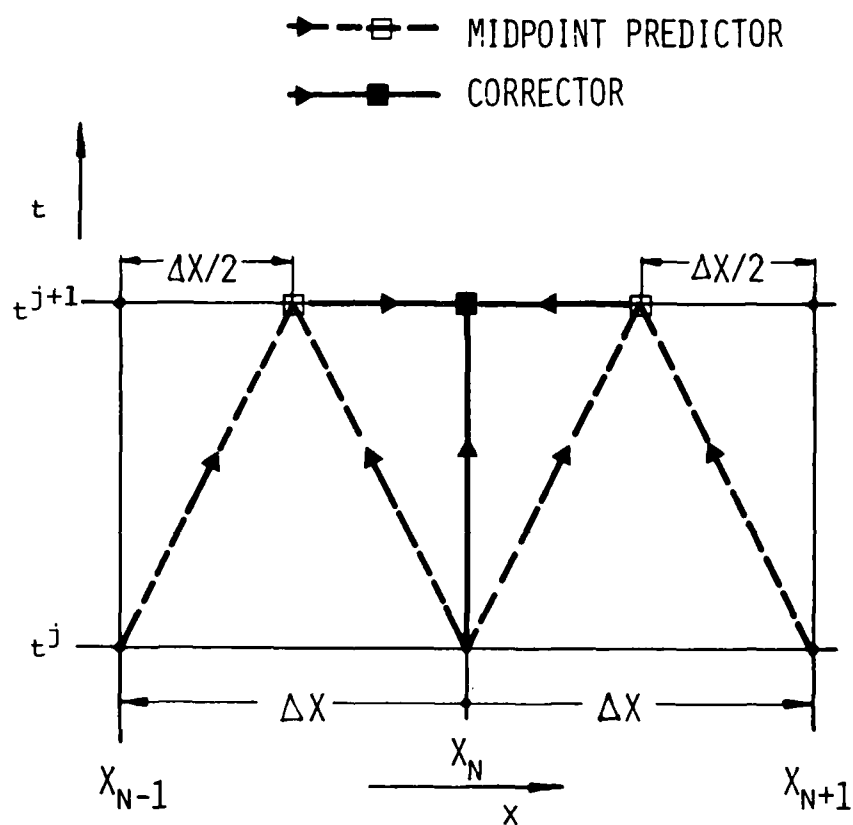
Fig. VIII.6

Computational molecule for the explicit Rubin-Burstein finite
difference algorithm. Arrows indicate participation in calcu-
lation of U-values at a particular point.
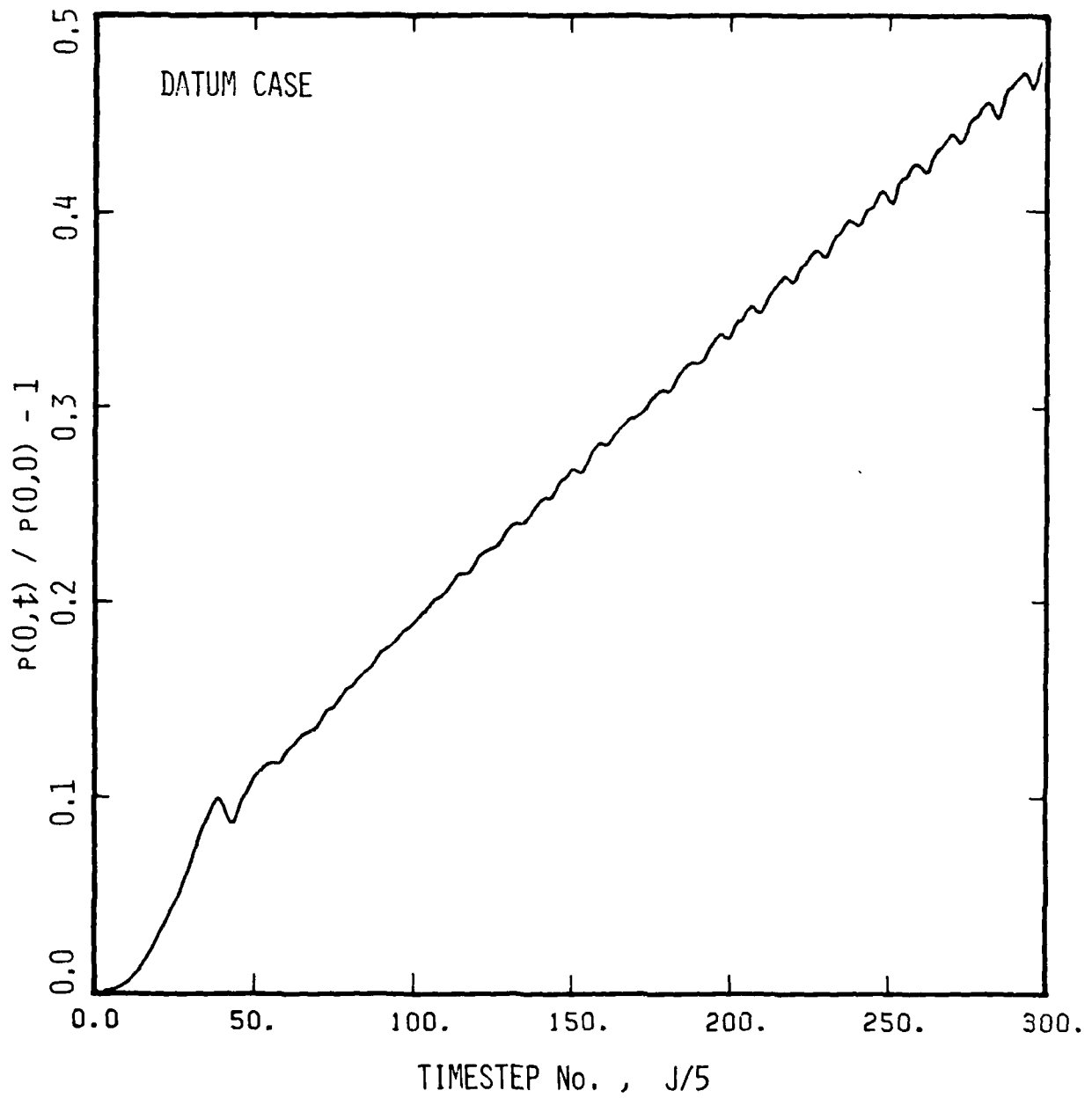
Fig. IX.la

Normalized head end pressure oscillations vs. dimensionless time.
Note the decay of the fundamental standing mode.
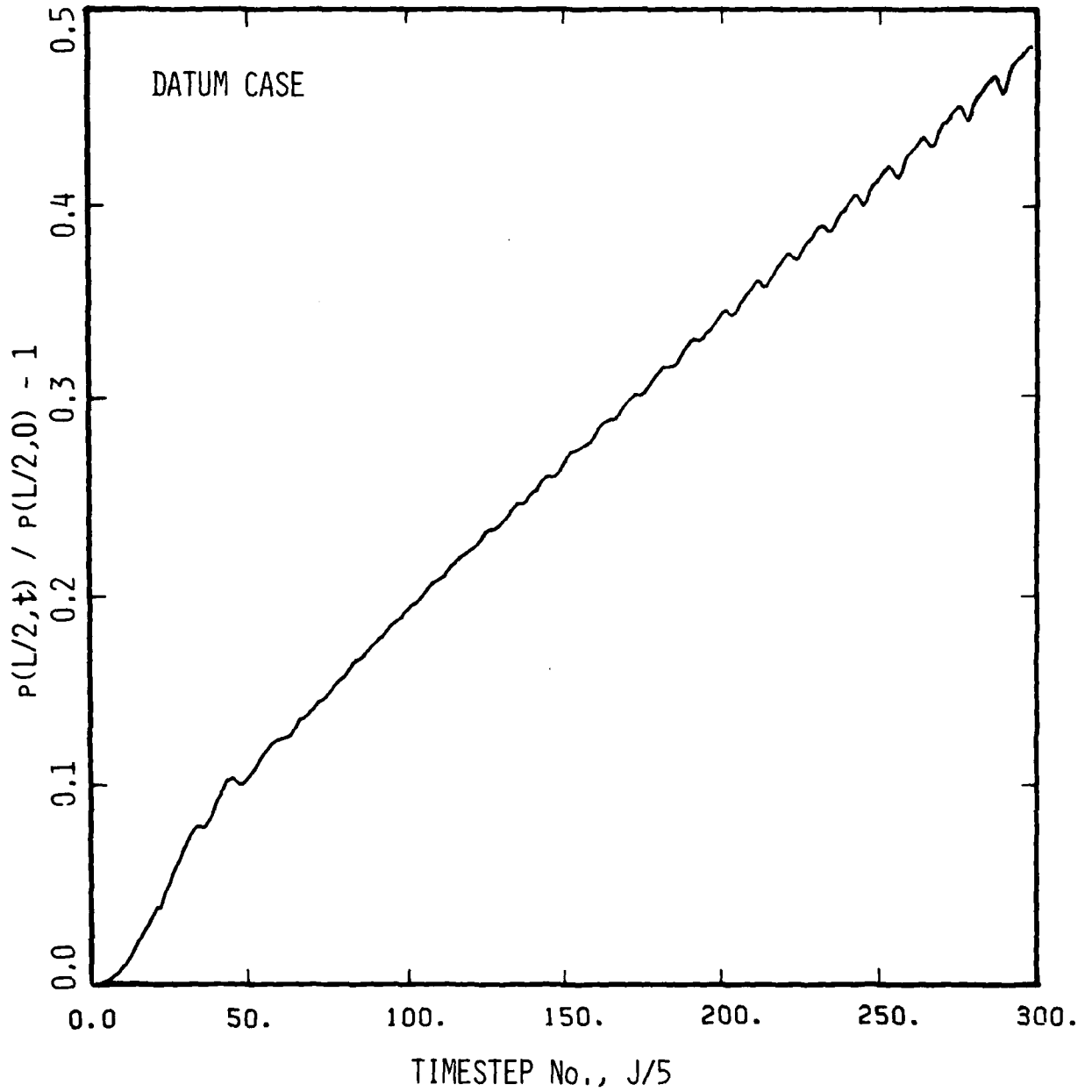
Fig. IX.1b

Normalized pressure oscillations vs. dimensionless time at chamber midpoint, x = L/2.
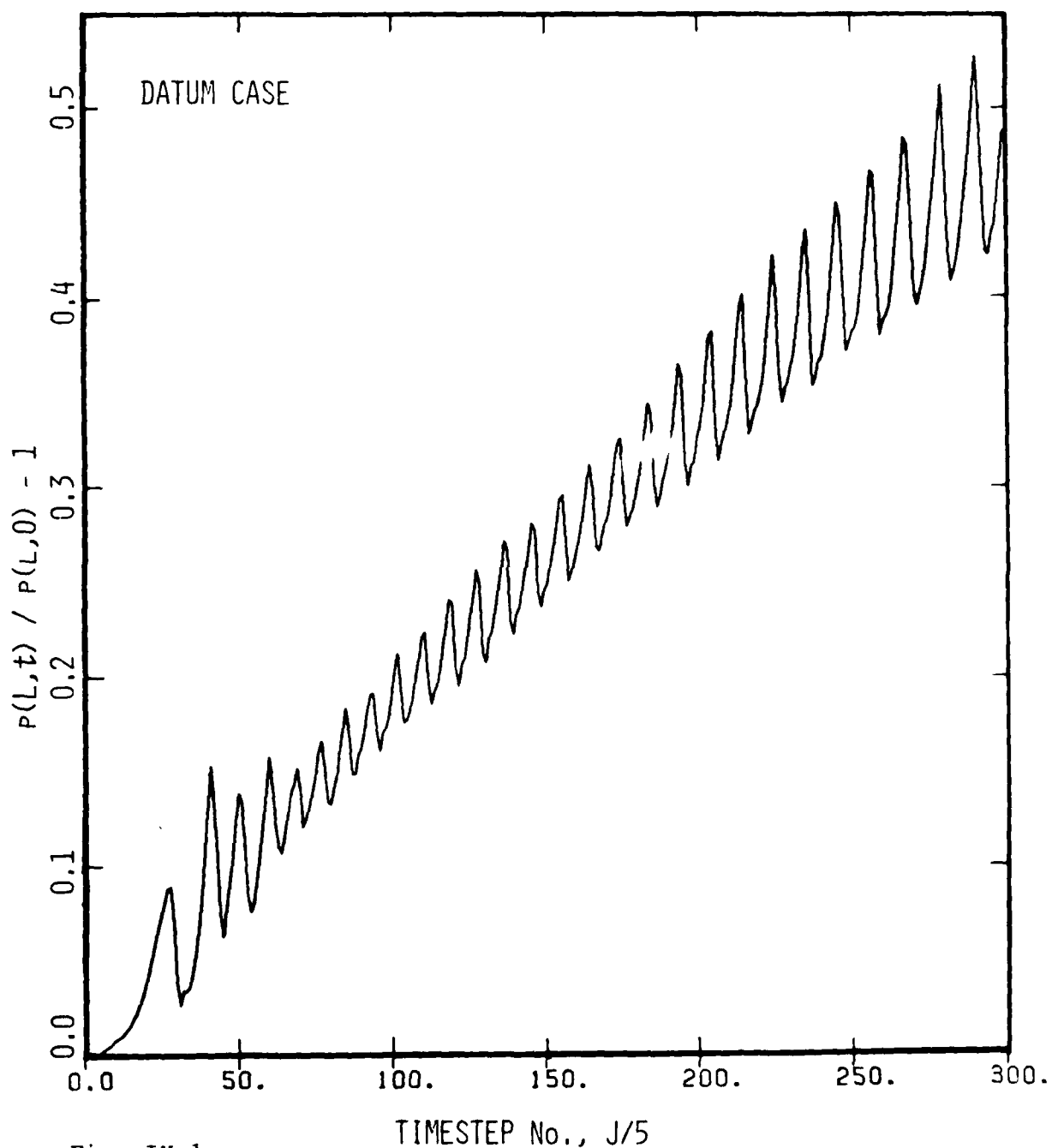
Fig. IX.1c

Normalized pressure oscillations vs. dimensionless time at the
chamber exit, x = L. These oscillations are in phase with those
at x = 0 and out of phase with those at x = L/2, indicating evo-
lution of the first harmonic standing mode. Note the slowly in-
creasing amplitude.
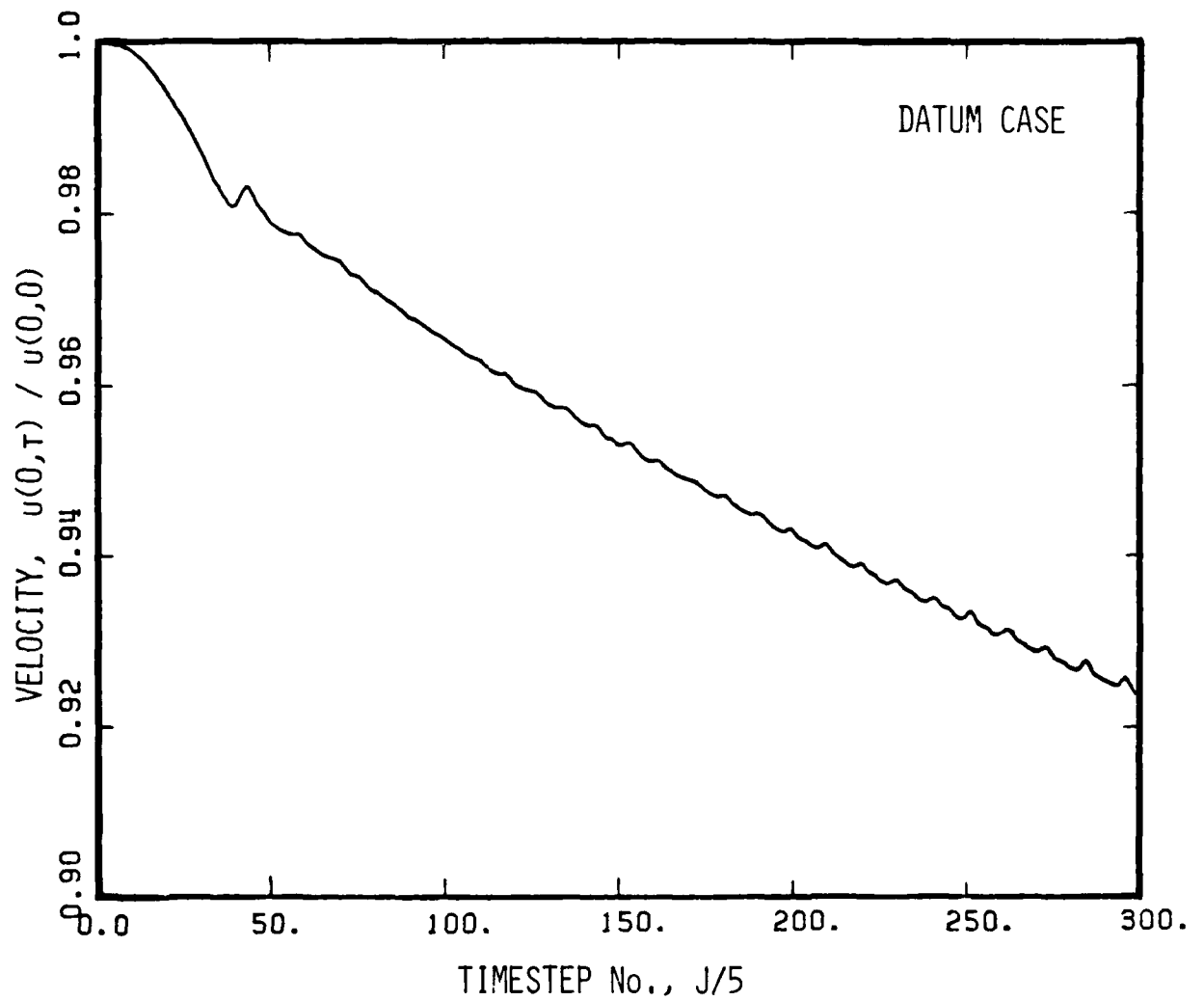
Fig. IX.2a

Normalized velocity vs. dimensionless time at x = 0. The decay
in the mean is associated with the mean pressure rise.
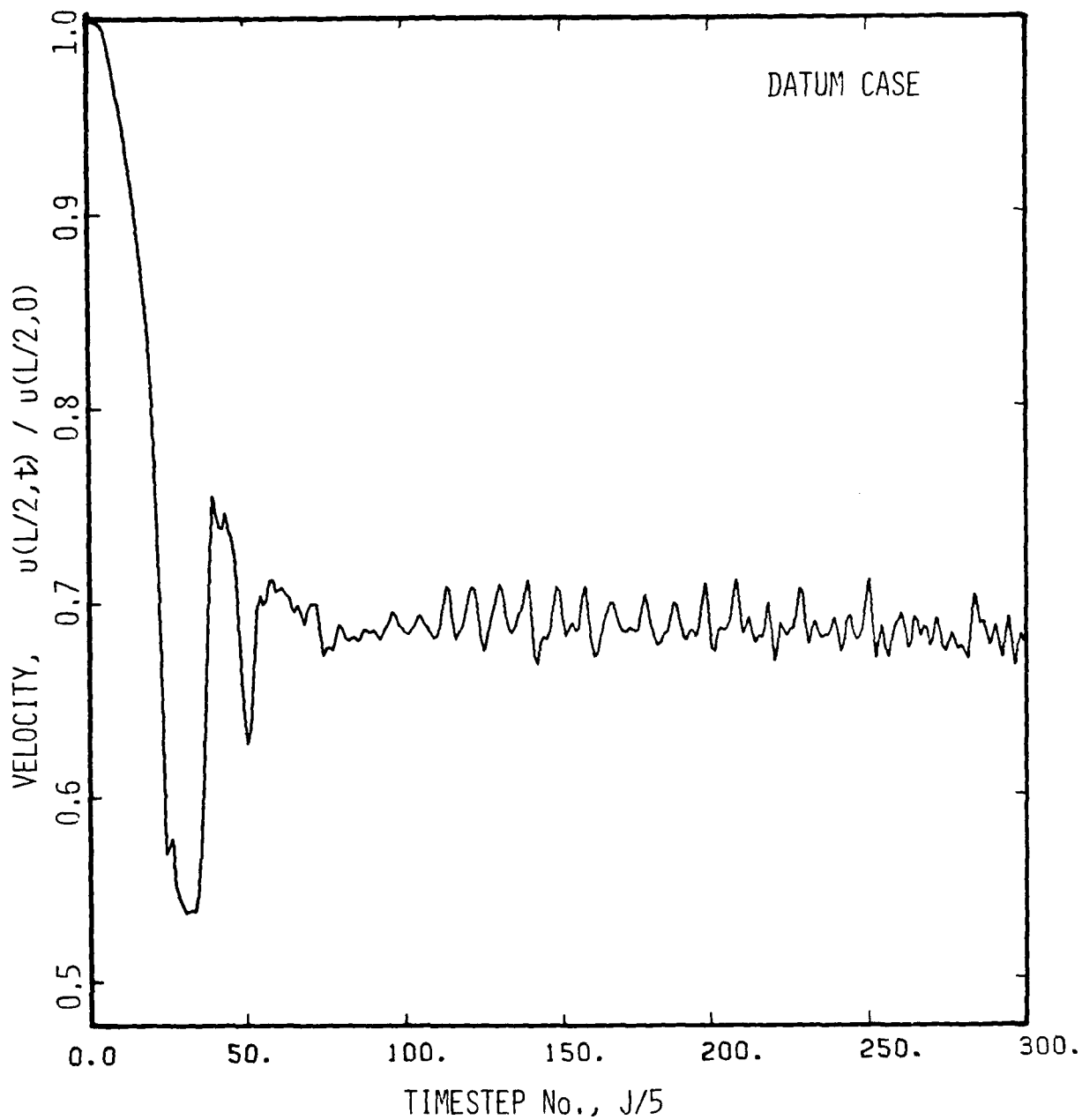
Fig. IX.2b

Normalized velocity vs. dimensionless time at x = L/2. The decay
of the fundamental mode (for which L/2 is an antinode) is shown;
persistent fluctuations at later stages are due to the presence
of mean flow (travelling waves).
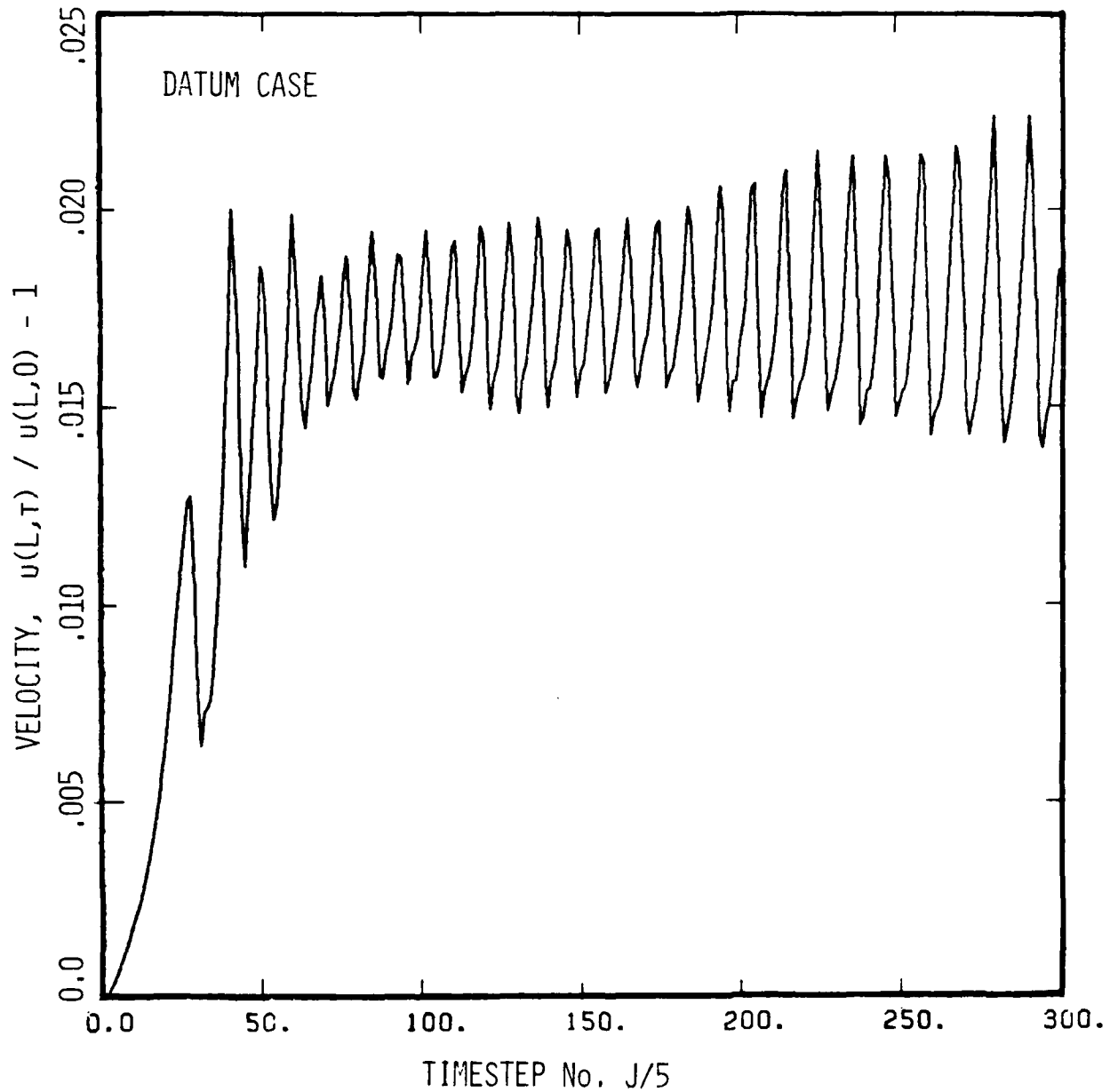
Fig. IX.2c

Normalized velocity at x = L vs. dimensionless time. Although
this is a velocity node (for the standing organ pipe modes),
highly-oscillatory behavior is shown, due to high travelling
wave content. High extent of erosive burning between x = L/2
and L causes the upward shift 'n mean velocity.
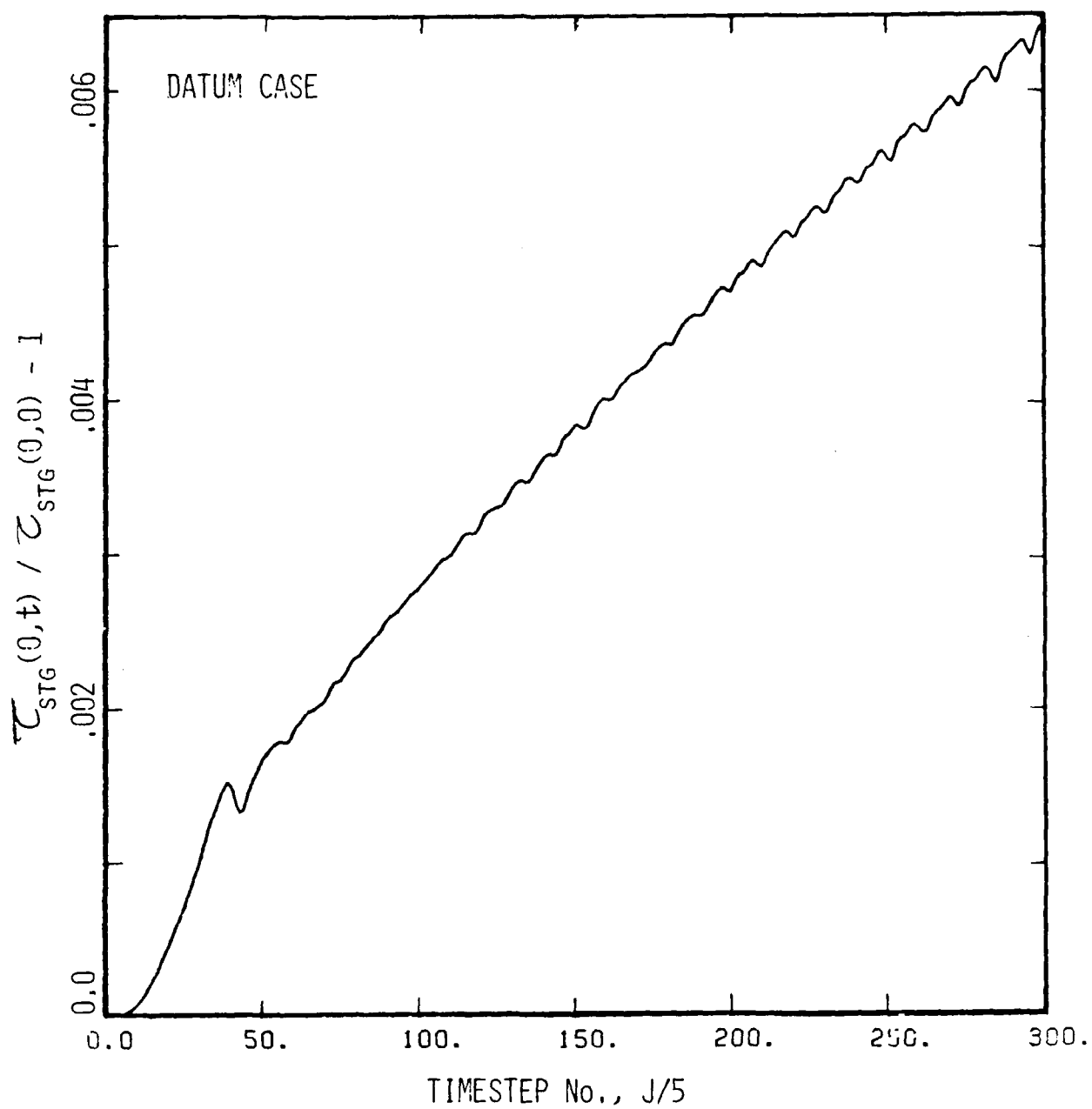
Fig. IX.3a

Normalized stagnation enthalpy at $x = 0^+$ vs. dimensionless time, showing evolution of first harmonic. The mean rise is due to pressure increase.
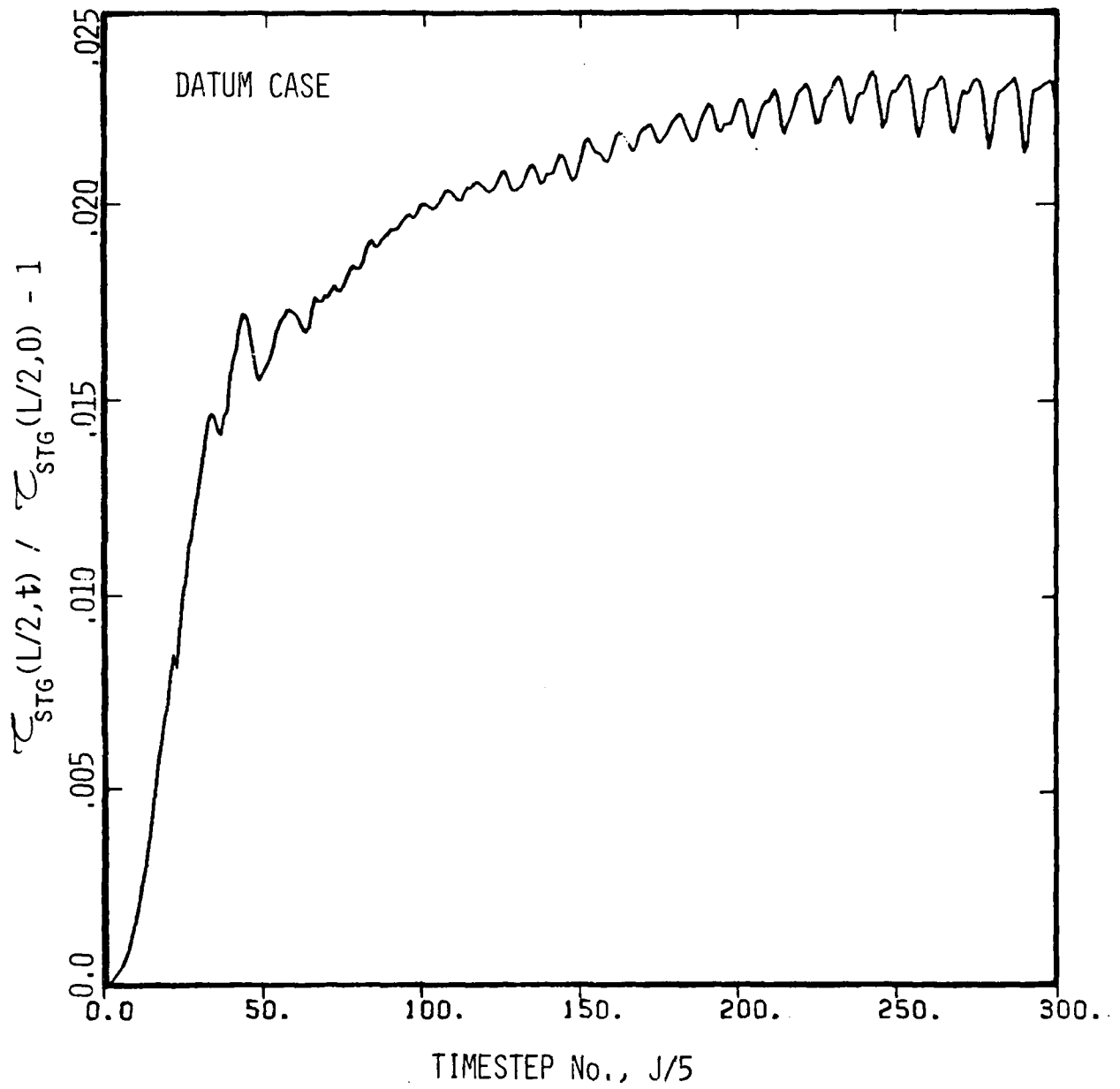
Fig. IX.3b

Normalized stagnation enthalpy at x = L/2 vs. dimensionless time.
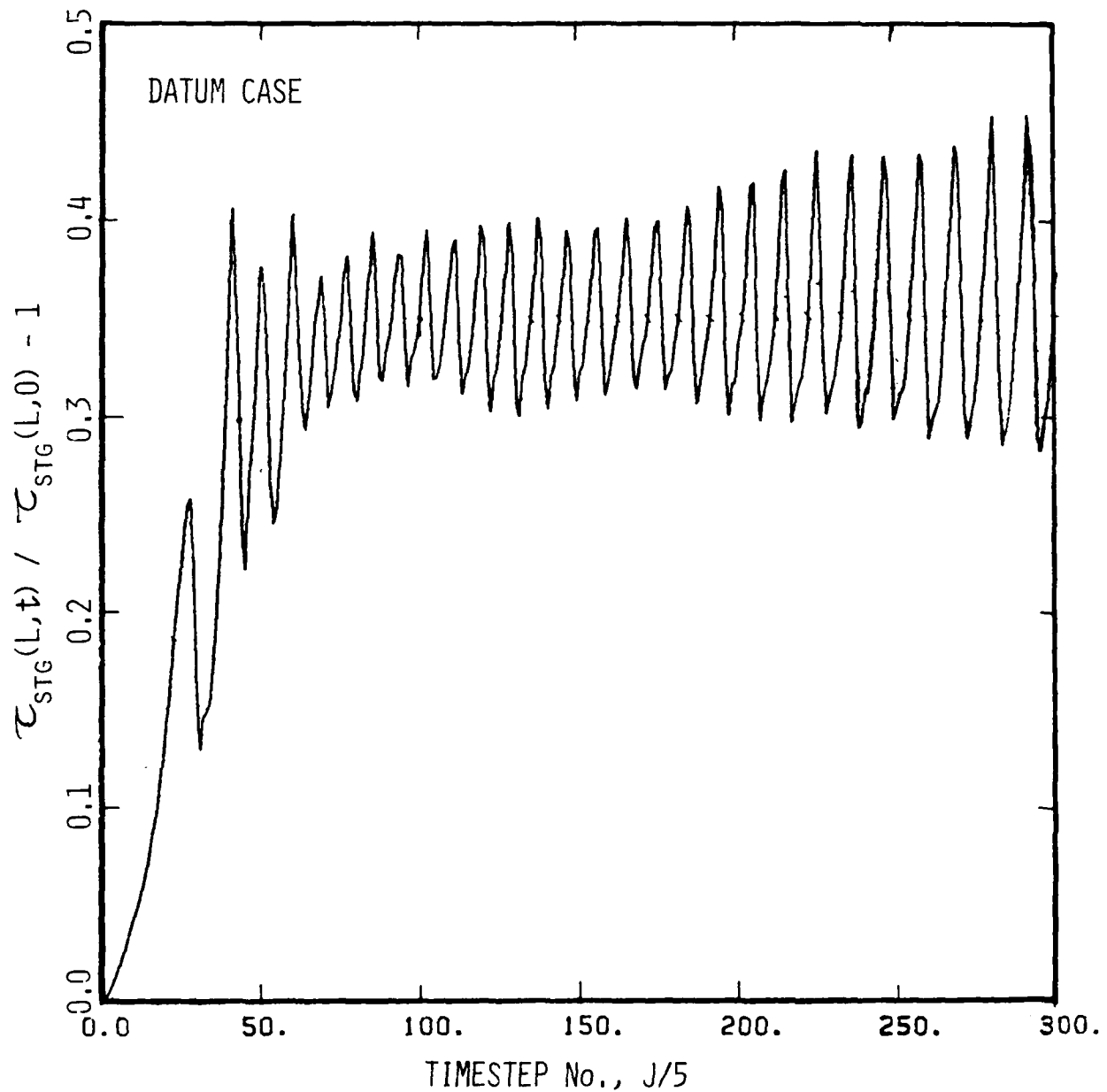
Fig. IX.3c

Normalized stagnation enthalpy at x = L vs. dimensionless time.
Amplitude of oscillations is much larger than at x = 0 or L/2,
resembling the behavior of velocity.
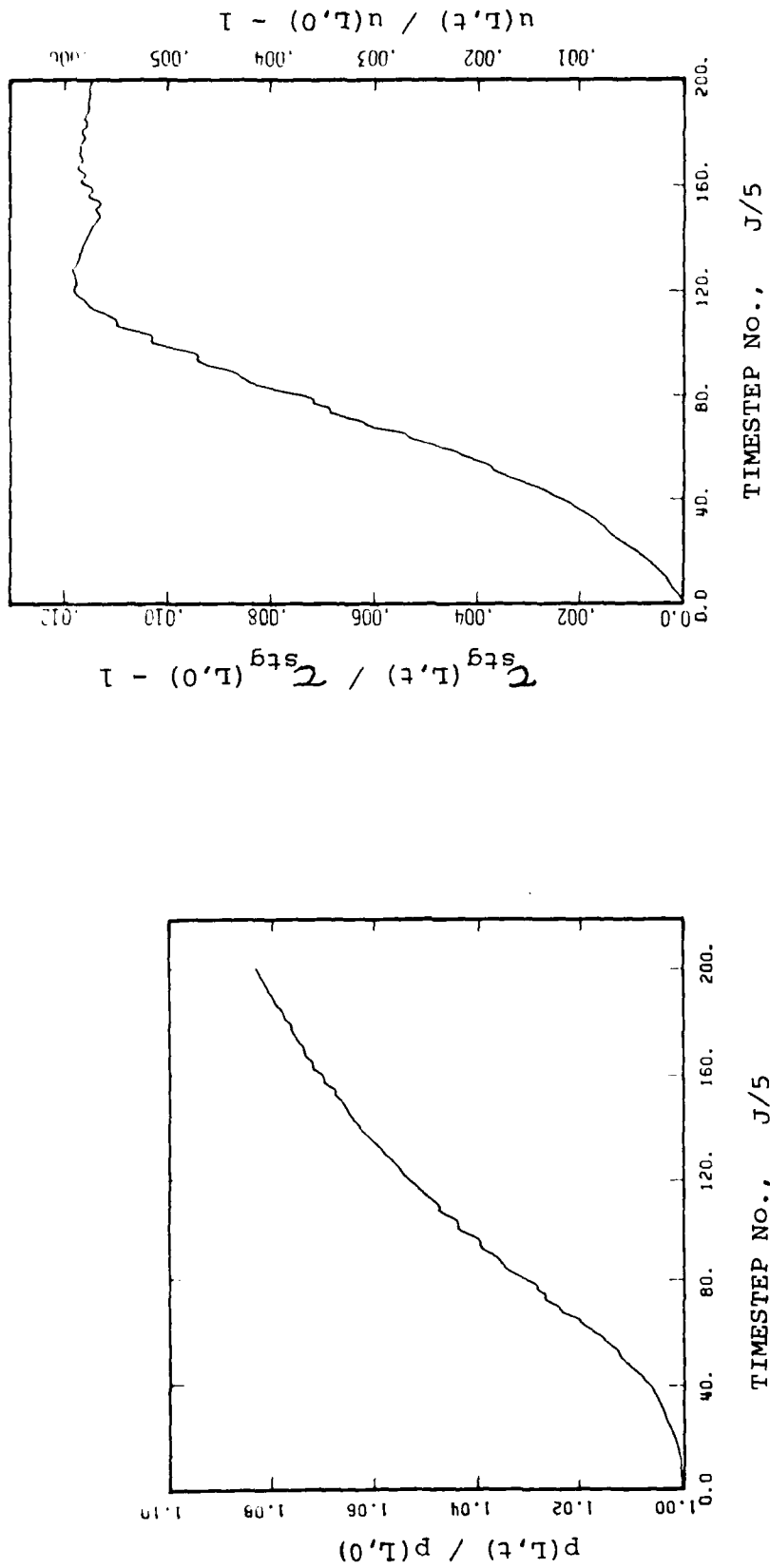
b. Stagnation enthalpy and velocity

a. Pressure

Fig. IX. 4

Normalized pressure, stagnation enthalpy and velocity fluctuations vs. dimensionless time, for case with vanishing coupling between core exothermicity and the acoustic field. Initial mean rise is followed by levelling-off. Note damping of fundamental mode, and then the first harmonic. Stagnation enthalpy ard velocity fluctuations are similar, due to negligible residual heat release in the ccre.

-260-
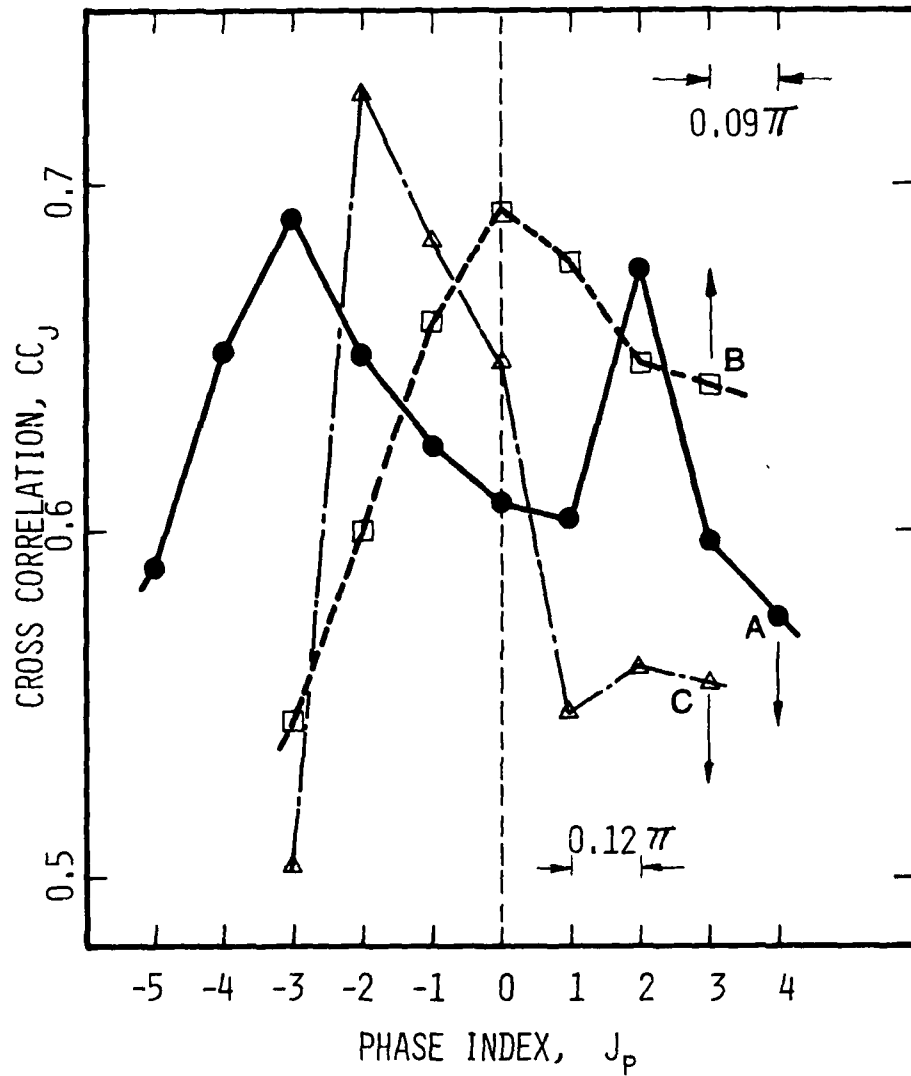
Fig. IX.5

Discretized cross correlations between normalized fluctuations of core exothermicity, $\hat{q}_R$, and pressure, $\hat{p}$, at x = L-Δx. Comparison between 3 cases:

CASE:	A	B	C
$\bar{p}$ (MPa)	5	5	2
d (cm)	1	0.6	1
4L/d	40	40	40
Blasius Coeff:	0.03	0.02	0.03
Coupling:	strong	vanishing	weak
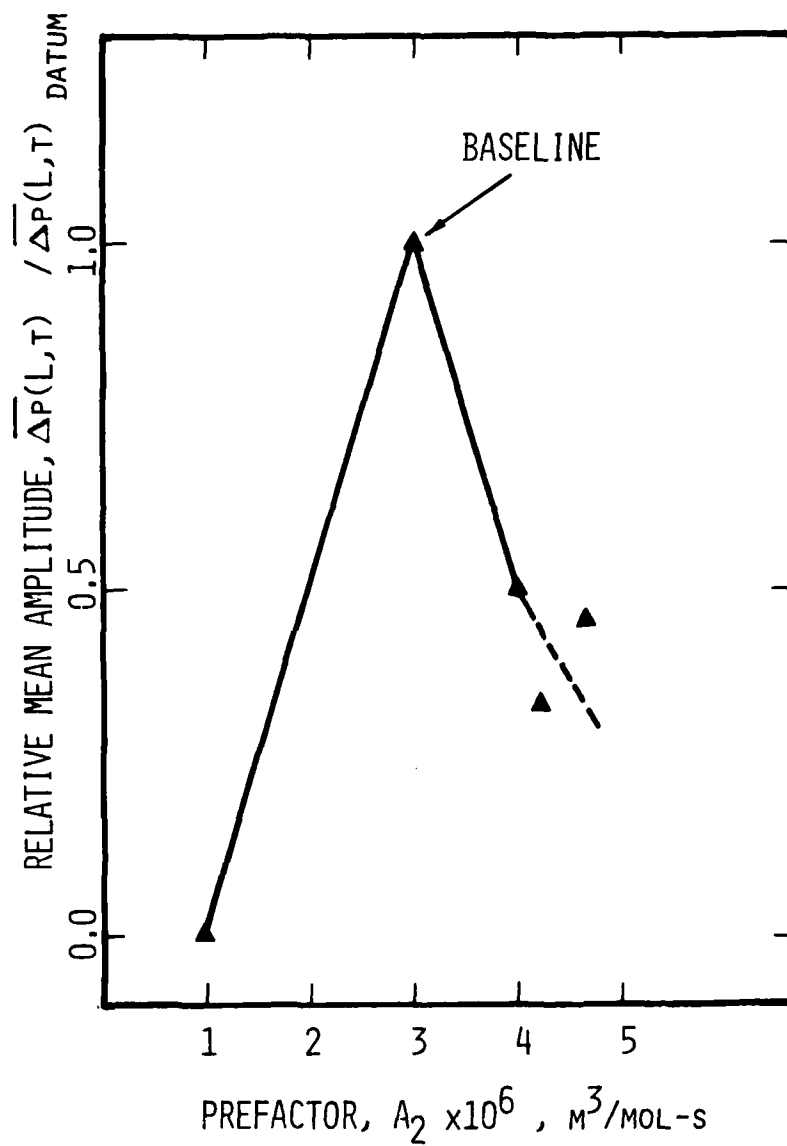
Fig. IX.6

Schematic comparison of mean amplitude of pressure oscillations
vs. value of the reaction prefactor for 5 cases tested, showing
peak at baseline data.

APPENDIX A

THERMOPHYSICAL PROPERTIES IN THE GAS PHASE

Within the framework of the nonlinear deflagration model, variable gas properties are required. Thermophysical properties such as thermal conductivity, specific heat, and diffusivity depend in general upon local composition $(Y_1, Y_2, \ldots Y_N)$ and temperature. In order to make the incorporation of such parameters in the numerical deflagration scheme feasible (in terms of the computational effort involved per gas phase integration), certain simplifications were necessary. The modeling involved is described herein.

For certain chemical species, the basic data required do not yet exist in the literature. Thus, various estimates are necessary; one such estimate is the calculation of $C_{p,RDX}$, the details of which are given here. In light of the approximations involved, it is difficult to assign an error margin to the calculations. Overall, a cautious estimate would be 10%, although in certain individual species parameters the error might be much larger.

In the following three main sections, detailed models are described for the specific heat, C_p, the thermal conductivity, λ, and the mixture diffusivity, ρD. Specific data are given in Tables A-1 through A-4 and Fig. A-1.

1. Specific Heat, C_p, of the Gas Mixture

Given the temperature and all species mass fractions at a point in the gas phase field, the specific heat is by definition

$$C_p = \sum_{i=1}^{N} Y_i C_{p,i}(T) \qquad \text{(A-1)}$$

where Y_i and $C_{p,i}$, $i = 1,2,\ldots N$ are the individual species mass fractions and specific heats respectively. $C_{p,i}$ vs temperature data are available for all species (except RDX) in the JANNAF Tables.[1]

To simplify the calculations in the computer program solving the gas-field deflagration problem, explicit linear temperature dependence was assumed for the $C_{p,i}$ values of the individual species

$$C_{p,i} \doteq A_i + B_i T \qquad \text{(A-2)}$$

in the range $T = 600$ K to 1300 K, typical to the near field in the gas. The corresponding A_i and B_i of Eq. (A-2) were obtained by least squares fitting of the $C_{p,i}$ data in this range of temperatures.

Thus, the specific heat of the gas mixture at any point in the field is given by

$$C_p = \sum_{i=1}^{N} Y_i (A_i + B_i T) \qquad (A-3)$$

Table A-2 contains the various A_i and B_i used in the program, in SI units.

2. Structural Estimate of C_p for Gaseous RDX

Tabulated C_p data for this compound do not exist, which makes it necessary to calculate C_p by structural analysis. Following the principle of energy equipartition and summing the translational, rotational, and vibrational contributions:

$$C_p = R_u + \frac{3}{2}R_u + \frac{3}{2}R_u + \sum_{j=1}^{3n^*-6} C_v(vib); \qquad (A-4)$$

n^* denotes the number of atoms per molecule and $3n^*-6$ the total number of vibrational degrees of freedom; for RDX these are 21 and 57, respectively.

The jth vibrational term is given by the Einstein equation:

$$C_v(vib)_j = R_u X_j^2 \exp(X_j)/(\exp(X_j) - 1)^2 \qquad (A-5)$$

where $\qquad X_j \equiv \theta_j/T$

and $\qquad \theta_j \equiv (hC/k)\omega_j = 1.43879\omega_j$

where k is the Boltzman constant, h is the Planck constant, and C the speed of light. $\omega_j(cm^{-1})$ is the fundamental harmonic oscillator wave number for the particular j^{th} vibrational mode. $T(K)$ is the absolute temperature and θ_j has the dimension of T.

The method of Benson[2] is followed in the above calculation. Most of the ω_j frequencies for RDX were categorized by Wood.[3] The data are summarized in Table A-1; wherever ω_j estimates were made, the source is indicated.

Utilizing Eqs. (A-5) and (A-4), $C_{p,RDX}$ can be calculated for the given wave numbers ω_j of Table A-1 at various temperatures. The results of this calculation are:

T(K)	$C_{p,RDX}$, cal/mol-K
600	74.20
700	82.39
800	88.75
900	93.74
1000	97.73

A plot of $C_{p,RDX}$ vs Temperature is given in Fig. A-1 together with the linear regression, obtained by least-squares fitting. The linear formula is:

$$C_{p,RDX} = 40.63 + 0.0584T \quad \text{(cal/mol-K)}$$
$$= 765.01 + 0.244T \quad \text{(J/kg-K)} \tag{A-6}$$

3. Thermal Conductivity, λ, of the Gas Mixture

The method outlined by Bird, Stewart, and Lightfoot[4] is utilized here, for calculation of the gas mixture thermal conductivity. Following Hirschfelder and Mason and Saxena,[5] the equation for λ is

$$\lambda = \sum_{i=1}^{N} \frac{X_i \lambda_i}{\sum_{j=1}^{N} X_j \Phi_{ij}} \tag{A-7}$$

where λ_i are the species thermal conductivities, and X_i the molar fractions, defined

$$X_i = (Y_i/W_i) \Big/ \sum_{j=1}^{N} (Y_j/W_j)$$

The dimensionless coupling coefficient Φ_{ij} is defined:

$$\Phi_{ij} = (1/\sqrt{8}) \left[1 + \left(\frac{\mu_i}{\mu_j}\right)^{1/2} \left(\frac{W_j}{W_i}\right)^{1/4} \right]^2 (1 + W_i/W_j)^{-1/2} \quad \text{for } i \neq j$$

$$\text{and} \quad \Phi_{ij} = 1 \quad \text{for} \quad i = j \tag{A-8}$$

μ_i in the last equation is the coefficient of viscosity for the ith species.

Evidently, the evaluation of λ at any point in the gas field requires X_i, $\lambda_i(T)$ and $\mu_i(T)$, $i = 1,2,...N$. The modeling of λ_i and μ_i is described in the following two sections.

a. The Coefficient of Thermal Conductivity, λ_i

Eucken's[6] formula for polyatomic gases is written:

$$\lambda_i = \mu_i (C_{pi} + \frac{5}{4} R_u/W_i)$$

The resulting approximation strongly *depends on the* accuracy of C_{pi} and μ_i; it was decided for this reason, as well as for retaining computational simplicity, to use existing $\lambda_i(T)$ data for obtaining an explicit linear temperature dependence:

$$\lambda_i \doteq F_i + E_i T \qquad (A-9)$$

similar to that for C_{pi}. In the range of temperatures from 600 K to 1300 K, $\lambda_i(T)$ data was used from several sources.[7,8,9] Because of the lack of specific data, RDX here was represented approximately by benzene (g). The values of F_i and E_i in SI units are given in Table A-3.

b. The Coefficient of Viscosity, μ_i

The Chapman-Enskog approximation[4] was utilized:

$$\mu_i \doteq 2.6693 \times 10^{-5} (W_i T)^{1/2} \Big/ (\sigma_i^2 \Omega_\mu) \qquad (A-10)$$

which was intended originally for monatomic gases but has been used successfully to approximate polyatomic, non-dense gases. The various parameters involved are:

μ_i (g/cm-s) = the viscosity coefficient

W_i (g/mol) = the molecular weight

σ_i (Å) = the minimal approach distance parameter for 2 colliding molecules

Ω_μ = $f(kT/\varepsilon_i)$, dimensionless collision integral, evaluated by using Chapman-Enskog theory with Lennard-Jones attractive potential.

Numerical values of the function Ω_μ vs $Z_i \equiv kT/\varepsilon_i$ are given in Table B-2 of Ref. 4. An excellent approximation for Ω_μ is obtained by a 2-parameter exponential regression, using least-squares fit. This yields the following expression:

$$\Omega_\mu \doteq 1.5418 \exp(-0.07433 Z_i) \qquad (A-11)$$

with $Z_i \equiv T/(\varepsilon_i/k)$ the dimensionless temperature. Values of σ_i and ε_i/k are given in Table B-1 of Ref. 4 for several of the species of interest here. For the rest, σ_i and ε_i/k were deduced from known[8,9] or estimated viscosity data. Combining Eqs. (A-10) and (A-11)

$$\mu_i \doteq \frac{2.6693 \times 10^{-5}}{1.5418} \frac{\sqrt{W_i}}{\sigma_i^2} \left(\frac{\varepsilon_i}{k}\right)^{1/2} \sqrt{Z_i} \exp(0.07433 Z_i) \qquad (A-12)$$

When $\mu_i(T_1)$ and $\mu_i(T_2)$ are given at the 2 known temperatures $T_1 \neq T_2$, (ϵ_i/k) and σ_i^2 may be found using Eq. (A-12).

Now it is possible to write a compact expression for $\mu_i(T)$:

$$\mu_i \doteq C_i \sqrt{Z_i} \; \exp(0.07433 Z_i) \qquad (A-13)$$

where

$$C_i \equiv \frac{2.6693}{1.54175} \times 10^{-5} \frac{\sqrt{W_i}}{\sigma_i^2} \left(\frac{\epsilon_i}{k}\right)^{1/2}, \quad g/cm\text{-}s \qquad (A-14)$$

The values of C_i, ϵ_i/k and σ_i, $i = 1,2,\ldots N$, are given in SI units in Table A-4.

Now it is possible to calculate λ of the mixture in a unified manner, using the data and equations given in the foregoing sections. The following sequence is used:

(1) T and $Y_1,Y_2,\ldots Y_N$ are given at the point of interest in the gas field.

(2) Using ϵ_i/k and C_i, $\mu_i(T)$ is found by Eq. (A-13) for all $i = 1,2,\ldots N$.

(3) Using μ_i and W_i, $i = 1,2,\ldots N$, the array Φ_{ij} is calculated, using Eq. (A-8).

(4) Using Y_i and W_i, $i = 1,2,\ldots N$, The various molar fractions X_i are calculated.

(5) Now the denominator of Eq. (A-7) can be calculated:

$$\sum_{j=1}^{N} \Phi_{ij}X_j, \quad i = 1,2,\ldots N$$

(6) Using F_i and E_i, the various $\lambda_i(T)$ are found by Eq. (A-9).

(7) Finally, the gas mixture thermal conductivity λ is calculated by Eq. (A-7).

The parameters A_i, B_i, F_i, E_i, C_i, ϵ_i/k and W_i are all incorporated in subprogram 'GDATA' of the overall deflagration computer scheme. C_p and λ calculations are carried out in the subprograms named 'CPG' and 'LAMDAG', in the manner described herein.

4. The Diffusivity, ρD, of the Gas Mixture

Given λ and C_p at any point in the gas, and assuming $\text{Le} \doteq 1$ for the mixture, the diffusivity is found directly by

$$\rho D \doteq \lambda/C_p$$

Utilizing the equation of state for ideal gas, ρ can be calculated and the mixture diffusion coefficient can be found from the above equation.

Unfortunately, in spite of the modeling introduced, a rather large computational effort is involved in the calculation of λ at each spatial mesh point in the gas for each integration cycle. Therefore, a simplification was sought; a natural choice for ρD is the simple power expression:

$$\rho D \simeq \left(\frac{\lambda}{C_p}\right)_s (T/T_s)^\alpha, \quad y > 0 \qquad \text{(A-15)}$$

with $\alpha = 0.67$, the above expression produced insignificant changes in the final results and, hence, was used whenever faster integration was desirable. Note that Eq. (A-15) applies only to the interior field points; at $y = 0^+$ (denoted here by subscript "s"), the strict λ-procedure of Section A.3 is applied.

REFERENCES

A1.   JANAF Thermochemical Tables, National Standard Reference Data Systems ,
      Washington, D.C., (2nd Edition), 1971.

A2.   Benson, S.W., Thermochemical Kinetics J.Wiley, N.Y., 1968, pp.30-36.

A3.   Wood, R., "The Infrared Spectrum and Structure of Cyclo Trimethylene
      Trinitramine (Cyclonite, RDX)" Advances in Molecular Spectroscopy Vol.2,
      1962, pp. 955-960.

A4.   Bird, R.B., Stuart, W.E. and Lightfoot, E.N. Transport Phenomena J.
      Wiley, N.Y., 1960, Sect. 8.3: "Theory of Thermal Conductivity of Gases
      at Low Density", pp. 253-260.

A5.   Hirschfelder, J.O., Jour. Chem. Phys., 26, 1957, pp.274-281 anu 282-285.
      Also,

      Mason, E.A. and Saxena, S.C., The Physics of Fluids Vol.1, 1958,
      pp.361-369.

A6.   Williams, F.A., Combustion Theory Addison - Wesley, Reading, Mass., 1965,
      pp. 414-429.

A7.   Handbook of Chemistry and Physics Weast, R.C. and Selby, S.M., Editors,
      The Chemical Rubber Co., Cleveland, Ohio, 48th Edition, 1967-68.

A8.   Touloukian, Y.M., et. al. Thermophysical Properties of Matter TPRC
      Series,
      Vol.3: "Thermal Conductivity of Liquids and Gases" . Also,
      Vol.11: "Viscosity".

A9.   Gallant, R.W., Physical Properties of Hydrocarbons Chap.24: "C1 - C4
      Aldehydes" Gulf Publishing Co., Houston, Texas, 1968.

A10. Valance, W.G., Personal Communication, Aug. 1974.
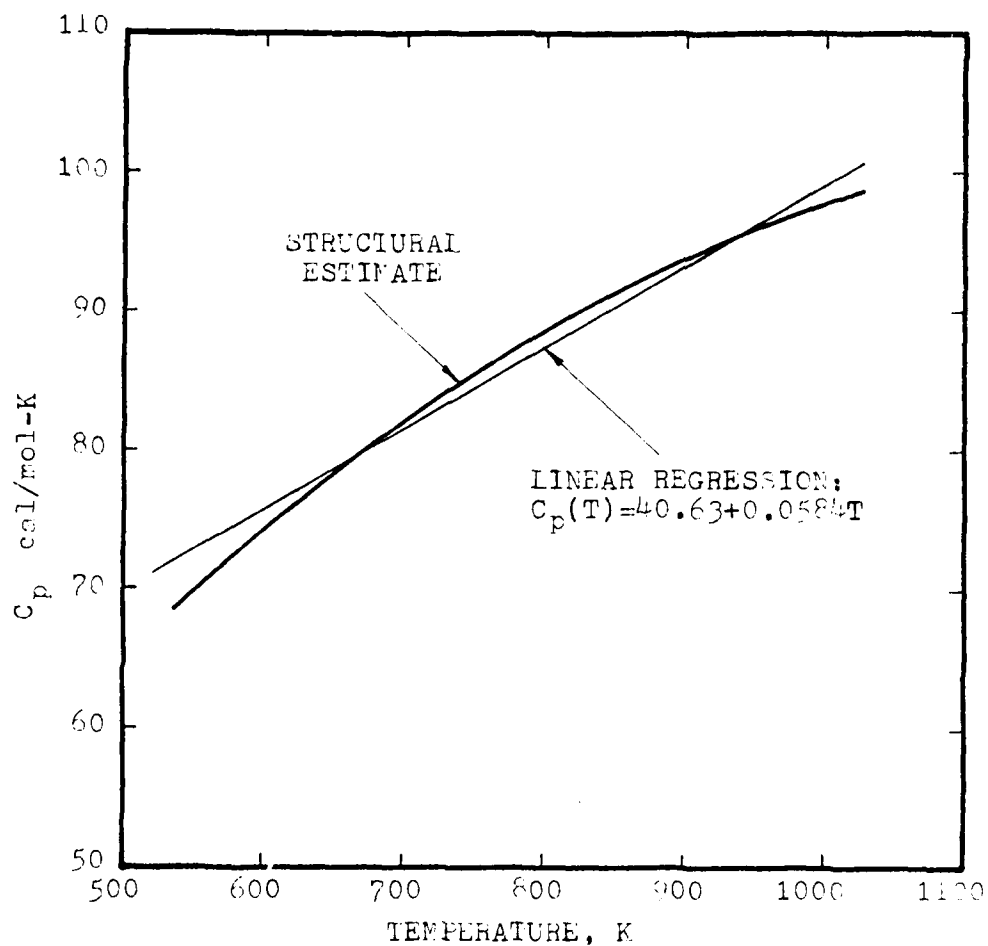
Fig. A.1

Isobaric specific heat of RDX, $C_{p,RDX}$, as function of temperature. Structural estimate is compared with a linear regression in the range 600 - 1000 K, for implementation in the deflagration model.

TABLE A-1

RDX VIBRATIONAL DATA FOR STRUCTURAL

ESTIMATE OF $C_{p,RDX}$[a]

DEGENERACY	TYPE	WAVE NO., ω_j (cm^{-1})
	A. 12 RDX Ring Vibrations	
3	C - N stretch	1000
3		1200
3		1000
3		800
	B. 18 CH_2 Vibrations	
3	Symmetrical stretch	2500
3	Asym. stretch	2700*
3	Deform.	1200
3	Twist	1000*
3	Wag	800*
3	Rock	1000*
	C. 18 NO_2 Vibrations	
3	Symmetrical stretch	1350
3	Asym. stretch	1500
3	Deform.	650
3	Twist	700*
3	Wag	700*
3	Rock	700*
	D. 9 N-N Vibrations	
3	Symmetrical stretch	1250
3		1000
3		800

[a]The data for this table was collected by W. Valance.[10]
*Data marked with asterisk are estimates from Hertzberg.[3]

TABLE A-2

PARAMETERS USED IN THE CALCULATION

OF SPECIFIC HEATS, $C_{pi} = A_i + B_i T$

i	SPECIES	A_i (J/kg-K)	B_i (J/kg-K^2)
1	RDX	765.0	0.2444
2	H_2O	1582.0	0.7037
3	CH_2O	1053.0	0.9532
4	CO_2	886.9	0.3215
5	CO	963.9	0.2071
6	N_2	953.0	0.2020
7	NO	930.5	0.1874
8	N_2O	927.2	0.2941
9	NO_2	841.1	0.2673

TABLE A-3

CONSTANTS FOR CALCULATION OF THE SPECIFIC

THERMAL CONDUCTIVITIES $\lambda_i \doteq F_i + E_i T$

i	SPECIES	F_i (W/m-K) $\times 10^2$	E_i (W/m-K^2) $\times 10^4$
1	RDX*	-3.65	1.429
2	H_2O	-1.684	1.058
3	CH_2O	-2.893	1.167
4	CO_2	+5.442	0.6197
5	CO	+1.567	0.4866
6	N_2	+1.759	0.4532
7	NO	+0.7254	0.6519
8	N_2O	-0.1369	0.7222
9	NO_2	+0.5262	0.6334

*RDX here approximated by benzene (gas) data.[8]

TABLE A-4

CONSTANT PARAMETERS FOR THE CALCULATION OF THE SPECIFIC

VISCOSITY COEFFICIENTS $\mu_i(T)$, cf. Eq. (A-13)

i	SPECIES	$\bar{W}_i$ (g/mol)	ε_i/k (K)	$\sigma_i(\overset{\circ}{A})$	C_i (kg/m-s) $\times$ 10^{+5}
1[a]	RDX	222	~440.0	~6.0	~1.50
2[a]	H_2O	18	82.1	3.81	0.458
3[a]	CH_2O	30	113.6	4.25	0.559
4	CO_2	44	190.0	3.996	0.992
5	CO	28	110.0	3.59	0.746
6	N_2	28	91.5	3.68	0.647
7	NO	30	119.0	3.47	0.859
8	N_2O	44	220.0	3.88	1.132
9[a]	NO_2	46	65.1	4.36	0.487

[a] ε_i/k and σ_i for the species marked by asterisk were calculated by available or estimated viscosity data.

APPENDIX B

CONCISE MODEL FOR THE LIQUID LAYER PROCESSES

OF DEFLAGRATING NITRAMINE MONOPROPELLANT

The assumption is made that all heat release associated with the liquid phase decomposition of nitramine is localized at the liquid/gas interface. This results in decoupling of the energy and species equations in the liquid. Particularly, the energy equation being now homogeneous (without the nonlinear source term) may be solved at once. The resulting thermal profile is then available for further solution of the single (nitramine) species equation.

The above assumption is based on the observation that the liquid layer is "thin" under the ambient conditions considered in the present study. The term "thin" means that the characteristic residence time in the liquid phase for a nitramine particle is much less than the characteristic time required for reaction for typical expected liquid phase temperatures. In other words, a characteristic thermal scale, y_m^*, representing the liquid layer thickness, is expected to be much smaller than a characteristic mean reactive length scale, y_R^*, based on a mean liquid phase temperature.

Letting

$$y_m^* \sim (\lambda_c/C_c)/m_p$$

$$y_R^* \sim m_p/\bar{\omega}_L(\bar{T}_1)$$

it is found that,

$$y_m^*/y_R^* \sim \frac{(\lambda_c/C_c)\bar{\omega}_L}{m_p^2} \sim 0(1/100) \quad .$$

where the condensed phase thermochemical data of Table III.1 is used, $\bar{\omega}_L$ is the mean reaction rate in the liquid and $\bar{T}_1 = 600$ K.

The analysis presented herein is intended to solve the liquid phase problem under the above assumption. It appears that analytical solution is possible, although closed-form solutions are not obtained.

1. Solution of the Energy Equation

In dimensionless form, the energy equation reads, for

$-a \leqslant \zeta < 0$

$$d^2\theta/d\zeta^2 - d\theta/d\zeta = 0 \qquad (B.1)$$

where
$$\theta \equiv (T-T_s)/\beta$$

$$\beta \equiv E_{ml}/R_u$$

$$\zeta \equiv y/(\lambda_c/C_c m_p)$$

and $a = y_m/(\lambda_c/C_c m_p)$ is the liquid layer thickness, which is unknown. β is the activation temperature in the Arrhenius expression for the liquid phase reaction. T_s is the liquid/gas interface temperature, and T_m is the melting temperature. The boundary conditions for Eq. (B.1) are:

$$\theta(-a) = (T_m-T_s)/\beta \equiv \theta_m$$

$$\theta(0) = 0 \ . \tag{B.2}$$

Note that $\theta \leq 0$ in the domain of interest.

The solution is,

$$\theta(\zeta) = C_1 \exp(\zeta) + C_2$$

After using the given BCs, the constants of integration C_1 and C_2 can be found. Thus,

$$\theta(\zeta) = \theta_m\left[1 - \exp(\zeta)\right]/\left[1 - \exp(-a)\right] \ . \tag{B.3}$$

Note that the denominator of the last equation will not vanish as long as $a \neq 0$, i.e., the liquid layer thickness is nonzero.

2. The Liquid Layer Thickness

Two auxiliary relations shall be used here in order to define the liquid layer thickness, y_m.

a. The energy balance at the liquid/solid interface, written in dimensional form:

$$\lambda_c dT/dy(-y_m^+) = \lambda_c dT/dy(-y_m^-) + m_p Q_m \ , \tag{B.4}$$

where the same properties regarding λ_c and C_c are assumed for both liquid and solid states. Superscript + and - denote liquid and solid sides of the interface respectively; Q_m denotes the heat of fusion per unit mass.

b. Total energy balance on the solid phase, for $-\infty \leq y < -y_m$ yields

$$\lambda_c dT/dy(-y_m^-) = m_p C_c (T_m - T_0) \qquad (B.5)$$

neglecting any heat sources or sinks in the solid, and assuming adiabaticity at $y = -\infty$. T_0 denotes the ambient solid temperature.

Combining Eqs. (B.4) and B.5),

$$\lambda_c dT/dy(-y_m^+) = m_p [Q_m + C_c (T_m - T_0)] \quad .$$

In dimensionless form, the last equation reads:

$$d\theta/d\zeta(-a^+) = [Q_m + C_c (T_m - T_0)]/C_c \beta \quad . \qquad (B.6)$$

Now, using the solution for $\theta(\xi)$ obtained in Eq. (B.3), the first derivative at $\zeta = -a$ can be written explicitly:

$$d\theta/d\zeta(-a^+) = \theta_m/[1 - \exp(a)] \quad . \qquad (B.7)$$

The liquid layer thickness, a, can be obtained explicitly using Eqs. (B.6) and (B.7):

$$a = \ln | [C_c (T_s - T_0) + Q_m]/[C_c (T_m - T_0) + Q_m] | \quad , \qquad (B.8)$$

and the dimensional expression is:

$$y_m = (\lambda_c/C_c m_p) a$$

so that y_m depends inversely on the mass burning rate, m_p, and logarithmically on T_s .

3. Evaluation of the Nitramine Mass Fraction at the Liquid Surface

It remains now only to calculate the nitramine mass fraction in the layer, using the thermal profile and layer thickness which were obtained previously.

Denoting by Y the nitramine mass fraction in the liquid (assuming decomposition products to be dissolved in the liquid nitramine), and neglecting molecular diffusion:

$$dY/d\zeta = -Y\Lambda_c \exp[-1/(\theta+\gamma)] \quad , \qquad (B.9)$$

where

$$\Lambda_c \equiv \alpha_c A_{ml}/r^2 \qquad (B.10)$$

and $\qquad 0 < \gamma \equiv T_s/\beta < 1 \quad .$

$\alpha_c \equiv \lambda_c/C_c\rho_c$, the thermal diffusivity of the liquid, and r is the linear regression rate of the propellant. (Recall that the coordinate origin $y = 0$ is fixed to the regressing liquid/gas interface.)

The BC, given at the liquid/solid interface is

$$Y(-a) = 1 \quad . \tag{B.11}$$

The solution to Eq. (B.9), satisfying Eq. (B.11) can be written in the form:

$$Y(\zeta) = \exp\left[-\Lambda_c \int_{-a}^{\zeta} \exp\left(-1/(\theta+\gamma)\right) d\zeta'\right] \tag{B.12}$$

where $\theta = \theta(\zeta)$ is given by Eq. (B.3). Thus, the problem now amounts to solution of the integral equation (B.12), or to solving the integral within the exponential, viz.,

$$I \equiv \int_{-a}^{\zeta} \exp\left[-1/(\theta+\gamma)\right] d\zeta' \quad . \tag{B.13}$$

The following transform is proposed:

$$\phi \equiv -1/(\theta+\gamma) \tag{B.14}$$

so it follows, using Eq. (B.3), that:

$$d\phi/\phi^2 = (d\theta/d\zeta)d\zeta = (\theta+c)d\zeta$$

$$= (b-1/\phi)d\zeta \tag{B.15}$$

where

$$c \equiv -\theta_m/(1-\exp(-a))$$

$$= [Q_m + C_c(T_s - T_0)]/C_c\beta \quad , \tag{B.16a}$$

and

$$b \equiv c - \gamma = (Q_m/C_c\beta) - T_0/\beta \quad . \tag{B.16b}$$

The second equality in Eq. (B.16a) was made by using the definition of a, Eq. (B.8).

Now, the integrand of Eq. (B.13) becomes, after using partial fractions:

$$\frac{e^\phi}{\phi(b\,\phi-1)} = \frac{-e^\phi}{\phi} + \frac{be^\phi}{b\phi-1} \quad . \tag{B.17}$$

The lower limit of the integration is:

$$\phi_m = -1/(\theta_m + \gamma) = -\beta/T_m \quad , \tag{B.18a}$$

and the upper limit, for the case of maximal ζ , i.e., $\zeta = 0$ is:

$$\phi_0 = -1/\gamma = -\beta/T_s > \phi_m \quad . \tag{B.18b}$$

Hence, $\phi_m < \phi < \phi_0 < 0$ shows the domain of interest to be on the negative part of the ϕ -axis.

Finally, the problem is reduced to solving the integrals $I = I_1 + I_2$, where

$$I_1 \equiv -\int_{\phi_m}^{\phi} \frac{\exp(\phi)}{\phi} \, d\phi \quad . \tag{B.19}$$

$$I_2 \equiv \int_{\phi_m}^{\phi} \frac{\exp(\phi)}{(\phi - 1/b)} \, d\phi \quad .$$

Observing Eq. (B.16b) for the parameter b, and the properties of Table III.1, it is evident that

$$-1/b = \beta/(T_0 - Q_m/C_c) > \beta/T_0$$

for practically interesting values of $T_0 > 100$ K. Thus,

$$-1/b > \beta/T_0 > \beta/T_m > \beta/T_s \quad .$$

Hence, the denominator of the integrand in I_2, namely $\phi - 1/b$ can never vanish in the domain of interest between T_m and $T_s > T_m$. Also, since $\phi_m < \phi_0 < 0$ strictly, ϕ will never vanish. Hence, it is expected that both I_1 and I_2 would exist, and the integration in both cases is not carried over any singular point.

(a) Solution of I_1

From Fig. B1, it is evident that the integrand in I_1, namely $f(\phi) \equiv \exp(\phi)/\phi$ is vanishing at $\phi = -\infty$ and both $\phi_m, \phi_0 \ll -1$, for typical thermochemical data taken from Table III.1. Hence, the integral is written conveniently in the form

$$-I_1 = \int_{\phi_m}^{\phi} f(\phi') d\phi' = \int_{-\infty}^{\phi} f(\phi') d\phi' - \int_{-\infty}^{\phi_m} f(\phi') d\phi' \tag{B.21}$$

where $$f(\phi) \equiv \exp(\phi)/\phi \quad .$$

The resulting integrals may be integrated by parts:

$$\int_{-\infty}^{\phi} \frac{e^{\phi} d\phi}{\phi} = \frac{e^{\phi}}{\phi} + \int_{-\infty}^{\phi} \frac{e^{\phi} d\phi}{\phi^2} \qquad (B.22)$$

The process of integration by parts may be repeated on the second member of Eq. (B.22), noting that $\exp(\phi)/\phi$, $\exp(\phi)/\phi^2$, etc. all vanish at the lower limit. After repeating the process n times (n not too large!),

$$\int_{-\infty}^{\phi} \frac{e^{\phi} d\phi}{\phi} = \frac{e^{\phi}}{\phi} \left[1 + \frac{1!}{\phi} + \frac{2!}{\phi^2} + \ldots + \frac{(n-1)!}{\phi^{n-1}} \right] + n! \int_{-\infty}^{\phi} \frac{e^{\phi} d\phi}{\phi^{n+1}} \qquad (B.23)$$

The residual, defined

$$\text{Res } (\phi;n) \equiv \left| n! \int_{-\infty}^{\phi} \frac{e^{\phi} d\phi}{\phi^{n+1}} \right| < \frac{n! e^{\phi}}{\left| \phi^{n+1} \right|} \qquad (B.24)$$

is bounded. It is evident now why n must not be too large--the reason is that $n!$ may surpass $\left| \phi^{n+1} \right|$ so that from a certain (critical) n and on, the residual will increase.

The asymptotic series, Eq. (B.23) for values of ϕ which are of practical interest here was found to converge very rapidly; indeed, four terms were found sufficient for proper representation.

Thus, the solution here is:

$$I_1 = - \frac{e^{\phi}}{\phi} \left[1 + \frac{1!}{\phi} + \frac{2!}{\phi^2} + \ldots + \frac{(n-1)!}{\phi^{n-1}} \right]$$

$$+ \frac{e^{\phi_m}}{\phi_m} \left[1 + \frac{1!}{\phi_m} + \frac{2!}{\phi_m^2} + \ldots + \frac{(n-1)!}{\phi_m^{n-1}} \right] - \text{Res } (\phi;n) \qquad (B.25)$$

Note that $\text{Res } (\phi;n) \gg \text{Res } (\phi_m;n)$, and it appears here as a decrement. In practical calculations it was found typically that the entire second member of Eq. (B.25), concerning ϕ_m, was negligible.

(b)   Solution of I_2

The integrand here is found to have two branches, as shown in Fig. B2.   A singular point appears at $\phi = 1/b$ but this point

lies outside of the integration domain. We are concerned here with the positive branch only of the integrand function,

$$g(\phi) = \exp\left[\phi /(\phi-1/b)\right] ; \qquad (B.26)$$

specifically, for $1 + 1/b \leq \phi \leq 0$. The lower bound is taken at the point where $g(\phi)$ has a minimum. This point is very close to the singular point $\phi = +1/b\sim (-100)$, where $g(1/b) \to +\infty$.

At the point $\phi^* = 1 + 1/b$, the value of the integrand is quite small, being

$$g(\phi^*) = \exp (1+1/b) \sim \exp (-100)$$

Thus, the point ϕ^* shall serve the same purpose as that of $\phi = -\infty$ in the integration of I_1, cf. Eq. (B.21). Here too, following the same procedure of (a) and repeatedly integrating by parts

$$\int_{1+1/b}^{\phi} \frac{e^{\phi}d\phi}{\phi-1/b} = \frac{e^{\phi}}{(\phi-1/b)} \left[1 + \frac{1!}{\phi-1/b} + \frac{2!}{(\phi-1/b)^2} + \dots \right.$$

$$\left. + \frac{(n-1)!}{(\phi-1/b)^{n-1}} \right]_{1+1/b}^{\phi} + n! \int_{1+1/b}^{\phi} \frac{e^{\phi}d\phi}{(\phi-1/b)^{n+1}} \qquad (B.27)$$

Note that $\phi-1/b > 0$ so $(\phi-1/b)^{n+1}$ will not have alternating signs. The upper limit on the number of terms considered concerning a critical n applies here, too: n should not exceed this value.

Thus, writing

$$I_2 \equiv \int_{\phi m}^{\phi} \frac{e^{\phi}d\phi}{(\phi-1/b)} = \int_{1+1/b}^{\phi} \frac{e^{\phi}d\phi}{\phi-1/b} - \int_{1+1/b}^{\phi m} \frac{e^{\phi}d\phi}{\phi-1/b} , \qquad (B.28)$$

and noting that the lower limit in the first member of Eq. (B.27) will cancel when used in Eq. (B.28). The solution therefore is:

$$I_2 = \frac{e^{\phi}}{\phi-1/b} \left[1 + \frac{1!}{\phi-1/b} + \frac{2!}{(\phi-1/b)^2} + \dots + \frac{(n-1)!}{(\phi 1/b)^{n-1}} \right]$$

$$- \frac{e^{\phi m}}{\phi_m-1/b} \left[1 + \frac{1!}{\phi_m-1/b} + \frac{2!}{(\phi_m-1/b)^2} + \dots + \frac{(n-1)!}{(\phi_m-1/b)^{n-1}} \right]$$

$$+ O\left(\frac{n!e^{\phi}}{(\phi-1/b)^{n+1}} \right) . \qquad (B.29)$$

Here, too, the residual term corresponding to ϕ_m is much smaller than that of ϕ . Actual calculations of the finite partial sums for I_1 and I_2, Eqs. (B.25) and (B.29), indicate:

(1) The four first terms of each of the series suffice for representation of both I_1 and I_2, with the error term being several orders of magnitude smaller than the leading term.

(2) The ϕ_m -members of both I_1 and I_2 series are much smaller than the residual terms due to the ϕ -members. Therefore, to a very good accuracey, the ϕ_m -terms can be discarded.

It can be concluded now, that the nitramine mass fraction at the $\zeta = 0$, inquid/gas interface (on the liquid side) can be found by

$$Y(0^-) = \exp[-\Lambda_c I] \tag{B.30}$$

where $I = I_1 + I_2$ as given by Eqs. (B.25) and (B.29), consisting of analytical expressions.

4. Conclusions

The preceding model for liquid phase processes was based on a number of simplifying assumptions. Of these, the strongest corresponds obviously to the removal of heat release by the liquid phase reaction and localizing it at the $\zeta = 0$ surface. Thus, the model solutions concerning liquid phase thickness, nitramine mass fraction $Y(0^-)$, and thermal gradient on the liquid side of the $\zeta = 0$ interface are expected to be accurate only as long as the assumption that $y_m^*/ y_R^* \ll 1$ holds.

Practical calculations were carried out with RDX liquid phase data using the present model, and compared with the calculations of a more comprehensive one, where the "thin" layer assumption was relaxed (namely, heat release in the liquid was considered). Very good agreement between the models was achieved, concerning $Y(0^-)$ and Y_m, the layer thickness, but not for $dT/dy(0^-)$, the thermal gradient. It is evident that with the thermochemical data used, the $Y_m^*/Y_R^* \ll 1$ assumption breaks down in the vicinity of $T_s \simeq 650$ K.

Utilizing other data, such as the average of several studies made by Thiokol for RDX shows excellent agreement for all three parameters of interest by the two models. This data, typically, has a reduced reaction rate pre-exponential term (A_{ml}) which directly decreases the ratio y_m^*/y_R^* .
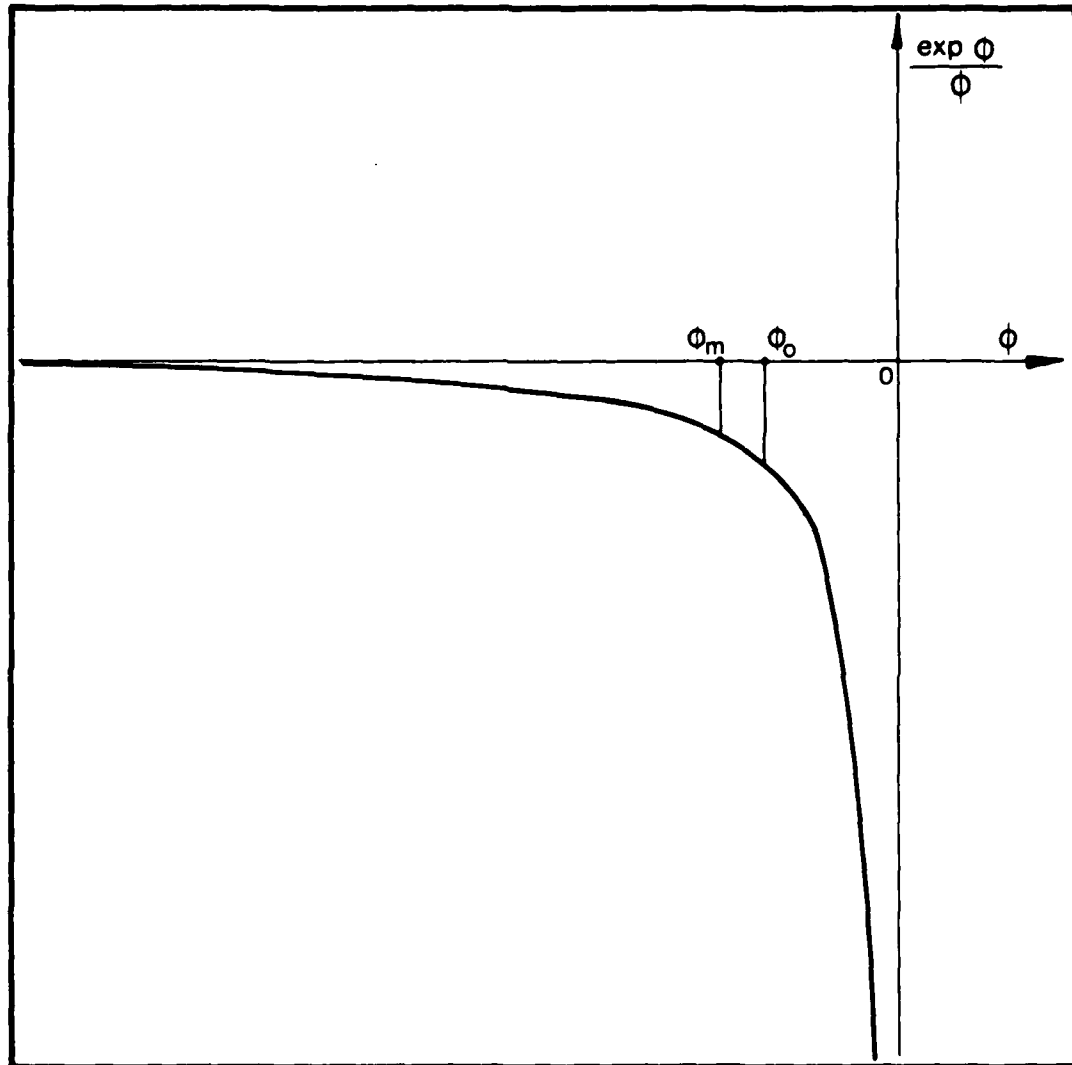
Fig. B.1
The integrand of I_1 in Eq. (B.19) shown schematically.
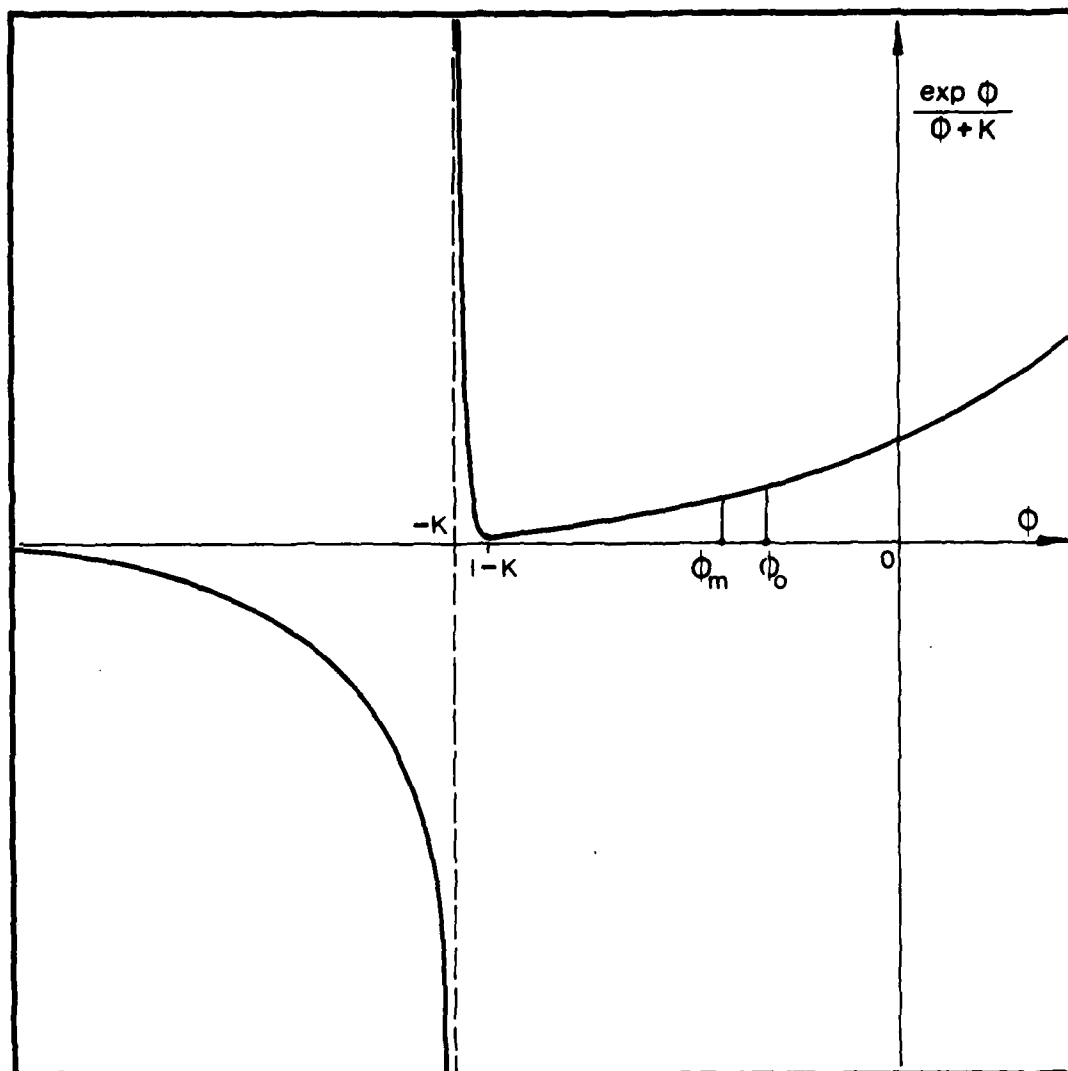
Fig. B.2

The integrand of I_2 in Eq. (B.20) shown schematically. The negative branch is not of interest. With K = 100, the minimum value of the function at $\phi = 1-K$ is much smaller than at ϕ_m .

APPENDIX C

THE NUMERICAL CODE FOR NITRAMINE DEFLAGRATION

AT STEADY STATE

A functional and structural description of the numerical computer code NTRCOM is provided herein, in the form of a user's manual. To facilitate independent use without having to refer to the full algorithm description, some of the mathematical detail of Chapter IV is repeated, in summary. As improvements and modifications to the program are continuously made, a standard format is used for internal division of the manual into sections, being more flexible to updating; this differs from the convention utilized in the rest of the thesis.

The program is written in FORTRAN IV, and consists of about 2000 lines of encoded statements. In order not to overburden this document with excessive bulk, the actual source listing of the program is excluded.

1. FUNCTIONAL STRUCTURE OF THE FINITE
DIFFERENCE ALGORITHM, NTRCOM

1.0 General Description

NTRCOM is the principal solution element of the nitramine monopropellant deflagration model. It combines condensed and gas phase integration procedures for given ambient (P,T_0) and burning rate data. A time-like relaxation procedure is utilized to obtain steady state solutions of the deflagration problem. These solutions satisfy the boundary conditions at the end of the near field in the gas and in the condensed phase; further, all of the conservation conditions related to chemical species and energy at the condensed-gas interface are satisfied, within the accuracy of the overall finite difference algorithm employed.

NTRCOM can be used as an element in the solution of the overall deflagration problem, where only ambient data (P,T_0) is prescribed and the burning rate, m, is solved for. The actual procedure involves NTRCOM in an iteration, with the nitramine evaporation law as auxiliary constraint for unique definition of m. The quality of these solutions naturally depends upon that of the available nitramine evaporation data.

Figure 1 depicts the general structure of NTRCOM. The solution procedure is contained in the subprogram group headed by RGAS. The calling subprogram CALGC serves as a link to the aforementioned overall deflagration solution.

Figure 2 depicts the logic of operation of the subprogram group under RGAS, using combined intermediate solutions of the condensed phase and gas phase fields. The remaining sections describe the functional operation of each element of the algorithm.

1.1 The Gas Phase Solution: TIMINT

The algorithm utilized to obtain numerical solution to the near field region in the gas is summarized in this section.

The $N + 1$ conservation equations for energy and $N = 9$ chemical species are cast in a one dimensional nonsteady form, which obtains a coupled, nonlinear parabolic system. The finite difference algorithm chosen for integration is generalized-implicit, using central differences in space. Thus, pseudo time-marching is employed to reach the sought steady state solution. Boundary data is perscribed as follows: at the inner boundary, $U(0^+,t) = f(t)$; at the outer boundary $\partial U/\partial y(L,t) = 0$. Initial data $U(y,0)$, is provided by a fictitious set of solution profiles.

Following quasi-linearization, the algorithm yields (at any pseudo time level) a coupled set of linear algebraic equations, in a block tri-diagonal matrix form. Solutions to this system are obtained by standard methods, employing upper-lower diagonal decomposition and Gaussian elimination; each solution passage is repeated in a predictor-corrector manner.

The predictor-corrector cycles within each pseudo time step are controlled from TIMINT, which calls for solution of the linear algebraic system.

The various U^j -dependent parameters, utilized in the gas field solution process, are calculated in COEFF. The block tri-diagonal elements corresponding to the interior gas field points are calculated in subprogram FORMQ, at each time level, and at both predictor and corrector modes. The $y = 0^+$ boundary data is utilized through subprogram BCALCQ. Subprogram SOLVEQ merely calls for the solution of the tri-diagonal matrix equation, which is made by the subprogram group under TRIBLC.

Figure 3 describes the logic of operation of TIMINT within a single time-like integration step.

1.2 Base Point Iterations: OBASE

The procedure generates initial values of the dependent variable vector U at the liquid-gas interface:

$$U_0^T = (Y_1(0^+) \quad Y_2(0^+) \cdots Y_N(0^+) \quad T_S) \quad ,$$

for the given set of data (T_0, P, m) these values are used to start the integration process. For this purpose, an initial estimate of the near-field in the gaseous deflagration region is made, assuming that nitramine decomposition is the only reaction occuring, that it goes to completion at the outer end of the near field, and that the condensed phase is chemically inert.

An overall energy balance obtains a single algebraic expression, in which the only unknown is T_S . This is made possible by use of the evaporation law, which yields the partial pressure of nitramine vapor,

$$P_{NTR}(0^+) = f(P; T_s)$$

and suitable Shvab-Zeldovich coupling terms among species, obtaining linear expressions:

$$Y_j(0^+) = f[Y_{NTR}(0^+)] \quad , \quad j = 2, 3 \cdots N \quad .$$

The energy balance expression is solved by a regula falsi procedure for T_s . In most cases tested, reasonable sets of initial data were obtained this way.

1.3 Initial Conditions: SDATA

Preliminary calculations are performed in SDATA, for the given data (P, m), following the convergence of the base point iterations which yield $U(y = 0^+, 0)$. The main calculations therein are summerized as follows:

a. The parameters $\bar{C}_p(0^+)$, $\bar{\lambda}(0^+)$, $\bar{W}(0^+)$ and $\rho(0^+)$ are calculated, based on the vector $U(y = 0^+,0)$.

b. The length of the region of interest in the gas is fixed as $XF = XSCALE*(\bar{\rho}D)_0/m$, where $(\bar{\rho}D)_0 = \bar{\lambda}(0^+)/\bar{C}_p(0^+)$, and the associated spatial increment is $DX = XF/NF$, with $NF \doteq 25$. The Length given by XF defines mostly the near field in the gas, where primary nitramine decomposition is dominant. Thus, for RDX and HMX simulations one should not expect to find $T_f \sim 3000$ K at the end of the zone; rather, temperatures achieved at $y \sim XF$ are close to 1300 K, with $XSCALE = 2$, typically. In the present second order accurate scheme, employing a uniform spatial mesh, a substantial increase in the size of the region (by increase of $XSCALE$ at constant NF) would result in an appreciable loss of accuracy, particularly near $y = 0^+$, where gradients are high. On the other hand, an appreciable decrease in the region length would tend to invalidate the adequacy of the outer boundary condition, $\partial U/\partial y(XF,t) = 0$.

c. A time step, $DT = TSCALE*DX/VS$, where $VS = m/\rho(0^+)$ is calculated, for the gas field integration. In spite of the gas phase problem being parabolic, and the implicit algorithm employed, DT may not be arbitrarily chosen, to avoid numerical instability. Values of $TSCALE \leq 1$ must be specified in most cases.

d. Initial profiles, for $U(y,0)$ are computed, using quadratic polynomials. The three coefficients for each component of U are determined by $U(y=0^+,0)$, $U(y=XF,0)$ and $\partial U/\partial y(XF,0) = 0$. The vector $U(XF,0)$ is estimated by imposing a fully reacted secondary flame at $y = XF$ (as calculated in $YFIN$) and the specified $TFIN = T(XF,0)$. These initial profiles are completely artificial, and serve merely to start the integration process. They must, however, be smooth enough, to minimize initial error propagation due to non-analiticity. Particularly, the condition that all mass fractions must sum to unity at all points $0 \leq y \leq XF$ was found very important.

e. The calculation of the $U(y,0)$ profiles is followed by calculation of the coefficients in the equations of motion at time level 0. This is required to properly start the predictor-corrector procedure in $TIMINT$.

1.4 The Condensed Phase Solution: RCND

The initial value problem corresponding to the original two-point boundary value problem in the liquid phase is solved by means of an RK-4 (fourth order Runge Kutta) integration marching forward from the solid/liquid interface, where $ZETA = 0$, to the liquid/gas interface. The only two dependent variables here are the total (convective and conductive) heat flux and distance, both in dimensionless form. The problem is solved in the phase-plane, and dimensionless temperature serves as the single independent variable.

This procedure yields solutions of the condensed phase profiles, but of these only the liquid side of the liquid-gas interface parameters are kept for purposes of the present combined gas-condensed phase solution. Unique solutions are generated for imposed data sets (T_0, T_s, m) The algorithm executing the condensed phase solution is contained in the subprogram group under RCND.

For a particular value of m, the boundary condition relaxation procedure at $y = 0$ (contained in SURG) may perscribe temporarily a value of T_s which is too high, such that $dT/dy = 0$ occurs for $T < T_s$ within the liquid field (followed by $dT/dy < 0$ as T becomes closer to T_s). The solution procedure is stopped in this instance, since the current value of T_s is out of range in terms of the existence of physically valid condensed phase solutions. To restart, a higher value of m is recommended. This would decrease the amount of the effective heat release in the layer since the dimensionless reaction rate is $\omega \sim 1/m^2$. The structure and logic of the particular section of the program dealing with the condensed phase solution is described by the block diagram and flow charts of Figures 4, 5, and 6, referring to the subprogram group RCND.

1.5 Time-like Relaxation of the $y = 0$ Boundary Conditions: SURG

The procedure is contained in subprogam SURG, utilizing the energy and chemical species conservation constraints at the liquid-gas interface. These $N + 1$ dimensionless conditions form algebraic relations, by which the dimensional dependent variable vector

$$U^T(y = 0^+, t^{j+1}) = (Y_1(0^+) \quad Y_2(0^+) \cdots Y_N(0^+) \quad T_s)^{j+1}$$

can be calculated at each time level. This is made possible by second order, 3-point representation of the gas side gradients, and naturally requires gas phase and condensed phase solutions at time level t^j. Thus, the $y = 0$ boundary values, U_0, are varied at each (pseudo) time level, in an attempt to relax or minimize the error in the interface constraints. In terms of the previously described gas phase solution procedure, this amounts to solving the parabolic gas phase problem with one set of boundary data being time dependent.

The boundary relaxation procedure is called from subprogram RGAS, after the gas field solution has advanced by one time step. It calls for condensed phase solution in RCND, utilizing the data (m, T_s^j).

The entire combined (condensed and gas phase) solution is considered converged to steady state only if both gas-field and $y = 0$ surface time-like variation is close enough to zero. A check on the convergence of the U_0^{j+1} vector is made at each time step in subprogram SURG. After convergence, the final residual errors in the interface constraints are calculated

in subprogram SGRAD, called from RGAS. The logic of operation of the $y = 0$ surface relaxation procedure is shown in Figure 7.

1.6 Utilities: Physical Parameters, Output and Algebraic Manipulations

The mean isobaric specific heat of the gas mixture, C_p and the heat conductivity thereof, , are calculated in subprograms CPG and LAMDAG respectively. The primary and secondary reaction rates, ω_1 and ω_2, are calculated in subprogram RRATE, but this calculation is made only for purposes of output. Given the values of the dependent variable vector, U, and ambient data (P), these subprograms calculate the values of the above physical constants at a point (y_n, t^j) . All three subprograms mentioned (and the first two in particular) require appreciable amounts of thermophysical data concerning individual species. These data are stored in subprogram GDATA, not included within the active input for each regular run; the information is passed through use of labeled common blocks.

Output for the final converged step (steady state solution) has the forms of printout, punched cards (both containing converged profile data and parameters of interest) and printer plots. The first two of these functions are performed by subprogram PRINT, along with a fair amount of calculations for output involving converged step data. The printer plots are called by subprogram PLUTO, and executed by FOXGRF.

Subprogram UNINTG executes the fourth-order Runge Kutta (RK4) procedure, required for the condensed phase solution. Subprogram TRIBLC heads a group of programs which perform block tri-diagonal linear system solution.

Functions VPXP and VAPR are used for calcultions involving the evaporation law for nitramine.

2.0 Description of Program Input

The discussion in this section coupled with the sample problems described in Section 4.0 will enable the user to prepare input for the program. The SI system of units is used as program input and in the internal calculations. However, since this is the period of transition to the SI units, some of the input descriptions indicate the conversion from the previously used units to the SI units and some of the program output is converted to more familiar units.

The input to the program is in four parts: a comment card identifying the run, followed by three sets of data input by means of the following three NAMELISTS:

a. NGAS -- data concerning the gas phase integration

b. NCND -- data concerning the condensed phase integration

c. NCOM -- data for execution of the solution process to the deflagration problem, combining condensed and gas phase integrations.

All input data are handled through a single subprogram, DLOAD, called once at the beginning of any particular run. DLOAD performs the following functions:

a. reading of the three groups of (NAMELIST) data and printing them out

b. calling subprogram GDATA which contains thermophysical properties of the species considered in the gas phase;   GDATA also calls for calculation of some of the gas-phase initial conditions (typically, mass fractions at the downstream-end of the flame, through subprogram YFIN).

c. calculation of constant parameters for both gas and condensed phases, which do not change during a single run.

The data are communicated to the rest of the program by means of several common blocks. A block diagram of the program input section is given in Figure 8 . A detailed description of the contents of the three NAMELISTS is given in the following sections. Unless indicated otherwise by the decimal or lack of decimal in the default value, the NAMELIST variables follow the usual Fortran conventions for fixed and floating numbers.

The usual caution should be used when building up a new input data set, e.g.,

(1) whenever practical, pattern new data sets after sample cases

(2) first check-out run should be for a short computer running time interval, i.e., a small value of ITSTEP,

(3) build up new data sets (which differ markedly from the familiar cases) by making a progression of check-out cases in which individual changes are explored, and

(4) examine the output for obvious inconsistencies or evidence of instabilities.

2.1 Input Pertaining to the Gas Phase

The following data is read in through NAMELIST 'NGAS'.

2.1.1 Initial Conditions

Computer Symbol	Symbol in Text	Description	Units
TF	T_f	Initial temperature at the $y = L$ point, for starting profiles only. (1300.)*	K

2.1.2 Primary Reaction Kinetic Parameters:

AHRN1	A_1	Pre-exponential factor for the primary (nitramine decomposition), overall reaction. (3.2E15, Robertson 1948)	s^{-1}
EB1	E_1	Activation temperature for the primary nitramine decomposition overall reaction; = activation energy (cal/mol)/R_u where R_u = 1.986 cal/mol-K. (41,500./1.986, Robertson 1948)	K
H1	Q_1	Heat of reaction for the primary nitramine decomposition (1st order overall), in the gas phase. (108,000. × 4.184)	J/mol

2.1.3 Secondary Reaction Kinetic Parameters:

AHRN2	A_2	Pre-exponential factor for the secondary (second order, overall) chemical reaction $NO_2 + CH_2O$.	m^3/mol-s
EB2	E_2	Activation temperature for the secondary (2nd order overall) reaction. (19,000./1.986, Pollard & Wyatt, 1949)	K
H2	Q_2	Heat of reaction for the secondary (2nd order overall), e.g., NO_2 + CH_2O reaction. (45,500. × 4.184)	J/mol

---

*Values in parentheses are default values.

2.1.4 Evaporation Parameters:

Computer Symbol	Symbol in Text	Description	Units
TRVAP	T_v	Evaporation law reference temperature. (A local temperature corresponding to liquid conditions.)	K
EVAP	E_v	Evaporation law activation temperature, [evap. energy (cal/mol)/ R_u]. Value is equal to the heat of vaporization, not the heat of sublimation.	K
PVAP	P_v	Evaporation law reference partial pressure (of nitramine, liquid/ gas), at the specified "TRVAP" reference temperature. Obtained from sublimation data.	MPa

2.1.5 Numerical Solution Parameters:

Computer Symbol	Symbol in Text	Description	Units
IF		Denotes total number of chemical species considered, must be $\leq$ 9. (9)	
MF		Total number of dependent variables = total number of species (IF) + temperature (1) (10)	
NF		Total number of interior mesh points in space (x), excluding the end points at x = 0 and x = L. Should not be more than 25 or less than 20. (25)	
KMAX		Maximum number of repeating corrector steps for each predictor-corrector (timelike implicit) integration. (2)	
THETA	θ	Dimensionless parameter for the generalized-implicit integration, 0.0 < THETA $\leq$ 1.0. (0.9)	
TSCALE		Dimensionless constant for stretching or contracting Δt (Δt is calculated in the program). Can range between 0.02 and 1.0. (1.)	

Computer Symbol	Symbol in Text	Description	Units
XSCALE	b	Dimensionless constant for stretching or contracting Δx (Δx calculated in the program). Can range between 0.5 and 3.0. (2.0)	
STEADY	(ϵ_t)	Tolerance for achievement of steady state by the time-like integration process. Checking temperature, if it changes at all nodes by less than STEADY, steady state is achieved. (0.1)	K
ITSTEP		Total number of time-like integration steps allowed (within which steady state should be achieved). (40)	

2.1.6 Stoichiometry of the Primary Reaction:

The overall nitramine decomposition step may be described in balanced form:

$$\nu'_{1,1} \, NTR \rightarrow \nu''_{1,2} \, H_2O + \nu''_{1,3} \, CH_2O + \nu''_{1,4} \, CO_2 + \nu''_{1,5} \, CO$$

$$+ \nu''_{1,6} \, N_2 + \nu''_{1,7} \, NO + \nu''_{1,8} \, N_2O + \nu''_{1,9} \, NO_2 \;\; .$$
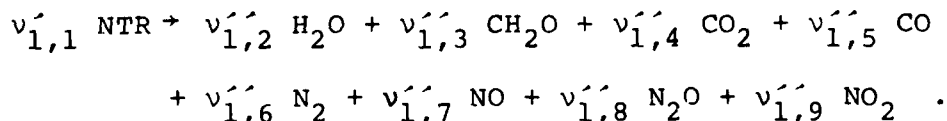
Computer Symbol	Symbol in Text	Description	Units
STOIC1	$(\nu''_{1,n} - \nu'_{1,n})$	The stoichiometric coefficient of the nth species in the overall primary decomposition reaction. STOIC1 = 0 for all specias not participating.	

2.1.7 Stoichiometry of the Secondary Reaction:

Same form as for primary reaction; for example:

$$\nu'_{2,9} \, NO_2 + \nu'_{2,3} \, CH_2O \rightarrow \nu''_{2,2} \, H_2O + \nu''_{2,4} \, CO_2 + \nu''_{2,5} \, CO$$

$$+ \nu''_{2,6} \, NO \;\; .$$
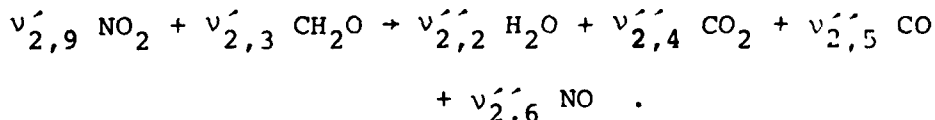
(species not participating were omitted)

Computer Symbol	Symbol in Text	Description
STOIC2	$(\nu''_{2,n} - \nu'_{2,n})$	Stoichiometric coefficient of the the nth species in the secondary reaction. STOIC2 = 0 for all species not participating.

2.2   Inputs that Pertain to the Condensed Phase

The following inputs are read in as part of NAMELIST NCND.

2.2.1   Liquid nitramine decomposition thermochemistry data:

Computer Symbol	Symbol in Text	Description	Units
AMELT1	A_{m1}	Pre-exponential factor for the primary overall decomposition in the liquid phase.	s^{-1}
EM1	E_{m1}	Activation temperature for primary overall decomposition in the liquid phase.	K
HM1	Δh_{m1}	Heat of reaction in the condensed phase. For nitramine decomposition, NITR(S1)→PRODUCTS(g) + HM1.	J/mol

2.2.2   Melting and evaporation data:

TM	T_m	Melting temperature of solid.	K
QMELT	Q_{melt}	Heat of fusion (melting) for nitramine.	J/mol
QVAP	Q_v	Heat of vaporization for nitramine. (Liquid to gas.)	J/mol

2.2.3   Condensed phase properties (liquid and solid properties are considered to be approximately equal):

RHOC	ρ_c	Density of condensed phase.	kg/m^3
CC	C_c	Specific heat of condensed phase.	J/kg-K
RLAMDA	λ_c	Thermal conductivity of condensed phase.	J/m-s-K
WMNTR	W_1	Molecular weight of nitramine.	kg/mol

2.2.4 Integration parameters used for internal control of solution (should not be changed by those unfamiliar with the method of solution):

Computer Symbol	Symbol in Text	Description	Units
MFM		Number of dependent variables integrated in the liquid phase program. Consists of: (a) temperature gradient, (b) distance in melt . (2)	
JFF		Number of interior nodal points in the condensed phase field numerical solution. (50)	

2.3 Inputs that Control Combined Solution

The following inputs are read in as part of NAMELIST NCOM:

2.3.1 Imposed Boundary and Ambient Conditions:

Computer Symbol	Symbol in Text	Description	Units
P	p	Pressure of current calculation not used in solution.	MPa
TO	T_0	Solid ambient temperature in semi-infinite slab. (298.0)*	K
RREF		Initial approximation of propellant regression rate, base point. (0.005)	m/s
TSB		Initial estimate for the condensed/gas interface temperature, to start base point iteration. (650.)	K

2.3.2 Base Point Iteration Control

The parameters in the following sections should not be changed by those unfamiliar with the method of solution.

DTS		Interface temperature increment for the base point iteration. (5.)	K
JBMAX		Maximal number of allowed base point iterations (regula falsi method). (15)	

2.3.3 Relaxation of the $y = 0^+$ Boundary Data

RBITE		Surface temperature (T_s) iteration parameter for damping oscillations during initial stages of relaxation procedure. (30.)	

*Values in parentheses are default values.

2.3.4 Parameters for External Solution Control

The following parameters are required
only when NTRCOM is utilized as an
element in a Newton-Raphson iterative
algorithm, to solve for the mass burning
rate, m .

Computer Symbol	Symbol in Text	Description	Units
ITER		Dimension of Newton Raphson iteration vector and error vector (deflagration problem solution process). (1)	
KFIN		Maximal number of regular Newton-Raphson iterations allowed with any single Jacobian (without re-computing the Jacobian matrix). (10)	
JACMAX		Maximum number of Jacobian matrix formations allowed in a single run. (4)	
PERT		Dimensionless perturbation parameter for use in the numerical formation of the Jacobian matrix. (0.01)	
BIT		Suppression factor for the Newton-Raphson correction vector (in order not to use its full length, to avoid divergence). (0.50)	
TOLZ		Dimensionless tolerance for error vector components in the Newton-Raphson scheme, to signal convergence. (0.005)	

3.0   Description of Output

Following the printing of input parameters, there are six major printout sections corresponding to output from the solution procedure in NTRCOM, for each single run.   These are:

  a)   Base-point iterations
  b)   Initial data
  c)   Condensed phase data
  d)   Relaxation of the $y = 0^+$ boundary data
  e)   Gas phase profiles from converged (or last) integration step
  f)   Final $y = 0$ interface data

Sections (c) and (d) are repeated at each integration step, as indicated by the "timestep No." caption; the first printout from the condensed phase corresponds to the initial data.

3.1   Base-Point Iterations Output

This section corresponds to output from the regula-falsi base point surface temperature (T_s^0) iteration procedure in OBASE. It contains four columns marked as follows:

  a)   J = iteration step number, the regula-falsi procedure. The first two lines denoted "0" correspond to the initial guess and a perturbation, respectively.
  b)   ERROR(K) = current iteration error, degrees K.
  c)   TS(K) = current T_s -iterate value, degrees K.
  d)   YR = nitramine mass fraction at the gas side of the concensed/gas interface, $Y_{NTR}(0^+) = f(P;T_s)$.

The last line of data corresponds to the converged case.   The criterion for convergence is calculated in OBASE and taken as $1/T_s^0$, where T_s^0 = the initial guess.

3.2   Initial Data

This printout section is generated by subprogram SDATA, called from RGAS after convergence of the base point iteration procedure. The printout is self-explanatory; it consists of $y = 0^+$ and initial data calculated therein, corresponding to the gas phase.

3.3   Condensed Phase Data

This printout section is generated in subprogram RCND, called from SURG each integration cycle.   It consists of two main parts. First, constant parameters, and boundary conditions at the solid-liquid interface; some of these parameters are T_s -independent,

and will remain invariant for all integration cycles within a single NTRCOM run. Second, solution data, given only at the liquid side of the $y = 0$ interface. Detailed profiles of the entire condensed phase solution are not given, as they can be obtained readily from the independent condensed phase program NTRCND. A detailed description follows.

a) Following "CONSTANT PARAMETERS FROM CDTA", a number of reference terms are printed:

$TSTR = T_s - T_m$, reference temperature

$QSTR = C_c * TSTR$, reference enthalpy

$HSTR = m * QSTR$, reference heat flux

$DELQ = [Q_{liq}/W_R]/QSTR$, normalized heat of reaction in the liquid

$CSZ = [C_c(T_m - T_0) + Q_m]/(Q_{liq}/W_R) - 1$, Shvab-Zeldovich type coupling term between total thermal flux and nitramine mass fraction

$XSCALE = (\lambda_c/C_c)/m$, length scale in the condensed phase

b) "INITIAL CONDITIONS AT THE SOLID-LIQUID INTERFACE":

$PHIO(0) = [C_c(T_m - T_0) + Q_m]/QSTR$, total dimensionless (convective and conductive) thermal flux in the liquid, in the direction of the solid

$DT/DY(0)$ = dimensional thermal gradient, on liquid side

$ZETA(0)$ = dimensionless distance in liquid

c) "CONDENSED PHASE SOLUTION AT LIQUID-GAS INTERFACE"

$YNTR(0^-)$ = nitramine mass fraction

$HCON = \lambda_c dT/dy(0^-)$, dimensional heat conduction into liquid

$HCON + YR*QV*MDOT = \lambda_c dT/dy(0^-) + Y_1(0^-)Q_v m$, dimensional heat feedback required from the gas phase to maintain the enegy balance at $y = 0$.

$YS(0^-)$ = mass fractions of all species considered in the program, at the liquid side of the $y = 0$ interface (spacing and order are same as those of the surface relaxation data printed out below)

3.4   Surface Relaxation Data at y = 0

The printout of this section is generated in subprogram SURGE, following "TIMESTEP NO.". Only two lines of data are printed:

$US(0^+)$ = the vector of boundary conditions
$(Y_1(0^+)Y_2(0^+)\cdots Y_9(0^+)T_s)$, at the gas side of
of the $\hat{y} = 0$ interface, for the current timestep.

$DELUS(0^+)$ = The vector of increments used to generate the current values of $US(0^+)$ from previous timestep data. $T_s(K)$ is given in dimensional form, but the corresponding incremental value is dimensionless, viz. $\Delta T_s/TREF$. A negative sign of any $DELUS(0^+)$ term denotes an increment, while a positive sign indicates a decrement. For the purpose of checking the gas field behavior, the above printouts are preceded by the temperatures from the two first interior field points, T_1 and T_2. These are are generated by RGAS.

3.5   Gas Phase Solution Output

The printout follows the "CONVERGED" or "UNCONVERGED" message, and occupies two pages of output. The first consists of parameter profiles, and the second of species and temperatu-re profiles throughout the gas phase regime. The first and last in each column of data correspond to the surface $y = 0^+$ and the final point $y = XF$, respectively. The column marked "N" denotes the current spatial notal point. A detailed description of the parameters in the first page is given as follows:

Y,MICRONS = distance in the gas field, from the liquid surface

CPBAR = mean isobaric specific heat of the gas mixture, J/Kg.K

1/WBAR = reciprocal mean molecular weight, mol/kg

WBAR,G/MOL = mean molecular weight

LAMDAG = λ_g, mean heat conductivity, J/m-s-K

RHOD = ρD, mean molecular diffusivity, Kg/m-s

DIFF = D, mean diffusion coefficient, m^2/s

RHOG = ρ, mean gas density, $WBAR*P/R_uT)$

DRHOD/DY = $d(\rho D)/dy$

RR1 = reaction rate constant for primary nitramine decomposition, $A_1 \exp(-E_1/T)$, 1/s

RR2 = reaction rate constant for the secondary reaction (NO_2+CH_2O), $A_2 \exp(-E_2/T)$, $m^3/mol-s$

OMEGA1 = $\rho * RR1 * Y_R/W_R$, overall primary reaction rate, mol/m^3-s

OMEGA2 = $\rho^2 * RR2 * (Y_3/W_3)(Y_q/W_q)$, overall secondary reaction rate, $mol/m^3.s$

Q1*OMG1 = Q1*OMEGA1, net heat production by primary reaction, $J/m^3.s$

K*DT/DY = $\lambda_g dT/dy$, conductive heat flux, in -y direction, $J/m^2.s$

DTAU/ΔZETA = dimensionless thermal gradient (the dimensionless conductive enthalpy flux per unit mass generated, m)

The second page of gas phase output consists of profiles for the nine species considered and temperature. The "TIME,SEC" message refers to the current pseudo-time, t^j, for the converged step printed.

3.6 $y = 0^+$ Surface Data

This printout section corresponds to final, converged step data. Four groups of parameters are given; according to order of appearance, these are summarized as follows:

a) Converged step solution vector at the $y = 0^+$ interface. The first two lines repeat the last printout from the surface relaxation procedure, cf. Section 3.4. In addition:

REDIF = dimensionless diffusive flux, on gas side. For chemical species, $-dY_K/d\zeta(0^+)$, and for temperature, $d\tau/d\zeta(0^+)$,

TOTAL FLUX = for chemical species, dimensionless convective and diffusive flux, $Y_K(0^-) - dY_K/d\zeta(0^+)$. For temperature, $d\tau/d\zeta(0^+)$ is repeated.

Each column of the above four lines of output corresponds to a chemical species, as indicated. The last column is for temperature.

The following line summarizes three parameters of interest: $\lambda dT/dy(0^+)$, the conductive heat feedback at the gas side, CPS = $\bar{C}p(0^+)$, the isobaric specific heat, and LAMDAGS = $\lambda(0^+)$, the heat conductivity. All are dimensional, and given for quick reference.

b) "REFERENCE PARAMETERS--" these terms were used for the normalization of the $y = 0$ interface constraints, and remain constant during the run.

$CPS\emptyset$ = reference specific heat

$TREF$ = reference temperature, $CPSO*TREF = Q1/W_R$

$HSCAL = m*CPS\emptyset*TREF$, reference heat flux

$RH\emptyset D/FLUX(0^+)$ = reference length scale in the gas, = $XF/XSCALE$

c) Evaporation law data is printed in the following three lines:

*"YNTRG---": The calculation of nitramine mass fraction by evaporation law involves the parameters EVAP, PVAP, TRVAP, and the converged step surface vector $U_s(0^+)$, excluding the nitramine mass fraction $Y_1(0^+)$.

*"ERR1---": The difference between the nitramine mass fraction, calculated by the evaporation law and that provided by the converged step.

*"REF.NTR···PVREF(MPA)=": Assuming that the evaporation law parameters EVAP and TRVAP are valid, the reference vapor pressure is re-calculated by letting ERR1 = 0, namely, using the $Y_1(0^+)$ of the converged step in the calculation. This parameter should be compared with the value of PVAP given in the input listing.

d) Finally, a table of dimensionless residuals of the $y = 0$ conservation conditions is printed. The order of the table (indicated by the serial number column, L) is identical to that of the dependent variable vector, U. To obtain an idea of the converged step accuracy, the values printed should be compared with unity.
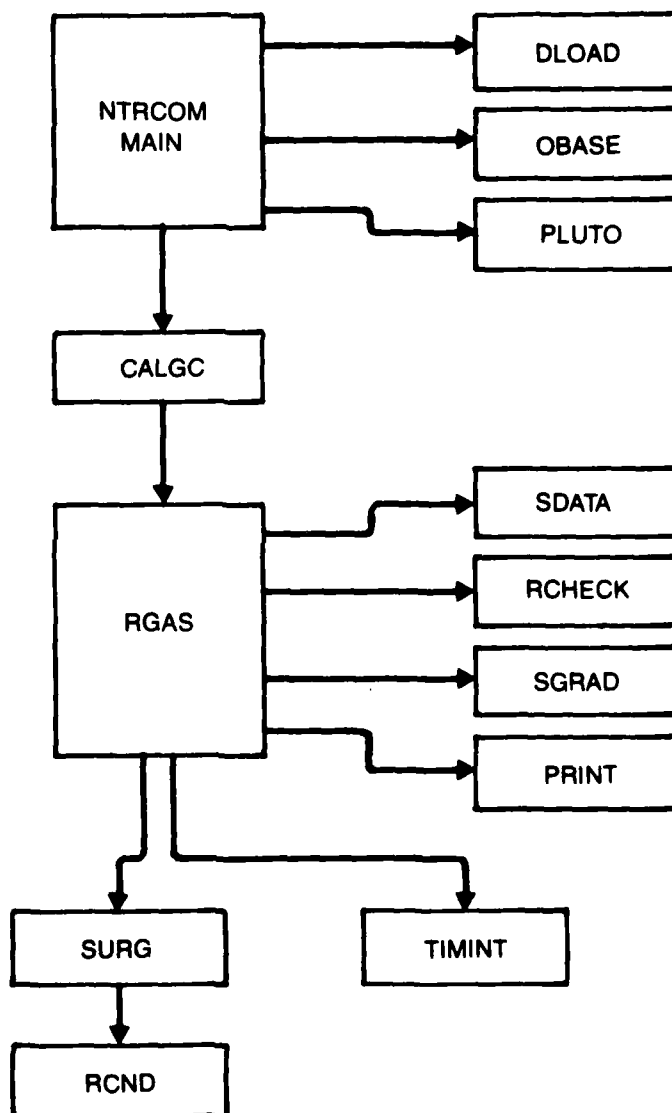
Fig. C.1.

NTRCOM STRUCTURE
Block diagram with principal components of the combined
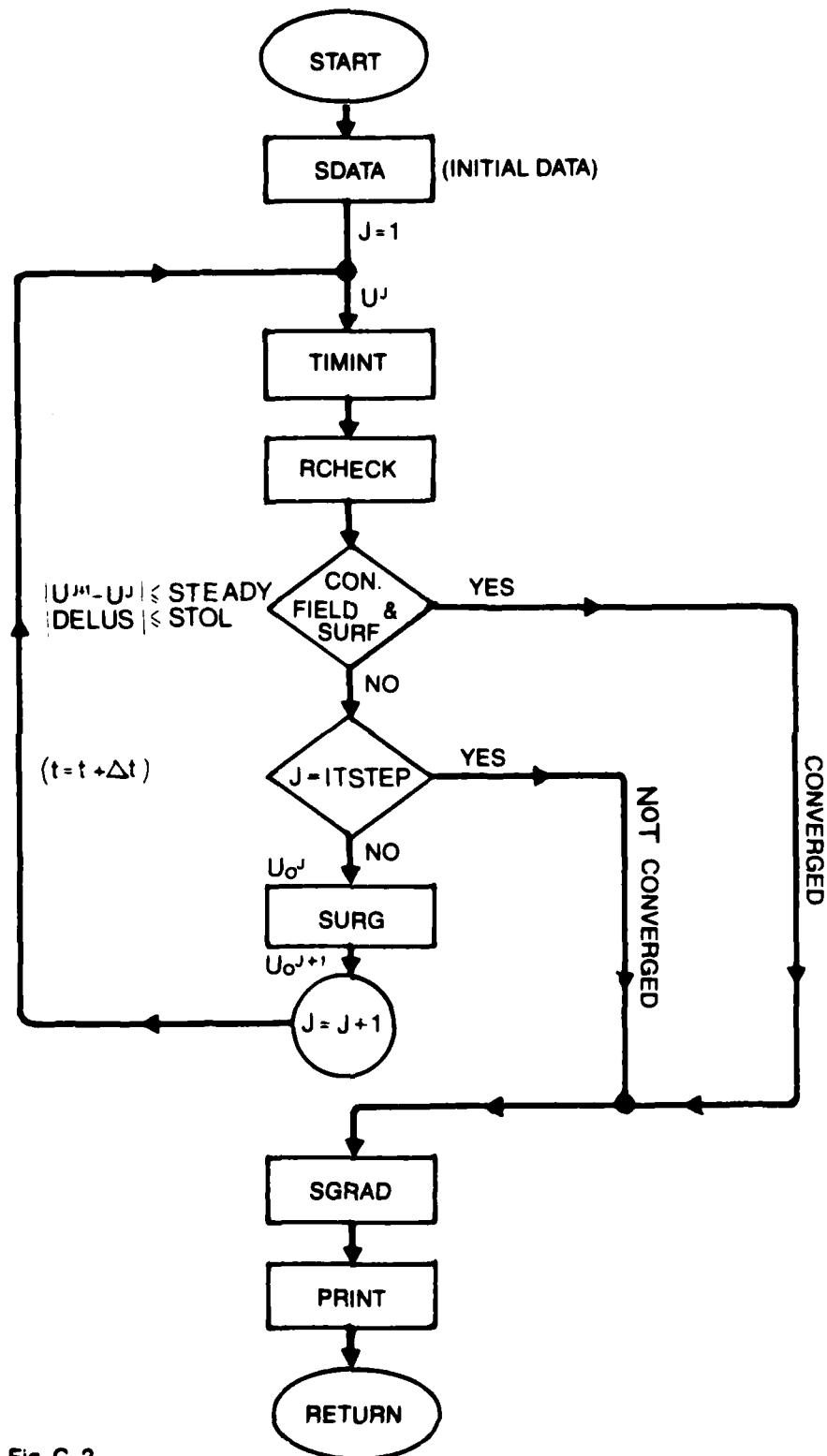condensed and gas phase program.

Fig. C. 2

RGAS FLOW CHART OF OVERALL INTEGRATION CONTROL:
TIMINT for the gas field, and SURG for the y = o surface and condensed phase.

```
                    ┌─────────┐
                    │  START  │
                    └─────────┘
                         │
                         ▼
        ┌────────────────────────────────────┐
        │      RHS OF GEN. IMPLICIT          │
        │           OPERATOR:                │
        │  R ᴶᴴ = (1/θ') U ' + (1—1/θ' ) R '  │
        │            (EXACT)                 │
        └────────────────────────────────────┘
                         │
                         ▼
        ┌────────────────────────────────────┐
        │        INITIAL PREDICTOR           │
        │      U ᴶᴴ,ᴾ = 2U '—U ¹'¹           │
        └────────────────────────────────────┘
                         │
                         ▼
        ┌──────────────────────┐   YES   ┌──────────┐
        │  TROUBLE SHOCTING    │────────▶│  ITERP   │
        │  VALUES OF U ' ⁺ ',ᴾ  │         └──────────┘
        │    OUT OF RANCE?     │
        └──────────────────────┘
              K = 1   │
                      ▼           U ᴶᴴ ᴾ
                ┌──────────┐
                │  COEFF   │
                └──────────┘
                      │
                      ▼
                ┌──────────┐       ┌──────────┐
                │  FORMQ   │──────▶│  BCALCQ  │
                └──────────┘       └──────────┘
                      │
                      ▼
                ┌──────────┐       ┌──────────┐
                │  SOLVEQ  │──────▶│  TRIBLC  │
                └──────────┘       └──────────┘
                      │
                      ▼
                     ( )   U ' ⁺ ',ᶜ
                      │
         K = K + 1    ▼
                     ( )
                      │
                      │  K = KMAX
                      ▼
                ┌─────────┐
                │ RETURN  │
                └─────────┘
```
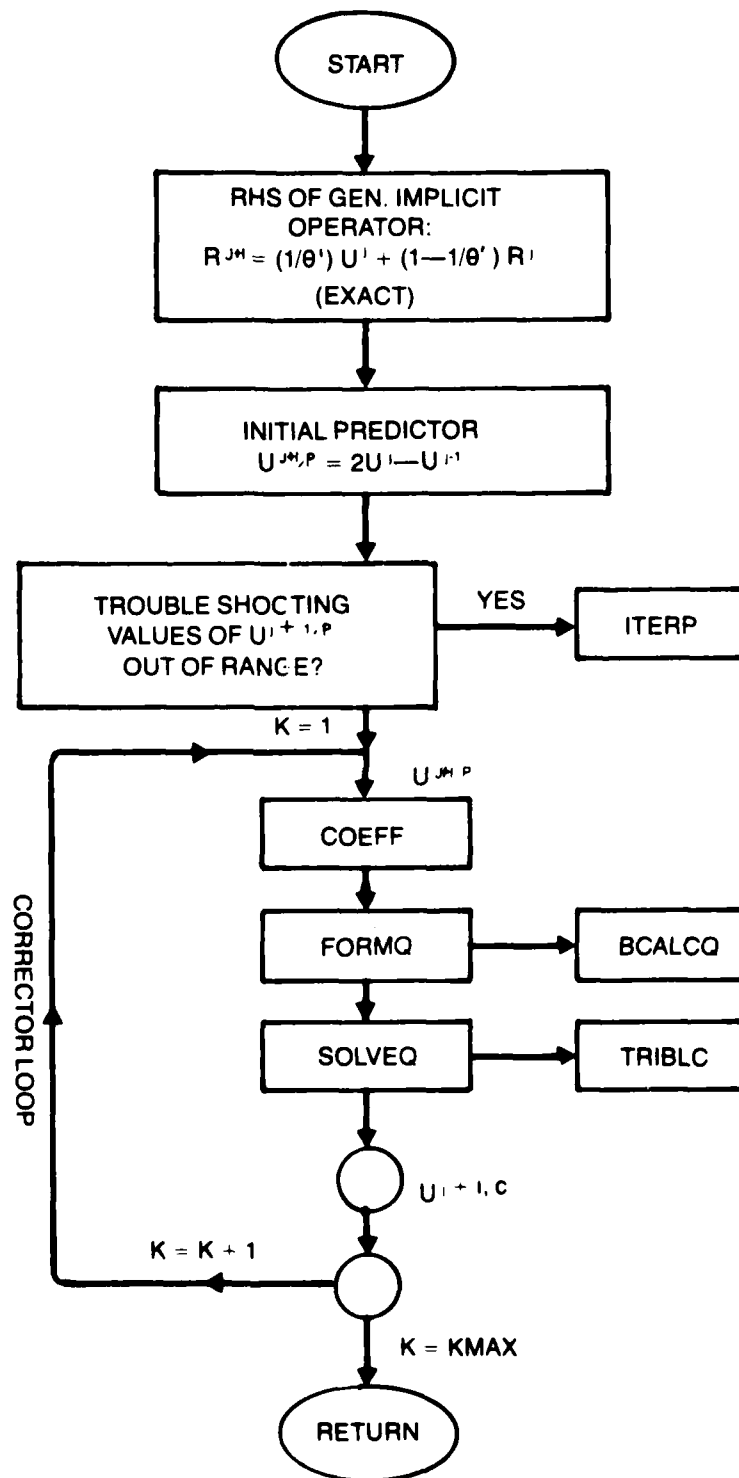
CORRECTOR LOOP

Fig. C.3

TIMINT: Generalized implicit pseudo-time marching algorithm, for gas field solution. (predictor-corrector)
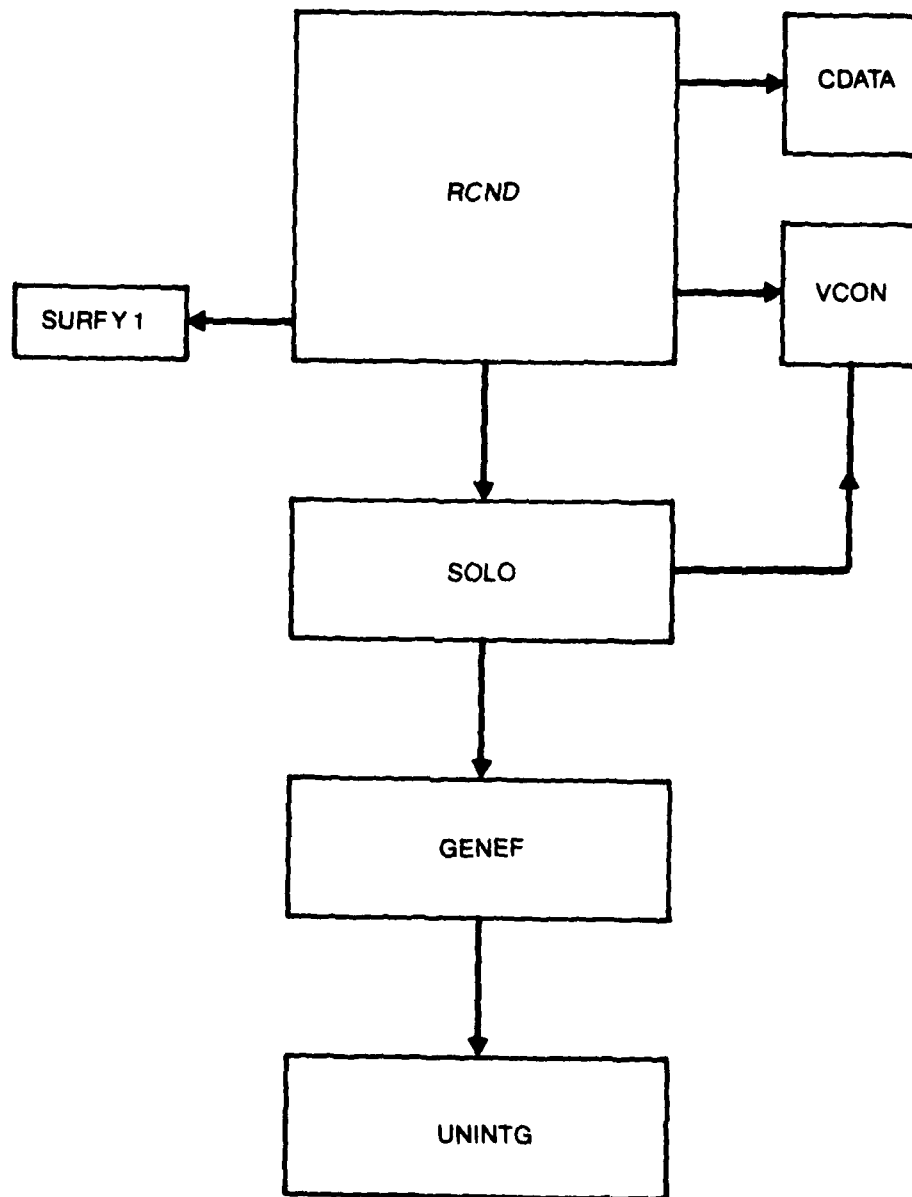
Fig. C.4

RCND: Block diagram of condensed phase integration section.
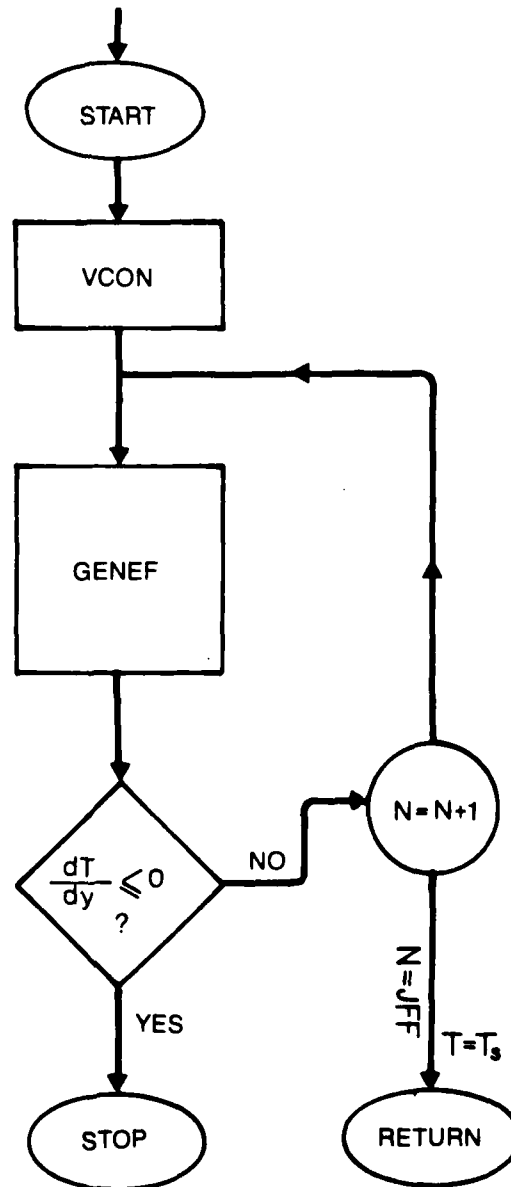
To,Ts AND INITIAL DATA @
SOLID-LIQUID INTERFACE

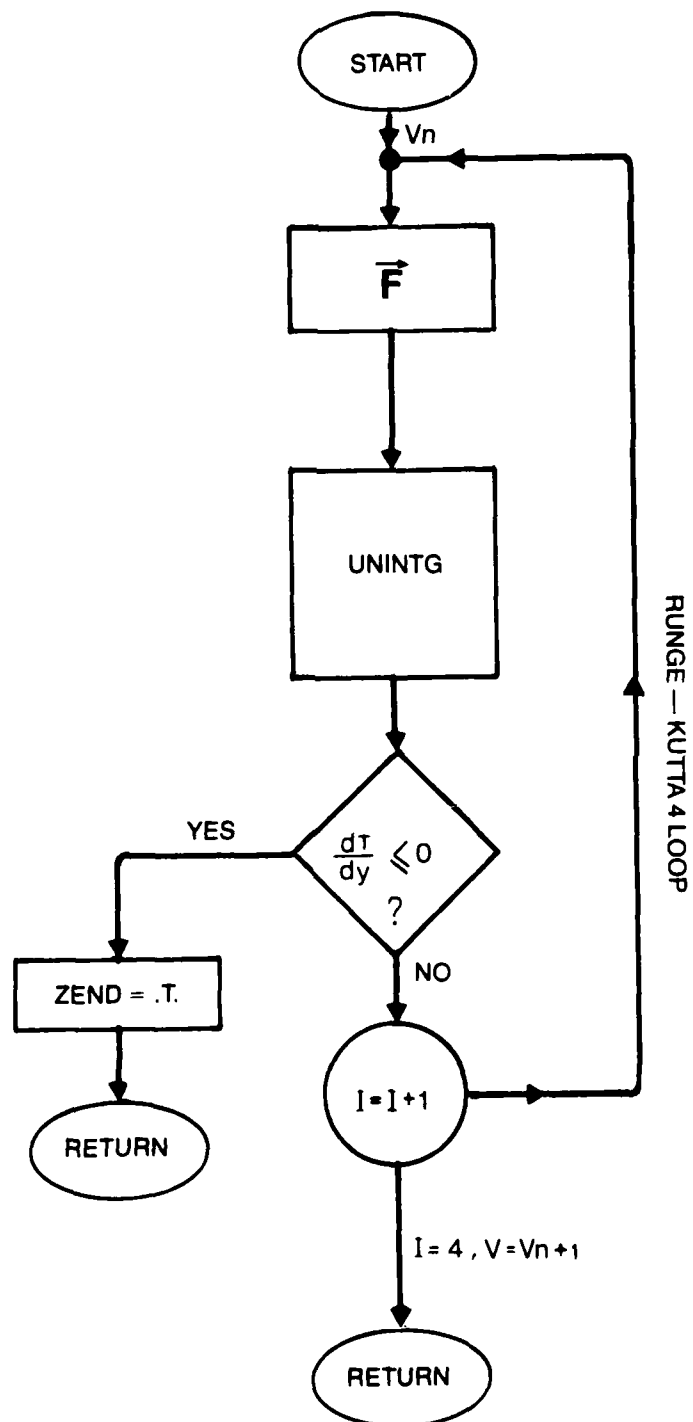Fig. C.5

SOLO: Overall condensed phase Integration Control.

Fig. C.6.

GENEF: Single integration step in the condensed phase, for the
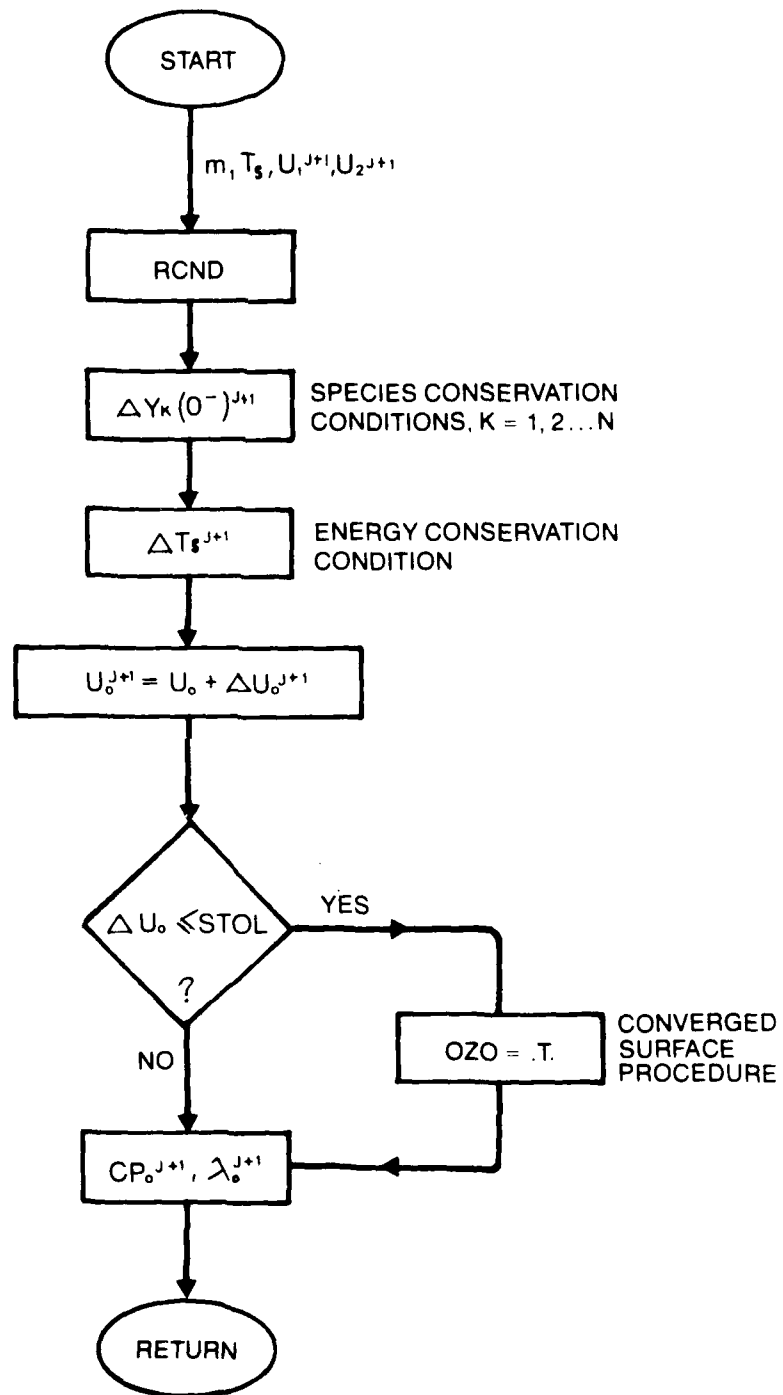equivalent initial value problem, $dv/d\tau_t = F$.

Fig. C. 7.

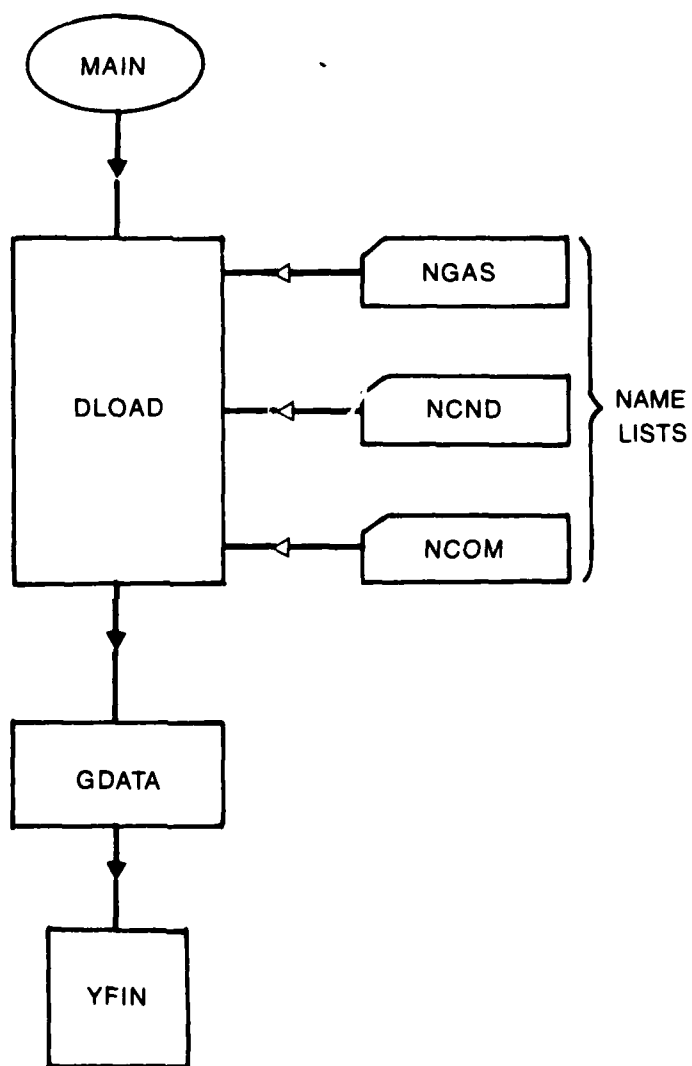SURG: Relaxation procedure for the $y = o$ (liquid-gas) boundary conditions, U_o

Fig. C.8.

Block diagram of data imput section for NTRCOM

APPENDIX D

THE REACTING WALL LAYER IN THE QUASI-STEADY MODE

The quasi-steady assumption affords great mathematical simplicity in the analysis of dynamic rocket chamber processes. This assumption is usually made with respect to the very thin gaseous deflagration region near the propellant surface for ammonium perchlorate composite propellants. The assumption is applicable whenever the characteristic time scale of the layer is much shorter or much longer than that associated with the imposed temporal variation in chamber properties. In the first instance, pertaining to the range of frequencies presently of interest, $\Omega \sim O(10^3 \text{ Hz})$, the layer is considered to adjust instantaneously to the local variation in chamber parameters. Thus, it would seem sufficient to state that the layer characteristic time, $\tilde{T}_L$, is such that $\tilde{T}_L \ll 1/\Omega$. The question remains, however, to what order of magnitude in the small parameter ε, associated with the layer, is the assumption valid. In other words, whether the quasi-steady assumption has any interaction with the nearfield and farfield formulation given in Chapters III and VI. This motivates a somewhat more detailed investigation, given herein.

1. Analysis of the Governing Equations

Considering a small region of burning propellant within the chamber, the quasi-one-dimensional assumption of Chapter VI is retained. Variation in any direction parallel to the propellant surface is considered negligible, and the only space coordinate of concern remains that perpendicular to the surface. The transverse (or axial) velocity component within the layer is also considered negligible, following the analysis of Section VI.B.

It remains then to investigate a nonsteady one-dimensional flame region where reactions are assumed to proceed in a pre-mixed manner. All the assumptions of Chapter III regarding the steady, normal deflagration of nitramine composite propellants are adopted, along with the overall flame field formulation therein.

No distinction between nearfield and farfield is made as yet, in order not to complicate this analysis unnecessarily. The dimensionless gaseous flame region equations are therefore written in nonsteady form, without referring to multiple space scales as follows. For $t > 0$ and $0 < \xi < +\infty$:

chemical species:

$$\Omega \frac{\partial}{\partial t}(\rho \phi_j) + \frac{1}{\tilde{T}_{L,1}}\left[V \frac{\partial \phi_j}{\partial \xi} - \frac{\partial^2 \phi_j}{\partial \xi^2} + F_j(\phi_1,\ldots\phi_T)\right] = 0,$$

$$j = 1,2\ldots N \qquad\qquad (D.1)$$

thermal enthalpy:

$$\frac{\Omega}{\gamma} \frac{\partial}{\partial t}(\rho \phi_T) + \frac{1}{\tilde{T}_{L,1}} \left[V \frac{\partial \phi_T}{\partial \xi} - \frac{\partial^2 \phi_T}{\partial \xi^2} + F_T(\phi_1, \ldots \phi_T) \right] = 0 \qquad (D.2)$$

overall continuity:

$$\Omega \frac{\partial \rho}{\partial t} + \frac{1}{\tilde{T}_{L,1}} \frac{\partial V}{\partial \xi} = 0 \qquad (D.3)$$

momentum:

$$\Omega \frac{\partial V}{\partial t} + \frac{1}{\tilde{T}_{L,1}} \left[V \frac{\partial v}{\partial \xi} - Pr \frac{\partial^2 v}{\partial \xi^2} + \frac{1}{\gamma M_L^2} \frac{\partial P}{\partial \xi} \right] - \frac{1}{\tilde{T}_{L,1}} \frac{\partial}{\partial \xi}(\tilde{\tau}_{11}^D) = 0$$

$$(D.4)$$

The dimensionless variables are defined:

$$\phi_T(\xi, t) = h_T/Q_1^*$$

$$\phi_j(\xi, t) = \bar{W} Y_j/W_j (\nu'' - \nu')_{\bar{k},j}, \quad j = 1, 2 \ldots N$$

where $(\nu'' - \nu')_{\bar{k},j} \neq 0$, and $\bar{k}$ denotes the reference reaction $V(\xi, t) \equiv m^*/m_0$, $\rho \equiv \rho^*/\bar{\rho}$, $P \equiv P^*/\bar{P}$, and $v \equiv V/\rho$.

The independent time and space variables are

$$t \equiv \Omega t^*, \quad \xi \equiv y^*/[\overline{\rho D}/m_0] \qquad (D.5)$$

Superscript star denotes dimensional properties, and overbar is used for reference values. m_0 denotes the non-perturbed, steady state propellant burning rate at the reference pressure.

The normalized sum of all chemical production terms is given by F_j and F_T, negative for production of chemical species or enthalpy. The mean Mach number is defined $M_L \equiv (m_0^2/\gamma \bar{P} \bar{\rho})^{1/2}$. The diffusional stress tensor is represented by the single, normal, Von Karman element

$$\tau_{11}^D = -\rho^* \sum_{j=1}^{N} Y_j v^j v^j$$

in dimensional form, v^j being the normal diffusional velocity of species j. After some manipulation and use of Fick's law, the above element reduces to the dimensionless form:

$$\tilde{\tau}_{11}^D \doteq -\rho \sum_{j=1}^{N} \frac{1}{Y_j} (\partial Y_j / \partial \xi)^2 \tag{D.6}$$

Recalling the discussion of Chapter VIII on time scales,

$$\tilde{T}_{L,1} \equiv [\overline{\rho D}/m_0] / (m_0/\overline{\rho}) \tag{D.7}$$

which is the diffusional time scale discussed therein. Ω in the above formulation represents a characteristic frequency associated with the imposed time variation. Thus, multiplying all the conservation equations through by $\tilde{T}_{L,1}$, the quantity

$$\Omega \tilde{T}_{L,1} = \tilde{T}_{L,1} / (\Omega^{-1}) \tag{D.8}$$

multiplies all the time derivatives; this factor is obviously the ratio of two time scales. The other reacting wall layer time scale considered in Section VIII.C is the one corresponding to the secondary reaction in the layer, $\tilde{T}_L$, such that

$$\tilde{T}_L \equiv \overline{\rho}/\overline{\omega}_{2,L} \gg \tilde{T}_{L,1} \tag{D.9}$$

In fact, $\tilde{T}_{L,1}/\tilde{T}_L \equiv \varepsilon$, with $0 < \varepsilon \ll 1$ defined by Eq. (III.30).

Defining now new, mutually independent space variables: $\zeta_1 \equiv \xi$ and $\zeta_2 \equiv \xi\varepsilon$; the corresponding dependent variables are denoted in general as $\Phi(t,\zeta_1,\zeta_2)$. Thus, for instance, the energy equation transforms to

$$\frac{\Omega \tilde{T}_{L,1}}{\gamma} \frac{\partial(\rho\Phi)}{\partial t} + \left[V\left(\frac{\partial \Phi}{\partial \zeta_1} + \varepsilon \frac{\partial \Phi}{\partial \zeta_2} \right) - \right.$$
$$\left. \left(\frac{\partial^2 \Phi}{\partial \zeta_1^2} + 2\varepsilon \frac{\partial^2 \Phi}{\partial \zeta_1 \partial \zeta_2} + \varepsilon^2 \frac{\partial^2 \Phi}{\partial \zeta_2^2} \right) - \Lambda\tilde{\omega}_1 - \varepsilon\tilde{\omega}_2 Q_2/Q_1 \right] = 0$$

$$\tag{D.10}$$

where $\tilde{\omega}_1$ and $\tilde{\omega}_2$ are the dimensionless reaction rates. Equation (D.10) shows clearly that in order to retain the nearfield and farfield resolution to lowest order in ε, terms up to $O(\varepsilon)$ should be conserved. Since $\gamma \sim O(1)$, the following condition may insure the validity of the quasi-steady assumption, up to second order in ε:

$$\Omega \tilde{T}_{L,1} \ll \varepsilon \tag{D.11a}$$

Hence, the relationship $\tilde{T}_{L,1}/\tilde{T}_L \equiv \epsilon$ implies

$$\Omega\tilde{T}_L \ll 1 \qquad\qquad (D.11b)$$

Obviously, it has been implicitly assumed in the last result that all of the normalized derivatives and production terms are $\sim O(1)$. Therefore, up to $O(\epsilon^2)$, the time derivative in the present formulation may be neglected, and the wall layer considered to adjust to temporal changes instantaneously.

There exists another possibility of application of the quasi-steady assumption, that is, when

$$\Omega\tilde{T}_{L,1} \gg 1 \qquad\qquad (D.12)$$

Here the layer is so slow in adjustment to the imposed variation that it remains essentially frozen at its initial configuration. This condition obviously has no interaction with the nearfield and farfield assumption, but its applicability is limited to ultrahigh frequencies.

Evidently, the quasi-steady assumption fails in the region

$$\tilde{T}_{L,1} < 1/\Omega < \tilde{T}_L \qquad\qquad (D.13)$$

The pressure dependence of $\tilde{T}_L$ and $\tilde{T}_{L,1}$ is given by

$$\tilde{T}_L^{-1} = \overline{\omega}_{2,L}/\overline{\rho} \sim P$$

$$\tilde{T}_{L,1}^{-1} = \frac{m_0^2/\overline{\rho}}{\overline{\rho D}} \sim P^{2n-1} \qquad\qquad (D.14)$$

where $n \simeq 0.8$ is the burning rate exponent for the pressure regime of interest, $1.0 < P < 6.0$ MPa. Equations (D.14) are the basis for Fig. VIII.3, which depicts the region on the $\Omega - P^*$ plane where the quasi-steady assumption regarding the reacting wall layer becomes inapplicable. A similar analysis for the gaseous deflagration region of a burning droplet was made by Bellan and Summerfield.

2. Conclusions

Observing now the conservation equations, several conclusions regarding the quasi-steady reaction zone formulation can be made.

   (a)   The overall continuity equation, (D.3), reduces to $\partial V/\partial \zeta = 0$ and hence

$$V = V(t) \qquad\qquad (D.15)$$

(b) The momentum equation, (D.4), leads to $\partial P/\partial \xi \doteq 0$, since $M_L^2 \ll 1$ is expected. Thus,

$$P = P(t) \tag{D.16}$$

which holds even without application of the quasi-steady assumption. No further information is expected from the momentum equation, and it may be dropped for the present purposes.

(c) The dimensionless equation of state is

$$P = \rho \phi_T \tag{D.17}$$

Thus, the spatial distributions of density and velocity are given by

$$\rho(\xi,t) = P(t)/\phi_T(\xi,t) \tag{D.18a}$$

$$v(\xi,t) = \phi_T(\xi,t)V(t)/P(t) \tag{D.18b}$$

using the single space-scale notation for simplicity.

(d) Up to $O(\epsilon^2)$, the dimensionless conservation equations for chemical species and enthalpy reduce to their steady state form. With the above precaution on the order of validity, the nearfield and farfield formulations of Chapters III and VI may be recovered.

(e) The boundary conditions associated with the governing equations given herein are treated explicitly in Chapter VIII, in the sections corresponding to the nonsteady condensed phase and source terms of the coreflow.

Once the quasi-steady assumption is justified, the reacting wall layer, within any interval in time, may be described by a succession of steady states, and thus would not introduce any dynamic effects into the system. Thus, variations in the coreflow properties would induce instantaneous adjustment of the wall layer. Considering the core-wall layer interface, the functional relations obtained for steady state interaction remain valid, and may be used to determine, at any instant, the interaction parameters θ_{fb} and ϵ_R or $\bar{T}^*$ defined in Chapter VI. In the solution process, the corresponding $d\tau/d\xi(0^+)$ is obtained; this, in turn, must be satisfied by the condensed phase nonsteady solution, through the proper interface conservation conditions. Therefore, it remains for an iterative solution, utilizing the steady state wall layer formulation, to satisfy both inner (propellant side) and outer (coreflow side) interface constraints.

It should be mentioned that for the cases of interest, $\Omega = \Omega_a^0 \sim \tilde{T}_p^{-1}$, where Ω_a^0 is the fundamental acoustic chamber mode, and $\tilde{T}_p$ the characteristic time scale associated with the condensed phase. Hence, different time scales are not expected to occur across the wall layer, which would have immensely complicated the problem.

APPENDIX E

CHARACTERISTICS OF THE CORE FLOWFIELD

The subject of the present analysis is the calculation of characteristic slopes (or eigenvalues of the determinantal equation) for the coreflow model given by Eqs. (VIII.48) and VIII.49). When these eigenvalues are obtained, a general classification of the system is possible. The analysis proceeds then to calculate a family of compatibility relations corresponding to these eigenvalues.

1. The Eigenvalues of the System

After some manipulation, the system of Eqs. (VIII.48), with $x_0 \equiv t$ and $x_1 \equiv x$, reads:

$$\frac{\partial u_1}{\partial x_0} + \frac{\partial u_2}{\partial x_1} = F_1 \tag{E.1}$$

$$\frac{\partial u_2}{\partial x_0} + 2u\frac{\partial u_2}{\partial x_1} - u^2 \frac{\partial u_1}{\partial x_1} + \frac{\gamma-1}{\gamma} \frac{\partial u_3}{\partial x_1} = F_2 \tag{E.2}$$

$$\frac{\partial u_3}{\partial x_0} + u\frac{\partial u_3}{\partial x_1} + \gamma h\frac{\partial u_2}{\partial x_1} - \gamma u h\frac{\partial u_1}{\partial x_1} = F_3 \tag{E.3}$$

$$\frac{\partial u_4}{\partial x_0} + u\frac{\partial u_4}{\partial x_1} + Y\frac{\partial u_2}{\partial x_1} - uY\frac{\partial u_1}{\partial x_1} = F_4 \tag{E.4}$$

where $u \equiv u_2/u_1$, $h \equiv u_3/u_1$ and $Y \equiv u_4/u_1$; the F terms were defined by Eqs. (VIII.49).

In short notation, the system of Eqs. (E.1) through (E.4)

$$A_{ij}^{1,0} \frac{\partial u_j}{\partial x_0} + A_{ij}^{0,1} \frac{\partial u_j}{\partial x_1} = F_i \tag{E.5}$$

where summation convention applies for repeated indices, and $A_{ij}^{1,0}, A_{ij}^{0,1}$ are the coefficient matrices. The corresponding determinantal equation is:

$$\left| A_{ij}^{1,0}\lambda - A_{ij}^{0,1} \right| = 0 \tag{E.6}$$

where $\lambda \equiv dx_1/dx_0$ is the eigenvalue. Written explicitly, the last equation is,

$$\Delta = \begin{vmatrix} -\lambda & 1 & 0 & 0 \\ -u^2 & (2u-\lambda) & (\gamma-1)/\gamma & 0 \\ -u\gamma h & \gamma h & (u-\lambda) & 0 \\ -uY & Y & 0 & (u-\lambda) \end{vmatrix} = 0$$

for which

$$[u^2 - \lambda(2u - \lambda)](u - \lambda)^2 - (u - \lambda)^2 a^2 = 0 \qquad (E.7)$$

where $a^2 \equiv (\gamma - 1)h$, the adiabatic speed of sound in the core gas mixture (frozen).

Equation (E.7) has four roots, as follows

$$\lambda_{I,II} = u \pm a \qquad (E.8a)$$

$$\lambda_{III} = \lambda_{IV} = u \qquad (E.8b)$$

where the (+) and (-) in Eq. (E.8a) correspond to λ_I and λ_{II}, respectively. Thus, the partial differential system, Eqs. (VIII.48), has all four characteristic roots real, with two of these repeated. The system is therefore hyperbolic in the general sense, despite the repeating of two of the roots. $\lambda_{I,II}$ are right and left-going Mach lines and $\lambda_{III,IV}$ is a particle path. The characteristic lines are not straight in the x,t plane, since $u(x,t)$ and $a(x,t)$ are variable.

2. Compatibility Relations

A system of ordinary differential equations holding along the characteristic lines is sought now. This amounts to transforming the original system to the characteristic plane. Calculation of these relations is described as follows.

The original system of equations (E.1-4) is now augmented by four additional relations, along the characteristic lines,

$$\frac{\partial u_i}{\partial x_0} + \frac{\partial u_i}{\partial x_1} \frac{dx_i}{dx_0} = \frac{du_i}{dx_0} \equiv \dot{u}_i \qquad (E.9)$$

where $dx_1/dx_0 \equiv \lambda$. The resulting eight algebraic equations, Eqs. (E.1-4) and (E.9) involve all the partial differential terms $\partial u_i/\partial x_k$, $k = 0,1$, as unknowns. The statement of Eq. (E.9) is equivalent to the requirement that the coefficient determinant of this system vanish, $\Delta = 0$. For compatibility, each of the determinants Δ_{ik} of the system [obtained by replacing the column corresponding to $\partial u_i/\partial x_k$ by the free-term vector

$(\dot{u}_i \quad F_i)]$ must also vanish by Kramer's rule; this should insure full indeterminacy of the partial differential unknowns. Thus,

$$\Delta_{ik} = 0 \qquad (E.10)$$

For Δ_{11} (corresponding to $\partial u_1/\partial x_1$), the determinant reduces to a 4 x 4 form, after some row and column manipulations:

$$\Delta_{11} = \begin{vmatrix} 1 & 0 & 0 & F_1 - \dot{u}_1 \\ 2u - \lambda & 0 & (\gamma-1)/\gamma & F_2 - \dot{u}_2 \\ \gamma h & 0 & u - \lambda & F_3 - \dot{u}_3 \\ Y & u - \lambda & 0 & F_4 - \dot{u}_4 \end{vmatrix} = 0$$

The resulting algebraic equation, after substitution of λ_I, λ_{II}, and λ_{III}, yields

$$\frac{\gamma-1}{\gamma}\left(\frac{du_3}{dt}\right)_{I,II} \pm a\left(\frac{du_2}{dt}\right)_{I,II} \mp ua\left(\frac{du_1}{dt}\right)_{I,II} = R_{I,II} \qquad (E.11a)$$

$$R_{I,II} \equiv \frac{\gamma-1}{\gamma}F_3 \pm aF_2 \mp uaF_1 \qquad (E.11b)$$

$$\frac{\gamma-1}{\gamma}\left(\frac{du_3}{dt}\right)_{III} - a^2\left(\frac{du_1}{dt}\right)_{III} = R_{III} \qquad (E.12a)$$

$$R_{III} \equiv \frac{\gamma-1}{\gamma}F_3 - a^2 F_1 \qquad (E.12b)$$

where $du_i/dt = \dot{u}_i$. To obtain an equivalent relationship for (du_4/dt) along the λ_{IV}-particle path, the process may be repeated with $\Delta_{31} = 0$. The resulting additional equation is:

$$\frac{\gamma-1}{\gamma}Y\left(\frac{du_3}{dt}\right) - a^2\left(\frac{du_4}{dt}\right)_{IV} = R_{IV} \qquad (E.13a)$$

$$R_{IV} \equiv \frac{\gamma-1}{\gamma}YF_3 - a^2 F_4 \qquad (E.13b)$$

Of course, the characteristic lines III and IV are identical.

Thus, the four compatibility relations, corresponding to the three distinct characteristics of the system are defined by Eqs. (E.11) through (E.13). They are utilized for the implementation of the boundary conditions in the numerical (finite difference) solution of the partial differential system, Eq. (VIII.48).

APPENDIX F

TREATMENT OF THE BOUNDARY CONDITIONS

IN THE NUMERICAL ALGORITHM

The modified Rubin-Burstein difference algorithm given by Eqs. (VIII.53) through (VIII.55), utilizes central differences in space for the representation of $\partial/\partial x$ derivatives. This leads to the requirement that all four dependent variables, U, must be specified at both $x = 0$ and $x = L$ boundaries. The four physically available boundary conditions are, therefore, augmented by the four available compatibility relations along the characteristic lines. These compatibility relations were derived in Appendix E.

1. The Head-End (x = 0) Boundary Conditions

Assuming all properties to be fully defined in the core flowfield up to the current time level, that is, for $t < t^j$, the following iterative procedure is utilized for calculation of U_0^{j+1}.

(a)   Initialization step:

The two-level, second-order-accurate formula is used for initial prediction:

$$U_0^{j+1,P} \approx 2U_0^j - U_0^{j-1} \qquad (F.1)$$

for the entire dependent variable vector. For $j = 1$, simply let $U_0^{j+1,P} \approx U_0^j$.

(b)   With $U_0^{j+1,P}$ given, the reacting wall layer and condensed phase solutions are generated at $x = 0$, as described in Section VIII.D. To maintain a finite Reynolds number, $R_{ex}(x = 0^+)$, a small standoff distance from the wall, $x_0/\Delta x \ll 1$, is imposed; the solution was found quite insensitive to actual x_0 values, as long as they remain small, due to the weak dependence on $R_{ex}^{-0.2}$.

The solutions at this step provide $(m, \ h^*, \ Y_F^*)$ at $x = 0^+$.

(c)   Corrector Step:

The following three relations are imposed physically by the particular position of the head-end boundary at the flame cutoff edge:

$$U_{0(1)}^{j+1,c} = U_{0(3)}^{j+1,P}/h^* \tag{F.2a}$$

$$U_{0(2)}^{j+1,c} = m \tag{F.2b}$$

$$U_{0(4)}^{j+1,c} = U_{0(1)}^{j+1,c} Y_F^* \tag{F.2c}$$

where the data from Step (b) is utilized. These relations are augmented by the left-running, II-characteristic compatibility condition given by Eq. (E.11). Replacing the time differentiations by difference quotients, the compatibility equation is written:

$$\Delta U_{(3)} = \frac{\gamma}{\gamma-1}\left[\Delta t \bar{R}_{II} + \bar{a}\left(\Delta U_{(2)} - \bar{u}\Delta U_{(1)}\right)\right] \tag{F.3}$$

Figure F.1 shows the II-characteristic segment of interest at the $x = 0^+$ boundary. This segment lies between the points $A(x_A, t^j)$ and $B'(0, t^{j+1})$.

The mean values of the coefficients in Eq. (F.3), denoted by overbar, are defined:

$$\bar{a} \equiv 0.5\left[(a^{j+1,P})_{B'} + (a^j)_A\right] \tag{F.4a}$$

where, generally, $a \equiv [(\gamma-1)U_{(3)}/U_{(1)}]^{1/2}$.

$$\bar{u} \equiv 0.5\left[(U_{(2)}^{j+1,P}/U_{(1)}^{j+1,P})_{B'} + (U_{(2)}^j/U_{(1)}^j)_A\right] \tag{F.4b}$$

$$\bar{R}_{II} \equiv 0.5\left[R_{II}(\vec{F}^{j+1,P})_{B'} + R_{II}(\vec{F}^j)_A\right] \tag{F.4c}$$

R_{II} is defined by Eq. (E.11b); it generally depends on the core source-term vector, $\vec{F}^T = (F_1\ F_2\ F_3)$. At the boundary point $B'(0, t^{j+1})$, the source terms are evaluated by using the wall layer and condensed phase solutions of Step (b) herein, along with the vector $U_0^{j+1,P}$. At the intermediate point, $A(x_A, t^j)$, the source terms are found by linear interpolation (at time level t^j) between their values at $B(0, t^j)$ and at $C(\Delta x, t^j)$.

The difference terms of Eq. (F.3) are defined:

$$\Delta U_{(k)} \equiv (U_{(k)}^{j+1,c})_{B'} - (U_{(k)}^j)_A \tag{F.4d}$$

with $k = 1, 2, 3$.

Now, since all the right hand side of Eq. (F.3) is fully defined, $\Delta U_{(3)}$ can be calculated:

$$U_{0(3)}^{j+1,c} = \Delta U_{(3)} + (U_{(3)}^{j})_A \qquad (F.5)$$

(d) Checking convergence:

When the following convergence criterion,

$$\max_{k} \left| \frac{U_{0(k)}^{j+1,c} - U_{0(k)}^{j+1,p}}{U_{0(k)}^{j}} \right| \leq \varepsilon_B \qquad (F.6)$$

is fulfilled, the procedure is stopped. If not, the iteration loop is repeated from Step (b), letting $U_0^{j+1,p} = U_0^{j+1,c}$. The value of $\varepsilon_B \simeq 1/1000$; the most sensitive parameter in the above check has been found to be $U_{(3)} = \rho h_T$.

The iteration procedure described herein, despite its crude appearance, has been found to converge within 3 iteration cycles under most conditions tested. Checking the residuals [at left hand side of Eq. (F.6)], shows accelerated convergence from cycle to cycle.

For clarification of the method by which the intermediate point location, x_A in Fig. F.1 , is defined, the reader is referred to the following section. The same method is used also for defining the location of the intermediate points, C, D in Fig. VIII.6b, at the x = L boundary.

2. Determination of the Intermediate Point 'A' at The x = 0 Boundary.

The characteristic line segment is straight, assuming small Δt. The II-characteristic segment of interest passes between the points $A(x_A, t^j)$ and $B'(0, t^{j+1})$, as shown in Fig. VIII.6a. The slope of the segment is defined by linear interpolation between the points $B(0, t^j)$ and $C(\Delta x, t^j)$; it therefore depends entirely on properties at time level t^j, consistent with the overall coreflow numerical algorithm, being explicit in its time marching.

The slope tangent is

$$\alpha = (1 - \Phi)\mu_B + \Phi\mu_C \qquad (F.7)$$

where $\mu_B \equiv (a - u)_B$, $\mu_C \equiv (a - u)_C$, and $0 \leq \Phi \equiv x_A/\Delta x \leq 1$. Observing the triangle $B'BA$, $x_A = \alpha\Delta t$. Thus, Φ and x_A may be solved for:

$$\phi = \mu_B \big/ [\mu_B - \mu_C + \Delta x/\Delta t] \qquad\qquad \text{(F.8a)}$$

$$x_A = \phi \Delta x \qquad\qquad \text{(F.8b)}$$

The parameter ϕ can now be used for calculating intermediate values of U_A^j and F_A^j, by linear interpolation, similar to that given by Eq. (F.7).

An identical procedure leads to the definition of the interior points D,F at the $x = L$ boundary, along with the associated ϕ-values. Note that the reason for point 'F' (for which the characteristic slope is $\sim a + u$) not coinciding with the last interior mesh-point, 'NF', is the CFL number, $B < 1$.

3. The Nozzle-End (X = L) Boundary Conditions

At this boundary, the only available physical condition corresponds to the Mach number, as imposed by the sonic nozzle constraint. The relationship is:

$$M^2(L,t^{j+1}) = \left(A_t(t^{j+1})/A \right)^2 \left\{ \frac{2}{\gamma+1} \left[1 + \frac{\gamma-1}{2} M^2(L,t^{j+1}) \right] \right\}^{\frac{\gamma+1}{\gamma-1}}$$

$$\text{(F.9)}$$

The Mach number corresponds to the frozen speed of sound, justified by the short nozzle assumption.

The given boundary constraint is augmented by three characteristic compatibility relations, along the I, III, and IV right-going characteristic lines. These allow the determination of the entire U_L^{j+1} vector, as required by the numerical scheme. An iterative procedure, similar to that for the $x = 0$ boundary, is utilized.

(a) Initialization step:

$$U_L^{j+1,P} = 2U_L^j - U_L^{j-1}$$

similar to Eq. (F.1).

(b) Calculation of the port exit section Mach number:

Equation (F.9) is implicit in $M^2(L,t^{j+1})$. For the current imposed value of throat area, $A_t(t^{j+1})$, $M^2(L,t^{j+1})$ is therefore calculated iteratively. A Newton Raphson procedure is used.

(c) Wall layer and condensed phase solution:

For the given $U_L^{j+1,p}$ core data; the source terms are calculated:

$$F_1^{j+1,p} \ \ldots \ F_4^{j+1,p}$$

(d) Corrector step:

The I,III-compatibility relations are used simultaneously, solving directly for $U_{L(1)}^{j+1,C}$ and $U_{L(3)}^{j+1,C}$, in the following manner.

$$\frac{\gamma-1}{\gamma}\Delta U_{(3)I} + \bar{a}_I \Delta U_{(2)I} - \overline{au}_I \Delta U_{(1)I} = \bar{R}_I \Delta t \qquad (F.10)$$

$$\frac{\gamma-1}{\gamma}\Delta U_{(3)III} - \overline{a^2}_{III} \Delta U_{(1)III} = \bar{R}_{III}\Delta t \qquad (F.11)$$

The I-characteristic segment is defined as FE' and the III-characteristic segment is DE', in Fig. F.2 . Accordingly, the mean properties, denoted by overbar in last two equations, are defined:

$$(\bar{\ })_I \equiv 0.5 \ [(\ )_{E'}^{j+1,p} + (\ )_F^j] \qquad (F.12a)$$

$$(\bar{\ })_{III} \equiv 0.5 [(\ )_{E'}^{j+1,p} + (\ )_D^j] \qquad (F.12b)$$

The associated difference terms are

$$\Delta U_{(k)I} \equiv [U_{(k)}^{j+1,c}]_{E'} - [U_{(k)}^j]_F \qquad (F.13a)$$

$$\Delta U_{(k)III} \equiv [U_{(k)}^{j+1,c}]_{E'} - [U_{(k)}^j]_D \qquad (F.13b)$$

for $k = 1,3$. The $\Delta U_{(2)I}$ term in Eq. (F.10) is treated explicity, letting

$$\Delta U_{(2)I} = M_L^{j+1}\left[(\gamma-1)U_{(1)E'}^{j+1,p} \ U_{(3)E'}^{j+1,p}\right]^{1/2} - U_{(2)F}^j \qquad (F.14)$$

Substitution of Eqs. (F.12) through (F.14) into Eqs. (F.10) and (F.11) results in a two-by-two, linear algebraic system:

$$X_1 - (\overline{au})_I X_2 = A_1$$

$$X_1 - (\overline{a^2})_{III} X_2 = A_2 \qquad (F.15)$$

where: $X_1 \equiv \dfrac{\gamma-1}{\gamma} U_{(3)E'}^{j+1,C}$, $\quad X_2 \equiv U_{(1)E'}^{j+1,C}$,

$$A_1 \equiv \overline{R}_I \Delta t - \overline{a}_I \Delta U_{(2)} + \frac{\gamma-1}{\gamma} U_{(3)F}^j - (\overline{au})_I U_{(1)F}^j$$

$$A_2 \equiv \overline{R}_{III} \Delta t + \frac{\gamma-1}{\gamma} U_{(3)D}^j - (\overline{a^2})_{III} U_{(1)D}^j$$

The solution is straightforward; the corrected values of $U_{(2)}^{j+1,c}$ and $U_{(4)}^{j+1,c}$ are obtained, in terms of X_1, X_2:

$$U_{(2)}^{j+1,c} = M_L^{j+1} [\gamma X_1 X_2]^{1/2} \qquad (F.16)$$

$$U_{(4)}^{j+1,c} = X_2 \frac{\overline{R}_{IV} \Delta t - \overline{a^2}_{IV} U_{(4)D}^j}{X_1 - \frac{\gamma-1}{\gamma} U_{(3)D}^j - \overline{a^2}_{IV} X_2} \qquad (F.17)$$

where $U_{(3)IV} = U_{(3)III}$, and $\overline{a^2}_{IV} = \overline{a^2}_{III}$;
Eq. (F.17) is derived from the difference-form of the IV-characteristic (particle path) compatibility relation, Eqs. (E.13a,b).

(e) Checking convergence:

This step is entirely identical to Step (d) in the x = 0 boundary calculations procedure of Section 1 herein, cf. Eq. (F.6).

   If the convergence criterion is not satisfied, a new iteration cycle is initiated, letting $U^{j+1,P} = U^{j+1,c}$, and re-starting at Step (c).

Similarly to the x = 0 boundary procedure, the present iteration procedure was found convergent within three to four iteration cycles, showing accelerated convergence.
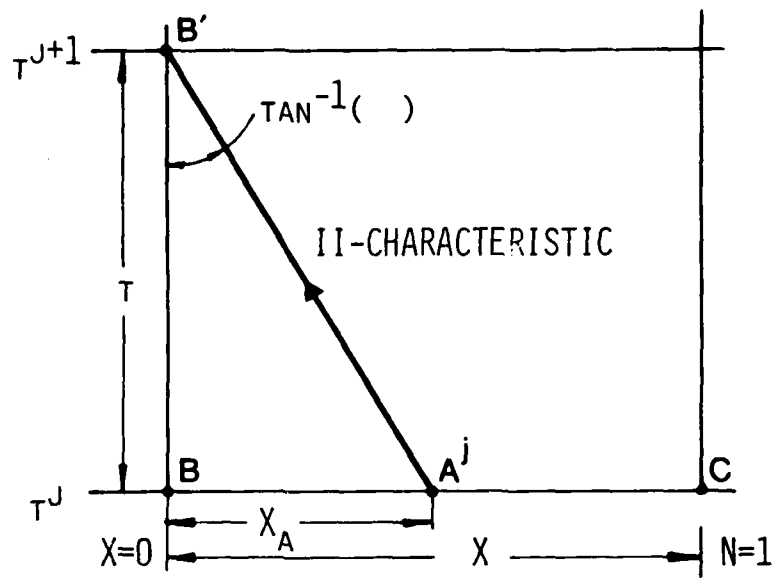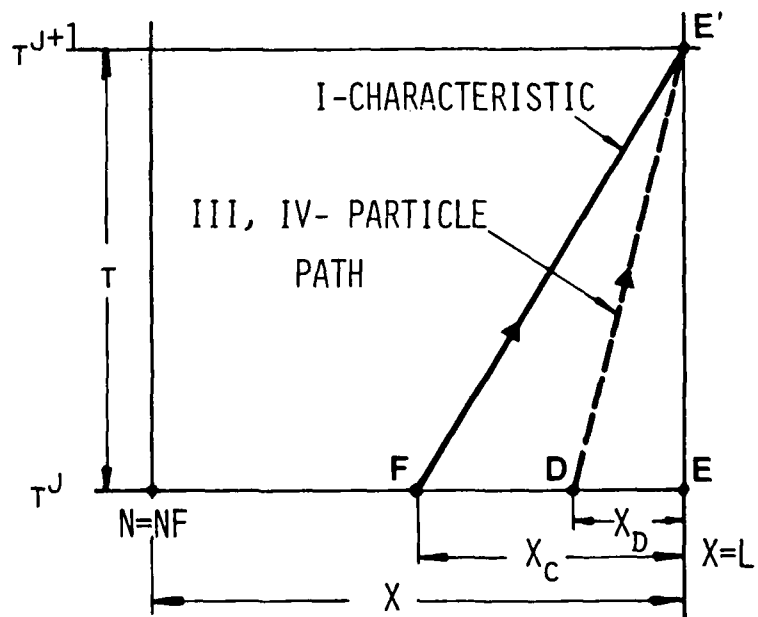
Fig. F.1

The x = 0 boundary configuration.

Fig. F.2

The x = L boundary configuration.

Appendix G

ERROR ANALYSIS FOR THE MODIFIED RUBIN-BURSTEIN
FINITE DIFFERENCE ALGORITHM

The present analysis is an extension of the numerical investigation in Section VIII.E. The original hyperbolic system is considered "in the small" for present purposes; the (linearized) exact operator is

$$\frac{\partial u}{\partial t} + C \frac{\partial u}{\partial x} = f u \tag{G.1}$$

and the numerical counterpart to the exact solution $u(x,t)$ being $U(x,t)$. The objective is to derive expressions for the amplitude and phase-velocity errors associated with the modified Rubin-Burstein finite difference algorithm and to demonstrate their dependence on the CFL number B and various values of $f\Delta t$. The nomenclature is the same as in Chapter VIII.

1. Amplitude Error and Spurious Dissipation

Following the von Neumann spectral analysis method, a single Fourier component of the numerical solution is considered,

$$U^{(k)}(x,t) = \hat{a}^{(k)}(t) \exp(ikx) \tag{G.2}$$

k is a wave number corresponding to the particular harmonic of interest; $a^{(k)}$ is the complex, time-dependent amplitude of the component. The amplification matrix is defined

$$\hat{Z} \equiv \hat{a}^{(k)}(t+\Delta t)/\hat{a}^{(k)}(t) \tag{G.3}$$

and is generally complex. Noting that the space increment operator may be expressed by

$$U_{n+\theta}^{(k)j} = \exp(ik\theta\Delta x) \cdot U_n^{(k)j}$$

substitution of Eq. (G.2) into the combined RB difference algorithm, Eq. (VIII.58), yields:

$$\hat{Z} = \hat{Z}_H + (f\Delta t)\left[(3+\cos k\Delta x)/4 - iB\sin k\Delta x\right] + $$
$$(f\Delta t)^2\left[1 + \cos k\Delta x\right]/4 \tag{G.4a}$$

The part corresponding to $f = 0$ is defined

$$\hat{Z}_H \equiv I - iB\sin k\Delta x + B^2(\cos k\Delta x - 1) \tag{G.4b}$$

and $B \equiv C\Delta t/\Delta x$.

Note that the stepwise stability requirement for the case $f = 0$ states simply that all eigenvalues of $\hat{z}_H$ must be smaller than unity, regardless of the exact solution. This type of stability argument is strictly ruled out whenever $f \neq 0$, and the two cases are not simply related.

The exact solution k^{th} Fourier component can be written as $u^{(k)}$ $(x,t) = b^{(k)}$ $(t) \exp(ikx)$. Substitution into the linearized system, Eq. (VIII.57), results in an ordinary differential equation for $b^{(k)}$; the solution yields:

$$\hat{z} = b^{(k)}(t+\Delta t)/b^{(k)}(t) = \exp(\tilde{f}\Delta t)\left[\cos ck\Delta t - i \sin ck\Delta t\right] \tag{G.5}$$

with $\tilde{f} = f$, and note that $C\Delta t = B\Delta x$, by definition. Considering only cases with $|f\Delta t| \ll 1$, the exponential term in the last equation can be expanded:

$$\exp(f\Delta t) = 1 + f\Delta t + (f\Delta t)^2/2! + h.o.t.$$

Substitution into Eq. (G.5) results in a hierarchy of components for various orders of $\tilde{f}\Delta t$. Comparison of the lowest order terms of $\hat{z}$ and $\hat{z}$ is given below. Throughout the remainder of the present section, the eigenvalues of $\hat{z}$ and $\hat{z}$ are considered. It can be shown that these are obtained by substitution of the eigenvalues of the matrix C (cf. Appendix E) in place of C, in Eqs. (G.4a,b) and (G.5). Extension of the results to the vector space is straightforward.

(1) Zeroth order, $(f\Delta t)^0$: The exact solution:

$$\hat{z}^{(0)} = \cos Bk\Delta x - i \sin Bk\Delta x \tag{G.6a}$$

The RB difference algorithm:

$$\hat{z}^{(0)} = (1-B^2) + B^2\cos k\Delta x - iB\sin k\Delta x \tag{G.6b}$$

which are in full agreement when $B = 1$.

(2) First order, $(f\Delta t)^1$:

$$\hat{z}^{(1)} = \hat{z}^{(0)}$$

$$\hat{z}^{(1)} = (3 + \cos k\Delta x)/4 - iB\sin k\Delta x \tag{G.6c}$$

In this instance, for $B = 1$, only the imaginary parts are in full agreement. However, for small wave numbers, i.e., $k\Delta x \ll 1$, good agreement can be expected for $B < 1$ as well. This can be observed by the complex-plane behavior of $\hat{z}$ and $\hat{z}$. $\hat{z}$ is always an ellipse, tangent to the interior of the circle $\hat{z}$ at the point $(1 + f\Delta t + (f\Delta t)^2/2! + ...)$ on the positive real axis. The tangency is implied by the RB difference algorithm, being of second order accuracy. Thus, for small values of the phase, $k\Delta x \ll 1$, the difference $|\hat{z} - \hat{z}|$ is small. For the finite space interval considered, L, the fundamental acoustic wave-number is $k_0 = 1/2L$. Typically, $\Delta x = L/25$; hence,

for this particular harmonic, $k_0 \Delta x \sim O(0.01) \ll 1$. Shorter wavelengths, however, would be more readily attenuated (for $f > 0$). This attenuation is due to spurious dissipation, introduced by the numerical approximation.

Spurious dissipation can be found already at zeroth order level, as shown by $|z^{(0)}| - |z^{(0)}| \neq 0$ for $B < 1$ in Eqs. (G.6a,b), regardless of the magnitude of Δt. The observation made by Rubin and Burstein[166] attributing the artificial viscosity in their algorithm to the diffusion-like, $0.5\ c^2\Delta t$ term [cf. third member on right hand side of Eq. (VIII.58)] is, therefore, somewhat misleading; it should hold only for an exact (discretized) time derivative.

The relative amplification error, defined in terms of the eigenvalues of $\hat{z}$ and $\hat{z}$,

$$E_a \equiv |\mathbb{Z}| / |z| - 1 \tag{G.7}$$

Note that $|z| = \exp(f\Delta t)$.

2. Phase Velocity Error

The rate of propagation of any particular Fourier wave-component in the physical system is given by the eigenvalues of the matrix C, namely, by the characteristic slopes $\lambda = dx/dt$. These are termed phase velocities[G1] and are equal for all wave lengths; this is not surprising, since the original linearized system, Eq. (G.1), is nondispersive. The subject of the present analysis is phase velocity difference, or error, between the linearized exact system and the RB algorithm.

The exact system phase velocity, cf. Eq. (G.5), is given by the identity

$$\lambda \equiv - Arg(z) / k\Delta t \tag{G.8a}$$

being a constant in the linearized system. The phase velocity of the numerical algorithm is defined analogously:

$$\lambda^* \equiv - Arg(\mathbb{Z}) / k\Delta t \tag{G.8b}$$

The relative phase velocity error is, therefore,

$$E_p \equiv \lambda^* / \lambda - 1 \tag{G.9}$$

Using now Eqs. (G.4a,b) with terms up to second order in $(f\Delta t)$,

$$E_p = \frac{-1}{Bk\Delta x}\ tg^{-1} \left[\frac{-B(1+f\Delta t)\sin k\Delta x}{1+B^2(\cos k\Delta x - 1) + f\Delta t(3\cos k\Delta x)/4} \right] \tag{G.10}$$

Evidently, $\lambda^*(k\Delta x)$ is not constant, so that distinct wave lengths

travel at different speeds in the numerical solution domain. By definition, this amounts to dispersion introduced by the particular difference approximation.[G2,G3]

When the only effect of interest is that of space discretization, the phase velocity of the difference scheme might take an alternate form. Consider for simplicity the single linear hyperbolic equation in the form of Eq. (G.1). The (complex) space discretization operator is denoted by $X(k\Delta x)$ for the particular Fourier component of wave number k. The time derivative is assumed exact. For the solution component given by Eq. (G.2), the resulting ordinary differential equation for $a^{(k)}(t)$ is

$$\frac{d}{dt} \ln \hat{a}^{(k)}(t) = \hat{X}(k\Delta x)$$ (G.11)

a solution of which is $\exp[t\hat{X}(k\Delta x)]$. To satisfy the exact differential operator of Eq. (G.1), the solution component must be of the form $\exp[ik(x - C^*t)]$. Thus, the space-discretization phase velocity, C^*, is defined

$$C^* \equiv Im\left[\hat{X}(k\Delta x)\right]/k$$ (G.12)

For the explicit, central space-difference algorithm,

$$\hat{X}(k\Delta x) = iC \sin k\Delta x /\Delta x + f$$

thus, by Eq. (G.12),

$$C^* = C \sin k\Delta x / k\Delta x$$

Equivalent definitions of the space-discretization phase velocity, C^*, have been used by Vichnevetsky[G3] to produce maps of the phase velocity and phase velocity error in the frequency domain, $(k\Delta x)$. Similar definition of C^* was utilized by Kreiss and Oliger,[G4] to compare the relative merits of second and higher order space discretization algorithms.

3. Discussion of Results

The amplification (or amplitude) error, Ea, defined by Eq.(G.7) was calculated by use of Eqs. (G.4a,b) and (G.5), including terms of order $(f\Delta t)^2$. Ea was plotted against phase angle, $k\Delta x$, in Figs. G.1 through G.3. In Fig. G.1, the CFL number, B, serves as parameter, at a fixed f t = 0.01. Evidently, as B is increased from 0.4 toward unity, regions of pure damping (B = 0.4) or pure amplification (B = 1) are traversed. The behavior is not necessarily monotonous for a given B, as shown by the peaking of the B = 0.9 and 0.95 curves. The effect of f t on the amplitude error at fixed B = 0.9 is shown in Fig. G.2; it ranges from pure damping at $f\Delta t = 0.005$ to pure amplification at $f\Delta t = 0.1$. For B = 0.5, the same parametric range of $f\Delta t$ produces damping only, which improves in a decelerating manner (i.e., Ea approaches zero) as $f\Delta t$ decreases, demonstrated in Fig. G.3. In general, all cases show tangency of the error curves to the abscissa at $k\Delta x = 0$, such that Ea is small within $k\Delta x < 0.1$. For larger phase angles, as $k\Delta x > 0.2$ (i.e., for smaller wave lengths) damping or amplification becomes more pronounced.

The phase velocity error, Ep, defined by Eq. (G.9) was calculated by use of Eqs. (G.4a,b) including terms of order $(f\Delta t)^2$. Ep was plotted against k x in Figs. G.4 through G.6, with the same parametric range of B and $f\Delta t$ conducted in Figs. G.1 through G.3, respectively. The effect of B is demonstrated in Fig. G.4: Ep < 0 for any B < 1. As B decreases, the phase velocity error becomes larger in absolute and negative; in other words, the same wave-length component (k) travels with less velocity (enhanced dispersion) in numerical space, as B is decreased at Δx = const. However, within $k\Delta x$ < 0.15, all departures from Ep = 0 are small (tangency at $k\Delta x$ = 0). The effect of $f\Delta t$ at B = 0.9 is shown in Fig. G.5: as $f\Delta t$ increases, Ep becomes larger in absolute and negative. For B = 0.5, all the different $f\Delta t$ curves coincide, as shown in Fig. G.6. This can be easily proven by substitution of B = 0.5 into Eq. (G.10). In general, Ep decreases (more negative) as $k\Delta x$ increases at fixed (B, $f\Delta t$). This behavior is termed normal dispersion,[G5] as smaller wave lengths (large $k\Delta x$) lag behind the larger ones (small $k\Delta x$).

Additional calculations made at B = 1 and $f\Delta t$ = 0 show that Ea = Ep = 0 uniformly, regardless of $k\Delta x$, recovering the well known result at zero forcing, f = 0.

In conclusion, the results of the error analysis indicate damping behavior (Ea < 0) and normal dispersion (Ep < 0) for B = 0.5. This particular CFL number obtains optimal values of the errors in absolute, for values of phase angle $k\Delta x$ < 0.2. Of course, other configurations may be better suited for investigations of other nature, e.g., when physical damping is sought within a system known to be amplifying.

References

G1. Vichnevetsky, R., Course Notes on Numerical Methods for Partial Differential Equations, Dept. of Computer Science, Rutgers University, NJ, 1974.

G2. Vichnevetsky, R. and Tomalesky, A. W., "Spurious Wave Phenomena in Numerical Approximations of Hyperbolic Equations", Proc. 5th Annual Princeton Conference on Information Science and Systems, Princeton University, Mar. 1971, pp. 357-363.

G3. Vichnevetsky, R. and DeSchutter, F., "Frequency Analysis of Finite Element and Finite Difference Methods for Initial Value Problems", Proc. AICA International Symposium on Advances in Computer Methods for Partial Differential Equations, July 1975, pp. 46-52.

G4. Kreiss, H. and Oliger, J., "Comparison of Accurate Methods for the Integration of Hyperbolic Equation", Tellus XXIV, 1972, No.3, pp. 199-215.

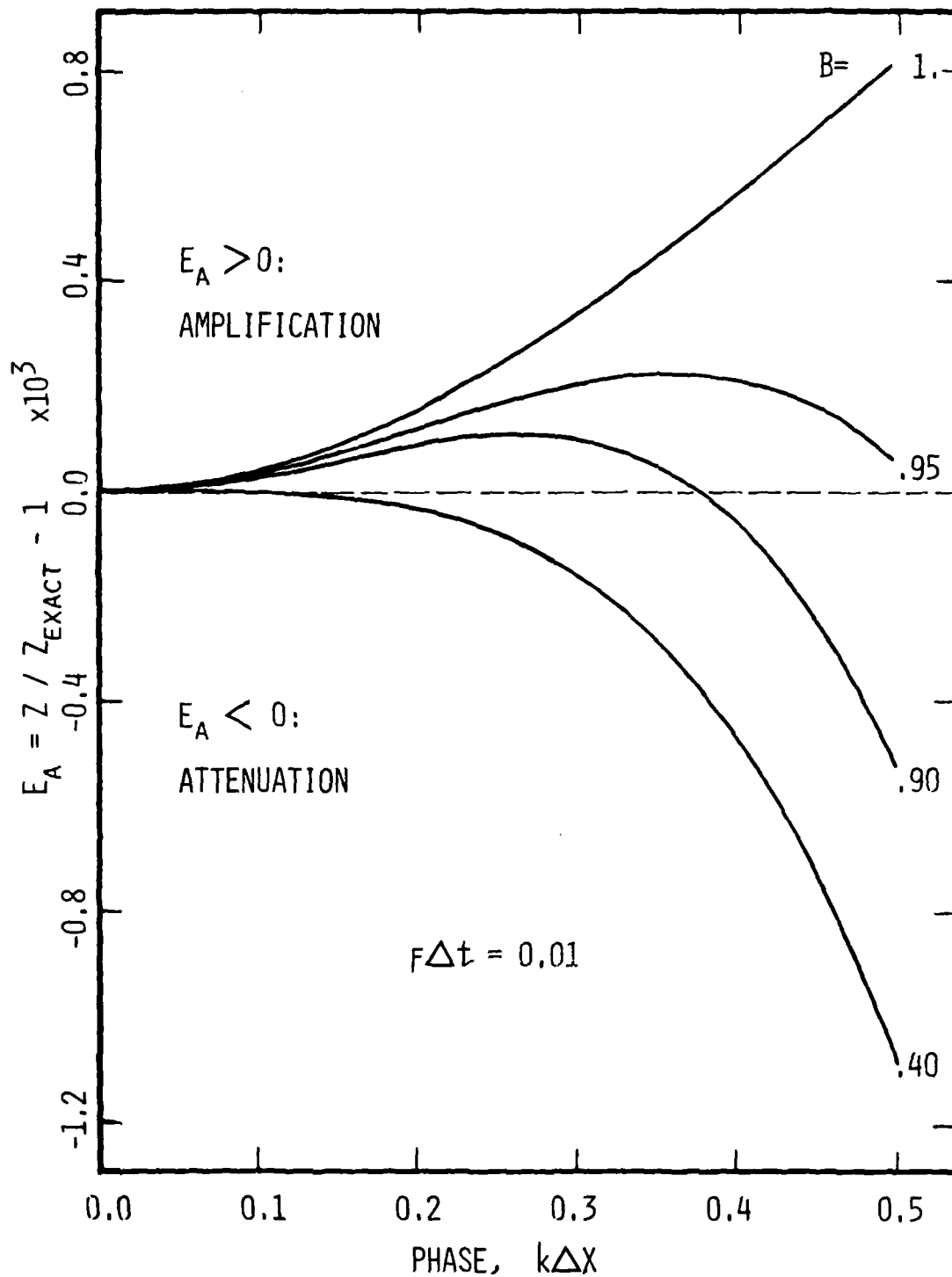G5. Sommerfeld, A., Mechanics of Deformable Bodies, Vol. II, Academic Press, NY, 1950, p. 172.

Fig. G.1

Stepwise amplitude error, E_a, vs. phase $k\Delta x$. The effect of CFL number B is demonstrated, at a fixed $f\Delta t = 0.01$.
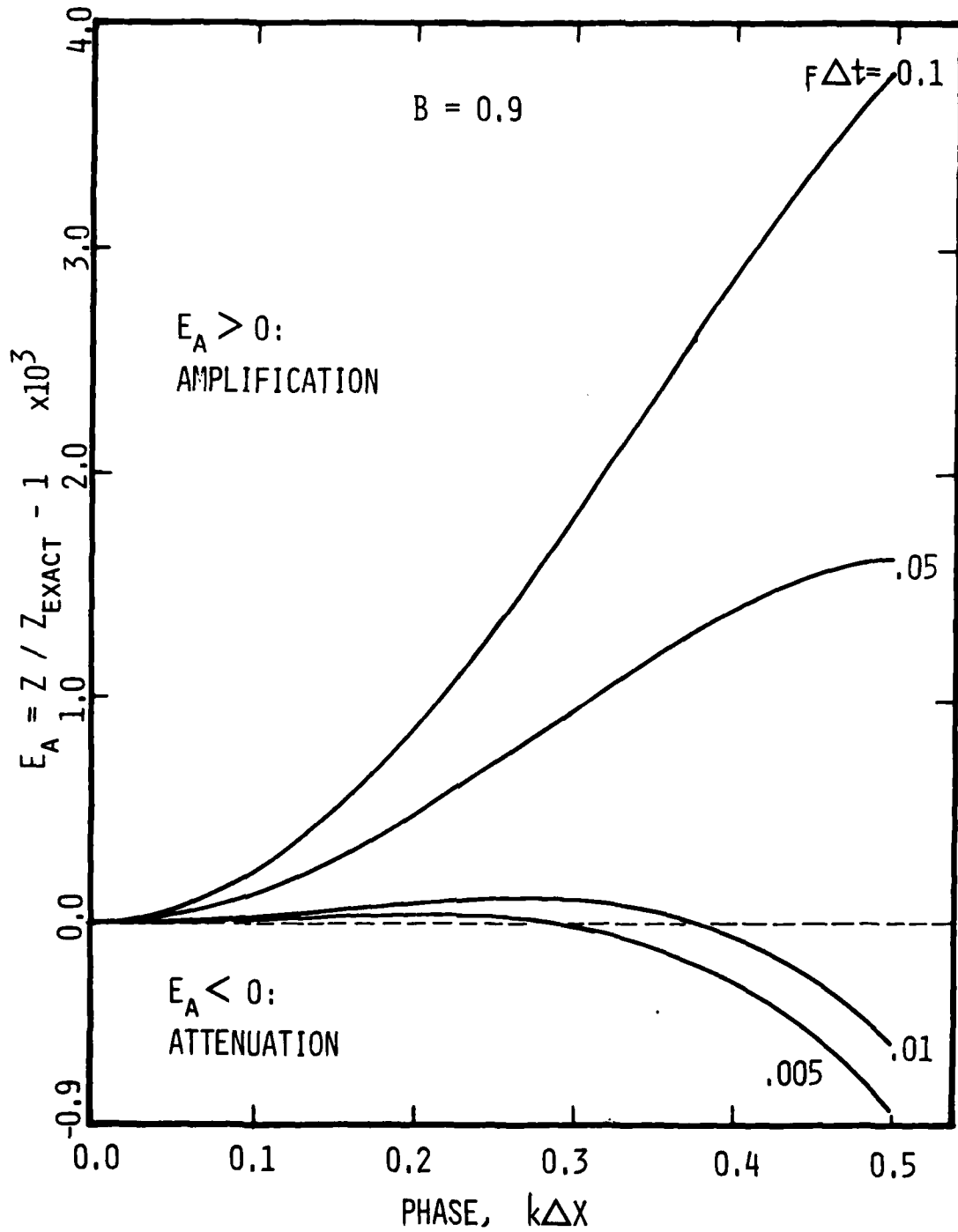
Fig. G.2

Stepwise amplitude error, E_a, vs. phase $k\Delta x$. The effect of linearized forcing term, $f\Delta t$, is shown, at a fixed CFL number, B = 0.9. Note regions of amplification.
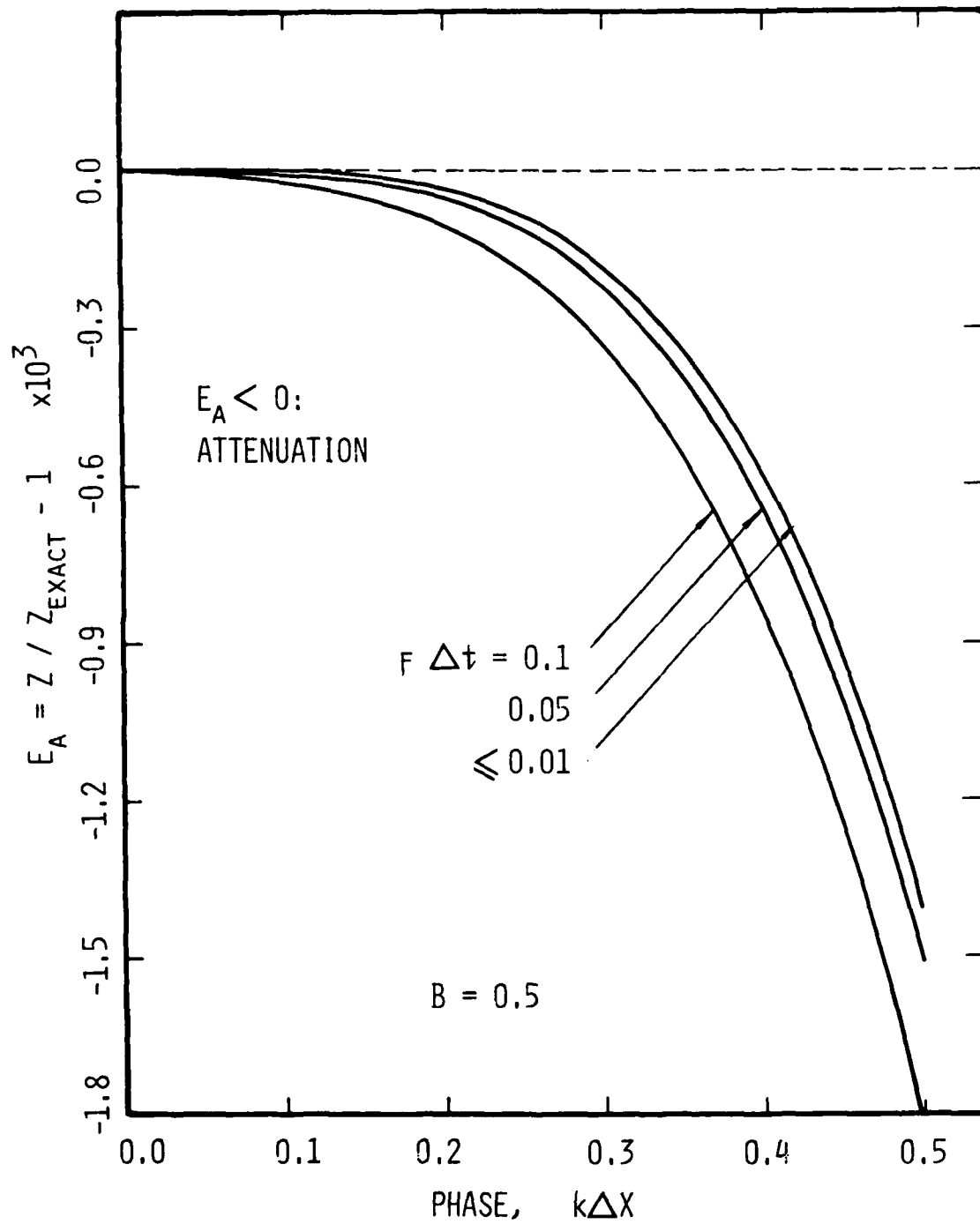
Fig. G.3

Stepwise amplitude error, E_a, vs. phase $k\Delta x$. At a fixed CFL number B = 0.5, varying $f\Delta t$ obtains attenuation only.
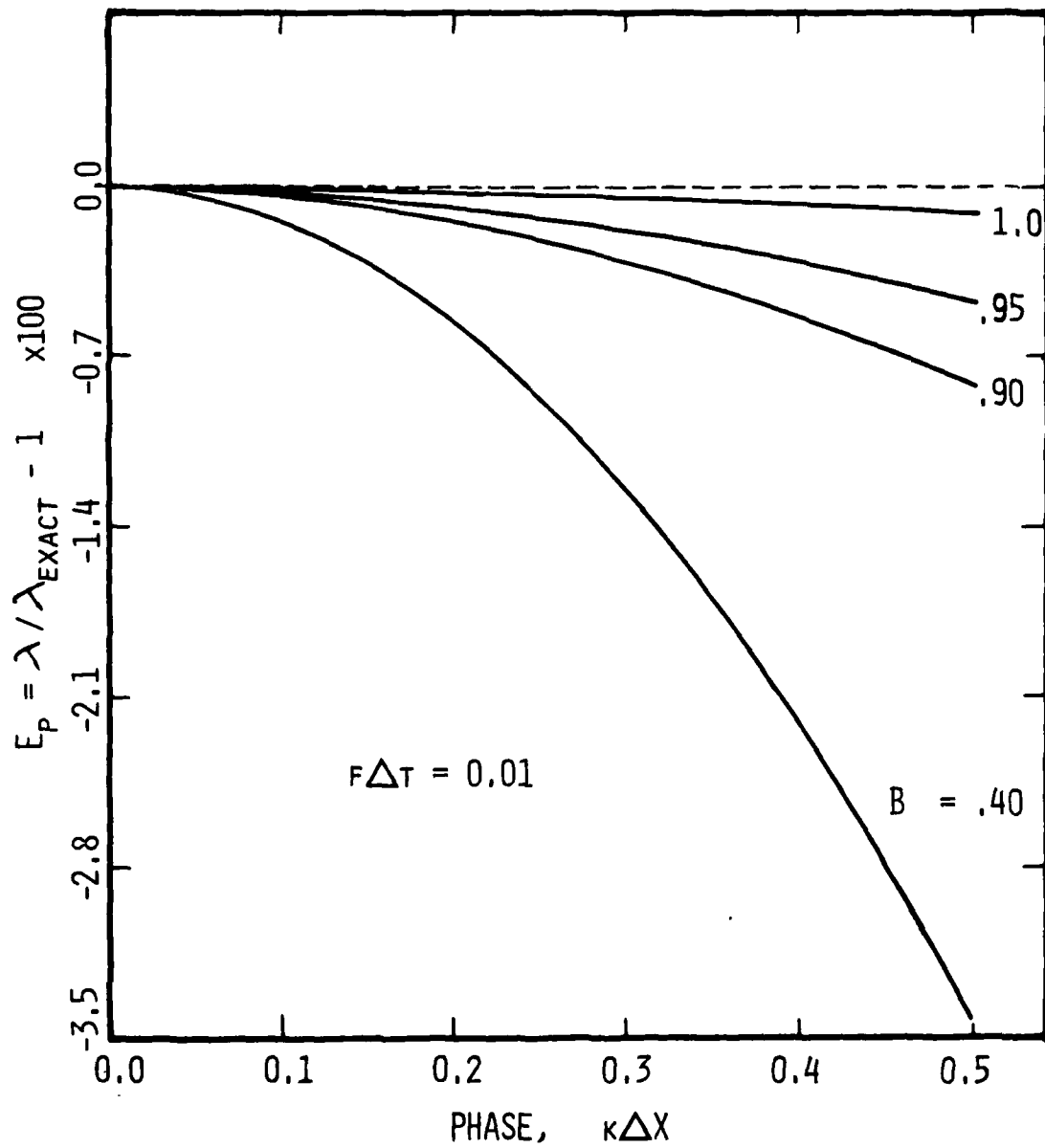
Fig. G.4

Stepwise phase velocity error, E_p, vs. phase $k\Delta x$. The effect of CFL number, B, is shown for a fixed $f\Delta t = 0.01$.
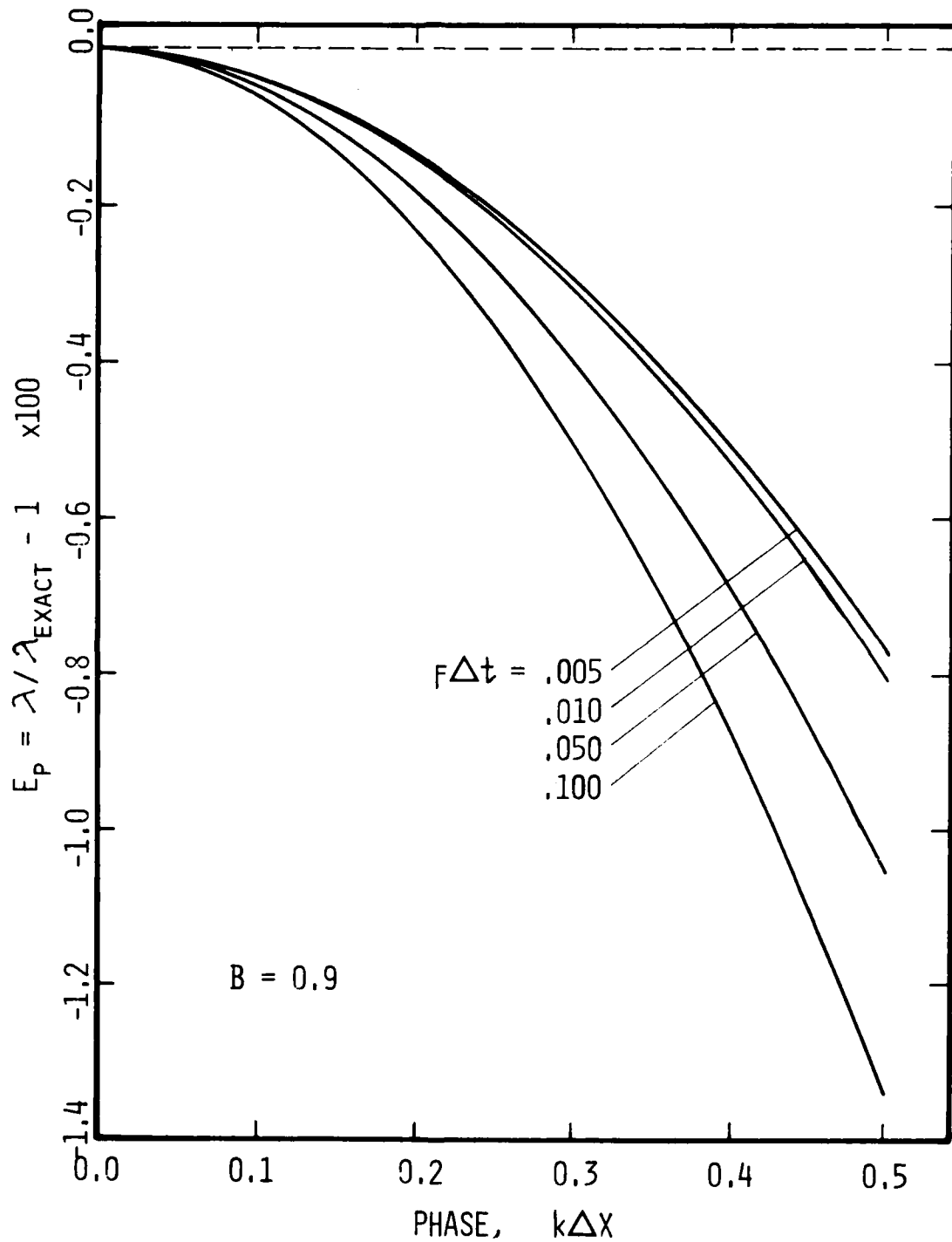
Fig. G.5

Stepwise phase velocity error, E_p, vs. phase $k\Delta x$. The effect of varying the linearized forcing term, $f\Delta t$, is shown, at a fixed CFL number B = 0.9.
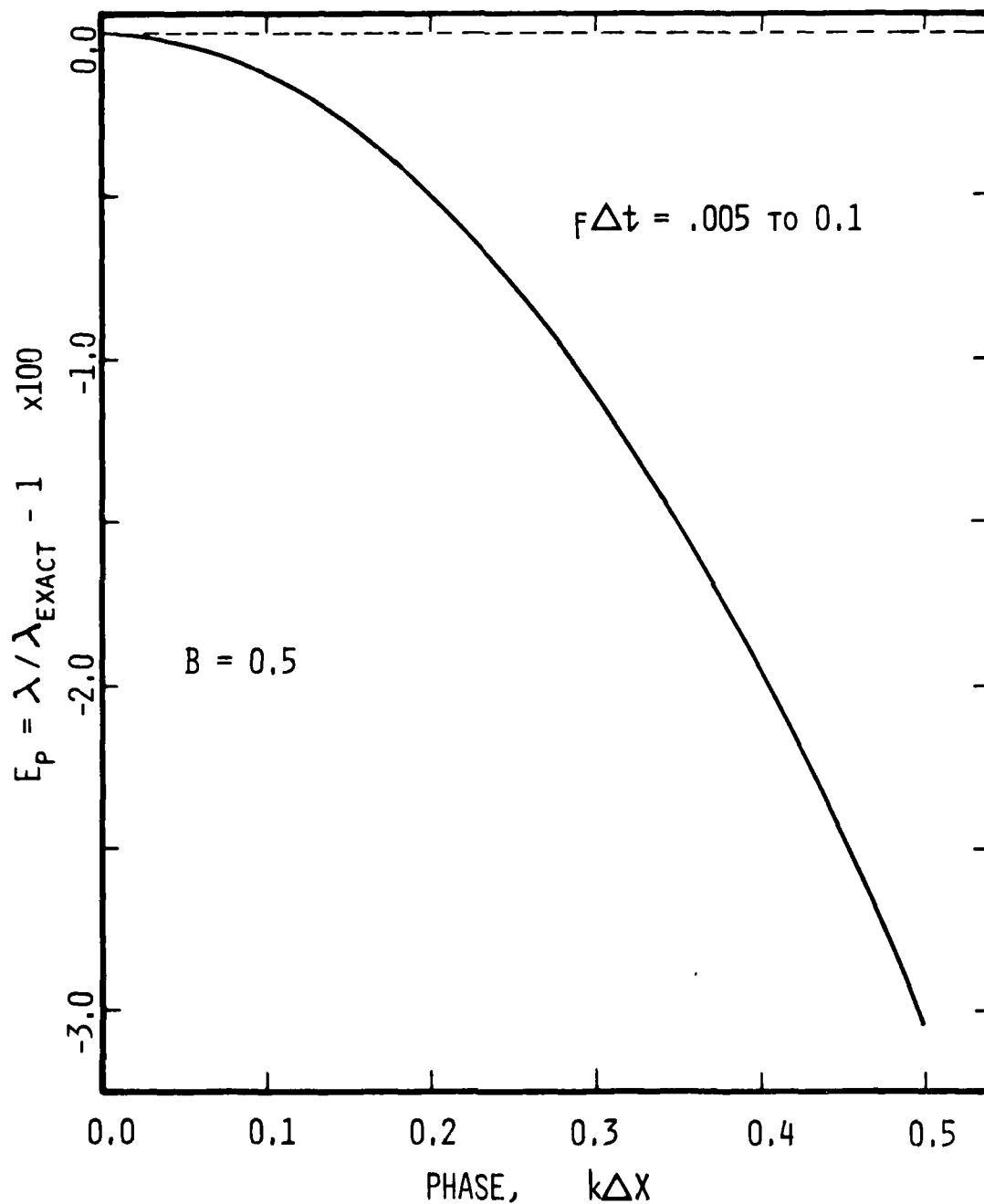
Fig. G.6

Stepwise phase velocity error, Ep, vs. phase k△x. When the CFL number is B = 0.5, a unique Ep distribution is obtained for all values of f△t.

REPORT DOCUMENTATION PAGE	READ INSTRUCTIONS BEFORE COMPLETING FORM

1. REPORT NUMBER	2. GOVT ACCESSION NO. AD-A085650	3. RECIPIENT'S CATALOG NUMBER

4. TITLE (and Subtitle) NITRAMINE MONOPROPELLANT DEFLAGRATION AND GENERAL NONSTEADY REACTING ROCKET CHAMBER FLOWS.	5. TYPE OF REPORT & PERIOD COVERED Technical Report.
	6. PERFORMING ORG. REPORT NUMBER MAE-1455

7. AUTHOR(s) Moshe Ben-Reuven and Leonard H. Caveny	8. CONTRACT OR GRANT NUMBER(s) N00014-75-C-0705

9. PERFORMING ORGANIZATION NAME AND ADDRESS Princeton University Princeton, NJ 08544	10. PROGRAM ELEMENT, PROJECT, TASK AREA & WORK UNIT NUMBERS

11. CONTROLLING OFFICE NAME AND ADDRESS Power Branch Office of Naval Research Washington, D.C.	12. REPORT DATE January 1980
	13. NUMBER OF PAGES 276

14. MONITORING AGENCY NAME & ADDRESS(if different from Controlling Office)	15. SECURITY CLASS. (of this report) UNCLASSIFIED
	15a. DECLASSIFICATION DOWNGRADING SCHEDULE

16. DISTRIBUTION STATEMENT (of this Report)

Approved for public release; distribution unlimited.

17. DISTRIBUTION STATEMENT (of the abstract entered in Block 20, if different from Report)

18. SUPPLEMENTARY NOTES

Partial support provided by U.S. Army Research Laboratory and the Air Force Rocket Propulsion Laboratory

19. KEY WORDS (Continue on reverse side if necessary and identify by block number)

Solid Propellant Combustion	Burning rate model	Acoustics
Nitramines	Reacting chamber flows	
HMX	Combustion instability	
RDX	Erosive burning	
Deflagration model	Velocity coupling	

20. ABSTRACT (Continue on reverse side if necessary and identify by block number)

A theoretical investigation is presented on the deflagration of cyclic nitramines (e.g., RDX and HMX), which are considered as highly-energetic components in solid propellant formulations for rocket motors. The first part of the study involves a steady state deflagration analysis of these monopropellants. This serves as a necessary preliminary step in the elucidation of these compounds within a propellant matrix. The analysis in the second part is aimed at the behavior of nitramine-like propellants within an

DD FORM 1473
1 JAN 73

20. Abstract - continued.

interior burning propellant grain. This was prompted by the no-
tion of thick overall gaseous flame zone associated with nitramine
compounds at pressures up to 5 MPa. The analysis revealed that
relatively small deviations from fully-burnt state at the wall
layer edge may be associated with appreciable burning rate pertur-
bations. The problem of dynamic coupling between the axial acous-
tic field and the pressure-sensitive residual reaction in the core
was addressed. A comparison of chemical relaxation (secondary
reaction) and fluid-dynamic timescales indicates possible areas
of Rayleigh-type coupling. This analysis points to the existence
of an additional component to acoustic instability, namely, an
acoustic coupling with heat addition by residual reaction in the
core.